INVESTIGATION OF UV-INDUCED GEOMETRICAL ISOMERISATION OF *HELICHRYSUM KRAUSSII* EXTRACTS AND THEIR INHIBITION POTENTIALS FOR ACID CORROSION OF MILD STEEL, ZINC AND ALUMINIUM

by

SITHUBA TSHEDZA

Student Number: 15003455

A thesis submitted in fulfillment of the requirements for the degree of

Doctor of Philosophy in Chemistry (MNPDPC)

Department of chemistry

Faculty of Science, Engineering, and Agriculture

University of Venda

Supervisor: Prof. L.C MURULANA

Co-Supervisor: Prof. M.M KABANDA

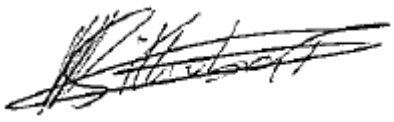
Co-Supervisor: Prof. N.E MADALA

November 2024

© University of Venda

DECLARATION

I, Tshedza Sithuba, declare that this thesis titled ‘’Investigation of UV induced geometrical isomerisation of *Helichrysum kraussii* extract and their inhibition potential for acid corrosion of mild steel, zinc and aluminium’’ is the results of a study carried out originally by me under the guidance and supervision of Prof L.C Murulana and co-supervision of Prof N.E Madala and Prof M.M Kabanda. This work is being submitted in fulfilment of the Doctor of Philosophy in Chemistry at the University of Venda and has not been submitted to any university for any degree and examination. Information I have collected from secondary sources has been properly acknowledged in the reference pages.

Signature:  Date: 25/02/2024

Tshedza Sithuba

© University of Venda

DEDICATION

This thesis is dedicated to my mother, I could not have done this without you. Thank you for your endless support throughout this journey.

© University of Venda

Table of Contents

DECLARATION i

Acknowledgement x

Abstract xi

List of abbreviations xiii

List of symbols xvii

List of figures xix

List of tables xxxi

CHAPTER 1 1

Introduction 1

1. Introduction 2

1.1. Background of the study 2

1.2. Justification of the study 4

1.2.1. Timeline of some of the significant incidents that occurred due to corrosion 5

1.3. Scope of the research 6

1.4. Problem statement 6

1.5. Research question 7

1.6. Aim and objectives of the study 8

CHAPTER 2 9

Literature review 9

2. Introduction 10

2.1. Definition of corrosion 10

2.2. Basic reactions during the corrosion process 11

2.3. Corrosive environment 14

2.4. Corrosion in different Media 15

2.5. Classification of corrosion 16

2.6. Types of corrosion 18

2.7. The rate of corrosion 25

© University of Venda

University of Venda
Creating Future Leaders

2.7.1. Methods of determining corrosion rate. 26
2.8. Factors affecting the rate of corrosion 36
2.8.1. Nature of the metal 37
2.8.2. Nature of the corroding environment 39
2.8.3. Other factors that affect the rate of corrosion may include: 41
2.9. Consequences of corrosion 41
2.10. Corrosion control method 43
2.10.1. Corrosion inhibitors 44
2.10.2. Proper selection of material 45
2.10.3. Cathodic protection 45
2.10.4. Linings, Coatings and Non-Metallic piping 45
2.11. Importance of corrosion inhibitors 46
2.12. Classification of corrosion inhibitors 46
2.12.1. Types of corrosion inhibitors 48
2.13. Toxicity of corrosion inhibitors 49
2.14. Metals usually used in corrosion studies. 50
2.15. Plant extracts as corrosion inhibitors 54
2.16. *Helichrysum kraussii* 56
2.17. Computational chemistry 57
2.18. Quantum chemistry 57
2.19. Quantum Chemical Calculations and their ability to estimate molecular properties 58
2.19.1. The Schrödinger equation 58
2.19.2. Approximation methods in quantum mechanics 59
2.19.3. Basis set 62
2.19.4. Semi-empirical and Ab initio methods emanating from the approximation approaches. 65
2.20. The molecular properties of interest in relation to metal corrosion inhibition 69
2.20.1. Total electronic energy of the molecule 69
2.20.2. Adsorption energy 70
2.20.3. Electron density 70
2.20.4. Frontier molecular orbitals and related properties 71
2.21. Metal surface from a crystal structure perspective 74

© University of Venda

2.21.1. Unit cells 74
2.21.2. Crystallographic planes 77
2.22. Molecular mechanics of chemistry 79
2.23. Effects of UV radiation on the chemicals or compounds 82
2.24. Literature review on the corrosion inhibition of metals using plant extracts in aqueous media. 83
CHAPTER 3 85
Experimental procedures 85
3.1. Materials 86
3.2. Corrosion inhibitors 86
3.3. Preparation of the extracts and solution preparation 87
3.4. Ultraviolet light (UV) 87
3.5. Gravimetric weight loss analysis 88
3.6. Liquid chromatography-mass spectrometry (LCMS). 89
3.7. Column chromatography 89
3.8. Fourier Transform Infrared Spectroscopy (FTIR). 89
3.9. Electrochemical studies 90
3.10. wettability study 91
3.11. Computational studies 91
3.11.1. DFT calculations 91
3.12. Scanning electron microscopy (SEM), energy dispersive spectroscopy (EDS) and X-ray diffraction (XRD) 93
RESULTS AND DISCUSSION 94
CHAPTER 4 95
Identification and isolation of compounds 95
4. Introduction 96
4.1. Liquid chromatography-mass spectrometry 96
4.1.1. Non-*Helichrysum kraussii* extract Controls (24 HOURS) 96
4.1.2. UV-radiated *H. kraussii* extract 97
4.2. Fourier Transform Infrared Spectroscopy (FTIR) 104

© University of Venda

University of Venda
Creating Future Leaders

4.3. Isolation of compounds causing corrosion inhibition 105
4.3.1. Column chromatography 107
CHAPTER 5 119
Non-radiated *H. kraussii* extract in hydrochloric acid 119
5. Introduction 120
Gravimetric analysis results 120
5.1. Weight loss 120
5.2. Corrosion rate and inhibition efficiency 122
5.3. Adsorption isotherm 127
5.4. The effects of temperature 133
5.5. Electrochemical analysis 140
5.5.1. Mild steel 140
5.5.2. Zinc metal 147
5.5.3. Aluminium metal 153
5.6. Fourier transform infrared spectroscopy (FTIR) 160
5.6.1. Mild steel 160
5.6.2. Zinc metal 162
5.6.3. Aluminium metal 164
CHAPTER 6 167
UV-radiated *H. kraussii* extract in Hydrochloric acid 167
6. Introduction 168
6.1. Weight loss 168
6.2. Corrosion rate and inhibition efficiency 169
6.3. Absorption isotherms 175
6.4. Thermodynamic parameters: Effect of temperature 179
6.5. Electrochemical analysis 185
6.5.1. Mild steel 185
6.5.2. Zinc metal 191
6.5.3. Aluminium metal 197
6.6. Fourier Transform Infrared Spectroscopy (FTIR) 204

© University of Venda

University of Venda
Creating Future Leaders

6.6.1. Mild steel 204
6.6.2. Zinc metal 206
6.6.3. Aluminium metal 208
CHAPTER 7 210
Non-radiated *H. kraussii* extract in sulphuric acid 210
7. Introduction 211
7.1. Weight loss analysis 211
7.2. Corrosion rate and inhibition efficiency 212
7.3. Adsorption isotherm 216
7.4. Temperature effect 219
7.5. Electrochemical analysis 223
7.5.1. Mild steel 223
7.5.2. Zinc metal 229
7.6. Fourier Transform Infrared Spectroscopy (FTIR) 235
7.6.1. Mild steel 235
7.6.2. Zinc metal 237
CHAPTER 8 240
UV-radiated *H. kraussii* in sulphuric acid 240
8. Introduction 241
8.1. Weight loss analysis 241
8.2. Corrosion rate and Percentage inhibition efficiency 242
8.3. Langmuir adsorption isotherm 246
8.4. Thermodynamics and kinetic parameters 249
8.5. UV-radiated H. *kraussii* extract in sulphuric acid 254
8.5.1. Mild steel 254
8.5.2. Zinc metal 260
8.6. Fourier Transform Infrared Spectroscopy (FTIR) 267
8.6.1. Mild steel 267
8.6.2. Zinc metal 269
CHAPTER 9 271
CONTACT ANGLES 271

© University of Venda

9. Introduction 272
9.1. Wettability study 272
9.1.1. Mild steel metal in 1.0 M HCl for non and UV-radiated *H. kraussii* extract 273
9.1.2. Mild steel metal in 1.0 M H_2SO_4 for non and UV-radiated *H. kraussii* extract 274
9.1.3. Zinc metal in 1.0 M HCl for non and UV-radiated *H. kraussii* extract 275
9.1.4. Zinc metal in 1.0 M H_2SO_4 for non and UV-radiated *H. kraussii* extract 276
9.1.5. Aluminium metal in 1.0 M HCl for non and UV-radiated *H. kraussii* extract 277
CHAPTER 10 278
Results and discussion on the computational studies on the interaction between selected inhibitors and metal surfaces 278
10. Introduction 279
This chapter presents and analyses the results on the interaction between the surface of the metal and selected inhibitor molecules. 279
10.1. Computational studies on the interaction between selected inhibitors and metal surfaces. 279
10.2. Interaction between aluminium metal surface and inhibitor molecules 281
10.3. Interaction between zinc metal surface and inhibitor molecules 292
10.4. Interaction between iron metal surface and inhibitor molecules 302
CHAPTER 11 310
Scanning electron microscopy, energy dispersive spectroscopy, and X-ray diffraction 310
11. Introduction 311
11.1. Surface morphology and elemental composition 311
11.1.1. Aluminium metal 311
11.1.2. Zinc metal 318
11.1.3. Mild steel metal 337
11.2. X-ray diffraction 355
11.2.1. Mild steel metal 357
11.2.2. Zinc metal 359
11.2.3. Aluminium metal 361
CHAPTER 12 362
Summary, conclusions and recommendations 362
12. Introduction 363

© University of Venda

12.1. Conclusion.....363

12.2. Contribution, recommendation and suggestions 365

References 366

© University of Venda

Acknowledgement

Firstly, I would like to thank God, the Almighty, who, without His grace, would not have made it possible for me to complete this thesis.

I extend my heartful thanks and my sincere appreciation to my supervisor, Prof L.C. Murulana, who was instrumental in this research and helped me throughout all the phases of this work, as well as provided guidance and insight during the completion of this dissertation.

I would also like to thank my co-supervisor, Prof M.M. Kabanda, who helped me a lot with computational chemistry, and Prof N.E. Madala for helping me with LCMS and isolating the compounds that were found to be the ones causing the corrosion inhibition.

I also thank the University of Venda community at large for providing me with a wonderful lifetime opportunity to pursue my studies with them. Without the University of Venda, this work was not going to be possible.

Last but not least, I would also like to thank my mother and family for the encouragement and support they showed me throughout this journey.

© University of Venda

Abstract

Corrosion is the destruction of material due to chemical or electrochemical processes. Corrosion can be controlled by using corrosion inhibitors. Recently, plants have been explored as possible green corrosion inhibitors because they are environmentally friendly, easy to dispose, easily accessible and cheaper to extract or convert to inhibitors. Plant's metabolites or chemical constituents undergo geometrical isomerisation under the influence of UV light radiation. These changes might affect the extract's ability to inhibit corrosion. In this study, the effect of the UV light radiation on the *Helichrysum kraussii (H. kraussii)* plant extract was investigated through comparison with the non-UV-radiated *H. kraussii* plant extracts for mild steel, zinc and aluminium metal corrosion in 1.0 M HCl and H_2SO_4 at 30-60 ℃. This investigation was made possible by using techniques such as gravimetric weight loss analysis, Liquid chromatography-mass spectrometry (LCMS), Fourier transform infrared spectroscopy (FTIR), electrochemical analysis, contact angle, Scanning electron microscopy (SEM), Energy dispersive spectroscopy (EDS), and quantum molecular dynamic simulations. LCMS confirmed the formation of geometrical isomerisation when the *H.kraussii* extract was exposed to UV radiation. From the gravimetric analysis data, the corrosion rate (C_R) was calculated and found to be decreasing with an increase in the concentration of the inhibitor extracts, with the highest concentration (1500ppm) at 30 ℃ having a corrosion rate of $3.92x10^{-4}$ and $1.70x10^{-4}$ $g.cm^2.h^{-1}$ for UV-radiated and non-radiated extract in 1.0 M H_2SO_4 for mild steel, respectively. Similar trends have been observed for the zinc and aluminium metals in HCl and H_2SO_4 solutions. The percentage inhibition efficiency (%IE) was found to increase with the increase in the two extract concentrations in the acidic media. In the presence of non-radiated extract, the % IE for mild steel in 1.0 M HCl was found to be 99.601% for 1500 ppm at 30 ℃. However, in the presence of UV-radiated *H. kraussii* extract, it was found to be 98.007%. The activation energy (E_a) values were found to increase with an increase in the concentration of both extract inhibitors. This suggests that the corrosion inhibition process of the three studied metals is through physisorption. The values of the change in Gibbs free energy (ΔG^o_{ads}) for both the extracts were found to be negative, indicating that the reaction between the inhibitor molecules and the metal surface was spontaneous. From the electrochemical impedance spectroscopy (EIS), the semi-circle diameter for mild steel and zinc metals and the circle diameter for the aluminium metal in the Nyquist plot was found to increase with an increase in the inhibitor concentration. The charge transfer resistance (R_{ct}) values were found to increase with an increase in the extract inhibitor concentrations. For mild steel in 1.0 M H_2SO_4, the R_{ct} values

© University of Venda

ranged between 8.751-26.52 Ωm^2 and 10.20-26.41 Ωm^2 for the UV-radiated and non-radiated extract, respectively. The introduction of the two extract inhibitors in the HCl and H_2SO_4 solution managed to reduce the corrosion current density (i_{corr}) for mild steel, zinc and aluminium metals. The i_{corr} values for mild steel in 1.0 M H_2SO_4 ranged between 397.202 - 1395.884 $mA.cm^{-2}$ and 343.358 – 1572.977 $mA.cm^{-2}$ for the UV-radiated and non-radiated extracts. FTIR performed on the coated mild steel, zinc, and aluminium surface showed functional groups such as C=C, O-H, and N-H for both extracts, which are known to be functional groups of the most effective corrosion inhibitors. Contact angles were used to study the surface morphology of the metals, and it was observed that introducing the extract inhibitors in aggressive solutions changed the metal's surface from hydrophilic to hydrophobic surface. Computational simulations have been studied to demonstrate the most conceivable adsorption arrangements or configurations between the metal surface and the inhibitor. Parallel configuration of the inhibitor molecules on the metal surface was found to be the best configuration, giving high adsorption energy. SEM showed that introducing the two extract inhibitors in the acidic solution protected the metal surface from developing deep pits caused by the acid attack. EDS showed that corrosion took place on the metal surface and that the extract inhibitors were adsorbed on the metal surface based on the functional groups such as oxygen, calcium and nitrogen obtained on the metal surface. X-ray diffraction showed the presence of oxide on the metal surface confirming that the corrosion process took place. Based on the results obtained, it was found that the non-radiated *H. kraussii* extract was found to be more effective in inhibiting the corrosion of mild steel, zinc and aluminium metals in 1.0 M HCl and H_2SO_4 than the UV-radiated *H. kraussii* extract. This suggests that the UV radiation decreases the inhibition efficiency of the *H. kraussii* extract as an efficient corrosion inhibitor for mild steel, zinc and aluminium metals in 1.0 M HCl and H_2SO_4. Therefore, it is recommended that the *H. kraussii* extract be used only as a corrosion inhibitor for mild steel, zinc, and aluminium metals in 1.0 M HCl and H_2SO_4 in its original state without being exposed to UV radiation.

Keywords: *Helichrysum Kraussii*, corrosion, UV-radiated, physisorption, Langmuir adsorption isotherm.

© University of Venda

University of Venda
Creating Future Leaders

List of abbreviations

%IE	Inhibition efficiency
AAS	Atomic adsorption spectroscopy
AC	Alternating current
ASTM-G15-08	American Society for Testing and Materials
AOs	Atomic orbitals
$\%IE_{PDP}$	Inhibition efficiency PDP
$\%IE_{EIS}$	Inhibition efficiency EIS
Al	Aluminium
AM1	Austin Model 1
BCC	Body-centred cubic
B3LYP	Becke, three-parameter, Lee-Yang-Parr
COSMO	Conductor-like screening model
CE	Counter electrode
CGTOs	Contracted Gaussian-type orbitals
CPE	Constant-phase element
DFT	Density functional theory
DZ	Double zeta
DND	Double-numerical +d
DZP	Double Zeta Polarization
DNP	Double numeric with polarization functions
EIS	Electrochemical impedance spectroscopy
E_{PP}	Passivation potential
FCC	Face-centred cubic
FT-IR	Fourier-transform infrared spectroscopy

© University of Venda

F	Farren height
FTIR	Fourier Transform Infrared
GGA	Generalized gradient approximation
GTO	Gaussian-type orbitals
GDP	Gross domestic product
H_2SO_4	Sulfuric acid
HCl	Hydrochloric acid
HOMO	Highest molecular orbital
HF	Hartree-Fock
HCP	Hexagonal close-packed
L	Inductance
LUMO	Lowest unoccupied molecular orbital
LCAO	Linear Combination of Atomic Orbital
LDR	Linear polarization resistance
LC/MS	Liquid chromatography/mass spectrometry
LDA	Local density approximation
MNDO	Modified Neglect of Diatomic Overlap
MS	Mild steel
MINTEK	Mining Technology
MIC	Microbiologically influenced corrosion
MCRs	Multi-component reactions
M	Molar
MP	Moller-Plesset
MP1	Moller-Plasset 1
MP2	Moller-Plesset 2

© University of Venda

University of Venda
Creating Future Leaders

M06	Minnesota Functional
MPPT	Moller-Plesset Perturbation Theory
NDDO	Neglect of differential diatomic overlap
NACE	National Association of Corrosion Engineers
IMPACT	International measures of prevention, application and Economics of corrosion technology
OCP	Open-circuit potential
OCV	Open circuit voltage
PGTOs	Primitive Gaussian-type orbitals
PBE	Perdew-Burke-Ernzerhof
PVC	Polyvinyl chloride
PDP	Potentiodynamic polarization
PDDG	Pairwise Distance-Directed Gaussian
PES	Potential energy surface
PM3	Parameterized Model number 3
PM6	Parameterized method number 6
5Z	Pentuple Zeta
pH	Potential of hydrogen
ppm	Parts per million
PZ	Quintuple Zeta
R	Resistance
RE	Reference electrode
TZ	Triple Zeta
SEM/EDS	Scanning electron microscopy/energy dispersive X-ray spectroscopy

© University of Venda

STO	Slater-type orbital
SZ	Single Zeta
SPC	Society for Protective Coatings
WE	Working electrode
Zn	Zinc
QZ	Quadruple Zeta
UV	Ultraviolet radiation
H. kraussii	*Helichrysum kraussii*
K_L	Dimensionless separation constant
Vdw	Van der Waals

© University of Venda

List of symbols

K	Kelvin temperature
℃	Degree Celsius
$\boldsymbol{\theta}$	Surface coverage
ΔE	Energy gap
$\mathbf{E_{HOMO}}$	Energy of the highest occupied molecular orbital
$\mathbf{E_{LUMO}}$	Energy of the lowest unoccupied molecular orbital
$\mathbf{K_{ads}}$	Equilibrium adsorption constant
$\boldsymbol{\rho}$	Corrosion rate
S	Surface area
h	Hours
R	Gas constant
$\Delta \boldsymbol{G^{o}_{ads}}$	Gibbs free energy of adsorption
$\mathbf{E_{corr}}$	Corrosion potential
$\boldsymbol{E_a}$	Activation energy
$\boldsymbol{i^{o}_{corr}}$	Corrosion current density without coating
$\boldsymbol{i_{corr}}$	Corrosion current density with coating
n	Constant phase element constant
$\mathbf{R_s}$	Solution resistance
$\mathbf{R_{ct}}$	Charge transfer resistance
$\boldsymbol{\beta_a}$	Anodic Tafel constant/slope
$\boldsymbol{\beta_c}$	Cathodic Tafel constant/slope
$\mathbf{C_{inh}}$	Concentrations of inhibitors/extracts
$\boldsymbol{\Delta H^{*}}$	Enthalpy of activation
$\boldsymbol{\Delta S^{*}}$	Entropy of activation
$\mathbf{C_R}$	Corrosion rate
ΔE	Relative energy
$\mathbf{E_{interaction}}$	Interaction energy

© University of Venda

W	Mass
O_2	Dioxide
CO_2	Carbon dioxide
C_{dI}	Double-layer capacitance
H_2S	Hydrogen sulphide
$Fe(OH)_2$	Iron(II) hydroxide
Fe_3O_4	Iron (II,III) oxide
Fe_2O_3	Iron (III) oxide
FeOOH	Iron oxyhydroxide
H_2O	Water
S	Sulphur
O	Oxygen
N	Nitrogen

© University of Venda

University of Venda
Creating Future Leaders

List of figures

CHAPTER 2

Figure 2. 1: Corrosion cell in which anode and cathode sites are occurring in the same metal 11

Figure 2. 2: Corrosion cell in which the anode and cathode reactions occur between two dissimilar metals 12

Figure 2. 3: The schematic diagram showing the electrochemical reaction of iron and water 14

Figure 2. 4: Common forms of corrosion. 18

Figure 2. 5: uniform corrosion 19

Figure 2. 6: Galvanic corrosion. 20

Figure 2. 7: Pitting corrosion. 21

Figure 2. 8: crevice corrosion. 21

Figure 2. 9: Example of Microbiological influenced corrosion 22

Figure 2. 10: Example of sweet corrosion. 23

Figure 2. 11: Example of sour corrosion. 23

Figure 2. 12: Example of fretting corrosion 24

Figure 2. 13: Example of intergranular corrosion 25

Figure 2. 14: Sinusoidal current response in a linear system 29

Figure 2. 15: Origin of Lissajous figure 30

Figure 2. 16: Nyquist plot with impedance Vector 31

Figure 2. 17: Simple equivalent circuit with one-time constant Z 31

Figure 2. 18: Bonde plots for the circuit in Figure 17 32

Figure 2. 19: Polarization curve for a corrosion process showing classical Tafel plots. 34

Figure 2. 20: Schematic diagram of PDP curves, (a) Activation controlled anodic/cathode reaction, with straight lines added to demonstrate Tafel extrapolation method for estimation of i_{corr} and E_{corr} (b) Cathode branch profile exhibits a constant/limiting current typical of diffusion-limited process. (c) An anodic branch profile is expected for a substrate undergoing passivation 35

Figure 2. 21: Schematic graph showing the possible changes in the PDP curve due to the addition of cathodic, anodic or mixed inhibitors. 36

Figure 2. 22: Classification of corrosion inhibitors. 47

Figure 2. 23: Internal corrosion of a crude oil pipeline made of mild steel 52

Figure 2. 24: Schematic diagram of the pitting corrosion of aluminium 54

Figure 2. 25: Basic parts of the plant and its common active compounds 56

© University of Venda

Figure 2. 26: A picture of the *H. Kraussii* plant [143].....57

Figure 2. 27: The FCC unit cell with atoms represented by hard-spheres (a), reduced spheres model (b), and the collection of spheres representing the FCC crystal structure (c), respectively 75

Figure 2. 28: The BCC unit cell with atoms represented by hard spheres (a), the reduced spheres model (b), and the collection of spheres representing the BCC crystal structure (c), respectively. 76

Figure 2. 29: The HCP unit cell with atoms represented by the reduced spheres model (a) and the collection of spheres representing the HCP crystal structure (b), respectively. 77

Figure 2. 30: Examples of different crystallographic phases.....78

Figure 2. 31: Schematic representations of energy contributions in a molecular mechanics system 80

CHAPTER 3

Figure 3. 1: *Helichrysum kraussii* plant used as corrosion inhibitor 86

CHAPTER 4

Figure 4. 1: Representative of LC-MS chromatogram showing separation of the different isomers of mono-acylated caffeoylquinic acid from non-radiated *H. kraussii* extracts at different retention time shaked for 24 hours.....97

Figure 4. 2: Representative of LC-MS chromatogram showing separation of the different isomers of mono-acylated caffeoylquinic acid from UV-radiated *H. kraussii* extracts at different retention time shaked for 3 hours.....97

Figure 4. 3: Representative of LC-MS chromatogram showing separation of the different isomers of mono-acylated caffeoylquinic acid from UV-radiated *H. kraussii* extracts at different retention time shaked for 6 hours.....98

Figure 4. 4: Representative of LC-MS chromatogram showing separation of the different isomers of mono-acylated caffeoylquinic acid from UV-radiated *H. kraussii* extracts at different retention time shaked for 9 hours.....99

Figure 4. 5: Representative of LC-MS chromatogram showing separation of the different isomers of mono-acylated caffeoylquinic acid from UV-radiated *H. kraussii* extracts at different retention time shaked for 12 hours.....100

Figure 4. 6: Representative of LC-MS chromatogram showing separation of the different isomers of mono-acylated caffeoylquinic acid from UV-radiated *H. kraussii* extracts at different retention time shaked for 15 hours.....100

Figure 4. 7: Representative of LC-MS chromatogram showing separation of the different isomers of mono-acylated caffeoylquinic acid from UV-radiated *H. kraussii* extracts at different retention time shaked for 18 hours.....101

© University of Venda

Figure 4. 8: Representative of LC-MS chromatogram showing separation of the different isomers of mono-acylated caffeoylquinic acid from UV-radiated *H. kraussii* extracts at different retention time shaked for 21 hours. 102

Figure 4. 9: Representative of LC-MS chromatogram showing separation of the different isomers of mono-acylated caffeoylquinic acid from UV-radiated *H. kraussii* extracts at different retention time shaked for 24 hours. 103

Figure 4. 10: FTIR spectra for *H. kraussii* plant extract (Black) and UV-radiated *H. kraussii* plant extract (Red). 104

Figure 4. 11: Sirius software showing all the possible compounds found in the *H. kraussii* plant. 106

Figure 4. 12: Sirius software showing all the possible compounds found in the UV-radiated *H. kraussii* plant. 107

Figure 4. 13: The graphical representation of the weight loss of mild steel metal. 109

Figure 4. 14: Representative of LC-MS chromatogram for the 15 different fractions collected from column chromatography showing separation of the different isomers of mono-acylated caffeoylquinic acid from non-radiated *H. kraussii* extracts at different retention times. 112

Figure 4. 15: Sirius software showing all the possible compounds found in fraction 8 of the *H. kraussii* plant. 114

Figure 4. 16: Sirius software showing all the possible compounds found in fraction 3 of the *H. kraussii* plant. 115

Figure 4. 17: Knapsak is used to confirm the family and structure of the compound. 116

Figure 4. 18**:** Schematic representation of how the isolated compounds formed geometrical isomers from trans to cis isomerisation. 117

CHAPTER 5

Figure 5. 1: Graph of inhibition efficiency using *H. kraussii* in 1.0 M HCl for mild steel at different temperatures. 126

Figure 5. 2: Graph of inhibition efficiency using *H. kraussii* in 1.0 M HCl for aluminium at different temperatures. 126

Figure 5. 3: Graph of inhibition efficiency using *H. kraussii* in 1.0 M HCl for zinc at different temperatures. 127

Figure 5. 4: Langmuir adsorption isotherm for the adsorption of *H. Kraussii* extract on mild steel metal in 1.0 M HCl at 30, 40, 50 and 60°C. 129

Figure 5. 5: Langmuir adsorption isotherm for the adsorption of *H. Kraussii* extract on zinc metal in 1.0 M HCl at 30, 40, 50 and 60°C. 129

Figure 5. 6: Langmuir adsorption isotherm for the adsorption of *H. Kraussii* extract on aluminium metal in 1.0 M HCl at 30, 40, 50 and 60°C. 130

Figure 5. 7: Arrhenius plots for mild steel metal corrosion in 1.0 M HCl solution in the absence and presence of different concentrations of *H. kraussii* as the inhibitor. 134

© University of Venda

Figure 5. 8: Arrhenius plots for zinc metal corrosion in 1.0 M HCl solution in the absence and presence of different concentrations of *H. kraussii* as the inhibitor. 134

Figure 5. 9: Arrhenius plots for aluminium metal corrosion in 1.0 M HCl solution in the absence and presence of different concentrations of *H. kraussii* as the inhibitor. 135

Figure 5. 10: Transition state plots showing the corrosion of mild steel metal in a 1.0 M HCl solution both with and without various concentrations of the *H. kraussii* inhibitor.....135

Figure 5. 11: Transition state plots showing the corrosion of zinc metal in a 1.0 M HCl solution both with and without various concentrations of the *H. kraussii* inhibitor.....136

Figure 5. 12: Transition state plots showing the corrosion of aluminium metal in a 1.0 M HCl solution both with and without various concentrations of the *H. kraussii* inhibitor.....136

Figure 5. 13: Open circuit voltage for mild steel in hydrochloric acid and *H. kraussii*. 140

Figure 5. 14: Nyquist plot of mild steel metal in 1.0 M HCl with and without various concentrations of *H. kraussii* extract inhibitor.....141

Figure 5. 15: Bode impedance magnitude plot (a) and Bode phase angle plot (b) of mild steel metal in 1.0 M Hydrochloric acid with and without various concentrations of *H. kraussii* extract inhibitor.....142

Figure 5. 16: Equivalent circuit model for blank and *H. kraussii* extract solution.....143

Figure 5. 17: Tafel plots for mild steel in 1.0 M HCl with and without different *H. kraussii* inhibitor extract concentrations.....145

Figure 5. 18: Open circuit voltage for zinc in 1.0 M HCl and *H. kraussii* extract. 148

Figure 5. 19: Nyquist plot of zinc metal in 1.0 M HCl with and without various *H. kraussii* extract inhibitor concentrations.....149

Figure 5. 20: Bode impedance magnitude plot (a) and Bode phase angle plot (b) of zinc metal in 1.0 M HCl with and without various concentrations of *H. kraussii* extract inhibitor. 150

Figure 5. 21: Tafel plots for zinc in 1.0 M HCl with and without various *H. kraussii* extract inhibitor concentrations. 151

Figure 5. 22: Open circuit voltage for aluminium 1.0 M HCl solution and *H. kraussii.*.....153

Figure 5. 23: Nyquist plot of aluminium metal in 1.0 M HCl with and without various concentrations of *H. kraussii* extract inhibitor.....154

Figure 5. 24: Bode impedance magnitude plot (a) and Bode phase angle plot (b) of aluminium metal in 1.0 M HCl with and without various concentrations of *H. kraussii* extract inhibitor. 155

Figure 5. 25: Equivalent circuit model for a blank solution and *H. kraussii* extract solution. 156

Figure 5. 26: Bode plots of aluminium metal in 1.0 M HCl with and without various concentrations of *H. kraussii* extract inhibitor.....159

Figure 5. 27: FTIR spectra for solid *H. kraussii plant* extract (Black), 1500 ppm *H. kraussii* plant extract – 1.0 M HCl solution (Red), the layer formed on mild steel metal exposed in 1500

© University of Venda

ppm *H. kraussii* plant extract – 1.0 M HCl solution (Green) and corrosion products formed on mild steel metal exposed in 1.0 M HCl solution (black). 161

Figure 5. 28: FTIR spectra for solid *H. kraussii* plant extract (Black), 1500 ppm *H. kraussii* plant extract – 1.0 M HCl solution (Red), the layer formed on mild zinc exposed in 1500 ppm *H. kraussii* plant extract – 1.0 M HCl solution (Green) and corrosion products formed on zinc exposed in 1.0 M HCl solution (black). 163

Figure 5. 29: FTIR spectra for solid *H. kraussii* plant extract (Black), 1500 ppm *H. kraussii* plant extract – 1.0 M HCl solution (Red), the layer formed on aluminium metal exposed in 1500 ppm *H. kraussii* plant extract – 1.0 M HCl solution (Green) and corrosion products formed on aluminium metal exposed in 1.0 M HCl solution (black). 165

CHAPTER 6

Figure 6. 1: The graph of inhibition efficiency using UV-radiated *H. kraussii* in 1.0 M HCl for mild steel at various temperatures.....173

Figure 6. 2: The graph of inhibition efficiency using UV-radiated *H. kraussii* in 1.0 M HCl for aluminium at various temperatures. 174

Figure 6. 3: The graph of inhibition efficiency using UV-radiated *H. kraussii* in 1.0 M HCl for zinc at various temperatures.....174

Figure 6. 4: Langmuir adsorption isotherm for the adsorption of UV-radiated *H. Kraussii* on mild steel metal in HCl at 30, 40, 50 and 60°C. 175

Figure 6. 5: Langmuir adsorption isotherm for the adsorption of UV-radiated *H. Kraussii* on zinc metal in HCl at 30, 40, 50 and 60°C. 176

Figure 6. 6: Langmuir adsorption isotherm for the adsorption of UV-radiated *H. Kraussii* on aluminium metal in HCl at 30, 40, 50 and 60°C.....176

Figure 6. 7: Arrhenius plots for mild steel metal corrosion in 1.0 M HCl medium with and without various concentrations of UV-radiated *H. kraussii* as the inhibitor. 180

Figure 6. 8: Arrhenius plots for zinc metal corrosion in 1.0 M HCl medium with and without various concentrations of UV-radiated *H. kraussii* as the inhibitor.....180

Figure 6. 9: Arrhenius plots for aluminium metal corrosion in 1.0 M HCl medium with and without various concentrations of UV-radiated *H. kraussii* as the inhibitor. 181

Figure 6. 10: Transition state plots for mild steel metal corrosion in 1.0 M HCl medium with and without various concentrations of UV-radiated *H. kraussii* as the inhibitor.....182

Figure 6. 11: Transition state plots for zinc metal corrosion in 1.0 M HCl medium with and without various concentrations of UV-radiated *H. kraussii* as the inhibitor. 182

Figure 6. 12: Transition state plots for aluminium metal corrosion in 1.0 M HCl medium with and without various concentrations of UV-radiated *H. kraussii* as the inhibitor.....182

Figure 6. 13: Open circuit voltage for mild steel in 1.0 M HCl medium and UV-radiated *H. kraussii* extract. 186

Figure 6. 14: Nyquist plot of mild steel metal in 1.0 HCl M with and without various concentrations of UV-radiated *H. kraussii* inhibitor compounds. 187

© University of Venda

Figure 6. 15: Bode impedance magnitude plot (a) and Bode phase angle (b) of mild steel metal in 1.0 M HCl with and without various concentrations of UV-radiated *H. kraussii* inhibitor compound.....188

Figure 6. 16: Tafel plots for mild steel in 1.0 M HCl with and without various UV-radiated *H. kraussii* inhibitor compound concentrations.....190

Figure 6. 17: Open circuit voltage for zinc in 1.0 M HCl solution and UV-radiated *H. kraussii*. 192

Figure 6. 18: Nyquist plot of zinc metal in 1.0 M HCl solution with and without various concentrations of UV-radiated *H. kraussii* inhibitor compounds. 193

Figure 6. 19: Bode impedance magnitude plot (a) and Bode phase angle plot (b) of zinc metal in 1.0 M HCl solution with and without various concentrations of UV-radiated *H. kraussii* extract inhibitor.....194

Figure 6. 20: Tafel plots for zinc in 1.0 M HCl solution with and without various UV-radiated *H. kraussii* inhibitor compound concentrations.....196

Figure 6. 21: Open circuit voltage for aluminium in 1.0 M HCl solution and UV-radiated *H. kraussii* extract.....198

Figure 6. 22: Nyquist plot of aluminium metal in 1.0 M HCl solution with and without the presence of various concentrations of UV-radiated *H. kraussii* inhibitor compounds. 199

Figure 6. 23: Bode impedance magnitude plot (a) and Bode phase angle plot (b) of aluminium metal in 1.0 M HCl solution with and without various concentrations of UV-radiated *H. kraussii* extract inhibitor. 200

Figure 6. 24: Tafel plots for aluminium in 1.0 M HCl solution with and without various concentrations of UV-radiated *H. kraussii* extract inhibitor.....202

Figure 6. 25: FTIR spectra for solid UV-radiated *H. kraussii* plant extract (Black), 1500 ppm UV exposed Helichrysum kraussii plant extract – 1.0 M HCl solution (Red), the layer formed on mild steel metal exposed in 1500 ppm UV-radiated *H. kraussii* plant extract – 1.0 M HCl solution (Green) and corrosion products formed on mild steel metal exposed in 1.0 M HCl solution (black). 204

Figure 6. 26: FTIR spectra for solid UV-radiated *H. kraussii* plant extract (Black), 1500 ppm UV-radiated *H. kraussii* plant extract – 1.0 M HCl solution (Red), the layer formed on zinc metal exposed in 1500 ppm UV-radiated *H. kraussii* plant extract – 1.0 M HCl solution (Green) and corrosion products formed on zinc metal exposed in 1.0 M HCl solution (black). 206

Figure 6. 27: FTIR spectra for solid UV-radiated *H. kraussii* plant extract (Black), 1500 ppm UV-radiated *H. kraussii* plant extract – 1.0 M HCl solution (Red), the layer formed on aluminium metal exposed in 1500 ppm UV-radiated *H. kraussii* plant extract – 1.0 M HCl solution (Green) and corrosion products formed on aluminium metal exposed in 1.0 M HCl solution (black). 208

CHAPTER 7

Figure 7. 1: The graph of inhibition efficiency using *H. kraussii* in 1.0 M H_2SO_4 for mild steel at various temperatures. 215

© University of Venda

Figure 7. 2: The graph of inhibition efficiency using *H. kraussii* in 1.0 M H_2SO_4 for zinc at various temperatures. 215

Figure 7. 3: Langmuir adsorption isotherm for the adsorption of *H. kraussii* extract on mild steel metal in 1.0 M H_2SO_4 at 30, 40, 50 and 60°C. 216

Figure 7. 4: Langmuir adsorption isotherm for the adsorption of *H. kraussii* extract on zinc metal in 1.0 M H_2SO_4 at 30, 40, 50 and 60°C. 217

Figure 7. 5: Arrhenius plots for mild steel metal corrosion in 1.0 M H_2SO_4 solution with and without various concentrations of *H. kraussii* as the extract inhibitor. 220

Figure 7. 6: Arrhenius plots for zinc metal corrosion in 1.0 M H_2SO_4 solution with and without various concentrations of *H. kraussii* as the extract inhibitor.....220

Figure 7. 7: Transition state plots for mild steel metal corrosion in 1.0 M H_2SO_4 medium with and without various concentrations of *H. kraussii* as the extract inhibitor.....221

Figure 7. 8: Transition state plots for zinc metal corrosion in 1.0 M H_2SO_4 medium with and without various concentrations of *H. kraussii* as the extract inhibitor. 221

Figure 7. 9: Open circuit voltage for mild steel in 1.0 M H_2SO_4 solution and *H. kraussii* extract. 224

Figure 7. 10: Nyquist plot of m mild steel metal in 1.0 M H_2SO_4 solution with and without various concentrations of *H. kraussii* extract inhibitor.....225

Figure 7. 11: Bode impedance magnitude plot (a) and the Bode phase angle plot (b) of mild steel metal in 1.0 M H_2SO_4 with and without various concentrations of *H. kraussii* inhibitor compound.....226

Figure 7. 12: Tafel plots for mild steel in 1.0 M H_2SO_4 with and without various *H. kraussii* extract inhibitor concentrations.....228

Figure 7. 13: Open circuit voltage for zinc in 1.0 M H_2SO_4 medium and *H. kraussii* extract. 230

Figure 7. 14: Nyquist plot of zinc metal in 1.0 M H_2SO_4 with and without various *H. kraussii* extract inhibitor concentrations.....231

Figure 7. 15: Bode impedance magnitude plot (a) and Bode phase angle plot (b) of zinc metal in 1.0 M H_2SO_4 with and without various concentrations of *H. kraussii* inhibitor compound. 232

Figure 7. 16: Tafel plots for zinc in 1.0 M H_2SO_4 with and without various concentrations of *H. kraussii* extract inhibitor. 234

Figure 7. 17: FTIR spectra for solid *H. kraussii* plant extract (Black), 1500 ppm *H. kraussii* plant extract – 1.0 M H_2SO_4 solution (Red), the layer formed on mild steel metal exposed in 1500 ppm *H. kraussii* plant extract – 1.0 M H_2SO_4 solution (Green) and corrosion products formed on Mild steel metal exposed in 1.0 M H_2SO_4 solution (black). 236

Figure 7. 18: FTIR spectra for solid *H. kraussii* plant extract (Black), 1500 ppm *H. kraussii* plant extract – 1.0 M H_2SO_4 solution (Red), the layer formed on zinc metal exposed in 1500 ppm *H. kraussii* plant extract – 1.0 M H_2SO_4 solution (Green) and corrosion products formed on zinc metal exposed in 1.0 M H_2SO_4 solution (black). 238

© University of Venda

CHAPTER 8

Figure 8. 1: The graph of inhibition efficiency using UV-radiated *H. kraussii* in 1.0 M H_2SO_4 for mild steel at various temperatures. 245

Figure 8. 2: The graph of inhibition efficiency using UV-radiated *H. kraussii* in 1.0 M H_2SO_4 for zinc at various temperatures. 246

Figure 8. 3: Langmuir adsorption isotherm for UV-radiated *H. Kraussii* extract adsorption on mild steel metal in H_2SO_4 at 30, 40, 50 and 60°C. 246

Figure 8. 4: Langmuir adsorption isotherm for UV-radiated *H. kraussii* extract adsorption on zinc metal in H_2SO_4 at 30, 40, 50 and 60°C. 247

Figure 8. 5: Arrhenius plots for mild steel metal corrosion in 1.0 M H_2SO_4 medium with and without various concentrations of UV-radiated *H. kraussii* as the inhibitor. 250

Figure 8. 6: Arrhenius plots for zinc metal corrosion in 1.0 M H_2SO_4 medium with and without various concentrations of UV-radiated *H. kraussii* as the extract inhibitor. 250

Figure 8. 7: Transition state plots for mild steel metal corrosion in 1.0 M H_2SO_4 medium with and without various concentrations of UV-radiated *H. kraussii* as the inhibitor. 250

Figure 8. 8: Transition state plots for zinc metal corrosion in 1.0 M H_2SO_4 medium with and without various concentrations of UV-radiated *H. kraussii* as the extract inhibitor. 251

Figure 8. 9: Open circuit voltage for mild steel in 1.0 M H_2SO_4 medium and UV-radiated *H. kraussii* extract. 254

Figure 8. 10: Nyquist plot of m mild steel metal in 1.0 M H_2SO_4 with and without various concentrations of UV-radiated *H. kraussii* inhibitor compounds. 255

Figure 8. 11: Bode impedance magnitude plot (a) and Bode phase angle plot (b) of mild steel metal in 1.0 M H_2SO_4 solution in the absence and presence of various concentrations of UV-radiated *H. kraussii* inhibitor compound. 256

Figure 8. 12: Tafel plots for mild steel in 1.0 M H_2SO_4 solution with and without different UV-radiated *H. kraussii* extract inhibitor concentrations. 258

Figure 8. 13: Open circuit voltage for zinc in 1.0 M H_2SO_4 medium and UV-radiated *H. kraussii.* 261

Figure 8. 14: Nyquist plot of zinc metal in 1.0 M H_2SO_4 solution with and without various concentrations of the UV-radiated *H. kraussii* extract inhibitor. 262

Figure 8. 15: Bode impedance magnitude plot (a) and Bode phase angle plot (b) of zinc metal in 1.0 M H_2SO_4 with and without various concentrations of UV-radiated *H. kraussii* extract inhibitor. 263

Figure 8. 16: Tafel plots for zinc in 1.0 M H_2SO_4 with and without different UV-radiated *H. kraussii* inhibitor extract concentrations. 265

Figure 8. 17: FTIR spectra for solid UV-radiated *H. kraussii* plant extract (Black), 1500 ppm UV-radiated *H. kraussii* plant extract – 1.0 M H_2SO_4 solution (Red), the layer formed on mild steel metal exposed in 1500 ppm UV-radiated *H. kraussii* plant extract – 1.0 M H_2SO_4 solution (Green) and corrosion products formed on Mild steel metal exposed in 1.0 M H_2SO_4 solution (black). 267

© University of Venda

Figure 8. 18: FTIR spectra for solid UV-radiated *H. kraussii* plant extract (Black), 1500 ppm UV-radiated *H. kraussii* plant extract – 1.0 M H_2SO_4 solution (Red), the layer formed on zinc metal exposed in 1500 ppm UV-radiated *H. kraussii* plant extract – 1.0 M H_2SO_4 solution (Green) and corrosion products formed on zinc metal exposed in 1.0 M H_2SO_4 solution (black). 269

CHAPTER 9

Figure 9. 1: Surface wettability behaviour of (a) polished untreated mild steel substrate, (b) mild steel substrate after 8 hours of immersion in 1.0 M HCl medium with no inhibitor, and (c) in the presence of 1500 ppm of Non-radiated *H. kraussii*. 273

Figure 9. 2: Surface wettability behaviour of (a) polished untreated mild steel substrate, (b) mild steel substrate after 8 hours of immersion in 1.0 M HCl medium with no inhibitor, and (c) in the presence of 1500 ppm of UV-radiated *H. kraussii*. 273

Figure 9. 3: Surface wettability behaviour of (a) polished untreated mild steel substrate, (b) mild steel substrate after 8 hours immersion time in 1.0 M H_2SO_4 medium without inhibitor, and (c) in the presence of 1500 ppm of Non-radiated *H. kraussii*. 274

Figure 9. 4: Surface wettability behaviour of (a) polished untreated mild steel substrate, (b) mild steel substrate after 8 hours of immersion in 1.0 M H_2SO_4 medium with no inhibitor, and (c) in the presence of 1500 ppm of UV-radiated *H. kraussii*. 274

Figure 9. 5: Surface wettability behaviour of (a) polished untreated zinc metal substrate, (b) zinc metal substrate after 8 hours of immersion in 1.0 HCl medium with no inhibitor, and (c) in the presence of 1500 ppm of Non-radiated *H. kraussii*. 275

Figure 9. 6: Surface wettability behaviour of (a) polished untreated zinc metal substrate, (b) zinc metal substrate after 8 hours of immersion in 1.0 M HCl medium with no inhibitor, and (c) in the presence of 1500 ppm of UV-radiated *H. kraussii*. 275

Figure 9. 7: Surface wettability behaviour of (a) polished untreated zinc metal substrate, (b) zinc metal substrate after 8 hours of immersion in 1.0 M H_2SO4 medium with no inhibitor, and (c) in the presence of 1500 ppm of Non-radiated *H. kraussii*. 276

Figure 9. 8: Surface wettability behaviour of (a) polished untreated zinc metal substrate, (b) zinc metal substrate after 8 hours of immersion in 1.0 M H_2SO_4 medium with no inhibitor, and (c) in the presence of 1500 ppm of UV-radiated *H. kraussii*. 276

Figure 9. 9: Surface wettability behaviour of (a) polished untreated aluminium metal substrate, (b) aluminium metal substrate after 8 hours of immersion in 1.0 M HCl medium with no inhibitor, and (c) in the presence of 1500 ppm of Non-radiated *H. kraussii*. 277

Figure 9. 10: Surface wettability behaviour of (a) polished untreated aluminium metal substrate, (b) aluminium metal substrate after 8 hours of immersion in 1.0 M HCl medium with no inhibitor, and (c) in the presence of 1500 ppm of UV-radiated *H. kraussii*. 277

CHAPTER 10

Figure 10. 1: Optimised structures for the isolated inhibitor compounds. The abbreviation FA denotes for ferulic acid, 4-P-CQ denotes for 4-P-Coumaroylquinic acid, 3-P-CCQ denotes 3-P-Coumaroyl-5-(E)-caffeic quinic acid, 1.3-DCAF denotes 1.3-Dicaffeoylquinic acid, C-Chec denotes Caffeoyl-checorin and CFQ denotes Caffeoyl-feruroyl-quinic acid. 280

© University of Venda

Figure 10. 2: Different adsorption geometries of ferulic acid (FA) molecules on the Al(111) surface in water solution. 283

Figure 10. 3: Different adsorption geometries of 4-P CQ acid molecule on the Al(111) surface in water solution. 285

Figure 10. 4: Different adsorption geometries of 3-P-CCQ acid molecule on the Al(111) surface in water solution. 287

Figure 10. 5: Different adsorption geometries of 1.3-DCAF acid molecule on the Al(111) surface in water solution. 288

Figure 10. 6: Different adsorption geometries of C-Chec molecule on the Al(111) surface in water solution. 290

Figure 10. 7: Different adsorption geometries of CFQ acid molecule on the Al(111) surface in water solution. 292

Figure 10. 8: Different adsorption geometries of ferulic acid (FA) molecules on the Zn(110) surface in water solution. 293

Figure 10. 9: Different adsorption geometries of 4-P CQ acid molecule on the Zn(110) surface in water solution. 295

Figure 10. 10: Different adsorption geometries of 3-P-CCQ acid molecule on the Zn(110) surface in water solution. 296

Figure 10. 11: Different adsorption geometries of 1.3-DCAF acid molecule on the Zn(110) surface in water solution. 298

Figure 10. 12: Different adsorption geometries of C-Chec molecule on the Zn(110) surface in water solution. 299

Figure 10. 13: Different adsorption geometries of CFQ acid molecule on the Zn(110) surface in water solution. 301

CHAPTER 11

Figure 11. 1: SEM images and EDS spectra of unexposed aluminium surface, Aluminium immersed in uninhibited 1.0 M HCl, and Aluminium immersed in *H. kraussii*-inhibited 1.0 M HCl solution. 312

Figure 11. 2: SEM images and EDS spectra of unexposed aluminium surface, Aluminium immersed in uninhibited 1.0 M HCl, and Aluminium immersed in UV-radiated *H. kraussii*-inhibited 1.0 M HCl solution. 313

Figure 11. 3: SEM image of the unexposed aluminium metal surface. 314

Figure 11. 4: SEM image of aluminium metal immersed in 1.0 M HCl solution. 315

Figure 11. 5: SEM image of aluminium metal immersed in 1.0 M HCl and *H. kraussii* - inhibited solution. 316

Figure 11. 6: SEM image of aluminium metal immersed in 1.0 M HCl and UV-radiated *H. kraussii* - inhibited solution. 317

© University of Venda

Figure 11. 7: SEM images and EDS spectra of unexposed zinc surface, zinc immersed in uninhibited 1.0 M HCl, and zinc immersed in UV-radiated *H. kraussii*-inhibited 1.0 M HCl solution.....319

Figure 11. 8: SEM images and EDS spectra of unexposed zinc surface, zinc immersed in uninhibited 1.0 M H_2SO_4, and zinc immersed in *H. kraussii*-inhibited 1.0 M H_2SO_4 solution. 320

Figure 11. 9: SEM images and EDS spectra of unexposed zinc surface, zinc immersed in uninhibited 1.0 M HCl, and zinc immersed in UV-radiated *H. kraussii*-inhibited 1.0 M HCl solution.....321

Figure 11. 10: SEM images and EDS spectra of unexposed zinc surface, zinc metal immersed in uninhibited 1.0 M H_2SO_4, and zinc immersed in UV-radited *H. kraussii*-inhibited 1.0 M H_2SO_4 solution. 322

Figure 11. 11: SEM image of unexposed zinc metal surface. 323

Figure 11. 12: SEM image of zinc metal immersed in 1.0 M HCl in solution. 325

Figure 11. 13: SEM image of zinc metal immersed in 1.0 M H_2SO_4 solution. 327

Figure 11. 14: SEM image of zinc metal immersed in 1.0 M HCl and *H. kraussii* - inhibited solution.....329

Figure 11. 15: SEM image of zinc metal immersed in 1.0 M H_2SO_4 and *H. kraussii* - inhibited solution.....331

Figure 11. 16: SEM image of zinc metal immersed in 1.0 M HCl and UV-radiated *H. kraussii* - inhibited solution. 333

Figure 11. 17: SEM image of zinc metal immersed in 1.0 M H_2SO_4 and UV-radiated *H. kraussii* - inhibited solution. 335

Figure 11. 18: SEM images and EDS spectra of unexposed mild steel surface, mild steel immersed in uninhibited 1.0 M HCl, and mild steel immersed in *H. kraussii*-inhibited 1.0 M HCl solution. 338

Figure 11. 19: SEM images and EDS spectra of unexposed mild steel surface, mild steel immersed in uninhibited 1.0 M H_2SO_4, and mild steel immersed in *H. kraussii*-inhibited 1.0 M H_2SO_4 solution. 339

Figure 11. 20: SEM images and EDS spectra of unexposed mild steel surface, mild steel immersed in uninhibited 1.0 M HCl, and mild steel immersed in UV-radiated *H. kraussii*-inhibited 1.0 M HCl solution. 340

Figure 11. 21: SEM images and EDS spectra of unexposed mild steel surface, mild steel immersed in uninhibited 1.0 M H_2SO_4, and mild steel immersed in *H. kraussii*-inhibited 1.0 M H_2SO_4 solution. 341

Figure 11. 22: SEM image of unexposed mild steel metal surface. 342

Figure 11. 23: SEM image of mild steel metal immersed in 1.0 M HCl solution. 344

Figure 11. 24: SEM image of mild steel metal immersed in 1.0 M H_2SO_4 solution. 346

© University of Venda

Figure 11. 25: SEM image of mild steel metal immersed in 1.0 M HCl and *H. kraussii* - inhibited solution. 348

Figure 11. 26: SEM image of mild steel metal immersed in 1.0 M H_2SO_4 and *H. kraussii* inhibited solution. 350

Figure 11. 27: SEM image of mild steel metal immersed in 1.0 M HCl and UV-radiated *H. kraussii* - inhibited solution. 352

Figure 11. 28: SEM image of mild steel metal immersed in 1.0 M H_2SO_4 and UV-radiated *H. kraussii* - inhibited solution. 354

Figure 11. 29: XRD spectra for mild steel metal in the absence (BM-HCl) and presence (HKM-HCl) of *H. kraussii* extract in HCl (a) and their scale spectra (b). 357

Figure 11. 30: XRD spectra for mild steel metal in the absence (BM-HCl) and presence (VHKM- HCl) of UV-radiated *H. kraussii* extract in HCl (a) and their scale spectra (b).....357

Figure 11. 31: XRD spectra for mild steel metal in the absence (BM-H_2SO_4) and presence (HKM- H_2SO_4) of *H. kraussii* extract in H_2SO_4 (a) and their scale spectra (b). 358

Figure 11. 32: XRD spectra for mild steel metal in the absence (BM- H_2SO_4) and presence (VHKM- H_2SO_4) of UV-radiated *H. kraussii* extract in H2SO4 (a) and their scale spectra (b). 358

Figure 11. 33: XRD spectra for zinc metal in the absence (BZ-HCl) and presence (HKZ- HCl) of *H. kraussii* extract in HCl (a) and their scale spectra (b). 359

Figure 11. 34: XRD spectra for mild steel metal in the absence (BZ-HCl) and presence (VHKZ-HCl) of UV-radiated *H. kraussii* extract in HCl (a) and their scale spectra (b). 359

Figure 11. 35: XRD spectra for zinc metal in the absence (BZ- H_2SO_4) and presence (HKZ-H_2SO_4) of *H. kraussii* extract in H_2SO_4 (a) and their scale spectra (b). 360

Figure 11. 36: XRD spectra for zinc metal in the absence (BM-H_2SO_4) and presence (VHKM-H_2SO_4) of UV-radiated *H. kraussii* extract in H_2SO_4 (a) and their scale spectra (b). 360

Figure 11. 37: XRD spectra for aluminium metal in the absence (BAL-HCl) and presence (VHKAL- HCl) of UV-radiated *H. kraussii* extract in HCl (a) and their scale spectra (b)...361

Figure 11. 38: XRD spectra for aluminium metal in the absence (BAL-HCl) and presence (VHKAL- HCl) of UV-radiated *H. kraussii* extract in HCl (a) and their scale spectra (b)...361

© University of Venda

List of tables

CHAPTER 4

Table 4. 1: Functional groups from the FTIR spectra.....105

Table 4. 2: Shows weight loss and percentage inhibition efficiency for the 15 fractions in 1.0 M H_2SO_4. 108

Table 4. 3: Isolated compounds causing corrosion inhibition. 117

CHAPTER 5

Table 5. 1: Gravimetric weight loss analysis in the presence of 1.0 M HCl and *H. kraussii* extract for mild steel, zinc and aluminium metal.....121

Table 5. 2: The corrosion parameters for mild steel, aluminium and zinc in aqueous solution of 1.0 M HCl in the absence and presence of different concentrations of *H. Kraussii* extract from weight loss measurements at four different temperatures (30 – 60° C).....122

Table 5. 3: Adsorption parameters from Langmuir Adsorption Isotherm plots for *H. kraussii* extract in 1.0 M HCl. 130

Table 5. 4: Dimensionless separation factor (K_L) at various *H. kraussii* concentrations at four various temperatures for metals corrosion in 1.0 M HCl.....132

Table 5. 5: Transition state and Arrhenius parameters for the adsorption of various concentrations of *H. kraussii* in 1.0 M HCl on mild steel, zinc and aluminium metal.....138

Table 5. 6: EIS parameters like the solution resistance (R_s), resistance of charge transfer (R_{ct}), constant phase element (CPE), constant phase element constant (n2), double layer capacitance (C_{dl}) and percentage inhibition efficiency ($\%IE_{EIS}$), using *H. kraussii* in 1.0 M HCl in mild steel metal.....144

Table 5. 7: PDP parameters, including anodic and cathodic Tafel slopes (βa and β_c), polarization resistance (R_P), corrosion potential (E_{corr}), and corrosion current density (i_{corr}), measured in 1.0 M HCl using different *H. kraussii* inhibitor concentrations.....146

Table 5. 8: EIS parameters like the solution resistance (R_s), resistance of charge transfer (R_{ct}), constant phase element (CPE), constant phase element constant (n2), double layer capacitance (C_{dl}) and percentage inhibition efficiency ($\%IE_{EIS}$), using *H. kraussii* in 1.0 M HCl in zinc metal.....150

Table 5. 9: PDP parameters, including anodic and cathodic Tafel slopes (βa and β_c), polarization resistance (R_P), corrosion potential (E_{corr}), and corrosion current density (i_{corr}), measured in 1.0 M HCl using different *H. kraussii* inhibitor concentrations.....152

Table 5. 10: EIS parameters like the solution resistance (R_s), resistance of charge transfer (R_{ct}), constant phase element (CPE), constant phase element constant (n1), double layer capacitance (C_{dl}) and percentage inhibition efficiency ($\%IE_{EIS}$), using *H. kraussii* in 1.0 M HCl in aluminium metal. 157

Table 5. 11: PDP parameters, including anodic and cathodic Tafel slopes (βa and β_c), polarization resistance (R_P), corrosion potential (E_{corr}), and corrosion current density (i_{corr}), measured in 1.0 M HCl using different *H. kraussii* inhibitor concentrations.....159

© University of Venda

Table 5. 12: Possible functional groups present in solid *H. kraussii* plant extract, corrosion products formed on mild steel metal exposed in 1.0 M HCl solution, 1500 ppm *H. kraussii* plant extract – 1.0 M HCl solution and layer formed on mild steel metal exposed in 1500 ppm *H. kraussii* plant extract – 1.0 M HCl solution. 161

Table 5. 13: Possible functional groups present in solid *H. kraussii* plant extract, corrosion products formed on zinc metal exposed in 1.0 M HCl solution, 1500 ppm *H. kraussii* plant extract – 1.0 M HCl solution and layer formed on zinc metal exposed in 1500 ppm *H. kraussii* plant extract – 1.0 M HCl solution.....163

Table 5. 14: Possible functional groups present in solid *H. kraussii* plant extract, corrosion products formed on aluminium metal exposed in 1.0 M HCl solution, 1500 ppm *H. kraussii* plant extract – 1.0 M HCl solution and layer formed on aluminium metal exposed in 1500 ppm *H. kraussii* plant extract – 1.0 M HCl solution. 165

CHAPTER 6

Table 6. 1: Gravimetric weight analysis in the presence of 1.0 M HCl and UV-radiated *H. kraussii* extract for mild steel, zinc and aluminium metals. 168

Table 6. 2: Corrosion parameters for aluminium, mild steel and zinc in an aqueous medium of 1.0 M HCl with and without various concentrations of UV-radiated *H. kraussii* extract from weight loss measurements at four (30 – 60° C) different temperatures.....170

Table 6. 3: Langmuir Adsorption Isotherm parameters for UV-radiated *H. kraussii* extract in 1.0 M HCl. 177

Table 6. 4: Dimensionless separation factor (K_L) at various *H. kraussii* concentrations at four various temperatures for metals corrosion in 1.0 M HCl.....178

Table 6. 5: Transition state and Arrhenius parameters for the adsorption of various concentrations of UV-radiated *H. kraussii* in 1.0 M HCl on mild steel, zinc and aluminium metal.....183

Table 6. 6: EIS parameters like the solution resistance (R_s), resistance of charge transfer (R_{ct}), constant phase element (CPE), constant phase element constant (n2), double layer capacitance (C_{dl}) and percentage inhibition efficiency ($\%IE_{EIS}$), using UV-radiated *H. kraussii* in 1.0 M HCl in mild steel metal. 188

Table 6. 7: PDP parameters, including anodic and cathodic Tafel slopes (βa and β_c), polarization resistance (R_P), corrosion potential (E_{corr}), and corrosion current density (i_{corr}), measured in 1.0 M HCl using various UV-radiated *H. kraussii* inhibitor concentrations.....190

Table 6. 8: EIS parameters like the solution resistance (R_s), resistance of charge transfer (R_{ct}), constant phase element (CPE), constant phase element constant (n2), double layer capacitance (C_{dl}) and percentage inhibition efficiency ($\%IE_{EIS}$), using UV-radiated *H. kraussii* in 1.0 M HCl in zinc metal. 194

Table 6. 9: PDP parameters, including anodic and cathodic Tafel slopes (βa and β_c), polarization resistance (R_P), corrosion potential (E_{corr}), and corrosion current density (i_{corr}), in 1.0 M HCl using various UV-radiated *H. kraussii* inhibitor concentrations. 196

Table 6. 10: EIS parameters like the solution resistance (R_s), resistance of charge transfer (R_{ct}), constant phase element (CPE), constant phase element constant (n1), double layer capacitance

© University of Venda

(C_{dl}) and percentage inhibition efficiency (%IE_{EIS}), using UV-radiated *H. kraussii* in 1.0 M HCl in aluminium metal.....201

Table 6. 11: PDP parameters, including anodic and cathodic Tafel slopes (βa and β_c), polarization resistance (R_P), corrosion potential (E_{corr}), and corrosion current density (i_{corr}), measured in 1.0 M HCl using various UV-radiated *H. kraussii* inhibitor concentrations.....203

Table 6. 12: Possible functional groups present in solid UV-radiated *H. kraussii* plant extract, corrosion products formed on mild steel metal exposed in 1.0 M HCl solution, 1500 ppm UV-radiated *H. kraussii* plant extract – 1.0 M HCl solution and layer formed on mild steel metal exposed in 1500 ppm UV-radiated *H. kraussii* plant extract – 1.0 M HCl solution.....205

Table 6. 13: Possible functional groups present in solid UV-radiated *H. kraussii* plant extract, corrosion products formed on zinc metal exposed in 1.0 M HCl solution, 1500 ppm UV-radiated *H. kraussii* plant extract – 1.0 M HCl solution and layer formed on zinc metal exposed in 1500 ppm UV-radiated *H. kraussii* plant extract – 1.0 M HCl solution.....207

Table 6. 14: Possible functional groups present in solid UV-radiated H. *kraussii* plant extract, corrosion products formed on aluminium metal exposed in 1.0 M HCl solution, 1500 ppm UV-radiated H. *kraussii* plant extract – 1.0 M HCl solution and layer formed on aluminium metal exposed in 1500 ppm UV-radiated *H. kraussii* plant extract – 1.0 M HCl solution.....209

CHAPTER 7

Table 7. 1: Gravimetric weight loss analysis in the presence of 1.0 M H_2SO_4 acid and *H. kraussii* extract for mild steel and zinc metal. 211

Table 7. 2: The corrosion parameters for mild steel and zinc in the aqueous solution of 1.0 M H_2SO_4 with and without various concentrations of *H. kraussii* extract from weight loss measurements at four various temperatures (30 – 60° C).....212

Table 7. 3: Adsorption parameters from Langmuir Adsorption Isotherm plots for *H. kraussii* extract in 1.0 M H_2SO_4.....217

Table 7. 4: Dimensionless separation factor (K_L) at various *H. kraussii* concentrations at four various temperatures for metals corrosion in 1.0 M H_2SO_4.....219

Table 7. 5: Transition state and Arrhenius parameters for the adsorption of various concentrations of *H. kraussii* in 1.0 M H_2SO_4 on mild steel and zinc metal. 222

Table 7. 6: EIS parameters like the solution resistance (R_s), resistance of charge transfer (R_{ct}), constant phase element (CPE), constant phase element constant (n2), double layer capacitance (C_{dl}) and percentage inhibition efficiency (%IE_{EIS}), using *H. kraussii* in 1.0 M H_2SO_4 in mild steel metal. 226

Table 7. 7: PDP parameters, including anodic and cathodic Tafel slopes (βa and β_c), polarization resistance (R_P), corrosion potential (E_{corr}), and corrosion current density (i_{corr}), measured in 1.0 M H_2SO_4 using different *H. kraussii* inhibitor concentrations.....228

Table 7. 8: EIS parameters like the solution resistance (R_s), resistance of charge transfer (R_{ct}), constant phase element (CPE), constant phase element constant (n2), double layer capacitance (C_{dl}) and percentage inhibition efficiency (%IE_{EIS}) using *H. kraussii* in 1.0 M H_2SO_4 in zinc metal.....232

© University of Venda

Table 7. 9: PDP parameters, including anodic and cathodic Tafel slopes (βa and β_c), polarization resistance (R_P), corrosion potential (E_{corr}), and corrosion current density (i_{corr}), measured in 1.0 M H_2SO_4 using different *H. kraussii* inhibitor concentrations.....234

Table 7. 10: Possible functional groups present in solid *H. kraussii* plant extract, corrosion products formed on mild steel metal exposed in 1.0 M H_2SO_4 solution, 1500 ppm *H. kraussii* plant extract – 1.0 M H_2SO_4 solution and layer formed on mild steel metal exposed in 1500 ppm *H. kraussii* plant extract – 1.0 M H_2SO_4 solution.....236

Table 7. 11: Possible functional groups present in solid *H. kraussii* plant extract, corrosion products formed on zinc metal exposed in 1.0 M H_2SO_4 solution, 1500 ppm *H. kraussii* plant extract – 1.0 M H_2SO_4 solution and layer formed on zinc metal exposed in 1500 ppm *H. kraussii* plant extract – 1.0 M H_2SO_4 solution.....238

CHAPTER 8

Table 8. 1: Gravimetric analysis in the presence of 1.0 M H_2SO_4 and UV-radiated *H. kraussii* extract for mild steel and zinc metals. 241

Table 8. 2: The corrosion parameters for mild steel, aluminium, and zinc in the aqueous solution of 1.0 M H_2SO_4 with and without various concentrations of UV-radiated *H. kraussii* extract from weight loss measurements at four various temperatures (30 – 60° C).....242

Table 8. 3: Adsorption parameters from Langmuir Adsorption isotherm plots for UV-radiated *H. kraussii* extract in 1.0 M H_2SO_4. 247

Table 8. 4: Dimensionless separation factor (K_L) at various *H. kraussii* concentrations at four various temperatures for metals corrosion in 1.0 M H_2SO_4.....249

Table 8. 5: Transition state and Arrhenius parameters for the adsorption of various concentrations of UV-radiated *H. kraussii* in 1.0 M H_2SO_4 on mild steel and zinc metal.....252

Table 8. 6: EIS parameters like the solution resistance (R_s), resistance of charge transfer (R_{ct}), constant phase element (CPE), constant phase element constant (n2), double layer capacitance (C_{dl}) and percentage inhibition efficiency (%IE_{EIS}), using UV-radiated *H. kraussii* in 1.0 M H_2SO_4 in mild steel metal. 257

Table 8. 7: PDP parameters, including anodic and cathodic Tafel slopes (βa and β_c), polarization resistance (R_P), corrosion potential (E_{corr}), and corrosion current density (i_{corr}), measured in 1.0 M H_2SO_4 using different UV-radiated *H. kraussii* inhibitor concentrations. 259

Table 8. 8: EIS parameters like the solution resistance (R_s), resistance of charge transfer (R_{ct}), constant phase element (CPE), constant phase element constant (n2), double layer capacitance (C_{dl}) and percentage inhibition efficiency (%IE_{EIS}), using UV-radiated *H. kraussii* in 1.0 M H_2SO_4 in zinc metal. 263

Table 8. 9: PDP parameters, including anodic and cathodic Tafel slopes (βa and β_c), polarization resistance (R_P), corrosion potential (E_{corr}), and corrosion current density (i_{corr}), measured in 1.0 M H_2SO_4 using different UV-radiated *H. kraussii* inhibitor concentrations. 265

Table 8. 10: Possible functional groups present in solid UV-radiated *H. kraussii* plant extract, corrosion products formed on mild steel metal exposed in 1.0 M H_2SO_4 solution, 1500 ppm

© University of Venda

UV-radiated *H. kraussii* plant extract – 1.0 M H_2SO_4 solution and layer formed on mild steel metal exposed in 1500 ppm UV-radiated *H. kraussii* plant extract – 1.0 M H_2SO_4 solution. 268

Table 8. 11: Possible functional groups present in solid UV-radiated *H. kraussii* plant extract, corrosion products formed on zinc metal exposed in 1.0 M H_2SO_4 solution, 1500 ppm UV-radiated *H. kraussii* plant extract – 1.0 M H_2SO_4 solution and layer formed on zinc metal exposed in 1500 ppm UV-radiated *H. kraussii* plant extract – 1.0 M H_2SO_4 solution.....270

CHAPTER 10

Table 10. 1: Optimised energies for stable FA acid adsorption sites on Al(111) surface. 283

Table 10. 2: Optimised energies for stable 4-P-CQ acid adsorption sites on Al(111) surface in solution.....285

Table 10. 3: Optimised energies for stable 3-P-CCQ acid adsorption sites on Al(111) surface. 287

Table 10. 4: Optimised energies for stable 1.3-DCAF acid adsorption sites on Al(111) surface. 289

Table 10. 5: Optimised energies for stable C-Chec acid adsorption sites on Al(111) surface. 290

Table 10. 6: Optimised energies for stable CFQ acid adsorption sites on Al(111) surface...292

Table 10. 7: Optimised energies for stable FA acid adsorption sites on Zn(110) surface. 294

Table 10. 8: Optimised energies for stable 4-P-CQ acid adsorption sites on Zn(110) surface in solution.....295

Table 10. 9: Optimised energies for stable 3-P-CCQ acid adsorption sites on Zn(110) surface. 297

Table 10. 10: Optimised energies for stable 1.3-DCAF acid adsorption sites on Zn(110) surface. 298

Table 10. 11: Optimised energies for stable C-Chec acid adsorption sites on Zn(110) surface. 299

Table 10. 12: Optimised energies for stable CFQ acid adsorption sites on Zn(110) surface.301

CHAPTER 11

Table 11. 1: Table showing the atomic number, element symbol, element name, concentration percentage and certainty of different regions on the aluminium metal surface. 314

Table 11. 2: Table showing the atomic number, element symbol, element name, concentration percentage and certainty of different regions on the aluminium metal surface. 315

Table 11. 3: Table showing the atomic number, element symbol, element name, concentration percentage and certainty of different regions on the metal surface. 316

Table 11. 4: Table showing the atomic number, element symbol, element name, concentration percentage and certainty of different regions on the aluminium metal surface. 317

© University of Venda

Table 11. 5: Table showing the atomic number, element symbol, element name, concentration percentage and certainty of different regions on the zinc metal surface.....324

Table 11. 6: Table showing the atomic number, element symbol, element name, concentration percentage and certainty of different regions on the zinc metal surface.....326

Table 11. 7: Table showing the atomic number, element symbol, element name, concentration percentage and certainty of different regions on the zinc metal surface.....328

Table 11. 8: Table showing the atomic number, element symbol, element name, concentration percentage and certainty of different regions on the zinc metal surface.....330

Table 11. 9: Table showing the atomic number, element symbol, element name, concentration percentage and certainty of different regions on the zinc metal surface.....332

Table 11. 10: Table showing the atomic number, element symbol, element name, concentration percentage and certainty of different regions on the zinc metal surface.....334

Table 11. 11: Table showing the atomic number, element symbol, element name, concentration percentage and certainty of different regions on the zinc metal surface.....336

Table 11. 12: Table showing the atomic number, element symbol, element name, concentration percentage and certainty of different regions on the mild steel metal surface.....343

Table 11. 13: Table showing the atomic number, element symbol, element name, concentration percentage and certainty of different regions on the mild steel metal surface.....345

Table 11. 14: Table showing the atomic number, element symbol, element name, concentration percentage and certainty of different regions on the mild steel metal surface.....347

Table 11. 15: Table showing the atomic number, element symbol, element name, concentration percentage and certainty of different regions on the mild steel metal surface.....349

Table 11. 16: Table showing the atomic number, element symbol, element name, concentration percentage and certainty of different regions on the mild steel metal surface.....351

Table 11. 17: Table showing the atomic number, element symbol, element name, concentration percentage and certainty of different regions on the mild steel metal surface.....353

Table 11. 18: Table showing the atomic number, element symbol, element name, concentration percentage and certainty of different regions on the mild steel metal surface.....355

© University of Venda

CHAPTER 1

Introduction

© University of Venda

1. Introduction

This introduction deliberates on the problems and background of corrosion on various metals. It also discusses this study's rationale, justification, aims and objectives.

1.1. Background of the study

Aggressive acids such as hydrochloric and sulphuric have long been intentionally used in the engineering and metallurgical process, which includes acid descaling, acid pickling, acid cleaning, oil-well acidizing implicating the utilisation of mineral acids and drilling processes in oil and gas exploration [1-6]. These processes are believed to be the leading root course of corrosion of metals typically used in industries. On the other hand, Metals and alloys are extracted into an elemental form from ores which occurs in their combined states [7]. The extracted metals in their elemental form tend to always strive to revert to their most stable states, like their sulphides, hydroxides or oxides. This tendency causes extracted metals to experience a variety of chemical reactions in different environments, which include atmospheric and marine conditions, like water, electrolytes, vapour or gases, and moisture, among others, resulting in the degradation of such metals [8]. As a result, lives and wealth have been lost in the past and continue to be lost in all engineering fields. Also, the cost of renewing damaged equipment in industry because of corrosion makes a fair share of the country's gross domestic product (GDP) [9]. This makes the corrosion of metals an enormous problem for industries and poses safety problems and economic loss. Explosions, pipeline leakage, and breakdown of production lines and equipment are some of the many safety problems implicating the corrosion of metals. Worldwide, using a 3.4% of global GDP (2013), the global cost of corrosion can then be estimated to be US$2.5 trillion [10], with the direct cost in South Africa estimated to be around R130 billion [11]. This puts industries on high alert to protect metallic equipment to lower the effects of safety and economic problems caused by corrosion. Metals such as mild steel, also called plain carbon steel, have become favourites for many structural and industrial applications because of their low cost and high strength-to-mass ratio. At the same time, it offers the qualities of materials suitable for a range of tasks. The only shortcoming is that its corrosion resistance is limited in acidic environments and suffers the most [12]. However, a counteracting factor in the form of an inhibitor can be introduced to prevent the rate at which the metals corrode in the presence of the acids and also to delay the inevitable process of metals reverting to their stable states. Organic and inorganic compounds, also known as traditional corrosion inhibitors, have been intensively used as corrosion

© University of Venda

inhibitors because of: the presence of heteroatoms like nitrogen, sulphur and oxygen, their excellent thermal stability, low water solubility, ease of addition, effectiveness over a broad pH range, high efficiency at low concentrations, limited or non-interactions with other coating components [13, 14]. The presence of heteroatoms on the compounds increases their polarity, allowing them to behave as surfactants in aqueous solutions. Organic compounds with significant molecular weight are also good candidates to be used effectively as corrosion inhibitors. However, due to their high cost of production, toxicity, non-biodegradability, change in laws, environmental hazard concerns and awareness, [15] the utilisation of inorganic and organic compounds as corrosion inhibitors has been heavily compromised, with the exceptions of a few once which are cheap and environmentally friendly. Engineers and scientists in the corrosion science field are currently using the one-step multi-component reactions (MCRs) method for the synthesis of organic inhibitors, which is also due to the growing ecological consciousness and stringent environmental regulations in all science and technology fields. The MCRs have become a significant tool for organic compound green synthesis, especially when used in conjunction with microwave and ultrasonic irradiation. [16-22]. The use of various plant extracts, ionic liquids and chemical medicines has also gained considerable recognition in developing green corrosion inhibitors, also known as green chemistry, to address the shortcomings caused by traditional inhibitors. Green Chemistry is a field of science, engineering, and technology that uses a collection of concepts and principles that minimize the discharge of environmentally malignant materials into the surrounding environment and the application of eco-friendly chemicals [23-25]. Plants contain various metabolites or chemical constituents. These metabolites are normally found in their trans-isomerisation state, however, when exposed to UV radiation, their geometry tends to change to cis-isomerisation. This shift might affect the inhibition potential of the plant as a corrosion inhibitor. This research project is dedicated to investigating the effect of UV-radiation on the corrosion inhibition potential of *H. kraussi*i plant extract for mild steel, zinc and aluminium metals corrosion in hydrochloric and sulphuric acids.

© University of Venda

1.2. Justification of the study

There are four major motives why corrosion of metals is studied. The first three motives are focused on social issues regarding (a) Human life and safety, (b) corrosion cost, and (c) material conservation [26]. The fourth motive is that corrosion is a formidable phenomenon to comprehend, and its study is a challenging and fascinating endeavour. The first three reasons are elaborated on further below and in the consequences of corrosion section [27].

- **Human life and safety**

The safety and health of people are always compromised when corrosion comes into play. Steel structures such as bridges can collapse due to metal failure because of corrosion, which can cause death and injuries. Some metals release rust when undergoing corrosion, which can be toxic and dangerous to humans. For example, iron releases iron oxide during corrosion, which is carcinogenic [27].

- **Corrosion cost**

On the corrosion account, the world economy trembles. The direct cost of corrosion globally, excluding resource waste, personal injuries caused by corrosion, and environmental impacts, is estimated to be between 3.1 and 3.5 % of the yearly global gross domestic product (GDP), or between 1.3 and 1.4 trillion euros [28]. This corrosion also has a severe impact on the environment, and according to a study conducted by MINTEK, the majority of steels created are used to replace those that have been damaged. Typically, these metals are created from ores, some of which are obtained by mining. The ongoing mining of these valuable ores indefinitely could lead to their depletion. Manufacturing these metals discharges huge amounts of carbon dioxide into the atmosphere, damaging the ozone layer and resulting in climate changes, leading to drought and other environmental hazards.

- **Material Conservation**

The main purpose of studying corrosion is to understand its mechanisms to find suitable ways to delay its tactics so that materials can perform their duties for a prolonged period with no risk of being damaged by corrosion. To date, there are many different methods that are highly recommended for controlling or delaying corrosion attacks. Such methods include the utilisation of corrosion inhibitors, material selection, etc. The shortcoming of these methods is that they cannot permanently get rid of corrosion but can only delay it for some time [27].

© University of Venda

Some other reasons to study corrosion are because of the major accidents that happened in the past so that we can gain knowledge and understanding on how to prevent such accidents from happening again. Below are some of the significant corrosion accidents and those counteracted from happening in the past events.

1.2.1. Timeline of some of the significant incidents that occurred due to corrosion

- On December 15, 1967, the Silver Bridge, a bridge across the Ohio River in the United States connecting Point Pleasant, West Virginia, Kranauga, and Ohio, collapsed, killing 46 people. The combined effects of stress and corrosion were said to be the cause of the bridge's downfall [27].
- On June 28, 1983, a 100-foot piece of a bridge span on a major US Interstate highway collapsed, killing three people and badly injuring three others. The rusting of a support pin was the cause of the collapse [27].
- On April 28, 1988, the cabin of a commercial aeroplane en-route from Hilo to Honolulu, Hawaii, suddenly disintegrated, killing the flight attendant and injuring 65 passengers. According to the report, the problem was caused by metal fatigue and corrosion combined [27].
- In February 2004, a nuclear power station in Ohio was shut down for routine maintenance, and a pineapple-sized hole in the reactor’s lid was discovered due to corrosion. The Nuclear Regulatory Commission stated in its assessment that the facility had been operating on the verge of a catastrophic nuclear accident [27].
- A 500-foot-long pedestrian bridge collapsed in a retail mall in the United States in July 2005. The accident likely happened after regular business hours, with no one harmed. The rusting of large metal bolts connecting the bridge to a parking garage and the shops in the mall was blamed for the bridge's structural breakdown [27].
- In December 2008, in suburban Washington, DC, a massive water main pipe broked, unleashing a torrent of water and forcing dramatic rescues of trapped cars. This tragedy reignited concerns about the safety of the country's outdated infrastructure [27].

© University of Venda

1.3. Scope of the research

The scope of the study reported in this research project covers the exploitation of the corrosion inhibition potential of UV-radiated and non-radiated *H. kraussii* extracts on mild steel, zinc and aluminium metals in 1.0 M sulphuric and hydrochloric acids. The potential of *H. kraussii* extracts as a corrosion inhibitor was exploited using gravimetric weight loss techniques, electrochemical techniques, quantum chemical methods, liquid chromatography-mass spectroscopy, and surface characterisation techniques such as contact angle, Fourier Transform Infrared spectroscopy, X-ray diffraction, Scanning electron microscopy and Energy dispersive spectroscopy.

1.4. Problem statement

All over the world, museum institutions are filled with different materials, like objects of industrial heritage, which are of sentimental value because of their historical, architectural, technological, and scientific value. Most of the equipment we have today in various sectors is just a modification of these old materials, making them precious and worthy of being conserved. Some of these historical sites consist of buildings, machinery, factories, mills, workshops, and mines [29]. Cities and parks in most countries are decorated with statues of heroes of our past as a way of honouring them. However, a significant part of these objects preserved in museums and statues in our cities are covered with rust, and some are even weathering away such that their mechanical structure is no longer intact. This happens because of the inevitable process of corrosion. The ores from which the metals are made are obtained through the process of mining. The mining process comes with many environmental hazards. The process of converting ores to desired metallic material requires a lot of energy, which in some cases comes in the form of electricity, which is one of the most expensive commodities [30]. Suppose materials, especially metallic ones, are not protected from corroding. In that case, more ores will be mined, resulting in environmental degradation and depletion of natural resources, and more energy will be used just to replace the damaged materials [31]. If possible, a convenient way of making different materials to withstand any condition to survive for eternity is swiftly needed to address the problem of corrosion. The most profound way of protecting metal from corrosion attack is by utilising corrosion inhibitors. Synthetic organic compounds were the most preferred inhibitors over inorganic compounds in the last decade. However, recently, researchers have shifted their focus to exploring plant extracts as potential

© University of Venda

corrosion inhibitors [32]. The shift was inspired by the high cost of production, toxicity, non-biodegradability, and environmental hazards posed by the organic and inorganic compounds. Green corrosion inhibitors originating from plant roots, leaves, and stem extracts have been dubbed to be cost-effective and biodegradable and pose little or no harm to the environment [33, 34]. This is the reason this study is dedicated to exploring plant extracts as corrosion inhibitors. Some corrosion effects include:

- Power plants, chemical processing plants and refineries shut down, leading to detrimental economic loss and production problems as more jobs will be lost, and the products produced by these factories might have to be imported from other countries.
- Corrosion products can find their way into the drinking and other aquatic water channels, resulting in their poisoning. Rapid corroding of metallic parts can lead to leaking containers, resulting in contamination of chemicals and explosion hazards [35].
- Metal corrosion leads to premature metal failure, resulting in death and loss of lives and vulnerable properties [12].

1.5. Research question

The research question for this study was what effect does the formation of geometrical isomers contained in *Helichrysum kraussii* extract formed due to UV radiation have on the corrosion inhibition efficiency of mild steel, zinc and aluminium metal in acidic media.

© University of Venda

1.6. Aim and objectives of the study

The aim of this study is to investigate the effect of UV radiation on the corrosion inhibition potential of *H. Kraussii* extracts for mild steel, zinc and aluminium metals in acidic environments.

The specific objectives of this study are to:

1. extract chemical constituents of *H. kraussii* leaves using different solvents with a Soxhlet extractor.
2. investigate UV-induced geometrical isomerisation of the chemical constituents using LCMS technique.
3. isolate compounds causing corrosion inhibition.
4. carry out quantum molecular dynamic calculations to study the adsorption and interaction energy between the metal surface and the inhibitor molecules.
5. investigate the corrosion inhibition potentials of the plant extracts for mild steel, zinc and aluminium in sulphuric and hydrochloric acid media and their adsorption characteristics on the metallic surface using gravimetric and electrochemical techniques.
6. study the metal surface wettability in the acidic environment before and after exposure to the extract inhibitor.
7. examine the surface morphology of the metals utilising scanning electron microscopy (SEM) coupled with energy dispersive spectroscopy (EDS) and identify the functional groups responsible for metal-inhibitor interactions by using Fourier transform infrared (FTIR) spectroscopy. X-ray diffraction (XRD) was also employed to find the crystalline plane formed on the surface of the metal and to confirm if the corrosion and corrosion inhibition process took place on the surface of the metals.

© University of Venda

CHAPTER 2

Literature review

© University of Venda

2. Introduction

This chapter deliberates on the problems of mild steel, zinc, and aluminium metal corrosion, corrosion inhibition, and mechanisms in hydrochloric and sulphuric acid mediums. The electrochemistry, computational techniques, and green corrosion inhibitor adsorption properties of corrosion applied to describe the properties of corrosion inhibitors are discussed herein. This chapter also discusses the rationale for the use of *H. kraussii* plant extract as a corrosion inhibitor and the effect of UV radiation on the plant extract metabolite geometry.

2.1. Definition of corrosion

Corrosion is a natural process that is influenced by changes in a material's energy levels [36]. Historically, the word corrosion generally comes from the Latin word ‘corrodere’, which literally translates as “gnaw into pieces”. In general language, corrosion is often understood to be something which eats or wears away gradually [37, 38]. Corrosion has been defined in a variety of ways. One report defines it as a spontaneous natural process that converts pure metals and their alloys into stable forms like their oxides, sulphides and hydroxides as a consequence of chemical and electrochemical reactions with the surrounding environments [36]. Some authors consider it an oxidation process through which an oxide layer forms on the metal surface going through such a process. Corrosion does not apply only to metallic materials but can also be seen in non-metallic materials like glass, plastic, concrete, ceramics, etc. The principles through which such materials undergo corrosion are quite different from those of metals. When it takes place in non-metallic materials, it is defined as the deterioration of the material caused by chemicals. Metallic corrosion is referred to as the interaction of a metal with its environment. Onen (2010) [39] stated that Fontana and Greene (1967) and Uhling (1971) defined corrosion as the undesirable deterioration of metal – a metal's interaction with its environment that alters its properties that need to be preserved. This definition caters to both the corrosion of metallic and non-metallic materials [39].

Generally, corrosion is defined as an electrochemical or chemical reaction of the metals with their environment, which causes the deterioration or destruction of the materials [40, 41]. This definition of corrosion is technically restricted to the corrosion of metals only and will be the one referred to in this study when the word corrosion is mentioned [42].

© University of Venda

2.2. Basic reactions during the corrosion process

In this study, corrosion taking place in an aqueous environment will be intensively explored. Such corrosion is regarded as an electrochemical process because it is a chemical reaction that is accompanied by the generation and transfer of electrons to electrochemically active species dissolved in the electrolyte [43]. For corrosion to occur, three elements of paramount importance must be present, which include the cathode (for reduction half-reaction), anode (for oxidation half-reaction) and electrolyte (e.g., water, acids or basic solutions). Depending on the type of electrolyte solution, electrochemical active species such as O_2, CO_2, H_2S, etc., are also essential elements for corrosion to occur at some point. The combination of the three elements is known as the corrosion cell. The cathode and anode are known as the electrodes and can be of the same metal with heterogeneous surface structures or different metals. As a result, corrosion occurs because of the electrical potential difference between the electrodes that must be electrically connected. The electrolyte is the solution responsible for conducting electric current between the two electrodes by the movement of the ions [44]**.** Below are the two figures showing the two possible ways in which corrosion can happen between the cathode and anode in the same metal and in different metals.

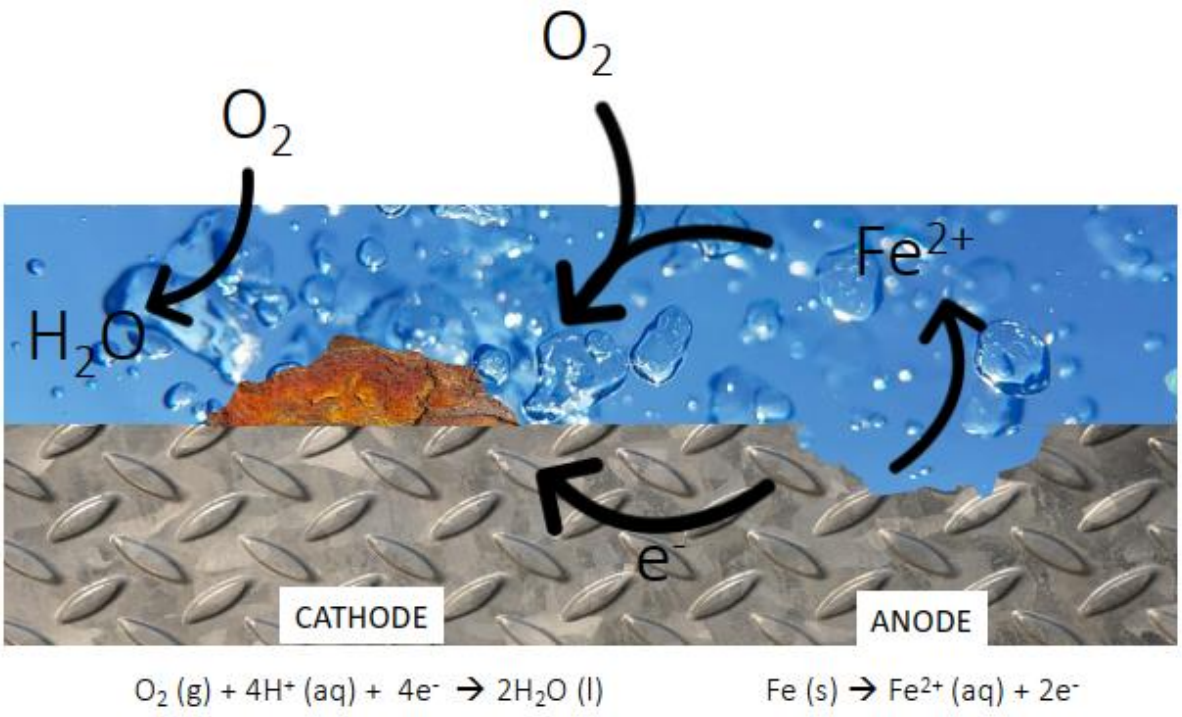


Figure 2. 1: Corrosion cell in which anode and cathode sites are occurring in the same metal [45].

© University of Venda

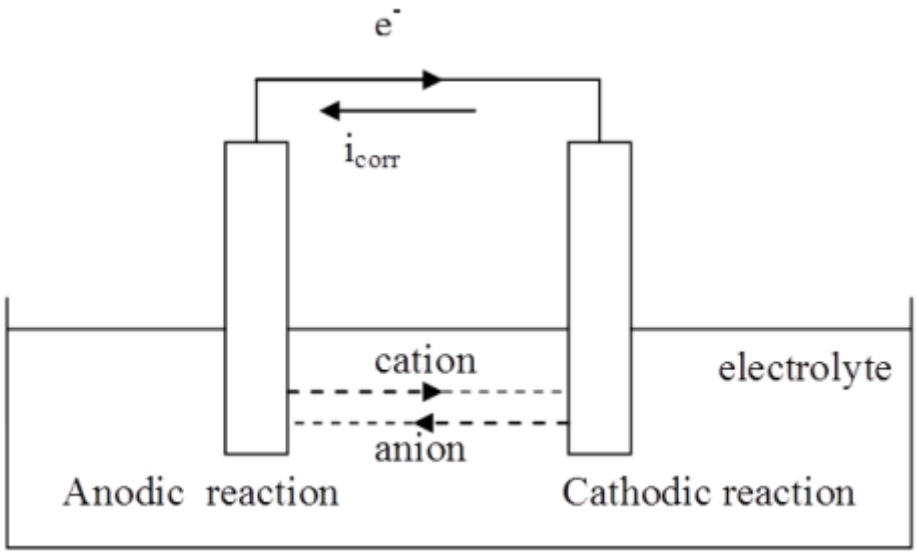


Figure 2. 2: Corrosion cell in which the anode and cathode reactions occur between two dissimilar metals [43].

The reactions and mechanisms taking place at the two electrodes (Cathode and anode) and the role of each during the process of corrosion are highlighted below.

Anode

In the electrochemical reaction, considering the metals, the anode is the region at which the metal is corroded (dissolved). The dissolved metal can either be transferred into the electrolyte solution as metal ions or be deposited back in the bulk metal surface as the corrosion products. In the case where the dissolved metal is transferred into the solution as positively charged metal ions, the ions move through the electrolyte, releasing the electrons which take part in the cathodic reaction or become deposited in the cathodic electrode. This process is called oxidation [44].

For instance, in the corrosion of iron metal, the metal ions are transferred into the electrolyte solution. The reaction process might occur in two steps, whereby the iron would be first oxidized into ferrous irons [45].

$$Fe \rightarrow Fe^{2+} + 2e^{-} \quad (1)$$

Depending on the corrosion potential, the ferrous ions can then be further oxidized into ferric ions:

$$Fe^{2+} \rightarrow Fe^{3+} \quad (2)$$

© University of Venda

In the case where the dissolved metal iron is deposited back onto the metal surface, which happens when the cathode and anode are of the same metal, the ferrous ions will be deposited on the metal surface depending on the electrolyte properties.

$$Fe^{2+} + 2OH^{-} \rightarrow Fe(OH)_2 \quad (3)$$

In most cases, rust in the form of iron hydroxide ($Fe(OH)_2$ is the deposited product.

The solid corrosion products that form on the surface of the metal may hinder the corrosion process. However, in the case of iron metal corrosion, the corrosion product films are weakly attached to the metal surface and are very porous, which can give access to the electrolyte solution to penetrate the metal surface, resulting in further corrosion.

Cathodic reaction.

The cathodic reaction plays a significant role in the equilibrium establishment of the corrosion system. It does this by balancing the anodic reaction with the reduction process on the cathode. This causes the electrons generated in the anodic site (oxidation half reaction) to be consumed at the cathode. It should always be kept in mind that the cathode and anode could be two different sites on the heterogeneous surface of one metal or different metal pieces [44]. In an aqueous acidic environment, in the void of dissolved oxygen, the cathodic reaction results in hydrogen evolution:

$$2H^{+} + 2e^{-} \rightarrow H_2 \quad (4)$$

When the dissolved oxygen is present, the cathodic reaction results in oxygen reduction, which is more thermodynamically favourable. This process proceeds in the acidic environment as follows [45],

$$O_2 + 4e^{-} + 4H^{+} \rightarrow 2H_2O \quad (5)$$

However, when dissolved oxygen and water are present, the cathodic half-reaction takes place in the form of Equation 6 as follows:

$$\frac{1}{2}O_{2\ (g)} + H_2O_{\ (l)} + 2e^{-} \rightarrow 2OH^{-}_{\ (aq)} \quad (6)$$

© University of Venda

Overall reaction

Equation 7 shows the overall reaction of iron metal with water and oxygen, which is a combination of the cathodic and anodic half-reactions.

$$Fe_{(s)} + \frac{1}{2}O_{2\ (g)} + H_2O_{\ (l)} \rightarrow Fe^{2+}{}_{(aq)} + 2OH^{-}{}_{(aq)} \quad (7)$$

Equation 7 can be simplified further and written in the form of Equation 8 [45].

$$Fe^{2+}{}_{(aq)} + 2OH^{-}{}_{(aq)} \rightarrow Fe(OH)_{2\ (aq)} \quad (8)$$

In some cases, the iron oxide $Fe(OH)_{2\ (aq)}$ can be oxidized to form brown-red $2Fe(OH)_{3\ (aq)}$ known as rust [43].

$$2Fe(OH)_{2\ (aq)} + H_2O_{(l)}H_2 + \frac{1}{2}O_{2\ (g)} \rightarrow 2Fe(OH)_{3\ (aq)} \quad (9)$$

The corrosion processes that occur on the iron metal surface can be detailed schematically using Figure 2.3.

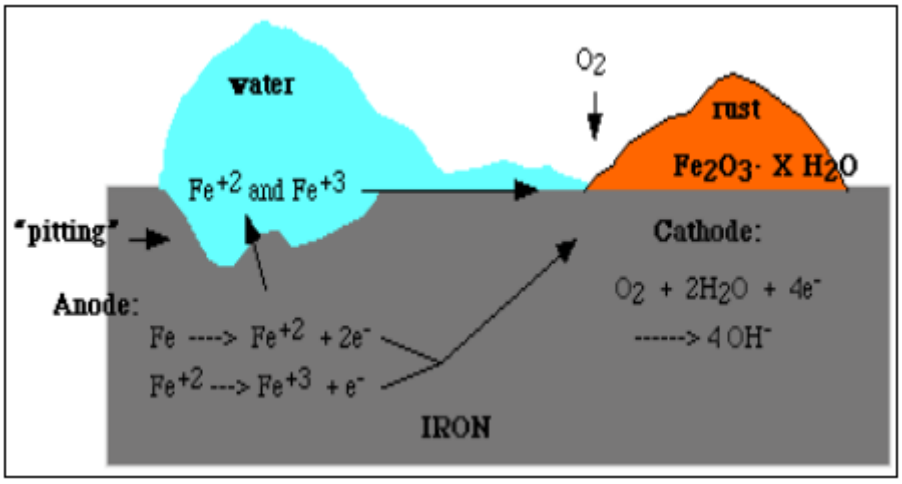


Figure 2. 3: The schematic diagram showing the electrochemical reaction of iron and water [46].

2.3. Corrosive environment

Different types of corrosion can be identified in various ways. One way to identify different types of corrosion is by the way in which the metal corrodes and the environment in which the metal corrodes [47]. Based on the environment in which the metal corrodes, two types of corrosion are likely to occur: wet and dry corrosion. Dry corrosion occurs when the corrodents

© University of Venda

are gases or vapours, and the environment is above the dew point, whereas wet corrosion occurs when the environment is electrolytic or aqueous [48]. This makes different types of environments in which the corrosion of material takes place to be very crucial in the understanding of corrosion studies. There are three main groups in which the types of corrosive environments are found. These groups include man-made environments (industrial molten metals and salts), atmospheric (rural and urban areas) and outer space (vacuum) environments [49]. These environments are said to be influenced by factors such as pressures and temperatures. For instance, high-temperature environments are linked with high metal corrosion rates [50].

2.4. Corrosion in different Media

There are three common media in which corrosion prevails the most. These include neutral, acids and basic (alkaline) media. Most of the equipment that is utilised in various industrial processes, like industrial water-colling systems [47], acid pickling, and coatings, are normally exposed to these types of media. This makes the three media highly regarded when studying the corrosion of materials, especially in different industrial sectors. The pH level of these three media helps differentiate them from one another. The pH level of a media ranging from 1 – 6 is said to be acidic in nature, those with a pH of 7 are said to be natural, and the most common example of such is pure water, while those media with a pH level ranging from 8 – 14 are said to be basic in nature.

Neutral Media

As mentioned above, water is an example of a neutral medium. When oxygen transported by air encounters water, it dissolves in water, which generally causes corrosion when the metal surface interacts with water [50]. For example, the reaction of zinc with water is given by Equation 7.

$$Zn_{\ (s)} + 2H_2O_{\ (l)} \rightarrow Zn(OH)_{2\ (s)} + H_{2\ (g)} \quad (10)$$

Alkaline

In the presence of dissolved oxygen, basic solutions such as sodium hydroxide can be corrosive to different materials. Below is the equation showing the example of the reaction of sodium hydroxide with zinc metal that leads to the deterioration of zinc metal.

$$Zn_{\ (s)} + 2NaOH_{(s)} \rightarrow Na_2ZnO_{2\ (g)} + H_{2\ (g)} \quad (11)$$

© University of Venda

Acidic Medium

An acidic environment or media can exist as a diluted or concentrated acid. The two vary in their strength in terms of their corroding capability. Diluted acids are extremely corrosive to metals when compared to concentrated acids. This is because the diluted acid to which the metal can be exposed contains more water than concentrated acids, resulting in a huge number of hydrogens being released in the process, which causes the metal to corrode [50]. For instance, zinc chloride is formed when zinc metal is exposed to diluted hydrochloric acid, and a substantial amount of hydrogen gas is released during the process. Equation 5 shows the reaction equation for such a process.

$$Zn_{\ (s)} + 2HCl_{\ (g)} \rightarrow ZnCl_{2\ (s)} + H_{2\ (g)} \quad (12)$$

Amongst the three media, acidic media are very strong corrosive media, and this is generally because acids have lower pH, which means that there are more free hydrogen ions, resulting in more hydrogens being given off, which leads to the corrosion of metals. Acids are also used in various industrial processes, such as the pickling process of metals and in the removal of the undesirable scale of rust. This is why acids such as hydrochloric and sulphuric acids are the most reported in most corrosion studies, as they have a vast application and aggression towards metallic materials.

2.5. Classification of corrosion

Corrosion has been categorised in various ways for easy recognition and identification. One technique separates corrosion into electrochemical and oxidation (or direct combination). One method divides corrosion into two types: electrochemical and oxidative (or direct combination). Another method distinguishes between low-temperature and high-temperature corrosion [36]. The most common classification of corrosion is the one that separates it into three factors: the nature of the corrodent (wet and dry corrosion), the mechanism of corrosion and the appearance of the corroded metal [51]. These three factors are further elaborated below. There are a number of different types of corrosion that can occur, and they are all identical in the sense that they involve the chemical process of corrosion but differ in how and where they attack the metal [52]. In oil and gas-producing industries, the most prevalent corrosion types are sour and sweet corrosion due to CO_2 and H_2S, respectively [53]. Other types of corrosion have been outlined in section 2.5.

© University of Venda

a) Nature of the corrodent

This classification is based on whether corrosion occurs in wet or dry settings. Moisture is required for wet corrosion, and dry corrosion usually involves the reaction with gases at elevated temperatures [54].

- Wet corrosion

  Wet corrosion occurs when a liquid is present. It occurs via electron transfer, which is comprised of two processes: reduction and oxidation. In reduction, the surrounding environment gains the electrons lost by the metal atoms in oxidation. The anode is the metal in which electrons are lost. The cathode is the liquid, gas, or metal that receives electrons. Compared to dry corrosion, wet corrosion is by far the most common type of corrosion.

- Dry corrosion

  The metal reacts with oxygen in the atmosphere in dry corrosion [55]. It is usually related to higher temperatures and occurs when no liquids are involved or when the temperature is higher than the dew point of the environment. In this regard, corrosion is usually caused by vapours and gases. In this process, the metal oxide reacts solely with the atmospheric environment.

  In this research, corrosion, which is influenced by the presence of liquids (wet corrosion), will be explored.

b) Mechanism of corrosion

According to this classification, corrosion can either occur through electrochemical or direct chemical reactions.

c) Corroded metal appearance

Corrosion can be localized or uniform. In localized corrosion, only tiny regions on the surface of the metal are affected. However, the metal corrodes at the same rate on the whole metal surface for uniform corrosion.

The morphology of the corrosion attack, which may be observed either under magnification or with the naked eye, is the best way to classify corrosion by appearance [56]. The image in Figure 2.4 depicts some of the most frequent types of corrosion and appearance.

© University of Venda

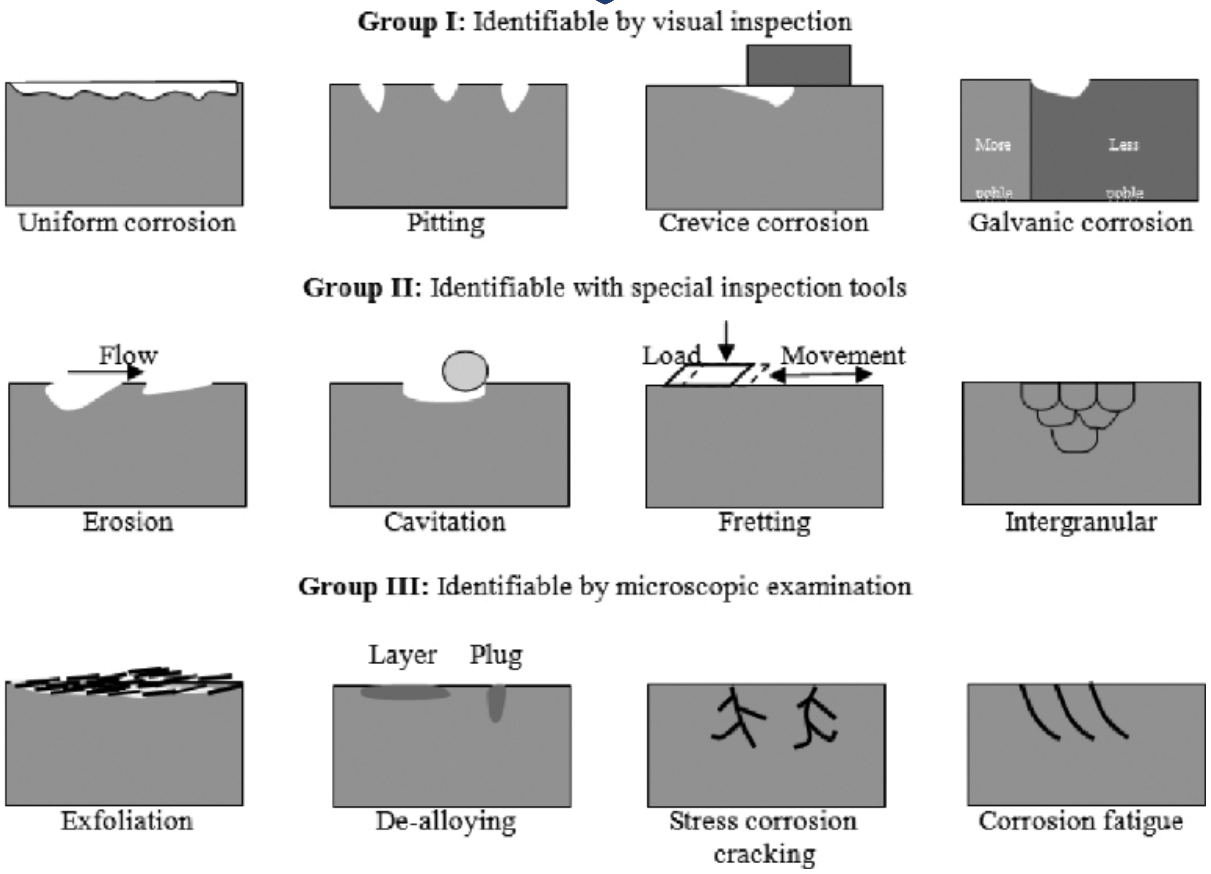


Figure 2. 4: Common forms of corrosion [57].

2.6. Types of corrosion

Not very often is the ratio of the corrosion attack to its depth used to classify the types of corrosion. If the corrosion attack depth to its ratio is much less than 1, the corrosion attack is called general corrosion. When the corrosion attack depth exceeds the width, the corrosion is known as localised corrosion. However, when the ratio gets much greater than 1, the corrosion attack is known as pitting corrosion [43]. Generally, corrosion is classified into different types based on the appearance of the corroded metal, the mechanism of attack, and the kind of environment to which the metal is exposed.

According to the type of reaction causing corrosion, corrosion can also be categorised into two groups, namely chemical and electrochemical corrosion [58, 59]. It is crucial to note that all the classification methods can be used simultaneously to come up with the most suitable type of corrosion.

© University of Venda

1. Chemical corrosion

Chemical corrosion is generally described as the spontaneous deterioration of metals without the exchange of charges with their environment, and it is said to be governed by the laws of ordinary heterogeneous kinetics.

2. Electrochemical corrosion

An electrochemical reaction is a type of corrosion involving the exchange of electrons between the metals and their surrounding environment. The electrochemical reaction takes place very frequently, and it causes more severe damage than chemical corrosion. This is the reason electrochemical corrosion is explored extensively. Based on the mode of destruction caused by electrochemical corrosion, it is further divided into the following categories.

- **Uniform corrosion**

Uniform corrosion takes place at nearly the same intensity on the whole surface of the metal [60]. It is also known as a general attack. Uniform corrosion results in huge weight loss and destruction of the metal [61]. The rusting of steel is a common example of uniform corrosion [43].



Figure 2. 5: uniform corrosion [55].

© University of Venda

- **Galvanic corrosion**

Galvanic corrosion occurs at the junction between two dissimilar metals put together in a corrosive electrolyte [62, 63]. Based on the position in the galvanic series, the metal which will act as the cathode will be protected from corrosion at the expense of the metal that will act as the anode. In cases where the anode metal is very small in relation to the cathode metal, the rate of corrosion experienced can be very high because the large cathodic metal influences corrosion at a relatively small anodic point [43].



Figure 2. 6: Galvanic corrosion [55].

- **Pitting corrosion**

Pitting is a localized type of corrosion that occurs when one part of the metal becomes anodic in comparison to the remainder of the metal's surface, resulting in holes on the metal's surface that can be small or large in diameter [43]. The pits that form can be close together or isolated, and they resemble a roughened surface. Metals that may produce a protective layer, such as magnesium and aluminium, are found to be the most vulnerable to this sort of corrosion. The grey or white powder is the corrosion by-product that generally occurs as a result of this type of corrosion. This by-product powder is commonly used as a pitting corrosion identification symbol. When by-product powder is removed from the metal surface, microscopic pits or holes appear. A large degree of destruction can be noticed on the metal when these little pits or holes in the metal surface penetrate deep into the metal structure. Materials with a high alloy content contribute less to the corrosion problem in instances where the conditions that cause fretting corrosion cannot be modified.

© University of Venda



Figure 2. 7: Pitting corrosion [55].

- **Crevice corrosion**

This type of corrosion occurs inside narrow gaps, such as contact regions between two parts and inside cracks where fluids from the environment have limited access [64]. It is mostly influenced by the difference in concentration of the chemical constituents, such as oxygen, between the entire metal and the crevice. In this case, the entire metal becomes the cathode, and the crevice becomes the anode [65]. This type of corrosion is also known as shielded corrosion. This is because crevice corrosion occurs where the surface is shielded, preventing oxygen from freely interacting with the surface of the metal. The passive film that results in some metals during the corrosion process often tends to break down in these areas.



Figure 2. 8: crevice corrosion [66].

© University of Venda

- **Microbiologically influenced corrosion**

Microbiologically influenced corrosion (MIC) is a localized aggressive type of corrosion caused by microorganisms, such as fungi, bacteria and microalgae, with bacteria being the main cause. MIC is also known as biocorrosion, microbially influenced corrosion or microbiological corrosion, and it leads to biodeterioration of material [67, 68]. The bacteria that cause it can be grouped into anaerobic and aerobic bacteria. The former does not require oxygen to be active, while the latter relies on oxygen to be active. The most reported microbiologically influenced corrosion-related damages to engineered systems such as offshore structures and ships are due to sulphate-reducing anaerobic bacteria [65]. The microorganism's activities initiate and accelerate this kind of corrosion. This is because, as part of their metabolism, microbiological aerobic bacteria generate highly corrosive species.



Figure 2. 9: Example of Microbiological influenced corrosion [67].

- **Sweet corrosion (CO_2 corrosion)**

At the temperatures experienced in oil and gas industries, dry CO_2 is not itself corrosive; however, when it is dissolved in an aqueous phase, it can spread out and cause an electrochemical reaction between steel and the aqueous phase in contact, the CO_2 will blend with water producing carbonic acid forming the fluid acid, which then causes the corrosion. Sweet corrosion generally takes advantage of the material at high temperatures [53].

© University of Venda



Figure 2. 10: Example of sweet corrosion [69].

- **Sour corrosion (H_2 corrosion)**

This type of corrosion is the most troubling in the drill pipe. It takes place as a result of the interaction of the metal with hydrogen sulphide and moisture. H_2S, like sweet corrosion, is not corrosive in and of itself, but it becomes corrosive in the presence of water, causing the pipe to lose flexibility. The dissolution of H_2S in water causes the formation of sulphuric acid (H_2SO_4), the source of hydrogen ions that cause corrosion. Iron sulphide and hydrogen gas are the corrosion products [53].



Figure 2. 11: Example of sour corrosion [69].

© University of Venda

- **Fretting Corrosion**

Fretting corrosion is a rapidly localized type of corrosion that occurs because of the attack on mated (fitted together) surfaces under load when a small amount of slips or frictional movement between the two surfaces is allowed [70]. It is usually observed in shifts, impact machinery, bearings, and gears mounted in vibrational machinery. This type of corrosion not only causes mechanical damage to the metal surface but also removes its protective film. As a result, the exposed damaged metal surface reacts with oxygen in the atmosphere, forming the metal oxide. The removal of the protective layer causes the acceleration of electrochemical corrosion.

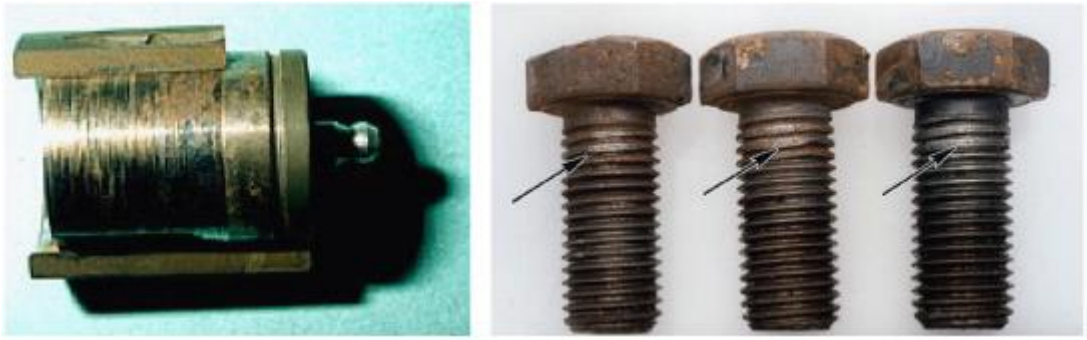


Figure 2. 12: Example of fretting corrosion [70].

- **Intergranular corrosion**

Metals and alloys contain small differentiable regions known as grains from a microscopic point of view. The orientation of the lattice (atomic arrangement) is identical within the individual grain. Each grain contains different orientations, and the boundary among the grains is known as the grain boundary. With this said, intergranular corrosion is a form of corrosion that attacks selectively at the grain boundaries of metals or alloys due to the presence of a secondary phase. It generally happens because of the metal's impurities or enrichment, which are usually present in very high concentrations close to the grain boundary [71]. The most common example of this kind of corrosion occurs in stainless steel. In the case of heating in the 950 – 1450 F temperature range or welding, stainless steel becomes susceptible to this type of corrosion [62]. This occurs because the chromium carbide, which is used to make steel, does not dissolve in this temperature range and tends to precipitate out of the grain to the grain boundary. This results in chromium depletion in the grain region next to the grain boundary. As a result, the region becomes anodic, and the grain boundary becomes cathodic. When the two different regions come in contact with the electrolyte, they tend to react, causing corrosion.

© University of Venda



Figure 2. 13: Example of intergranular corrosion [72].

2.7. The rate of corrosion

The rate of corrosion has been explained and expressed in various ways. Generally, it is described as a technique that is used to measure how rapidly any material deteriorates after a specific time in a particular environment [73]. It is also defined as the corrosion effect on a material per unit of time. For example, during the corrosion studies through gravimetric weight loss, the amount of weight (mass) lost by the corroded metal in every unit of time is referred to as the rate of corrosion. It is crucial to note that the corrosion rate differs for every metal and its extent [74], varies with time, may not be the same at all points of the corroding surface, and depends on the environmental conditions and the kind of metal under study. This is the reason why the corrosion rate report should include information on the time, dependency, type and location of the corrosion effect [32]. Expanding on why the corrosion rate differs for every metal. Some metals are resistant to corrosion; for illustration, aluminium forms aluminium oxide when it comes into contact with oxygen (in water, soil, or the air). This generated coating of aluminium oxide is chemically bonded to the metal's surface and protects the core aluminium from further reaction. Because zinc metals lack the ability to produce such coatings, their corrosion rates are substantially higher than those of aluminium. Metals like copper have a limited ability to create this layer, resulting in significant corrosion rates. The mathematical expression of the rate of corrosion used relies on the type of corrosion effects and technical

© University of Venda

system. In some cases, the rate of corrosion can be expressed as a penetration rate (an increase in the depth of corrosion per unit time, mils/yr). It is also expressed as the mass of metal lost per unit area of surface per unit time (m/yr, g/sq) [36]. For this study, the corrosion rate will be expressed based on the following mathematical expression,

$$\rho = \left(\frac{\Delta w}{st}\right) \tag{13}$$

where ρ is the corrosion rate ($g.cm^{-2}.h^{-1}$), s is the surface area of the materials (cm^2), w is the average weight loss of the materials (g), and t is the immersion time (h).

2.7.1. Methods of determining corrosion rate.

The rate of corrosion can be determined using a variety of techniques. The rate of corrosion in uniformly corroding metals can be determined using any of the methods listed below [75].

- Weight loss
- Electrochemical techniques
- Chemical analysis of the solution
- Weight gain
- Gasometric techniques
- Inert marker method
- Thickness measurements
- Electrical resistance probes
- Electrical resistance probes

For this study, only the first two methods will be undertaken to study the rates of corrosion of mild steel, zinc and aluminium metals in an acidic environment. These methods are briefly elaborated on.

2.7.1.1. Weight loss method

In this method, the metal sample is first weighed and then put in the corrosive environment for a certain period. After that period elapses, the metal is removed from the corrosive environment and cleaned for any corrosion products on its surface. It is then dried before being weighed again to get the mass difference or weight loss. Any solid corrosion products on the metal's surface must be removed for this method to work. Chemicals or electrochemical procedures,

© University of Venda

which are usually specific to the metal being treated, can be utilised to eliminate persistent and rigid corrosion products on the metal surface. If the corrosion products are non-adherent and loose, mechanical methods such as brushing and wiping the metal surface can be used to remove them [76].

2.7.1.2. Chemical analysis of the solution

When a metal corrodes in an electrolyte with a constant volume, the corroding metal's cations build up in the solution. As time progresses, the solution gets more concentrated in the dissolved cation. As a result, determining the corrosion rate requires chemical analysis of extracted aliquots of the solution as a function of time. Two popular techniques utilised in this method are atomic adsorption spectrophotometry (AAS) and standard colourimetric procedures in the visible range [75]. AAS is employed to analyse the solution of the corroded metal. AAS is very useful because it requires a very small sample size. The sample is weighed before being sprayed onto the instrument's flame and atomized. Light of the correct wavelength for the element being studied is directed through the flame, and the sample's atoms absorb part of it. The amount of light absorbed in a solution is equivalent to the element's concentration. The AAS approach is capable of detecting trace elements down to parts per million [77]. It's also worth noting that the methods by which the samples are analysed vary depending on the instrument version.

2.7.1.3. Electrochemical techniques

None of the approaches listed above can provide information about the underlying cause of the corrosion, except electrochemical techniques. Electrochemical techniques have these qualities, as well as the ability to control the electrode potential to prevent corrosion. These techniques include electrochemical impedance spectroscopy (EIS), potentiodynamic polarization (PDP), open circuit voltage (OCV), linear polarization resistance (LPR) method, galvanostatic polarization, and cyclic voltammetry measurements. In this work, only the first three electrochemical techniques, EIS, PDP and OCV, will be exploited [75].

- **Electrochemical impedance spectroscopy (EIS)**

Electrochemical impedance spectroscopy (EIS), also referred to as the AC impedance method, involves applying a sinusoidal perturbation in the form of potential or current over a specific frequency range to the cell. If a sinusoidal potential excitation is administered to the cell, an

© University of Venda

AC signal is produced that may be evaluated as a sinusoidal function sum. The EIS technique employs a non-destructive process in the OCV mode that forces either an oxidation or a reduction reaction to occur. This is due to the use of very small excitation amplitudes, which are typically between 5 and 10 mV peak to peak, resulting in no or minor perturbations of the electrochemical test system. In recent years, EIS has enjoyed a successful ride in its utilisation for corrosion studies because of the advantage it gives for the corrosion characterisation of different oxide layers on the surface of the metal. This technique may also differentiate between the electric and dielectric properties of individual contributions of components under study, as well as provide information about the corrosion process on the substrate surface [78].

Theory and representation of complex impedance values

Definition of Impedance

The concept of electrical resistance is very well known, and it is described as the circuit element's ability to withstand the flow of electrical current. It can be mathematically represented by Ohms law, which defines resistance in terms of the ratio between current I and voltage E.

$$R = \frac{E}{I} \tag{14}$$

Although Equation 14 is a well-known relationship, it can only be applied to one circuit element, commonly called the ideal resistor. The following are some of the simplifying properties of this ideal resistor: (i) It obeys Ohm's law at all current and voltage levels, (ii) Its resistance value is frequency independent, and (iii) AC current and voltage signals passing through a resistor are in phase. Nevertheless, the real world comprises of elements that display much more complex behaviour. These elements advocate for the usage of impedance, which is a more broad circuit characteristic, rather than the simple concept of resistance [79]. Impedance is also a measurement of a circuit's ability to withstand the electrical flow of current, similar to resistance. However, it is not confined to the three simplifying features described above, unlike resistance.

Electrochemical impedance is often measured by applying an AC voltage to an electrochemical cell and then monitoring the current that passes through it. For example, if a sinusoidal potential is applied, the outcome is an AC current signal, which may be analysed as a sinusoidal function sum. When measuring electrochemical impedance, a tiny excitation signal is used to make the

© University of Venda

cell's response pseudo-linear. The current response to a sinusoidal potential in a pseudo-linear system is sinusoidal with equal frequency but displaced in phase [79].

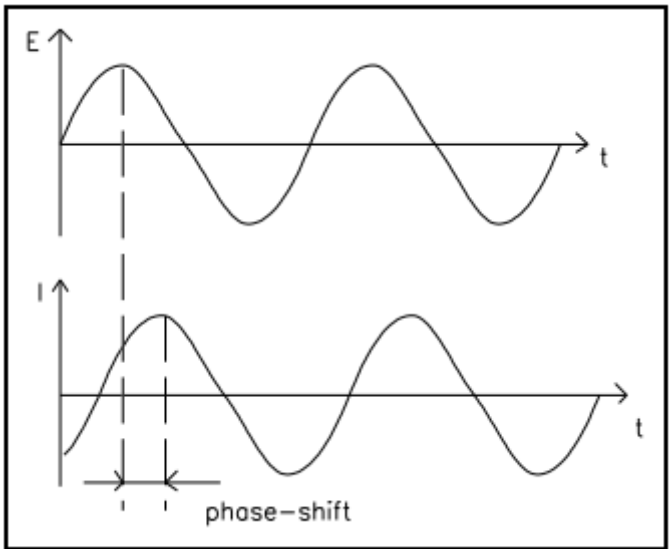


Figure 2. 14: Sinusoidal current response in a linear system [79].

The excitation signal can be mathematically expressed as a function of time and has a form,

$$E_t = E_0 \sin(\omega t) \tag{15}$$

where E_t is the potential at the time t, E_0 is the amplitude of the signal, and w is the radial frequency. The mathematical relationship between frequency (hertz) and ω (second/radians) is given as,

$$\omega = 2\pi f. \tag{16}$$

The response signal, I_t is shifted in phase (ϕ) and has a different amplitude, I_0, in a linear system,

$$I_t = I_0 sin(\omega t + \phi) \tag{17}$$

A similar expression to Ohm's law that enables the calculation of the system's impedance is as follows,

$$Z = \frac{E_t}{I_t} = \frac{E_0 sin(\omega t)}{I_0 sin(\omega t + \phi)} = Z_0 \frac{sin(\omega t)}{sin(\omega t + \phi)} \tag{18}$$

As a result, the impedance is expressed in terms of the magnitude, Z_0, and a phase shift, ϕ .

© University of Venda

An Oval known as the Lissajous figure results if the applied sinusoidal signal E(t) is plotted on the X-axis of a graph and the sinusoidal response signal (t) on the Y-axis. The study of Lissajous Figures on oscilloscope screens was the standard method of measuring impedance before modern EIS equipment became available [80].

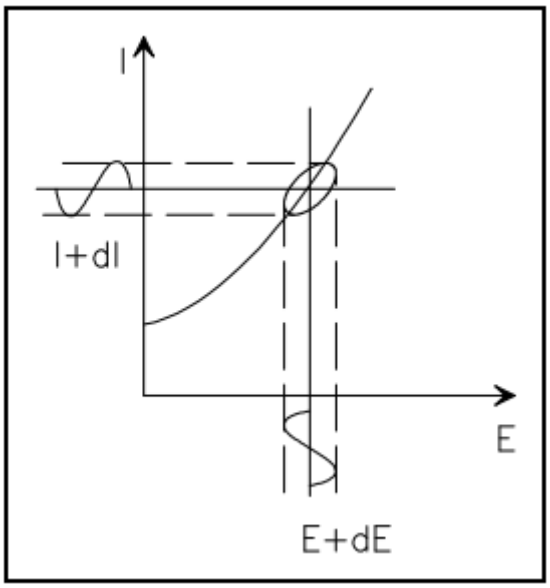


Figure 2. 15: Origin of Lissajous figure [79].

With Euler's relationship, given as:

$$exp(j\phi) = cos\phi + jsin\phi \tag{19}$$

it is possible to express the impedance as a complex function. The potential is described as follows,

$$E_t = E_0\, exp(j\omega t) \tag{20}$$

and the current response is as follows,

$$I_t = I_0\, exp(j\omega t - \phi) \tag{21}$$

The impedance is then represented as a complex number,

$$Z(\omega) = \frac{E}{I} = Z_0 exp(j\phi) = Z_0(cos\phi + jsin\phi) \tag{22}$$

© University of Venda

Data representation.

From Equation 22, the expression for $Z(\omega)$ is composed of a real and an imaginary part. A Nyquist plot is obtained by plotting the real part on the X-axis and the imaginary part on the Y-axis of a graph (Figure 2.16).

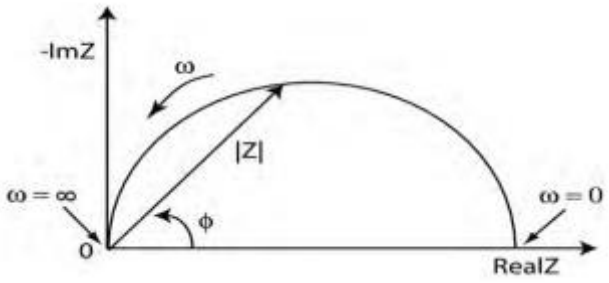


Figure 2. 16: Nyquist plot with impedance Vector [79].

In the plot above, the impedance can be expressed as a vector (arrow) of length $|Z|$. The angle between this vector and the X-axis, commonly called the phase angle'', is ϕ.

The major disadvantage of the Nyquist plot is that when looking at any data point on the plot, one cannot tell what frequency was used to record that point. The Nyquist plot in Figure 2.16 resulted from the electrical circuit in Figure 2.17. The semicircle is characteristic of a single time constant. Electrical impedance plots often contain several semicircles. Usually, only a portion of a semicircle is seen [80].

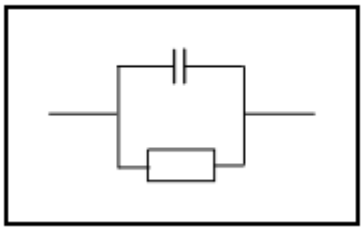


Figure 2. 17: Simple equivalent circuit with one-time constant $|Z|$ [79].

Impedance can also be presented in the form of a Bode plot. The impedance is plotted with log frequency on the X-axis, and both the absolute values of the impedance ($|Z| = Z_0$) and the phase shift on the Y-axis. The Bode plot for the electrical circuit in Figure 17 is shown in Figure 18. The Bode plot does show the frequency information.

© University of Venda

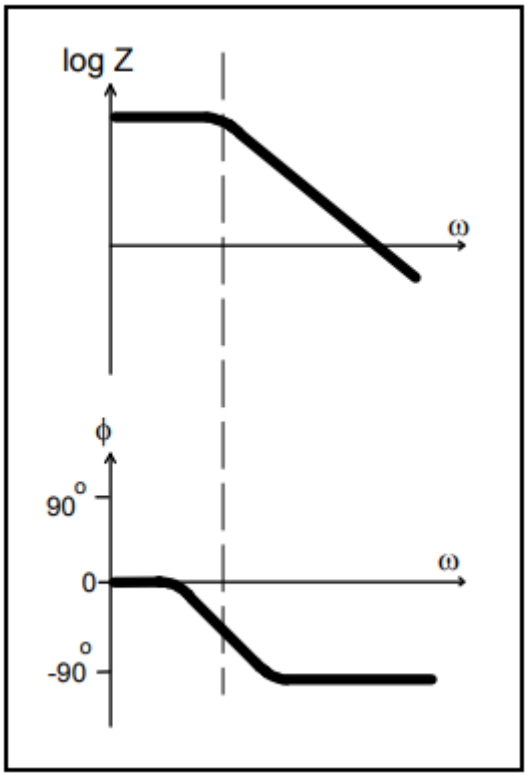


Figure 2. 18: Bonde plots for the circuit in Figure 17 [57].

- **Potentiodynamic polarization (PDP)**

Potentiodynamic polarization is an electrochemical technique that is normally conducted with three electrodes in an electrochemical cell, which are the reference electrode (RE), working electrode (WE), and counter electrode (CE). The metal whose corrosion process is being studied is known as the working electrode. RE is utilised as a reference when measuring the working electrode potential; therefore, current does not flow through it. The function of CE in the electrochemical cell is to give an electron source for WE. The three electrodes are all connected to a potentiostat, which permits the user to vary the metal sample potential in a controlled manner and measure the current flowing as a function of applied potential. The equilibrium potential attained by metal when there is no electrical connection is known as the open circuit potential (OCP). Prior to any electrochemical corrosion measurement taken, it is important for the metal to assume a stable OCP value [37].

PDP measurements are executed by scanning the sample potential from below and above the E_{corr} value to get the anodic and cathodic branches. The acceptable potential scan range is usually around several hundred millivolts. The data obtained is often plotted as a Log of current density versus the potential, as shown in Figure 2.19, which is known as the polarization curve.

© University of Venda

The current potential curves obtained under steady-state conditions are referred to as polarization curves. However, when the potential curve is obtained under potentiodynamic conditions, the curve is referred to as the potentiodynamic polarization curve.

Since the polarization curve depicts a profile showing the activation of the controlled cathode or anode reaction as the linear region as the potential is polarised away from the E_{corr} value, Corrosion current density (i_{corr}) and corrosion rate can be obtained by the Tafel extrapolation of the cathodic and/ or anodic branches of the polarization curve. This method takes the anodic and cathodic reaction as exhibiting the Tafel behaviour,

$$E = a + bLogi \tag{23}$$

This equation is derived from the Butler-Volmer equation, which depicts how the electrode current depends on potential. a and b are the constants, with b usually known as the Tafel slope and is often expressed in Mv/decate.

The Tafel extrapolation method has a shortcoming, which is the large potential excursion away from the E_{corr}, which can cause the modification of the sample surface. This means that if, for some reason, the measurements have to be repeated, the sample should be re-prepared exactly as before and must be allowed to stabilize in the electrolyte until such time a steady E_{corr} is achieved. This makes this method unsuitable for studies requiring pseudo-continuous measurements of i_{corr} values [81].

© University of Venda

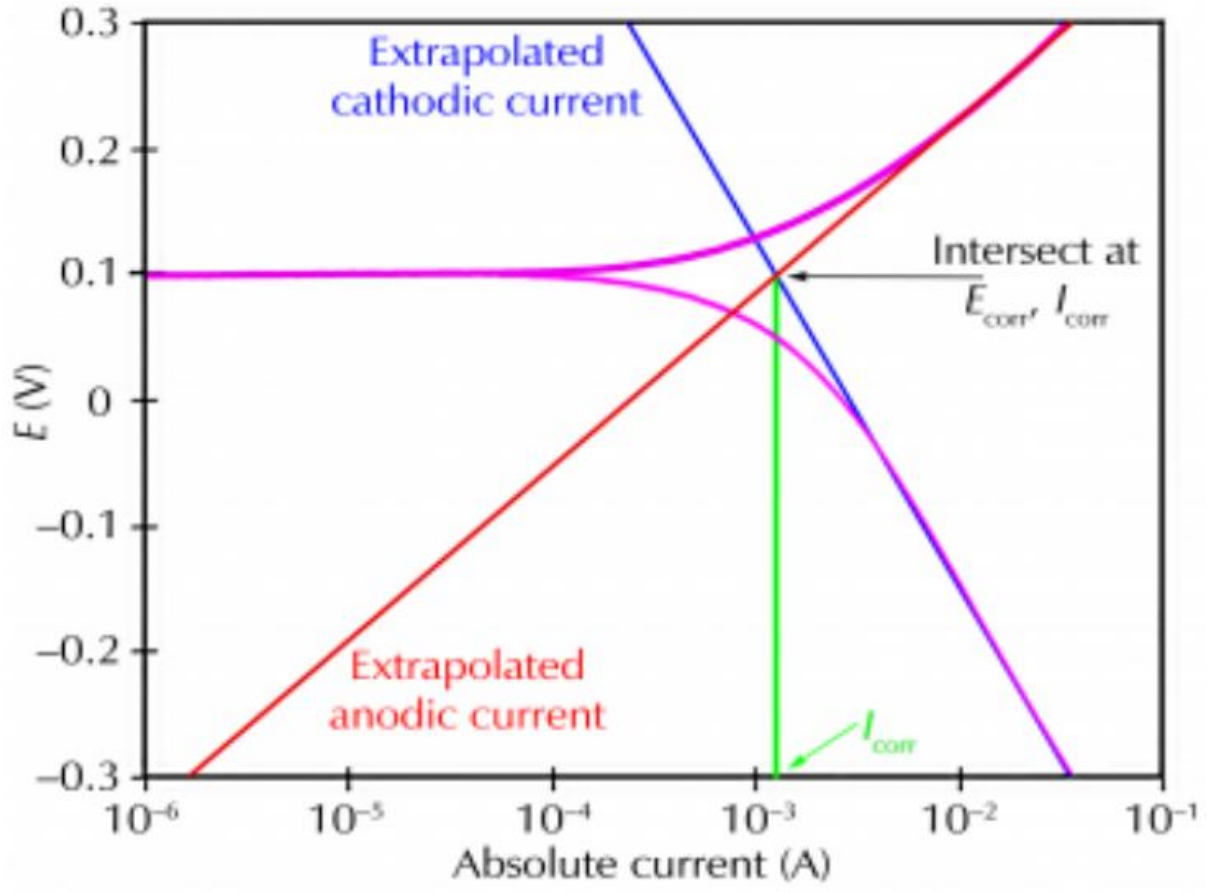


Figure 2. 19: Polarization curve for a corrosion process showing classical Tafel plots [37].

More information about interfacial electrochemistry, the presence of diffusion-controlled reactions and substrate passivation can be found in the PDP curve. For instance, in Figure 2.20 b., the cathodic profile shows that the cathodic reaction has a limited diffusion because a constant current (i1) is observed as the potential is varied. Figure 2.20 c. depicts a PDP profile consistent with a substrate going through passivation upon anodic polarization. At the anodic branch (more positive potential than E_{corr}), the corrosion current increases and reaches a maximum at the passivation potential (Epp) and then decreases. A small or low corrosion current is maintained as the potential is increased until the film is broken down because of pitting.

© University of Venda

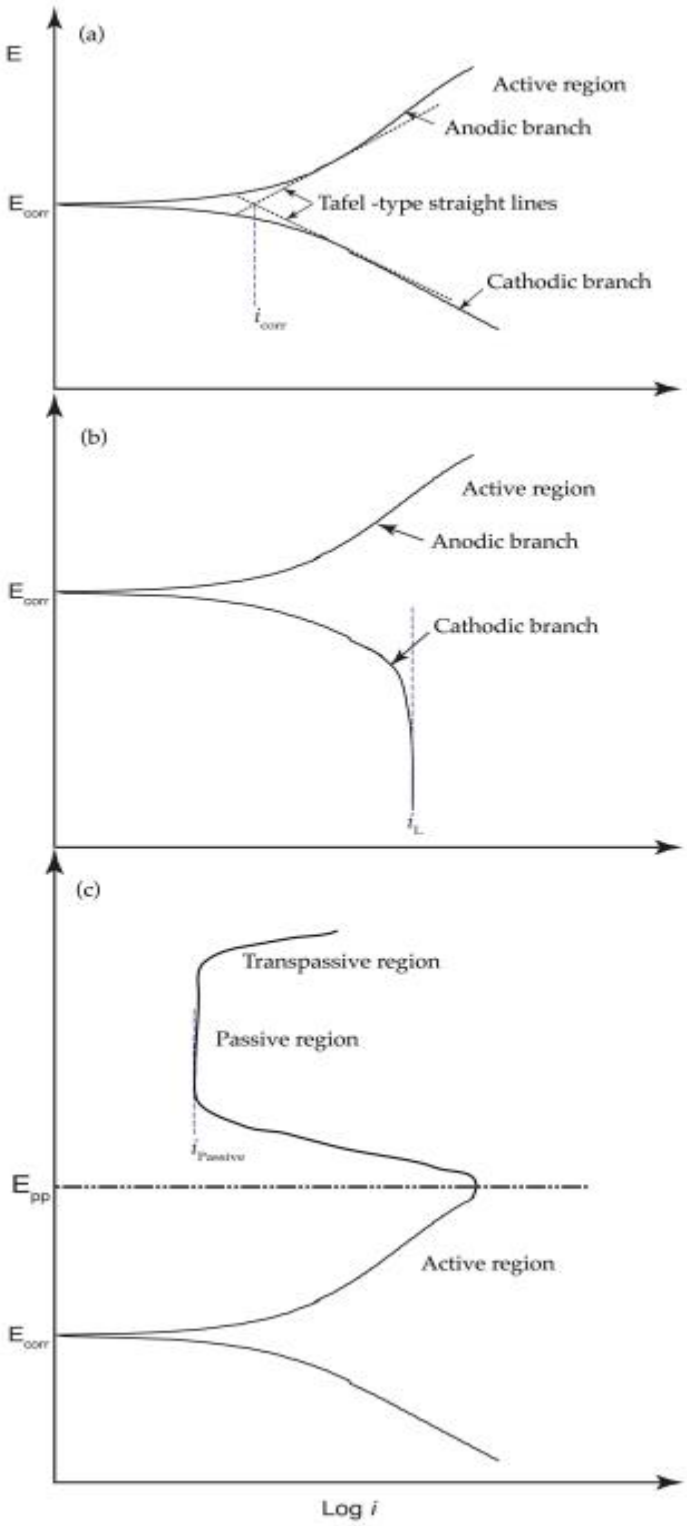


Figure 2. 20: Schematic diagram of PDP curves, (a) Activation controlled anodic/cathode reaction, with straight lines added to demonstrate Tafel extrapolation method for estimation of i_{corr} and E_{corr} (b) Cathode branch profile exhibits a constant/limiting current typical of diffusion-limited process. (c) An anodic branch profile is expected for a substrate undergoing passivation [53, 81].

© University of Venda

PDP measurements are very important for understanding corrosion. This is because the inhibitor may interfere with either cathodic, anodic or both reactions, which results in the corresponding shifts in E_{corr} values. Figure 2.21 shows how the shifts are structured and presented.

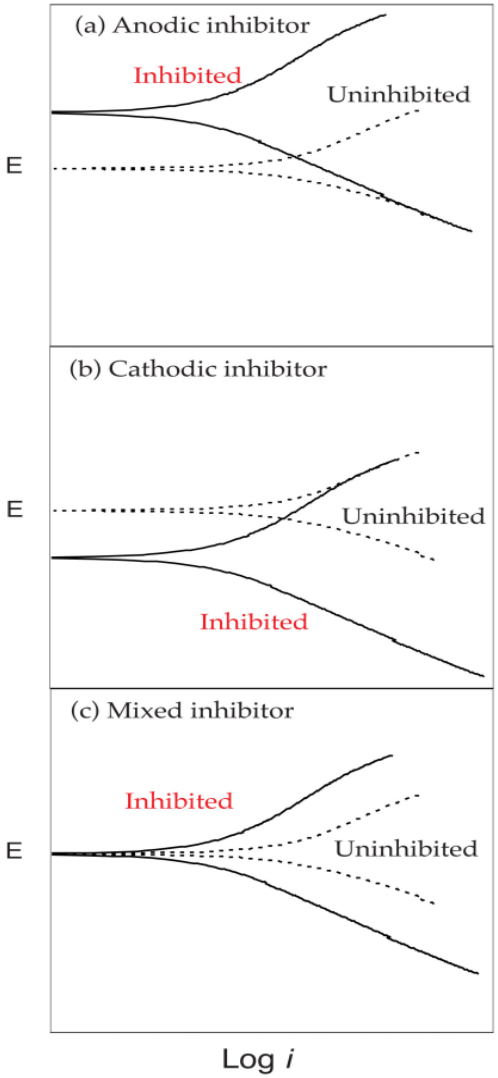


Figure 2. 21: Schematic graph showing the possible changes in the PDP curve due to the addition of cathodic, anodic or mixed inhibitors [53, 81].

2.8. Factors affecting the rate of corrosion

The metal is always shielded from corrosion if the chemicals and characteristics of the metal in its manufactured state remain effective. The rate and degree of corrosion of metal are determined by two fundamental factors: the nature of the metal (primary factor) and the nature of the corroding environment (secondary factor) [36].

© University of Venda

2.8.1. Nature of the metal

- **Purity of metal**

Impurities on the surface of the metal usually form a very small electrochemical cell under suitable environmental conditions and increase the rate at which the metal undergoes corrosion [36].

- **The surface state of the metal**

Smooth or polished surfaces are not easily attacked by corrosion compared to rough surfaces with different kinds of imperfections, such as dislocations and point defects [82]. The surface ratio of the cathode and anode directly affects the rate of corrosion. Sacrificial anodes are often utilised to prevent galvanic corrosion. Surface modification can hinder the reaction rate because the corrosion attack, in the simplest case, only takes place on the metal surface. Several methods, such as electroplating, spraying, painting, and cladding, can be used to protect the surface of the metal [83].

- **Position in gravimetric series**

Galvanic corrosion is a form of corrosion that occurs when two different metals are placed together in a corrosive electrolyte. A galvanic cell is another name for the complete corrosion process. Metals that are found at a higher position in the gravimetric series are more reactive and have a higher tendency for corrosion. Metals discovered at lower positions in the gravimetric series have the opposite effect [84]. The potentials of the metals are measured in comparison to the reference electrode in this series. When two metals that are far apart from the gravimetric series are joined together in the presence of a corrosive electrolyte, the galvanic corrosion speeds up. However, the opposite is the case when two metals that are very close to each other in the gravimetric series are placed together in the presence of an electrolyte since the rate of galvanic corrosion is substantially minimized. Gold is the least active metal in the galvanic series, whereas magnesium is the most active [85].

- **Protective film**

Aluminium metal is capable of forming a passive oxide layer that operates as a physical barrier between the corrosive medium and the metal, protecting the metal from corrosion. However, in other metals, such as iron, where rust is produced as a corrosion product, the oxide layer produced is not passive and is soluble, making the oxide layer ineffective in reducing the corrosion rate. Other metals such as zinc, molybdenum and tantalum are capable of forming a

© University of Venda

non-porous, insoluble oxide film in nature with very low electronic and ionic conductivity, making the layer effective in preventing further corrosion in such metals. Besides forming protective layers, these metals are also capable of self-repairing themselves when destroyed [86].

- **The physical state of the metal**

The orientation of the crystals, size, grain, and stress are some of the physical states of the metal that are crucial in determining the corrosion rate. For example, if the metal grain size is small, the rate of corrosion increases because the metal's solubility increases as its size increases. Microbial corrosion is one type of corrosion that increases with an increase in the grain size [87].

- **Reactivity of metals**

Passive metals, since they produce an extremely protective and thin oxide film on the surface of the metal, do not corrode often. Such metals include Titanium, Nickel, chromium, cobalt, etc [88]. This oxide layer formed is also able to repair itself during cracking.

- **The volatility of corrosion product**

Volatility is the ability of something to evaporate rapidly under normal conditions. In this context, volatile corrosion products rapidly escape the metal's surface, exposing the metal's inner layer for further corrosion attack [89]. This makes the corrosion in such metals to be continuous

- **Solubility of corrosion products**

Soluble corrosion products in the corrosive medium do not protect the metal from further corrosion but expose the inner layer of the metal, increasing the corrosion rate. The opposite is true when the corrosion products are insoluble in the corroding media. Therefore it can be said that the rate of corrosion depends on the solubility of the meta1 [90].

© University of Venda

2.8.2. Nature of the corroding environment

- **The effect of Temperature**

An increase in temperature can increase the rate of almost all chemical and electrochemical reactions. The greatest effect of temperature change is experienced when the rate-determining step is the activation process [52]. Reactions involved in the corrosion process are mostly electrochemical in nature; hence, they are also greatly influenced by the change in temperature. This is due to the fact that the temperature increase influences an increase in the conductance of the corrosive media, thereby resulting in an increase in the diffusion rate. Based on the amount of the activation energy, if diffusion rates are doubled for a given rise in temperature, the activation process may be boosted by 10 - 100 times [91]. Passivity decreases with increasing temperature in some instances, resulting in an increase in corrosion rate. A chemical reaction is expected to accelerate with an increase in temperature, increasing the corrosion rate based on thermodynamic principles [92, 93].

- **The effect of Humidity**

Humidity refers to the quantity of water vapour or moisture in the air. The time in which the metal is subjected to moisture or humidity (time of wetness) contributes greatly to speeding up the corrosion of that metal [94]. This happens when the oxygen in the atmosphere, the water in the moisture, and the metal react. It can be said that the more the metal is subjected to moisture and a watery environment, the more the metal is likely to be prone to corrosion. It can also be said that an increase in the amount of humidity also increases the corrosion rate because the humidity contains the electrolyte that is important for corrosion to occur [95].

- **The effect of pH**

The pH of a solution affects the supersaturation of a chemical or electrochemical reaction, which influences the development of a protective layer, directly affecting the rate of corrosion. The increase in the solution pH results in high supersaturation, which then causes an increase in the film's precipitation rate [96]. However, corrosion was found to occur more frequently in acidic media (pH 7) than in neutral (pH = 7) or alkaline (pH > 7) media [97]. In basic or alkaline conditions, metals like zinc, palladium, and aluminium usually form complexes, which is why they corrode considerably faster in alkaline media. At very high pH, metals like iron produce a protective iron oxide film that inhibits corrosion. However, catastrophic corrosion takes place at very low pH levels. The pH has a significant impact on the corrosion of all metals. Since a lower pH enhances the rate of hydrogen evolution, which speeds up the corrosion process, a

© University of Venda

lower pH increases the speed at which the metal corrodes [98]. The corroding metal surface may display activity, passivity, or immunity in situations where the pH of the corrosive medium changes

- **Effect of atmospheric gases present in the air**

Gases like carbon dioxide, sulphur dioxide, water, etc., present in the atmosphere or fumes of acids like nitric acid, sulphuric acid [99], etc., form the medium, which is more acidic above the metal surface because these gases are soluble in water to form acids. Acids have more conducting power, enhancing the corrosion rate.

- **Effects of the nature of the electrolyte present**

For corrosion to occur, an electrolyte must be present in most cases. For example, an electrolyte such as hydrogen chloride or sodium chloride contains anions such as chloride that destroy the protective layer on the surface of the metal. This causes the inner metal surface to be exposed to further corrosion. However, some anions in the electrolyte, such as sulphite, and silicates form an insoluble film on the surface of the metal that protects the metal from corroding further [100].

- **Effects of concentration of oxygen**

In the presence of moisture and oxygen, the rate of corrosion accelerates. Corrosion is more likely to occur in an oxygen-deficient environment, although the corrosion rate is much slower [101]. When a metal is exposed to an aqueous medium, and one region of the metal containing more oxygen interacts with an electrolyte than the other area of the metal, the greater oxygen concentration area is cathodic compared to the remaining surface. As a result, differential aeration creates numerous concentration cells, which enhances the rate of corrosion because of the electrochemical process. The rate of corrosion decreases in the presence of dry oxygen.

© University of Venda

2.8.3. Other factors that affect the rate of corrosion may include:

- **Availability of corrosion inhibitors:**

Corrosion inhibitors are chemical substances that, when added to the corrosive environment in minute quantities, limit the corrosive environment's aggressiveness on a metal. It has been largely observed that when the inhibitor concentration increases, the corrosion rate decreases. However, when the inhibitor concentration is reduced, the rate of corrosion increases [39, 41, 42, 49].

- **Fluid speed**

Diffusion effects are the main causes of corrosion by the motion of fluids. When metals that are protected by chemical coatings are subjected to fluids carrying fast-moving particles, they experience this type of corrosion. The chemical coating is scraped off by the fast-moving particles in the fluids, leaving the metal vulnerable to corrosion. High fluid velocity is considered to be linked to increased corrosion [50].

2.9. Consequences of corrosion

Corrosion tremendously impacts our communities and poses serious threats to important aspects of our daily lives, such as health, economics, safety, and cultural and technological advancement [102].

- **Economic effects**

In 2016, the National Association of Corrosion Engineers (NACE) released the Internal Measures of Prevention, Application and Economics of Corrosion Technology (IMPACT), which appraised the global cost of corrosion to be around 3.4% of the Global Domestic Product (GDP), equivalenting to approximately $2.5trillion U.S dollars [103]. The direct cost of corrosion in the United States in 2011 was 3.1% of the $15.1 trillion US gross domestic product (GDP), which in the same year was $468.1 billion. Based on a 1998 NACE study, the indirect cost of corrosion is estimated to be greater than or equal to the direct cost [104]. Through the application of the already available corrosion control measures, it is estimated that between 15 and 35% of the cost of corrosion can be saved, which is between $ 375 and $875 billion annually on a global basis [10]. These figures clearly show the impact of corrosion. Major challenges experienced in industrial sectors, people's lives, and the nation are due to the economic effects of the consequences of corrosion, which have led to the great loss of

© University of Venda

resources, properties, and productivity in various sectors. For example, in oil and gas sectors, pipelines, electrical power and chemical processing plants are affected by corrosion, which in some cases leads to their shutdown and loss of jobs and valuable resources. Hot water heaters, such as gassers and electric kettle also experience corrosion which may lead to their malfunction earlier than their life span, even worse if left unattended, such corrosion can contribute to a bitter taste of water because of the unalleviated level of toxic metals such as zinc, copper and lead which can cause health problems.

- **Health effects**

In recent years, the health medical sector has been skyrocketing with new inventions made possible by technological advancement. The use of prostheses such as implants, plates, pacemakers and hip joins has brought quite a revolutionary change in our medical sector. However, despite these new developments, corrosion always becomes a stumbling block and hinders further developments. For instance, fractures of weight-bearing prosthetic devices, broken connections in pacemakers, and failures through inflammation caused by corrosion products in tissues around implants are some of the problems caused by corrosion[105]. With all these challenges, all is not lost since prosthetic devices are constantly improving, taking into account corrosion every day [15].

- **Technological effect**

Technology is the driving force leading to the 4^{th} industrial revolution. It is used as a measure of how developed the country is. However, most technological endeavours and advances are hindered by corrosion. This is because materials that would have been used for certain technological advances are expected to endure very harsh conditions of high temperatures, high pressure, and very corrosive environments [105]. For example, in the energy sector, corrosion affects the machines utilised to drill oil in the sea and land, compromising the quality of the oil and the advancement in this sector. Due to global warming, corrosion is becoming a massive problem since high temperatures also influence it, and this is sabotaging the innovation of workable technological systems [58].

- **Cultural effects**

All over the world, museums are filled with various artefacts of the past generation. These precious treasures are of paramount importance in terms of preserving the culture of one group of people. These artefacts are also used to narrate the lives of our ancestors to the next

© University of Venda

generation. They are also used as a means of tourist attraction. However, these artefacts are becoming endangered by corrosion. Some of these artefacts are deteriorating in such a way that they even lost their appearance. Because of that, many museums around the world even go as far as hiring corrosion experts to protect these artefacts [105]. Depending on culture, some worship these artefacts as their gods, and this shows how sentimental they are to humans. The aforementioned corrosion effects demonstrate its consequence on people's day-to-day lives, and as such, measures to prevent and control it must be applied [15].

- **Safety effects**

If corrosion cannot be eradicated, all metallic materials, such as steel structures, bridges, aircraft and cars, and the lives and safety of people will always be compromised. When steel structures and bridges collapse due to corrosion effects, many people can lose their lives, and some get badly injured [105]. The property will also not be spared. This shows that not only will people's safety be in danger, but many essential properties will also be affected. More money will be distributed to replace the damaged properties caused by corrosion, and above that, the indirect cost of corrosion, like natural resources, potential hazards, and loss of lives, will also be accounted for financially. As such, people's daily lives, industries, and the world have been affected deeply by corrosion [15].

2.10. Corrosion control method

Since there are numerous types of corrosion, several corrosion control methods can also be employed. A suitable corrosion control method must be chosen based on factors which include the nature of the corrodent environment, the type of corrosion, the cost of the corrosion control method, the application, and the type of metal [37]. These methods increase the life span and usefulness of different metals so that they can perform their assigned duties for a longer time than untreated metals. Coating, inhibitors, cathodic and anodic protection, surface cleaning and inspection, and material selection are just a few of the strategies that can be utilised to control the corrosion of metals. In this study, corrosion inhibitors will be used to control the corrosion of mild steel, aluminium and zinc in hydrochloric and sulphuric acids as corrosive media. Some of the methods of controlling corrosion are discussed further below.

© University of Venda

2.10.1. Corrosion inhibitors

Corrosion inhibition is one of many protective measures against metal corrosion attacks [106]. As a way of controlling corrosion in industries, inhibitors are often added to the corrosive environment, which in most cases is the acids used. According to the American Society for Testing and Materials (ASTM-G15-08), a corrosion inhibitor is a chemical substance or a mixture of chemical substances that decreases or prevents corrosion in corrosive environments when present in proper concentrations and forms [107]. Corrosion inhibitors, on the other hand, are defined by the National Association of Corrosion Engineers (NACE) as a chemical that, when applied to a corrosive environment in minute concentrations, delays the corrosion of the material. Recently, the use of corrosion inhibitors has enjoyed the preference as a first choice in controlling the corrosion of metals. The reason behind its preference is that it is economical, effective, and convenient, and it can be added in situ during the manufacturing process, making it the most flexible way of controlling corrosion [108-113]. Inhibitors can be found naturally, and some are artificially added as an alternative for corrosion control. Artificially introduced inhibitors find applications in processes such as acid descaling, pickling, cleaning, etc [39, 114]. Corrosion inhibitors are often organic or inorganic compounds that are soluble in the corrosive medium and eventually form a protective film on the metal's cathodic or anodic area. Compounds that provide good corrosion inhibition have been found to contain oxygen, nitrogen, phosphorus and sulphur heteroatoms, π-electrons in conjugated double or triple bonds and aromatic rings. It has been discovered that nitrogen-containing organic compounds work best as inhibitors for hydrochloric acid media, while those that contain sulphur atoms have been found to provide maximum inhibition performance in sulphuric acid media [115]. Corrosion inhibitors that combine two or more different heteroatoms mentioned above have also shown remarkable corrosion inhibition in acidic environments [116]. In other instances, two or more compounds can be combined to achieve better inhibition in the corrosive environment, generally known as synergism. Toxicity has seen a sharp decrease in the use of synthetic organic compounds as corrosion inhibitors. Recently, the use of plant parts extracts as corrosion inhibitors has received huge attention because of their non-toxicity.

© University of Venda

2.10.2. Proper selection of material

The choice of material is usually chosen during the design phase, and it is based on criteria such as the material's chemical, visual, mechanical, and physical properties, as well as its cost. Titanium, for example, has a high corrosion resistance but is much more expensive than steel and is not as ductile as steel. Carbon steel is the greatest material of choice in the oil production system, especially for materials such as vessels, wells, tanks, and pipelines, due to its excellent mechanical qualities and low cost. Nonetheless, in circumstances where very high corrosion resistance material is required, other metals, such as stainless steel or cobalt-chromium metals, may be used as alternatives [44].

2.10.3. Cathodic protection

Cathodic protection works by polarizing the material that is to be protected to more negative potentials than that of the corrosion potential, therefore preventing the corrosion of the material (Anodic reaction) thermodynamically. For this procedure to work out, the external power supply can be used. Another useful method is the utilisation of sacrificial anodes. In this regard, the anode is composed of a very active metal compared to the metal to be protected. The metal becomes the cathode of the new corrosion cell. If the sacrificial anode is the one continuing to corrode, the cathodic metal will always be protected. Underground structures or materials, such as water storage tanks, ship hills, buried pipelines, and marine facilities, are typically protected with this type of corrosion protection [44].

2.10.4. Linings, Coatings and Non-Metallic piping

The lining is a form of a coating that is used internally. The coating is generally described as the application of thin material, usually in the form of a liquid or powder, that, when it solidifies, becomes continuously and firmly attached to the material that is being protected. The lining is a name given to a coating that is being applied internally. Several requirements must be met for a good coating, such as that it must be flexible, have good adhesion, have no porosity, be resistant to chemical attacks from the fluids to be contacted, and be stable at the working temperatures. For a variety of applications, non-metallic piping is recommended since it does not corrode but instead deteriorates. Polyvinyl chloride (PVC) is one of the types of this non-metallic piping and is mostly preferred for this category because it can be softened, reshaped and reheated repeatedly without destroying it. In situations of high pressure and

© University of Venda

weight, PVC and other polymer-based materials are not a good choice for use because material integrity is of paramount importance, and in this regard, the application is usually limited to metals.

2.11. Importance of corrosion inhibitors

In the United States and some other countries, education on corrosion is a very crucial aspect. There are degree programs, certificate programs, general education and training, and company in-house training based on corrosion. Some national universities even provide corrosion control courses in their engineering programmes. Organizations such as the National Association of Corrosion Engineers (NACE) and the Society for Protective Coatings (SPC) give courses and certificates from basic corrosion to coating inspectors and cathodic protection specialists. All of this points to the importance of corrosion control and its global economic impact [117].

Scientists are interested in the use of corrosion inhibitors as a way of managing corrosion for two important reasons. Firstly, safety concerns such as industrial corrosion can cause process breakdowns that can lead to the release of chemicals which are harmful to human health and the environment. Secondly is the economic issue. According to NACE research published in March 2016, corrosion damages amount to roughly 3.4 % of the global domestic product (GDP) or around $2.55 trillion US dollars. According to some research, the cost of corrosion in 2002 was projected to be approximately $300 billion [118] [119].

2.12. Classification of corrosion inhibitors

Corrosion inhibitors can be divided into two distinct types: environmental conditioners and interface inhibitors. The first reduces corrosion by scavenging the corrosive substances on the medium. Scavengers can be employed to reduce corrosion in alkaline solutions where oxygen reduction is a frequent cathodic reaction [101, 102]. Interface corrosion inhibitors form a protective layer on the metal surface to control corrosion. The interface inhibitors can be divided into two subcategories: vapour and liquid phase inhibitors. The vapour phase inhibitors are also referred to as volatile corrosion inhibitors and are defined as compounds that can be carried into a closed environment by the volatilization from the source to the site of corrosion [102]. In boilers, volatile corrosion inhibitors are utilised to prevent corrosion in the condenser tubes by being transported with steam. Depending on the electrochemical reactions they inhibit,

© University of Venda

the liquid phase inhibitor is further divided into cathodic, anodic, and mixed corrosion inhibitors [45]. As displayed in the diagram below, the anodic and mixed corrosion inhibitors can also be subcategorised further.

Corrosion inhibitors hinder the corrosion process by:

- the electrical resistance of the metallic surface
- diminishing the diffusion of ions to the metal surface.
- increasing the anodic or cathodic polarization behaviour, which can be monitored through the Tafel plots.

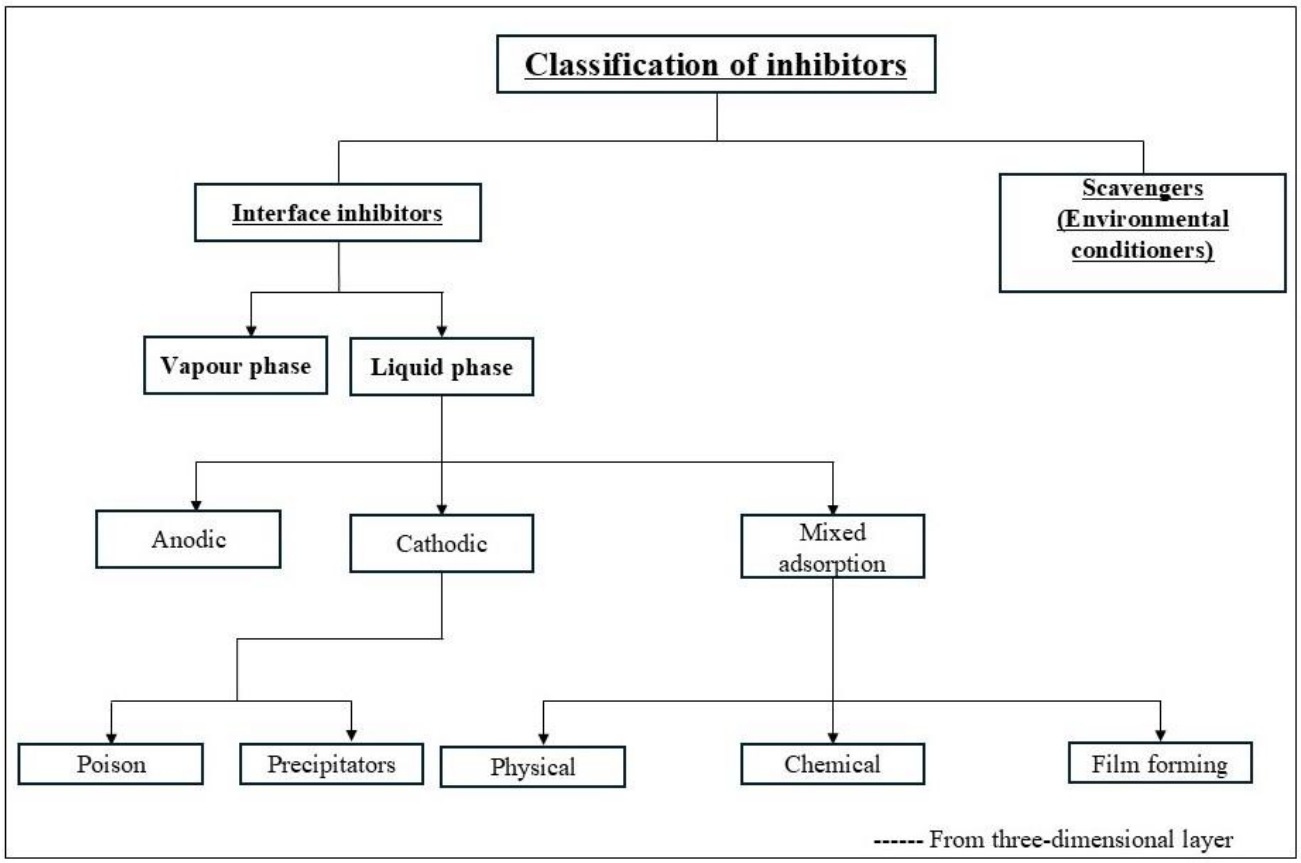


Figure 2. 22: Classification of corrosion inhibitors [52, 120, 121].

© University of Venda

2.12.1. Types of corrosion inhibitors

- Organic inhibitors

Organic compounds that are used as inhibitors work by adsorbing on the surface of the metal, also referred to as film formation. They can also act as anodic, cathodic or a combination of anodic and cathodic inhibitors, which are referred to as mixed inhibitors. Organic inhibitors with high inhibition efficiency and low environmental hazard are the most desired [103]. These inhibitors need to be soluble in the medium surrounding the metal since they are known to generate a protective hydrophobic coating on the metal's surface that acts as a barrier to the electrolyte's dissolution [104]. Because they feature ionizable hydrophobic portions, organic compounds utilized as corrosion inhibitors are highly effective when polar functional groups, such as S, O, and N atoms, pi electrons, and heterocyclic compounds, occur in the molecule [36, 122]. The adsorption process is started by this polar functionality, which acts as the reaction centre. When it comes to inhibiting corrosion, organic molecules with pi bonds outperform organic acids that contain nitrogen, oxygen, and sulfur. Although they function well, their toxicity to the environment and biological systems makes them less appealing for utilization [105].

- **Anodic (Passivating) Corrosion Inhibitors**

Anodic inhibitors are typically used in near-neutral fluids where hydroxides or oxides, which are soluble corrosion products, are generated [45]. In order to prevent the anodic metal dissolution reaction, they promote the production of passivating layers. As a result, another name for anodic inhibitors is passivating inhibitors [123]. Instead of being inhibited, corrosion may worsen when the anodic inhibitor concentration is too low. The critical concentration at which inhibitors become effective is determined by the type and concentration of aggressive ions [97, 102]. The metallic surface is pressed into the passivation range by a large anodic shift in the corrosion potential caused by anodic inhibitors. Oxidizing anions and non-oxidizing ions are the two types of passivating inhibitors. To passivate steel, non-oxidizing ions, which include tungstate, molybdate, and phosphate, need oxygen to be present. Oxidizing anions, which include substances like nitrite, nitrate, and chromate, passivate the steel in the absence of oxygen. Due to their efficiency, these inhibitors are the most often utilised. Inhibitors such as chromium have recently been utilised in several applications, such as refrigerators and rectifiers, because of their affordability.

© University of Venda

- **Cathodic Corrosion Inhibitors**

Cathodic inhibitors work to prevent corrosion by increasing the surface impedance and blocking the diffusion of reducible species to cathodic areas by decreasing the rate of reduction (cathodic poisons) or precipitating, especially in the cathodic areas (cathodic precipitators) [124]. Cathodic inhibitors can provide inhibition through three different mechanisms: cathodic precipitates, cathodic poisons, and oxygen scavengers. In contrast, cathodic poisons such as sulphides and selenides are adsorbed on the surface of the metal, whereas compounds of arsenic, bismuth, and antimony are reduced at the cathode and result in a metallic coating. Inorganic anions like borates, silicates, and phosphates create a protective film in near-neutral and alkaline solutions that slow the diffusion of oxygen to the metal's surface, reducing the cathodic reaction rate. Cathodic precipitators, such as zinc, magnesium, and calcium ions, shield the metal from corrosion by precipitating as oxides and adding an additional layer of protection to the metal. Oxygen scavengers are known to prevent cathodic depolarization caused by oxygen, which prevents corrosion. At room temperature, sodium sulphate is the oxygen scavenger that is most frequently used [36].

- **Mixed Corrosion Inhibitors**

Mixed corrosion inhibitors work by suppressing both the reactions of the anode and cathode [36, 124]. They accomplish this by adhering to the entire metal surface and creating a thin protective layer. The precipitates that form on the metal's surface as a result of the film's formation inadvertently restrict both cathodic and anodic sites. Film-forming inhibitors and adsorption inhibitors are other names for mixed inhibitors. They are now among the most preferred concrete inhibitors. The most common mixed corrosion inhibitors are phosphates and silicates. Sodium silicate is used in residential water softeners to avoid the occurrence of rust in water. Mixed corrosion inhibitors are able to limit the corrosion rate of metals without significantly changing the corrosion potential. The overall effects on the corrosion potential are insignificant but may move either towards the anodic or cathodic site [50].

2.13. Toxicity of corrosion inhibitors

In the industrial sectors, the application of corrosion inhibitors as a measure of controlling corrosion is the most preferred among other techniques. This is purely because these measures happen to give high corrosion inhibition or protection. Regardless of their high percentage inhibition, the majority of these corrosion inhibitors, which are mostly organic or inorganic,

© University of Venda

are known to be harmful and toxic to the environment [125]. For example, sodium chromate was mainly utilised as a booster or additive for corrosion inhibitors in aqueous heating and cooling systems. However, since it was accused of having the potential to cause cancer (carcinogenic), it is no longer in use. Acetylenic alcohols, which were normally used as acidizing inhibitors due to their effectiveness, easy availability, and inexpensiveness, also ran out of favour because they were only effective at high concentrations and very toxic, causing difficulty in handling and disposal of waste [44].

Another reason for their depreciated use was that they produce toxic vapours under acidizing process conditions. Another example is that of theorea derivatives used in the past as corrosion inhibitors. However, since they were found to isomerize into toxic compounds and also speed up hydrogen uptake by metals, they were considered unsafe for usage. Another toxicity of corrosion inhibitors can be illustrated based on the use of n-alkanethiols as corrosion control for copper and iron metals, which provided very high inhibition efficiency. Its range of usage in the industries depreciated rapidly because of its toxicity [44].

Although many toxic inhibitors have been scraped off for usage, there are still a lot of toxic corrosion inhibitors in use. With this regard, it is still in the best interest of scientists to find inhibitors that will be able to provide high corrosion protection efficiency for different metals with no hazardous impact on both living organisms and the environment. This initiative is also driven by the call for green chemistry. Recently, many corrosion studies have shifted the focus to the utilisation of natural products, such as different plants, as corrosion inhibitors since they pose little or no environmental impact [126].

2.14. Metals usually used in corrosion studies.

- **Zinc**

Zinc is one of the most widely utilised metals in different industrial processes. It finds its greatest use in iron's galvanization (protective coating). This is possible because zinc is found higher on the electrochemical scale than iron, thereby reducing it to the metal through cathodic protection, eliminating rust in the process [127].

Zinc has the ability to slow down corrosion by generating an insoluble basic carbonate layer that adheres tightly to its surface. Zinc still experiences the most corrosion when compared to aluminium but less when compared to mild steel alloy. The environment that the zinc metal

© University of Venda

finds itself in significantly impacts how quickly it corrodes. For instance, it has been discovered that zinc corrodes least quickly in conditions with pH levels between 6.5 and 12.

Zinc corrodes rapidly in conditions like acidic solutions and marine, making it unsuitable for use in these environments. As a result, zinc must be protected from these conditions. For example, Corrosion occurs when sulphate ions come into contact with zinc, and the behaviour takes the form of the half-reactions shown below [74].

The zinc is first oxidized into zinc 2+ ions according to Equation 24, given as,

$$Zn_{(s)} \rightarrow Zn^{2+}{}_{(aq)} + 2e^{-} \quad (24)$$

Then, the hydrogen ions are reduced to hydrogen gas by taking up the two electrons of the oxidized zinc, as shown in Equation 25, given as,

$$2H^{+}{}_{(aq)} + 2e^{-} \rightarrow H_{2\,(g)} \quad (25)$$

When Equations 24 and 25 combine, the final reaction is produced in the form of Equation 26, given as,

$$Zn_{(s)} + H_2SO_{4\,(l)} \rightarrow ZnSO_{4\,(aq)} \quad (26)$$

- **Mild steel**

Mild steel is also known as steel or iron, and when subjected to an alkaline environment, its surfaces form passive layers. The corrosion process is initiated when the passivating layer dissolves in chloride ions. This is due to the fe^{3+} ion's ease of hydrolysis exposure, which means that if an oxygenated differential cell is made in a salt chloride environment, there will be a very high chloride concentration within the small crevices or cracks. The passivating layer dissolves as a result of the increased acidity brought on by the hydrolysis of the iron. The passivating layer is composed of two layers, the inner first layer being magnetite or Fe_3O_4 and the outer second layer being feOOH, commonly known as rust. The movement of oxygen and other corrosives is made feasible by pores in the outer layer that extend all the way down to the inner layer. Because of the diffused oxygen through the pores, the Magnetite will become oxidized to hydrated fe_2O_3 and feOOH. The pores in the inner layer of Magnetite will be greatly enlarged due to the acid dissolving the oxide on the steel surface if exposed to an acidic environment. This will allow the Fe ions to reach the metal's surface [128]. The majority of steels produced are exposed to outdoor environments, frequently in extremely polluted

© University of Venda

environments where corrosion is far more severe than in pristine rural settings. The illustration below depicts how corrosion from brine water affects the steel.

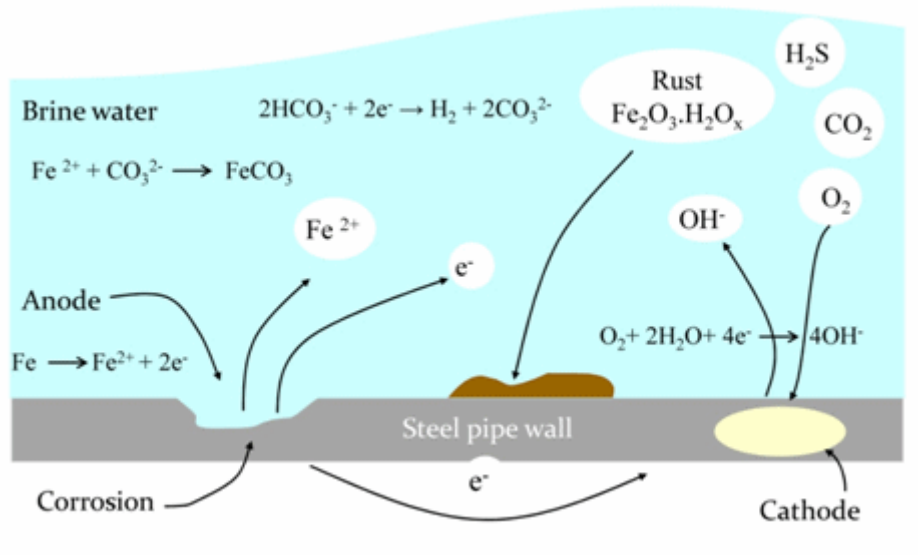


Figure 2. 23: Internal corrosion of a crude oil pipeline made of mild steel [93].

Another example of mild steel reaction with H_2SO_4 can be well represented with iron using the following two half-reactions expressed by Equations 28 and 29:

$$Fe_{(s)} \rightarrow Fe^{2+}{}_{(aq)} + 2e^- \quad \text{(oxidation)} \tag{27}$$

$$2H^+{}_{(aq)} + 2e^- \rightarrow H_{2\,(g)} \quad \text{(reduction)} \tag{28}$$

Even though mild steel corrodes in concentrated sulfuric acid at a relatively low rate, little corrosion can still occur. The reaction products from this corrosion process, as shown in Equation 29, are iron sulphate and hydrogen gas.

$$Fe_{(s)} + H_2SO_{4\,(l)} \rightarrow FeSO_{4\,(s)} + H_{2\,(g)} \tag{29}$$

The comparatively thin iron sulphate layer can be disturbed by high acid velocities or other liquid disturbances. Because hydrogen can essentially wipe off the mechanically fragile iron sulphate layer, which is the sole thin layer protecting the steel from corrosion, it is recognised to be a concern for the corrosion of mild steel in sulfuric acid conditions.

© University of Venda

- **Aluminium**

Aluminium metal is the second most utilised metal in the universe behind steel, with an annual consumption of about 25 million metric tons [129]. Aluminium and its alloys have various applications in engineering due to their electrical and thermal conductivity, light and heat reflectivity, the combination of strength with lightness and good corrosion resistance [39]. It is regarded as one of the metals having a high affinity for oxygen and is particularly reactive. It is also considered to be active because of its natural ability to oxidize quickly. The fact that it oxidises swiftly by nature adds to the idea that it is active. In addition, aluminium metal has excellent resistance to a wide range of chemical agents, including sulfuric acid. This resistance is attributed to its oxide layer, which is produced on its surface and is inert and has a protective character. Aluminium quickly interacts with oxygen present (in the water, soil, or air) to produce aluminium oxide, which then forms the oxide layer. This layer of formed aluminium oxide protects the aluminium core from any further reactions and is chemically bonded to the metal's surface. The film made of aluminium oxide is durable, tenacious, and immediately self-renewing. This is a particularly distinct type of steel corrosion (oxidation) in which rust builds up on the metal surface and later peels off, exposing the fresh metal to corrosion. The formation of the oxide layer causes the rate of corrosion of aluminium in most environments to decrease rapidly with time, a phenomenon which is impossible to find in other metals such as zinc and mild steel [39]. Because of these advantages, it is no surprise that it is extensively used for ground transport, automotive industries, ship and aerospace building [129]. However, aluminium is no match for corrosion since it gets consumed quickly when exposed to other harsh environmental conditions that remove the oxide covering film. Aluminium's protective oxide film is typically stable in the pH range of 3.5 to 8.5, according to the US Army Corps of Engineers. However, the oxide layer becomes unstable and finally breaks down in extremely acidic and basic environments, and its automatic renewal may not occur with sufficient speed to prevent the metal from being exposed and undergoing corrosion again.

Chloride and fluoride ions, which have the capacity to destroy the oxide film and cause corrosion, are typically responsible for aluminium metal corrosion. When chloride ions are present in the solution, aluminium metals are known to suffer pitting corrosion [70]. The following is a description of the chemical processes involved in the pitting corrosion of aluminium metal.

© University of Venda

First, as Equation 30 shows, the aluminium metal oxidises.

$$Al_{(s)} \rightarrow Al^{3+}{}_{(aq)} + 3e^- \quad (30)$$

Following this, the aluminium 3+ ion and water undergo a reaction to form the aluminium hydroxide, as shown in Equation 31.

$$Al^{3+}{}_{(aq)} + 3H_2O_{(l)} \rightarrow Al(OH)_{3\ (l)} + 3H^+{}_{(aq)} \quad (31)$$

According to the reaction in Equation 32, the process involving hydrogen evolution occurs at the intermediate cathode given as,

$$2H^+{}_{(aq)} + 2e^- \rightarrow H_{2\ (g)} \quad (32)$$

Finally, the reaction of oxygen reduction occurs according to Equation 33, given as,

$$O_{2\ (g)} + 2H_2O_{(l)} + 4e^- \rightarrow 4OH^-{}_{(aq)} \quad (33)$$

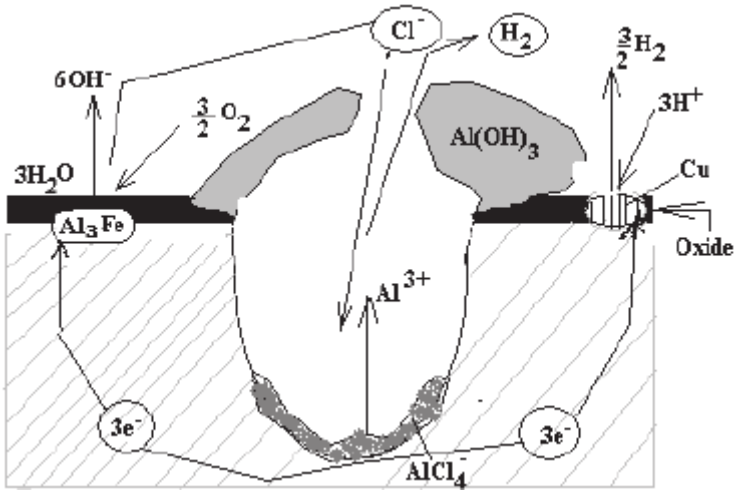


Figure 2. 24: Schematic diagram of the pitting corrosion of aluminium [71].

2.15. Plant extracts as corrosion inhibitors

The exploitation of natural products as corrosion inhibitors can be dated back as early as the middle of the 19th century. Baldwin was issued the very first patent in natural products corrosion inhibition, in which he used molasses and vegetable oils for pickling steel sheets in acids. In the early days of the utilisation of natural products as inhibitors, Marangoni and Slephanelli inhibited the corrosion of iron in acids using extracts of glue, gelatina and bran [130].

© University of Venda

Plants are made up of different kinds of chemicals, and among those, the non-nutritive components that are importantly responsible for the plant's colour, taste, and smell are called phytochemicals [131]. The phytochemicals can be classified into groups such as terpenoids, organic compounds and polyphenols, which can also be classified further into other groups. The phytochemicals have molecular structures resembling synthetic organic compounds, which can be used as corrosion inhibitors [9]. With that said, plants are largely considered to be the source of naturally occurring compounds. Most of these compounds contain complex molecular structures and have various physical, chemical and biological properties. A handful of these compounds have found a number of uses in traditional applications like biofuels, pharmaceuticals and as traditional remedies [132]. These compounds are leached out of the plant in the form of a crude known as an extract. This extract is regarded as a solution made up of active principles of plant parts and a particular medium functioning as a solvent [133]. The extracts are normally obtained from the entire plant or parts that contain high concentrations of the active principles generally known as phytochemicals, as shown in Figure 2.25, which shows the different kinds of phytochemicals which are obtained at various parts of the plant [134-138]. In all the extraction techniques, such as Soxhlet and maceration extraction, the yield of the extract depends solely on the polarity of the solvent utilised. The active principles found in a particular extract determine the properties of its purpose; hence, a particular plant based on its concentrations and active principles can be linked with some benefits. In most cases, the extracts are mainly recognised for their antiviral, antioxidant, antimicrobial and anti-inflammatory effects. The extracts of plant leaves, flowers, seeds, and fruits contain active compounds that are very promising as corrosion inhibitors for various aggressive environments. The corrosion inhibition provided by these extracts can be said to have a synergistic effect [133]. Natural products (plant extracts) have recently enjoyed the first-choice priority as corrosion inhibitors for metals in different corrosive media. This is because plant extracts are eco-friendly, low-cost, bio-degradable, and easily available [132].

© University of Venda

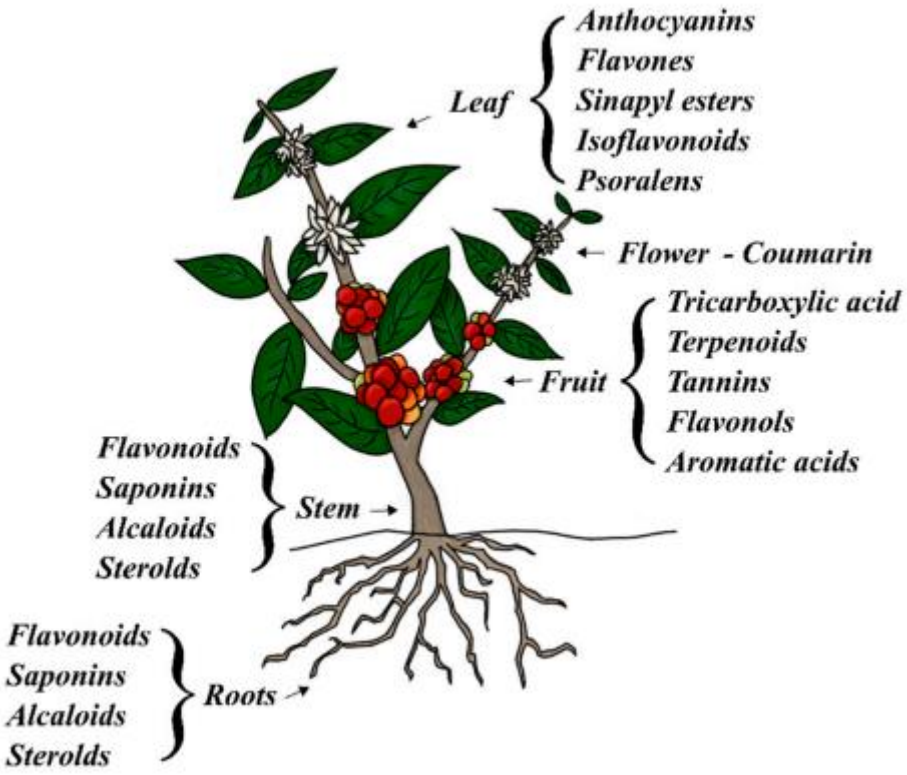


Figure 2. 25: Basic parts of the plant and its common active compounds [133, 139]

2.16. *Helichrysum kraussii*.

Helichrysum consists of about 500-600 species in the Asteraceae family, Inuleae tribe and Gnaphaliinnae subtribe. They are abundantly found in Africa, with reportedly about 244-250 species in South Africa and Namibia, with large morphological diversity [140]. These species are also found in Australia, southern Europe, southern India, south-west Asia and Sri Lanka. Because of their large morphological diversity, this species was subdivided into 30 morphological groups based on the size and shape of their flower head as distinctive characteristics. The stem part is usually woolly, and the flower heads occur in compact, solitary or spreading inflorescence. The Helichrysum name was generated from the Greek words Helios (sun) and chrysos (gold) based on the attractive yellowish flowers displayed by its species [140]. *Helichrysum* species have been largely explored by indigenous people to treat many diseases like infections, wounds, respiratory conditions, coughs, fever, colds and headaches [141]. *H. Kraussii,* which is normally used to treat tuberculosis, is a perennial, much-branched aromatic shrublet plant [142]. It normally grows in a profusion of sandy soil and rocky places [142]. Based on my knowledge, there is no existing research or documentation on the use of this plant for corrosion inhibition studies.

© University of Venda



Figure 2. 26: A picture of the *H. Kraussii* plant [143].

2.17. Computational chemistry

Computational chemistry is a field that uses computer simulations to help solve important chemical problems, from chemical thermodynamics problems to molecular structural problems, reaction mechanisms, reaction kinetics, etc. [37]. It makes use of theoretical chemistry methods blended into effective computer programs to calculate the structures, properties, and interactions of molecules. Computational chemistry can be exploited through different methods, like density functional theory (DFT), semiempirical, and ab initio, which have been discussed below.

2.18. Quantum chemistry

In the past decades, a number of various models have been developed to calculate the energies and molecular structures of different compounds. These models can be categorised into two important models: molecular mechanics and quantum chemical models. In place of tacticle models, molecular mechanics paired with computer graphics have recently been used to visualize quantity steric and molecular shapes. On the other hand, quantum chemical

© University of Venda

calculations provide an actual prospect of complementing experiments to find and investigate new chemistry [144]. Quantum chemistry is a field of chemistry that uses the methods of quantum mechanics to tackle important chemical problems, from chemical thermodynamics to molecular structural problems, reaction mechanisms, reaction kinetics, etc [37].

The reason behind chemists' increased utilization of these calculations, specifically the quantum chemical calculations, is that the theories behind the calculations have recently moved to a point where different relevant quantities like the reaction energies and molecular equilibrium geometry can be found with enough accuracy [144].

2.19. Quantum Chemical Calculations and their ability to estimate molecular properties

2.19.1. The Schrödinger equation

The Austrian physicist Erwin Schrödinger proposed an equation for finding the wavefunction of any system in 1926, which is now called the Schrödinger equation [145]. It is the key equation in quantum mechanics that generally describes the behaviour of quantum systems, such as molecules, atoms, and subatomic particles. This equation is a partial differentiation that describes the relationship between the wavefunction of a system and its energy [145]. Molecular geometry describes the molecules in terms of minimal energy configurations of the nuclei and quantum mechanics based on the interactions among electrons and the nuclei. The Schrödinger equation is the foundation of quantum mechanical techniques, and it may be precisely solved for the special situation of a single particle in three dimensions, such as a hydrogen atom. The Schrödinger equation is given as

$$\left[-\frac{1}{2}\nabla^2 - \frac{Z}{r}\right]\Psi(r) = E\Psi(r) \tag{34}$$

where the parameters in the square brackets represent the potential and kinetic energy of an electron placed at a distance r from a nucleus of charge Z for one hydrogen. Ψ is the function of electron coordinates, E is the electronic energy in atomic units, and $\Psi(r)$ is the wavefunction fully detailing the movement of the electron.

The Schrödinger equation can be generalised to a multielectron, multinuclear system as follows [146],

$$\hat{\mathrm{H}}\Psi = E\Psi \tag{35}$$

© University of Venda

where Ψ is a many-electron wavefunction, and $\hat{H}$ is the Hamiltonian operator, which in atomic units is given by Equation 36 as [147]

$$\hat{H} = -\frac{1}{2}\sum_i^{electrons} \nabla_i^2 - \frac{1}{2}\sum_A^{nuclei} \frac{1}{M_A}\nabla_A^2 - \sum_i^{electron}\sum_A^{nuclei} \frac{Z_A}{r_{iA}} + \sum_i^{electron}\sum_{<j} \frac{1}{r_{ij}} + \sum_A^{nuclei}\sum_{<B} \frac{Z_A Z_B}{R_{AB}} \quad (36)$$

where M_A is the ratio of the mass of the nucleus, A to the mass of an electron, Z is the nuclear charge, r_{iA} is the distance between electron i and nucleus A, r_{ij} is the distance between electrons i and j, and R_{AB} is the distance between nuclei A and B [148, 149].

2.19.2. Approximation methods in quantum mechanics

The Schrödinger equation cannot be solved for multiple electrons, even for a two-electron system like the hydrogen molecule or helium atom, and in such circumstances, approximation has to be introduced to provide practical methods. Below are some of the approximation methods that can be utilised.

(a). Born-Oppenheimer approximation

The Born-Oppenheimer approximation serves as the foundation for practically all computations involving electronic structure. By assuming that the electronic and nuclear motions can be separated, it considerably simplifies the Schrödinger equation [150]. The Schrödinger equation can be simplified to accommodate molecular systems by making assumptions that there was no nuclei movement and only electrons move. However, the Born-Oppenheimer approximation outlines that the nuclei move at a slower rate than the rate at which the electrons move, which is equivalent to the speed of light, and this approximation leads to an electronic Schrödinger equation given as [149],

$$\hat{H}^{el}\Psi^{el} = E^{el}\Psi^{el} \quad (37)$$

$$\hat{H}^{el} = -\frac{1}{2}\sum_i^{electrons} \nabla_i^2 - \sum_i^{electron}\sum_A^{nuclei} \frac{Z_A}{r_{iA}} + \sum_i^{electron}\sum_{<j} \frac{1}{r_{ij}} \quad (38)$$

where the parameters are the same as those described in Equation 36. Since it is 0, the quantity describing nuclear kinetic energy is not present in the equation above. In Equation 36, the nuclear-nuclear coulomb term is a constant. To produce the system total energy E, the last part of Equation 35 must be added to the electronic energy E^{el} as follows,

© University of Venda

$$E = E^{el} + \sum_{A}^{nuclei} \sum_{<B} \frac{Z_A Z_B}{R_{AB}} \quad (39)$$

where the parameters are the same as those described in Equation 36. In the electronic Schrödinger equation, the nuclear mass does not form part of the equation, such that the Born-Oppenheimer approximation holds true, indicating that the causes of mass effects on chemical reactivities and molecular characteristics are distinct.

(b). Hartree-Fock approximation

The Hartree-Fock approximation implements the Born-Oppenheimer approximation since its electronic Schrödinger equation is intractable. This method is predicated on the idea that in a multi-electron system, electrons move independently of one another [50, 149]. This motion guarantees that the motion of one electron has no impact on the motions of the other electrons and that it is unaffected by the motion of the other electrons. This means that the overall wavefunction is antisymmetric upon switching the coordinates of the electrons because it is expressed as a Slater determinant (single determinant) given as [144],

$$\Psi = \frac{1}{\sqrt{N!}} \begin{vmatrix} x_{1(1)} & x_2(1) \cdots\cdots x_n(1) \\ x_1(2) & x_2(2) \cdots\cdots x_n(2) \\ x_1(N) & x_2(N) \cdots\cdots x_n(N) \end{vmatrix} \quad (40)$$

where xi is a spin-orbital and is the product of spatial function or molecular orbital, Ψi, and a spin function, α or β.

The set of molecular orbitals resulting in the lowest energy is found through the self-consistent procedure. The Hartree-Fock method is the original SCF method; however, the SCF methods also involve density functional procedures. The following equation is the result of all SCF operations given as

$$f(i)x^{(X_i)} = \varepsilon x^{(X_i)} \quad (41)$$

$$f(i) = -\frac{1}{2}\nabla_i^2 + v^{eff}(i) \quad (42)$$

where X_i is the spin and spatial coordinates for the electron i, x is the spin orbitals, and v^{eff} is the effective potential depending on the SCF methodology.

© University of Venda

(c). Linear Combination of Atomic Orbital approximation (LCAO)

The Hartree-Fock approximation leads to a couple of differential equations, referred to as the Hartree-Fock equations, each involving various coordinates of a single electron. Although these equations can be numerically solved, it is beneficial to include the Hartree-Fock equations in a set of algebraic equations. For the hydrogen atom, it can be expected that one-electron solution for many-electron molecules will closely imitate the one-electron solutions. The molecular orbitals are presented in the form of a linear combination of a basis set (a finite set) of predefined functions referred to as the basis functions, ϕ. Equation 43 is referred to as the linear combination of atomic orbitals, also called the LCAO approximation given as [151],

$$\Psi_i = \sum_{\mu}^{basis\ function} C_{\mu i}\phi_{\mu} \tag{43}$$

where c is the unknown coefficient of molecular orbital, usually known as the molecular orbitals. ϕ are often called atomic orbitals because they are often centred at the nuclear positions.

When the LCAO and the Hartree-forck approximations are combined and introduced to the electronic Schrödinger equation, the Roothaan-Hall equation emerges, given as

$$Fc = \sum Sc \tag{44}$$

where S is the overlap matrix, c represents the orbital energies, and F is the Fock matrix; similar to the Hamiltonian in the Schrödinger equation, its elements are given by

$$F_{ocv} = H_{core\ ocv} + J_{ocv} - K_{ocv} \tag{45}$$

where H core represents the core Hamiltonian, and it's given as

$$H_{\mu v}^{core} = \int \phi_{\mu}(\boldsymbol{r}) \left[-\frac{1}{2}\nabla^2 - \sum_{A}^{nuclei} \frac{Z_A}{r}\right] \phi_v(\boldsymbol{r}) d\boldsymbol{r} \tag{46}$$

The coulomb and exchange elements are given as

$$J_{\mu v} = \sum_{\lambda}^{basis} \sum_{\sigma}^{functions} P_{\lambda\sigma}\big((\mu v|\lambda\sigma)\big) \tag{47}$$

$$K_{\mu v} = \frac{1}{2}\sum_{\lambda}^{basis} \sum_{\sigma}^{functions} P_{\lambda\sigma}\big((\mu v|\lambda\sigma)\big) \tag{48}$$

© University of Venda

where P is the density matrix, the elements of which involve a product of two molecular orbital coefficients summed over all occupied molecular orbitals, given as

$$P_{\lambda\sigma} = 2\sum_{i}^{occupied\ molecular\ orbitals} C_{\lambda i}C_{\sigma i} \quad (49)$$

where $(\mu v|\lambda\sigma)$ are the two-electron integrals, the number of which increases as the fourth power of the number of basis functions, and since they are very numerous, the evaluation and processing of two-electron integrals constitute the major time-consuming steps given as [144],

$$(\mu v|\lambda\sigma) = \iint \phi_\mu(r_1)\phi_v(r_1)\left[\frac{1}{r_{12}}\right]\phi_\lambda(r_2)\phi_\sigma(r_2)dr_1dr_2. \quad (50)$$

2.19.3. Basis set

A basis set is a mathematical description of a system's orbitals that is employed in modelling or approximating theoretical calculations. It is regarded as a set of basic functional building blocks that can be stacked to have desired features. Stacking in mathematics means adding things after multiplying each of them by their own constant [152]. For example, the basis set can be given as

$$\psi = a_1\phi_1 + a_2\phi_2 + \ldots + a_k\phi_k \quad (51)$$

where ψ is the basis set, K is the size of the basis set, ϕ_1, ϕ_2,…., ϕ_k are the bais functions and a_1, a_2 ,…., a_k are the normalization constants [152].

- **Types of basis set**

There are two basis set types: Slater-type orbitals (STO) and Gaussian-type orbitals (GTO). The two basis sets can also be called the atomic orbitals (AOs), which are used in the calculations of the electronic structure [153].

(a). Slater-type orbital (STO)

The Slater-type orbital is an excellent approximation to atomic orbital wavefunctions, but it is difficult to evaluate [154]. The slater-type orbital takes the form,

$$x_{\zeta,n,l,m}(r,\theta,\varphi) = NY_{l,m}(\theta,\varphi)r^{n-1}e^{-\zeta r} \quad (52)$$

where N is the normalization constant, $Y_{l,m}$ are the spherical functions, ζ is the orbital exponent, and n is the principal quantum number.

(b). Gaussian-type orbital (GTO)

© University of Venda

Gaussian-type orbitals are the most used in most ab initio methods and in cartesian coordinates because molecular integrals are easy to derive and encode from them. The GTO is given as

$$x_{\zeta,n,l,m}(r,\theta,\varphi) = NY_{l,m}(\theta,\varphi)r^{2n-2-1}e^{-\zeta r^2}, \quad (53)$$

$$x_{\zeta,l_x,l_y,l_z} = Nx^{l_x}y^{l_y}z^{l_z}e^{-\zeta r^2}, \quad (54)$$

and the type of orbital is determined by the sum of $l_{x,}l_{y,}l_z$.

The GTOs are regarded as being inferior to STOs because of two problems generated by their dependence on r^2. Firstly, the tail of the GTO wave function is poorly represented as a result of the early dips from the core as compared to the STOs. The second problem is that the GTO has a zero slope at the nucleus, which makes them not sufficiently represent the behaviour near the nucleus, as compared to STO, which contains a discontinuous derivative. In order to get the same level of accuracy as STOs, three times as many GTOs as STOs are needed [153, 155].

- **Classification of GTO**

Suppose the GTO basis set, which is defined by the number of functions of each type (s-,p-,d-, etc.), is selected. In that case, parameters such as the values of the exponent for each function and the way to combine the functions in a fixed linear combination are combined to get large degrees of freedom [153].

The combination of the complete set of basis functions, called the primitive GTOs (PGTOs), into a smaller set of functions generating linear combinations is known as contraction of the basis set, and the functions obtained are called contracted GTOs (CGTOs).

The classification can also be made based on the number of functions used to describe the AOs. The minimal basis set, which is the smallest possible number of functions, uses only enough functions to contain all the electrons of the neutral atoms. These are known as the single Zeta (SZ), and for helium or hydrogen, it represents a single s-function (1s); for the first row of the periodic table, it implies two s-functions (1s and 2s) and the set of p-functions (2px, 2py, and 2pz) [153].

The basis functions can be duplicated in one set, generating the Double Zeta (DZ), which utilises two s-functions (1s and 1s') for helium and hydrogen, four functions and (1s, 1s', 2s and 2s') and two sets of p-functions for the elements in the row, as an improvement. This gives a better description of the electron distribution. The increment of the basis set results in a Triple Zeta (TZ) having three times as many functions as the minimum basis. Names such as

© University of Venda

Quadruple Zeta (QZ) and Quintuple or Pentuple Zeta (PZ or 5Z) are also used for the following levels of the basis sets. The increase in the number of functions makes it possible to describe the bond in all directions and environments. The valence electrons are heavily affected by the chemical environment, as opposed to the core electrons, which are not related to chemical bonding and are treated with minimal basis sets. Chemical bonding takes place between the valence orbitals, and this causes the valence electrons to be treated with larger basis sets like TZ or DZ. In this case, the split valence basis set is used to reduce the time required for large molecule calculations [153]. Some of the most recognised split-valence basis sets are those found in the Pople group, which includes the 3-21G, 6-31G, and 6-311G basis sets. These basis sets can be selectively augmented with diffuse and/or polarization functions [154].

(a) Polarization functions

The size of the basis set can be increased by the use of polarization functions. Polarization functions are utilised on the orbitals of higher angular momentum and allow atomic electron density to be polarized to obtain a good representation of the electron density of the molecules. For example, in hydrogen, which only contains spherical (s) orbitals when bonded to an atom with very low electronegativity like lithium, the electron density changes from being spherical and the introduction of a p-orbital will change the electron density in the direction of the bond, which is its polarization. The most utilised polarization functions are the p-, d-, or f- orbitals, and they are used to polarize the previous functions. For example, p-orbitals polarize s-orbital, and d-orbitals polarize p-orbitals. For example, after polarization, the naming becomes Double Zeta plus Polarization (DZP) type basis for a DZ basis with a single set of polarization functions added [153]. The polarization functions bring about flexibility by including higher orbital types, like p-orbitals on hydrogen or d-orbitals on carbon; these are represented by listing the extra functions included, e.g. (d, p) or by adding one (*) or two (**) asterisks, after the basis set name. For example, the 6-31G*basis is the same as 6-31G(d), and for hydrogen, the basis set can be 6-31G**, which is identical to 6-31G(d,p) (double split-valence with polarization) with 2 number of functions [155].

(b) Diffuse functions

Diffuse functions are very shallow Gaussian functions that accurately represent the electron distribution at a distance from the nucleus, which can be essential when there are loosely bound anions, electrons, or excited states [153]. The diffuse functions are the s- and p- functions, and they are presented before the G. The introduction of diffuse functions is denoted by one (+) or two (++) plus signs or by the prefix aug- [154]. The first + indicates one set of diffuse s- and

© University of Venda

p- functions for heavy metals, and the second + indicates that the diffuse s-function is added to hydrogen [155]. Examples of diffusion functions include 6-311+G(2df) for elements like aluminium, sodium, silicon and magnesium, and 6-311++G(2df,2p) for first raw elements and hydrogen [156]. The example of a diffuse function basis set using the aug- prefix can be aug-cc-pVTZ [157].

The example of a diffuse function basis set using the aug- prefix can be aug-cc-pVTZ [157].

2.19.4. Semi-empirical and Ab initio methods emanating from the approximation approaches.

The approximation approach to the Shrödinger equation, when combined together, can result in what is known as semi-empirical and ab initio methods. Semi-empirical methods solve the Shrödedinger equation by introducing some empirical data into the equation. Ab initio methods, on the other hand, solve the Shrödinger equation from the first principle; this means without introducing experimental data. In the subsections below, we describe a few of the semi-empirical and ab initio methods.

2.19.4.1. Semi-empirical models

Semi-empirical models reduce the complexity of the Hartree-Fock models by only considering the valence electrons and restricting the basis set to the smallest possible amount of valence representation [149]. The central approximation of this model is to ensure that the atomic orbitals residing on various atomic centres do not overlap in order to reduce the overall computation. The advantage generated by this approximation is the speed of computational calculations, which is faster than the ab initio calculations. Another advantage is that semi-empirical methods can support an experimental finding on any number of fronts, in a sense that theoretical studies can also be performed on large molecules that are computationally out of reach by ab initio methods. Modified Neglect of Diatomic Overlap (MNDO), Austin Model 1(AM1) and Parametric Method 3 (PM3) are some examples of semi-empirical methods and are briefly described below [144].

(a). Modified Neglect of diatomic overlap (MNDO)

The modified neglect of diatomic overlap is a revamped version of the Neglect Diatomic differential overlap (NDDO). The spectroscopic data produced for all isolated atoms are used to parametrize the one-centre - two-centre integrals in this model. The MNDO used only the s

© University of Venda

and the p orbitals basis sets, but the new MNDO/d models use an additional orbital basis set, d. The description of all the d-block elements as well as the hypervalent sulphur species, is made possible by the newly added d orbital basis set. Due to significant intermolecular repulsion forces and lack of proper accuracy on the results of the heats of formation, MNDO has the disadvantage of being unable to accurately explain the hydrogen bond [50].

(b). Austin Model 1(AM1)

The Austin Model 1 approach is excellent for describing hydrogen bonding. Despite the fact that this model employs a unique expression for nuclear-nuclear core repulsion, it approximates the two-electron integrals. The van der Waals interactions are taken care of by this unique expression since it introduces attractive forces that are not physical. The basicities of molecules are systematically over-estimated, and this is the disadvantage of the AM1 method [144].

(c). Parametric method 3 (PM3)

The functional group-specific modification of the core repulsion function is used in the parametric method 3 (PM3) model. The van der Waals attraction between atoms is explained by the pairwise distance-directed Gaussian (PDDG) modification. The PM3 with the PDDG is the ideal tool for usage with molecules that have forces of attraction and repulsion between their atoms. Another advantage of PM3 is that it can estimate the heat of formation [144]. The disadvantage of PM3 is that molecular conformational energies and the explanation for radicals are not very accurate; another disadvantage of PM3 is the overestimation of the activation barriers [50].

2.19.4.2. Ab Initio method

This method uses pure theoretical principles to compute quantum and molecular chemical parameters and does not involve experimental data. The quantum chemical calculations used in the ab initio approach are only solved using mathematical procedures, like utilising easy mathematical expressions that represent wavefunction with a finite basis set [37]. This implies that the Schrödinger equation is solved without ignoring other integrals on the equation or by introducing other parameters, as is the case with the semi-empirical method.

© University of Venda

(a). Hartree-Fock (HF) method

One of the earliest and simplest approximations in quantum chemistry is the Hartree-Fock (HF) method. It predicts that a collection of molecular orbitals (MOs) can be used to approximate the many-electron wave function as a single Slater determinant. The HF approach is inaccurate for systems with substantial electron correlation because it ignores the effects of electron-electron correlation. The electron-electron correlation refers to the deviation from the main field approximation used to define electrons' behaviour in many electron systems. The main-field approximation is a method used to simplify the treatment of complex many-body systems, like those that involve electrons in atoms, molecules or solids [158].

(b). Moller-Plesset theory (MP2)

The second Mollar-Plesset theory is the simplest wavefunction-based electron correlation method. It provides systematics improvement in optimized geometries and other molecular properties relative to the HF theory. In a five-page note from 1934, Moller and Plesset1 (MP1) explained how second-order perturbation theory can be used to correct the Hartree-Fock (HF) method for electron pair correlation. Moller-Plesset perturbation theory, also known as MPPT or just MP in the literature, is the current name for this method. Although first generally disregarded, MPPT has significantly influenced the advancement of quantum chemical ab initio methods during the past 40 years [159]. The MP2 correlation energy correction is given as [159],

$$E_{MP}^{(2)} = \sum_{s>0} \frac{V_{0s} V_{s0}}{E_0 - E_s} \tag{55}$$

where $E_{MP}^{(2)}$ is the second Mollar-Plesset energy, V_{0s} is the finite matrix element.

(c). Density functional theory (DFT)

DFT can be seen as a wave function-based approach despite being frequently linked to density functional approximations. Instead of the many-electron wave function, DFT approximations use electron density. Electron density is defined as the multiple integral over all of the electrons' spin coordinates and over all but one of the spatial variables as [37],

$$\rho(\underset{r}{\rightarrow}) = N \int \ldots \int \left| \Psi(\underset{x_1}{\rightarrow}, \underset{x_2}{\rightarrow}, \ldots \underset{x_N}{\rightarrow} \right|^2 d\underset{x_1}{\rightarrow} d\underset{x_2}{\rightarrow} \ldots d\underset{x_N}{\rightarrow} \tag{56}$$

where $\rho\left(\underset{r}{\rightarrow}\right)$, determine the probability of finding any of the N electrons within volume element $d\underset{x}{\rightarrow}$.

© University of Venda

This probability density has to satisfy certain unique properties. The mathematical proof of Hohenberg-Kohn theorem found that the total energy (E[ρ]) associated with the electron density can be written as the summation of the kinetic energy of the electron (T[ρ]), nuclear energy due to the nuclei-electron attraction ($E_{Ne}[\rho]$) and the energy term due to electron-electron repulsion ($E_{ee}[\rho]$) given as [37],

$$E[\rho] = E_{Ne}[\rho] + T[\rho] + E_{ee}[\rho]. \quad (57)$$

Commonly used functionals include Local Density Approximation (LDA) and Generalised Gradient Approximation (GGA).

- **Local Density Approximation (LDA)**

By taking into account the electron density at a specific point in space, LDA attempts to approximate the exchange-correlation energy density functional. It predicts that the system's overall electron exchange-correlation energy is constant, and for non-realistic cases, the LDA is given as [160],

$$E_{XC}[n] = \int n(r)\epsilon_{XC}[n(r)]dr \quad (58)$$

where $E_{XC}[n]$ is the exchange-correlation energy and $\epsilon_{XC}[n]$ is energy of the exchange-correlation per electron in a homogeneous electron gas with a constant density n.

For many molecular characteristics, LDA performs admirably, but it has trouble representing systems with large nonlocal correlation effects [161].

- **Generalised Gradient Approximation (GGA)**

GGA enhances the LDA by taking into account the gradient of the electron density. It is possible to capture some nonlocal correlation effects more accurately by including the density gradient. The GGA is given as [162],

$$E_{XC}^{GGA}[n_\uparrow, n_\downarrow] = \int d^3r\, f(n_\uparrow, n_\downarrow, \nabla n_\uparrow, \nabla n_\downarrow) \quad (59)$$

where E_{XC}^{GGA} is the exchange-correlation energy foR GGA, $n_\uparrow, n_\downarrow$ are the spin densities.

Although GGAs are more precise than LDAs for a variety of systems, they still have problems representing strongly coupled systems [161]. In such cases, hybrid generalized gradient approximation methods were introduced. These methods are formed by combining the Hartree-Fock exchange and the DFT exchange-correlation functionals. These functionals intend to capture both short-range and long-range electron correlation effects. A few well-known

© University of Venda

examples include Becke, three-parameter, Lee-Yang-Parr (B3LYP), Perdew-Erzerhof hybrid functional with 25% exact exchange (PBE0), and Minnesota functional (M06). Although hybrid functionals need more computation than pure DFT functionals, they can offer better accuracy [161].

The B3LYP exchange-correlation hybrid density functional is expressed as a linear combination of the Hatree-Fock exchange operator. (E_{xHF}), the Becke88 GGA exchange functional (ΔE_{xB88}) and the LDA exchange functional (E_{xLDA}) as [163],

$$E_{xB3LYP} = 0.2E_{xHF} + 0.8E_{xLDA} + 0.72\Delta E_{xB88}. \quad (60)$$

2.20. The molecular properties of interest in relation to metal corrosion inhibition

Some molecular properties can be estimated using quantum chemical methods, which provide insight into the effectiveness of corrosion inhibitors and their interactions with the metal surface when studying metal corrosion inhibition. The following are some molecular properties of interest [164].

2.20.1. Total electronic energy of the molecule

The total electronic energy of a molecule is an essential parameter in corrosion studies that can be used to shed light on the system's stability and reactivity. The energy associated with how the electrons are arranged and how they interact with one another inside a chemical atom is known as electronic energy.

In quantum mechanics, electronic structure calculations are used to determine the molecule's electronic energy. With the aid of calculations, the system's electronic wavefunction and related energy are obtained through solving the Schrödinger equation. The density functional theory (DFT), Hatree-Fock (HF) and post-Hatree-Fock approaches are some of the computational techniques that can be used to solve the Schrödinger equation [5].

The electronic energy of a molecule is very important because it can be used to determine the properties that are relevant to corrosion investigations, such as

- **Bond energies**

The electronic energy determines how strongly a molecule's chemical bonds are held together. Weaker bonds are more likely to break during corrosion processes.

© University of Venda

- **Reaction energies**

The energy shift resulting from a corrosion reaction can be calculated by comparing the electronic energies of the reactant and product molecules. When the reaction energies are found to be positive, the corrosion is said to be energetically unfavourable.

- **Stability**

Chemical structures which are more stable are generally associated with lower electronic energy. Stable corrosion intermediates or products can be found by investigating the relative electronic energies of different molecule structures.

- **Charge distribution**

The charge distribution within a molecule can be determined using electronic energy. The insight into the system's reactivity and the possibility of electron transfer processes involved in corrosion can be found by understanding the distribution of positive and negative charges [7].

2.20.2. Adsorption energy

Adsorption energy determines the strength of interaction between the surface of the metal and the corrosion inhibitor molecules. High adsorption energy is associated with strong binding of the inhibitor molecules on the surface of the metal, indicating an effective corrosion inhibitor.

2.20.3. Electron density

The electron arrangement in a corrosion inhibitor molecule is very important in understanding the charge distribution and electronic structure. It also helps understand the electron transfer processes during the corrosion inhibition mechanism.

The substituent effect in aromatic region substituted compounds can be determined by using the value of the Hammett substituent constant (σ). The substituent effect on the cyclic and aliphatic substituted compounds can be determined by the values of the Taft constant (σ^*). The Hammett constant reflects the entire electron density. The Hammett constant equation can be given as [165-167],

$$log \frac{K_R}{K_H} = \rho\sigma \tag{61}$$

where K_R and K_H are the equilibrium constants for organic compounds with and without substituents, respectively, ρ is the reaction parameter whose value mainly depends upon the

© University of Venda

nature of the reaction, and σ is the Hammett constant, which reflects the total electronic effect on the reaction centre

From the literature, it is known that the electronic donating substituents correspond to negative values of (σ). This means that the substituents that have higher negative values of (σ) are associated with higher corrosion inhibition potential, while those with less negative values of (σ) are associated with less corrosion inhibition potential. Substitutes such as -OH, -NH_3, -OMe and -CH_3 are some of the known electron-donating substituents and have negative values of (σ). These substituents increase the electron density of the compound at the donor site [165]. They are believed to increase the electron density either by + I-effect (inductive effect) and/ or +R-effect (resonance effect). For example, Methyl groups are expected to increase the electron density through their + I-effect; therefore, methyl groups containing compounds show remarkably high corrosion inhibition potential as compared to the non-substituted compound. However, the increased inhibition potential of –OH substituted compounds can be explained using its + R effect. Because of its + R-effect, the –OH substituent increases the electron density at the donor sites and overall adsorption tendency [165].

2.20.4. Frontier molecular orbitals and related properties

The frontier molecular orbitals for a molecule are the lowest unoccupied molecular orbital (LUMO) and the highest molecular orbital (HOMO). These orbitals are utilized to determine the electron donating and accepting ability and the reactivity ability of molecules; in our case, this would be the corrosion inhibitor molecules [168]. The most interesting features relative to HOMO and LUMO orbitals include the energy of the individual orbitals, the HOMO-LUMO energy gap, electronegativity, etc. Below is a discussion of some of the properties related to the two orbitals.

(a). The energy of the HOMO and LUMO orbitals

The energy of the HOMO indicates the capacity of a molecule to donate electrons to the metal's unoccupied molecular orbitals, while the energy of the LUMO indicates the capacity of the molecule to accept electrons from the occupied molecular orbital in the metal [168]. Since the HOMO energy gives details on the electron-donating capacity of molecules, the higher values would make it simpler for the molecule to donate electrons during the reaction, improving the inhibitor's adsorption on the metal surface and adsorption efficiency [169]. High values of the E_{LUMO} indicate the increased electron-accepting capability of a molecule. Therefore, it can be

© University of Venda

concluded that the binding capacity of the inhibitor to the metal surface rises with rising energy values of the HOMO and decreasing energy values of the LUMO [168]. The E_{HOMO} and E_{LUMO} values are used when comparing the strength of two or more inhibitor molecules since there is no energy value range that determines the strength of the inhibitor molecules.

(b). The energy gap

The energy gap is the energy difference between HOMO and LUMO. It is highly important since it provides more details on the molecule's reactivity with different chemical species. Strong values are typically linked to low reactivity, whereas molecules with an energy gap exhibit strong reactivity. The energy gap is given as

$$\Delta E = E_{LUMO} - E_{HOMO} \quad (62)$$

where ΔE is the energy gap, E_{LUMO} is the LUMO energy, and E_{HOMO} is the HOMO energy.

(c). Electronegativity

The HOMO and the LUMO are related to the electronegativity of the molecules given as [170],

$$\chi \cong -\tfrac{1}{2}(E_{HOMO} + E_{LUMO}) \quad (63)$$

where χ is the electronegativity, E_{LUMO} is the LUMO energy, and E_{HOMO} is the HOMO energy.

This molecular reactivity parameter is important because it measures the power of the group of atoms or electrons to attract electrons toward itself. Electronegativity is a significant parameter, a numerical value taken into account to forecast the electron transfer between the metal and the inhibitor [171]. It is also known that inhibitor molecules with high electronegativity values cannot be excellent corrosion inhibitors, while those with low electronegativity values can act as good corrosion inhibitors. Tüzün, B., and Kaya, C. (2018) reported on this [172].

(d). Global hardness and Global softness

This parameter is very helpful in measuring the resistance of an atom to a charge transfer, and it is defined as

$$\eta \cong -\tfrac{1}{2}(E_{HOMO} - E_{LUMO}). \quad (64)$$

Global softness is a molecular reactivity parameter that is utilised to describe a molecule's stability and reactivity. It is related to the global hardness as [170],

$$\sigma = \frac{1}{\eta} \quad (65)$$

© University of Venda

where σ is the global softness, and η is the global softness.

(e). Ionization energy (I)

The ionization energy is very important because of its relationship to the energy needed to extract an electron from a molecule. The energy released by the molecule during chemical reactions with other chemical species when an electron is lost is approximated by the ionization energy. This parameter is related to the energy of the HUMO through the equation given as

$$I \cong - E_{HOMO} \quad (66)$$

where I is the ionization energy, E_{HOMO} is the energy of the Highest Occupied Molecular Orbital.

Ionization energy is also used to measure the chemical reactivity of a molecule. Therefore, high ionization energy indicates high chemical inertness and stability, while low ionization energy indicates the high reactivity of the molecule. In corrosion studies, highly reactive molecules are believed to be effective corrosion inhibitors, as observed by Akbas, E. (2019) [168].

(f). Global electrophilicity index

This parameter gives details on the electrophilicity of the molecule and the capability of a molecule to perform as an electrophile. Good electrophiles have high values of the global electrophilicity index, while molecules with low values are regarded as good nucleophiles. The global electrophilicity index of the molecule is associated with the global hardness and electronegativity based on Equation 67 given as [171],

$$\omega = \frac{\chi^2}{2\eta} \quad (67)$$

where ω is the global electrophilicity index, χ is the electronegativity.

Since the global electrophilicity index measures the tendency of molecules to accept electrons. Inhibitor molecules with low global electrophilicity index are termed nucleophiles. They are good corrosion inhibitors since they can donate electrons to the metal surface, thereby forming a protective film on the metal surface, as reported by Akbas (2019) [168].

(g). Molecular geometry

The size and shape of the inhibitor molecule play a crucial role in the inhibitor's efficiency. Inhibitors with large sizes and appropriate shapes allow for efficient metal surface coverage,

© University of Venda

thereby preventing the corrosive species from reaching the surface of the metal. The geometry of molecules affects their properties, such as reactivity and solubility. This is why it is important to understand the geometry of molecules to understand their behaviour. Inhibitors with planer geometry are highly effective as corrosion inhibitors compared to any other geometry of the same inhibitor. Sánchez-Eleuterio et al. (2023) reported on this [173]. This is because planar geometry gives a wide range of possible interactions between the inhibitor molecules and the metal surface since, in planar geometry, the inhibitor lays flat on the surface of the metal [170].

2.21. Metal surface from a crystal structure perspective

All solid materials can be categorized based on the regularity with which the ions or atoms are arranged with regard to one another [174]. Crystalline materials are those in which atoms are placed in repeating arrays over a large atomic distance in such a way that upon solidification, the atoms will position themselves in a repetitive three-dimensional pattern so that each atom is bonded to its nearest neighbour atoms. In the description of crystalline structures, atoms or ions are considered solid spheres with well-defined diameters. This is known as the atomic hard-sphere model, whereby spheres representing nearest neighbour atoms touch one another. Metals, some polymers, and certain ceramic materials form crystalline structures under normal solidifications. In the context of crystal structure, sometimes the term lattice is used, and in this regard, the lattice means a three–dimensional array of points coinciding with atoms' positions. With that said, a metal surface can be described in terms of its lattice arrangement and surface planes. Metals have a crystalline structure, meaning their atoms are arranged in a regular and repeating pattern.

2.21.1. Unit cells

The order of the atoms in the crystalline solids indicates that small groups of atoms form a repetitive pattern. It is thus very important to subdivide the structures into small repeating entities called unit cells when describing the crystal structures. The unit cell is, therefore, the basic unit or building block of the crystal structure and defines the crystal structure based on its geometry and the position of the atoms. There are generally seven different types of unit cells, which are:

© University of Venda

- Cubic
- Tetrahedral
- Orthorhombic
- Hexagonal
- Monoclinic
- Triclinic

For most common metals, there are three relatively simple cubic crystal structures: face-centred cubic, body-centred cubic, and hexagonal close-packed crystal structures, which are briefly described in the subsequent paragraphs.

(a) Face-centred cubic crystalline structures

The crystal structure for metals that has a cubic geometry unit cell with atoms positioned at each of the eight corners and the centres of all the cube faces is called the face-centred cubic (FCC) crystal structure. Metals such as aluminium, copper, gold, and silver have an FCC crystal structure. FCC has an atomic packing factor of 0.74. There are two atoms per unit cell, and the coordination number is 8 [175]. Figure 2.27 shows the FCC unit cell with atoms represented by hard spheres (a), the reduced spheres model (b), and the collection of spheres representing the FCC crystal structure (c), respectively.

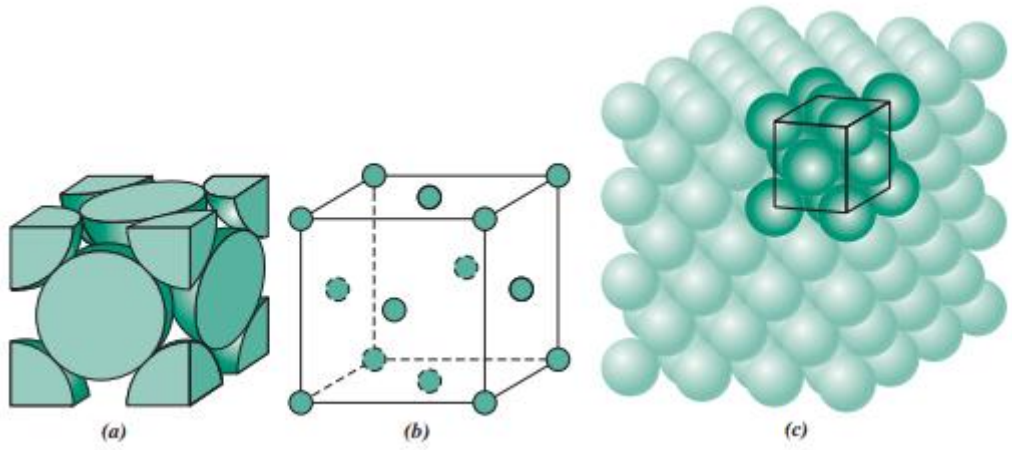


Figure 2. 27: The FCC unit cell with atoms represented by hard-spheres (a), reduced spheres model (b), and the collection of spheres representing the FCC crystal structure (c), respectively [175].

© University of Venda

(b) Body-centred cubic crystal structure

The body-centred cubic (BCC) crystal structure has a cubic unit cell with atoms positioned at all eight corners and a single atom at the cube's centre. Metals such as iron, chromium, tungsten, etc., show a BCC crystal structure. The BCC has an atomic packing factor of 0.68, 4 atoms per unit cell, and a coordination number of 12.

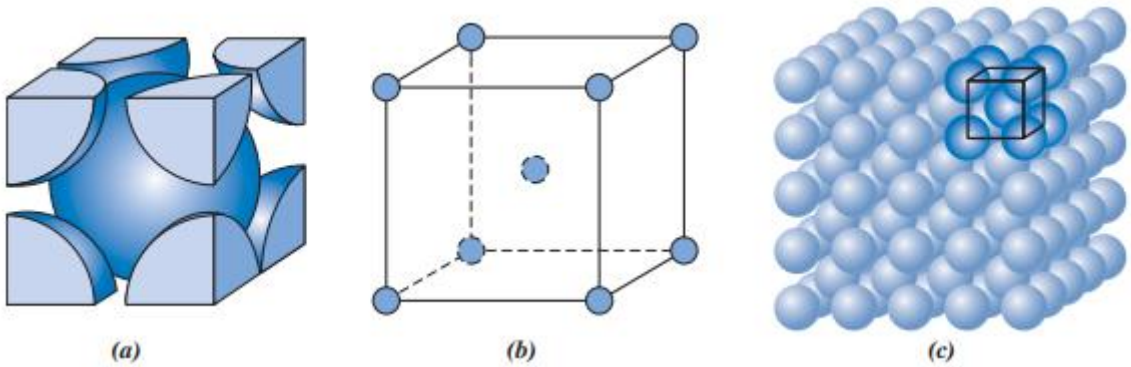


Figure 2. 28: The BCC unit cell with atoms represented by hard spheres (a), the reduced spheres model (b), and the collection of spheres representing the BCC crystal structure (c), respectively [175].

(c) Hexagonal close-packed crystal structure

Not all metals possess cubic symmetry unit cells; some possess the hexagonal unit cell. HCP is one of the most common structures of metallic crystals and contains six atoms from the regular hexagon, which surrounds one atom in the centre. Another plane is placed halfway up the unit cell with three more atoms located at the interstices of the hexagonal closed-packed planes. Examples of metals that undergo HCP are Cadium, Magnesium, zinc, and titanium [175].

© University of Venda

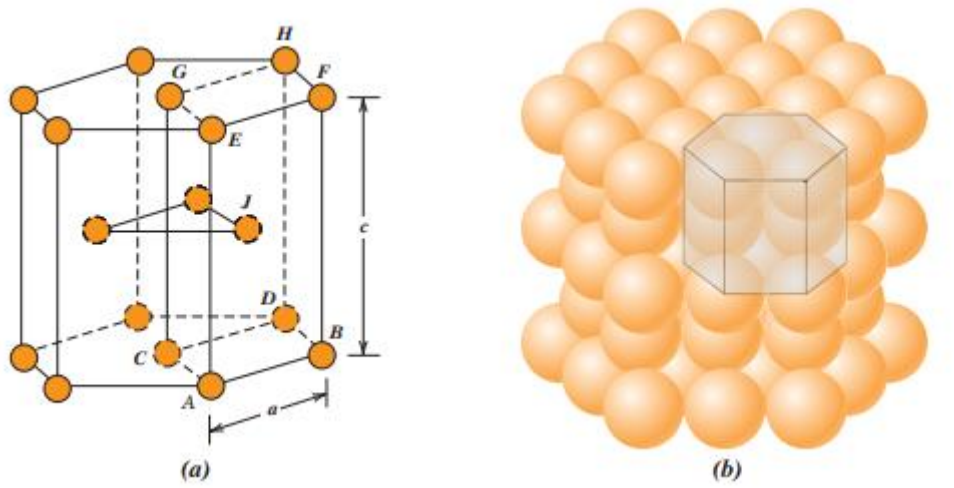


Figure 2. 29: The HCP unit cell with atoms represented by the reduced spheres model (a) and the collection of spheres representing the HCP crystal structure (b), respectively [175].

2.21.2. Crystallographic planes

The crystallographic planes are imaginary planes within a crystal lattice that are defined by the position of the atoms in the crystal. The Miller indices are used to describe the orientation of the crystal planes within a structure. They are specified by (hkl), in which h, k, and l are integers representing the intercepts of the plane with the crystallographic axes. They are defined as the reciprocals of the intercepts made by the planes on the three axes. However, the miller indices for the hexagonal closed-packed crystal structures are different because of the hexagonal symmetry [175]. Therefore, its miller indices are specified by [hkil], in which h, k, i, and l are also integers. Some examples of the most common crystal structures are listed below [176].

© University of Venda

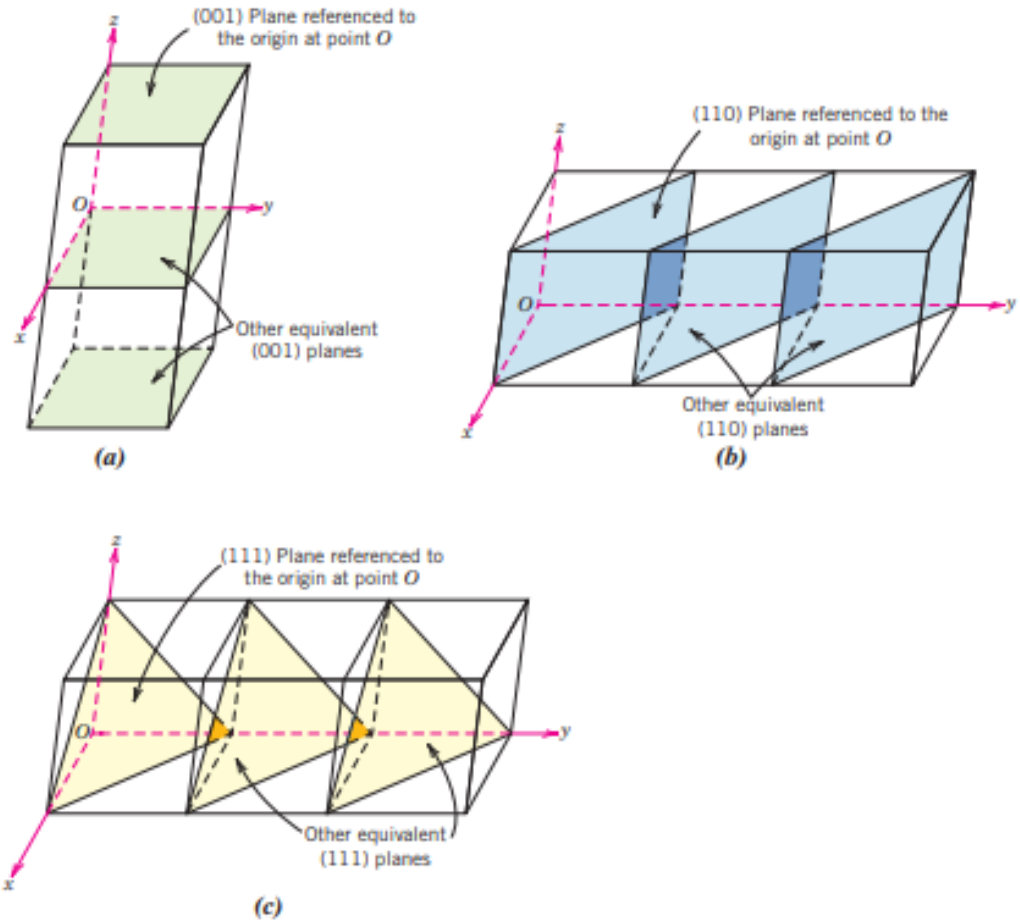


Figure 2. 30: Examples of different crystallographic phases [175].

It is worth noting that there are many different planes for different crystal structures. However, the section below only focuses on the most common planes found in FCC, BCC, and HCP crystal structures.

In FCC, the most common planes are (100), (110), and (111), and their miller indices are given as follows. The (100) plane intercepts the x-axis at a/2 and does not intercept the y and z-axes, such that the miller indices are (1,0,0). The plane (110) intercepts the x,y, and z axes at a/2, a/2, and a/2, respectively, such that the miller indices are (1,1,1). The (111) plane intercepts the x,y, and z axes at a/2, a/2, and a/2, respectively, such that the miller indices are (1,1,1).

The body-centred crystal structure has the following most common possible Miller indices. The (100) plane intercepts the x-axis at a/2 and does not intercept the y and z-axes; hence the miller indices are (1,0,0). The (110) plane intercepts the x,y, and z axes at a/2, a/2, and a/2, respectively, such that the miller indices are (1,1,1). The (111) plane intercepts the x,y, and z axes at a, a, and a, respectively, such that the Miller indices are (1,1,1).

© University of Venda

The Hexagonal closed packed crystal structure has the following possible miller indices. The (1000) plane is perpendicular to the hexagonal axis and passes through the centres of the hexagonal faces, such that the miller indices are (1,0,0,0) [176]. The (1010) plane is perpendicular to the hexagonal axis and intercepts the hexagonal faces at the edges' midpoints, such as Miller indices (1,0,1,0). The (1120) is inclined to the hexagonal axis and intercepts the hexagonal faces at the centres of the edges, such that the miller indices are (1,1,2,0).

2.22. Molecular mechanics of chemistry

Molecular mechanics depicts molecules based on the bonded atoms which have been diverted from some idealised geometry because of non-bonded van der Waals and Coulombic interactions. This differs from quantum chemical models, which do not make any reference to chemical bonding. Some factors that make the molecular mechanics models successful include the ability to transfer geometrical parameters from one molecule to another and the predictable dependence of the parameters on atomic hybridization. For instance, the carbon-carbon single bond lengths are normally found in the range from 1.45 to 1.55 Å and also increase in length with increasing p character of the carbon hybrids. This makes it possible to come up with an accurate guess at the molecular geometry based on angles, torsion angles, and bond lengths only if the molecules have already been represented based on a particular violent structure [144].

The energy of molecules in molecular mechanics is reported based on the sum of contributions coming from distortions from ideal stretch contributions “bond distances’’, bend contribution (bond angles), torsion contribution (torsion angles), and Coulombic and Van der Waals interactions (contributions due to non-bonded molecules). It is generally called the strain energy, which suggests that it reflects the strain inherent to a real molecule relative to some idealised form.

$$E^{strain} = \sum_{A}^{bonds} E_A^{stretch} + \sum_{A}^{bond\ angles} E_A^{bend} + \sum_{A}^{torsion\ angles} E_A^{torsion} + \sum_{A}^{non-bonds\ atoms} \sum_{B} E_{AB}^{non-bonded} \quad (68)$$

© University of Venda

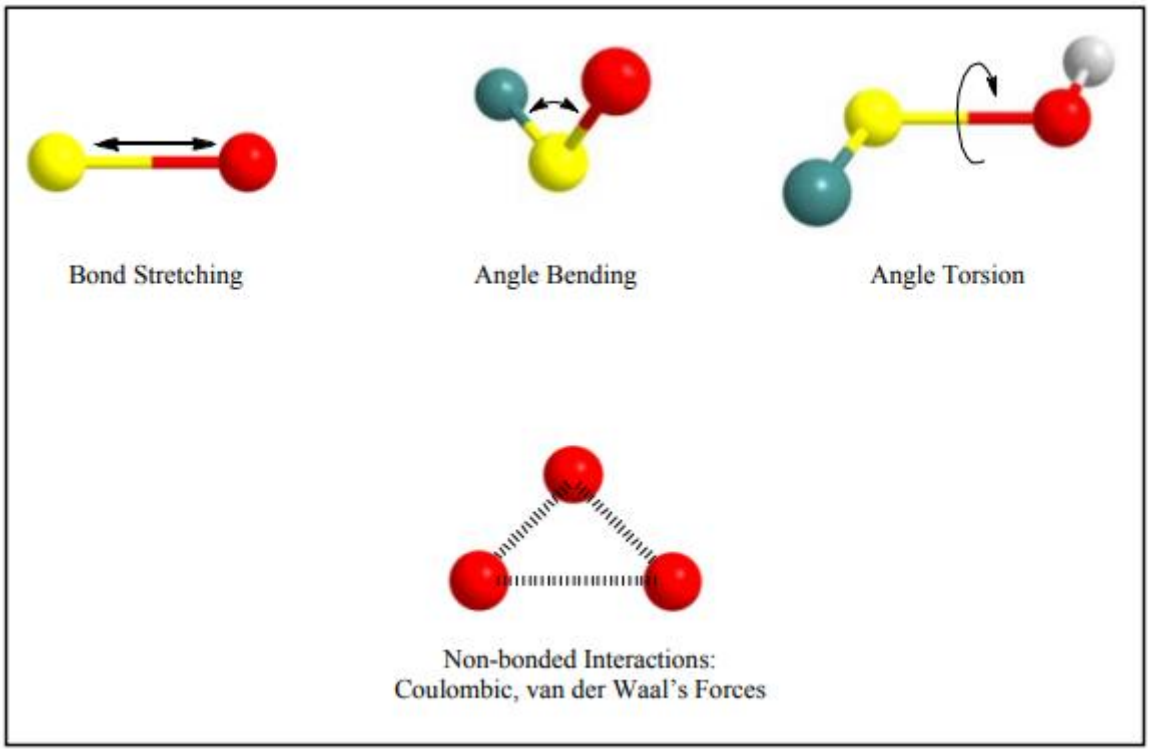


Figure 2. 31: Schematic representations of energy contributions in a molecular mechanics system [149].

Here, the first three summations are over all bonds, all bond angles and all torsion angles. In contrast to quantum chemistry calculations, where the bonding information is part of the output, molecular mechanics calculations include bonding information as an input. The last summation is over all the non-bonded pairs of atoms.

However, the bend and stretch terms are generally expressed in the form of Hook's law quadratic forms given as

$$E^{strech}(r) = \frac{1}{2}K^{strech}(r - r^{eq})^2 \quad (69$$

$$E^{strech}(\alpha) = \frac{1}{2}K^{bend}(\alpha - \alpha^{eq})^2 \quad (70)$$

Where α and r are the bond angles and distance, respectively, k^{bend} and k^{strech} are the bend and stretch force constraints, respectively, α^{eq} and r^{eq} are the ideal equilibrium bond angle and bond length obtained either from correct quantum chemical calculations or from experiments, respectively. In order to account for the correlations between bend and stretch components, the

© University of Venda

molecular mechanic's models can also involve cross terms, the cubic and higher order contributions [144].

The appropriate description of the torsion potential demands a form that reflects its inherent periodicity. For instance, the three-fold periodicity or rotation of the carbon-carbon bond in ethane may be depicted using the following functional form equation,

$$E^{torsion}(\omega) = K^{torsion3}[1 - cos3(\omega - \omega^{eq})] \quad (71)$$

where $k^{torsion3}$ is treated as a parameter, ω^{eq} is the ideal torsion angle, and ω is the torsion angle. The contribution of the bond torsion to the total energy may also need to involve terms which are one-fold and two-fold periodic.

$$E^{torsion}(\omega) = K^{torsion1}[1 - \cos(\omega - \omega^{eq})] + K^{torsion2}[1 - cos2(\omega - \omega^{eq}) + K^{torsion3}[1 - cos3(\omega - \omega^{eq})] \quad (72)$$

This equation is a shortened version of the Fourier series. The difference in energy between the trans (180°) and cis (0°) conformers is accounted for by a one-fold term, while the variation in energy between the perpendicular (90°, 270°) and planer (0°, 180°) conformers are accounted for by the two-fold term. However, molecular models may also involve higher-order and cross terms and terms to account for asymmetrical environments.

The non-bonded interactions usually include the summation of Coulombic interactions and Van der Waals (VDW) interactions [144] given as

$$E^{non-bonded}(r) = E^{VDW}(r) + E^{Coulombic}(r) \quad (73)$$

In order to account for interactions like those of hydrogen bonding, additional non-bonded terms may be included [177].

The interactions of Van der Waals are often represented as the total of attractive and repulsive terms.

$$E^{VDW}(r) = \varepsilon\left[\left(\frac{r^o}{r}\right)^{12} - 2\left(\frac{r^o}{r}\right)^{6}\right] \quad (74)$$

where r is the non-bonded distance, and ε and r^o are parameters. This functional form accommodates both the inherent size requirements of atoms as well as the weak attraction forces between separated atoms by providing a very high energy barrier inside the sum of van

© University of Venda

der Waals radii for the two atoms involved and a shallow energy well at larger separations. The Coulombic term considers the interactions between charges.

$$E^{coulombic}(r) = \frac{qq}{r} \quad (75)$$

In this case, the atomic charges, q, can either be considered as parameters or derived from quantum chemical calculations, and r is the non-bonded distance. The total molecular charge, which is 0 in the case of a neutral molecule, must be equal to the sum of the atomic charges [144].

2.23. Effects of UV radiation on the chemicals or compounds

The sun is the biggest energy source for the earth and releases a wide range of wavelengths, but only visible, Infrared and ultraviolet (UV) light reaches the earth's surface. UV light is divided into three bends of spectra, which are UVC (200 – 280 nm), UVB (280 – 315) and UVA (315 – 400 nm) [178]. Before these lights reach the earth's surface, they pass through a layer called the ozone layer. This layer functions as a filter of the UV and only emits UV wavelengths ranging from 100 to 315 nm. This means that the ozone layer completely eliminates the UVC and a large part of UVB, making only The UVA and a small amount of UVB reach the earth. Different polymeric materials have recently been utilised in various applications like marine industries, protective coatings, aerospace, and civil engineering. The performance or usage of the polymer-based material for various applications is affected by its durability. The polymers are damaged or harmed by UV radiation. When the polymer is exposed to UV light, a process known as photodegradation is started, affecting the polymers' chemical, mechanical and physical properties. The sun's UV light generates free radicals on the polymer-based material surface. The generated radicals are very active in destroying the polymeric structures. The UV light energy is normally higher than the chemical bond’s strength of bonds such as the C-N, H-O, C-C and O-O in the polymer, which makes these chemical bonds to be prone to break, resulting in photodegradation. The use of inorganic and organic UV absorbers can reduce the photodegradation of the polymer. How these UV absorbers operate differs based on the type of material. The inorganic UV absorbers usually scatter light, and the organic UV absorbers generally convert UV light to heat, Higher wavelength and radical interceptors, which capture the free radicals [179]. The above example of the degradation of polymer materials from UV light exposure is ideal proof that UV negatively affects the chemical components of the materials. Due to climate changes influenced by global

© University of Venda

warming through various activities that damage the ozone layer, more UV light will reach the earth, posing more threats to the polymers, some of which are used as protective coats. It is, therefore, vital to find the inhibitors that can withstand the UV light attacks and still function to their optimum ability.

2.24. Literature review on the corrosion inhibition of metals using plant extracts in aqueous media.

Muthukumarasamy et al. (2020) conducted a study on the prevention of corrosion in mild steel exposed to hydrochloric acid by using an extract derived from Tunbergia fragrant. Ethanol was employed as a solvent to remove the inhibitor from the plant material, resulting in the acquisition of the crude form. The undiluted extract was introduced into the pickling solution containing hydrochloric acid at varying strengths. The corrosion inhibition efficacy of mild steel was determined using gravimetric analysis and electrochemical analysis. The obtained results demonstrate that the extract effectively hinders the corrosion of mild steel by up to 81% in a 1 M HCl solution. The data from the gravimetric weight loss analysis showed that it followed the Langmuir adsorption isotherm, with physical adsorption being the dominant factor. Increasing the concentration of the extract resulted in a drop in the corrosion current density, leading to an increase in the percentage inhibition efficiency (%IE). The Nyquist plot generated by Potentiodynamic polarization revealed that the size of the semicircle exhibited a rise as the concentration of the inhibitor rose [180].

Berrissoul et al. (2020) used Lavandula Mairei Humbert (LM) extract as an eco-friendly inhibitor for mild steel corrosion in 1 M HCl. Weight loss analysis, electrochemical measurements, X-ray Photoelectron Spectroscopy (XPS0 and Scanning Electron Microscopy (SEM) techniques were used to examine the mild steel corrosion. From the results obtained, it was found that the use of LM extract managed to significantly minimize the mild steel rate of corrosion. The highest inhibition was found to be 92% at 303 K for 0.4 g/L concentration. The LM adsorption on a mild steel surface was observed to obey the Langmuir adsorption isotherm. The continuous decrease in corrosion rate and anodic Tafel slope degression, with a rise in the concentration of LM extract, supported the limited dissolution of the mild steel metal [181].

Ruvubu (2021) investigated the corrosion inhibition ability of green eco-friendly lignin and its sulfonated product of natural polymer on mild steel corrosion in 0.1 M HCl. The lignin was extracted using an acidic precipitation technique from the bunch of palm oil fruit and

© University of Venda

characterised by FTIR to find and ensure functional groups found in the plant extract. The extracted lignin was subjected to a sulfonation reaction to produce sulfonated lignin. Potentiodynamic polarization, gravimetric analysis and FTIR techniques were used to carry out the study. It was reported that sulfonated lignin was an excellent corrosion inhibitor compared to lignin in the same condition since sulfonated lignin showed the highest corrosion inhibition efficiency of 98.2% for 2.0 mM inhibitor concentration. The lignin achieved the highest corrosion inhibition efficiency of 92.9% for 4.0 mM inhibitor concentration. The Tafel polarization curves showed that the introduction of both lignin and sulfonated lignin at different concentrations to the corrosive medium resulted in the reduction of anodic and cathodic current densities and the corrosion current densities for inhibited systems when their concentration increased. This observation concluded that both lignin and sulfonated lignin functioned as a mixed type of corrosion inhibitor. The data obtained from FTIR showed that the extraction of lignin from selected agro wastes and modification into sodium lignosulfonate was efficient [182].

© University of Venda

CHAPTER 3

Experimental procedures

© University of Venda

3.1. Materials

Mild steel, zinc, and aluminium metals weighing around 3.200 g, 2.500 g, and 1.000 g, respectively, were purchased and cleaned before use to prevent any interfence in the surface. The metals had a 1 cm^2 small hole in the middle and a surface area of 6 cm^2. The hydrochloric and sulphuric acid were used to prepare the corrosive solution, and the methanol used for extraction was procured from Sigma-Aldrich. Epoxy resin and the catalyst used to prepare the samples for electrochemical studies were purchased from Build It South Africa, Thohoyandou branch.

3.2. Corrosion inhibitors

Two kinds of *H. kraussii* plant leaf extracts were generated, with one being exposed to UV light radiation and the other not exposed, which was also used as a control variable. The two extracts are utilised in this study as possible corrosion inhibitors. Figure 3.1 shows the pictures of the *H. kraussii* plants utilised in this study as corrosion inhibitor.



Figure 3. 1: *Helichrysum kraussii* plant used as corrosion inhibitor

© University of Venda

3.3. Preparation of the extracts and solution preparation

The plant leaves were collected in the Vhembe district, Thohoyandou Phiphidi area in September (Sring season), and dried at room temperature for five days. The leaves were not dried in direct sunlight to avoid the damage that the sun's rays could have on the potential components found in the plant. The leaves were then ground until the powder formed. 2g of the ground leaves were weighed and transferred to the 20 ml centrifuge tube containing 20 ml of 80% analytical grade methanol solution (4:1 ratio of methanol and water). The 80% concentration of methanol was selected due to its exceptional solvent features for extraction. This is because most extracts exhibit higher solubility in polar solvents, and 80% methanol possesses greater polar characteristics, as reported by Chigayo et al. (2016) [183]. The mixture was then shaken in a dragon shaker for 24 hours. After 24 hours, the extraction residual was filtered using filter paper and then taken to rotary vapour to remove methanol and water. The remaining jelly-like extract was dried and weighed before being digested with 1.0 M of H_2SO_4 and HCl solution in a 1000 mL volumetric flask as the stock solution. 100, 300, 600, 900, 1200 and 1500 ppm were prepared from the stock solution with 1.0 M H_2SO_4 and HCl in a 1000 mL volumetric flask and used as the corrosion inhibitor test solution. In order to obtain a large amount of extract at once, 100g of the ground leaves powder can also be extracted using a Soxhlet extractor with methanol and water in a 4:1 ratio for 24 hours at 60°C in a water bath until all the methanol evaporates [32]. The extraction residual will then be filtered using the filter paper and then taken to rotary vapour to remove excess methanol and water [33]. The 1.0 M HCl was prepared by diluting the exact amount of 37% analytical-grade (AR) HCl in a 1000 ml volumetric flask [184, 185]. The 1.0 M H_2SO_4 was also prepared by diluting the exact amount of 32% analytical-grade H_2SO_4 in a 100 ml volumetric flask. Plant leaves were used instead of other parts of the tree like roots, stems and branches because cutting those on a tree might endanger the tree. Another reason is that previous studies have also shown that molecules that undergoes geometrical isomerization are mostly found in leaves [186].

3.4. Ultraviolet light (UV)

Some of the liquid extract obtained after filtering the solid extract was transferred in a quart tube and then placed inside the UV lamp for 24 hours. After the mentioned time elapsed, the extract was rotary vapoured to remove methanol and water until a dark black liquid jelly-like extract was obtained, which was then dried until it solidified. In this case, two extracts were

© University of Venda

used for the corrosion inhibition test: the UV-radiated extract and the non-UV-radiated extract (control).

3.5. Gravimetric weight loss analysis

80 ml of 100 ppm prepared extract solution in 1.0 M HCl was transferred into a 100 ml beaker. Mild steel metal was then immersed in the 100 ppm solution by suspending it using glass robs and hooks so that it did not touch the beaker. The beaker was then put inside the water bath, which was maintained at 30 ℃ for 8 hours. After the 8 hours had elapsed, the beaker was removed from the water bath, and the metal was then washed with distilled water and brushed with a glass wipe cleaner. The metal was left to dry for 10 minutes before being re-weighed. The procedure was first performed for 1.0 M HCl solution, generally known as a blank test or control test. The weight loss obtained from the blank and inhibitor tests was then compared to get the percentage inhibition efficiency. The blank test procedure was also repeated for 40, 50 and 60 ℃ for 1.0 M H_2SO_4. However, the inhibition test procedure was also repeated for mild steel, zinc and aluminium metals in 100, 300, 600, 900, 1200 and 1500 ppm in 1.0 M HCl and H_2SO_4 at 30, 40, 50 and 60 ℃.

The difference in mass for metals obtained is used to calculate the corrosion rate. The corrosion rate was calculated from the change in weight of the metal using Equation 13.

The degree of surface coverage, which suggests how much of the metal surface the extract managed to cover, was also calculated from the corrosion rate equation

$$\theta = \left(1 - \frac{\rho 1}{\rho 2}\right) \tag{76}$$

where θ is the degree of surface coverage, ρ_1 and ρ_2 is the corrosion rate of metal in the presence and absence of the inhibitor.

The percentage inhibition efficiency (%IE) was calculated by multiplying the degree of surface coverage Equation 76 by 100,

$$\%IE = \left(1 - \frac{\rho 1}{\rho 2}\right) \times 100\% \tag{77}$$

where %IE is the percentage inhibition efficiency, ρ_1 and ρ_2 have similar descriptions as above.

© University of Venda

3.6. Liquid chromatography-mass spectrometry (LCMS).

LCMS has been employed to verify the main phytochemical constituents of the *H. kraussii* extract. It was also utilized to verify the impact of UV light on *H. kraussii* extract metabolites. The analysis of the non-radiated and UV-radiated *H. kraussii* extracts was performed using a liquid chromatography–quadrupole time-of-flight tandem MS instrument (LCMS-9030 qTOF, Shimadzu Corporation, Kyoto, Japan) equipped with a Shim-pack Velox C18 column (100 mm × 2.1 mm, particle size 2.7 µm) (Shimadzu Corporation, Kyoto, Japan). The column oven temperature was maintained at 55 °C, and analytes were separated using a 53-minute binary gradient following the method described by Ramabulana et al. (2021) [187]. The chromatographic eluents were subjected to analysis using the qTOF high-definition mass spectrometer in negative mode, with consistent conditions including an interface voltage of 4.0 kV, interface temperature of 300 °C, detector voltage of 1.8 kV, heat block temperature of 400 °C, nebulisation and dry gas flow rate of 3 L/min, DL temperature of 280 °C, and flight tube temperature of 42 °C. Sodium iodide (NaI) was employed as a calibration solution to ensure high mass accuracy. MS 1 and MS 2 spectra were acquired for all m/z values within the range of 100-1000 (precursor m/z isolation window).

3.7. Column chromatography

Column chromatography was performed with the stationary phase containing silica gel packed in a column and the mobile phase (5% methanol and 95% ethyl acetate) being run through the column after loading the extract on top of the stationary phase. The mobile phase transports the compounds in the mixture at varying rates depending on their affinities to the stationary and mobile phases. Finally, the compound components and the mobile phase can be collected [188]. Fifteen fractions were collected and analysed further for their chemical constituents.

3.8. Fourier Transform Infrared Spectroscopy (FTIR).

Among all infrared spectroscopy, the Fourier transform infrared is the most reliable, well-known Analytical technique utilised to identify functional groups of organic molecules [189]. It is widely used because it is fast, more sensitive, precise, and does not destroy the sample under study. All the IR spectroscopies are based on the principle that the IR radiation infiltrates the sample such that a certain amount of radiation is absorbed by the sample, which then gets recorded. Since every sample or compound produces a different spectrum, it is possible to

© University of Venda

distinguish different compounds. The infrared portion of the electromagnetic spectrum is located between the microwave and UV visible light regions, in the wavenumber range of 1.3 x 10^4 – 3.3 x 10^1 cm^{-1}. The inhibitor layer that had been adsorbed to the surface of mild steel, zinc, and aluminium metals in 1.0 M HCl and H_2SO_4 at 30 °C was scraped off using a spatula before the samples were subjected to FTIR analysis. The technique was similarly carried out on the metals at 30 °C in the absence of the inhibitors; however, the metal's acid-corroded layer was peeled off and examined this time. The pure extracts, water, acid solutions, inhibitor acid solution, and pure metals were also analysed under the FTIR for precise comparison of which functional groups are causing the corrosion inhibition. Therefore, FTIR was utilized to study the *H. kraussii* extract functional groups before and after exposure to UV radiation. Additionally, it was utilized to examine the adsorption film on mild steel, zinc, and aluminium metal both before and after being submerged in the test solution.

3.9. Electrochemical studies

Electrochemical measurements were conducted using the SP-150 Biologic instrument, which makes use of a three-electrode electrochemical cell equipped with EC-lab software. The counter electrode (CE) was utilised in the form of a graphite rod, and mild steel, zinc and aluminium metals were used as the working electrodes (WE). Meanwhile, the reference electrode (RE) was utilised in the form of Ag/AgCl filled with 4.0 M KCl solution. The three electrodes were all plunged into the beaker containing the electrolyte solution, which in this study was the acid and the inhibitor acid solution, carefully ensuring that the RE was very close to the WE electrode so that the voltage IR drop could be minimised. The electrochemical cell was connected to the potentiostat, and the electrolyte and the three electrodes were kept under steady conditions at 303 K for all the measurements.

However, before the electrochemical measurements were taken, the metal was allowed to corrode freely in Open Circuit Potential (OCP) for 1 hour to stabilise the system and to obtain reliable results [190]. The two most important electrochemical techniques after the OCP, Electrochemical impedance spectroscopy (EIS) and potentiodynamic polarization (PDP) spectroscopy, also known as Tafel curve, were analysed. The EIS measurements were performed by using the AC signal to analyse the electrochemical system frequency response at 5 mV sinusoidal perturbation in 100 kHz to 100 mHz range.

© University of Venda

From the data obtained in the EIS measurements, the corrosion inhibition efficiency was calculated using Equation 78 [191-193].

$$\%IE_{EIS} = \left(\frac{R_{ct} - R^0_{CT}}{R_{ct}}\right) \times 100 \quad (78)$$

where R_{ct} and $R°_{ct}$ are the charge transfer resistance in the presence and absence of the extract inhibitor.

While in the PDP experiments, the corrosion inhibition was calculated as [192],

$$\%IE_{PDP} = \left(\frac{i^0_{corr} - i_{corr}}{i_{corr}}\right) \times 100 \quad (79)$$

where i^0_{corr} and i_{corr} are the corrosion current density values with and without the presence of the extract inhibitor.

3.10. wettability study

The wettability of mild steel, zinc and aluminium metals was investigated with contact angle surface measurements using Wenzel model since the surface of the metal after corrosion was rough, but still homogenous. The images were taken with a high-resolution camera set to macro. The drop angle was analysed using ImageJ software coupled with drop analysis-LB-ADSA. The drop was dropped on the metal surface using a pipette.

3.11. Computational studies

3.11.1. DFT calculations

The quantum chemical calculations were performed using the DMol3 module, which is based on density functional theory (DFT) in the Material Studio 2020 software [194-196]. The Perdew-Burke-Ernzerhof (PBE) functional was selected in the numerical-based DFT module DMol3 and complemented with generalised gradient approximation (GGA) and the double numerical basis set (DNP 4.4) to optimise the geometry of the selected inhibitors and metal surface [197-199]. GGA was used to approximate the exchange-correlation functional since it gives a better overall electronic system description [200]. The van der Waals (vdW) interactions between the isolated compounds and the selected surfaces of the metal were accurately accounted for using DFT-D. The DNP adds a polarization d-function on all non-hydrogen atoms and a polarization p-function on hydrogen atoms. The DFT semi-core

© University of Venda

pseudopots (DSPP) were used to account for relativistic effects inorder to balance calculation accuracy and computational efficiency and to accelerate the self-consistent field (SCF) charge density convergence [199]. These settings were used to get a general overview of the reactivity of the molecules under study [201]. The COSMO solvation model (defining water as the solvent) was employed to simulate the aqueous phase and generate the sigma profile.

Quantum chemical studies are a very helpful technique in explaining the relationship between the inhibition efficiency of a corrosion inhibitor and its molecular structure [39]. Recently, theoretical calculation techniques have become useful and effective in simulating the behaviour of corrosion inhibitors on the surface of the metal. This is actually performed to avoid the cost and energy consumption of the experimental tests [202]. The most stable adsorption configurations of ferulic acid, 4-P-coumarouyl quinic acid, 3-P-Coumaroyl-5-(E)-caffeic-quinic acid, 1.3-Dicaffeoylquinic acid, Caffeoyl-checorin and Caffeoyl-feruroyl-quinic acid in aluminium, zinc and mild steel metals, and their adsorption energy were investigated and displayed in Figure 10.2 – 10.13. The released adsorption energy when the relaxed adsorbate components of the six compounds are adsorbed on the metal surface was obtained by using Equation 80 given as [203],

$$E_{ads} = E_{Total} - (E_{adsorbate} + E_{substrate}), \quad (80)$$

where E_{Total} is the energy of the substrate (metal)-adsorbate (inhibitor) configuration, $E_{adsorbate}$ and $E_{Substrate}$ are the energy of extract molecules and the metal surface, respectively. The binding or adsorption energy is known as the energy needed to separate a particle from the system [204]. It is known that the adsorption energy of the inhibitor molecule on the metal surface is directly linked to the inhibitor's inhibitory efficiency [205].

The binding energy is related to the interaction energy by [206-208],

$$E_{adsorption} = - E_{interaction} \quad (81)$$

$$E_{binding} = - E_{adsorption} \quad (82)$$

The inhibitor molecule's interaction with the Al(111), Zn(110) and Fe(110) surfaces in an aqueous corrosive media at 298 K was simulated using the Material Studio 2020 software. The interaction phenomena between the *H. kraussii* extract metabolites, and the three metals surfaces were simulated in a three-dimensional box with the following periodic boundary conditions: 14.317145 x 17.317145 x 24.675696 $Å^3$, 24.734 x 23.078711 x 22.6649 $Å^3$ and 12.411876 x 12.411876 x 24.053702 $Å^3$ Al(111), Zn(110) and Fe(110), respectively, with a

© University of Venda

vacuum of 20 Å on the z-axis for the purpose of separating periodic repetition [203]. The simulation box for all the metals was constructed by employing the supercell of dimensions 5 x 5. The inhibitor molecules were then placed on the slab with the space for the relaxation of all atoms except the bottom atomic layers [209].

3.12. Scanning electron microscopy (SEM), energy dispersive spectroscopy (EDS) and X-ray diffraction (XRD)

SEM-EDS is a primary method employed to investigate and analyse the elemental composition of corrosion-related samples on the surface. The SEM examination offers insights into the morphology [210] and corrosion type of the metal surface. On the other hand, EDS is employed for elemental analysis [211]. The surface morphology of mild steel, zinc and aluminium metal immersed in the 1.0 M HCl and H_2SO_4 corrosive solution before and after the introduction of 1500 ppm of non-radiated and UV-radiated *H. kraussii* at 30 ℃ was done by SEM analysis using Phenom pro x instrument coupled with EDS for elemental composition at 15 Kv point and different magnification range (80 µn-930x, 30 µn -2050x and 20 µn -4000x). The X-ray diffraction (Rigaku instrument) was used to conduct the XRD analysis on the scratched mild steel, zinc and aluminium metal oxide film formed on the surface of the metals after the corrosion process at 2θ from (1-80˚). This technique was performed in the absence and presence of 1500 ppm of non-radiated and UV-radiated *H. kraussii* extract in 1.0 M HCl and H_2SO_4 solutions.

© University of Venda

RESULTS AND DISCUSSION

© University of Venda

CHAPTER 4

Identification and isolation of compounds

© University of Venda

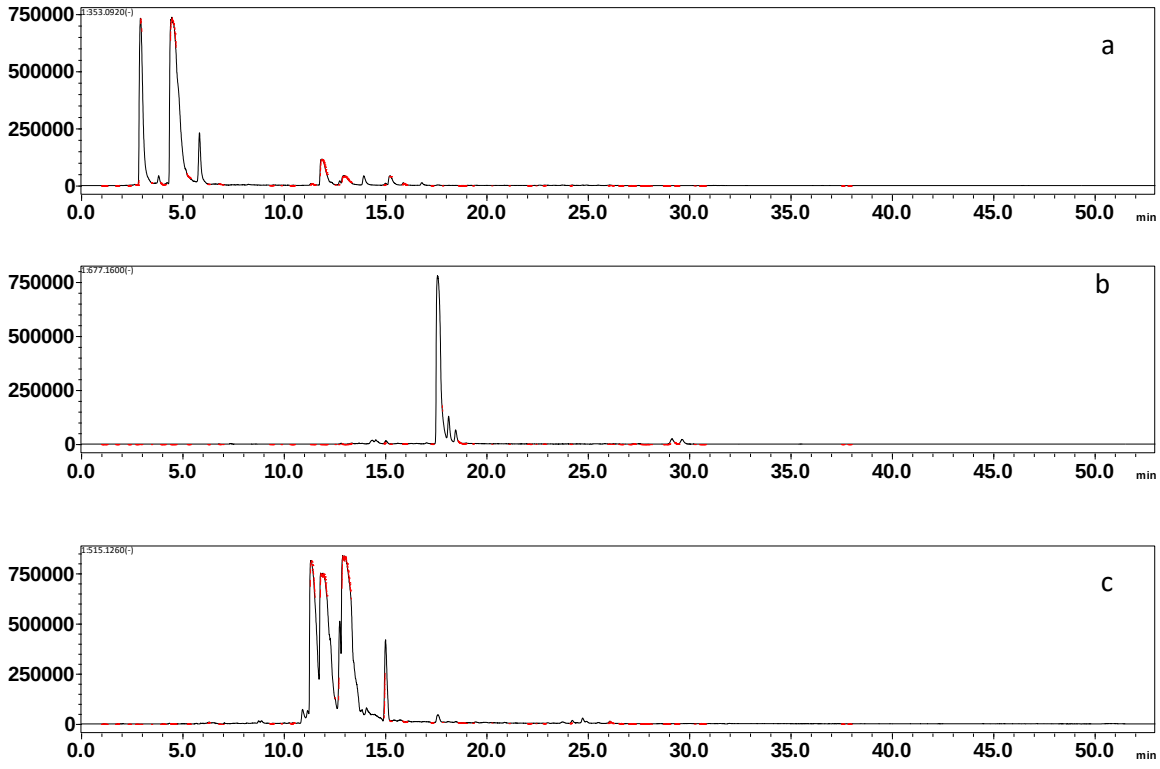
4. Introduction

This chapter discusses and shows the effect of UV radiation on *H. kraussii* plant extract and the isolation process for the compounds believed to be causing corrosion inhibition.

4.1. Liquid chromatography-mass spectrometry

Liquid chromatography-mass spectrometry (LC-MS) stands as a crucial analytical method employed for the quantification, separation, and classification of both identified and unidentified chemicals. This technique enhances comprehension of the structural and chemical attributes of diverse molecules. Particularly, it is ideal for measurements of small molecules. LC-MS delivers pronounced sensitivity and selectivity, proving valuable in the examination of trace amounts of substances, as seen in the complex composition of plant extracts [212]. Sections 4.1.1., 4.1.2 and 4.4 show some LCMS spectra for both the non-radiated and UV-radiated *H. kraussii* extract.

4.1.1. Non-*Helichrysum kraussii* extract Controls (24 HOURS)



© University of Venda

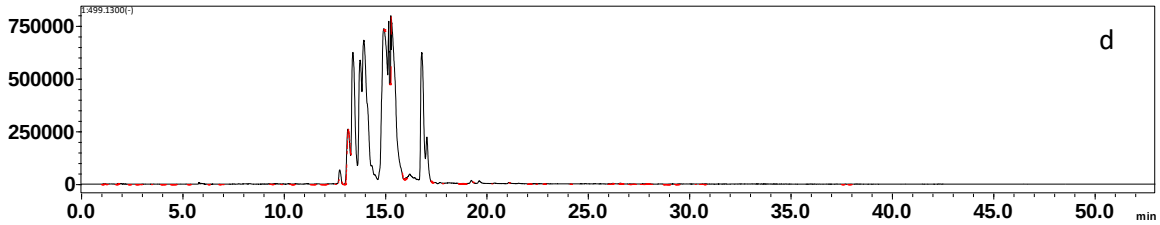


Figure 4. 1: Representative of LC-MS chromatogram showing separation of the different isomers of mono-acylated caffeoylquinic acid from non-radiated *H. kraussii* extracts at different retention time shaked for 24 hours.

4.1.2. UV-radiated *H. kraussii* extract

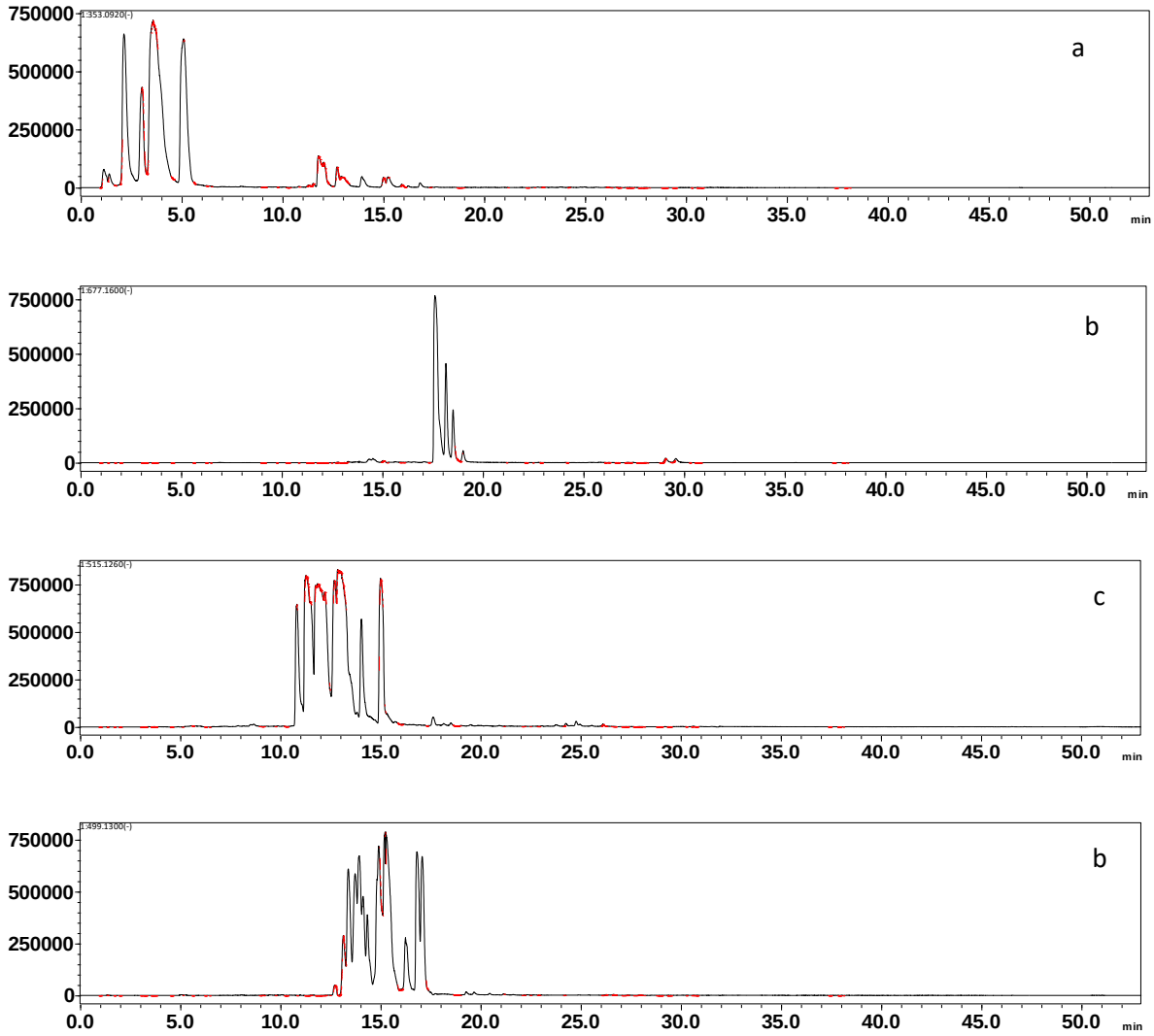


Figure 4. 2: Representative of LC-MS chromatogram showing separation of the different isomers of mono-acylated caffeoylquinic acid from UV-radiated *H. kraussii* extracts at different retention time shaked for 3 hours.

© University of Venda

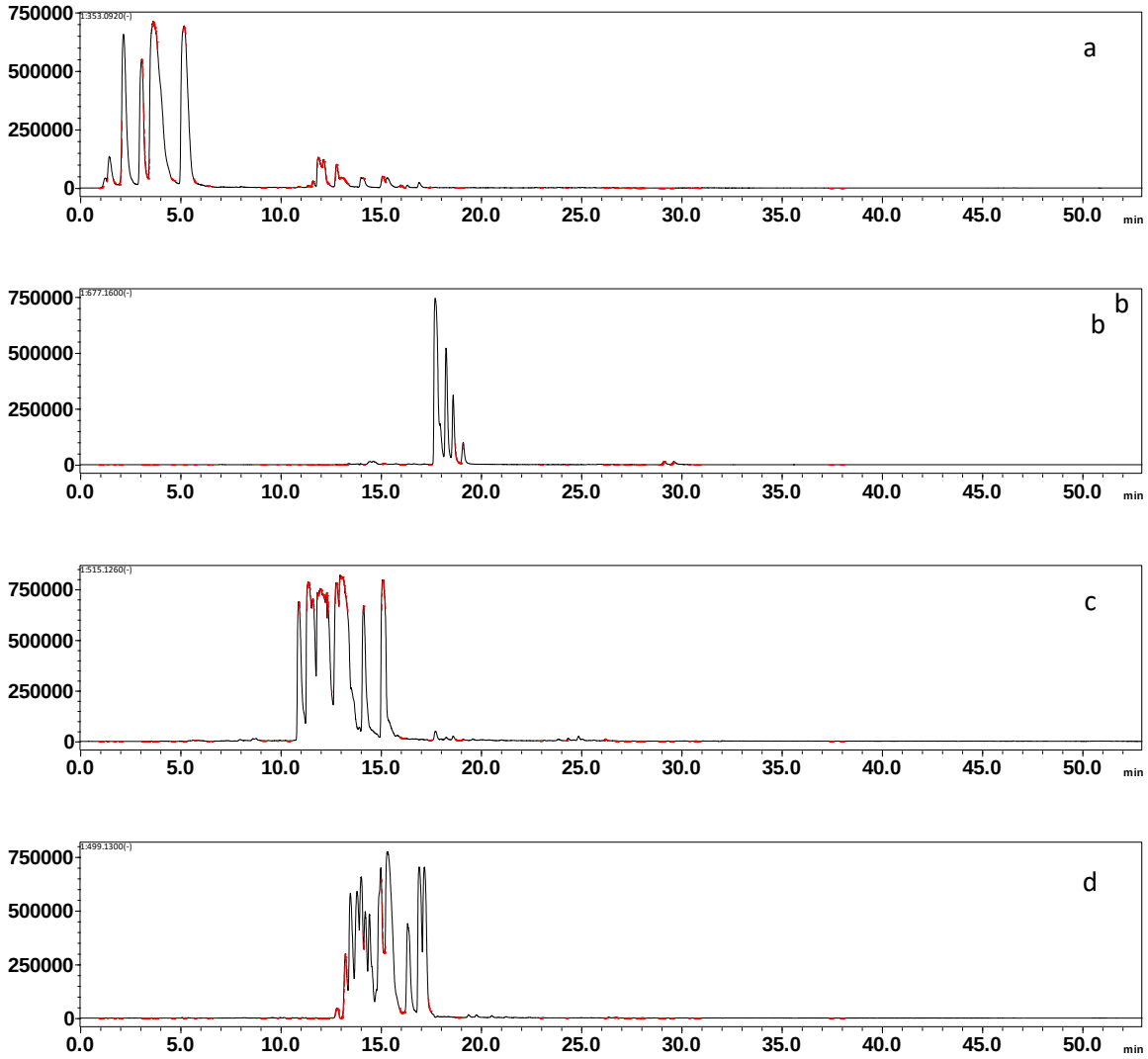
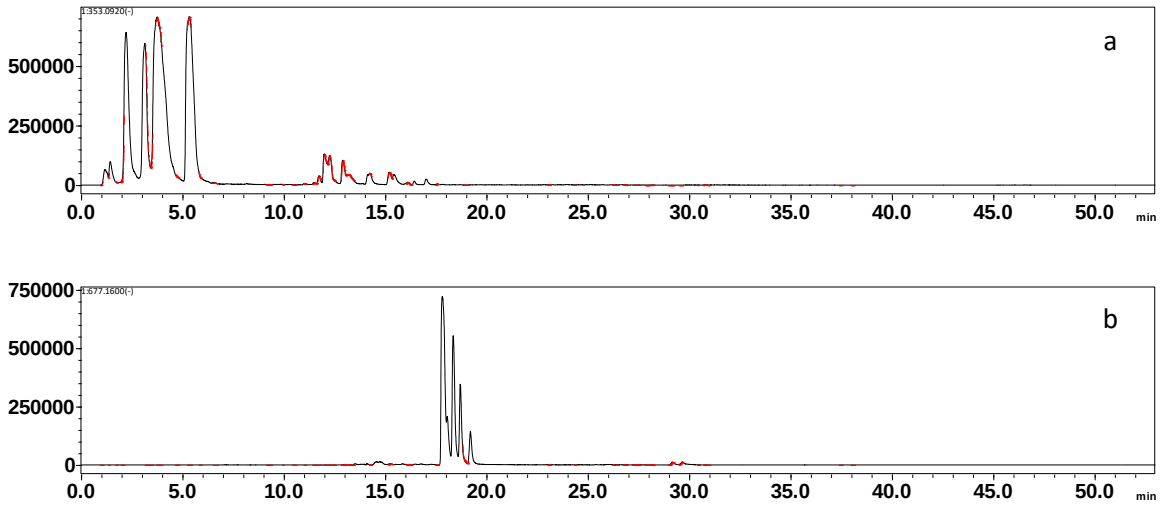


Figure 4. 3: Representative of LC-MS chromatogram showing separation of the different isomers of mono-acylated caffeoylquinic acid from UV-radiated *H. kraussii* extracts at different retention time shaked for 6 hours.



© University of Venda

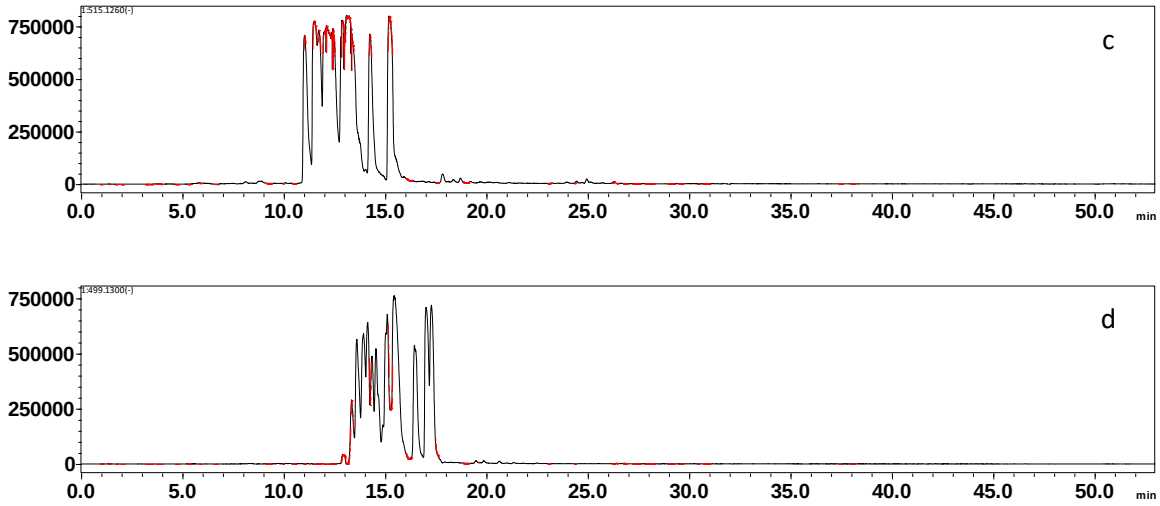
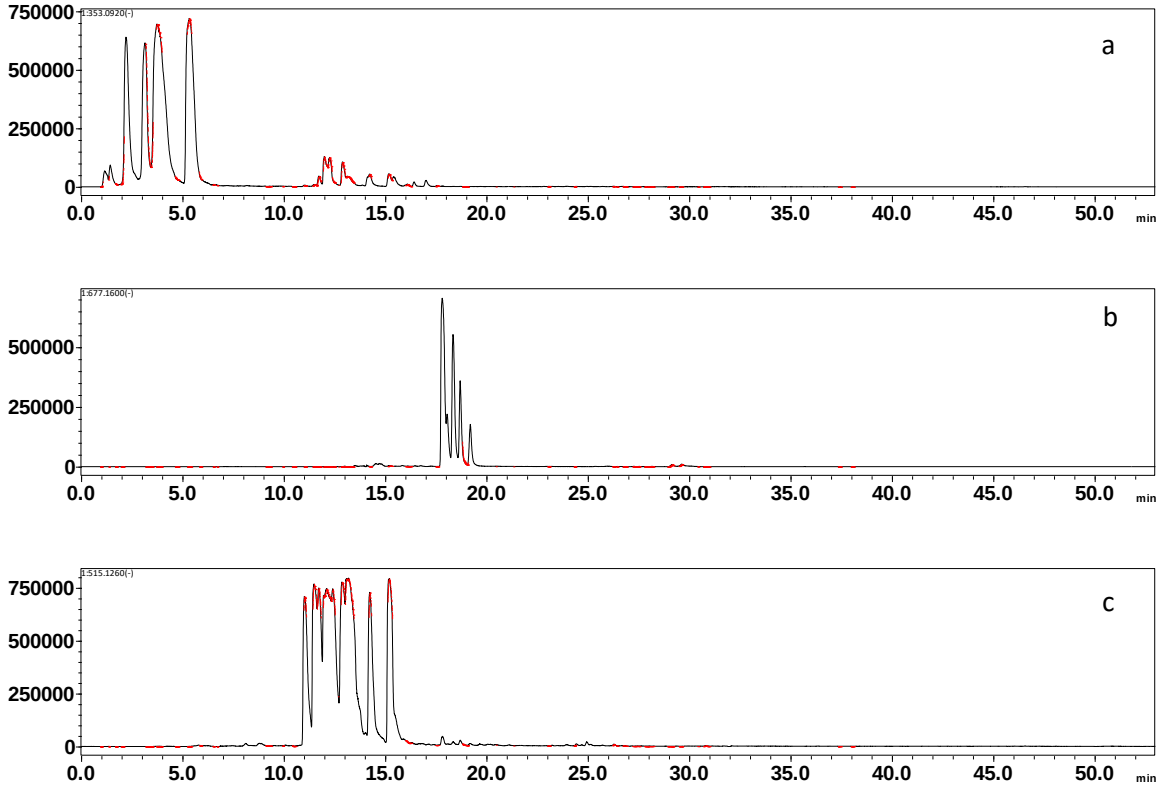


Figure 4. 4: Representative of LC-MS chromatogram showing separation of the different isomers of mono-acylated caffeoylquinic acid from UV-radiated *H. kraussii* extracts at different retention time shaked for 9 hours.



© University of Venda

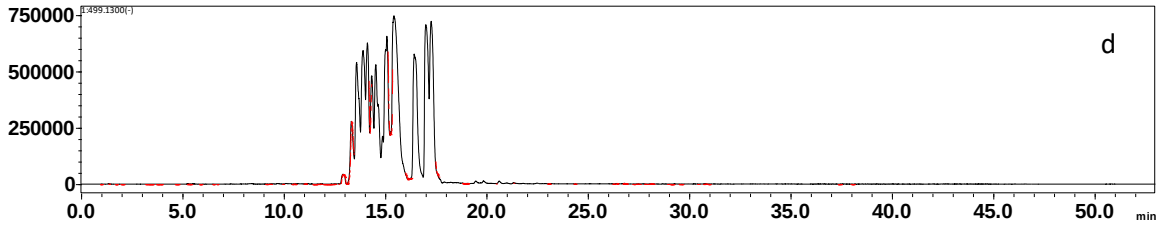


Figure 4. 5: Representative of LC-MS chromatogram showing separation of the different isomers of mono-acylated caffeoylquinic acid from UV-radiated *H. kraussii* extracts at different retention time shaked for 12 hours.

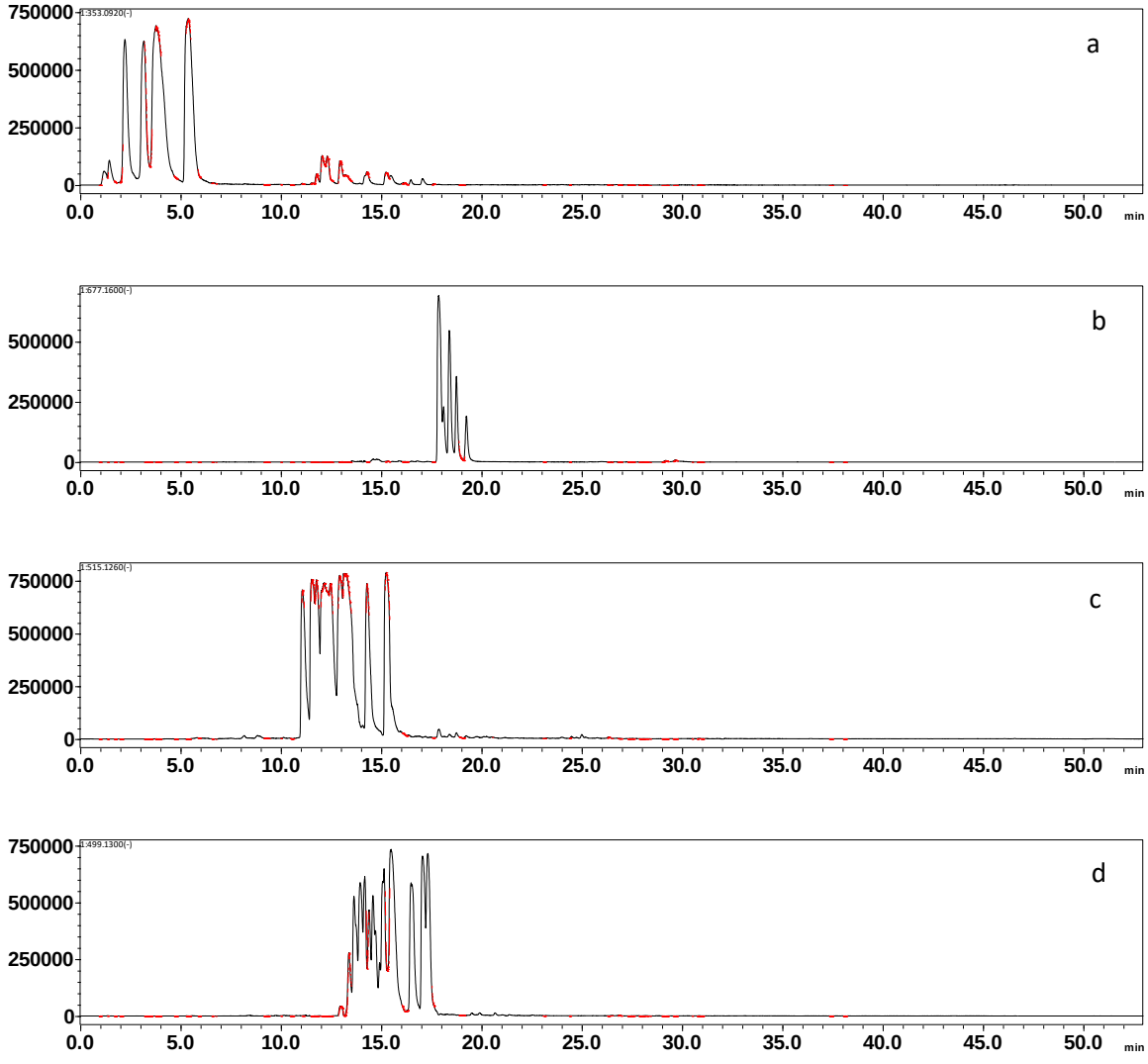


Figure 4. 6: Representative of LC-MS chromatogram showing separation of the different isomers of mono-acylated caffeoylquinic acid from UV-radiated *H. kraussii* extracts at different retention time shaked for 15 hours.

© University of Venda

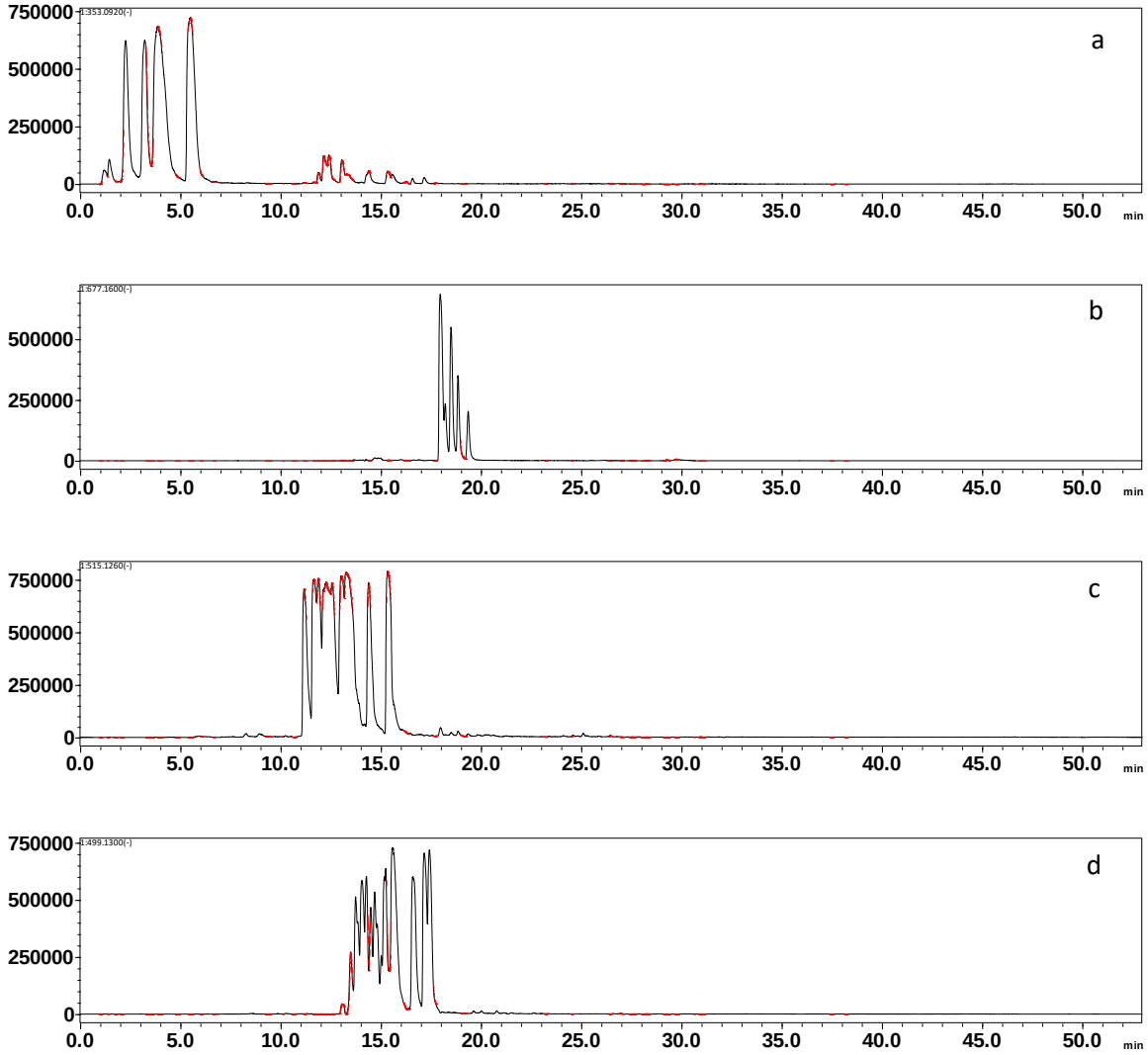
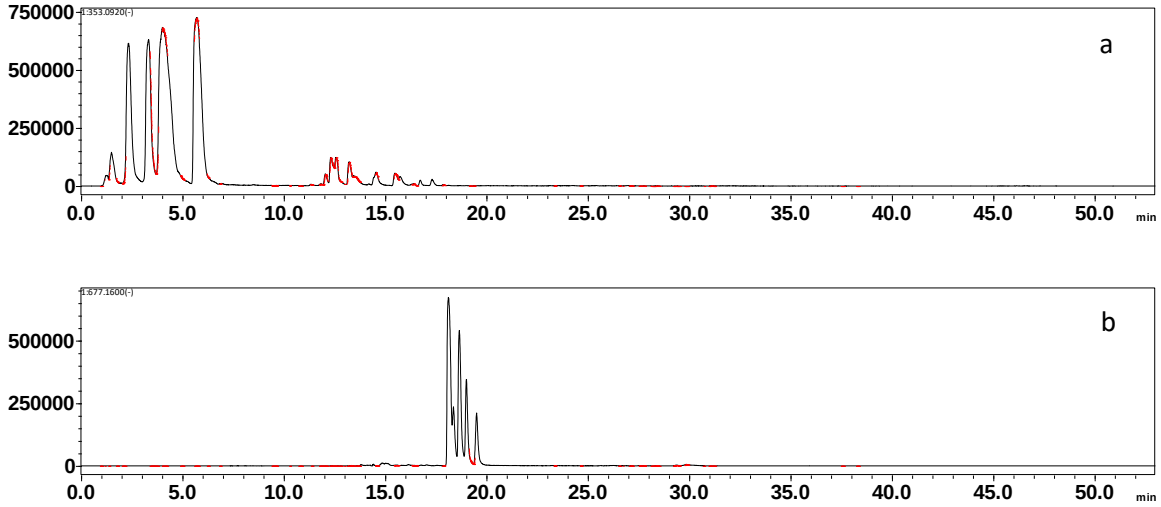


Figure 4. 7: Representative of LC-MS chromatogram showing separation of the different isomers of mono-acylated caffeoylquinic acid from UV-radiated *H. kraussii* extracts at different retention time shaked for 18 hours.



© University of Venda

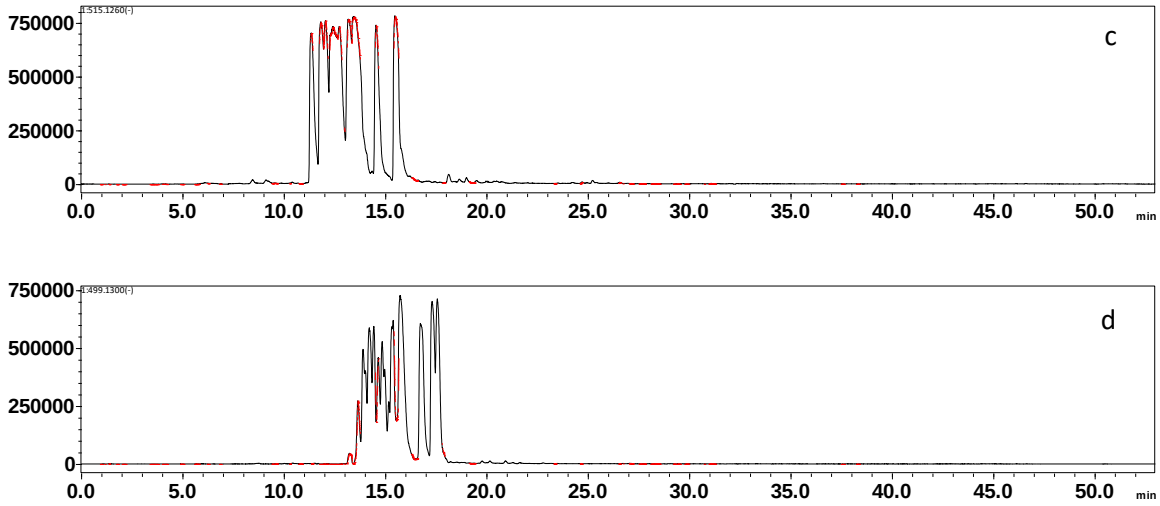
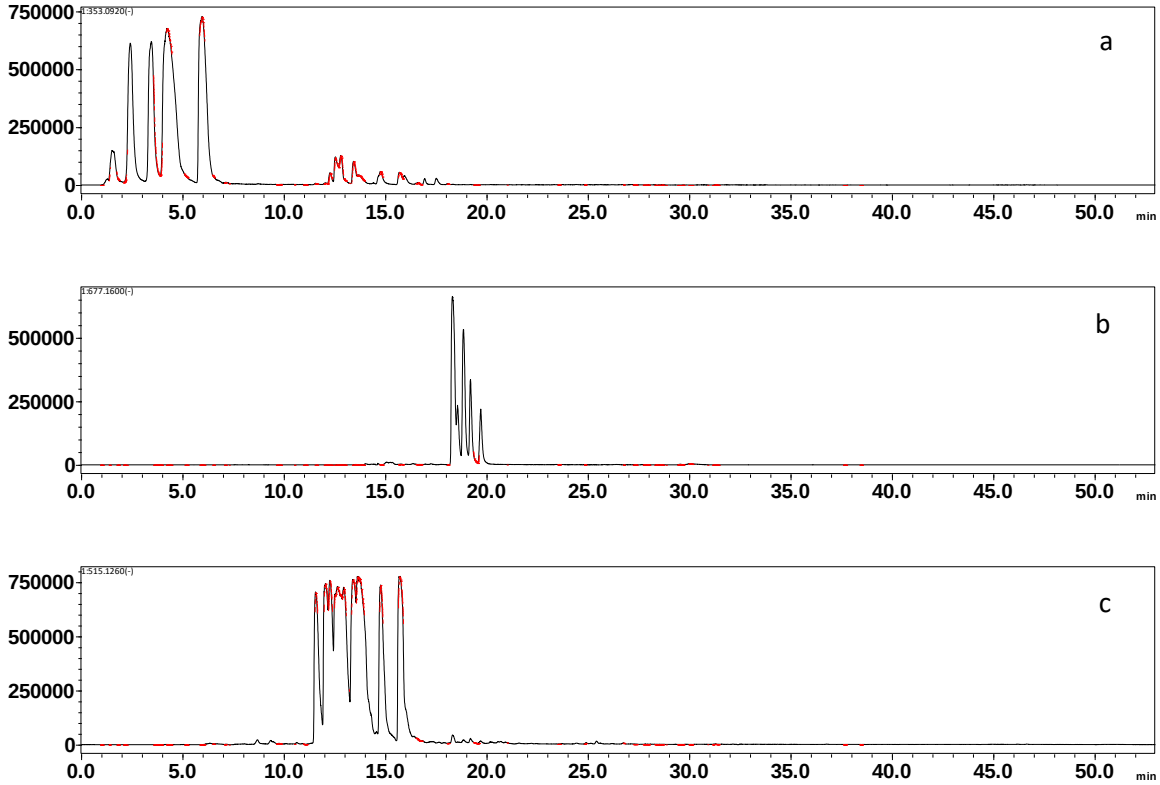


Figure 4. 8: Representative of LC-MS chromatogram showing separation of the different isomers of mono-acylated caffeoylquinic acid from UV-radiated *H. kraussii* extracts at different retention time shaked for 21 hours.



© University of Venda

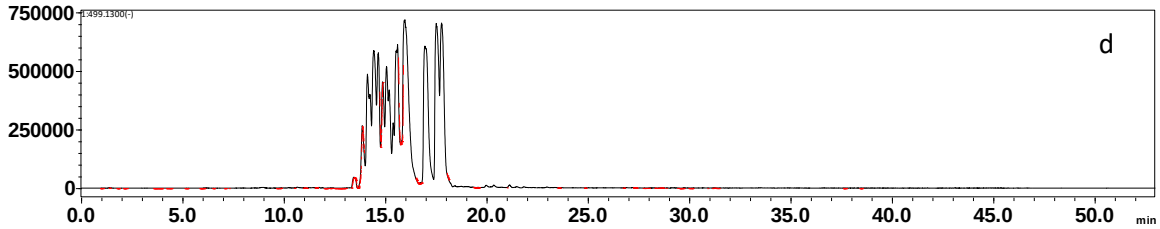


Figure 4. 9: Representative of LC-MS chromatogram showing separation of the different isomers of mono-acylated caffeoylquinic acid from UV-radiated *H. kraussii* extracts at different retention time shaked for 24 hours.

Some of the compounds found in Plants are said to undergo geometrical isomerisation when exposed to UV radiation. Naturally, plants are found in their trans isomerisation, and when exposed to UV, some of the compounds found in the plant can undergo Cis geometrical isomerisation. The *H. kraussii* plant extract was exposed to UV radiation in order to see if the compounds found in the plant extract undergo geometrical isomerisation under the influence of UV radiation. In order to achieve that, the two *H. kraussii* extracts (UV-radiated and non-radiated) were run on LCMS, and the data obtained is shown in Figure 4.1 - 4.9. The non-radiated extract was put in the dark for 24 hours before being run on LCMS. The UV-radiated extract was placed under UV light for 24 hours while monitoring and extracting a small amount of the sample from the quarts tube after each and every 3 hours and then analysed under LCMS, as shown in Figures 4.2- 4.9. A change in the peak intensity and emergence of new peaks was obtained after the first 3 hours, confirming the formation of the geometrical isomers with respect to the unexposed extract. At around m/z 0.0 – 0.7, it can be observed that after the UV exposure of the *H. kraussii* extract, there was an increase in the peaks intensity and the emergence of new peaks in Figure 4.2 (a) compared to Figure 4.1 (a). From all the other 3 hours, there was no significant change in the spectra for 24 hours as compared to the spectrum of Figure 4.2. This observation is an indication that 3 hours was enough to cause the geometrical isomerisation on the extract metabolites and that the prolonged exposure time did not have a significant impact. However, 24 hours was taken as the standard time of exposure for the UV-radiated *H. kraussii* extract.

© University of Venda

4.2. Fourier Transform Infrared Spectroscopy (FTIR)

Figure 4.10 and Table 4.1 show the spectrum and the detected functional groups for *H. kraussii* extract (Black) and UV-radiated *H. kraussii* extract (Red). Since the UV light exposure only transforms the geometrical isomerisation of plant extract, usually from their trans to cis isomerisation, it is therefore expected that no new functional groups will be formed, and no disappearance of functional groups will occur [213, 214]. This is because the geometrical isomerisation only changes the orientation of the functional group and not the functional groups present. This means that the two extracts will have similar functional groups, with only a slight shift in the adsorption regions. From the table, it can be observed that all the extracts contain functional groups such as O-H alcohol, N-H amine and amide, C-O ketone and aldehyde, NO_2 nitro, C≡C alkyne amongst others, which are known good functional groups to cause inhibition efficiency. Even though geometrical isomers do not cause the change in the functional group, there was a bit of variation in the functional groups detected. The pure *H. kraussii* extract contains functional groups such as Sp^3 C-H (C-C-H), C≡C alkyne, amine C-N and C=C alkene, which are not present in the UV-*radiated H. kraussii* extract. Meanwhile, the UV-radiated *H. kraussii* extract contains functional groups such as Sp C-H (C≡C-H) and C-H aromatic, which are not present in the non-radiated *H. kraussii* extract. One of the main reasons for this unexpected functional group variation is because the instrument peaked them with a very low insignificant intensity, which might have caused them not to appear on both extracts. The most common functional groups where peaked at around 3260 – 3600 cm^{-1}.

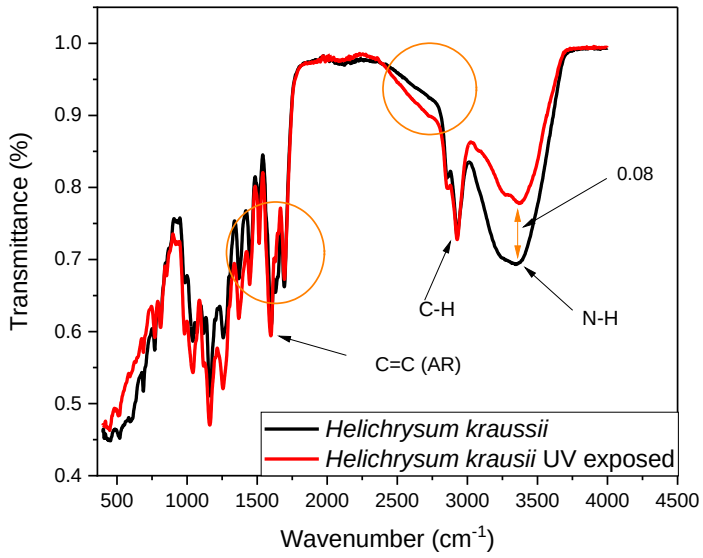


Figure 4. 10: FTIR spectra for *H. kraussii* plant extract (Black) and UV-radiated *H. kraussii* plant extract (Red).

© University of Venda

Table 4. 1: Functional groups from the FTIR spectra

	Functional Groups	
Bands position (cm^{-1})	**Solid *H. kraussii***	**UV-radiated *H. kraussii***
2400 – 3600	O-H Carboxylic acid	O-H Carboxylic acid
3300 – 3500	O-H alcohol	O-H alcohol
3200 – 3400	N-H amine N-H amide	N-H amine N-H amide
3260 – 3390		Sp C-H (C≡C-H)
2850 – 2960	Sp^3 C-H (C-C-H)	
2100 – 2250	C≡C alkyne	
1680 – 1720	C=O ketone C=O aldehyde	C=O ketone C=O aldehyde
1600 – 1650	C=C alkene	
1500 – 1570	NO_2 Nitro C=C aromatic	NO_2 Nitro C=C aromatic
1450 – 1470		
1180 – 1360	amine C-N	
1000 – 1200	Sp^3 C-O	Sp^3 C-O
900 – 1000		C-H aromatic
600 – 900	C-Cl chloride C-C alkane C-H aromatic	C-Cl chloride C-C alkane C-H aromatic

4.3. Isolation of compounds causing corrosion inhibition

Sirius 5.5.7 software was used to identify the compounds, number of compounds, molar masses, and molecular formulae of compounds that were possibly found in non-radiated and UV-radiated extracts. Two thousand three hundred ninety-seven (2397) compounds were found in the non-radiated extract, and two thousand three hundred and eighty-four (2384) in the UV-radiated extract, compounds were found as displayed in figures 4.11 and 4.12.

© University of Venda

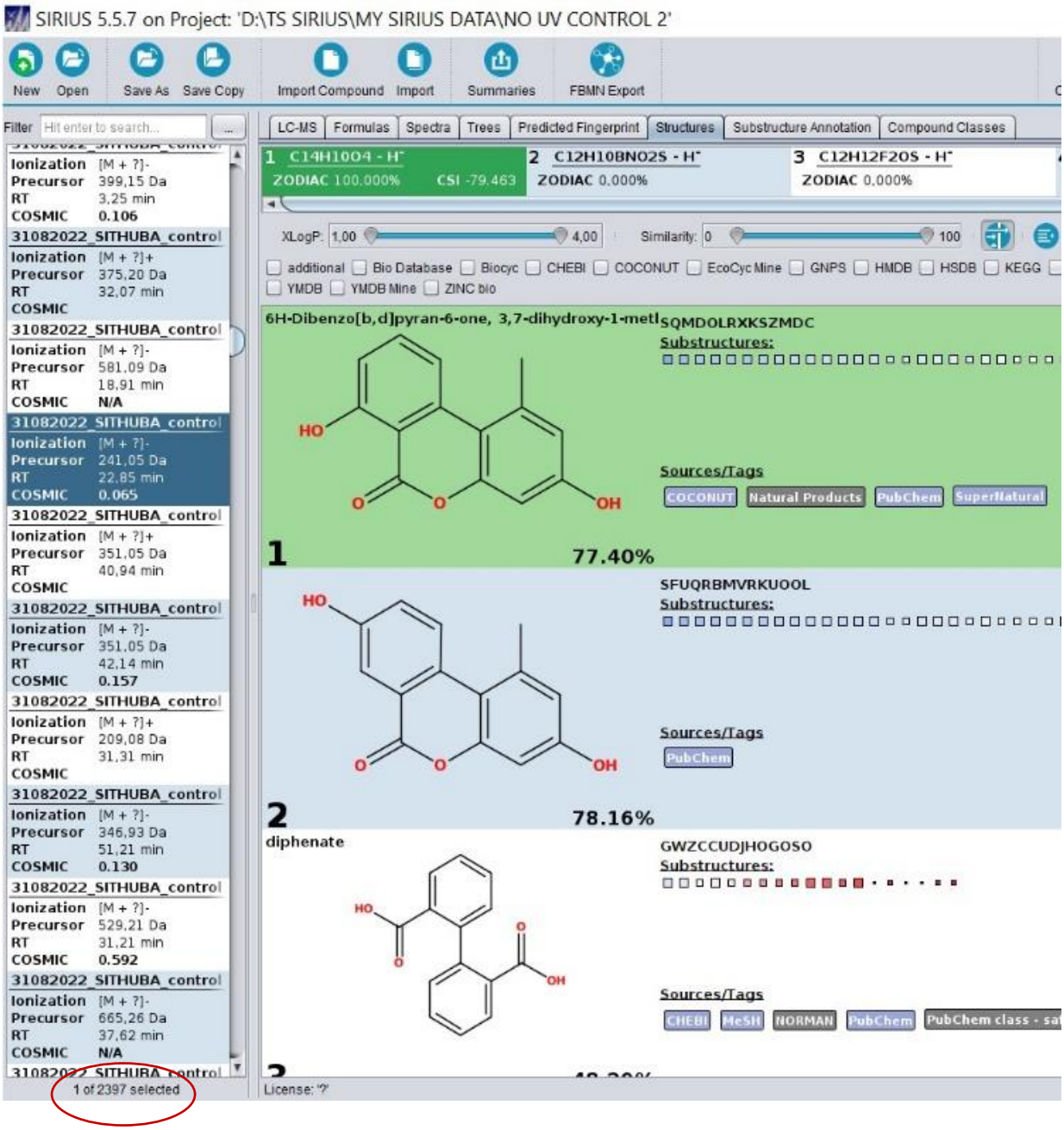


Figure 4. 11: Sirius software showing all the possible compounds found in the *H. kraussii* plant.

© University of Venda

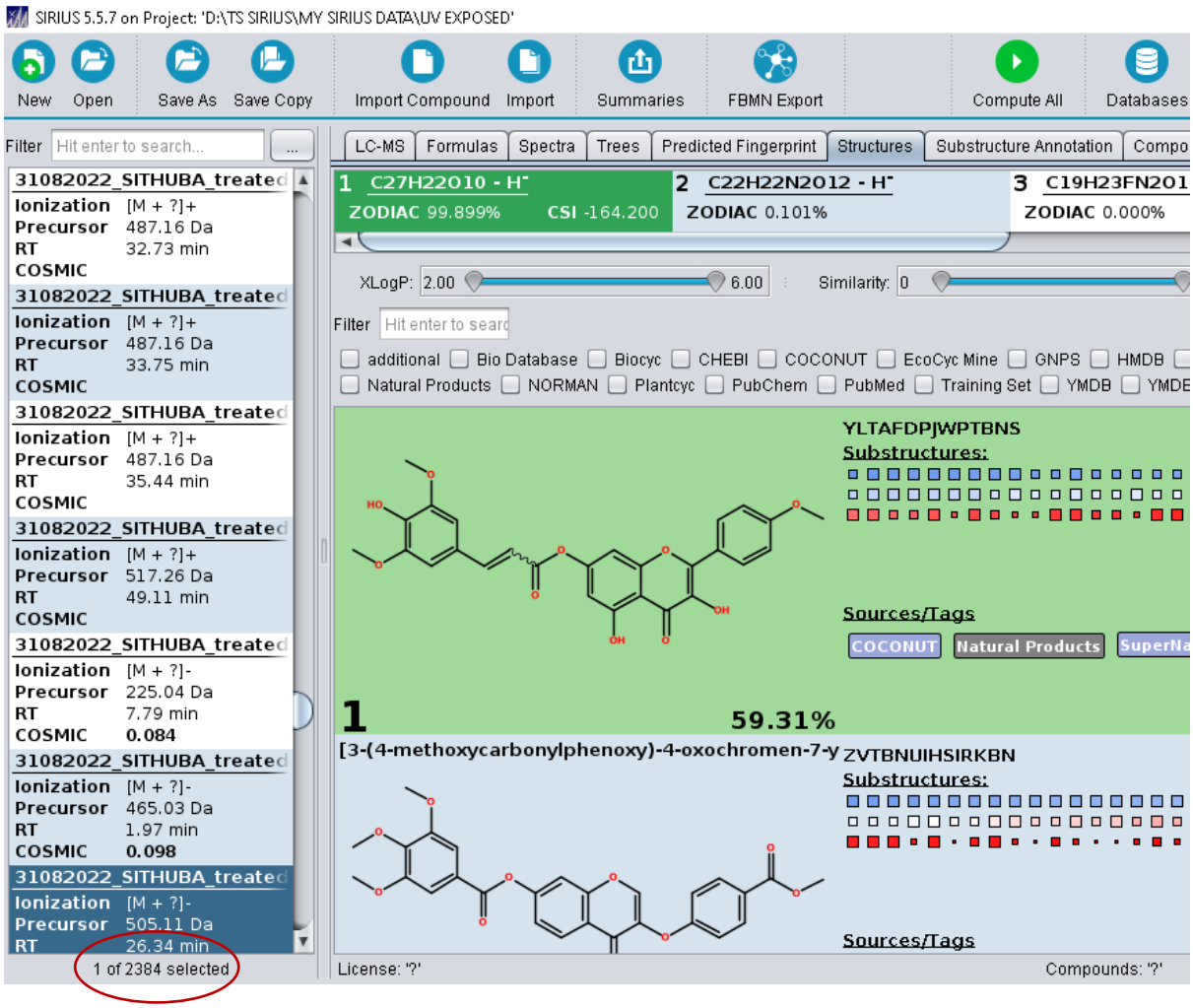


Figure 4. 12: Sirius software showing all the possible compounds found in the UV-radiated *H. kraussii* plant.

4.3.1. Column chromatography

Column chromatography is the most common, simple, and effective technique used to separate and purify different extracts. Liquids and solids can be purified and separated using this technique. It is composed of a solid stationary phase that separates and adsorbs the compounds passing through it with the aid of a liquid mobile phase [188, 215]. Column chromatography was used to separate the metabolites found in the *H. kraussii* extract. Table 4.2 shows the weight loss and inhibition efficiency for the 15 fractions collected.

© University of Venda

Table 4. 2: Shows weight loss and percentage inhibition efficiency for the 15 fractions in 1.0 M H_2SO_4.

Metal	Temperature	Fraction number	Weight loss (g)	% Inhibition
Mild steel	30 ^{0}C	0	0.4894	
		1	0.5276	-7.8055
		2	0.2215	54.7405
		3	0.1418	71.0257
		4	0.2979	39.1295
		5	0.3589	26.6653
		6	0.4095	16.3261
		7	0.4114	15.9379
		8	0.5171	-5.6600
		9	0.5332	-8.7454
		10	0.4979	-1.7368
		11	0.4757	2.7993
		12	0.5027	-2.7176
		13	0.5005	-2.2681
		14	0.6281	-28.3408
		15	0.3298	32.6114

The non-radiated extract was run through the column chromatography with 5% methanol and 95% ethyl acetate as the mobile phase. Fifteen fractions were collected from the column, the gravimetric analysis was performed for each fraction, and the percentage inhibition efficiency was calculated. Fraction number 3 gave the highest corrosion inhibition efficiency of 71.0257 %. Fraction number 14 gave the lowest inhibition efficiency of -28.3408 %. It was concluded that the fractions that gave the lowest or negative inhibition efficiency contained the compounds that mostly enhanced the corrosion of the metals, while those that gave the positive inhibition efficiency contained most of the compounds that caused the corrosion inhibition of the metals. All 15 fractions were also run on LCMS; their chromatogram is listed in Figure 4.13.

© University of Venda

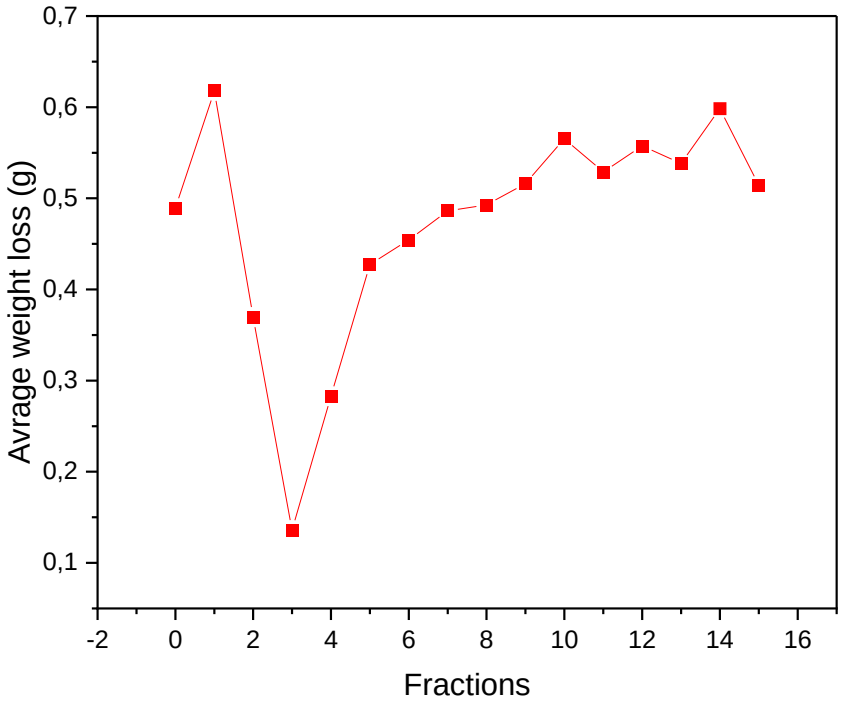
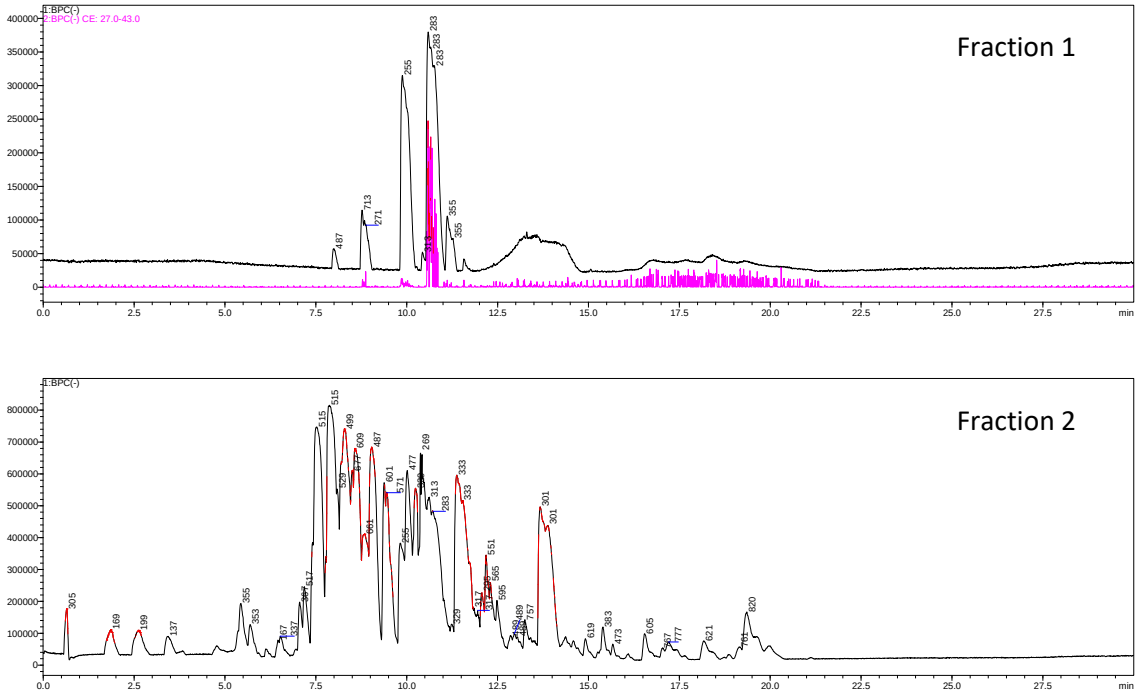
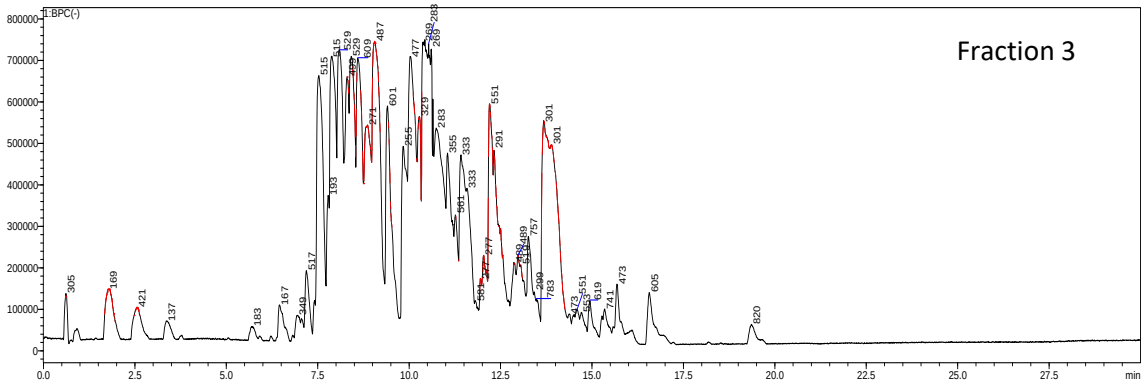
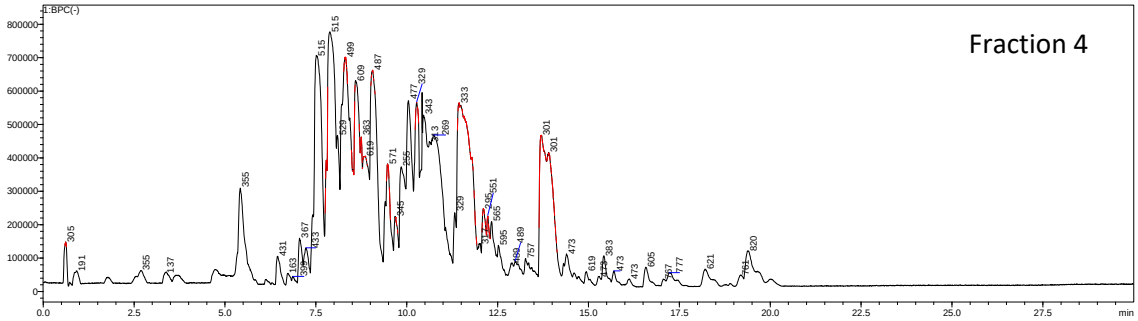


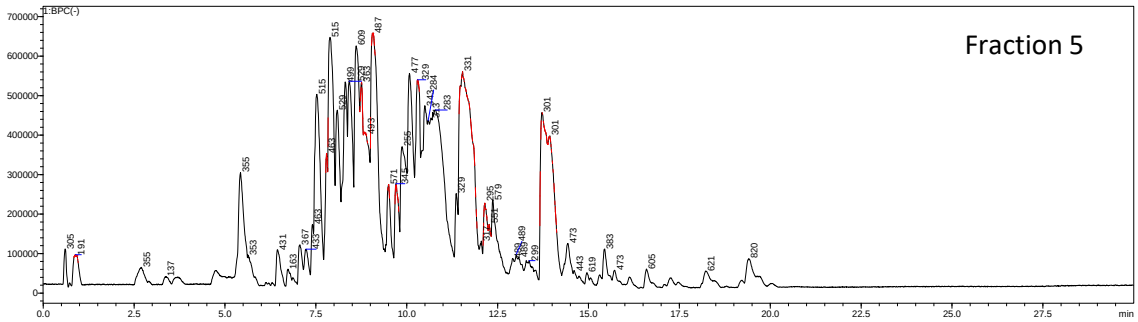
Figure 4. 13: The graphical representation of the weight loss of mild steel metal.

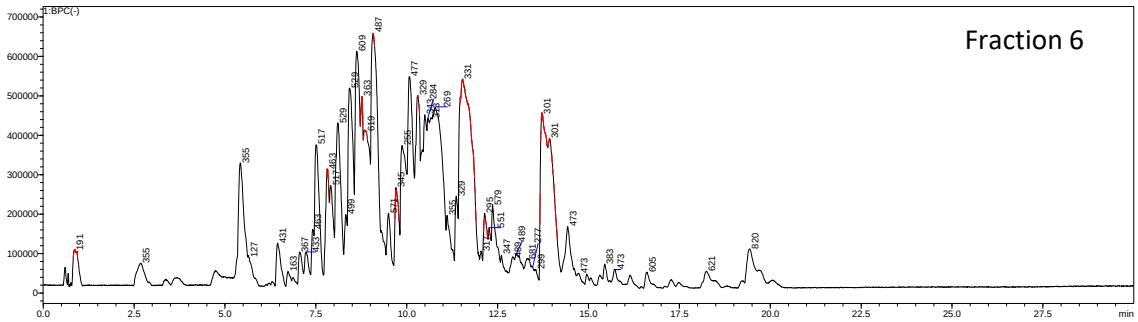


© University of Venda

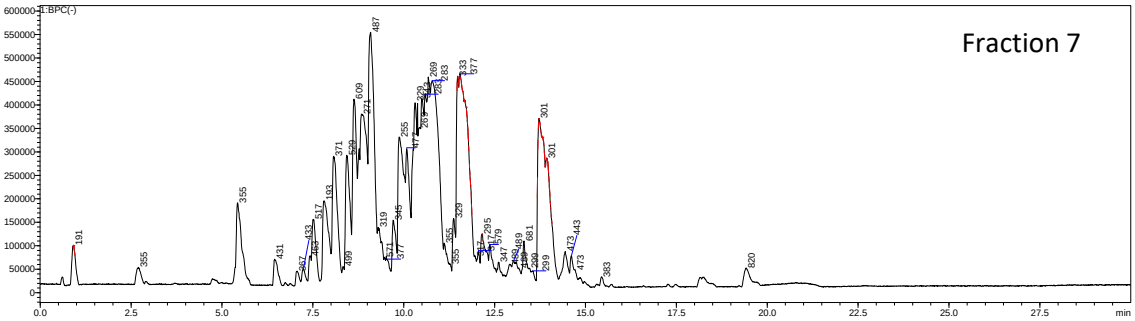


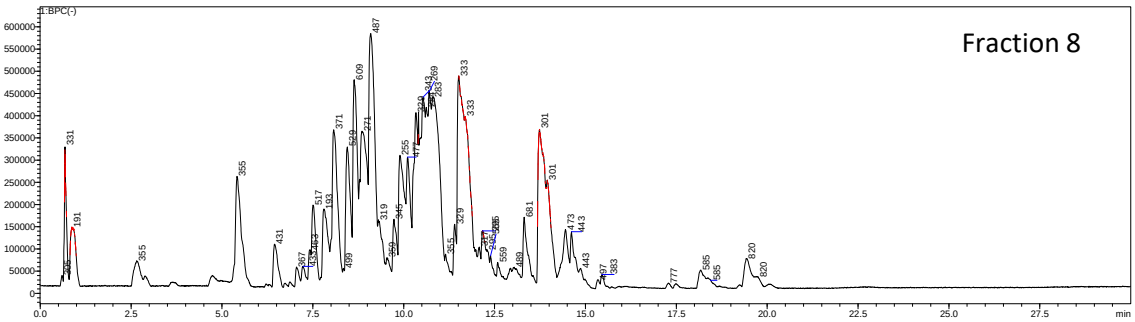


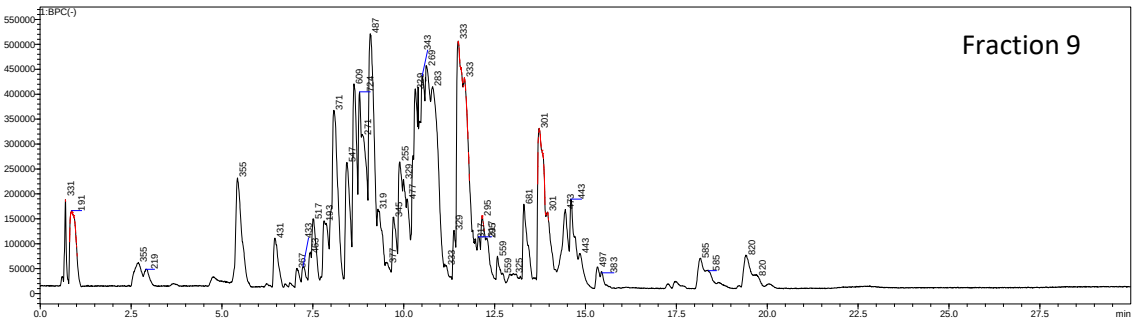


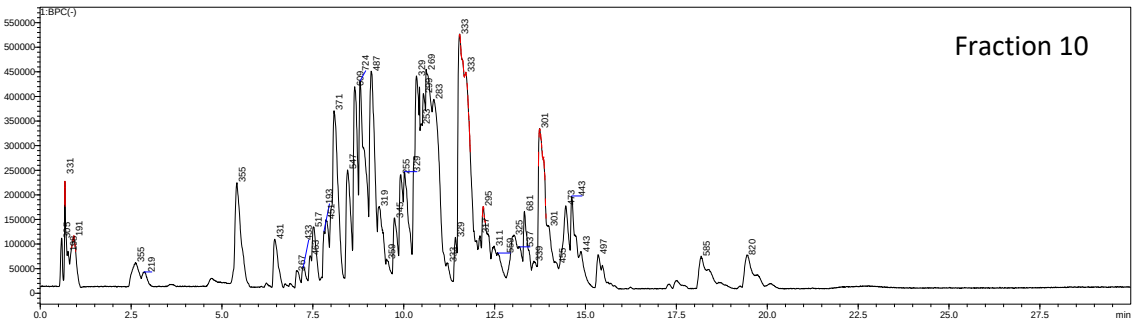


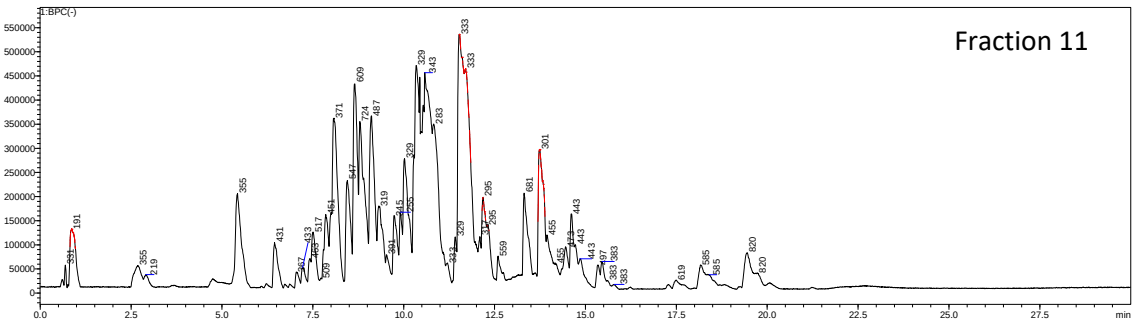
© University of Venda











© University of Venda

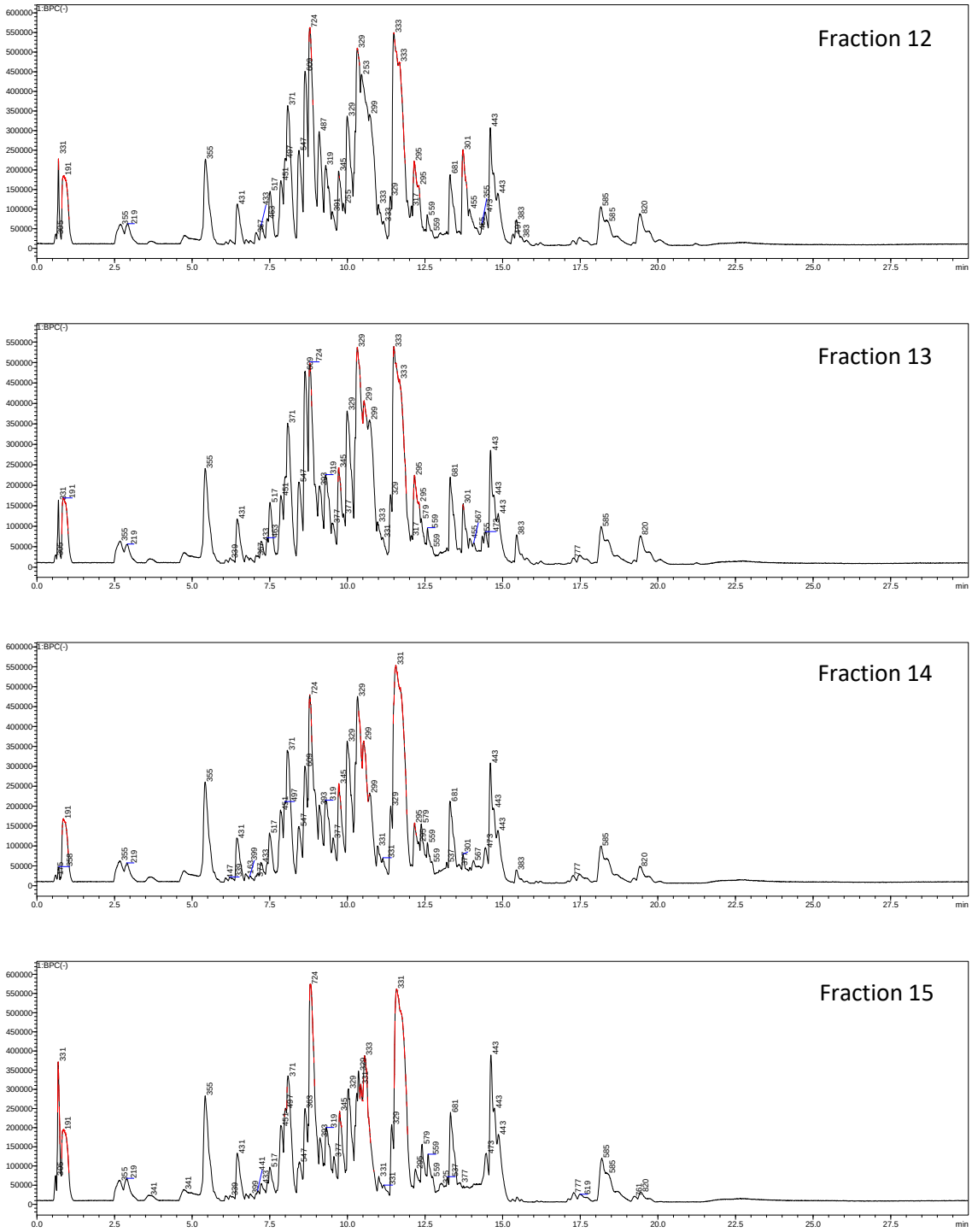


Figure 4. 14: Representative of LC-MS chromatogram for the 15 different fractions collected from column chromatography showing separation of the different isomers of mono-acylated caffeoylquinic acid from non-radiated *H. kraussii* extracts at different retention times.

© University of Venda

The elimination process was used to distinguish the compounds that cause the corrosion inhibition and those that enhance the metal's corrosion by running the m/z data obtained from LCMS in SIRIUS software. The extract itself, before column chromatography, had 2397 compounds. However, after running the column, fraction number 3, which gave the highest inhibition, was now found to contain 863 compounds and fraction number 8, which contains compounds that mostly enhance the corrosion of the metal, was found to have 768 compounds. All the compounds found in fraction eight were eliminated in fraction 3, and only a few were left, which are considered to be the ones among the compounds causing corrosion inhibition. Fractions 3 and 8 were taken for further analysis based on their position in the column extract constituent's collection since they might contain most of the extract constituents and because one gives positive inhibition and the other negative inhibition. This is the justification why fraction 14, which appeared to have the lowest inhibition efficiency, was not chosen for further analysis since it might be containing mostly the compounds from the mobile phase based on its position in the column extract constituents. Besides its position in the column extract constituent's collection, fraction number 3 chromatogram contains many peaks which are high in intensity and correspond to the number of compounds and their abundance compared to the other fractions chromatograms, which might be the reason for its high inhibition efficiency.

© University of Venda

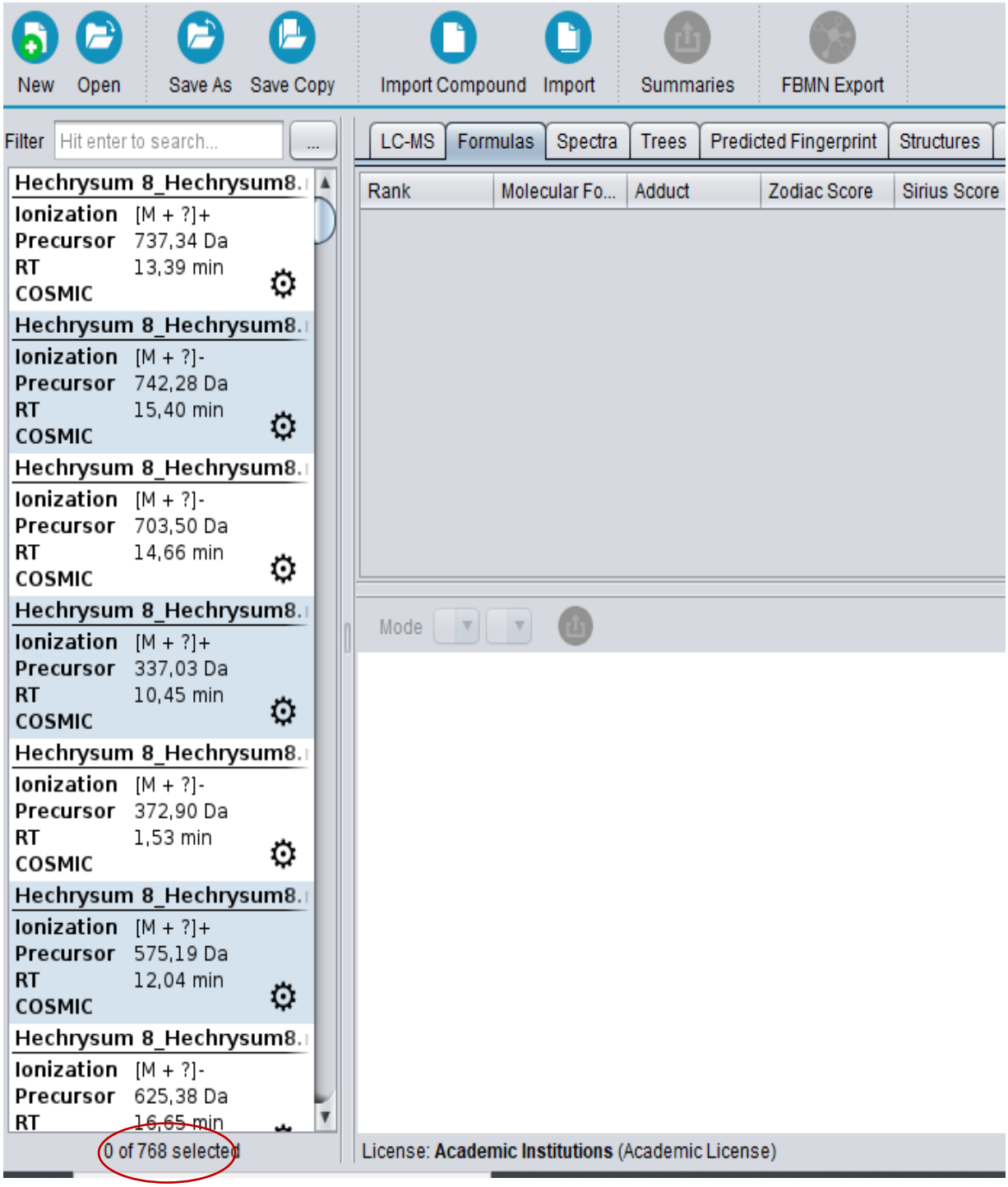


Figure 4. 15: Sirius software showing all the possible compounds found in fraction 8 of the *H. kraussii* plant.

© University of Venda

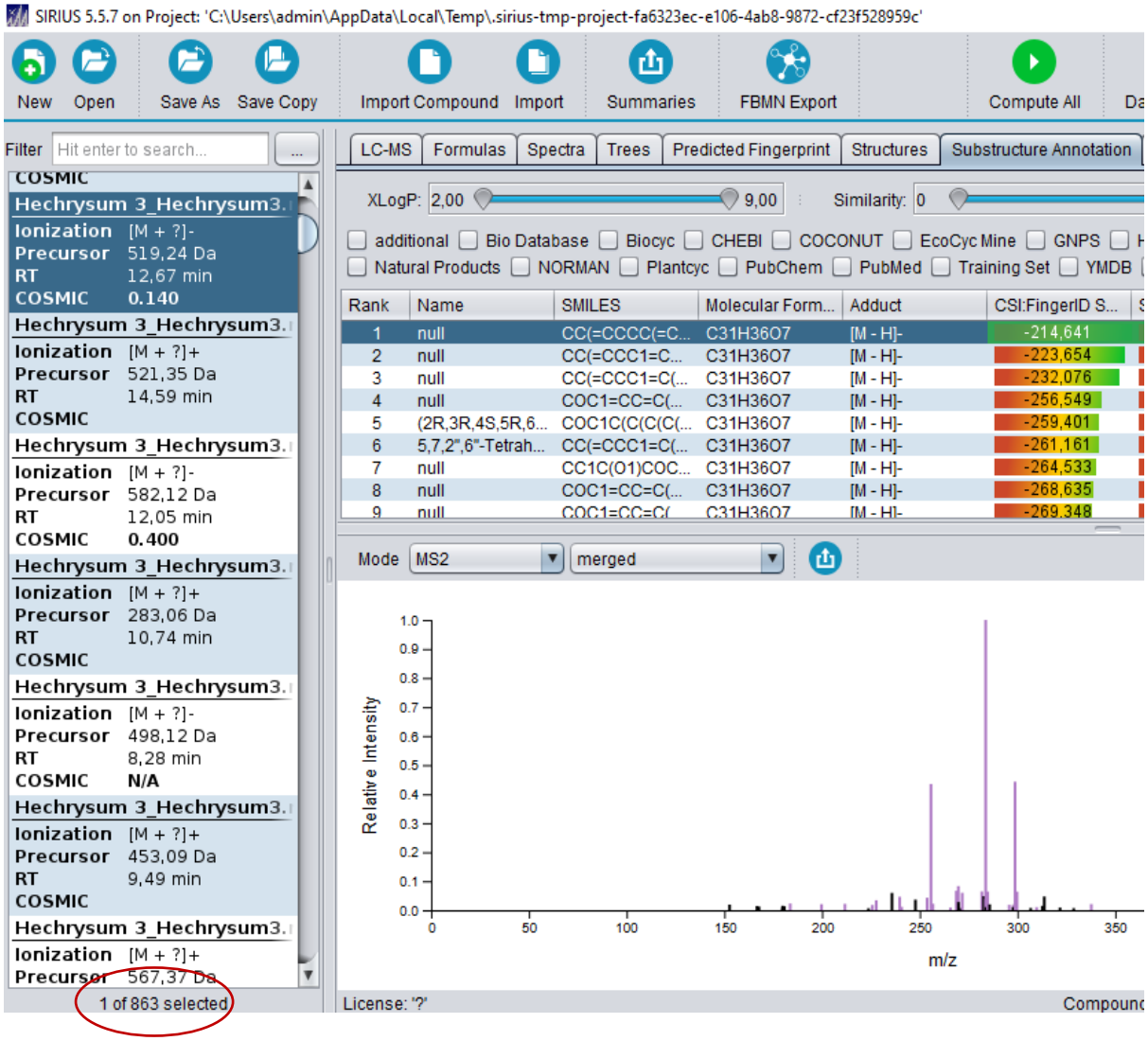
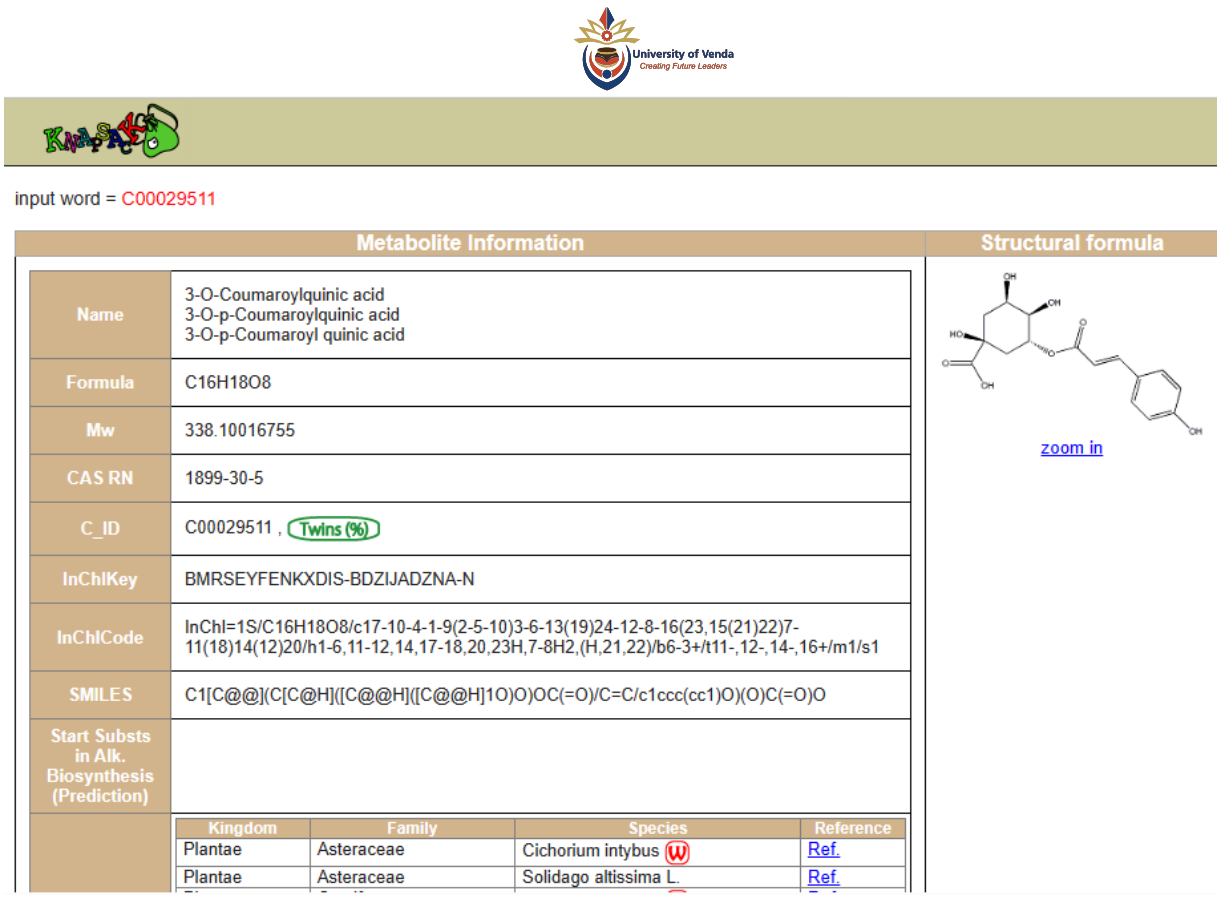


Figure 4. 16: Sirius software showing all the possible compounds found in fraction 3 of the *H. kraussii* plant.

From the compounds left after elimination based on fraction number 3. Molecular networking was used to further isolate and identify the compounds found in the plant extract. After that, Knapsack was used to confirm if the compounds obtained fall within the family of the *H. kraussii* plant. The *H. kraussii* plant falls within the Asteraceae family. The compounds found not to fall within the Asteraceae family were then eliminated. After that

© University of Venda



input word = C00029511

Metabolite Information	
Name	3-O-Coumaroylquinic acid 3-O-p-Coumaroylquinic acid 3-O-p-Coumaroyl quinic acid
Formula	C16H18O8
Mw	338.10016755
CAS RN	1899-30-5
C_ID	C00029511 , Twins (%)
InChIKey	BMRSEYFENKXDIS-BDZIJADZNA-N
InChICode	InChI=1S/C16H18O8/c17-10-4-1-9(2-5-10)3-6-13(19)24-12-8-16(23,15(21)22)7-11(18)14(12)20/h1-6,11-12,14,17-18,20,23H,7-8H2,(H,21,22)/b6-3+/t11-,12-,14-,16+/m1/s1
SMILES	C1[C@@](C[C@H]([C@@H]([C@@H]1O)O)OC(=O)/C=C/c1ccc(cc1)O)(O)C(=O)O
Start Substs in Alk. Biosynthesis (Prediction)	

Kingdom	Family	Species	Reference
Plantae	Asteraceae	Cichorium intybus W	Ref.
Plantae	Asteraceae	Solidago altissima L.	Ref.

Structural formula

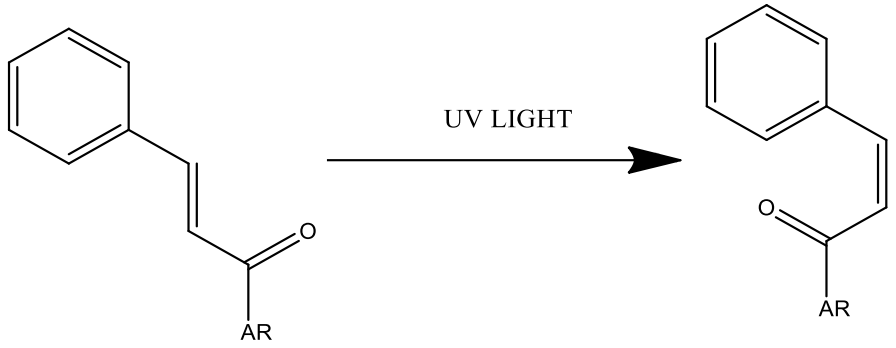
zoom in

Figure 4. 17: Knapsak is used to confirm the family and structure of the compound.

It is known that plants contain thousands of compounds. In terms of corrosion inhibition studies, some of these compounds can enhance corrosion, while some can impede it, especially in acidic environments for various metals. In this study, six compounds, namely ferulic acid, 4-P-coumaroylquinic acid, 3-P-coumaroyl-5-(E)-caffeic-quinic acid, 1.3-dicaffeoylquinic acid, caffeoyl-checorin, and caffeoyl-feruroyl-quinic acid, were identified through isolation using LC-MS [216], SIRUS software, column chromatography, molecular networking and Knapsack as compounds that are causing the corrosion inhibition of aluminium metal synergically. These compounds are listed in Table 4.4.

Plants are normally found in their trans isomerisation, but their geometry changes to cis isomerisation when exposed to UV light. In this study, all the isolated compounds contain cinnamic acid; this means that for cis isomerisation to form, the substituent molecule represented by AR attached to cinnamic acid will shift to form cis isomerisation. It can be observed that all the compounds in Table 1 are in their trans isomerisation state. When UV-radiation is applied, all these compounds will transform to their cis isomerisation state according to the schematic representation in Figure 4.18.

© University of Venda

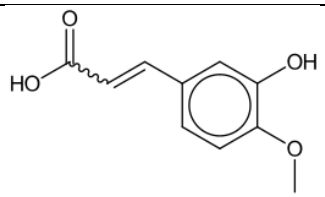
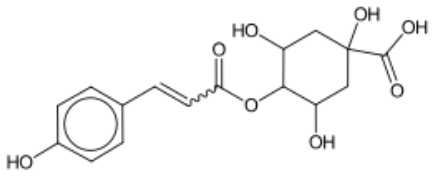
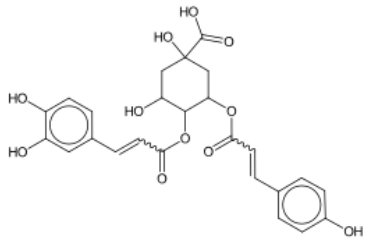


trans-Cinnamic acid

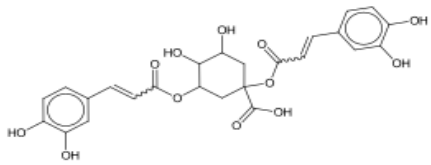
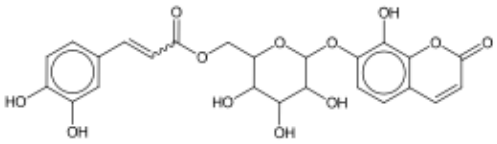
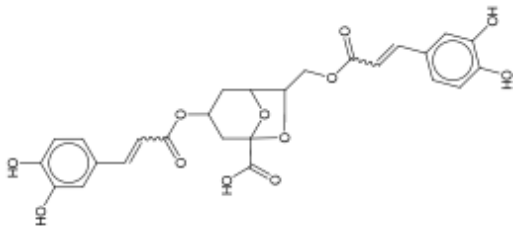
Cis-Cinanmic acid

Figure 4. 18**:** Schematic representation of how the isolated compounds formed geometrical isomers from trans to cis isomerisation.

Table 4. 3: Isolated compounds causing corrosion inhibition.

No.	Name of compound	Molecular formula	Molar mass
1	 Ferulic acid (	$C_{10}H_{10}O_4$	193.05
2	 4-P-Coumaroylquinic acid	$C_{16}H_{18}O_8$	337.09
3	 3-P-Coumaroyl-5-(E)-caffeic- quinic acid	$C_{26}H_{24}O_{11}$	499.13

© University of Venda

4	 1.3-Dicaffeoylquinic acid	$C_{25}H_{24}O_{12}$	515.12
5	 Caffeoyl-checorin	$C_{24}H_{22}O_{12}$	501.11
6	 Caffeoyl-feruroyl-quinic acid	$C_{26}H_{22}O_{12}$	526.45

© University of Venda

CHAPTER 5

Non-radiated *H. kraussii* extract in hydrochloric acid

© University of Venda

5. Introduction

In this chapter, the results obtained for *H. kraussii* plant extract as a corrosion inhibitor for mild steel, zinc and aluminium metal in hydrochloric acid using gravimetric analysis, adsorption isotherm, the effect of temperature, electrochemistry, and Fourier transform infrared spectroscopy are discussed.

Gravimetric analysis results

The gravimetric method is the simplest and most widely used procedure to monitor various material's corrosion behaviour. It provides a fundamental understanding of the correlation between the concentration of the extract inhibitor and the efficiency of corrosion resistance. [217, 218]. Its vast usage is influenced by its inexpensiveness, ease of carrying out, and reliable results. It is also known that the weight loss experiment is the most convenient classic and common corrosion test technique that can quantitatively analyse the corrosion resistance abilities of inhibitors [219]. This method was performed for mild steel, aluminium, and zinc metals in 1.0 M HCl in the non-existence and existence of non-radiated and UV-radiated *H. kraussii* extract. This method was also performed for mild steel and zinc for both extracts, but this time in 1.0 M H_2SO_4 solution. The results obtained are displayed in the form of tables and figures in Chapters 5 - 8, which have also been discussed comprehensively. The metals were immersed in the corrosive solution for 8 hours at four various temperatures (30, 40, 50 and 60 ℃) and six inhibitor extract concentrations (100, 300, 600, 900, 1200 and 1500 ppm). Based on the gravimetric results obtained, parameters such as corrosion rate, percentage inhibition efficiency, surface coverage, equilibrium constant, Gibbs free energy, correlation coefficient, slopes, apparent activation energy, change in entropy and enthalpy will be determined, which helps to characterise the two inhibitor extracts efficiency as corrosion inhibitors for the three studied metals in hydrochloric and sulphuric acid environments.

5.1. Weight loss

The corrosion rate can be determined by conducting experiments that involve measuring the loss of mass. These experiments also serve as the foundation for developing corrosion inhibitors and evaluating their potential effectiveness. [220]. The mass loss of mild steel, zinc and aluminium metals obtained after gravimetric analysis has been tabulated in Table 5.1. The

© University of Venda

weight loss was calculated by subtracting the mass of the metal before gravimetric analysis and the mass after gravimetric analysis.

Table 5. 1: Gravimetric weight loss analysis in the presence of 1.0 M HCl and *H. kraussii* extract for mild steel, zinc and aluminium metal.

Inhibitor	**Metal**	**Concentration (ppm)**	**Weight loss (g)**			
			30° C	40° C	50° C	60° C
***H. kraussii* extract**	Mild steel	0.00	0.1446	0.2997	0.5872	0.9731
		100	0.0249	0.1633	0.4184	0.8602
		300	0.0092	0.0288	0.3039	0.6520
		600	0.0051	0.0121	0.0513	0.4966
		900	0.0021	0.0099	0.0349	0.1590
		1200	0.0007	0.0075	0.0311	0.1520
		1500	0.0006	0.0073	0.0309	0.0454
	Aluminium	0.00	0.5457	0.6949	0.6209	0.7168
		100	0.2362	0.4690	0.4950	0.5763
		300	0.1687	0.3710	0.4111	0.5682
		600	0.1256	0.3020	0.3922	0.5604
		900	0.0779	0.3011	0.3896	0.5467
		1200	0.0750	0.2688	0.3827	0.5103
		1500	0.0748	0.2388	0.3796	0.4987
	Zinc	0.00	0.2549	0.4053	0.6411	1.1229
		100	0.1418	0.2170	0.4583	0.8741
		300	0.1141	0.1615	0.3271	0.6704
		600	0.1085	0.1279	0.2379	0.4670
		900	0.1056	0.1198	0.1649	0.3687
		1200	0.1055	0.1094	0.1296	0.2239
		1500	0.1040	0.1075	0.1271	0.1620

Table 5.1 shows the weight loss of mild steel, aluminium, and zinc metals in the presence of 1.0 M HCl. It can be seen that the mass loss of the three metals decreases with an increasing extract inhibitor concentration. However, as the temperature increased, the mass loss of the metals also increased. The 0.00 ppm shows the weight loss of the metals in the absence of the inhibitor at the four different studied temperatures. Aluminium metal was the worst affected

© University of Venda

by the presence of hydrochloric acid since its weight loss is the highest at all temperatures and concentrations compared to the other two metals.

Meanwhile, mild steel metal was the least affected, as evident in the weight loss at the temperatures and concentrations studied compared to the other two metals. The decrease in the mass loss of the three metals as the inhibitor concentration increases provides strong evidence that the introduction of inhibitors in the aggressive acid solution effectively reduces the corrosion rate of the metal. The increase in weight loss with temperature shows that the extract inhibitor utilized is very effective at lower temperatures.

5.2. Corrosion rate and inhibition efficiency

The rate of corrosion and inhibition efficiency are very useful in determining the inhibitor's effectiveness in counteracting the corrosive medium's aggressiveness for different materials. The difference in mass for metal obtained after gravimetric analysis was used to calculate the corrosion rate using Equation 13. The degree of surface coverage (θ), which suggests how much of the surface of the metal the inhibitor managed to cover, was also calculated from the corrosion rate equation using Equation 76. The percentage inhibition efficiency (%IE) was also calculated by multiplying the degree of surface coverage equation by 100 to give Equation 77. The data obtained using these equations are tabulated in Table 5.2.

Table 5. 2: The corrosion parameters for mild steel, aluminium and zinc in aqueous solution of 1.0 M HCl in the absence and presence of different concentrations of *H. Kraussii* extract from weight loss measurements at four different temperatures (30 – 60° C).

Inhibitor	**Metal**	**Temperature (° C)**	**Inhibitor Concentration (ppm)**	**Corrosion rate ($g.cm^{-2}.h^{-1}$)**	**Inhibition Efficiency (%)**	**Surface coverage (θ)**
			0.00	0.001505		
			100	0.000259	82.791	0.82791
		30	300	0.000096	93.621	0.93621
			600	0.000053	96.478	0.96478
			900	0.000022	98.538	0.98538
			1200	0.000007	99.535	0.99535
			1500	0.000006	99.601	0.99601
			0.00	0.003119		
			100	0.0016996	45.508	0.45502

© University of Venda

***H. Kraussii* extract**	Mild steel	40	300	0.0002997	93.912	0.93912
			600	0.000126	95.960	0.95960
			900	0.000103	96.698	0.96698
			1200	0.000078	97.499	0.97499
			1500	0.000076	97.563	0.97563
		50	0.00	0.006111		
			100	0.004355	28.735	0.28735
			300	0.003163	48.241	0.48241
			600	0.000534	91.262	0.91262
			900	0.000363	94.027	0.94027
			1200	0.000324	94.698	0.94698
			1500	0.000322	94.731	0.94731
		60	0.00	0.010128		
			100	0.008953	11.602	0.11602
			300	0.006789	32.996	0.32996
			600	0.005168	48.973	0.48973
			900	0.001655	83.659	0.83659
			1200	0.001582	84.380	0.84380
			1500	0.000473	95.330	0.95330
	Aluminium	30	0.00	0.005679		
			100	0.002458	56.718	0.56718
			300	0.001756	69.079	0.69079
			600	0.001307	76.985	0.76985
			900	0.000811	83.719	0.83719
			1200	0.000781	86.248	0.86248
			1500	0.000778	86.300	0.86300
		40	0.00	0.006331		
			100	0.004881	22.903	0.22903
			300	0.003861	39.014	0.39014
			600	0.003143	50.355	0.50355
			900	0.003134	50.500	0.50500
			1200	0.002798	55.805	0.55805
			1500	0.002485	60.749	0.60749
			0.00	0.006842		

© University of Venda

		50	100	0.005152	24.700	0.24700
			300	0.004279	37.460	0.37460
			600	0.004082	40.339	0.40339
			900	0.004055	40.734	0.40734
			1200	0.003983	41.786	0.41786
			1500	0.003951	42.254	0.42254
		60	0.00	0.007460		
			100	0.005998	19.598	0.19598
			300	0.005914	20.724	0.20724
			600	0.005832	21.825	0.21825
			900	0.005690	23.727	0.23727
			1200	0.005311	28.807	0.28807
			1500	0.005190	30.423	0.30423
	Zinc	30	0.00	0.002653		
			100	0.001476	45.873	0.45873
			300	0.001186	55.296	0.55296
			600	0.001129	57.444	0.57444
			900	0.001099	58.575	0.58575
			1200	0.001098	58.613	0.58613
			1500	0.001082	59.216	0.59216
		40	0.00	0.004218		
			100	0.004218	46.468	0.46468
			300	0.002258	60.147	0.60147
			600	0.001681	68.445	0.68445
			900	0.001331	70.436	0.70436
			1200	0.001247	73.020	0.73020
			1500	0.001138	73.471	0.73471
		50	0.00	0.006672		
			100	0.004770	28.507	0.28507
			300	0.003404	48.981	0.48981
			600	0.002476	62.890	0.62890
			900	0.001713	74.326	0.74326
			1200	0.001349	79.781	0.79781
			1500	0.001323	80.171	0.80171

© University of Venda

		60	0.00	0.011687		
			100	0.009097	22.161	0.22161
			300	0.006977	40.301	0.40301
			600	0.004860	58.364	0.58364
			900	0.003837	67.169	0.67169
			1200	0.002330	80.063	0.80063
			1500	0.001686	85.574	0.85574

Table 5.2 demonstrates a clear inverse relationship between the rate of corrosion and the concentration of the inhibitor, indicating that as the inhibitor concentration increases, the rate of corrosion decreases. This behaviour suggests that the corrosive solution's ability to destroy the metal was impeded as the concentration of the inhibitor in the solution increased. This means that more inhibitor molecules were accessible for adsorption to the metal's surface. Upon analysing the %IE, it was seen that both mild steel and aluminium exhibited a parallel pattern, wherein their values improved as the concentration of the inhibitor increased. However, as the temperature increases, there is a decrease in the inhibition efficiency [221, 222]. This observation was also reported by Ahmed et al. (2023) [223]. At a specific temperature, an equilibrium between the two processes, inhibitor adsorption and desorption, exists at the metal surface. As the temperature rises, the equilibrium between the processes of adsorption and desorption shifts, causing a faster desorption rate than adsorption until the equilibrium is restored at a new value of the equilibrium constant. This behaviour explains the reduced inhibitory efficiency at higher temperatures [224]. The trend in the zinc %IE differed from that of the mild steel and aluminium metals since the %IE was found to rise with rising temperature and inhibitor concentration. The extract inhibitor adsorption on the surface of the metal is believed to be a quasi-substitution process [225].

Figures 5.1-5.3 show the variation in the %IE for the three studied metals. It can be observed from the figures that the rise in the inhibitor concentration results in a rise in the inhibitor's %IE. This is a result of increased inhibitor molecules in the solution as the concentration of the inhibitor is increased, which means that more molecules are available to be adsorbed onto the metal surface, thereby hindering the corrosion of the metals. As the temperature increases, the percentage inhibition is also found to increase for zinc metal, unlike for mild steel and aluminium metals.

© University of Venda

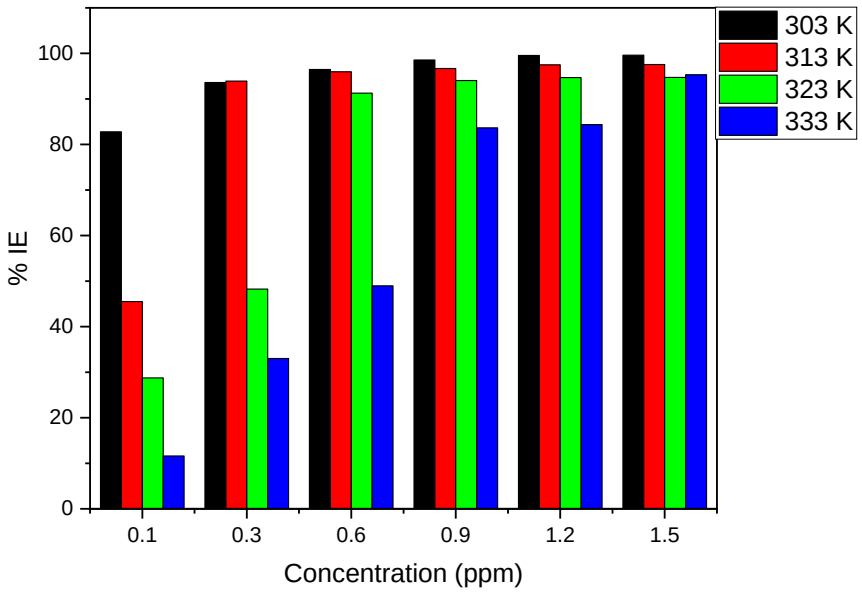


Figure 5. 1: Graph of inhibition efficiency using *H. kraussii* in 1.0 M HCl for mild steel at different temperatures.

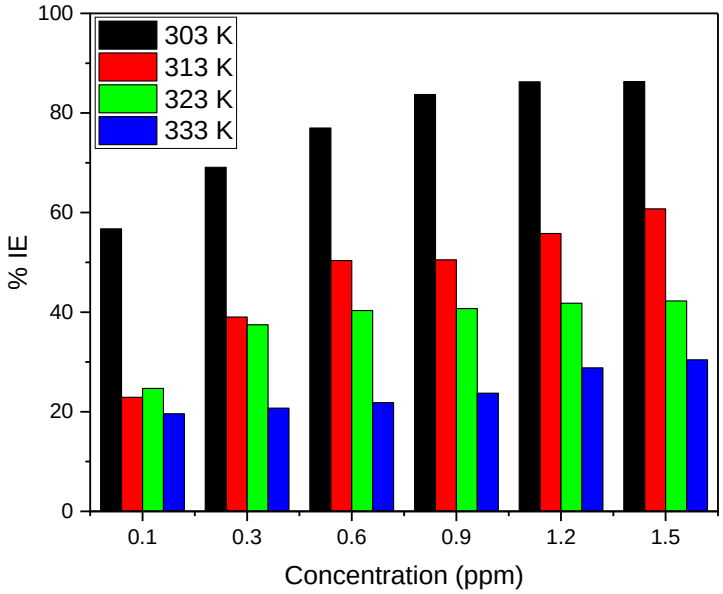


Figure 5. 2: Graph of inhibition efficiency using *H. kraussii* in 1.0 M HCl for aluminium at different temperatures.

© University of Venda

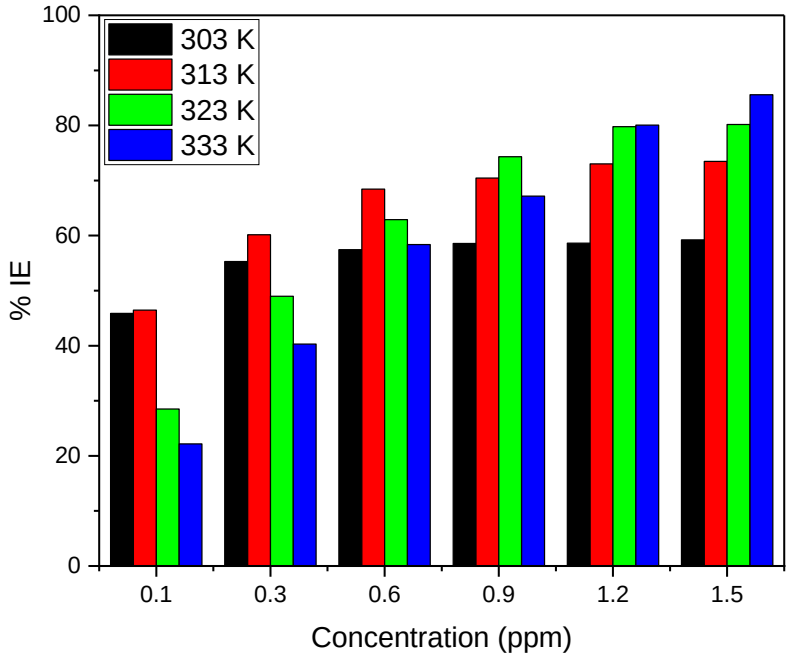


Figure 5. 3: Graph of inhibition efficiency using *H. kraussii* in 1.0 M HCl for zinc at different temperatures.

5.3. Adsorption isotherm

The adsorption isotherm describes the depth of interaction of molecules of different inhibitors with each other and the metal surface [53, 226, 227]. It is also very significant in determining the mechanism of corrosion inhibition [228]. Thermodynamic parameters are useful in studying the inhibitive mechanism [229]. The type of adsorption isotherm gives information regarding adsorbed molecule's interaction among themselves and their interactions with the surface of the electrode [230]. The interaction happens in such a way that the inhibitors displace the water molecules, which can be represented by the conjectural Equation 83 given as [37],

$$Inh_{(sol)} + H_2O_{(ads)} \leftrightarrow Inh_{(ads)} + xH_2O_{(sol)} \quad (83)$$

where the mole ratio x represents the amount of H_2O molecules substituted by the inhibitor's molecules.

The best adsorption isotherm model that describes the adsorption of the non-radiated *H. kraussii* extract on mild steel, zinc and aluminium metals in 1.0 M HCl was found by fitting the rate of corrosion and the inhibitor's degree of surface coverage into different adsorption isotherm models such as Flory Huggins, Langmuir, El Awady, Temkin, and Freundlich which are expressed in linear form as highlighted in the equations below [231].

© University of Venda

Langmuir adsorption isotherm model [232-234]

$$\frac{C_{inh}}{\theta} = \frac{1}{K_{ads}} + C_{inh} \quad (84)$$

Temkin adsorption isotherm model [231]

$$\theta = InC_R + K_{ads} \quad (85)$$

El-Awady's adsorption isotherm model [231]

$$\log\left(\frac{\theta}{1-\theta}\right) = y \log C_R + \log K, \; K_{ads} = K^{1/y} \quad (86)$$

Flory-Huggins adsorption isotherm model [232, 235]

$$\log\frac{\theta}{C_R} = b(1-\theta) + \log K_{ads} \quad (87)$$

Freundlich adsorption isotherm model [231, 236]

$$\log\theta = \log K_{ads} + n \log C_R \quad (88)$$

However, based on the linearity attained by the isotherm plot shown in Figures 5.4–5.6 and the proximity of the correlation coefficient values to unity, it was discovered that the gravimetric data acquired in all the isotherm models investigated precisely obeyed the Langmuir adsorption isotherm [37, 237-242]. The Langmuir equation is given in Equation 84, where C_{inh} is the concentration of the inhibitor, θ is the degree of surface coverage, and K_{ads} is the adsorption equilibrium constant, which is the intercept of the straight line. The values of K_{ads} are correlated to the Gibbs free energy (ΔG^{O}_{ads}) using the following equation,

$$\Delta G^{O}_{ads} = -RT \ln(K_{ads}) \quad (89)$$

where R is the gas constant, and T is the absolute temperature.

Since K_{ads} is given in g/L, the values of K_{ads} obtained must be multiplied by 1000 to make it dimensionless. This means that the equation must be multiplied and modified to become Equation 90 in order to obtain the correct values of ΔG^{O}_{ads} [243].

$$\Delta G^{O}_{ads} = -RT \ln(1000K_{ads}) \quad (90)$$

© University of Venda

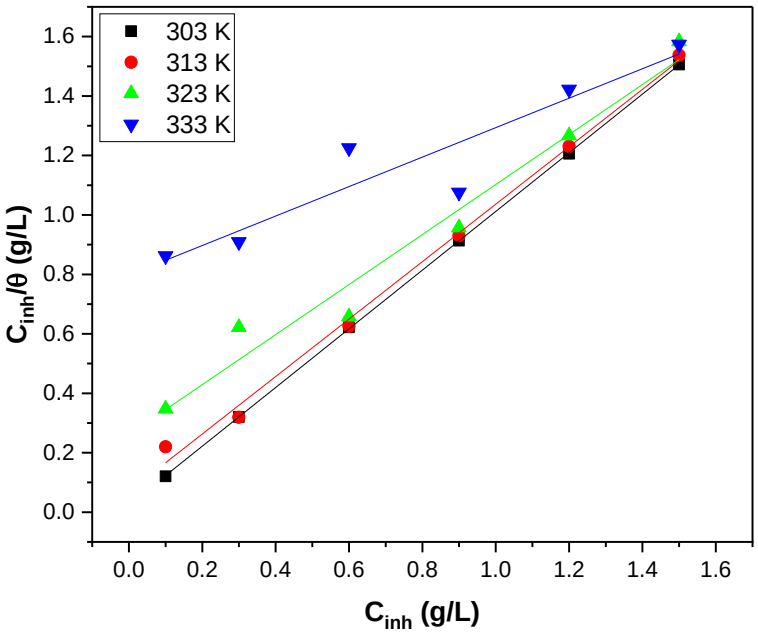


Figure 5. 4: Langmuir adsorption isotherm for the adsorption of *H. Kraussii* extract on mild steel metal in 1.0 M HCl at 30, 40, 50 and 60°C.

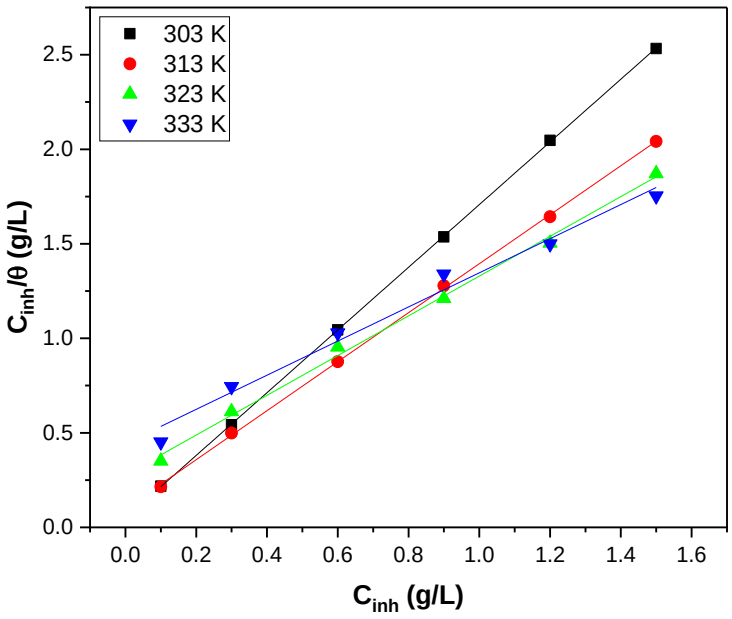


Figure 5. 5: Langmuir adsorption isotherm for the adsorption of *H. Kraussii* extract on zinc metal in 1.0 M HCl at 30, 40, 50 and 60°C.

© University of Venda

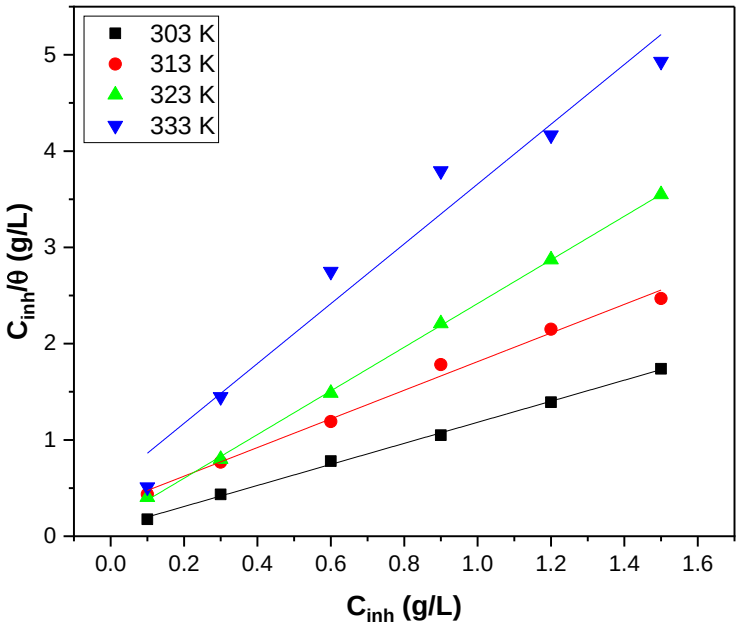


Figure 5. 6: Langmuir adsorption isotherm for the adsorption of *H. Kraussii* extract on aluminium metal in 1.0 M HCl at 30, 40, 50 and 60°C.

From the Langmuir plots, adsorption parameters such as the r^2 values, slope, $K_{ads,}$ and ΔG^{O}_{ads} were obtained and presented in Table 5.3. The r^2 values for non-radiated *H. kraussii* extracts did not show any particular trend with regard to temperature, but they were obtained to be close to unity, which indicates the accuracy of the adsorption isotherm explored. The slope values also range around 1, which confirms the linearity of the plots.

Table 5. 3: Adsorption parameters from Langmuir Adsorption Isotherm plots for *H. kraussii* extract in 1.0 M HCl.

Inhibitor	**Metals**	**Temperature (° C)**	**r^2**	**Slope**	**K_{ads} (L/g)**	**$-\Delta G^{o}_{ads}$ (kJ.mol^{-1})**
***H. Kraussii* extract**	Mild steel	30	0.99996	0.98714	40749.80	44.145
		40	0.99492	0.96637	14349.26	42.886
		50	0.96306	0.84148	3835.09	40.713
		60	0.84826	0.49569	1253.26	38.876
	Aluminium	30	0.99806	1.09355	11130.90	40.876
		40	0.99011	1.4872	3064.85	38.869
		50	0.99957	2.2680	6730.38	42.223
		60	0.95411	3.10647	1814.45	39.901

© University of Venda

	Zinc	30	0.99996	1.65841	20462.45	42.410
		40	0.9997	1.29583	10125.56	41.979
		50	0.99595	1.05112	3596.86	40.540
		60	0.9796	0.90281	2253.67	40.501

The adsorption equilibrium constant values are positive, indicating the potential for the inhibitor molecules to be adsorbed onto the surface of the metal [231]. It is generally known that K_{ads} signifies the strength between the adsorbate and the adsorbent [244]. It is also known that large values of K_{ads} indicate effective adsorption and, hence stronger protection capacity, just like what has been obtained in this study [245]. The K_{ads} values were calculated from Figures 5.4 and 5.6 and found to be ranging from 1253.26 – 40749.80, 1814.45 – 11130.90, and 2253.67 – 20462.45 L/g for mild steel, aluminium and zinc metals for non-radiated *H. kraussii* extracts, respectively, supporting the strong adsorption of the *H. kraussii* extract on the surface of the metal. The K_{ads} values are also found to be decreasing with an increase in temperature, which is an indication that, at higher temperatures, the inhibitor molecules adsorbed onto the metal surface tend to desorb. From the literature, the inhibitors can make a strong chemical bond when the values of ΔG^{O}_{ads} are around or more than -40 kJ.mol$^{-1,}$ and the electrostatic bond can be formed if the ΔG^{o}_{ads} is around -20 kJ.mol^{-1}. In this study, the values of the ΔG^{O}_{ads} are negative for the three metals studied. For mild steel, aluminium and zinc metals ΔG^{O}_{ads} values are around -40 kJ.mol^{-1} meaning that the adsorption of the extract inhibitor forms a strong chemical bond [246]. The negative values in ΔG^{O}_{ads} guarantee that the adsorption process is spontaneous and that the adsorbed film is stable on the surface of the metal [247].

The r^2 value is not sufficient to conclude that the given data obeys the Langmuir adsorption isotherm. Even though the r^2 values, which are close to unity, just like in Table 5.3, suggest a good fit, the corresponding gradient for zinc and aluminium metal is slightly above 1, which is inconsistent with Langmuir adsorption assumption of monolayer inhibitor molecules adsorption on the metal surface. This inconsistency may be due to different shortcomings that arise when utilizing Langmuir adsorption isotherm to fit data of common metal inhibition phenomena. For example, these shortcomings arise from the fact that monolayer inhibitor adsorption is only feasible on homogeneous metal surfaces and does not require the diffusion of adsorbed molecules at any temperature. But for a typical acid inhibition system like the one being studied, it is definitely not possible to accept these assumptions because there may be

© University of Venda

interactions and influences from foreign ions in the same solution, and some adsorption processes may be potentially dependent and selective with respect to the types of charges on the metal surface [248]. In order to explain this shortcoming, another physical characteristic of the adsorption isotherm must be taken into account in the form of a dimensionless separation constant (K_L), given as,

$$K_L = \frac{1}{1+K_{ads}C_{inh(\frac{g}{l})}} \quad (91)$$

Where C_{inh} is the extract inhibitor concentration in g/L. Table 5.4 shows the K_L values for the three studied metals at various temperatures and concentrations of the extract inhibitor. The value of $K_L < 1$ means that the experimental data fit the Langmuir adsorption isotherm and that the adsorption process is favourable. When $K_L > 1$, the adsorption process is not favourable and becomes irreversible when $K_L = 1$. The K_L average values obtained in Table 5.4 are all below unity, meaning the adsorption isotherm is favourable and that the experimental data fit the Langmuir adsorption isotherm.

Table 5. 4: Dimensionless separation factor (K_L) at various *H. kraussii* concentrations at four various temperatures for metals corrosion in 1.0 M HCl.

Metal	**Concentration (ppm)**	**Temperature (℃)**			
		30	40	50	60
Mild steel	100	0.0002453398	0.000696415	0.002600719	0.007916027
	300	0.0000817933	0.000232246	0.000868412	0.002652675
	600	0.0000408983	0.000116137	0.000434395	0.001328099
	900	0.0000272659	0.000077427	0.000289638	0.000885791
	1200	0.0000204496	0.000058072	0.000217245	0.000664491
	1500	0.0000163597	0.000046458	0.000173803	0.000531663
	Average	0.0000721178	0.000204459	0.000764035	0.002329791
Aluminium	100	0.000897594	0.003252191	0.001483596	0.005481104
	300	0.000299377	0.001086419	0.000495022	0.001833735
	600	0.000149711	0.000543505	0.000247572	0.000917709
	900	0.000099812	0.000362402	0.000165062	0.000611993
	1200	0.000074861	0.000271826	0.000123801	0.000459065
	1500	0.000059890	0.000217473	0.000099044	0.000367286
	Average	0.000263541	0.000955636	0.000435683	0.001611815

© University of Venda

Zinc	100	0.000488460	0.000986625	0.002772495	0.004417605
	300	0.000162874	0.000329092	0.000925876	0.001476885
	600	0.000081443	0.000164573	0.000463153	0.000738988
	900	0.000054297	0.000109721	0.000308816	0.000492780
	1200	0.000040723	0.000082293	0.000231630	0.000369631
	1500	0.000032579	0.000065836	0.008018531	0.000295726
	Average	0.000143396	0.000289690	0.002120083	0.001298602

5.4. The effects of temperature

The temperature effect on inhibition is complicated due to various alterations that may occur on the metal's surface, like rupture, desorption, rapid etching, decomposition, and or rearrangement of inhibitors [224, 249]. The experimental tests were undertaken to investigate the impact of temperature on the reaction. The temperature range of 303 – 333 K was chosen, and the experiments were carried out in the non-existence and existence of different concentrations of the extract inhibitor in a 1.0 M HCl solution. Based on the obtained results, it is evident that a rise in temperature leads to a higher rate of corrosion, regardless of whether an inhibitor is present or not. At lower temperatures, the hydrogen atom's adsorption blocks the cathodic area of the metal, while at higher temperatures, the hydrogen atoms are deabsorbed. The rise in temperature leads to a corresponding expansion in the cathodic area and an acceleration in the rate of corrosion. The activation energy, entropy, and enthalpy are calculated from the Arrhenius and transition states plot shown in Figures 5.7 – 5.12. The Arrhenius equation was used for the activation energy analysis [250].

© University of Venda

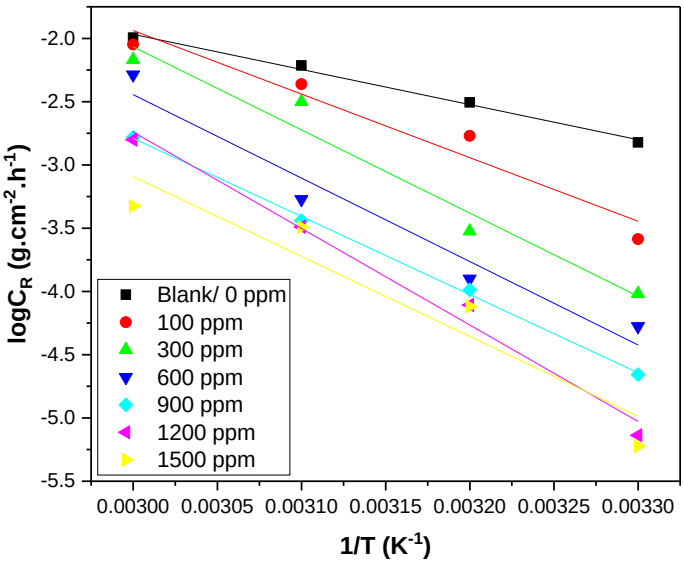


Figure 5. 7: Arrhenius plots for mild steel metal corrosion in 1.0 M HCl solution in the absence and presence of different concentrations of *H. kraussii* as the inhibitor.

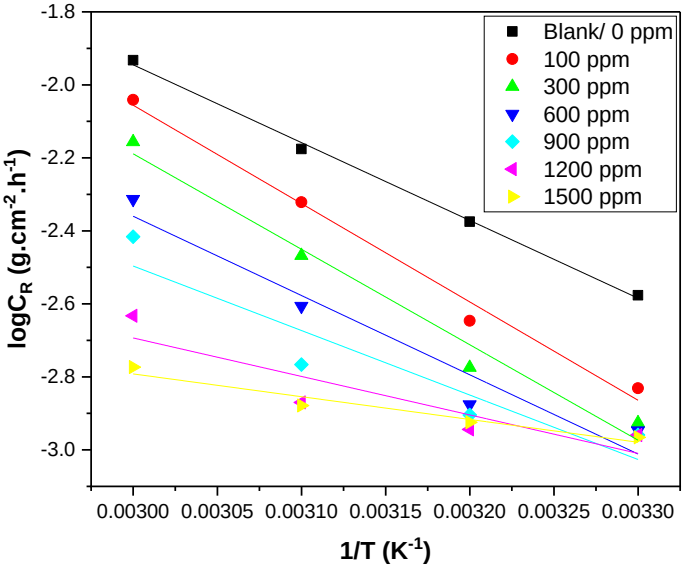


Figure 5. 8: Arrhenius plots for zinc metal corrosion in 1.0 M HCl solution in the absence and presence of different concentrations of *H. kraussii* as the inhibitor.

© University of Venda

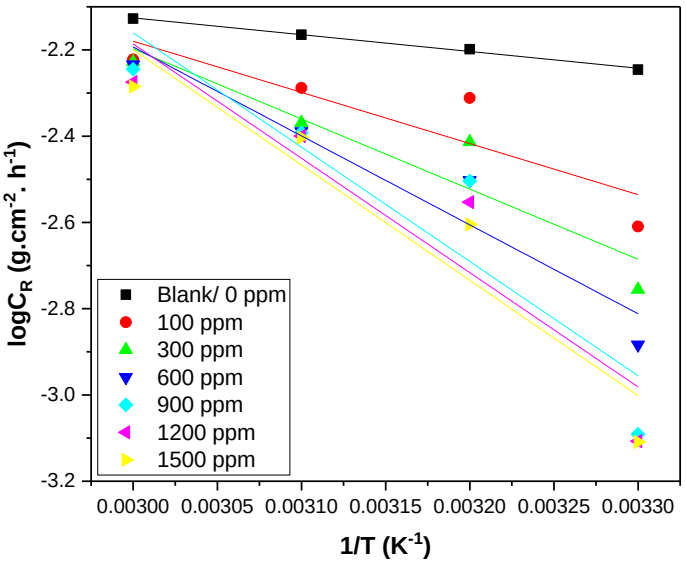


Figure 5. 9: Arrhenius plots for aluminium metal corrosion in 1.0 M HCl solution in the absence and presence of different concentrations of *H. kraussii* as the inhibitor.

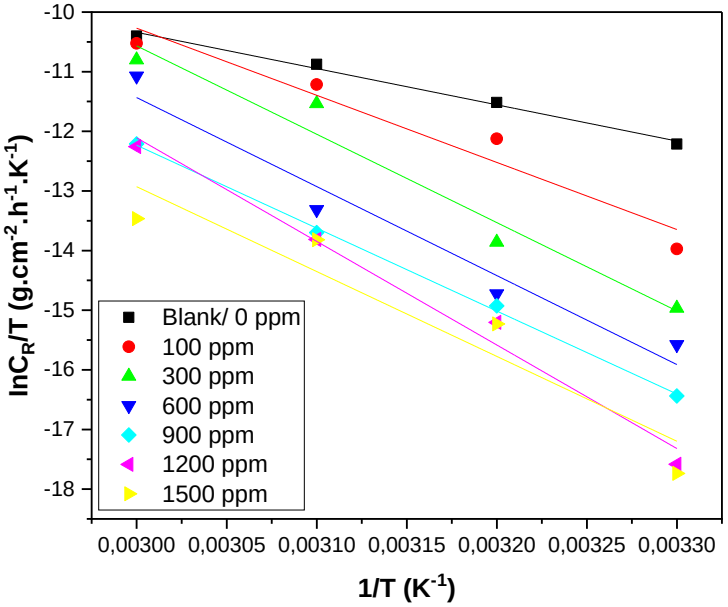


Figure 5. 10: Transition state plots showing the corrosion of mild steel metal in a 1.0 M HCl solution both with and without various concentrations of the *H. kraussii* inhibitor.

© University of Venda

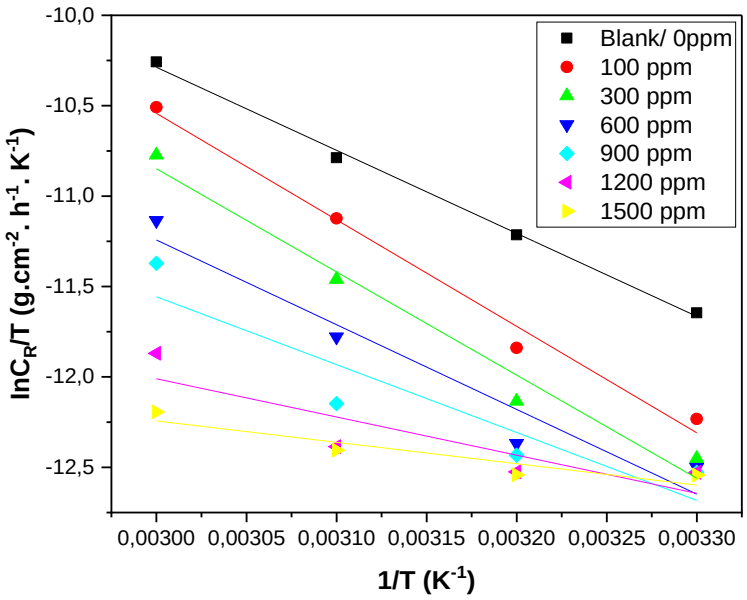


Figure 5. 11: Transition state plots showing the corrosion of zinc metal in a 1.0 M HCl solution both with and without various concentrations of the *H. kraussii* inhibitor.

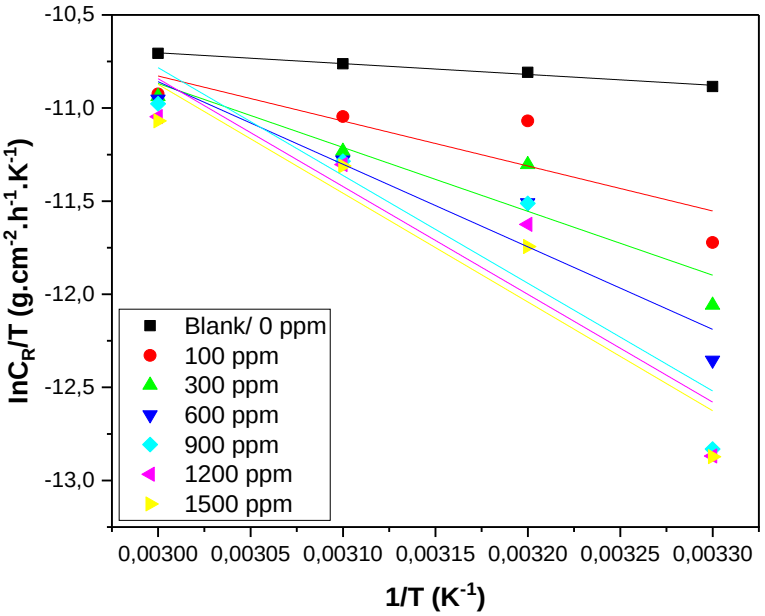


Figure 5. 12: Transition state plots showing the corrosion of aluminium metal in a 1.0 M HCl solution both with and without various concentrations of the *H. kraussii* inhibitor.

The activation energy (E_a) is utilised to study the effects of different temperatures on the mechanism and efficiency of inhibitors. The Arrhenius plot and its equation were used to estimate the activation energy in this regard [251].

© University of Venda

The Arrhenius equation, which may be used to evaluate the activation energy, is the mathematical expression between the temperature and the corrosion rate given as

$$log\ C_R = log\ A - \frac{E_a}{2.303RT} \quad (92)$$

where A is the frequency factor (Arrhenius pre-exponential factor), R is the gas constant (8.3145 $Jk^{-1}mol^{-1}$), E_a is the corrosion activation energy, T is the absolute temperature, and C_R is the corrosion rate in ($g.cm^{-2}.h^{-1}$), Plotting the logarithm of the corrosion rates of aluminium, zinc, and mild steel in HCl in both the existence and non-existence of the concentration of the inhibitor against the reciprocal of the examined absolute temperatures resulted in the construction of best-fit lines, with the slope of the lines being E_a/2.303R. Figures 5.7 - 5.9 depict this.

In accordance with the inhibitor's reactions to temperature and comparing the blank and inhibitor activation energies, Radovici (1965) and Laaroussi et al. (2022) differentiated the inhibitors-metal interaction into three groups [252, 253]:

1. Inhibitors where the E_a value is lower compared to the one attained in the blank solution while the %IE increases with temperature increase. This is an indication of a chemical interaction.

2. Inhibitors whose inhibition efficiency is unaffected by temperature change. Regardless of whether inhibitors are present or not, the perceived activation energy remains constant.

3. Inhibitors whose inhibitory effectiveness declines as temperature rises. The apparent activation energy discovered is higher than that in the blank solution. This observation is an indication of an electrostatic or physical adsorption

The results show that the activation energy values are higher than that of the blank solution, increasing with an increase in concentration at lower concentrations and decreasing at higher concentrations for mild steel and aluminium metals. This discovery suggests that the inhibitor is undergoing physical adsorption on the metal surface [242]. However, for the zinc metal, the activation energy at the first three concentrations (100, 300 and 600 ppm) of the inhibitor was found to be higher than that of the blank, but for the last three concentrations (900, 1200 and 1500 ppm), they were found to be less than that of the blank. Furthermore, it was demonstrated that they also diminished as the concentration of the inhibitor extract escalated. This

© University of Venda

observation indicates that the inhibitor was adsorbed onto the metal surface through a mix of physisorption and chemisorption.

Table 5. 5: Transition state and Arrhenius parameters for the adsorption of various concentrations of *H. kraussii* in 1.0 M HCl on mild steel, zinc and aluminium metal.

Inhibitor	**Metals**	**Concentration of inhibitors (ppm)**	E_a **(kJ.mol^{-1})**	ΔH^* **(kJ.mol^{-1})**	ΔS^* **(J.mol^{-1}.k^{-1})**
***H. kraussii* extract**	Mild steel	0.00	53.15624	-6.90261	-308.05998
		100	96.21347	95.52072	3.42156
		300	125.8355	123.19279	84.16284
		600	126.27074	124.11269	79.71965
		900	116.5643	115.62576	47.61122
		1200	146.06127	144.43068	135.05847
		1500	120.96322	11.83261	49.92780
	Aluminium	0.00	7.45098	4.83305	-272.04780
		100	22.70528	20.08451	-227.33016
		300	31.148912	28.52663	-202.33903
		600	39.48589	36.86308	-177.23195
		900	50.74604	48.12017	-142.85086
		1200	51.20158	48.13538	-143.2975
		1500	50.76117	48.57639	-142.2276
	Zinc	0.00	40.80559	38.18216	-168.54342
		100	51.58991	48.96426	-138.31580
		300	50.07643	47.45060	-145.40475
		600	41.57899	38.95485	-174.16726
		900	33.83235	31.21051	-200.01155
		1200	20.18517	17.56483	-244.71970
		1500	11.94662	09.83888	-269.83481

Using the transition state equation provided in Equation 93, the values of change in enthalpy of activation (ΔH*) and change in entropy of activation (ΔS*) were determined,

$$In\left(\frac{C_R}{T}\right) = \left[In\left(\frac{C_R}{h}\right) + \left(\frac{\Delta S^*}{2.303R}\right)\right] + \left(\frac{-\Delta H^*}{2.303R}\right)\left(\frac{1}{T}\right) \quad (93)$$

© University of Venda

where h is the Planck's constant, the entropy change and activation enthalpy, respectively, are represented by ΔS* and ΔH*. Plots of ln (CR/T) against 1/T are shown in Figures 5.10–5.12. The best-fitted data has an intercept of ΔS*/2.303R and a slope of -ΔH*/R. The values of the E_a, ΔH*, and ΔS* are displayed in Table 5.5.

It was discovered that the ΔS* values for zinc metal were negative and dropped as the concentration of inhibitor increased. This finding implies that the rate of disorderliness decreases as one moves from the reactants to the activated complex [231]. For mild steel metal, the values of the ΔS* are larger when the extract inhibitor is present than when it is not, indicating that the randomness increased as the reaction progressed from the reactant to the activated complex [254]. The ΔS* values in the presence of the extract inhibitor are positive for mild steel, as observed by Yadav et al. (2010) [255]. This observation suggests that the system transitioned from a more random arrangement to a less ordered one [256]. In the rate-determining step, the activated complex symbolizes association instead of dissociation, as indicated by the negative values of ΔS* of activation in both the presence and absence of the two extract inhibitors [257, 258]. For aluminium metal, the inhibited values of ΔS* are more positive than the blank. This finding can be explained as a result of water molecules' desorption during the inhibitor's adsorption [253].

The values of the ΔH* obtained were positive for all three metals. The positive values of ΔH* reflect that the mild steel dissolution reaction between the surface of the metal and the inhibitor was endothermic, meaning that the dissolution of mild steel, zinc and aluminium metal in HCl is a difficult process [259]. This observation also suggests that the dissolution process of mild steel, zinc, and aluminium metals is low in the presence of the inhibitor extract [242]. For aluminium metal, ΔH* values were observed to rise with the rising concentration of extract inhibitors, indicating high protection efficiency [260]. The rise in the ΔH* with the concentration of the extract inhibitor is associated with a minimized dissolution of the metal [261]. For zinc metal, the ΔH* values were found to decrease with increasing inhibitor concentration [231], suggesting that the decrease in the zinc corrosion rate in HCl is not mainly governed by the kinetic activation parameters [262]. For mild steel metal, the values of ΔH* did not follow a particular trend but increased in the presence of the extract inhibitor [263].

© University of Venda

5.5. Electrochemical analysis

5.5.1. Mild steel

5.5.1.1. Open circuit voltage (OCV)

The OCV was performed on a mild steel electrolyte system in the absence and presence of various concentrations of the extract. The results are presented in Figure 5.13. The variation of the free potential during a corrosion test is the initial indication of the corrosion extent during the immersion in the corrosive electrolyte [264]. The OCV measurements were performed between 0 and 3600 seconds to monitor the OCV variation with time. The OCV is performed before any electrochemical measurements (EIS and PDP) to avoid potential drift during the accumulation of the data [245]. From the OCV curve, it can be observed that the behavioural adjustment of the electrical double layer of the mild steel surface in 1.0 M HCl medium when there is no inhibitor is similar in shape to its adjustment in the presence of 100, 300, 600, 900, 1200 and 1500 ppm inhibitor concentrations. The potential starts with a high value for each curve and decreases as the curve progresses. Local potential fluctuations were observed in the extract inhibitor's presence [265].

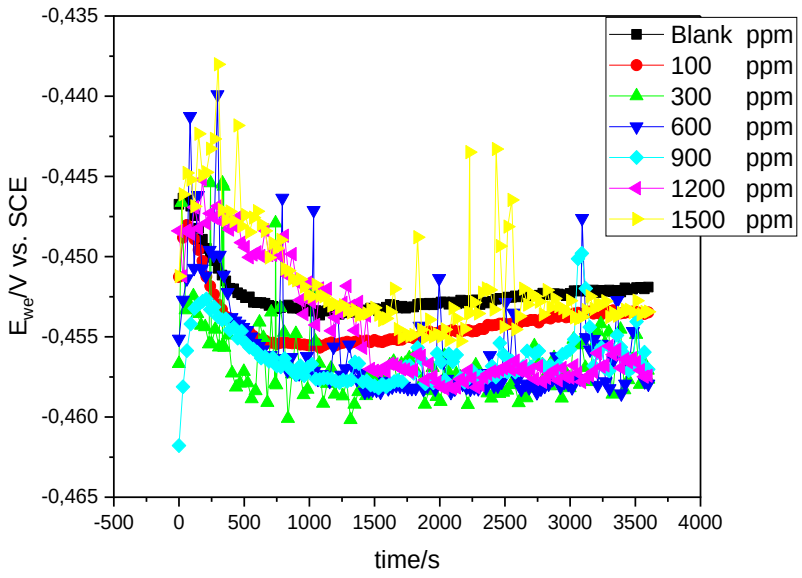


Figure 5. 13: Open circuit voltage for mild steel in hydrochloric acid and *H. kraussii*.

© University of Venda

5.5.1.2. Electrochemical impedance spectroscopy (EIS)

The EIS is one of the electrochemical methods that focuses on measuring and controlling the fundamental properties of electrochemical reactions [266]. EIS experiments were conducted for this system to have an understanding of the capability of the coating to protect the metal from defects coming from the reactivity or adhesion of the interface through the water uptake corresponding to an accumulation of molecules of water at the metal [267]. The mild steel Nyquist plot in acidified 1.0 M HCl medium in the absence and presence of different concentrations of *H. kraussii* extract after one hour of OCV immersion time is displayed in Figure 5.14. The impedance shape did not change upon introducing the extract inhibitor compared to the blank test [168], suggesting that introducing the inhibitor in the corrosive medium did not change the corrosion mechanism process. When the inhibitor was added to the corrosive medium, the diameter of the semi-circle increased as the inhibitor concentration increased. This suggests that the inhibitor was absorbed onto the metal surface, creating a protective coating for the metal. The Nyquist curves of the coated and uncoated cases show a single semicircle, suggesting that the acidic dissolution of mild steel involves a single charge transfer mechanism [268]. The imperfection of the semicircles is usually pointed out to the roughness and heterogeneous nature of the mild steel surface [269].

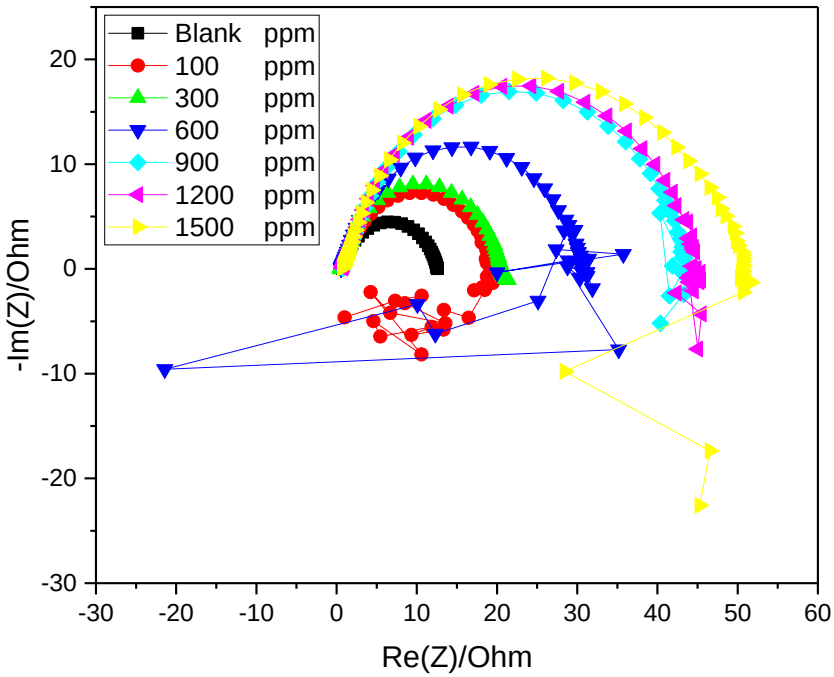


Figure 5. 14: Nyquist plot of mild steel metal in 1.0 M HCl with and without various concentrations of *H. kraussii* extract inhibitor.

© University of Venda

Figures 5.15 a and b show the Bode impedance plot and the phase angle plot highlighting the responses of the impedance of the samples during the 1-hour exposure in the blank and the inhibited solutions. At higher frequencies, the impedance was found to be decreasing, and the phase angle was found to be increasing with time. Coatings using inhibitors protect metallic surfaces from corrosion by isolating the metal from the corrosive environment [270]. The Bode phase angle plots supplement the Bode modulus and Nyquist plots in revealing the number of capacitive loops in the impedance measurements. Single minimum deflections corresponding to single capacitative loops can be observed in the blank and inhibited system. The Bode phase angle plots in the corrosive electrolyte show that the capacitative behaviour of mild steel metal surface displays a single relaxation process both in the uninhibited and inhibited system [245], indicating the excellent performance of the *H. kraussii* as a corrosion inhibitor [271]. The phase angles are prone to higher values, indicating the passive surface on the mild steel electrode [272].

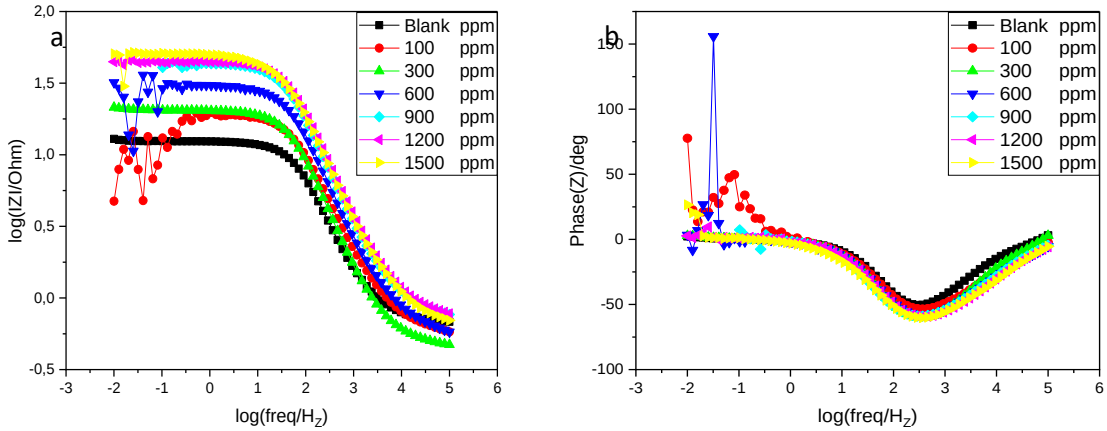


Figure 5. 15: Bode impedance magnitude plot (a) and Bode phase angle plot (b) of mild steel metal in 1.0 M Hydrochloric acid with and without various concentrations of *H. kraussii* extract inhibitor.

The impedance response was obtained by fitting the equivalent circuit represented in Figure 5.16 to provide a precise match for the experimental outcome, which yielded the parameters obtained in Table 5.6 and the calculated electrochemical impedance spectroscopy percentage inhibition efficiency (%IE_{EIS}). The circuit is comprised of R1, which is the solution resistance (Rs) [273, 274], R2, which is the charge transfer resistance (R_{ct}) and Q2, which is the constant phase element (CPE) [275]. The CPE is associated with the capacitance of the double layer (C). The utilisation of the CPE instead of the capacitor is vital to compensate for the deviation

© University of Venda

of the ideal dielectric behaviour related to the inhomogeneous surface of the electrode [276, 277].

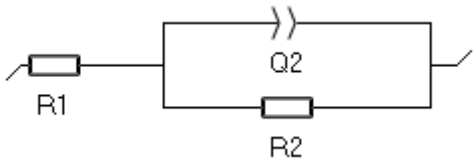


Figure 5. 16: Equivalent circuit model for blank and *H. kraussii* extract solution.

The CPE is made up of a coefficient n and a component Q_{dl} that measure many physical processes, such as the creation of porous layers, inhibitor adsorption, surface roughness, and surface inhomogeneousness. The double-layer capacitance (C_{dl}) can be simulated from CPE using Equation 94,

$$C_{dI} = Q_{dI} \times (2\pi f_{max})^{n-1} \quad (94)$$

However, for this study, the CdI was calculated from R_{ct} by using Equation 94 [278],

$$C_{dI} = \frac{1}{2\pi f_{max} R_{ct}} \quad (94)$$

where, fmax on the Nyquist plot stands for the frequency at which the imaginary value reaches a maximum. With the increase in concentration of extract inhibitor, the R_{ct} rises noticeably while the C_{dl} falls. A system that corrodes more slowly is correlated with a high charge transfer resistance (R_{ct}).

The drop in C_{dl} compared to the blank solution implies that the inhibitor molecules work by adsorbing at the interface between the metal and the solution. This phenomenon may be attributed to a reduction in the local dielectric constant or an augmentation in the electrical double-layer thickness. The Helmholtz model can be used to explain the decline in C_{dl} values:

$$C_{dI} = A\frac{\varepsilon\varepsilon_0}{d} \quad (94)$$

where d is the film's thickness, A is the electrode's surface area, ε_0 is the air's permittivity, and ε is the local dielectric constant. It is possible to hypothesize that the decline in C_{dl} values results from inhibitor molecules gradually replacing water molecules on the electrode surface, which decreases the degree of metal dissolution [279]. A single capacitive loop represents the results obtained both in the absence and presence of the *H. kraussii* extract [280].

© University of Venda

The time constant is used to obtain information about the charge and discharge of the double-layer electrical layer in the metal solution interface [281]. The circuit utilised to fit the impedance data contains only one time constant because it contains only one parallel combination of R_{ct} and CPE. The time constant τ is given by the following equation as reported by Fernine et al. (2022) and Alias (1992) [282, 283],

$$\tau = C_{dI} \times R_{ct} \quad (95)$$

The time constant values in Table 5.6 are found to be decreasing with increasing inhibitor concentration for mild steel metal. This observation implies that the adsorption time of the *H. kraussii* extract on the mild steel metal is low, which suggests a fast adsorption process [282]. The time constant is also found to have a direct proportional relationship with the double-layer capacitance.

Table 5. 6: EIS parameters like the solution resistance (R_s), resistance of charge transfer (R_{ct}), constant phase element (CPE), constant phase element constant (n2), double layer capacitance (C_{dl}) and percentage inhibition efficiency ($\%IE_{EIS}$), using *H. kraussii* in 1.0 M HCl in mild steel metal.

Inhibitor	**Metal**	**Conc. (ppm)**	R_s **(Ωcm^2)**	**CPE (F.s$^{(a-1)}$) x 10^{-3}**	**n2**	R_{ct} **(Ωcm^2)**	**C$_{dl}$ (μF/cm^{-2})**	**τ (s)**	%IE
H. kraussii extract	Mild steel	00	0.7022	0.5784	0.8253	11.87	3004.929	0.0357	
		100	0.6354	0.2323	0.8792	8.688	2527.626	0.0220	-36.63
		300	0.4941	0.4086	0.8435	20.21	974.1753	0.0197	41.27
		600	0.6318	0.2527	0.8396	22.43	608.7365	0.0137	47.08
		900	0.7928	0.2714	0.8051	43.23	217.3209	0.0094	72.54
		1200	0.799	0.2324	0.8078	44.54	247.0994	0.0110	73.35
		1500	0.7188	0.2730	0.7976	48.07	181.8023	0.0087	75.29

The smaller charge transfer resistance values illustrate that during the electrochemical measurement, an efficient electron transfer occurred in the interfaces between the electrolyte and the electrode [272]. The R_{ct} values rise with rising extract inhibitor concentration, with the highest concentration having a charge transfer of 48.07 Ωcm^2 compared to the blank, which is 11.87 Ωcm^2. This observation reveals an increased protective influence of the inhibitor [284]. The rise in the R_{ct} with inhibitor concentration increased the %IE. The optimum %IE was found to be 75.29 % for the highest concentration. From the literature, the constant phase element (n)

© University of Venda

values, which can only reach a maximum of 1, have several meanings. The value of n equal to 1 represents the capacitor, 0 represents the inductor, and -1 represents the inductance [285]. From the results obtained, the values of n are approaching 1, which suggests that the constant phase element resembles the capacitor.

5.5.1.3. Potentiodynamic polarization (PDP)

Polarization study is an excellent and useful technique for investigating corrosion mechanisms. The kinetics of the anodic and cathodic reactions can be understood using the polarization curve. The kinetics of corrosion reactions can be measured by using polarization techniques [227]. It is used to calculate the electrochemical parameters like corrosion cathodic and anodic Tafel slopes (β_c and β_a), current density (i_{corr}), corrosion potential (E_{corr}) [286], and the percentage inhibition efficiency ($\%IE_{PDP}$), and these are tabulated in Table 5.7. The mechanism of the process can determine if the inhibition that took place in the Tafel slopes is anodic, cathodic, or a mixture of anodic and cathodic reactions (mixed type). The E_{corr} values will be decided by the type of inhibitor utilised. Figure 5.17 displays the Tafel plot for mild steel in 1.0 M HCl solution in the non-existence and existence of *H. kraussii* extract. It can be observed that the plots lacked a consistent trend; however, in most cases, it was observed that the plots for the inhibitor were shifted to the lower i_{corr} values. It can also be seen that the anodic site curve shifted to the positive potential. In contrast, the cathodic site curve shifted towards the negative potentials, decreasing the rate of corrosion current densities, indicating that the inhibitor works as a mixed type [206].

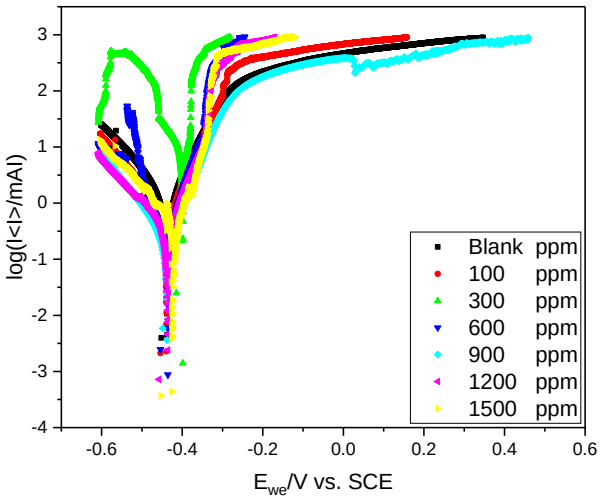


Figure 5. 17: Tafel plots for mild steel in 1.0 M HCl with and without different *H. kraussii* inhibitor extract concentrations.

© University of Venda

Table 5. 7: PDP parameters, including anodic and cathodic Tafel slopes (βa and β_c), polarization resistance (R_P), corrosion potential (E_{corr}), and corrosion current density (i_{corr}), measured in 1.0 M HCl using different *H. kraussii* inhibitor concentrations.

Inhibitor	**Inhibitor Conc. (ppm)**	**-E_{corr} (mV) With Ag/AgCl**	**i_{corr} (mA.cm^{-2})**	**R_P (Ω)**	**β_a (mV.dec^{-1})**	**β_c (mV.dec^{-1})**	**% IE$_{PDP}$**
Blank	0.00	-436.943	1471.823	16.1	81.5	130.0	
H. kraussii extract	100	-398.674	5404,492	0.43	15.8	51.6	-267.197
	300	-403.777	805.154	19.4	56.0	242.7	45.295
	600	-439.113	598.269	26.3	64.5	107.0	59.352
	900	-435.427	481.088	40.9	66.7	171.4	67.313
	1200	-436.081	269.061	31	46.4	69.4	81.719
	1500	-438.448	237.880	68.4	61.4	105.7	83.838

The i_{corr} results decrease as the concentration of the extract inhibitor increases relative to the blank sample [287], in which the inhibition efficiency also increased to achieve the maximum value of 83.838%. This results from the increase in the electrode surface fraction that is blocked by adsorption [288]. Both the anodic and cathodic Tafel slopes were reduced upon introducing an inhibitor in the aggressive electrolyte, indicating that the inhibitor suppressed both anodic and cathodic reactions, with the cathodic reaction being the most affected [289, 290]. When the anodic and cathodic slope values exhibit a valuable trend, it suggests that multiple mechanisms were involved in inhibiting corrosion rather than just the adsorption effect. These mechanisms may include the participation of other species or anions present in the aggressive electrolyte [261]. The values of the polarization resistance were generally observed to increase with rising concentration of extract inhibitor.

In most cases, the inhibitor's E_{corr} values are observed to have shifted towards more positive values relative to the blank system E_{corr} value. From the literature, the inhibitor can be categorised as cathodic, anodic or mixed inhibitor type based on the shifting of the E_{corr} values of the inhibited system compared to the uninhibited system. Therefore, the change in E_{corr} is a measure of the inhibitory mechanism. Suppose the shift is greater than -85 mV. In that case, the inhibitor can be classed as cathodic or anodic, depending on the primary influence on the specific (anodic or cathodic) processes. If the shift is less than -85 mV, the inhibitor can be classified as mixed type [261, 291]. In the current study, the E_{corr} difference is less than -85

© University of Venda

mV, suggesting that the inhibition is a mixed type in its inhibition action. It can be said that the inhibitor restricts both the anodic and cathodic reactions by forming a film on the surface of the metal, which indirectly leads to the blockage of cathodic and anodic reaction sites [268].

5.5.2. Zinc metal

5.5.2.1. Open circuit voltage

The OCV, also known as the corrosion potential (E_{corr}), alludes to the working electrode's potential when no external current is applied to the system. It is widely known that the OCV values of the metal with inhibitors are higher than those without inhibitors. When the inhibition coating on the metal fades away over time, the OCV values tend to become more negative until they equal the corrosion potential of the metal substrate. The OCV measurements can also give information about the disbandment of the coatings and the passive or active states of the metal substrate. For instance, a shift in the OCV towards more positive values when the inhibitors are present in the system is an indication of corrosion inhibition. The zinc electrode OCV-time profile in a corrosive medium was observed for 3600 s, which was sufficient to establish equilibrium for the corrosion system [292]. The OCV of the blank reached a maximum of -480 V, then suddenly dropped again and continued to decrease steadily until 3400 s. As can be observed from Figure 5.18, the time profile of the bare metal has a more negative potential than the inhibited metal profile, which shifted towards a less negative potential. This suggests that anodic protection could be the favoured process. No stable trend is observed in the OCV variation with time for the electrodes without or with varying concentrations of the inhibitor, suggesting that the plant extract acts as a mixed inhibitor type [293]. The oscillations in the OCV plots are an indication of the formation of the corrosion product layer and the destruction of the surface of the metal. In the inhibitor free-solution, the OCV potential moved towards the negative potential direction, indicating the corrosion products' desorption on the surface of the metal [294].

© University of Venda

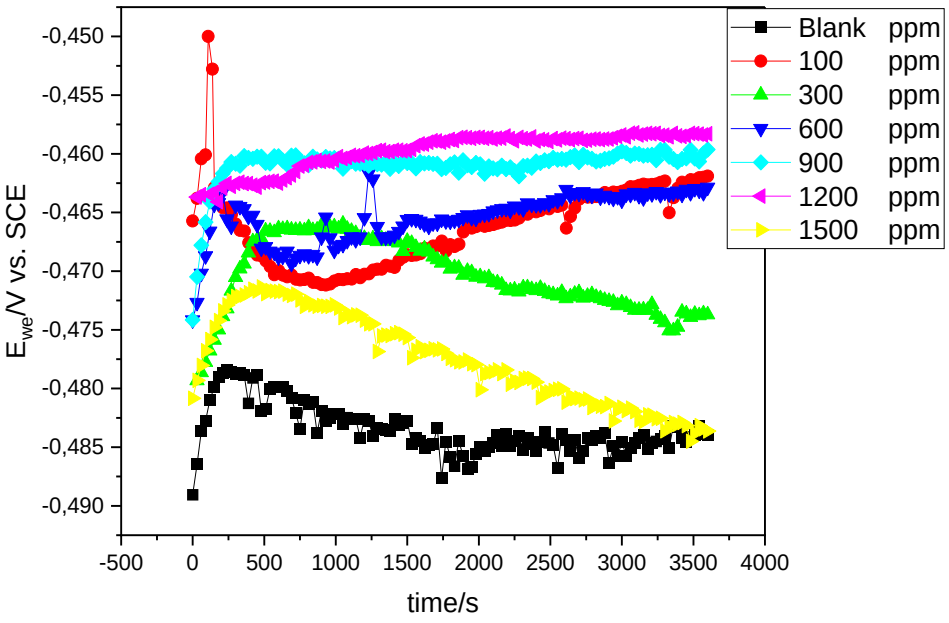


Figure 5. 18: Open circuit voltage for zinc in 1.0 M HCl and *H. kraussii* extract.

5.5.2.2. Electrochemical impedance spectroscopy (EIS)

EIS was used to evaluate the investigated sample's electrochemical properties and water uptake behaviour [199]. The Bode and Nyquist plots obtained from the impedance response after the OCV was run in the absence of the current for 3600s are displayed in Figures 5.19 and 5.20. Figure 5.19 shows that the Nyquist plots form a semi-circle both in the inhibited and uninhibited system, suggesting that introducing the *H. kraussii* extract on the corrosive solution did not change the corrosion mechanism. As the inhibitor concentration rises, it is observed that the semi-circle diameter increases as well, as reported by Bijapur et al. (2023) [295]. This indicates the adsorption of the inhibitor on the zinc metal surface, shielding it from corrosion attack. This is because the extract molecule adsorption reduces the active corrosion regions on the surface of the metal [296]. From the literature, it is said that surface heterogeneity is the sole cause of the semicircle's imperfection, as can be observed in the Nyquist plot [297]. Similar results of imperfect semi-circles have also been observed by Fouda et al. (2023) [298].

© University of Venda

University of Venda
Creating Future Leaders

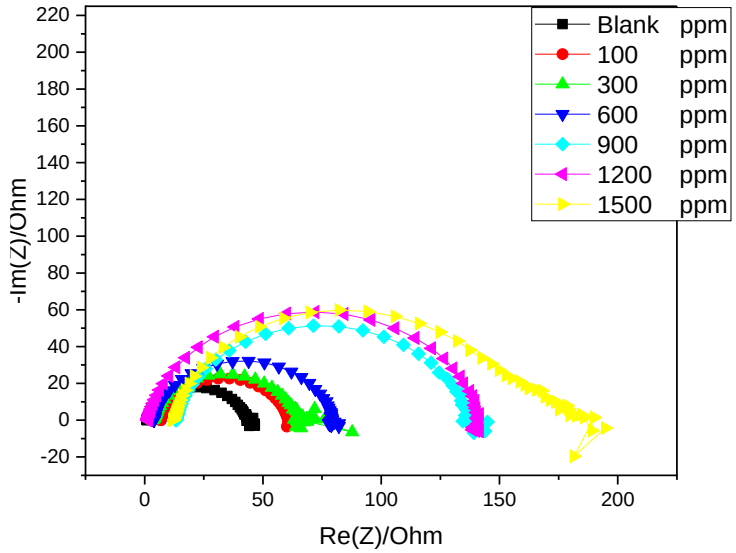


Figure 5. 19: Nyquist plot of zinc metal in 1.0 M HCl with and without various *H. kraussii* extract inhibitor concentrations.

The Bode phase angle and impedance modulus plots for zinc metal in 1.0 M HCl solution with and without *H. kraussii* extract inhibitor are shown in Figure 5.20. The figure's observation indicates that the interfacial impedance rises as the inhibitor concentration increases. The phase angle at high frequencies gives a basic notion of the performance of the corrosion inhibition. The more the phase angles shift towards negative values, the more capacitive the electrochemical behaviour [299]. The Bode plots show a single peak in the phase angle plot, indicating the occurrence of a single charge transfer process in the corrosion of the zinc metal. The height of the phase angle peak increased with increasing extract inhibitor concentration compared to the blank solution test, suggesting that a more capacitative metal electrolyte interference response occurs when the inhibitor is present [300]. The extraction of the impedance parameters was performed by fitting the equivalent circuit represented in Figure 5.16 to the Nyquist plot, and the parameters obtained are tabulated in Table 5.8.

© University of Venda

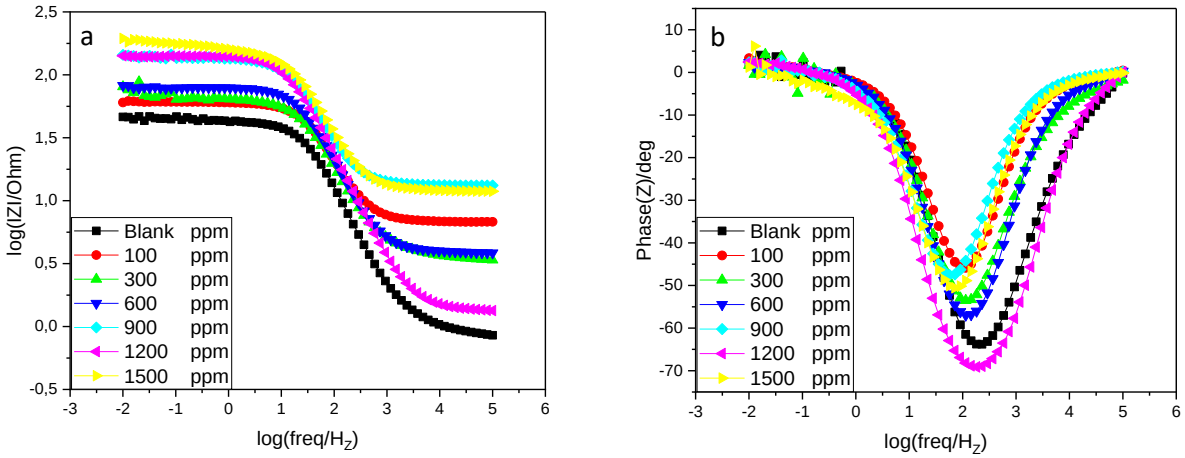


Figure 5. 20: Bode impedance magnitude plot (a) and Bode phase angle plot (b) of zinc metal in 1.0 M HCl with and without various concentrations of *H. kraussii* extract inhibitor.

Table 5. 8: EIS parameters like the solution resistance (R_s), resistance of charge transfer (R_{ct}), constant phase element (CPE), constant phase element constant (n2), double layer capacitance (C_{dl}) and percentage inhibition efficiency ($\%IE_{EIS}$), using *H. kraussii* in 1.0 M HCl in zinc metal.

Inhibitor	**Metal**	**Conc. (ppm)**	**R_s (Ωcm^2)**	**CPE ($F.s^{(a-1)}$) $x10^{-3}$**	**n2**	**R_{ct} (Ωcm^2)**	**C_{dl} ($\mu F/cm^{-2}$)**	**τ (s)**	**%IE**
***H. kraussii* extract**	Zinc	00	0.913	0.2794	0.8654	43.53	210.3134	0.0092	
		100	6.788	0.1671	0.8932	54. 00	130.2263	0.0070	19.39
		300	3.545	0.2382	0.8432	63.98	100.1167	0.0064	31.96
		600	3.902	0.1470	0.8973	75.57	65.4852	0.0049	42.40
		900	13.23	0.1355	0.8850	124.6	25.0596	0.0031	65.06
		1200	1.361	0.1339	0.8870	139.9	19.3614	0.0027	68.88
		1500	11.85	0.1425	0.8466	160.8	16.5505	0.0027	72.93

It can be observed from Table 5.8 that as extract inhibitor concentration rises, the R_{ct} values also rise, indicating that the metal surface becomes more resistant to corrosion because of the extract adsorption [296]. The increase in the R_{ct} values resulted in an increase in zinc metal inhibition efficiency. The phase shift constant n explains what the CPE stands for. For n=1, it implies that the CPE is a capacitance, n=0 a resistance, and n=-1 an inductance [285]. From the results obtained, the values of n are leading towards 1, which means that the CPE in this study represents capacitance. From the table, it can be observed that the interface of the double-

© University of Venda

layer capacitance (C_{dl}) decreases with the rising concentration of extract inhibitor. The gradual alteration in water molecules caused by the inhibitor molecules adhering to the zinc surface and forming a layer could be the reason for the decrease in C_{dI} values [301]. The C_{dl} decreased from 210.3134 μF/cm^{-2} of the blank to 16.5505 μF/cm^{-2} for the maximum concentration. The time constant values in Table 5.8 are found to be decreasing with increasing inhibitor concentration for zinc metal. This observation implies that the adsorption time of the *H. kraussii* extract on the zinc metal is low, which suggests a fast adsorption process [282]. The time constant is also found to have a direct proportional relationship with the double-layer capacitance.

5.5.2.3. Potentiodynamic polarization (PDP)

Figure 5.21 shows the Tafel plot for zinc metal in 1.0 M HCl medium in the absence and presence of the extract inhibitor. It is evident from Figure 5.21 that polarization curves are shifted to lower corrosion current density upon the introduction of the inhibitor relative to the uninhibited system [302]. It can also be noted that cathodic and anodic branches are present, which indicates that introducing the inhibitor in the corrosive solution did have an impact on the anodic and cathodic corrosion of zinc metal. Through the cathodic and anodic junction extrapolation, electrochemical parameters like corrosion potential (E_{corr}), polarization resistance (R_P), corrosion current density (i_{corr}), and anodic and cathodic Tafel slopes (β_a and β_c) and the calculated potentiodynamic polarization percentage inhibition efficiency (%IE_{PDP}) are tabulated in Table 5.9.

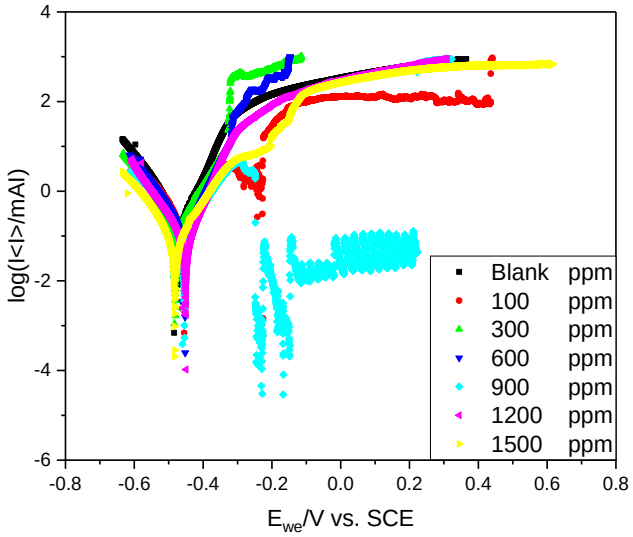


Figure 5. 21: Tafel plots for zinc in 1.0 M HCl with and without various *H. kraussii* extract inhibitor concentrations.

© University of Venda

Table 5. 9: PDP parameters, including anodic and cathodic Tafel slopes (βa and β_c), polarization resistance (R_P), corrosion potential (E_{corr}), and corrosion current density (i_{corr}), measured in 1.0 M HCl using different *H. kraussii* inhibitor concentrations.

Inhibitor	**Inhibitor Conc. (ppm)**	**-E_{corr} (mV) With Ag/AgCl**	**i_{corr} (mA.cm^{-2})**	**R_P (Ω)**	**β_a (mV.dec^{-1})**	**β_c (mV.dec^{-1})**	**% IE_{PDP}**
H. kraussii extract	0.00	-471.330	285.912	66.2	70.5	89.3	
	100	-454.806	235.802	86.3	85.5	109.4	17.5263
	300	-479.970	134.016	106	48.6	76.9	53.127
	900	-454.251	131,868	167	96.9	109.1	53.878
	600	-452.259	104.452	118	63.5	76.7	63.467
	1500	-483.745	60.923	221	85.5	72.0	78.692
	1200	-450.322	59.599	180	56.9	71.0	79.155

Table 5.9 shows that in most cases, the inhibitor's E_{corr} values are found to have shifted towards more positive values relative to the blank system E_{corr} value. From the literature, the inhibitor can be categorised as cathodic, anodic, or mixed inhibitor type based on the shifting of E_{corr} values of the coated system in comparison with the uncoated system. The E_{corr} value variation between the uncoated and coated system greater than -85 mV is dedicated to the cathodic or anodic type of inhibitor. The E_{corr} value less than -85 mV is attributed to the mixed inhibitor type. In the current study, the E_{corr} difference is less than -85 mV, suggesting that the inhibitor acts as a mixed type in its inhibition action. It can be said that the inhibitor inhibits both the anodic and cathodic reactions by creating a film on the surface of the metal, which leads to the indirect blockage of the cathodic and anodic reaction sites. The Tafel slope values (β_a and β_c) show variation upon the inhibitor introduction in the corrosive electrolyte in relation to the blank system. The variation in the β_a and β_c slope values may be due to several factors, such as the working electrode composition, the concentration of the electrolyte, the charge transfer coefficient, and the scan rate. The values of β_a and β_c can also be used to describe the magnitude of the variation of the E_{corr} values in categorising the inhibiting effects of the extract as anodic, cathodic or mixed type. From Table 5.9, it can be seen that the values of β_a and β_c do not follow a stable trend, which is an indication that the addition of the extract inhibitor affects both the anodic and cathodic half-reactions and that the rate of the anodic and cathodic inhibition differs with inhibitors concentrations. Based on the significant difference between the β_a and β_c of the blank system and the inhibited system, it is noted that the inhibition effects of the extract are cathodic dominating. In the table, it is evident that the values of i_{corr} decrease with the rising

© University of Venda

extract concentration, which leads to the increase in %IE, which suggests the adsorption of the inhibitor on the metal surface, forming the protective film hindering the metal corrosion [302].

5.5.3. Aluminium metal

5.5.3.1. Open circuit voltage

Figure 5.22 shows the open circuit voltage for the aluminium metal in hydrochloric acid for different concentrations of *H. kraussii* extract. The OCV was run for 3600 s to stabilize the system in order to get reliable results when running the EIS and PDP. It was performed in 1.0 M HCl solution with and without the various extract inhibitor concentrations at 303 K, and its response is presented in Figure 5.22. The OCV for the blank is found to have shifted towards more negative potential than the OCV for the three concentrations of the inhibitor (100, 600 and 1500 ppm), which are found to have shifted towards the more noble values. It can also be observed that the OCV for the three concentrations of the inhibitor (300, 900 and 1200 ppm) has shifted towards the more negative potential compared to blank system OCV. This is an indication that the aluminium metal was strongly attacked by corrosion, as confirmed by the low inhibition efficiency for the first two concentrations in Table 5.10. The oscillations in the OCV plots are an indication of the corrosion product layer formation and the destruction that occurred on the surface of the metal [303].

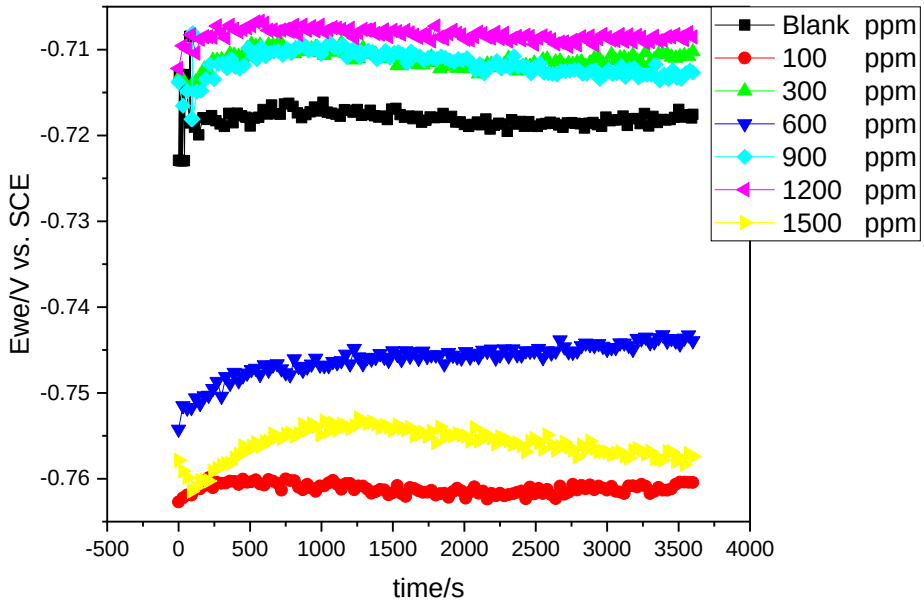


Figure 5. 22: Open circuit voltage for aluminium 1.0 M HCl solution and *H. kraussii.*

© University of Venda

5.5.3.2. Electrochemical impedance spectroscopy (EIS)

The EIS is a non-destructive method that can be utilised to find the corrosion mechanism at the solution or metal interface with and without the inhibitor in a 1.0 M HCl corrosive solution [303]. It is also widely known that the formation of the inhibitor layer on the metal surface leads to a rise in the corrosion system impedance, which also increases the charge transfer resistance. The increase in the charge transfer resistance in relation to the blank system results in the inhibition system increase [303]. Figures 5.24 and 5.23 show the Bode and Nyquist plots from the impedance response. The magnitude of the impedance at low frequencies in the Bode plots and the circle's diameter indicates the aluminium complex's performance [304]. The Nyquist plot for the uninhibited and the inhibited solution formed a depressed circle. The circles increase in diameter with an increase in the inhibitor concentration with respect to the uninhibited system, which is an indication that the inhibitor was adsorbed onto the surface of the metal, forming a protective film. The shape of the circles is the same both in the absence and presence of the inhibitor, which indicates that the inhibitor's addition in the corrosive solution did not change the corrosion mechanism [305].

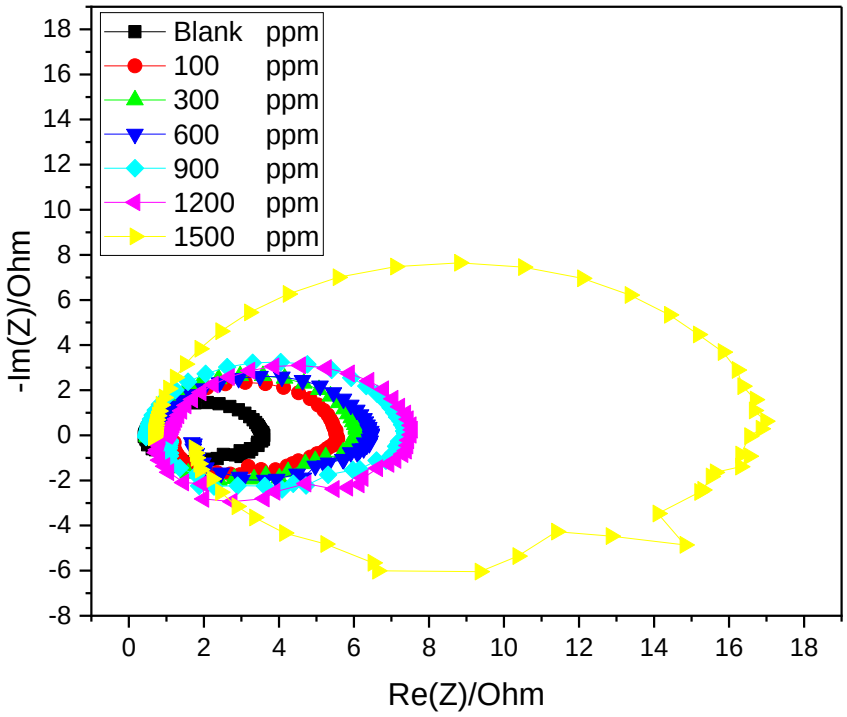


Figure 5. 23: Nyquist plot of aluminium metal in 1.0 M HCl with and without various concentrations of *H. kraussii* extract inhibitor.

© University of Venda

The Bode plots with and without different concentrations of *H. kraussii* are given in Figure 5.24. The inhibition effect of *H. kraussii* can be explained easily from the observation of the low-frequency impedance modulus. It can be observed that the low-frequency modulus in the presence of various concentrations of the *H. kraussii* is more than in comparison to the blank system. This observation is a clear indication that the adsorption of the *H. kraussii* extracts on the surface of the metal improves the corrosion resistance of aluminium metal [306]. The phase angle maxima values in the presence of different *H. kraussii* concentrations are approaching 90 ˚C, with 1200 ppm concentration at 60 ˚C. This trend is an indication that there is merely one time constant related to the electrical double-layer formation at the solution-surface interface [307].

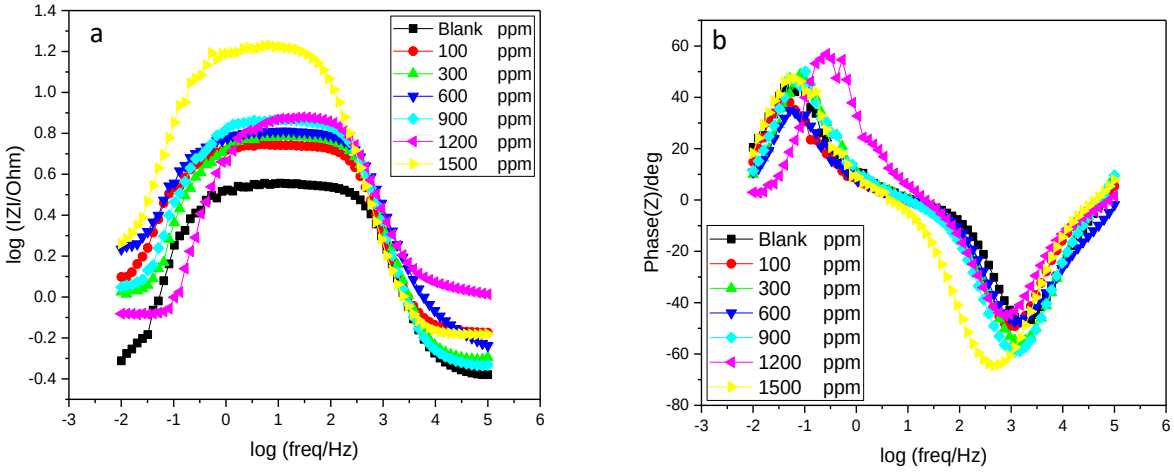


Figure 5. 24: Bode impedance magnitude plot (a) and Bode phase angle plot (b) of aluminium metal in 1.0 M HCl with and without various concentrations of *H. kraussii* extract inhibitor.

Electrochemical parameters, like R1 which is solution resistance (R_s), R2 which is charge transfer resistance (R_{ct}), inductor (L3), Q1 which is constant phase element (CPE), n1 which is constant phase element constant, and Resistor (R3), were all obtained by fitting Nyquist data into Figure 5.25 circuit and their values are presented in Table 5.10. The fitted charge transfer values were used to calculate the percentage inhibition efficiency using Equation 78, and its values are also presented in Table 5.10.

© University of Venda

University of Venda
Creating Future Leaders

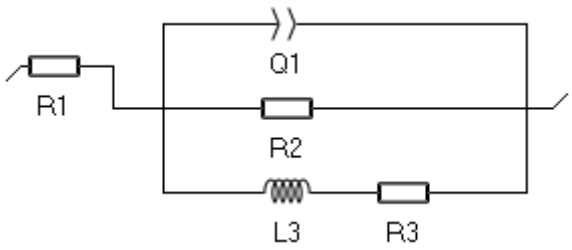


Figure 5. 25: Equivalent circuit model for a blank solution and *H. kraussii* extract solution.

© University of Venda

Table 5. 10: EIS parameters like the solution resistance (R_s), resistance of charge transfer (R_{ct}), constant phase element (CPE), constant phase element constant (n1), double layer capacitance (C_{dl}) and percentage inhibition efficiency ($\%IE_{EIS}$), using *H. kraussii* in 1.0 M HCl in aluminium metal.

Inhibitor	**Metal**	**Concentration (ppm)**	***R_s*** **(Ωcm^2)**	**CPE ($F.s^{(a-1)}$)**	**n1**	***R_{ct}*** **(Ωcm^2)**	**L3 (H)**	**R3 (Ωcm^2)**	**C_{dl} ($\mu F/cm^{-2}$)**	**τ (s)**	**$\%IE_{EIS}$**
H. kraussii extract	Aluminium	00	0.4339	$0.1063x10^{-3}$	0.9669	2.976	2.519	0.0512	36838.1142	0.1096	-
		100	0.6841	$94.84x10^{-6}$	0.9911	4.613	6.737	0.5501	15070.7097	0.0695	35.49
		300	0.5055	$73.33x10^{-6}$	0.9915	5.297	3.354	0.5036	11902.7156	0.0630	43.82
		600	0.6243	$0.1447x10^{-3}$	0.8891	5.657	7.034	1.3000	10871.4751	0.0615	47.39
		900	0.4778	$81.52x10^{-6}$	0.9896	6.483	4.456	0.6223	7915.4010	0.0513	54.10
		1200	1.037	$0.2067x10^{-3}$	0.8737	6.799	0.7676	-0.2443	7437.9316	0.0508	56.22
		1500	0.66	$0.1216x10^{-3}$	0.9779	15.26	12.29	1.2630	1697.7264	0.0259	80.50

From Table 5.10, the values of R_{ct} are observed to be increasing with increasing concentration of the inhibitor. This finding suggests that the inhibitor was adsorbed onto the surface of the metal, thereby protecting the metal from corrosion. The increase in the R_{ct} yielded an increase in the percentage inhibition efficiency. The maximum %IE was found to be 80.50% for the highest concentration of 1500 ppm. The constant phase element exponent (n1) values describe the corrosion process on the metal surface. Its values range from -1 to 1 [308], in which -1 represents the inductance, 1 represents the capacitor, and zero represents the resistor [309]. From the table, it can be observed that the values of n are approximately approaching 1, which suggests that the interface is of a capacitive nature. The high value of n is a proof that the extract formed a film on the surface of aluminium metal and improved its homogeneity.

© University of Venda

The CPE values do not form a proper trend, but generally, they are found to decrease with increasing extract inhibitor concentration. This is an indication of the inhibitor adsorption on the surface of the metal hindering the formation of hostile and corrosion cells. The solution resistance values did not show any particular trend, but their values in the presence of various concentrations of the inhibitor are higher than that of the blank system. The time constant values in Table 5.10 are found to be decreasing with increasing inhibitor concentration for aluminium metal. This observation implies that the adsorption time of the *H. kraussii* extract on the aluminium metal is low, which suggests a fast adsorption process [282]. The time constant is also found to have a direct proportional relationship with the double-layer capacitance. The double layer capacitance (C_{dl}) decreases with increasing inhibitor concentration, indicating that introducing the extract inhibitor in the corrosive solution increases the aluminium metal corrosion resistance [310]. The decrease in C_{dl} can be caused by the progressive replacement of water molecules and other ions that were originally adsorbed on the electrode surface during the adsorption of inhibitor molecules on the steel surface [311].

5.5.3.3. Potentiodynamic polarization (PDP)

The potentiodynamic curves were obtained through the application of a potential of 250 mV in relation to the corrosion potential of the electrochemical system for aluminium metal corrosion with and without various extract inhibitor concentrations and in the corrosive electrolyte of 1.0 M HCl at 303 K. The curve is displayed in Figure 5.26. Tafel plots are very helpful in categorising the inhibitors as cathodic, anodic, or mixed inhibitors based on Tafel constants. It can be observed from the Tafel plots that the introduction of the inhibitor in the corrosive electrolyte managed to reduce both the cathodic and anodic current densities in relation to that of the blank system. This is indicative of the formation of the inhibitor film on the surface of the metal, preventing corrosion. Different electrochemical parameters like the corrosion current density (i_{corr}), corrosion potential (E_{corr}), polarization resistance (R_P) and anodic and cathodic Tafel constants (β_a and β_c) were acquired through the Tafel extrapolation method. The percentage inhibition efficiency ($\%IE_{PDP}$) calculated using the corrosion current density values, and all these parameters are tabulated in Table 5.11.

© University of Venda

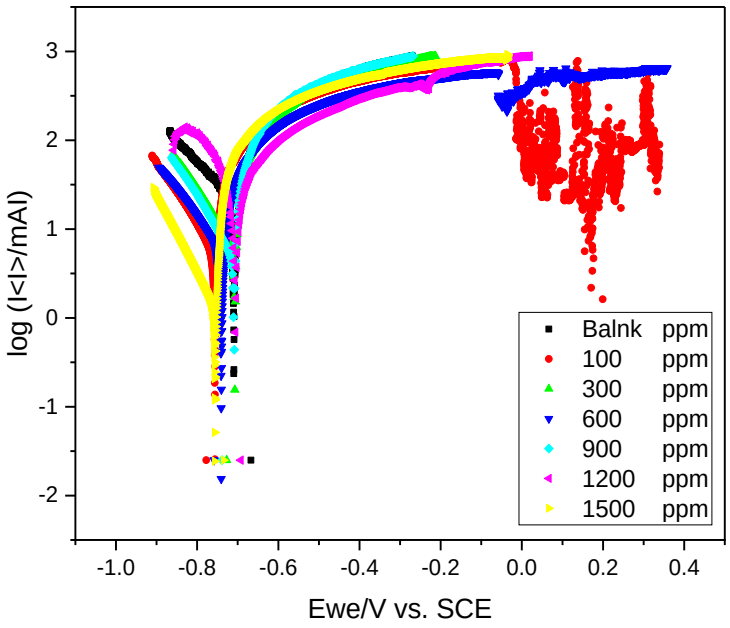


Figure 5. 26: Bode plots of aluminium metal in 1.0 M HCl with and without various concentrations of *H. kraussii* extract inhibitor.

Table 5. 11: PDP parameters, including anodic and cathodic Tafel slopes (βa and β_c), polarization resistance (R_P), corrosion potential (E_{corr}), and corrosion current density (i_{corr}), measured in 1.0 M HCl using different *H. kraussii* inhibitor concentrations.

Inhibitor	**Inhibitor Conc. (ppm)**	**-E_{corr} (mV) With Ag/AgCl**	**i_{corr} (mA.cm^{-2})**	**R_P (10^{-1}) (Ω)**	**β_a (mV.dec^{-1})**	**β_c (mV.dec^{-1})**	**% IE_{PDP}**
Blank	00	-709.347	23517.404	0.768	86.3	249.6	
UV-radiated *H. kraussii* extract	1200	-709.425	13297.926	0.488	35.8	46.2	43.45
	600	-740.520	5951.620	1.71	48.5	158.7	74.56
	300	-706.514	5781.870	0.967	24.0	132.6	75.41
	900	-709.135	5773.445	0.994	25.0	145.7	75.45
	100	-755.856	5530.814	1.24	31.8	137.5	76.48
	1500	-756.390	1395.980	1.71	14.8	116.0	94.06

Examination of the parameters in Table 5.11 reveals that the E_{corr} values did not show any stable trend but, in most cases, were found to be shifting cathodically in the presence of the inhibitor. From the literature, it is largely said that if the shifting of the E_{corr} values in the absence and presence of the inhibitor is less than -85 mV, the inhibitor is categorised as a mixed type, and if the shift is greater than that, the inhibitor is either categorised as an anodic or

© University of Venda

cathodic inhibitor. Based on the results obtained, the E_{corr} difference between the inhibitor and the blank system is less than -85 mV, indicating that the inhibitor works as a mixed type. From the table, it is clear that the values of the Tafel constants were affected by the presence of the inhibitor in the corrosive electrolyte, which is an indication of the modification of the mechanism of anodic aluminium dissolution and cathodic hydrogen evolution [312]. This insight also complements the suggestion that the inhibitor was acting as a mixed-type inhibitor, which adsorbs on the active sites of the aluminium surface. It is also observed that the i_{corr} values decreased with an increase in the inhibitor concentrations with respect to that of the blank system. This decrease yielded an increase in the percentage inhibition efficiency with regard to the blank system. This observation suggests the formation of the protective layer in the aluminium metal surface. The highest %IE was found at the maximum concentration of 1500 ppm with a value of 94.06%.

5.6. Fourier transform infrared spectroscopy (FTIR)

The FTIR analysis was performed on mild steel, zinc, and aluminium samples immersed for 8 hours in 37% HCl solutions with and without the inclusion of 1500 ppm concentration of the *H. kraussii* inhibitor extract. The complementary IR measurements proved the adsorption of the extract inhibitor molecules on the surface of the metal [313]. The spectra obtained are presented in the section below.

5.6.1. Mild steel

Figure 5.27 shows the spectra of four samples analysed for their functional groups, as the figure legend elaborates. From the figure, it can be observed that there was a variation in the adsorption transmittance for the four spectra. In the presence of HCl for mild steel, the plant extract was affected the most since most of the functional groups present in it were not retained on the metal surface after gravimetric analysis, as can be observed in Table 5.12. The only functional groups retained after gravimetric analysis in the presence of the extract inhibitor are C=C alkene, NO_2 nitro, C=C aromatic, Sp^3 C-O and C-H aromatic, which are believed to be the ones causing the corrosion inhibition.

© University of Venda

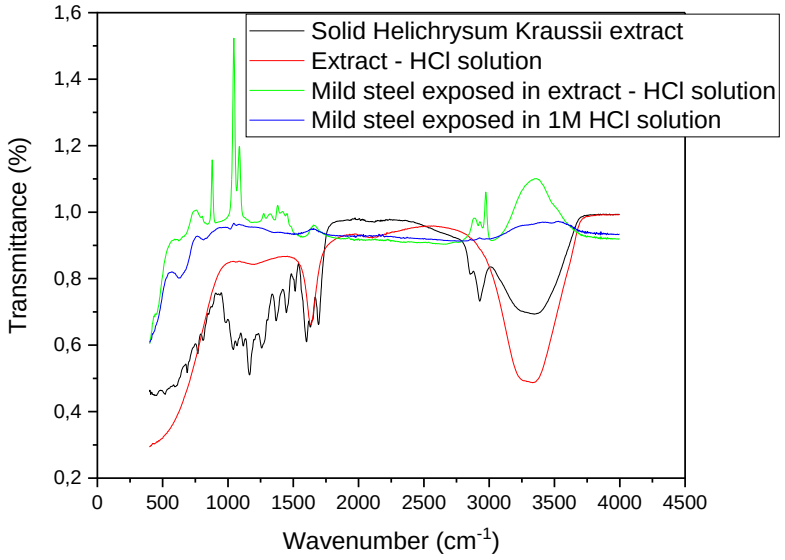


Figure 5. 27: FTIR spectra for solid *H. kraussii plant* extract (Black), 1500 ppm *H. kraussii* plant extract – 1.0 M HCl solution (Red), the layer formed on mild steel metal exposed in 1500 ppm *H. kraussii* plant extract – 1.0 M HCl solution (Green) and corrosion products formed on mild steel metal exposed in 1.0 M HCl solution (black).

Table 5. 12: Possible functional groups present in solid *H. kraussii* plant extract, corrosion products formed on mild steel metal exposed in 1.0 M HCl solution, 1500 ppm *H. kraussii* plant extract – 1.0 M HCl solution and layer formed on mild steel metal exposed in 1500 ppm *H. kraussii* plant extract – 1.0 M HCl solution.

	Functional Groups			
Bands position (cm^{-1})	**Solid *H. kraussii***	**Mild steel metal exposed in HCl blank solution**	***H. kraussii* - HCl solution**	**Mild steel metal exposed in *H. kraussii* - HCl solution**
2400 - 3600	O-H Carboxylic acid		O-H Carboxylic acid	
3300 - 3500	O-H alcohol		O-H alcohol	
3200 - 3400	N-H amine N-H amide		N-H amine N-H amide	
3260 - 3390			Sp C-H (C≡C-H)	
2850 - 2960	Sp^3 C-H (C-C-H)			
2700 - 2900				
2200 - 2270				
2100 - 2250	C≡C alkyne		C≡C alkyne	

© University of Venda

1680 - 1720	C=O ketone C=O aldehyde			
1600 - 1650	C=C alkene	C=C alkene	C=C alkene	C=C alkene
1500 - 1600				
1500 - 1570	NO_2 Nitro C=C aromatic	NO_2 Nitro C=C aromatic		NO_2 Nitro C=C aromatic
1450 - 1470		C-H alkane		
1180 - 1360	amine C-N			
1200 - 1250				
1000 - 1200	Sp^3 C-O	Sp^3 C-O		Sp^3 C-O
900 – 1000				
600 – 900	C-Cl chloride C-C alkane C-H aromatic			C-H aromatic

5.6.2. Zinc metal

As outlined in Figure 5.28 legend, the figure represents the FTIR spectra of the four samples analysed for their functional groups. According to the literature, the appearance and disappearance of the functional groups and the shift in the position of the spectra symbolise the interaction of the extract inhibitor with the surface of the metal [314], which, therefore, might lead to corrosion inhibition. Table 5.13 represents all the possible functional groups on the four spectra in Figure 5.28. Only a few functional groups on the plant extract were also present on the zinc metal surface after gravimetric analysis in the presence of the extract, which can be said to hinder the corrosion process. These functional groups include C≡C alkyne, C=C alkene, Sp^3 C-O, C-Cl chloride and C-H aromatic.

© University of Venda

University of Venda
Creating Future Leaders

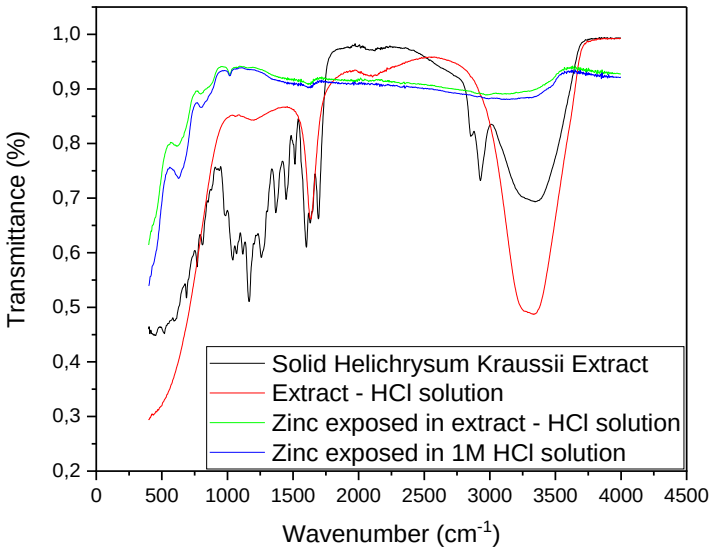


Figure 5. 28: FTIR spectra for solid *H. kraussii* plant extract (Black), 1500 ppm *H. kraussii* plant extract – 1.0 M HCl solution (Red), the layer formed on mild zinc exposed in 1500 ppm *H. kraussii* plant extract – 1.0 M HCl solution (Green) and corrosion products formed on zinc exposed in 1.0 M HCl solution (black).

Table 5. 13: Possible functional groups present in solid *H. kraussii* plant extract, corrosion products formed on zinc metal exposed in 1.0 M HCl solution, 1500 ppm *H. kraussii* plant extract – 1.0 M HCl solution and layer formed on zinc metal exposed in 1500 ppm *H. kraussii* plant extract – 1.0 M HCl solution.

	Functional Groups			
Bands position (cm^{-1})	**Solid *H. kraussii***	**Zinc metal exposed in HCl blank solution**	***H. kraussii* - HCl solution**	**Zinc metal exposed in *H. kraussii* - HCl solution**
2400 – 3600	O-H Carboxylic acid		O-H Carboxylic acid	
3300 – 3500	O-H alcohol		O-H alcohol	
3200 – 3400	N-H amine N-H amide		N-H amine N-H amide	
3260 – 3390			Sp C-H (C≡C-H)	
2850 – 2960	Sp^3 C-H (C-C-H)			
2700 – 2900				
2200 – 2270				
2100 – 2250	C≡C alkyne		C≡C alkyne	C≡C alkyne
1680 – 1720	C=O ketone			

© University of Venda

	C=O aldehyde			
1600 – 1650	C=C alkene		C=C alkene	C=C alkene
1500 – 1600		C=C alkene		
1500 – 1570	NO_2 Nitro C=C aromatic			
1450 – 1470				
1180 – 1360	amine C-N			
1200 – 1250				
1000 – 1200	Sp^3 C-O	Sp^3 C-O		Sp^3 C-O
900 – 1000				
600 – 900	C-Cl chloride C-C alkane C-H aromatic	C-Cl chloride C-H aromatic		C-Cl chloride C-H aromatic

5.6.3. Aluminium metal

Figure 5.29 shows the four spectra obtained from the FTIR instrument; the green spectrum was plotted separately to show the clear variation of the absorption bands. This is because it appeared to be a straight line in the combined spectra plot due to the variation in the spectrum scale. Generally, all the spectra show variations, which is strong evidence of the adsorption of the extract inhibitor on the surface of the metal. The disappearance and appearance of functional groups, especially in the green spectrum compared with the black spectrum, indicates the inhibitor adsorption on the metal surface, therefore causing corrosion inhibition. Table 5.14 shows all the possible functional groups that might be present in the four samples analysed. Looking at the first and the last columns, it can be said that most of the functional groups present in the first (black) column disappeared in the last (green) column, indicating poor adsorption of the extract on the metal surface. The functional groups which were found to have been attached on the metal surface after gravimetric analysis in the presence of the extract inhibitor, which can be said to be the ones causing the corrosion inhibition, are C≡C alkyne, C=O ester, C=O ketone, C=O amide, NO_2 nitro and C=C aromatic.

© University of Venda

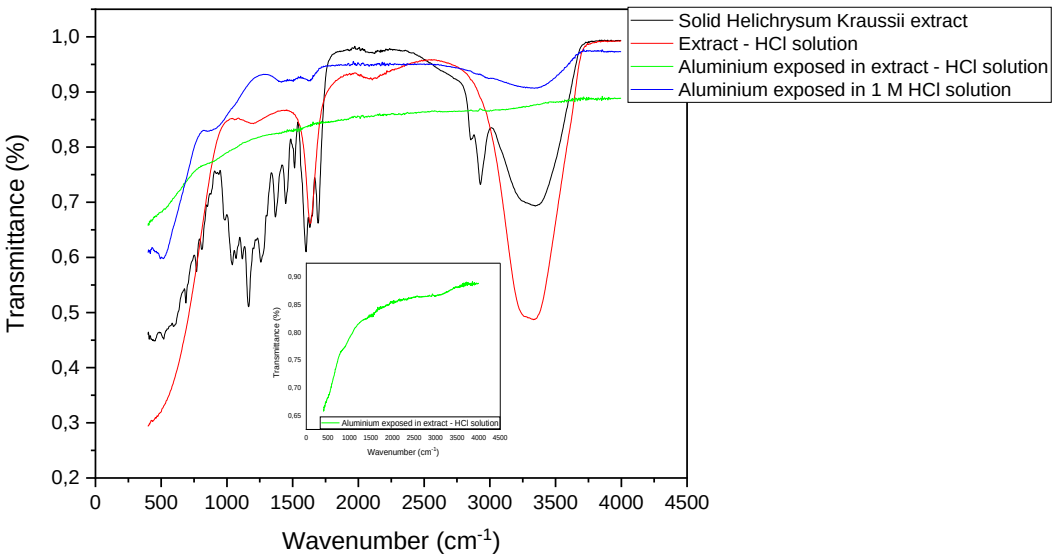


Figure 5. 29: FTIR spectra for solid *H. kraussii* plant extract (Black), 1500 ppm *H. kraussii* plant extract – 1.0 M HCl solution (Red), the layer formed on aluminium metal exposed in 1500 ppm *H. kraussii* plant extract – 1.0 M HCl solution (Green) and corrosion products formed on aluminium metal exposed in 1.0 M HCl solution (black).

Table 5. 14: Possible functional groups present in solid *H. kraussii* plant extract, corrosion products formed on aluminium metal exposed in 1.0 M HCl solution, 1500 ppm *H. kraussii* plant extract – 1.0 M HCl solution and layer formed on aluminium metal exposed in 1500 ppm *H. kraussii* plant extract – 1.0 M HCl solution.

	Functional Groups			
Bands position (cm^{-1})	**Solid *H. kraussii***	**Aluminium metal exposed in HCl blank solution**	***H. kraussii* - HCl solution**	**Aluminium metal exposed in *H. kraussii* - HCl solution**
3590 – 3600				O-H Carboxylic acid
2400 – 3600	O-H Carboxylic acid		O-H Carboxylic acid	O-H Carboxylic acid
3300 – 3500	O-H alcohol	O-H alcohol	O-H alcohol	
3200 – 3400	N-H amine N-H amide		N-H amine N-H amide	
3260 – 3390		Sp C-H (C≡C-H)	Sp C-H (C≡C-H)	
2850 – 2960	Sp^3 C-H (C-C-H)			
2700 – 2900				
2200 – 2270				

© University of Venda

2100 – 2250	C≡C alkyne		C≡C alkyne	C≡C alkyne
1730 – 1750				ester C=O
1680 – 1720	C=O ketone C=O aldehyde			C=O ketone amide C=O
1600 – 1650	C=C alkene	C=C alkene	C=C alkene	
1500 – 1600				
1500 – 1570	NO_2 Nitro C=C aromatic			NO_2 Nitro C=C aromatic
1450 – 1470				
1180 – 1360	amine C-N			
1200 – 1250				
1000 – 1200	Sp^3 C-O			
900 – 1000				
600 – 900	C-Cl chloride C-C alkane C-H aromatic			

© University of Venda

CHAPTER 6

UV-radiated *H. kraussii* extract in Hydrochloric acid

© University of Venda

6. Introduction

In this chapter, the results obtained for UV-radiated *H. kraussii* plant extract as a corrosion inhibitor for mild steel, zinc and aluminium metal in hydrochloric acid using gravimetric analysis, adsorption isotherm, the effect of temperature, electrochemistry, and Fourier transform infrared spectroscopy are discussed.

6.1. Weight loss

The weight loss of zinc, mild steel and aluminium metals obtained after gravimetric analysis in 1.0 M HCl with and without various concentrations of UV-radiated *H. kraussii* extract have been tabulated in Table 6.1. The difference in mass of the metals was calculated by subtracting the mass of the metal before gravimetric analysis and the mass of the metal after gravimetric analysis.

Table 6. 1: Gravimetric weight analysis in the presence of 1.0 M HCl and UV-radiated *H. kraussii* extract for mild steel, zinc and aluminium metals.

Inhibitor	**Metal**	**Concentration (ppm)**	**Weight loss (g)**			
			30° C	40° C	50° C	60° C
UV-radiated *H. kraussii* extract	Mild steel	0.00	0.1446	0.2997	0.5872	0.9731
		100	0.0563	0.1740	0.4119	0.7676
		300	0.0197	0.0547	0.2838	0.6637
		600	0.0129	0.0231	0.2170	0.4426
		900	0.0116	0.0229	0.1107	0.3629
		1200	0.0102	0.0177	0.0351	0.2974
		1500	0.0029	0.0109	0.0238	0.1706
	Aluminium	0.00	0.5457	0.6083	0.6574	0.7168
		100	0.2148	0.5072	0.6135	0.6421
		300	0.1712	0.4467	0.5699	0.6109
		600	0.1407	0.3127	0.5242	0.5476
		900	0.1161	0.2955	0.4868	0.5234
		1200	0.0949	0.2730	0.4768	0.5241
		1500	0.0835	0.2677	0.4583	0.5521
		0.00	0.2549	0.4053	0.6411	1.1229
		100	0.1586	0.2321	0.4226	0.7507

© University of Venda

	Zinc	300	0.1311	0.1604	0.3410	0.5678
		600	0.1143	0.1370	0.2296	0.4491
		900	0.1112	0.1157	0.1815	0.3607
		1200	0.1054	0.1120	0.1549	0.2956
		1500	0.1051	0.1091	0.1279	0.2828

Table 6.1 shows that the weight loss of all three metals decreases with rising inhibitor concentration. This indicates that introducing the inhibitors in the corrosive medium counteracts the aggression of the corrosive acid on the metal. However, as the temperature increased, the metal weight loss was found to be increasing. The 0.00 ppm shows the metal's weight loss when no inhibitors are involved at the four different investigated temperatures normally referred to as the blank. The weight loss of the metal, when there was no inhibitor involved at 60 ℃, was in the following sequence: zinc > mild steel > aluminium. Based on the blank results, it can be said that the zinc metal was the most affected by the hydrochloric acid solution among the three metals utilized. This is because zinc is higher in the electrochemical series than aluminium metals, making it more reactive. Even though mild steel is less reactive than aluminium, it corrodes faster than aluminium because aluminium metal can form an insoluble residue on the metal surface, preventing it from reacting further with acid [315]. Zinc and mild steel do not possess this property as effectively as aluminium. However, with the addition of the extract inhibitor in the acidic corrosive solution, it was found that the weight loss of aluminium metal was the highest at all the temperatures and concentrations compared to the other two metals, with the highest weight loss at the maximum temperature amounting to 0.6421 g. Mild steel metal was the least affected, as evidenced by the weight loss at the temperatures and concentrations studied compared to the other two metals. The reduction in the weight loss of the three metals with increasing extract inhibitor concentration is solid evidence that introducing the inhibitors on the aggressive acid solution reduced the rate at which the metals corrode. The increase in weight loss with rising temperature shows that the inhibitor utilized is very effective at lower temperatures.

6.2. Corrosion rate and inhibition efficiency.

The rate of corrosion determines the degree and rate at which the metal is affected by the corrosion. The corrosion rates and the percentage inhibition efficiency are very useful in determining the inhibitor's effectiveness in inhibiting the corrosion process of the metals in an acidic environment. The corrosion parameters, such as the corrosion rate (C_R), percentage

© University of Venda

inhibition efficiency (%IE) and surface coverage (θ), were all calculated using Equations 13, 77 and 76, respectively.

Table 6. 2: Corrosion parameters for aluminium, mild steel and zinc in an aqueous medium of 1.0 M HCl with and without various concentrations of UV-radiated *H. kraussii* extract from weight loss measurements at four (30 – 60° C) different temperatures.

Inhibitor	**Metal**	**Temperature (° C)**	**Inhibitor Concentration (ppm)**	**Corrosion rate ($g.cm^{-2}.h^{-1}$)**	**Inhibition Efficiency (%IE)**	**Surface coverage (θ)**
	Mild steel	30	0.00	0.001505		
			100	0.000586	61.063	0.61063
			300	0.000205	86.379	0.86379
			600	0.000134	91.096	0.91096
			900	0.000121	91.960	0.91960
			1200	0.000106	92.957	0.92957
			1500	0.000030	98.007	0.98007
		40	0.00	0.003119		
			100	0.001811	41.937	0.41937
			300	0.000569	81.757	0.81757
			600	0.000240	92.305	0.92305
			900	0.000238	92.369	0.92369
			1200	0.000184	94.101	0.94101
			1500	0.000113	96.377	0.96377
		50	0.00	0.00611		
			100	0.004287	29.848	0.29848
			300	0.002954	51.661	0.51661
			600	0.002258	63.050	0.63050
			900	0.001152	81.149	0.81149
			1200	0.000365	94.027	0.94027
			1500	0.000248	95.991	0.95991
		60	0.00	0.010128		
			100	0.007989	21.120	0.21120
			300	0.006908	31.793	0.31793
			600	0.004606	54.522	0.54522
			900	0.003777	62.707	0.62707

© University of Venda

			1200	0.003095	69.441	0.69441
			1500	0.001776	82.464	0.82464
		30	0.00	0.005679		
			100	0.002236	60.627	0.60627
			300	0.001782	68.621	0.68621
			600	0.001464	74.221	0.74221
			900	0.001208	78.729	0.78729
			1200	0.000988	82.603	0.82603
			1500	0.000869	84.698	0.84698
		40	0.00	0.006331		
			100	0.005279	16.617	0.16617
			300	0.004649	26.568	0.26568
			600	0.003254	48.602	0.48602
			900	0.003075	51.602	0.51429
			1200	0.002841	55.126	0.55126
			1500	0.002786	55.994	0.55994
		50	0.00	0.006842		
			100	0.006385	6.679	0.06679
			300	0.005931	13.1315	0.13315
			600	0.005456	20.257	0.20257
			900	0.005066	25.957	0.25957
			1200	0.004962	27.477	0.27477
			1500	0.004770	30.284	0.30284
		60	0.00	0.007460		
			100	0.006683	10.416	0.10416
			300	0.006358	14.772	0.14772
			600	0.005699	23.606	0.23606
			900	0.005447	26.984	0.26984
			1200	0.005455	26.877	0.26877
			1500	0.005746	25.992	0.25992
		30	0.00	0.002653		
			100	0.001651	37.769	0.37769
			300	0.001364	48.587	0.48587
			600	0.001190	55.145	0.55145
***UV-radiated H. Kraussii* extract**	Aluminium					

© University of Venda

			900	0.001157	56.389	0.56389
			1200	0.001096	58.688	0.58688
			1500	0.001094	58.764	0.58764
			0.00	0.004218		
			100	0.002416	42.722	0.42722
		40	300	0.001669	60.432	0.60432
			600	0.001426	66.193	0.66193
			900	0.001204	71.456	0.71456
			1200	0.001166	72.357	0.72357
			1500	0.001135	73.092	0.73092
	Zinc		0.00	0.006672		
			100	0.004398	31.083	0.34083
		50	300	0.003549	46.808	0.46808
			600	0.002390	64.179	0.64179
			900	0.001889	71.688	0.71688
			1200	0.001612	75.839	0.75839
			1500	0.001331	80.051	0.80051
			0.00	0.011687		
			100	0.007813	33.148	0.33148
		60	300	0.005909	49.440	0.49440
			600	0.004674	60.007	0.60007
			900	0.003754	67.879	0.67879
			1200	0.003077	73.672	0.73672
			1500	0.002943	74.818	0.74818

Table 6.2 shows that introducing the corrosion inhibitor on the corrosive medium reduced the rate at which the metal corrodes compared to its absence. Zheng et al. (2023) [316] reported similar observation. It was discovered that the rate of corrosion decreased as the inhibitor's concentration increased [317]. This is because more molecules were available in the reaction to adsorb on the metal surface and lessen the impact of the acid attack. The %IE was found to increase with increasing extract inhibitor concentration. This suggests that the extract inhibitor has strong inhibiting potential [318]. However, as the temperature increased, the %IE was found to decrease. The highest inhibition was found at the lowest temperature and highest concentration of the inhibitor for mild steel metal, equivalent to 98.007 %. The surface

© University of Venda

coverage values reveal how much of the metal surface was covered by the extract inhibitor. It has a value ranging from 0 to 1, with one indicating that the inhibitor efficiently covered the surface of the metal [319]. From the values of θ inspection in the table, it is found that they are increasing with the rising concentration of the extract inhibitor, reaching values close to 1 at the maximum concentration, suggesting that the inhibitor managed to cover most of the surface of the metal forming a protective layer thereby protecting the metal from acid corrosion attack. The layer formed by the adsorption of the extract inhibitor on the surface of the metal blocks the active sites and isolates the metal surface from the acidic environment [320].

Figures 6.1-6.3 show the graphical variation in the percentage inhibition efficiency for mild steel, zinc and aluminium metals in UV-radiated *H. kraussii* extract in the presence of 1.0 M HCl. The trend in the figures explains exactly what has been tabulated in Table 6.1. The %IE is observed to increase with increasing extract inhibitor concentration and decrease with an increase in temperature. This observation indicates that the extract inhibitor functions optimally at lower temperatures. This also means that high temperatures lowered the metal's corrosion resistance [231, 321].

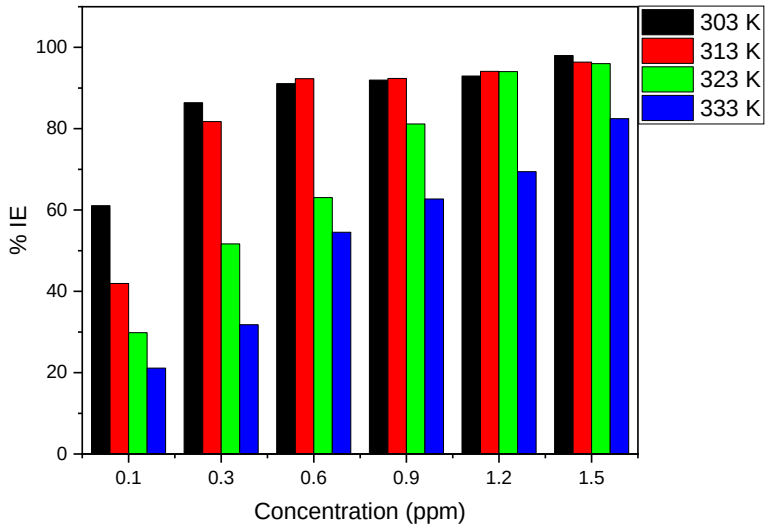


Figure 6. 1: The graph of inhibition efficiency using UV-radiated *H. kraussii* in 1.0 M HCl for mild steel at various temperatures.

© University of Venda

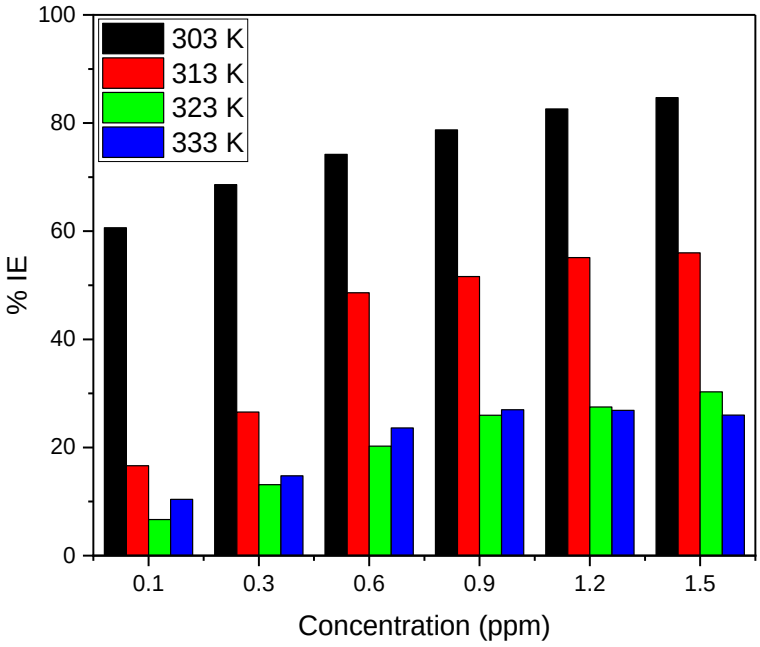


Figure 6. 2: The graph of inhibition efficiency using UV-radiated *H. kraussii* in 1.0 M HCl for aluminium at various temperatures.

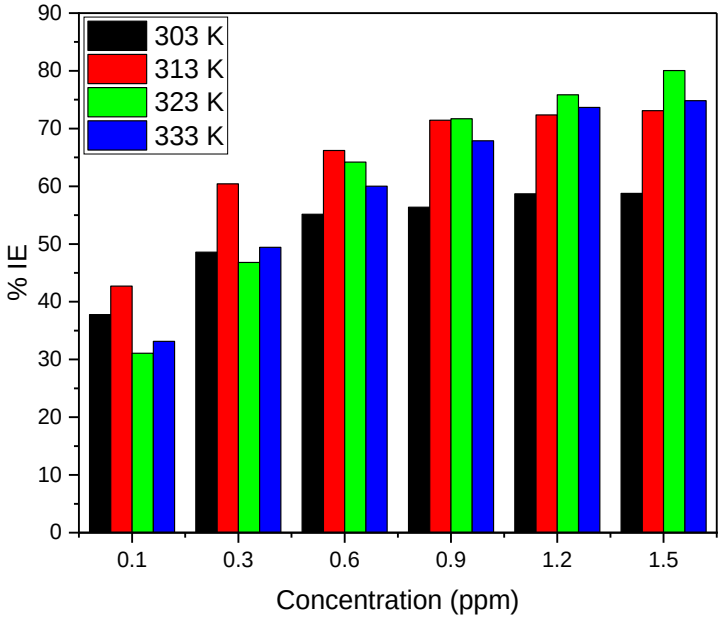


Figure 6. 3: The graph of inhibition efficiency using UV-radiated *H. kraussii* in 1.0 M HCl for zinc at various temperatures.

© University of Venda

6.3. Absorption isotherms

Adsorption isotherm is an essential tool in studying the *H. kraussii* extract distribution in the mild steel, zinc and aluminium metals and the aqueous solution, providing effective information on the equilibrium adsorption capacity of the extract [322]. The adsorption isotherm describes the depth of interaction of molecules of different inhibitors with the metal surface [226]. The interaction happens in such a way that the inhibitors displace the water molecules, which can be represented by the conjectural equation given in Equation 81.

The best adsorption isotherm model that describes the adsorption of the UV-radiated *H. kraussii* extract on mild steel, zinc and aluminium metal in 1.0 M HCl was found by fitting the rate of corrosion and the inhibitor's degree of surface coverage into different adsorption isotherms models like Frendlich, Temkim, Langmuir, Flory Huggins and El Awady adsorption isotherm. However, in all the isotherm models explored, the gravimetric data obtained were found to obey the Langmuir adsorption isotherm perfectly based on the closeness of the correlation coefficient values to unity and the linearity achieved by the isotherm plots in Figures 6.4 – 6.6 [237]. The equilibrium constant value (K_{ads}) is correlated to the Gibbs free energy (ΔG^{o}_{ads}) using Equation 90 [323].

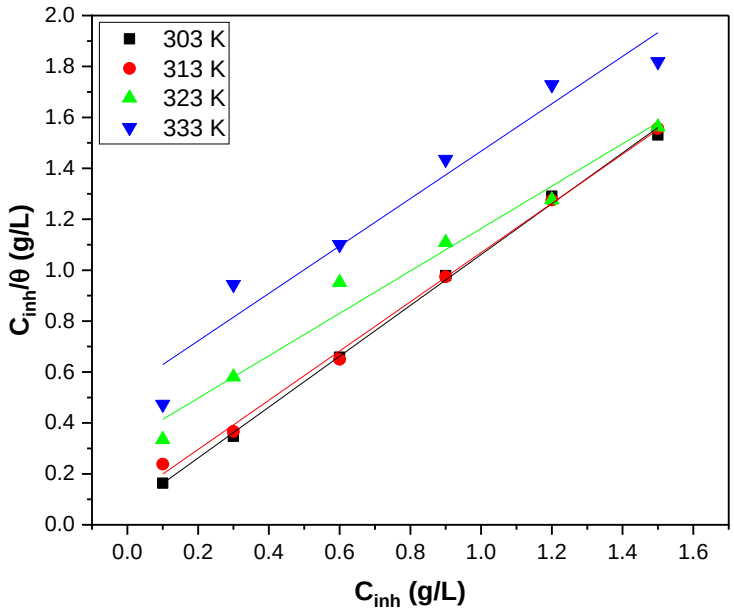


Figure 6. 4: Langmuir adsorption isotherm for the adsorption of UV-radiated *H. Kraussii* on mild steel metal in HCl at 30, 40, 50 and 60°C.

© University of Venda

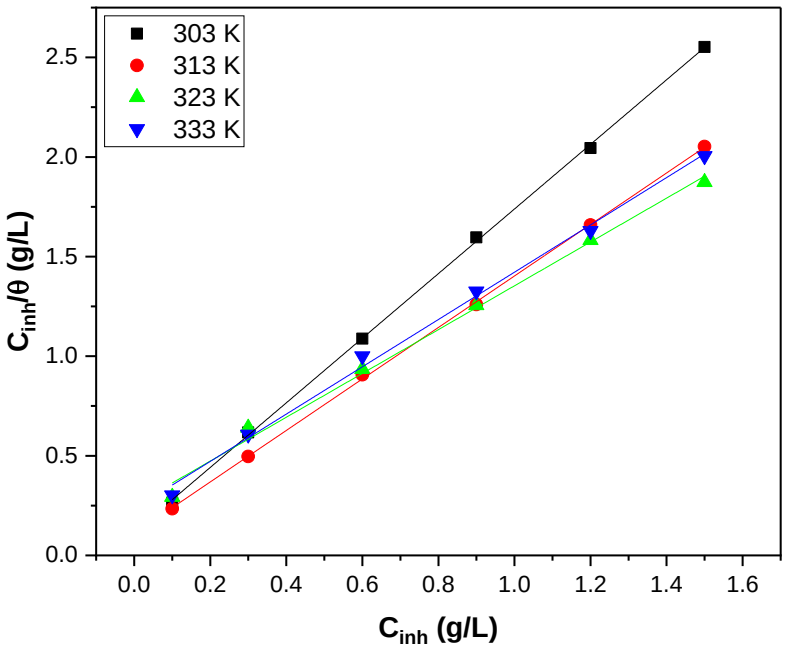


Figure 6. 5: Langmuir adsorption isotherm for the adsorption of UV-radiated *H. Kraussii* on zinc metal in HCl at 30, 40, 50 and 60°C.

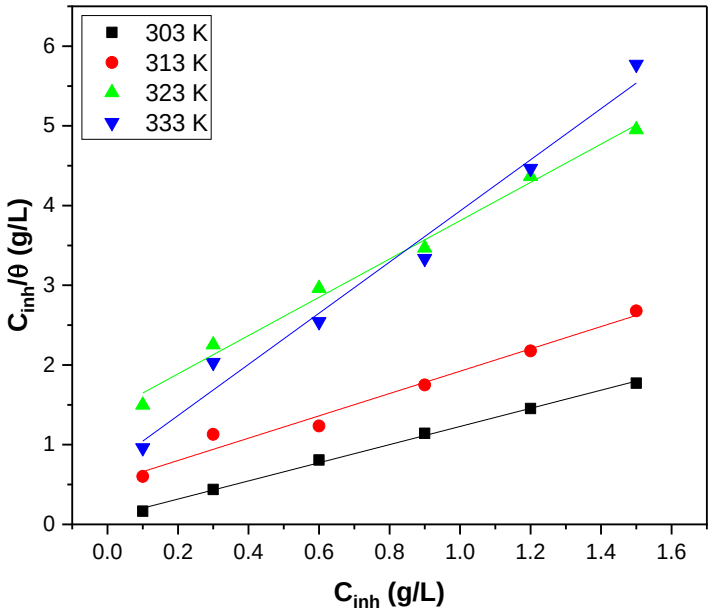


Figure 6. 6: Langmuir adsorption isotherm for the adsorption of UV-radiated *H. Kraussii* on aluminium metal in HCl at 30, 40, 50 and 60°C.

The Langmuir Adsorption Isotherm parameters for UV-radiated *H. kraussii* extract in 1.0 M HCl, such as the equilibrium constant (K_{ads}), Gibbs free energy ($-\Delta G^{o}_{ads}$), correlation coefficient (r^2) and the slope values are tabulated in Table 6.3.

© University of Venda

Table 6. 3: Langmuir Adsorption Isotherm parameters for UV-radiated *H. kraussii* extract in 1.0 M HCl.

Inhibitor	**Metals**	**Temperature (° C)**	**r^2**	**Slope**	**K_{ads} (L/g)**	**$-\Delta G^o_{ads}$ (kJ.mol^{-1})**
UV-radiated *H. Kraussii* extract	Mild steel	30	0.99796	0.99853	15933.72	41..780
		40	0.99680	0.96650	9748.49	41.880
		50	0.96940	0.96940	3024.62	40.075
		60	0.93972	0.93119	1865.43	39.978
	Aluminium	30	0.99709	1.13858	11112.35	40.872
		40	0.97396	1.40039	1917.32	37.648
		50	0.98940	2.40266	710.25	36.184
		60	0.97669	3.20939	1382.30	39.148
	Zinc	30	0.99962	1.62191	8537.52	40.208
		40	0.99965	1.29262	9076.88	41.694
		50	0.99300	1.10000	3945.40	40.789
		60	0.99551	1.18738	4267.49	42.269

The equilibrium constant (K_{ads}) values represent the inhibitor's adsorption degree onto the metal surface. The high values of the K_{ads} at lower temperatures represent the stronger formation of the bond between the extract inhibitor molecules and the metal surface studied. Meanwhile, the drop at higher temperatures represents the weakening of the absorbed film on the metal surface. The value of K_{ads} also provides information about the ratio of the adsorbent to adsorptive concentration [324]. From the literature, the negative values of the ΔG^o_{ads} suggest that the reaction between the inhibitor molecules and the metal surface is spontaneous and also signifies the stability of the adsorbed layer on the metal surface [169, 325, 326]. The values of ΔG^o_{ads} can be grouped into three categories. The values of ΔG^o_{ads} ranging from -40 kJ.mol^{-1} and above signify the chemisorption type of adsorption. In contrast, those ranging around -20 kJ.mol^{-1} and lower signify a physisorption kind of adsorption between the metal and the inhibitor molecules and the values between -20 kJ.mol^{-1} and -40 kJ.mol^{-1} and the combination of the values below and above those, signifies the mixed type of adsorption. Chemisorption refers to the transfer or electron sharing between the substrate surfaces and the adsorbate (inhibitors) molecules, leading to the formation of the coordinate type of bond formation. Physisorption is referred to as the electrostatic interaction between the charged surface of the

© University of Venda

metal substrate and the charged adsorbate (inhibitor). The table shows that the values of ΔG^{o}_{ads} for zinc are greater (more negative) -40 kJ.mol^{-1}, which indicates that the inhibitors absorb through chemisorption kind of adsorption [327]. However, for mild steel and aluminium metal, the ΔG^{o}_{ads} values are around -40 kJ.mol^{-1} with some greater than -40 kJ.mol^{-1} and some less but all very close to -40 kJ.mol^{-1}, suggesting a mixed type of adsorption with chemisorption dominating in mild steel metal. The trend in the ΔG^{o}_{ads} values describe the nature of adsorption between the corrosion inhibitor and the surface of the metal. The increase in the values of ΔG^{o}_{ads} (less negative) as the temperature increases temperature signifies exothermic adsorption dominance, while a decrease with an increase in temperature signifies an endothermic type of adsorption. From the table, the values of the ΔG^{o}_{ads} did not follow any particular trend but, in most cases, were found to increase with the increase in temperature, suggesting exothermic adsorption.

Table 6.4 shows the dimensionless separation constant (K_L) for the different concentrations of UV-radiated extract inhibitor for the three metals studied and four different temperatures. These values are calculated using Equation 91. From Table 6.3, it can be observed that the slope values of zinc and aluminium metal are slightly above unity, which is inconsistent with the Langmuir adsorption isotherm assumption of monolayer adsorption of inhibitor molecules on the surface of the metal and the fact that this study involves the use of acids. K_L is introduced to solve this inconsistency and to complement the r^2 values in Langmuir adsorption isotherm. The K_L average values are less than unity, suggesting a favourable adsorption process and that the experimental data fit the Langmuir adsorption isotherm.

Table 6. 4: Dimensionless separation factor (K_L) at various *H. kraussii* concentrations at four various temperatures for metals corrosion in 1.0 M HCl.

Metal	**Concentration (ppm)**	**Temperature** (℃)			
		30	40	50	60
Mild steel	100	0.000627206	0.001024749	0.003295306	0.005332111
	300	0.000209156	0.000341816	0.001100854	0.001783711
	600	0.000104589	0.000170937	0.000550730	0.000892652
	900	0.000069729	0.000113965	0.000367221	0.000595278
	1200	0.000052297	0.000085476	0.000275441	0.000446525
	1500	0.000041838	0.000068382	0.000220365	0.000357252
	Average	0.000184136	0.000300888	0.000968319	0.001567921
Aluminium	100	0.000899091	0.005188552	0.013884068	0.007182360
	300	0.000299877	0.001735521	0.004671260	0.002405639
	600	0.000149961	0.000868514	0.002341098	0.001204268
	900	0.000099979	0.000579177	0.001561951	0.000803168

© University of Venda

	1200	0.000074986	0.000434446	0.001171921	0.000602497
	1500	0.000059990	0.000347587	0.000937756	0.000482055
	Average	0.000263980	0.001525633	0.004094676	0.002113331
Zinc	100	0.001169930	0.001100488	0.002528189	0.002337820
	300	0.000390281	0.000367099	0.000844153	0.000780490
	600	0.000195179	0.000183583	0.000422255	0.000390397
	900	0.000130128	0.000122396	0.000281543	0.000260299
	1200	0.000097599	0.000091800	0.000211172	0.000195237
	1500	0.000078081	0.000073441	0.000168945	0.000156195
	Average	0.000343533	0.000323134	0.000742709	0.000686740

6.4. Thermodynamic parameters: Effect of temperature

Temperature plays a crucial role in the corrosion of different metals. The corrosion kinetics process attains the character of a diffusion process, whereby at lower temperatures, the quantity of the inhibitor molecules present on the surface of the metal is higher than at higher temperatures. Therefore, the high inhibition efficiency at minimum temperatures may be attributed to the high activation energy present for the adsorption process and the inhibitor molecule's high rate of diffusion [39].

The Arrhenius equation is the most efficient tool for evaluating the effect of temperature on adsorption behaviour and determining activation parameters for zinc, mild steel, and aluminium metals. The Arrhenius equation is given by Equation 92 [169, 328]. The corrosion rate logarithm ($logC_R$) of the three studied metals at 1.0 M HCl in the absence and presence of the inhibitors concentrations was plotted against the reciprocal of the absolute studied temperature($\frac{1}{T}$). The line of best fit was then constructed, with E_a/2.303R being the slope of the lines. The plots are represented by Figures 6.7 – 6.9.

© University of Venda

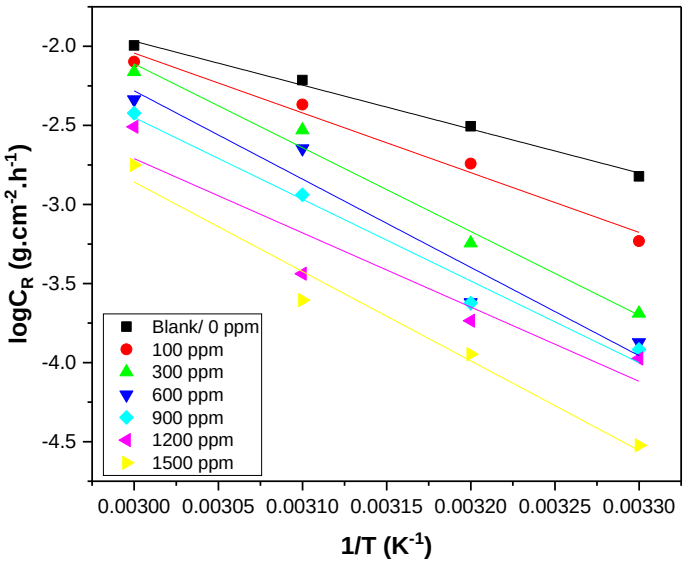


Figure 6. 7: Arrhenius plots for mild steel metal corrosion in 1.0 M HCl medium with and without various concentrations of UV-radiated *H. kraussii* as the inhibitor.

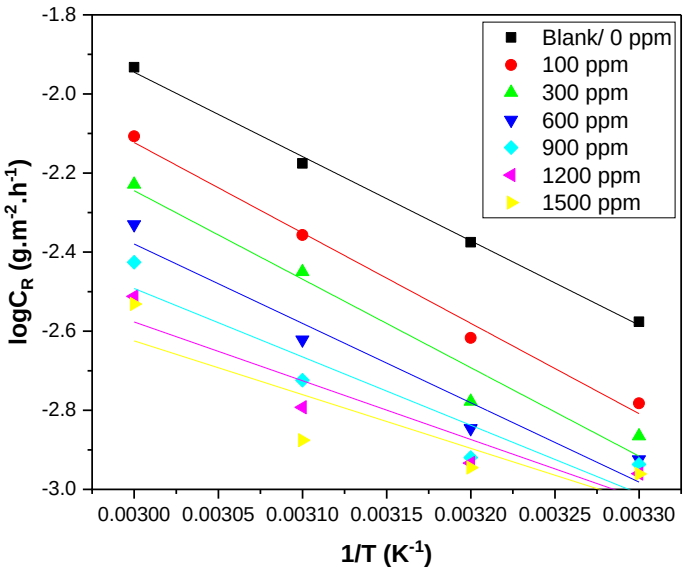


Figure 6. 8: Arrhenius plots for zinc metal corrosion in 1.0 M HCl medium with and without various concentrations of UV-radiated *H. kraussii* as the inhibitor.

© University of Venda

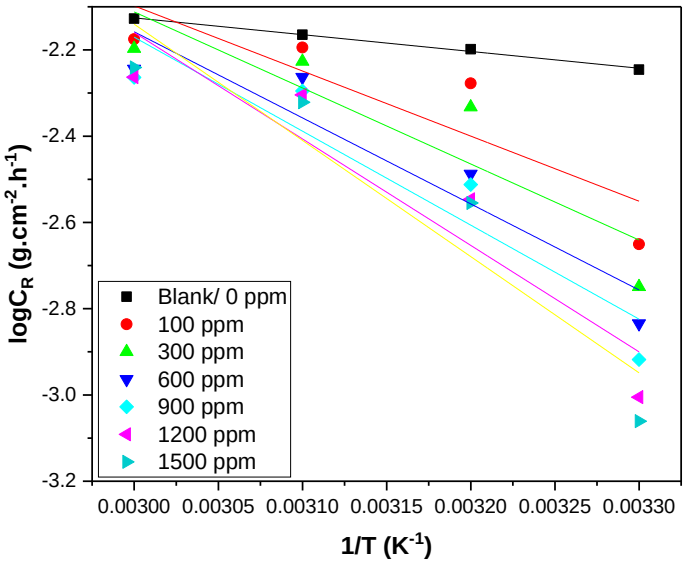
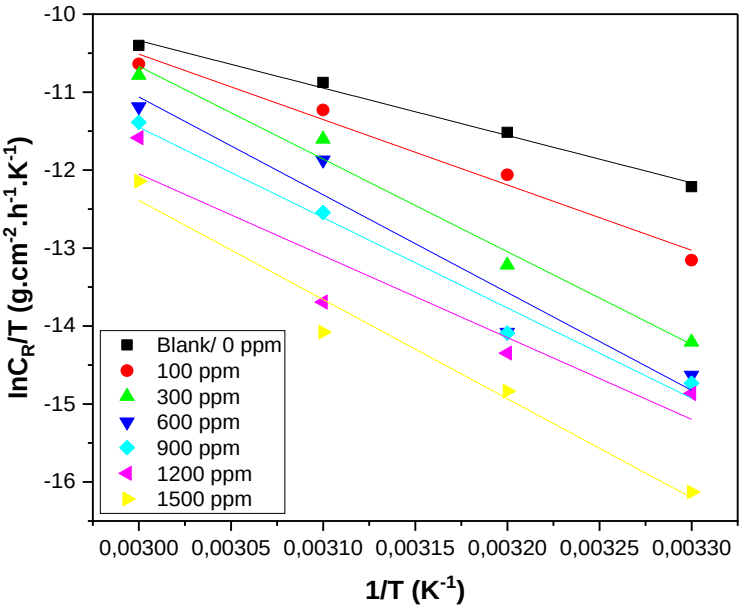


Figure 6. 9: Arrhenius plots for aluminium metal corrosion in 1.0 M HCl medium with and without various concentrations of UV-radiated *H. kraussii* as the inhibitor.

Equation 93 was utilized to get the values of the change in entropy of activation (ΔS*) and change in enthalpy of activation (ΔH*) based on the transition state plots presented below. Plots of ln (CR/T) versus 1/T are displayed in Figures 6.10 – 6.12, with best-fitted data having an intercept of ΔS*/2.303R and a slope of -ΔH*/R. Table 6.5 shows the E_a, ΔH*, and ΔS* values.



© University of Venda

Figure 6. 10: Transition state plots for mild steel metal corrosion in 1.0 M HCl medium with and without various concentrations of UV-radiated *H. kraussii* as the inhibitor.

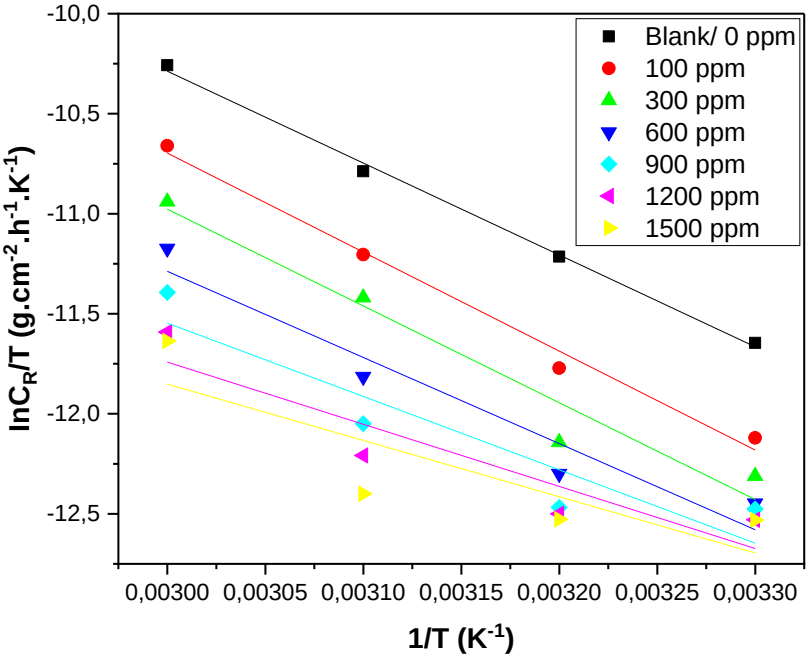


Figure 6. 11: Transition state plots for zinc metal corrosion in 1.0 M HCl medium with and without various concentrations of UV-radiated *H. kraussii* as the inhibitor.

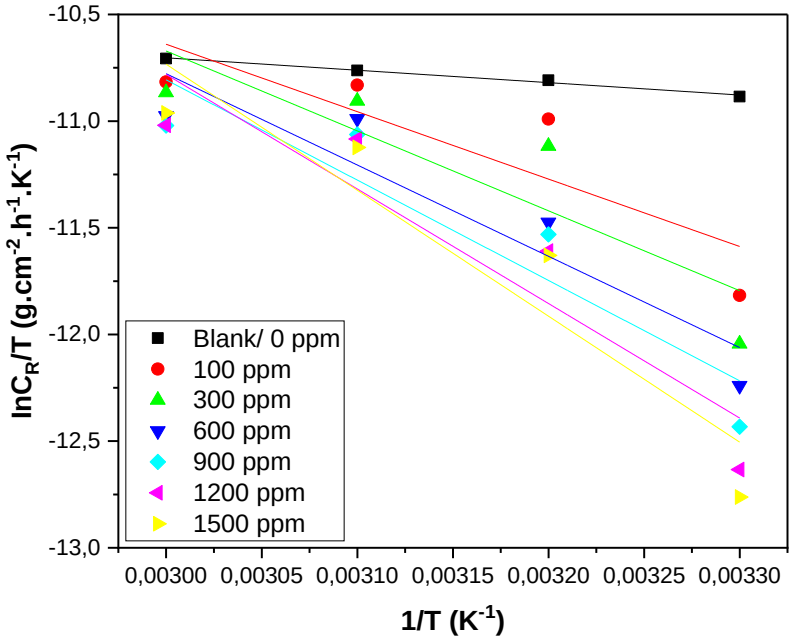


Figure 6. 12: Transition state plots for aluminium metal corrosion in 1.0 M HCl medium with and without various concentrations of UV-radiated *H. kraussii* as the inhibitor.

© University of Venda

Table 6. 5: Transition state and Arrhenius parameters for the adsorption of various concentrations of UV-radiated *H. kraussii* in 1.0 M HCl on mild steel, zinc and aluminium metal.

Inhibitor	**Metals**	**Concentration of inhibitors (PPM)**	E_a **(kJ.mol^{-1})**	ΔH^* **(kJ.mol^{-1})**	ΔS^* **(J.mol^{-1}.k^{-1})**
UV-radiated *H. kraussii* extract	Mild steel	0.00	53.15623	50.53104	-131.93043
		100	72.34225	69.71317	-75.82726
		300	101.44957	98.81459	10.15340
		600	106.88874	104.25132	23.22853
		900	98.95742	96.32323	-3.79168
		1200	89.872899	87.24056	-36.01511
		1500	108.34679	105.71188	16.57452
	Aluminium	0.00	7.45098	4.83305	-272.04780
		100	28.90550	26.27523	-207.19245
		300	33.75844	31.13622	-192.87314
		600	38.20525	35.58199	-180.42517
		900	41.72585	39.10193	-170.09765
		1200	47.26335	44.63864	-153.27949
		1500	51.59680	48.97091	-139.92465
	Zinc	0.00	40.80559	38.188476	-168.53460
		100	43.76094	41.136990	-163.08329
		300	42.84909	40.224980	-168.14831
		600	38.42488	35.801900	-184.00090
		900	33.10874	30.486690	-202.09866
		1200	28.44728	25.825590	-217.70331
		1500	26.01277	23.391930	-225.91987

Activation energy is regarded as the minimum energy required for the corrosion process to proceed [329]. Therefore, a rise in activation energy due to a higher concentration of extract inhibitor indicates that the corrosion reaction is becoming more difficult to proceed with. This trend was observed for aluminium metal, with the values of E_a in the presence of the extract inhibitor greater than the blank value [325, 330]. With that said, high activation energy values are a perfect indication that the inhibitor provides strong inhibition action by elevating the energy barrier of the corrosion process [324]. The table shows that the values of *Ea* for the zinc

© University of Venda

metal are generally decreasing as the extract inhibitor concentration increases. For mild steel metal, the E_a values increase with an increase in the extract inhibitor concentration (100 – 300 ppm) and then decrease from (900 -1200 ppm) and increase again at the highest concentration of 1500 ppm.

The values of (ΔH^*) and (ΔS^*) were determined from the transition state plot slope $-\Delta H^*/2.303R$ [331] and intercept $In(C_R/h+\Delta S^*/R)$. The values of the ΔH^* are used to determine if the reaction between the inhibitor and the surface of the metal is exothermic or endothermic. An exothermic reaction is one in which heat is given off the reaction and is represented by the negative values of the ΔH^* and suggests either physisorption or chemisorption kind of adsorption. In the exothermic reaction, chemisorption is differentiated from physisorption by assuming the adsorption heat of a chemisorption process approaches 100 $kJ.mol^{-1}$, while the absolute value of a physisorption process is lower than 40 $KJ.mol^{-1}$ [332]. An endothermic reaction is one in which heat is adsorbed onto the reaction and is represented by the positive values of the change in enthalpy, suggesting a chemisorption kind of adsorption. In this study, the values of the ΔH^* obtained are positive, indicating that the dissolution process of the metals studied is endothermic [333-335], further suggesting a chemisorption kind of adsorption. The values of the ΔS^* are used to describe the disorder taking place in the system. From Table 6.5, it can be observed that the values of the ΔS^* are negative, suggesting that the disorder taking place in the reaction decreased. This also suggests that the disorder of the product is less than the disorder of the reactant [324, 325].

© University of Venda

6.5. Electrochemical analysis

6.5.1. Mild steel

6.5.1.1. Open circuit voltage (OCV)

The OCV was used to investigate the amount of current flowing and resistance value [336] in the absence and presence of the UV-radiated *H. Kraussii* extract. Figure 6.13 shows the OCV-time curve for the working electrode corrosion of the bare mild steel substrate and various concentrations of UV-radiated *H. kraussii* extract. For the best reliability, accuracy and interpretation of the OCV plots, the OCV-time profile for mild steel dissolution in 1.0 M HCl solution was run for 3500 s. From the literature, the straight-line OCV-time curves indicate the dissolution of the surface of the metal oxide layer and the adsorption of the extract inhibitor at the metal interface [297]. Figure 6.13 shows that the OCV plots for both the uninhibited and inhibited systems reached equilibrium or constant flow at 1000 s, and most of the curves started to proceed in a straight-line form. From the figure, it can also be observed that the OCV for the inhibitor free-solution was shifted towards less positive potential values, indicating the corrosion product's desorption on the metal surface [294]. However, upon introducing the UV-radiated *H. kraussii* extract, the OCV was observed to have shifted towards more positive potential. This observation suggests that the extract was adsorbed at the metal interface. After 3000 s, the time profiles reached a straight-line steady state, which indicates that the adsorption and desorption of the extract on the surface of the metal have reached dynamic equilibrium for the blank and 100 ppm concentration [337].

© University of Venda

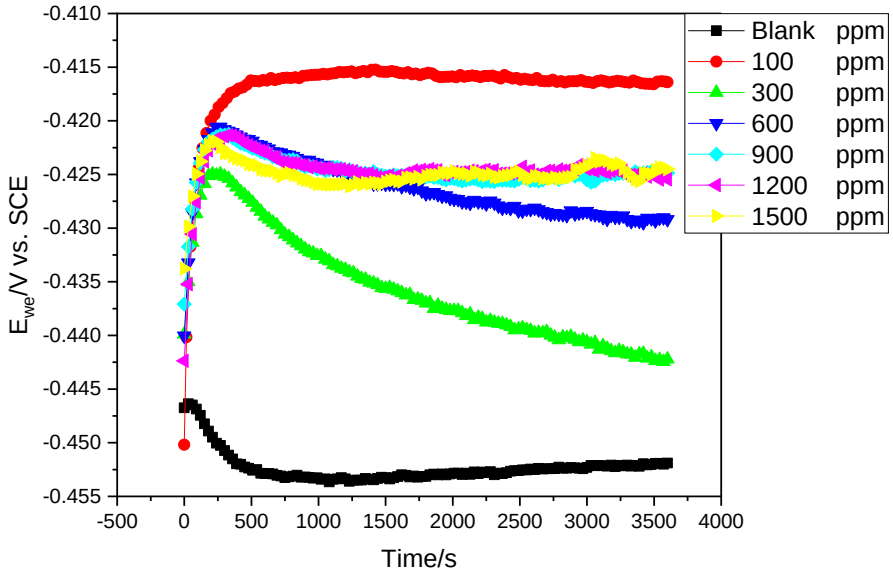


Figure 6. 13: Open circuit voltage for mild steel in 1.0 M HCl medium and UV-radiated *H. kraussii* extract.

6.5.1.2. Electrochemical impedance spectroscopy (EIS)

The EIS is an electrochemical technique used to analyse the response of the corroding electrodes to small amplitude varying the potential signals of widely alternating frequency [338]. The EIS was utilised to study the behaviour of mild steel in the presence of UV-radiated *H. kraussii* extract. This method relies on the measurements of the impedance of the double layer at the metal–solution interface. The Nyquist plots obtained for mild steel in the void of and with the presence of six concentrations of the UV-radiated *H. kraussii* extract are shown in Figure 6.14. From the figure, it can be observed that the plots have a semi-circle shape, which increases with an increase in the extract inhibitor concentrations. The semi-circle for the blank and the inhibitor concentrations resemble similar shapes, which shows that introducing the extract in the corrosive electrolyte did not change the corrosion mechanism. The Nyquist semi-circles are imperfect due to the metal solid surface roughness and inhomogeneities [339].

© University of Venda

University of Venda
Creating Future Leaders

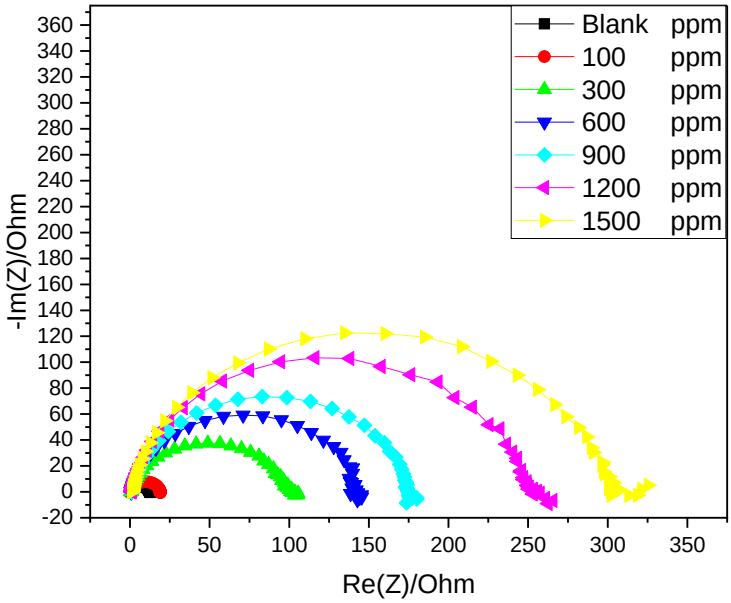


Figure 6. 14: Nyquist plot of mild steel metal in 1.0 HCl M with and without various concentrations of UV-radiated *H. kraussii* inhibitor compounds.

Nyquist has some shortcomings, such as when viewing the data point on the plot, it is difficult to tell what frequency was utilised to record that point. Impedance such as Bode plots is essential to making the correct interpretation. Unlike the Nyquist plot, the Bode plots shows the frequency information. The impedance measurements technique is applied to study the pitting corrosion and other localised corrosion [340]. Figure 6.15 represents the Bode and phase angle plots. The phase angles are found to shift to lower frequencies when the inhibitor is introduced to the aggressive solution [341], suggesting the inhibition of mild steel corrosion. It was observed that the peaks of the Bode plots represent a single time constant. It was also found that the impedance modulus increased with the increase in UV-radiated *H. kraussii* extract concentration in the studied frequency range. Correspondingly, the phase angle increased with the inhibitor concentration within the studied frequency range [337]. The extraction of the impedance parameters was performed by fitting the equivalent circuit represented in Figure 5.16 to the Nyquist plot, and the parameters obtained are tabulated in Table 6.6.

© University of Venda

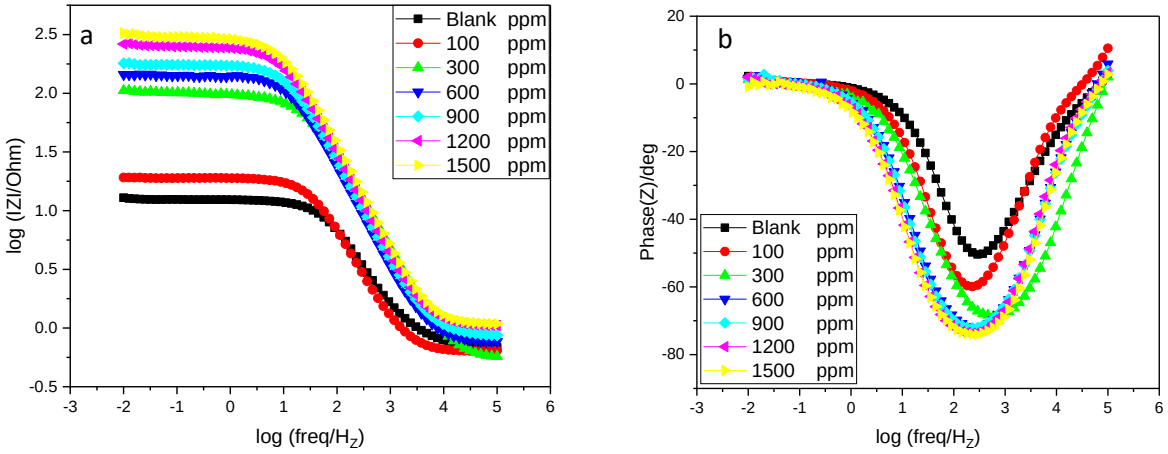


Figure 6. 15: Bode impedance magnitude plot (a) and Bode phase angle (b) of mild steel metal in 1.0 M HCl with and without various concentrations of UV-radiated *H. kraussii* inhibitor compound.

Table 6. 6: EIS parameters like the solution resistance (R_s), resistance of charge transfer (R_{ct}), constant phase element (CPE), constant phase element constant (n2), double layer capacitance (C_{dl}) and percentage inhibition efficiency ($\%IE_{EIS}$), using UV-radiated *H. kraussii* in 1.0 M HCl in mild steel metal.

Inhibitor	**Metal**	**Conc. (ppm)**	**R_s (Ωcm^2)**	**CPE ($F.s^{(a-1)}$**	**n2**	**R_{ct} (Ωcm^2)**	**C_{dl} ($\mu F/cm^{-2}$)**	**τ (s)**	**$\%IE_{EIS}$**
UV-radiated *H. kraussii* extract	Mild steel	00	0.7022	$0.5784x10^{-3}$	0.8253	11.87	3004.9292	0.0357	
		100	0.6328	$0.4412x10^{-3}$	0.8885	18.42	1315.4232	0.0242	35.56
		300	0.5533	$0.1224x10^{-3}$	0.8556	99.17	42.7576	0.0042	88.03
		600	0.7654	$0.1316x10^{-3}$	0.892	141.7	18.9964	0.0027	91.62
		900	0.876	$0.1150x10^{-3}$	0.8907	174.7	12.5380	0.0022	93.21
		1200	1.039	$96.81x10^{-6}$	0.8996	249.8	6.1594	0.0015	95.25
		1500	1.066	$83.37x10^{-6}$	0.8984	300.6	4.3406	0.0013	96.05

From Table 6.6 of the results, it can be observed that the R_{ct} values are found to increase with increasing extract inhibitor concentration. This indicates the adsorption of inhibitor on the surface of the metal, leading to the protective layer's formation and minimising the corrosion rate [29]. The increase in the $_{Rct}$ values with the extract inhibitor concentration increases the %IE. At the maximum concentration, the %IE was found to be 96.05%. The values of the constant phase element exponent (n2) are utilised to describe the corrosion process on the

© University of Venda

surface of the metal. Its values range from -1 to 1, where -1 represents the inductance, 1 represents the capacitor [342], and 0 represents the resistor. From the table, it can be observed that the values of n are approximately approaching 1, which suggests that the interface has a capacitive nature. The high values of n are used to prove that the extract formed a film on the surface of mild steel metal and improve its homogeneity. The CPE values did not form a proper trend, but generally, they were found to be decreasing with increasing extract concentration. This is an indication of the inhibitor adsorption on the surface of the metal hindering the formation of hostile and corrosion cells. The time constant values in Table 6.6 are found to be decreasing with increasing inhibitor concentration for mild steel metal. This observation implies that the adsorption time of the UV-radiated *H. kraussii* extract on the mild steel metal is low, which suggests a fast adsorption process [282]. The time constant is also found to have a direct proportional relationship with the double-layer capacitance. The double-layer capacitance is calculated using Equation 94. The defensive film development on the metal interface can be due to the significant decrease in the double-layer capacitance (C_{dI}) with increasing inhibitor concentration [343]. The C_{dI} decreases from 3004.9292 $\mu F/cm^{-2}$ for the blank to 4.3406 $\mu F/cm^{-2}$ for the highest concentration. Decreases in the local dielectric constant and/or increases in the thickness of the electrical double layer can cause a decrease in C_{dl}, indicating that molecules can be inhibited through adsorption at the metal/solution interface, which is facilitated by an increase in surface coverage (θ) [343, 344].

6.5.1.3. Potentiodynamic polarization (PDP)

The purpose of the polarization measurements is to examine the anodic and cathodic reaction kinetics. The Tafel plot for mild steel in 1.0 M HCl solutions in the absence and presence of various UV-radiated *H. kraussii* inhibitor concentrations is shown in Figure 6.16. The figure shows that introducing an extract inhibitor in the corrosive medium lowered both the anodic and cathodic corrosion current density. This observation indicates that the inhibitor hinders both the anodic dissolution of metal reactions and cathodic H_2 evolution [29]. The extrapolation of the anodic and cathodic branches junction yielded the electrochemical parameters like the corrosion potential (E_{corr}), corrosion current densities (i_{corr}), Polarization resistance (R_P), anodic and cathodic Tafel slopes (β_a and β_C). These parameters and the calculated potentiodynamic polarization percentage inhibition efficiency ($\%IE_{PDP}$) are tabulated in Table 6.7.

© University of Venda

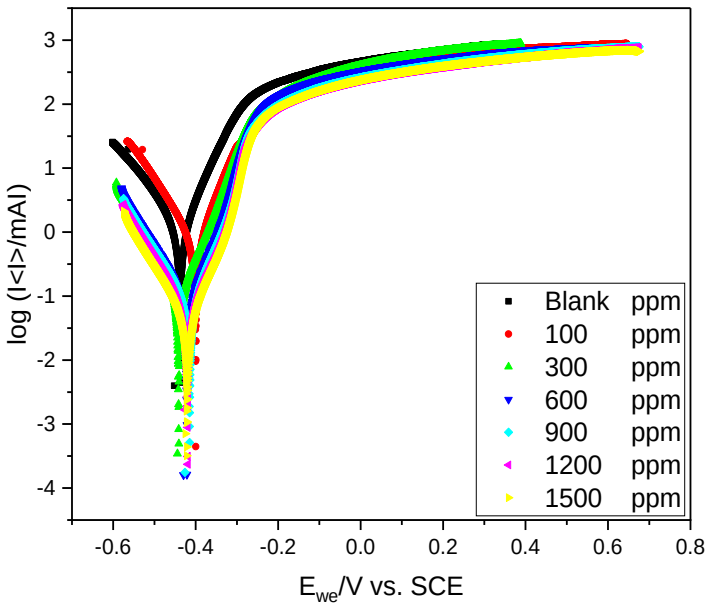


Figure 6. 16: Tafel plots for mild steel in 1.0 M HCl with and without various UV-radiated *H. kraussii* inhibitor compound concentrations.

Table 6. 7: PDP parameters, including anodic and cathodic Tafel slopes (βa and β_c), polarization resistance (R_P), corrosion potential (E_{corr}), and corrosion current density (i_{corr}), measured in 1.0 M HCl using various UV-radiated *H. kraussii* inhibitor concentrations.

Inhibitor	**Inhibitor Conc. (ppm)**	**$-E_{corr}$ (mV) With Ag/AgCl**	**i_{corr} (mA.cm^{-2})**	**R_P (10^{-1}) (Ω)**	**βa (mV.dec^{-1})**	**βc (mV.dec^{-1})**	**% IE_{PDP}**
Blank	0.00	-437.952	1593.060	16.1	84.8	134.4	
UV-radiated *H. kraussii* extract	100	-400.060	806.132	22.5	71.2	106.2	49.40
	300	-440.883	180.290	210.786	70.6	106.3	88.68
	600	-421.771	96.653	172	61.0	97.6	93.93
	900	-414.680	73.457	210	58.3	98.8	95.39
	1200	-418.375	57.274	286	59.5	97.1	96.40
	1500	-421.496	43.068	362	58.0	94.9	97.30

From inspection of Table 6.7 of results, it is found that with the introduction of the UV-radiated *H. kraussii* extract inhibitor, the E_{corr} values were shifted to the more positive or active (noble) direction following the OCV trend as reported by He et al. (2023) [345], suggesting a large number of inhibitor molecules being adsorbed on the metal solution interface [346]. It is widely known that if the displacement of the E_{corr} values between the inhibited and uninhibited system is higher than -85 mV, the inhibitor can be classified as either an anodic or cathodic type. Also,

© University of Venda

if the displacement of E_{corr} value is less than -85 mV, the inhibitor is classified as a mixed type. In this study, the largest displacement obtained was -37.892 mV, suggesting that the UV-radiated *H. kraussii* extract may be classified as a mixed inhibitor type. This suggests that the addition of the extract in 1.0 M HCl medium reduced both the cathodic hydrogen evolution reaction and anodic mild steel metal dissolution [347]. The values of the i_{corr} decrease with an increase in the extract's concentration, which suggests that the inhibitor was adsorbed onto the metal surface as reported by Luo et al. (2024), thereby hindering corrosion of the metal. This decrease in the i_{corr} results in an increase in %IE [29]. It can also be observed that the inhibition efficiency is directly proportional to the inhibitor concentration, and this indicates that the inhibitor was adsorbed on the mild steel metal, thereby covering its surface. The value of the polarization resistance of the blank system is lower than that of the inhibited system. These values are also observed to be increasing with increasing extract inhibitor concentration, with the maximum concentration recording 362 Ω as compared to 16.1 Ω of the blank system. It is also observed that the β_a and β_c values varied with respect to those of the blank upon the introduction of the extract inhibitor. This behaviour suggests that the UV-radiated *H. kraussii* extract is a mixed type of inhibitor and tends to manage both anodic metal dissolution and cathodic hydrogen evaluation [348]. The values of β_c are found to be higher than the β_a values, which suggests the cathodic action of the inhibitor. Larger values of the Tafel slopes can be associated with the surface kinetic process instead of the controlled diffusion process [349].

6.5.2. Zinc metal

6.5.2.1. Open circuit voltage (OCV)

The OCV, also known as the corrosion potential (E_{corr}), allude to the working electrode's potential when no external current is applied to the system. It is widely known that the OCV values of the inhibited metal are more positive than those of the uninhibited metal. When the inhibition coating on the metal fades away over time, the OCV values tend to become more negative until they equal the corrosion potential of the metal substrate. The OCV measurements can also give information about the disbandment of the coatings and the passive or active states of the metal substrate; for instance, a shift in the OCV towards more positive values when the inhibitors are present in the system is an indication of corrosion inhibition. The zinc OCV-time profile in a corrosive medium was run for 3600 s, which was sufficient to make the corrosion system reach equilibrium [292]. As can be observed from Figure 6.17, the time profile of the bare metal has a more negative potential than the inhibited metal profile, which shifted towards

© University of Venda

a less negative potential. This suggests that the most favoured process could be anodic protection. The shift towards a more negative potential direction for the inhibitor free-solution is an indication of the corrosion product's desorption on the metal surface [294]. No stable trend is observed in the OCV variation with time for the electrodes without or with varying concentrations of the inhibitor except for 600 ppm concentration, indicating that the extract functions as a mixed type of inhibitor [293]. In the inhibitor free-solution, the OCV potential moved towards the negative potential direction, indicating the corrosion product's desorption on the metal surface [294].

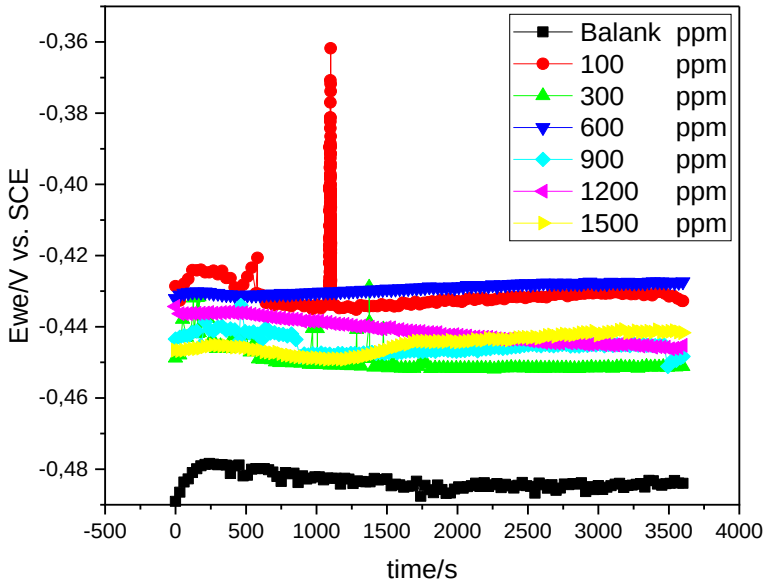


Figure 6. 17: Open circuit voltage for zinc in 1.0 M HCl solution and UV-radiated *H. kraussii.*

6.5.2.2. Electrochemical impedance spectroscopy (EIS)

The Nyquist plot obtained from electrochemical impedance spectroscopy (EIS) for zinc in 1.0 M HCl solution at 303 K is displayed in Figure 6.18. The depressed semi-circle in the Nyquist plots illustrates surface inhomogeneity of structural or interfacial origin, like those found in the adsorption process, while the single semi-circle indicates that capacitance was primarily responsible for controlling the corrosion process [350]. The diameter of the semi-circles represents the charge transfer resistance values, indicating the decrease in the rate of corrosion. The Nyquist plot with and without the extract inhibitor is of the same shape, suggesting that the corrosion mechanism was not tempered by introducing the extract inhibitor in the corrosive electrolyte.

© University of Venda

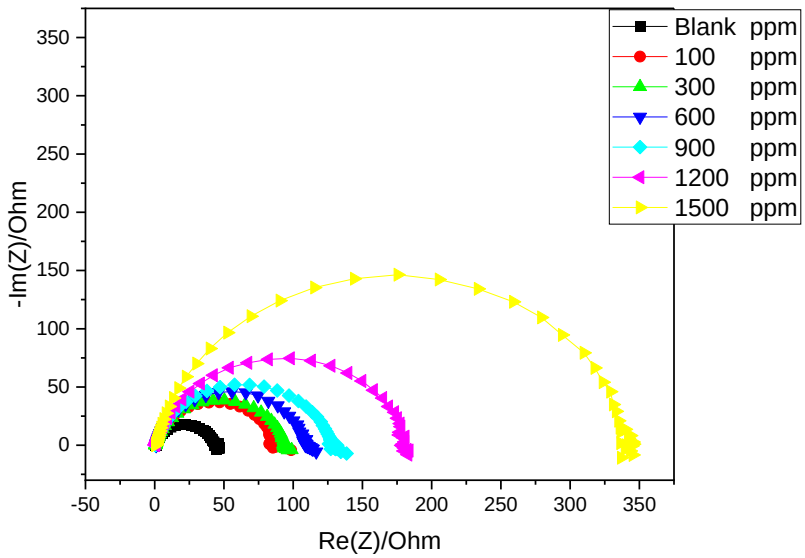


Figure 6. 18: Nyquist plot of zinc metal in 1.0 M HCl solution with and without various concentrations of UV-radiated *H. kraussii* inhibitor compounds.

Figure 6.19 shows the bode plots. The impedance spectra exhibit a single capacitive loop, which corresponds to a single time constant in the Bode plots, both in the absence and presence of the extract inhibitor. The phase angle increases in the negative direction with increasing extract inhibitor concentration, suggesting that the extract inhibitor will be more effective at higher concentrations [351]. The high-frequency time constant indicates the presence of the inhibitor coating in contact with the electrolyte. In contrast, the intermediate and low-frequency time constants are connected to the corrosion process at the surface of the metal's unprotected locations. The phase angle shows a wide single peak, indicating a one-time constant both with and without the extract inhibitor present [352]. The extraction of the impedance parameters was performed by fitting the equivalent circuit represented in Figure 5.16 to the Nyquist plot, and the parameters obtained are tabulated in Table 6.8.

© University of Venda

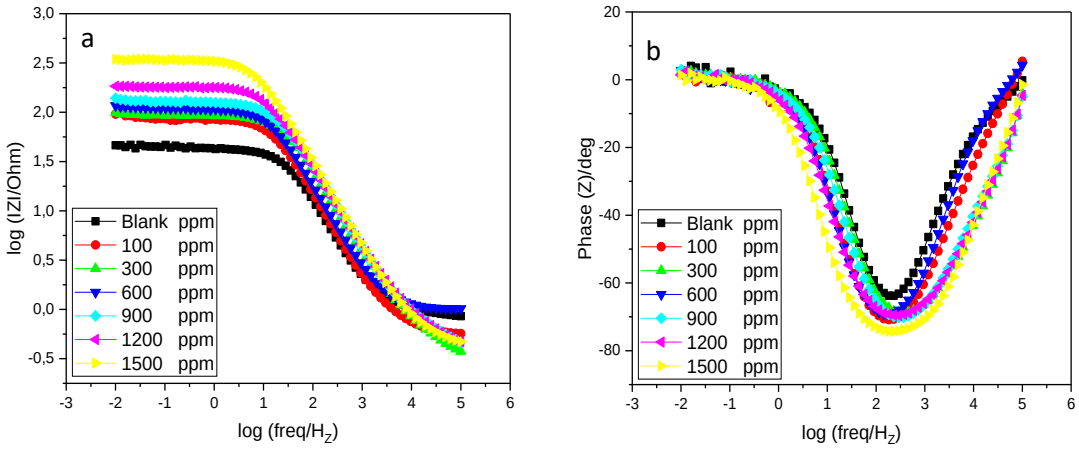


Figure 6. 19: Bode impedance magnitude plot (a) and Bode phase angle plot (b) of zinc metal in 1.0 M HCl solution with and without various concentrations of UV-radiated *H. kraussii* extract inhibitor.

Table 6. 8: EIS parameters like the solution resistance (R_s), resistance of charge transfer (R_{ct}), constant phase element (CPE), constant phase element constant (n2), double layer capacitance (C_{dl}) and percentage inhibition efficiency ($\%IE_{EIS}$), using UV-radiated *H. kraussii* in 1.0 M HCl in zinc metal.

Inhibitor	**Metal**	**Conc. (ppm)**	R_s **(Ωcm^2)**	**CPE (F.s$^{(a-1)}$ x10^{-3}**	**n2**	R_{ct} **(Ωcm^2)**	**C$_{dl}$ (μF/cm^{-2})**	**τ (s)**	**%IE$_{EIS}$**
UV-radiated *H. kraussii* extract	Zinc	00	0.9131	0.2794	0.8645	43.53	210.3134	0.0092	
		100	0.6004	0.2226	0.8768	87.46	49.8319	0.0044	50.229
		300	0.4032	0.1694	0.8376	95.26	43.1793	0.0041	54.304
		600	1.024	0.1788	0.8838	109.4	28.0217	0.0031	60.210
		900	0.5101	0.1477	0.8421	130.1	17.7873	0.0023	66.541
		1200	0.4935	0.1578	0.8318	184.0	11.5847	0.0021	76.342
		1500	0.4947	0.1099	0.8719	345.3	3.1478	0.0011	87.383

From Table 6.8 examination, the values of the R_{ct} were found to increase with increasing extract's inhibitor concentrations, reaching a maximum of 345.3 Ωcm^2, which yielded the maximum inhibition efficiency of 87.383 %. The increase of R_{ct} with increasing extract inhibitor concentration causes an increase in the calculated double-layer capacitance (C_{dl}) values. The reduction in C_{dl} implies that the inhibitor molecule functions through adsorption at the metal/solution interface, which may lead to an increase in the electrical double layer's

© University of Venda

thickness or a decrease in the local dielectric constant [353]. The time constant values are found to be decreasing with increasing inhibitor concentration for zinc metal. This observation implies that the adsorption time of the UV-radiated *H. kraussii* extract on the zinc metal is low, which suggests a fast adsorption process [282]. The time constant is also found to have a direct proportional relationship with the double-layer capacitance. The constant phase element exponent (n2) values describe the corrosion process on the surface of the metal. Its values range from -1 to 1, with -1 representing the inductance, 1 representing the capacitor [351], and 0 representing the resistor. The table shows that the n values do not show any particular trend and are approximately approaching 1, suggesting that the interface is capacitive. The high values of n indicate that the extract enhanced the homogeneity of the zinc metal surface by forming a film on it. Although the CPE values do not properly trend, they typically decrease as the extract concentration rises. This shows that the extract is adsorbed to the surface of the metal and prevents the development of hostile and corrosion cells. The high value of n proves that the extract formed a film on the surface of zinc metal and improved its homogeneity. The CPE values do not form a proper trend, but generally, they are found to be decreasing with an increase in the extract concentration. This is an indication of the extract adsorption on the metal surface hindering the formation of the hostile and corrosion cells.

6.5.2.3. Potentiodynamic polarization (PDP)

The Tafel plot for UV-radiated *H. kraussii* extract is displayed in Figure 6.20. The figure shows that both the cathodic and anodic branches are represented and shifted to the lower corrosion current density, especially on the cathodic branch. The shift into the lower corrosion current density symbolises that the inhibitor was adsorbed onto the surface of the metal. The electrochemical parameters like corrosion current density (i_{corr}), corrosion potential (E_{corr}), and anodic and cathodic Tafel slopes (β_a and β_c) were acquired through the cathodic and anodic branches junction extrapolation method, and they are tabulated in Table 6.9 together with the calculated potentiodynamic polarization percentage inhibition efficiency ($\%IE_{PDP}$).

© University of Venda

University of Venda
Creating Future Leaders

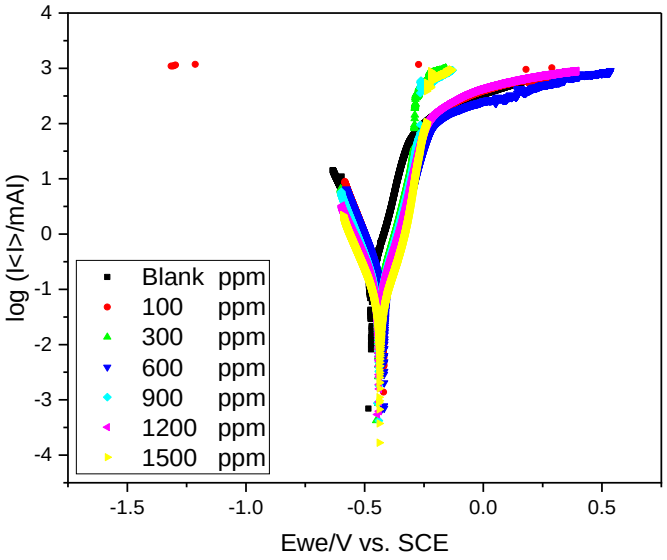


Figure 6. 20: Tafel plots for zinc in 1.0 M HCl solution with and without various UV-radiated *H. kraussii* inhibitor compound concentrations.

Table 6. 9: PDP parameters, including anodic and cathodic Tafel slopes (βa and β_c), polarization resistance (R_P), corrosion potential (E_{corr}), and corrosion current density (i_{corr}), in 1.0 M HCl using various UV-radiated *H. kraussii* inhibitor concentrations.

Inhibitor	**Inhibitor Conc. (ppm)**	**-E_{corr} (mV) With Ag/AgCl**	**i_{corr} (mA.cm^{-2})**	**R_P (10^{-1}) (Ω)**	**β_a (mV.dec^{-1})**	**β_c (mV.dec^{-1})**	**% IE_{PDP}**
Blank	0.00	-471.581	323.795	66.2	76.4	94.9	00
UV-radiated *H. kraussii* extract	100	-418.886	132.531	144	65.9	90.3	59.069
	300	-441.886	93.280	133	65.8	76.6	71.192
	600	-417.711	92.600	150	70.0	92.6	71.402
	900	-440.241	68.996	177	65.8	74.1	78.691
	1200	-438.695	68.264	193	72.5	80.6	78.918
	1500	-438.031	32.620	375	74.6	69.9	89.926

From the literature, it is largely said that if the shifting of the E_{corr} values in the absence and presence of the inhibitor is less than -85 mV, the inhibitor is categorised as a mixed type [354], and if the shift is greater than that, the inhibitor is either categorised as an anodic or cathodic inhibitor. Based on the results obtained in Table 6.8, the E_{corr} difference between the inhibitor and the blank system is less than -85 mV, indicating that the inhibitor works as a mixed type [217, 355]. In the presence of the inhibitor, the E_{corr} values are found to have shifted more

© University of Venda

towards the positive potential than the blank system. The corrosion current densities were reduced upon introducing the inhibitor in the corrosive solution, which indicates the inhibitor's mixed-type behaviour. From the table, it is observed that upon the increment of the extract inhibitor concentration, the inhibition efficiency was found to be increasing, while the corrosion current density was decreasing due to the adsorption of the extract inhibitor molecules on the zinc metal surface [350]. The values of β_a and β_c showed variation with respect to that of the blank system upon introducing the extract, indicating that the extract managed to suppress both the cathodic and anodic reactions. With that said, the UV-radiated *H. kraussii* extract acts as a mixed inhibitor [356]. The values of β_a and β_c showed no significant change, also confirming the suggestion that the investigated extract inhibitor is a mixed-type [357].

6.5.3. Aluminium metal

6.5.3.1. Open circuit voltage (OCV)

The OCV for aluminium metal performed for 3600 s in 1.0 M HCl solution with and without extract inhibitor at 303 K is presented in Figure 6.21. When it comes to 1.0 M HCl containing UV-radiated *H. kraussii* inhibitor, the OCV potentials for two inhibitor concentrations, 300 and 100 ppm, shifted towards more negative potentials with respect to the uncoated solution (blank). The remaining concentrations of UV-radiated *H. kraussii* extract (600, 900, 1200 and 1500 ppm) shifted towards the more positive potentials, indicating the adsorption of the UV-radiated *H. kraussii* on the metal surface and its impact on the anodic corrosion reaction [358]. The shift towards lower potentials in the smaller concentrations of the UV-radiated *H. Kraussii* is an indication that the aluminium metal was strongly attacked by corrosion, as confirmed by the low inhibition efficiency for the first two concentrations in Table 6.10. The oscillations in the OCV plot are an indication of the corrosion product layer formation and the metal surface destruction [303]. It can be observed from Figure 6.21 that 200 s was sufficient time to get a steady-state potential.

© University of Venda

University of Venda
Creating Future Leaders

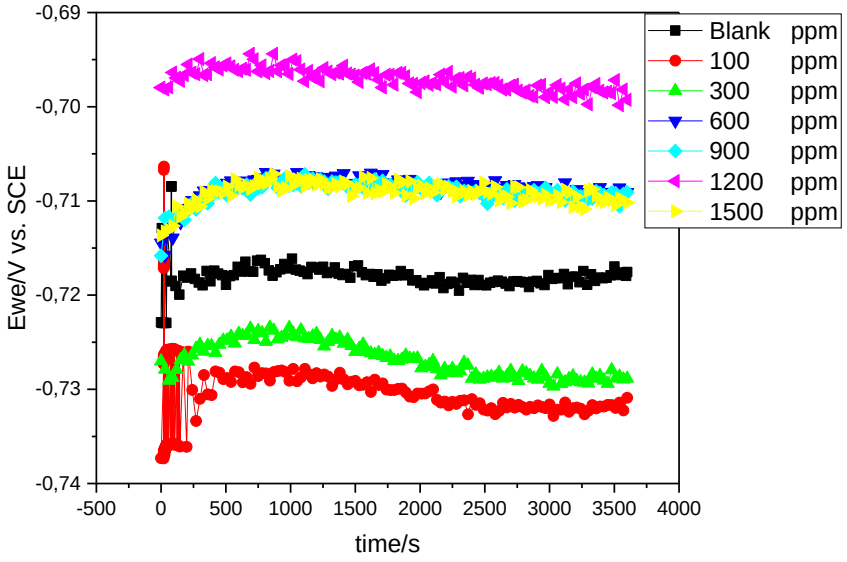


Figure 6. 21: Open circuit voltage for aluminium in 1.0 M HCl solution and UV-radiated *H. kraussii* extract.

6.5.3.2. Electrochemical impedance spectroscopy (EIS)

Figure 6.22 shows the Nyquist plot of aluminium metal in 1.0 M HCl medium with and without various UV-radiated *H. kraussii* extract concentrations at 303 K. EIS is known as a non-destructive technique that can be utilised to find the corrosion mechanism at the solution or metal interface, with and without the inhibitor. Additionally, it is widely recognized that the formation of the inhibitor layer on the metal surface results in an augmentation of the impedance of the corrosion system, consequently leading to an elevation in the resistance to charge transfer. The increase in the charge transfer resistance in relation to the blank system leads to an increase in the inhibition system [303]. The Nyquist plot for the blank and the inhibited solution formed a depressed circle. The circles increase in diameter with an increase in the concentration of the extract inhibitor with respect to the uninhibited system, which suggests that the inhibitor was adsorbed to the surface of the metal, forming a protective film [359]. The circles are of the same shape both with and without the inhibitor, indicating that the addition of the inhibitor did not change the corrosion mechanism [305].

© University of Venda

University of Venda
Creating Future Leaders

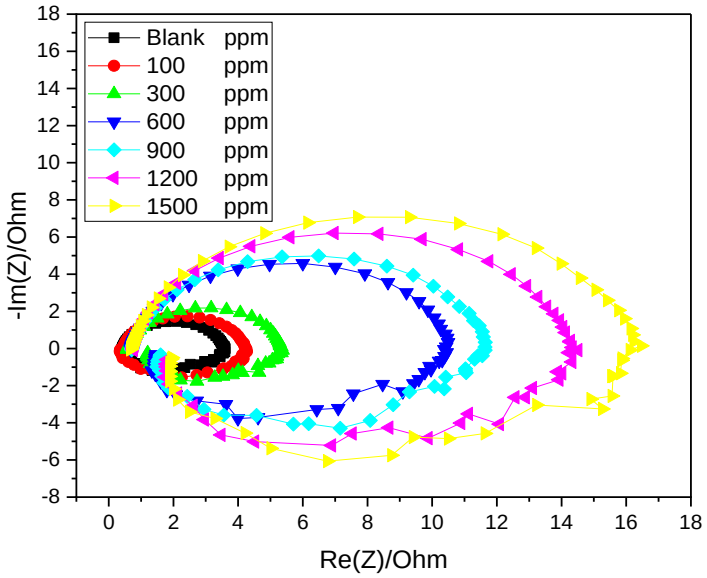


Figure 6. 22: Nyquist plot of aluminium metal in 1.0 M HCl solution with and without the presence of various concentrations of UV-radiated *H. kraussii* inhibitor compounds.

Figure 6.23 depicts the phase angle and the Bode magnitude plots with and without the presence of the maximum concentration of the extract inhibitor. The lower angle observed for 300 ppm at around -1.3 Hz is an indication of the inhomogeneous surface compared to the blank system [360]. The phase angles exhibit a positive correlation with the inhibitor concentration in the presence of the inhibitor extracts, indicating strong adsorption of the extract inhibitor onto the metal surface [361]. The maximum phase angle was observed for 1500 ppm to be around -62 ℃. The extraction of the impedance parameters was performed by fitting the equivalent circuit represented in Figure 5.26 to the Nyquist plot, and the parameters obtained are tabulated in Table 6.10.

© University of Venda

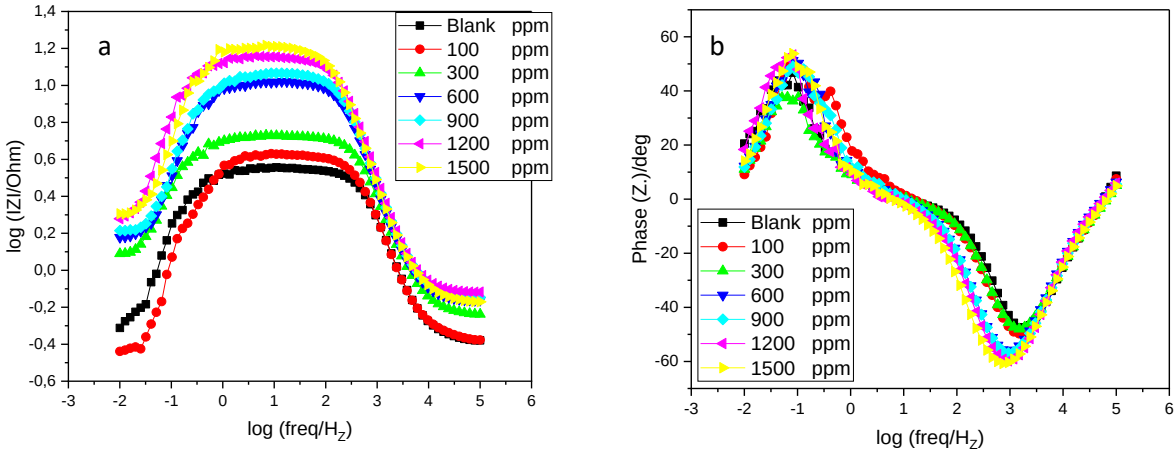


Figure 6. 23: Bode impedance magnitude plot (a) and Bode phase angle plot (b) of aluminium metal in 1.0 M HCl solution with and without various concentrations of UV-radiated *H. kraussii* extract inhibitor.

From the inspection of Table 6.10, it can be noted that the R_{ct} values increase with the increase in the concentration of the extract inhibitor. This observation suggests that the inhibitor was adsorbed on the surface of the metal, thereby protecting the metal from corrosion. The increase in the R_{ct} yielded an increase in the percentage inhibition efficiency. The optimum %IE was found to be 80.054 % for the highest concentration of 1500 ppm. From the table, the double-layer capacitance (C_{dl}) decreases with an increase in the extract inhibitor concentration as opposed to the trend in the R_{ct} values. The decrease in C_{dl} suggests an increase in the double-layer thickness and a decrease in the local dielectric constant [362]. The C_{dl} dropped to 2655.8652 µF/cm^{-2} in the highest concentration from 36838.1142 µF/cm^{-2} in the blank solution. The values of the constant phase element exponent (n) describe the corrosion process on the metal surface. Its values range from -1 to 1, where -1 represents the inductance, 1 represents the capacitor, and 0 represents the resistor [311, 359]. From the table, it can be observed that the values of n are approximately approaching 1, which suggests that the interface is of a capacitive nature. The high value of n proves that the extract formed a film on the surface of aluminium metal and improved its homogeneity. The CPE values do not form a proper trend, but generally, they are found to decrease with an increase in the extract concentration, indicating adsorption of the extract on the metal surface hindering the formation of the hostile and corrosion cells. The time constant values are found to be decreasing with increasing inhibitor concentration for aluminium metal. This observation implies that the adsorption time of the UV-radiated *H. kraussii* extract on the aluminium metal is low, which suggests a fast

© University of Venda

adsorption process [282]. The time constant is also found to have a direct proportional relationship with the double-layer capacitance.

Table 6. 10: EIS parameters like the solution resistance (R_s), resistance of charge transfer (R_{ct}), constant phase element (CPE), constant phase element constant (n1), double layer capacitance (C_{dl}) and percentage inhibition efficiency ($\%IE_{EIS}$), using UV-radiated *H. kraussii* in 1.0 M HCl in aluminium metal.

Inhibitor	**Metal**	**Conc. (ppm)**	**R_s (Ωcm^2)**	**CPE ($F.s^{(a-1)}$)**	**n1**	**R_{ct} (Ωcm^2)**	**L3 (H)**	**R3 (Ωcm^2)**	**C_{dl} ($\mu F/cm^{-2}$)**	**τ (s)**	**$\%IE_{EIS}$**
UV-radiated *H. kraussii* extract	Aluminium	00	0.4339	$0.1063X10^{-3}$	0.9669	2.976	2.519	0.0512	36838.1142	0.1096	-
		100	0.4172	$79.71X10^{-6}$	1.0000	3.564	1.285	$54.83x10^{-18}$	25735.3607	0.0917	16.498
		300	0.5955	$0.1012X10^{-3}$	0.9453	4.566	4.971	0.6608	17090.1998	0.0780	33.823
		600	0.7022	$88.98X10^{-6}$	0.9553	9.362	5.215	0.7166	6667.0371	0.0624	68.212
		900	0.8303	$56.88X10^{-6}$	1.0000	9.906	5.376	$13.09x10^{-3}$	5936.5755	0.0588	69.958
		1200	0.7922	$53.21X10^{-6}$	1.0000	12.81	11.98	0.9705	2137.6493	0.0274	76.7681
		1500	0.6963	$98.11X10^{-6}$	0.9370	14.92	8.473	1.226	2655.8652	0.0396	80.054

6.5.3.3. Potentiodynamic polarization

The potentiodynamic curves were obtained through the application of a potential of 250 mV with regards to the corrosion potential of the electrochemical system for aluminium metal corrosion with and without various extract inhibitor concentrations and in the corrosive electrolyte of 1.0 M HCl at 303 K. The curve is displayed in Figure 6.24. Tafel plots are very helpful in categorising the inhibitors as cathodic, anodic or mixed inhibitors based on Tafel constants. It can be observed from the Tafel plots that the introduction of the inhibitor in the corrosive electrolyte managed to shift the anodic and cathodic Tafel curves towards lower corrosion current densities in relation to those of the blank system [296].

© University of Venda

This is an indication of the formation of the extract inhibitor film on the surface of the metal, preventing corrosion. Different electrochemical parameters such as the corrosion potential (R_P), corrosion current density(i_{corr}), and Tafel constants (β_a and β_c) were obtained through the extrapolation method, and the percentage inhibition efficiency (%IE_{PDP}) was calculated using the corrosion current density values and the results obtained are tabulated in Table 6.11.

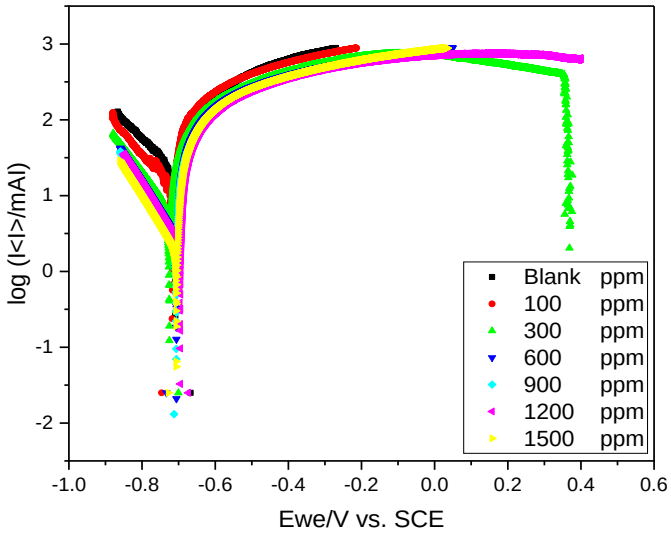


Figure 6. 24: Tafel plots for aluminium in 1.0 M HCl solution with and without various concentrations of UV-radiated *H. kraussii* extract inhibitor.

© University of Venda

Table 6. 11: PDP parameters, including anodic and cathodic Tafel slopes (βa and β_c), polarization resistance (R_P), corrosion potential (E_{corr}), and corrosion current density (i_{corr}), measured in 1.0 M HCl using various UV-radiated *H. kraussii* inhibitor concentrations.

Inhibitor	**Inhibitor Conc. (ppm)**	**-E_{corr} (mV) with Ag/AgCl**	**i_{corr} (mA.cm^{-2})**	**R_P (10^{-1}) (Ω)**	**β_a (mV.dec^{-1})**	**β_c (mV.dec^{-1})**	**% IE_{PDP}**
Blank	00	-709.347	23517.404	0.768	86.3	249.6	
UV-radiated *H. kraussii* extract	100	-716.631	19273.773	0.647	56.0	406.7	18.045
	300	-724.868	6629.255	1.17	34.3	151.2	71.811
	600	-706.892	2946.643	1.34	18.9	131.2	87.470
	900	-705.927	2583.881	1.47	15.9	132.0	89.013
	1200	-695.748	2371.490	1.54	18.1	130.3	89.916
	1500	-707.309	1927.672	1.59	15.7	129.9	91.803

Examination of the parameters in Table 6.11 reveals that the E_{corr} values did not show any stable trend but, in most cases, were found to be shifting cathodically in the presence of the inhibitor. From the literature, it is largely said that if the shifting of the E_{corr} values in the absence and presence of the inhibitor is less than -85 mV, the inhibitor is categorised as a mixed type, and if the shift is greater than that, the inhibitor is either categorised as a cathodic or anodic inhibitor. Based on the results obtained, the E_{corr} difference between the inhibitor and the blank system is less than -85 mV, suggesting that the inhibitor works as a mixed type [363]. From the table, it is clear that the values of the Tafel constants were affected by the presence of the inhibitor in the corrosive electrolyte, which is an indication of the modification of the mechanism of anodic aluminium dissolution and cathodic hydrogen evolution [206, 312]. This insight also complements the suggestion that the inhibitor was acting as a mixed-type inhibitor, which adsorbs on the active sites of the aluminium surface. It is also observed that the i_{corr} values decreased with increasing inhibitor concentrations compared to the blank system [296]. This decrease yielded an increase in the %IE with regard to the blank system. This observation suggests the formation of the protective film in the aluminium metal surface. The highest %IE obtained at the highest concentration (1500 ppm) was 91.03%.

© University of Venda

6.6. Fourier Transform Infrared Spectroscopy (FTIR)

6.6.1. Mild steel

Figure 6.25 displays the four spectra of the four samples analysed by the FTIR instrument. The blue line spectrum was plotted alone to show a clear variation since the mixed spectra did not show clear variation due to the different spectrum scales on the x-axis. It can be observed that the spectra show the variation in the adsorption bands, which can be said to be one of the indications that adsorption on the metal surface took place, especially looking at the black and green spectrum. From Table 6.12, the mild steel metal subjected to UV-radiated *H. kraussii* extract was compared for its functional group due to adsorption with the UV-radiated *H. kraussii* extract to find which functional groups were attached on the metal surface after gravimetric analysis. It can be observed that O-H carboxylic acid, C-C alkane, C-H aromatic were retained after the gravimetric analysis, which corresponds exactly to those observed in the Pure extract. However, it can be observed that new functional groups were formed that were not present in the pure extract, such as C-H alkane and aldehyde. The carboxylic acid at around 2400-3600 cm^{-1} and the C-H aromatic at around 600-900 cm^{-1} are known to be some of the functional groups that enhance the inhibition efficiency.

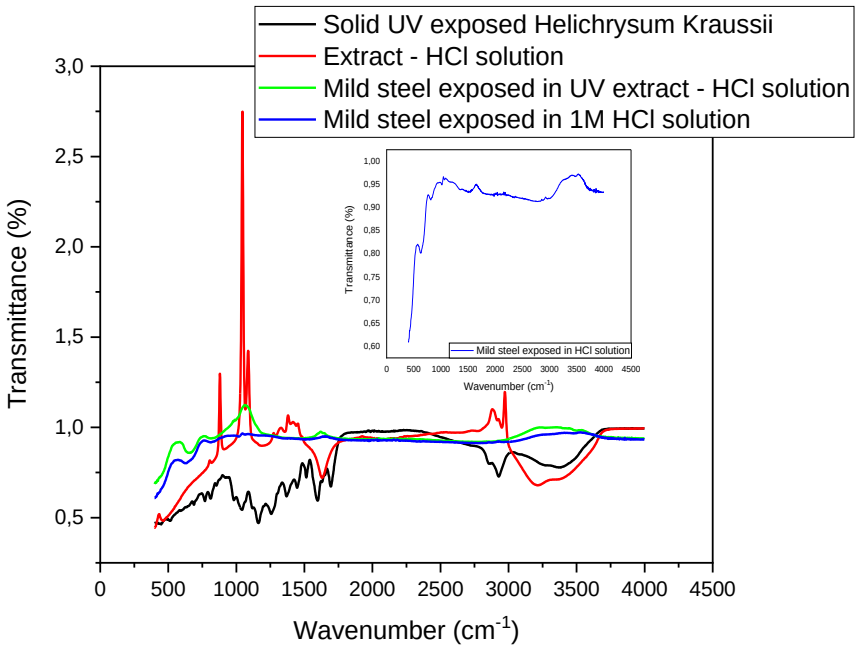


Figure 6. 25: FTIR spectra for solid UV-radiated *H. kraussii* plant extract (Black), 1500 ppm UV exposed Helichrysum kraussii plant extract – 1.0 M HCl solution (Red), the layer formed on mild steel metal exposed in 1500 ppm UV-radiated *H. kraussii* plant extract – 1.0 M HCl

© University of Venda

solution (Green) and corrosion products formed on mild steel metal exposed in 1.0 M HCl solution (black).

Table 6. 12: Possible functional groups present in solid UV-radiated *H. kraussii* plant extract, corrosion products formed on mild steel metal exposed in 1.0 M HCl solution, 1500 ppm UV-radiated *H. kraussii* plant extract – 1.0 M HCl solution and layer formed on mild steel metal exposed in 1500 ppm UV-radiated *H. kraussii* plant extract – 1.0 M HCl solution.

	Functional Groups			
Bands position (cm^{-1})	**Solid UV-radiated *kraussii* extract**	**Mild steel metal exposed in HCl blank solution**	**UV-radiated *H. kraussii* - HCl solution**	**Mild steel metal exposed in UV-radiated *H. kraussii* - HCl solution**
2400 – 3600	O-H Carboxylic acid		O-H Carboxylic acid	O-H Carboxylic acid
3300 – 3500	O-H alcohol			
3200 – 3400	N-H amine N-H amide		N-H amine N-H amide	
3260 – 3390	Sp C-H (C≡C-H)			
2850 – 2960			Sp^3 C-H (C-C-H)	Sp^3 C-H (C-C-H) C-H aldehyde
2700 – 2900				
2200 – 2270				
2100 – 2250			C≡C alkyne	
1680 – 1720	C=O ketone C=O aldehyde			
1600 – 1650		C=C alkene	C=C alkene	
1500 – 1600				
1500 – 1570	NO_2 Nitro C=C aromatic	NO_2 Nitro C=C aromatic		
1450 – 1470		C-H alkane		C-H alkane
1180 – 1360			amine C-N	
1200 – 1250				
1000 – 1200	Sp^3 C-O	Sp^3 C-O	Sp^3 C-O	
900 – 1000	C-H aromatic		C-H aromatic	
600 – 900	C-Cl chloride C-C alkane C-H aromatic			C-C alkane C-H aromatic

© University of Venda

6.6.2. Zinc metal

Figure 6.26 shows the FTIR spectra of the solid UV-radiated *H. kraussii* extract, pure metal, UV-radiated *H. kraussii* extract – HCl solution and the zinc metal subjected to UV-radiated *H. kraussii* extract – HCl solution. It can be observed that there was a variation in the peaks, especially looking at the pure extract and that of the metal exposed to the extract–HCl solution, which is a good sign that adsorption did take place. Table 6.13 shows the functional groups associated with the adsorption peaks. Looking at the first and the last column in the table, it can be observed that functional groups such as O-H carboxylic acid and Sp^3 C-O were peaked, indicating that they are responsible for causing corrosion inhibition, thereby reducing the metal's corrosion rate.

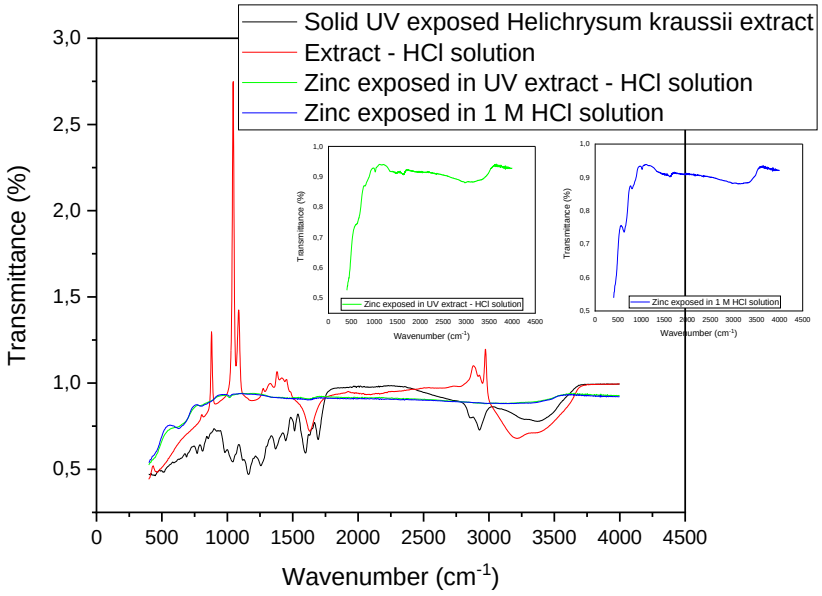


Figure 6. 26: FTIR spectra for solid UV-radiated *H. kraussii* plant extract (Black), 1500 ppm UV-radiated *H. kraussii* plant extract – 1.0 M HCl solution (Red), the layer formed on zinc metal exposed in 1500 ppm UV-radiated *H. kraussii* plant extract – 1.0 M HCl solution (Green) and corrosion products formed on zinc metal exposed in 1.0 M HCl solution (black).

© University of Venda

Table 6. 13: Possible functional groups present in solid UV-radiated *H. kraussii* plant extract, corrosion products formed on zinc metal exposed in 1.0 M HCl solution, 1500 ppm UV-radiated *H. kraussii* plant extract – 1.0 M HCl solution and layer formed on zinc metal exposed in 1500 ppm UV-radiated *H. kraussii* plant extract – 1.0 M HCl solution.

	Functional Groups			
Bands position (cm^{-1})	**Solid UV-radiated *H. kraussii* extract**	**Zinc metal exposed in HCl blank solution**	**UV-radiated *H. kraussii* - HCl solution**	**Zinc metal exposed in UV-radiated *H. kraussii* - HCl solution**
2400 – 3600	O-H Carboxylic acid		O-H Carboxylic acid	O-H Carboxylic acid
3300 – 3500	O-H alcohol			
3200 – 3400	N-H amine N-H amide		N-H amine N-H amide	
3260 – 3390	Sp C-H (C≡C-H)			
2850 – 2960			Sp^3 C-H (C-C-H)	
2700 – 2900	Sp^3 C-O			
2200 – 2270	Sp^3 C-O			
2100 – 2250			C≡C alkyne	
1680 – 1720	C=O ketone C=O aldehyde			
1600 – 1650		C=C alkene	C=C alkene	C=C alkane
1500 – 1600				
1500 – 1570	NO_2 Nitro C=C aromatic			
1450 – 1470				C-H alkane
1180 – 1360			amine C-N	
1200 – 1250				
1000 – 1200	Sp^3 C-O	Sp^3 C-O	Sp^3 C-O	Sp^3 C-O
900 – 1000	C-H aromatic		C-H aromatic	
600 – 900	C-Cl chloride C-C alkane C-H aromatic	C-Cl chloride C-H aromatic		

© University of Venda

6.6.3. Aluminium metal

Figure 6.27 shows the spectra for the four samples displayed in Table 6.14, and it can be observed that there was a variation in all the spectra. In the presence of aluminium metal, a number of functional groups present in the pure extract were also found on the surface of the metal exposed to the extract and HCl solution, which shows that the extract managed to adsorb very well on the metal surface. These functional groups are O-H carboxylic acid, N-H amine and amide, C=O ketone and aldehyde, C=C alkene, C=C aromatic, and NO_2 Nitro. These groups are very well known to cause corrosion inhibition.

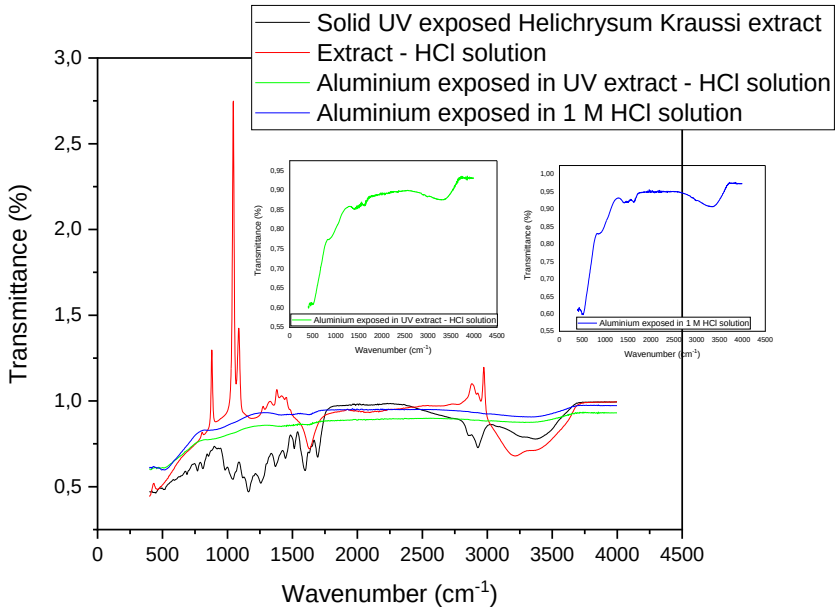


Figure 6. 27: FTIR spectra for solid UV-radiated *H. kraussii* plant extract (Black), 1500 ppm UV-radiated *H. kraussii* plant extract – 1.0 M HCl solution (Red), the layer formed on aluminium metal exposed in 1500 ppm UV-radiated *H. kraussii* plant extract – 1.0 M HCl solution (Green) and corrosion products formed on aluminium metal exposed in 1.0 M HCl solution (black).

© University of Venda

Table 6. 14: Possible functional groups present in solid UV-radiated H. *kraussii* plant extract, corrosion products formed on aluminium metal exposed in 1.0 M HCl solution, 1500 ppm UV-radiated H. *kraussii* plant extract – 1.0 M HCl solution and layer formed on aluminium metal exposed in 1500 ppm UV-radiated *H. kraussii* plant extract – 1.0 M HCl solution.

	Functional Groups			
Bands position (cm^{-1})	**Solid UV-radiated *H. kraussii***	**Aluminium metal exposed in HCl blank solution**	**UV-radiated *H. kraussii* - HCl solution**	**Aluminium metal exposed in UV-radiated *H. kraussii* - HCl solution**
2400 – 3600	O-H Carboxylic acid		O-H Carboxylic acid	O-H Carboxylic acid
3300 – 3500	O-H alcohol	O-H alcohol		
3200 – 3400	N-H amine N-H amide		N-H amine N-H amide	N-H amine N-H amide
3260 – 3390	Sp C-H (C≡C-H)	Sp C-H (C≡C-H)		
2850 – 2960			Sp^3 C-H (C-C-H)	
2700 – 2900				
2200 – 2270				
2100 – 2250			C≡C alkyne	
1680 – 1720	C=O ketone C=O aldehyde			C=O ketone C=O aldehyde
1600 – 1650		C=C alkene	C=C alkene	C=C alkene
1500 – 1600				
1500 – 1570	NO_2 Nitro C=C aromatic			NO_2 Nitro C=C aromatic
1450 – 1470				C-H alkane
1180 – 1360			amine C-N	
1200 – 1250				
1000 – 1200	Sp^3 C-O		Sp^3 C-O	
900 – 1000	C-H aromatic		C-H aromatic	
600 – 900	C-Cl chloride C-C alkane C-H aromatic			

© University of Venda

CHAPTER 7

Non-radiated *H. kraussii* extract in sulphuric acid

© University of Venda

7. Introduction

In this chapter, the results obtained for *H. kraussii* plant extract as a corrosion inhibitor for mild steel and zinc metal in sulphuric acid using gravimetric analysis, adsorption isotherm, the effect of temperature, electrochemistry, and Fourier transform infrared spectroscopy are discussed.

7.1. Weight loss analysis

The weight loss method is utilized to monitor the corrosion of metal samples by keeping them in a specific environment for a given period, after which the metal sample is removed from that environment, and the change in mass before and after exposure is determined. It is also considered to be the most basic, precise, and accurate method for finding the corrosion rate of the metal [227]. The weight loss of mild steel and zinc metal for non-radiated *H. kraussii* extract in 1.0 M H_2SO_4 solution at four various temperatures is reported in Table 7.1.

Table 7. 1: Gravimetric weight loss analysis in the presence of 1.0 M H_2SO_4 acid and *H. kraussii* extract for mild steel and zinc metal.

Inhibitor	**Metal**	**Concentration (ppm)**	**Weight loss (g)**			
			30° C	40° C	50° C	60° C
***H. kraussii* extract**	Mild steel	0.00	0.4894	0.8193	1.3652	2.0949
		100	0.3654	0.6722	1.1544	1.8981
		300	0.2766	0.5347	1.0275	1.7110
		600	0.1700	0.3864	0.8532	1.4537
		900	0.0583	0.2430	0.6846	1.3337
		1200	0.0283	0.2106	0.6347	1.2582
		1500	0.0163	0.1812	0.4977	1.0376
	Zinc	0.00	0.5213	0.8274	1.3785	2.1379
		100	0.2554	0.4664	0.8933	1.6619
		300	0.1835	0.3830	0.6155	1.2035
		600	0.1389	0.2831	0.5419	0.9826
		900	0.1235	0.1587	0.4321	0.8225
		1200	0.1120	0.1555	0.3820	0.7373
		1500	0.1105	0.1333	0.2997	0.6124

© University of Venda

Table 7.1 shows the weight loss of mild steel and zinc metals in the presence of 1.0 M H_2SO_4. It can be seen that the weight loss of the two metals decreased with increasing inhibitor concentration [364, 365]. However, as the temperature increased, the weight loss of the metals was found to be increasing. The 0.00 ppm shows the weight loss of the metals in the absence of the inhibitors at the four different studied temperatures. Mild steel metal was the worst affected in the presence of 1.0 M H_2SO_4 since its weight loss is the highest at all temperatures and concentrations compared to those of zinc metals. The reduction in the weight loss of the two metals with an increase in the inhibitor concentration is solid evidence that the presence of the inhibitors in the aggressive acid solution managed to reduce the rate at which the metal corrodes. The increase in weight loss with an increase in the temperature shows that the inhibitor utilized is very effective at lower temperatures.

7.2. Corrosion rate and inhibition efficiency

The corrosion rate, surface coverage and inhibition efficiency are calculated to study the corrosion rate of mild steel and zinc metals in the presence of 1.0 M H_2SO_4. The calculations were done for four various temperatures and six concentrations of the extract and the blank solutions. These parameters are tabulated in Table 7.2.

Table 7. 2: The corrosion parameters for mild steel and zinc in the aqueous solution of 1.0 M H_2SO_4 with and without various concentrations of *H. kraussii* extract from weight loss measurements at four various temperatures (30 – 60° C).

Inhibitor		**Temperature (° C)**	**Inhibitor Concentration (ppm)**	**Corrosion rate ($g.cm^{-2}.h^{-1}$)**	**Inhibition Efficiency (%)**	**Surface coverage (θ)**
		30	0.00	0.005094		
			100	0.003803	25.344	0.25344
			300	0.002879	43.483	0.43483
			600	0.001770	65.253	0.65253
			900	0.000607	88.084	0.88084
			1200	0.000295	94.209	0.94209
			1500	0.000170	96.663	0.96663
		40	0.00	0.008527		
			100	0.006996	17.955	0.17955
			300	0.005565	34.737	0.34737

© University of Venda

			600	0.004022	52.832	0.53832
			900	0.002529	70.341	0.70341
			1200	0.002192	74.293	0.74923
			1500	0.001886	77.882	0.77882
	Mild steel		0.00	0.014209		
			100	0.012015	15.455	0.15455
		50	300	0.010694	24.738	0.24738
			600	0.008880	37.504	0.37504
			900	0.007125	49.856	0.49856
			1200	0.006606	53.508	0.53508
			1500	0.005180	63.544	0.63455
			0.00	0.021303		
			100	0.019755	09.393	0.09393
***H. Kraussii* extract**		60	300	0.017807	18.328	0.18328
			600	0.015130	30.606	0.30606
			900	0.013881	36.334	0.36334
			1200	0.013095	39.939	0.39939
			1500	0.010799	50.470	0.50470
			0.00	0.005426		
			100	0.002658	51.014	0.51014
		30	300	0.001910	64.799	0.64799
			600	0.001446	73.351	0.73351
			900	0.001285	76.318	0.76318
			1200	0.001166	78.511	0.78511
			1500	0.001150	78.806	0.78806
			0.00	0.008611		
			100	0.004854	43.630	0.43630
		40	300	0.003986	53.710	0.53710
			600	0.002946	65.788	0.65788
			900	0.001652	80.815	0.80815
			1200	0.001618	81.210	0.81210
			1500	0.008550	83.893	0.83893
	Zinc					
			0.00	0.014347		
			100	0.009297	35.199	0.35199

© University of Venda

		50	300	0.006406	55.350	0.55350
			600	0.005640	60.689	0.60689
			900	0.004497	68.655	0.68655
			1200	0.003976	72.287	0.72287
			1500	0.002391	78.260	0.78260
		60	0.00	0.022251		
			100	0.017296	22.269	0.22269
			300	0.012526	43.706	0.43706
			600	0.010227	54.038	0.54038
			900	0.008560	61.530	0.61530
			1200	0.007674	65.512	0.65512
			1500	0.006374	71.354	0.71354

From Table 7.2, it can be observed that the rate of corrosion of the metal was found to decrease with increasing inhibitor concentration [364-366]. This observation suggests that the increase in the inhibitor molecules in the corrosive solution managed to hinder the corrosion process. The decrease in the extract inhibitor concentration resulted in an increase in the surface coverage. It can be observed that the %IE rises with rising extract inhibitor concentration and decreases with rising temperature of the environment [303]. This increase in %IE is because of the number of inhibitor molecules available for adsorption as the inhibitor concentration increases to form a protective film over the metal surface active sites [367]. The highest inhibition was obtained at the minimum studied temperature of 30 ˚C and the highest inhibitor concentration equivalating to 96.663 and 78.806 % for mild steel and zinc metals, respectively. These findings suggest that the inhibitor extract functions optimally at lower temperatures compared to high temperatures. The surface coverage values give the extent to which the inhibitor managed to cover the metal surface, thereby causing corrosion inhibition. The surface coverage values are observed to rise with rising inhibitor concentration [368]. Values amounting to 1 suggest that the inhibitor managed to cover the whole surface of the metals. From the table observation, it can be noted that at high concentrations, the surface coverage values are close to 1, which explains the high inhibition obtained at such concentrations.

The variation of the %IE of the two studied metals in 1.0 M H_2SO_4 is graphically presented in Figures 7.1 and 7.2. From the figures, it's evident the %IE increases with increasing inhibitor concentration.

© University of Venda

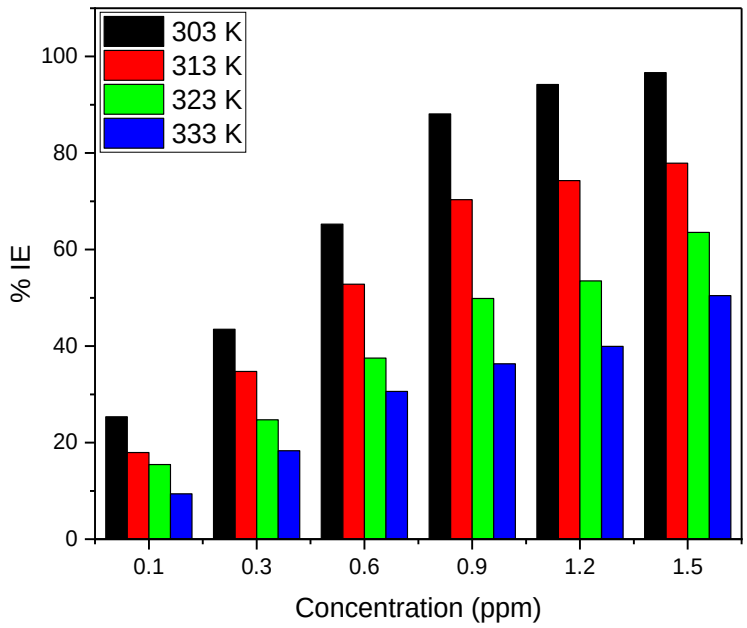


Figure 7. 1: The graph of inhibition efficiency using *H. kraussii* in 1.0 M H_2SO_4 for mild steel at various temperatures.

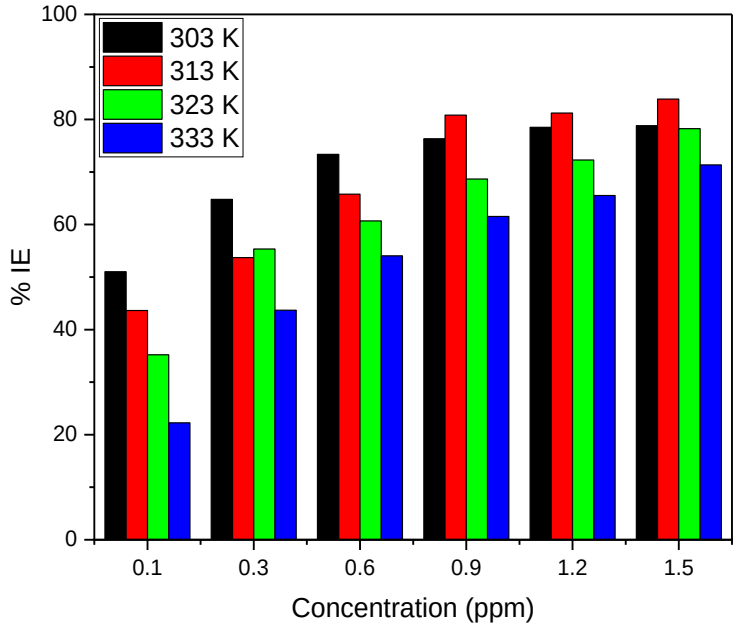


Figure 7. 2: The graph of inhibition efficiency using *H. kraussii* in 1.0 M H_2SO_4 for zinc at various temperatures.

© University of Venda

7.3. Adsorption isotherm

Adsorption isotherms are helpful in describing the interaction of the metal sample and the inhibitor [369]. It is also used to obtain information about the equilibrium between the inhibitor adsorbed and present in the bulk solution. The best isotherm should graphically result in a straight line, with the regression coefficient value equal to unity [227]. The Langmuir adsorption isotherm plots are displayed in Figures 7.3 and 7.4. The adsorption parameters such as regression coefficient (r^2), slope, equilibrium constant (K_{ads}), and the change in Gibbs free energy ($-\Delta G^o_{ads}$) are tabulated in Table 7.3.

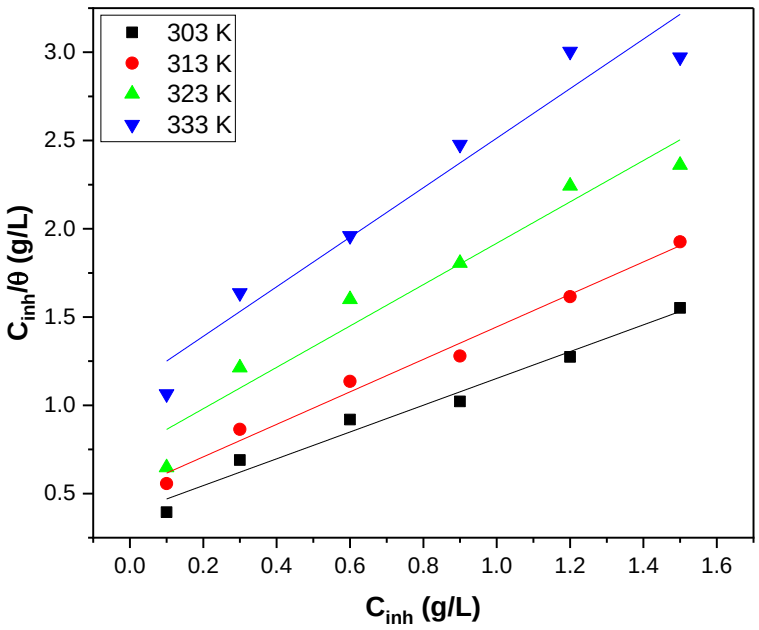


Figure 7. 3: Langmuir adsorption isotherm for the adsorption of *H. kraussii* extract on mild steel metal in 1.0 M H_2SO_4 at 30, 40, 50 and 60°C.

© University of Venda

University of Venda
Creating Future Leaders

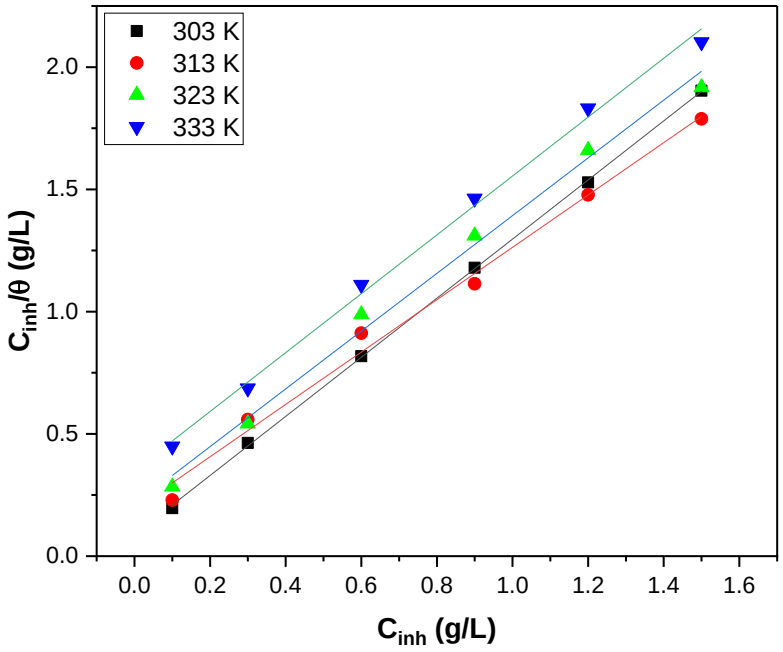


Figure 7. 4: Langmuir adsorption isotherm for the adsorption of *H. kraussii* extract on zinc metal in 1.0 M H_2SO_4 at 30, 40, 50 and 60°C.

Table 7. 3: Adsorption parameters from Langmuir Adsorption Isotherm plots for *H. kraussii* extract in 1.0 M H_2SO_4.

Inhibitor	**Metals**	**Temperature (° C)**	**r^2**	**Slope**	**K_{ads} (L/g)**	**$-\Delta G^o_{ads}$ (kJ.mol^{-1})**
***H. Kraussii* extract**	Mild steel	30	0.97096	0.75901	2542.52	37.158
		40	0.98274	0.92045	1909.09	37.637
		50	0.93304	1.17186	1340.05	37.889
		60	0.93297	1.40332	900.87	37.962
	Zinc	30	0.99973	1.2086	11352.03	40.926
		40	0.98882	1.07061	5198.05	40.244
		50	0.99128	0.04950	4723.22	41.272
		60	0.99544	1.20393	2851.28	41.152

The data obtained from the gravimetric analysis was tested into different isotherms like Frumkin, Temkin, Freundlich, Flory-Huggins and Langmuir in search of the best adsorption isotherm that fit the data perfectly [370]. Langmuir adsorption isotherm was the best isotherm, with r^2 values obtained from the linear diagrams very close to unity. It can then be said that the

© University of Venda

adsorption of *H. kraussii* extracts on mild steel and zinc metal surfaces proceeds through the Langmuir adsorption isotherm given by Equation 84 [337]. The equilibrium constant (K_{ads}) is correlated to the Gibbs free energy (ΔG^{o}_{ads}) using Equation 90. K_{ads} values are known to show the strength between the adsorbent and adsorbate. It is also known that large values of K_{ads} are an indication of effective adsorption and, hence stronger protection capacity [371]. The K_{ads} values were calculated from Figures 7.3 and 7.4 and found to range from 900.87 – 2542.52 L/g and 2851.28 – 11352.03 L/g for mild steel and zinc metals, respectively, supporting the strong adsorption of *H. kraussii* extract on the surface of the metals.

From Table 7.3, it can be observed that the values of ΔG^{o}_{ads} for both metals are negative, which suggests a spontaneous adsorption route [371]. From the literature, it is generally known that the ΔG^{o}_{ads} values around -20 kJ.mol^{-1} or less are an indication of physisorption kind of adsorption, while those around -40 kJ.mol^{-1} or more are consistent with chemisorption [206]. From the table, the values of ΔG^{o}_{ads} for mild steel metal are less than -40 kJ.mol^{-1} and greater than -20 kJ.mol$^{-1,}$ suggesting that the studied inhibitor adsorbs through a mixed-type of adsorption. However, for zinc metal, the values obtained are all greater than -40 kJ.mol$^{-1,}$ indicating chemical adsorption of the extract on the zinc metal surface. The values of ΔG^{o}_{ads} are also found to be decreasing (more negative) with an increase in the temperature of the reacting vessel, which also suggests a shift towards chemisorption [337].

The r^2 value is not sufficient to conclude that the experimental data fits the Langmuir adsorption isotherm. Another important adsorption parameter must be introduced to complement the r^2 values in concluding that the experimental data fit the Langmuir adsorption isotherm in the form of dimensionless separation constant (K_L). Table 7.4 shows the values of K_L for mild steel and zinc metal in four various concentrations of non-radiated *H. kraussii* extract inhibitor. These values are calculated using Equation 91. In Table 7.4, the K_L average values of mild steel and zinc metal at all four temperatures are less than unity, suggesting that the experimental data fit the Langmuir adsorption isotherm, and that the adsorption process is favourable.

© University of Venda

Table 7. 4: Dimensionless separation factor (K_L) at various *H. kraussii* concentrations at four various temperatures for metals corrosion in 1.0 M H_2SO_4.

Metal	**Concentration (ppm)**	**Temperature (℃)**			
		30	40	50	60
Mild steel	100	0.003917697	0.005210803	0.007407133	0.010978515
	300	0.001309319	0.001742989	0.002481297	0.003686486
	600	0.000655088	0.000872255	0.001242190	0.001846647
	900	0.000436821	0.000581672	0.000828470	0.001231856
	1200	0.000327651	0.000436318	0.000621481	0.000924177
	1500	0.000262138	0.000349085	0.000497247	0.000739478
	Average	0.001151452	0.001532187	0.002179636	0.003234527
Zinc	100	0.000880124	0.001920104	0.002112727	0.003494939
	300	0.000293547	0.000640855	0.000705255	0.001167700
	600	0.000146795	0.000320530	0.000352742	0.000584191
	900	0.000097868	0.000213710	0.000235189	0.000389537
	1200	0.000073403	0.000160290	0.000176402	0.000292181
	1500	0.000058723	0.000128237	0.000141127	0.000233758
	Average	0.000258410	0.000563955	0.000620574	0.001027051

7.4. Temperature effect

The effect of temperature on metal corrosion is a vital aspect of corrosion studies. In a neutral solution, the temperature increase can have useful effects on the overpotential of oxygen diffusion and depolarisation rate, with the possibility of oxygen drop. In the acidic solution, the corrosion exponentially rises with rising temperature because of the decreased hydrogen overpotential, resulting in speedy hydrogen evolution [372]. The effect of temperature on zinc and mild steel surface corrosion was exploited in the absence and presence of various inhibitor concentrations using Arrhenius and transition state equations, which yielded the activation energy (E_a), change in enthalpy (ΔH^*), and change in entropy (ΔS^*), which are tabulated in Table 7.5. These parameters were calculated based on the Arrhenius (Figures 7.5 and 7.6) and transition state plots (Figures 7.7 and 7.8).

© University of Venda

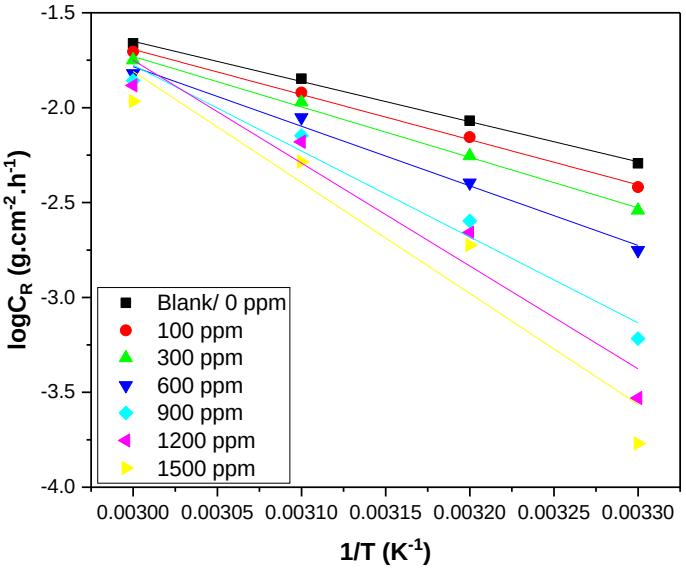


Figure 7. 5: Arrhenius plots for mild steel metal corrosion in 1.0 M H_2SO_4 solution with and without various concentrations of *H. kraussii* as the extract inhibitor.

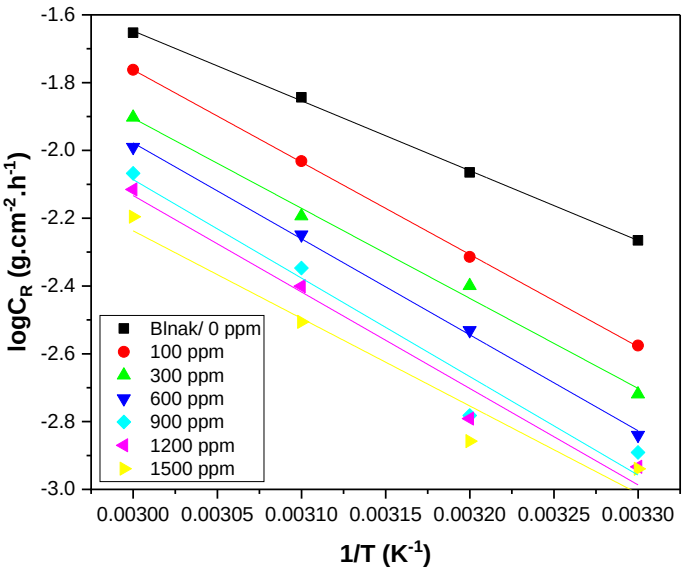


Figure 7. 6: Arrhenius plots for zinc metal corrosion in 1.0 M H_2SO_4 solution with and without various concentrations of *H. kraussii* as the extract inhibitor.

© University of Venda

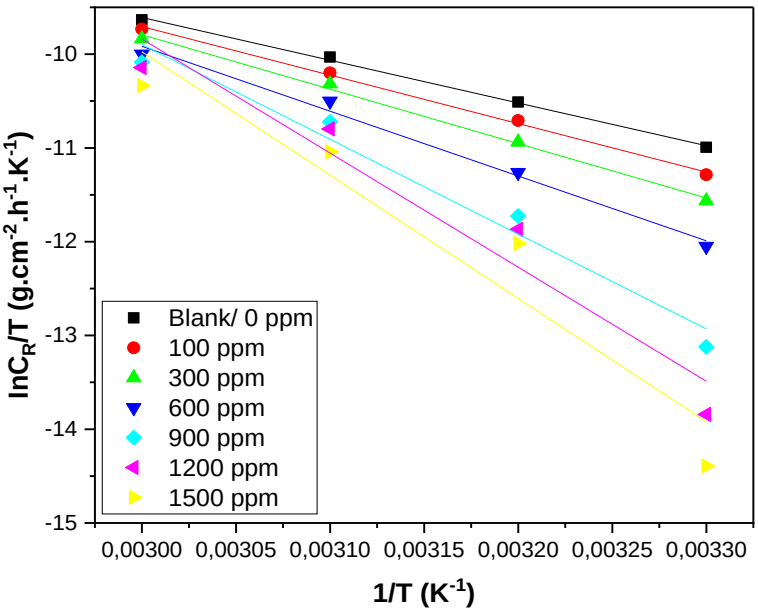


Figure 7. 7: Transition state plots for mild steel metal corrosion in 1.0 M H_2SO_4 medium with and without various concentrations of *H. kraussii* as the extract inhibitor.

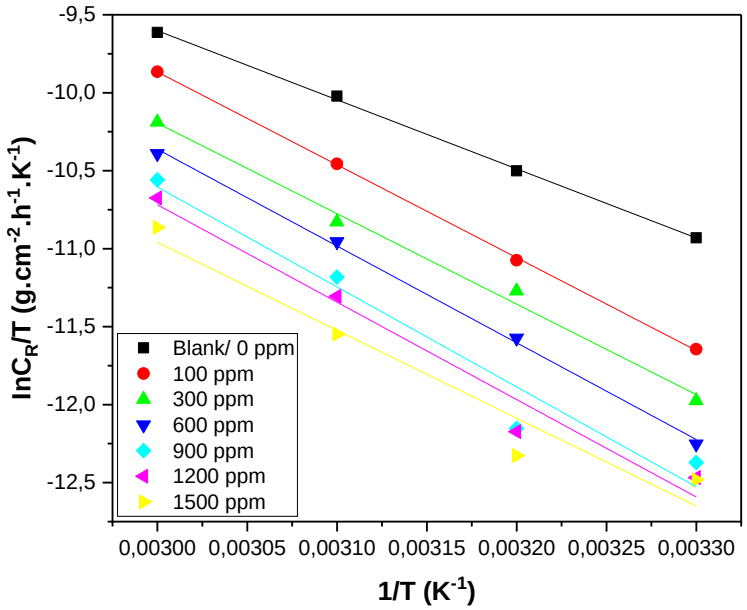


Figure 7. 8: Transition state plots for zinc metal corrosion in 1.0 M H_2SO_4 medium with and without various concentrations of *H. kraussii* as the extract inhibitor.

© University of Venda

Table 7. 5: Transition state and Arrhenius parameters for the adsorption of various concentrations of *H. kraussii* in 1.0 M H_2SO_4 on mild steel and zinc metal.

Inhibitor	**Metals**	**Concentration of inhibitors (ppm)**	E_a **(kJ.mol^{-1})**	ΔH^* **(kJ.mol^{-1})**	ΔS^* **(J.mol^{-1}.k^{-1})**
***H. kraussii* extract**	Mild steel	0.00	40.52047	37.89666	-163.75609
		100	45.60206	42.97765	-149.32345
		300	50.89080	48.18802	-134.4161
		600	60.11760	57.49011	-107.53253
		900	86.69428	84.06226	-27.65604
		1200	103.80232	101.16676	21.14770
		1500	111.971	109.33484	47.51277
	Zinc	0.00	39.45161	36.82816	-166.90787
		100	52.13008	49.50378	-131.08003
		300	50.86534	48.23965	-137.60333
		600	54.20480	51.57859	-128.97887
		900	55.63766	53.27219	-125.91065
		1200	54.48513	51.85912	-131.11187
		1500	49.46138	46.83641	-148.17281

The addition of the inhibitor extract in the corrosive solution increased the activation energy to values higher than that of the uninhibited solution. This behaviour indicates that the corrosion process in the inhibited solution has greater energy barriers, which are linked to either physical adsorption or the weak chemical interaction between the inhibitor molecules and the metal surface [373]. The table shows that the E_a values are increasing with an increase in the inhibitor concentrations for both mild steel and zinc metals, reaching maximum values of 111.971 and 55.638 kJ.mol^{-1}. However, for zinc metal, the increase was halted at 900 ppm and then decreased going forward to the highest concentration, but the values were still higher than that of the blank solution. The decrease at higher temperatures was reported in other literature, and it was explained that at elevated levels of inhibition, the total corrosion reaction shifts from the uncovered part of the metal surface to the covered part [374]. The activation energy values which become unchanged or lower in the inhibited solution than that of the uninhibited solution are an indication of the chemical adsorption mechanism, which results in the formation of the film layer on the surface of the metal and the increase in the surface area of the metal covered by the inhibitor molecules as the temperatures increase. Such behaviour also supports the existence of both physical and chemical adsorption on the surface of the metal [374].

© University of Venda

The change in entropy and enthalpy were obtained from the transition state plot, given by Equation 93. The enthalpy values obtained are positive, which is an indication of an endothermic reaction. The dissolution of metal is known to be an endothermic reaction [375]. The change in enthalpy values was found to be rising with rising extract inhibitor concentration. High values of enthalpy when *H. kraussii* is present indicate that more energy must be supplied to the system to drive the corrosion process. This suggestion is due to the formation of a protective film on the surface of the metal [376]. The entropy values in the presence of the extract inhibitors have been found to be lower than in the absence of the extract inhibitor. This observation is an indication of the decrease in the disorder in the electrolyte when the inhibitor molecules are absorbed onto the metal surface [375].

7.5. Electrochemical analysis

7.5.1. Mild steel

7.5.1.1. Open circuit voltage (OCV)

The effect of *H. kraussii* extract on the potential-time behaviour of mild steel was traced in a stagnant 1.0 M H_2SO_4 solution over 1 hour period. Figure 7.9 shows the variation of the OCV of the working electrode in the absence and presence of the various concentrations of the extract inhibitor. The OCV potentials of the inhibited solution shifted distinctly towards the direction of the cathodic region compared to the blank test potential. This is an indication that the extract inhibitor has a significant inhibitory effect on the cathodic mild steel dissolution reaction. The mild steel OCV curve stabilized after soaking in the sulphuric acid solution for 3600 s; however, a clear stability was obtained at around 750 s, and this strongly proves that the electrode surface reached a stable state before other electrochemical operations were performed [371]. The potential of the blank solution increases because of the formation and thickening of the oxide layer on the surface of the metal and because there is a specific surface adsorption effect [377].

© University of Venda

University of Venda
Creating Future Leaders

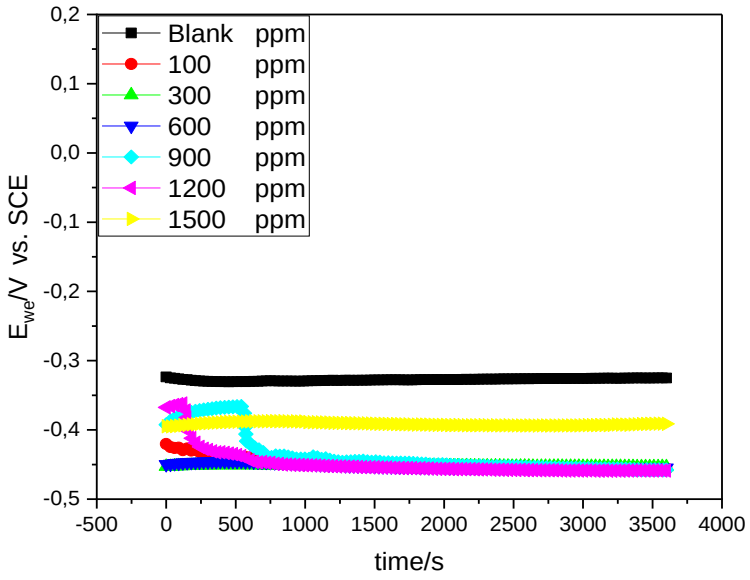


Figure 7. 9: Open circuit voltage for mild steel in 1.0 M H_2SO_4 solution and *H. kraussii* extract.

7.5.1.2. Electrochemical impedance spectroscopy (EIS)

EIS gives a remarkable understanding of the inhibitor's electrochemical interactions and the metal's surface. The ability of *H. kraussii* extract to inhibit corrosion on a mild steel metal surface in the corrosive acidic medium in comparison to an uninhibited mild steel metal was studied using the EIS technique at open circuit voltage after one hour immersion time. Figure 7.10 displays the Nyquist plot for mild steel in 1.0 M H_2SO_4 solution in the absence and presence of various concentrations of *H. kraussii* extract. From the figure observation, single semi-circles were observed in the non-existence and existence of the corrosion inhibitor, which increases in diameter with an increase in the inhibitor concentration [378]. This behaviour is indicative that the inhibitor was adsorbed onto the metal surface, protecting the metal from corrosion. The semi-circles are observed to be of the same shape in the absence and presence of the inhibitor, suggesting that the addition of the inhibitor in the corrosive electrolyte did not change the corrosion mechanism and that the corrosion action is under the charge transfer control [372].

© University of Venda

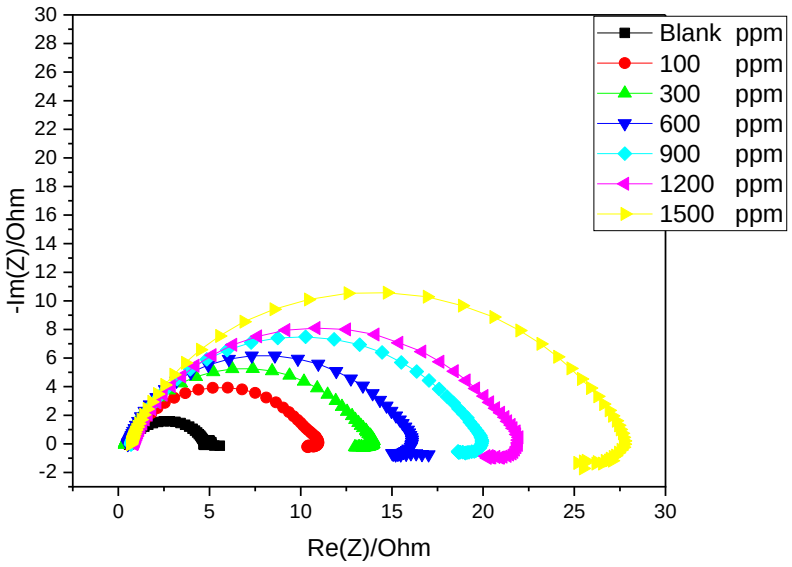


Figure 7. 10: Nyquist plot of m mild steel metal in 1.0 M H_2SO_4 solution with and without various concentrations of *H. kraussii* extract inhibitor.

Bode plots obtained for mild steel in 1.0 M H_2SO_4 with and without different *H. kraussii* extract concentrations are shown in Figure 7.11. The Bode plot displays that the impedance rises with rising plant extract concentration, and the one-time constant curve of the Bode plot supports a single charge transfer mechanism. Also, the Nyquist plots display a single semi-circle over the studied frequency range, which relates to the one-time constant in the Bode plot. This finding confirms the single charge transfer mechanism and the increase in inhibition efficiency as inhibitor concentration increases [379]. This observation also further indicates that the electrochemical process taking place is generally controlled by charge transfer. The single phase peak observed in the phase angle also indicates that there is a one-time constant for the system under investigation, which can be related to the electrical double layer [379]. The extraction of the impedance parameters was performed by fitting the equivalent circuit represented in Figure 5.16 to the Nyquist plot, and the parameters obtained are tabulated in Table 7.6.

© University of Venda

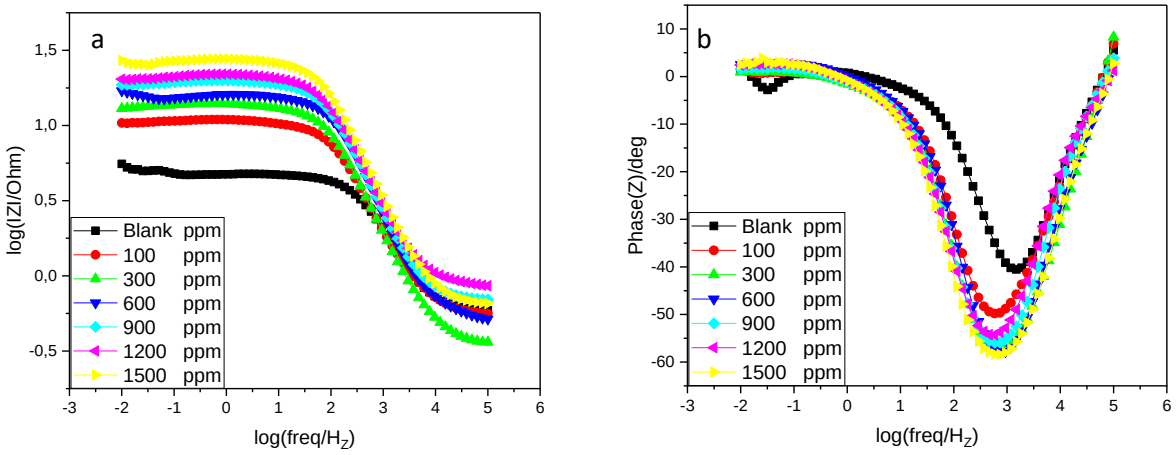


Figure 7. 11: Bode impedance magnitude plot (a) and the Bode phase angle plot (b) of mild steel metal in 1.0 M H_2SO_4 with and without various concentrations of *H. kraussii* inhibitor compound.

Table 7. 6: EIS parameters like the solution resistance (R_s), resistance of charge transfer (R_{ct}), constant phase element (CPE), constant phase element constant (n2), double layer capacitance (C_{dl}) and percentage inhibition efficiency ($\%IE_{EIS}$), using *H. kraussii* in 1.0 M H_2SO_4 in mild steel metal.

Inhibitor	**Metal**	**Conc. (ppm)**	R_s **(Ωcm²)**	**CPE (F.s$^{(a-1)}$ x10^{-3}**	**n2**	R_{ct} **(Ωcm²)**	C_{dl} **(μF/cm^{-2})**	**τ (s)**	**%IE$_{EIS}$**
H. kraussii extract	Mild steel	00	0.5866	0.3379	0.8377	4.221	23890.6700	0.1008	
		100	0.5664	0.4287	0.8177	10.2	3974.2726	0.0405	58.62
		300	0.3653	0.3513	0.8397	13.33	2273.6495	0.0303	68.33
		600	0.5395	0.2179	0.8606	15.29	1689.1418	0.0258	72.39
		900	0.6945	0.2318	0.8535	18.76	1133.0194	0.0213	77.50
		1200	0.8719	0.2414	0.8436	20.46	961.2586	0.0197	79.37
		1500	0.652	0.2010	0.8449	26.41	570.3171	0.0151	84.02

From the examination of Table 7.6, the values of the R_{ct} were found to rise with the concentration of the inhibitor [380]. This suggests that the inhibitor was adsorbed onto the metal surface, leading to the protective film's formation and minimising the corrosion rate [29]. The increase in the R_{ct} values with the inhibitor concentration leads to a rise in the inhibition efficiency, with the maximum concentration having a percentage inhibition efficiency of 84.02 %. The constant phase element exponent (n) values describe the corrosion process on the metal surface. Its values range from -1 to 1, in which the value of -1 represents the inductance, 1

© University of Venda

represents the capacitor, and 0 represents the resistor [381]. From the table, it can be observed that the values of n are approximately approaching 1, which suggests that the interface has a capacitive nature. The high value of n proves that the extract formed a film on the surface of mild steel metal and improved its homogeneity. The CPE values do not form a proper trend but generally are found to decrease with increasing extract concentration. This is an indication of the adsorption of extract inhibitor on the surface of the metal delaying hostile and corrosion cell formation. The double-layer capacitance (C_{dl}) positively correlates with the local dielectric constant and negatively correlates with the thickness of the double layer. Therefore, the decrease in C_{dl} in the Table 7.6 suggests an increase in the thickness of the double layer or a decrease in the local dielectric constant, which may be caused by the adsorption of the extract inhibitor molecules on the mild steel/HCl interface [382]. The time constant values exhibit a decreasing trend as the inhibitor concentration for mild steel metal increases. This observation indicates that the adsorption time of the *H. kraussii* extract on the aluminium metal is short, indicating a rapid adsorption process [282]. It has been observed that the time constant is directly proportional to the double-layer capacitance.

7.5.1.3. Potentiodynamic polarization

The polarization plots are a sentimental approach to studying the corrosion mechanism and comprehending the kinetics of both the anodic and cathodic reactions [269]. Figure 7.12 shows the Tafel plot for mild steel in 1.0 M H_2SO_4 solution in the absence and presence of *H. kraussii* extracts. From the figure, it can be observed that the introduction of the corrosion inhibitor in the corrosive solution managed to reduce both the anodic and cathodic current densities, indicating that the inhibitor was adsorbed onto the metal surface blocking the active sites, thereby forming a film on the metal surface. The Tafel plot extrapolation yielded the electrochemical parameters like corrosion potential (E_{corr}), polarization resistance (R_P), corrosion current density (i_{corr}), and anodic and cathodic Tafel slopes (β_a and β_c) and the calculated potentiodynamic polarization percentage inhibition efficiency ($\%IE_{PDP}$) which are presented in Table 7.7.

© University of Venda

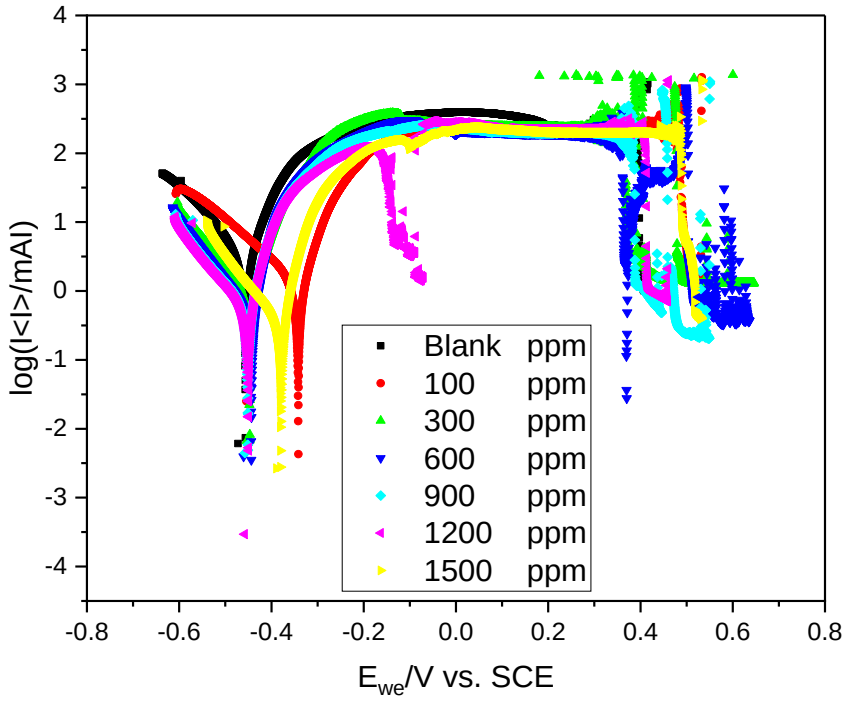


Figure 7. 12: Tafel plots for mild steel in 1.0 M H_2SO_4 with and without various *H. kraussii* extract inhibitor concentrations.

Table 7. 7: PDP parameters, including anodic and cathodic Tafel slopes (βa and β_c), polarization resistance (R_P), corrosion potential (E_{corr}), and corrosion current density (i_{corr}), measured in 1.0 M H_2SO_4 using different *H. kraussii* inhibitor concentrations.

Inhibitor	**Inhibitor Conc. (ppm)**	**-E_{corr} (mV) with Ag/AgCl**	**i_{corr} (mA.cm^{-2})**	**R_P (Ω)**	**β_a (mV.dec^{-1})**	**β_c (mV.dec^{-1})**	**% IE_{PDP}**
Blank	0.00	-456.498	3556.426	5.64	74.5	143.0	
H. kraussii extract	100	-341,029	1572.977	13.3	67.1	190.8	67.940
	300	-446.874	1022.143	14.8	57.6	135.0	75.590
	600	-443.471	480.792	19.6	37.3	117.5	88.602
	900	-450.921	561.726	20.3	45.8	131.1	86.511
	1200	-449.277	468.606	21.7	42.3	129.4	88.408
	1500	-380.537	343.358	27.7	39.1	121.9	91.776

The E_{corr} values difference between the inhibitor extract concentration and the blank system are within -85 mV as reported by Liu et al. (2023) [383], which is an indication that the extract behaviour is of a mixed type of inhibitor [217]. In the presence of the inhibitor, the E_{corr} values

© University of Venda

are found to have shifted more towards the positive potential. The i_{corr} values were reduced upon the addition of the inhibitor in the corrosive solution, which is an indication of a strong inhibitor and the protective layer formation on the metal surface. From Table 7.7, it is observed that upon the increment of the inhibitor concentration, the inhibition efficiency was mostly found to be increasing with an outlier at 600 ppm, while the corrosion current density decreased because of the inhibitor molecule's adsorption on the mild steel metal surface [350]. The values of the cathodic and anodic Tafel slopes showed variation with respect to that of the blank upon introducing the extract inhibitor, indicating that the extract managed to suppress anodic and cathodic reactions. With that said, the *H. kraussii* extract acts as a mixed inhibitor [356].

7.5.2. Zinc metal

7.5.2.1. Open circuit voltage

Figure 7.14 shows the OCV-time profile for zinc metal in 1.0 M H_2SO_4 solution in the non-existence and existence of *H. kraussii* extract. The figure shows that the zinc OCV-time profile in a corrosive medium was observed for 3600 s, sufficient for establishing corrosion system equilibrium [292]. As can be observed from Figure 7.13, the time profile of the bare metal has a more negative potential than the inhibited metal profile, which shifted towards a less negative potential. This suggests the most favoured process could be anodic protection. The shift towards the less negative potential also indicates the adsorption of the investigated inhibitor molecules on the active corrosion centres on the surface of the metal [384]. The shift in the OCV potential of the inhibitor free-solution towards the more negative potential direction indicates the desorption of the corrosion products on the metal surface [294]. No stable trend is observed in the OCV variation with time for the electrodes without or with varying concentrations of the inhibitor. This indicates that the extract functions as a mixed type of inhibitor [293]. In the inhibitor free-solution, the OCV potential moved towards the negative potential direction, indicating the corrosion product desorption on the metal surface [294].

© University of Venda

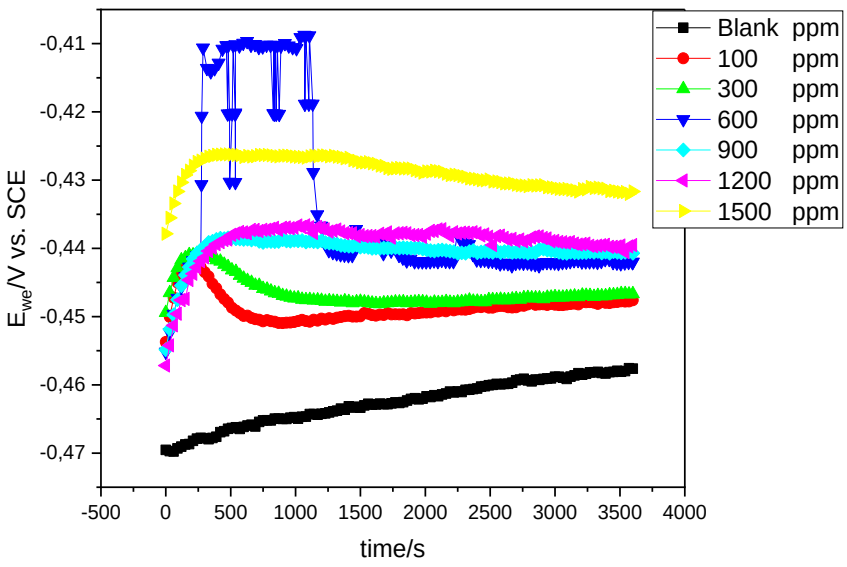


Figure 7. 13: Open circuit voltage for zinc in 1.0 M H_2SO_4 medium and *H. kraussii* extract.

7.5.2.2. Electrochemical impedance spectroscopy (EIS)

The corrosion inhibition process of zinc metal in 1.0 M H_2SO_4 solution in the absence and presence of different concentrations of *H. kraussii* extract can be studied preciously from EIS tests. The Nyquist plot is presented in Figure 7.14. The figure shows that the Nyquist plots possess the imperfect depressed single capacitive loop with a uniform shape in the absence and presence of the extract [385], suggesting that no corrosion mechanism change took place [386]. This finding is complemented by the occurrence of the single, one-time constant model in the Bode plots. The figure shows that the semi-circle diameter increases with increasing inhibitor concentration, indicating the adsorption of the inhibitor molecules on the metal surface, forming a protective film against the aggressive electrolyte attack [269].

© University of Venda

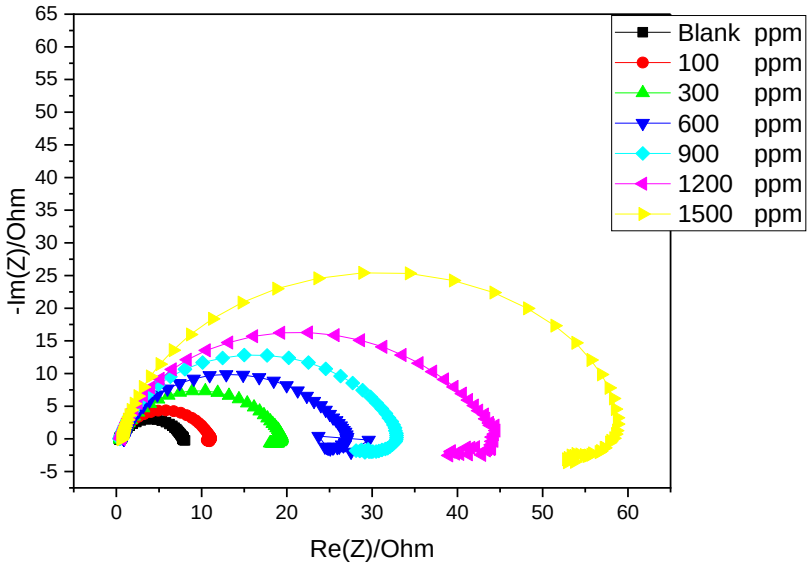


Figure 7. 14: Nyquist plot of zinc metal in 1.0 M H_2SO_4 with and without various *H. kraussii* extract inhibitor concentrations.

The Nyquist plot does not have the capability to display any frequency value, and in order to correct this, Bode plots were introduced to show the frequency behaviour of the corrosion process [387]. Figure 7.15 shows the Bode magnitude (a) and phase plots (b). The Bode plot was obtained by plotting the logarithm of the impedance modulus and the phase angle displacement as a function of the frequency logarithm [388]. It can be observed that the loglZl increased with an increase in the extract inhibitor concentration, [389] reaching a maximum of 1.8 Ω. The phase angles in the presence of the extract inhibitor are higher than that of the blank solution. The extraction of the impedance parameters was performed by fitting the equivalent circuit represented in Figure 5.16 to the Nyquist plot, and the parameters obtained are tabulated in Table 7.8.

© University of Venda

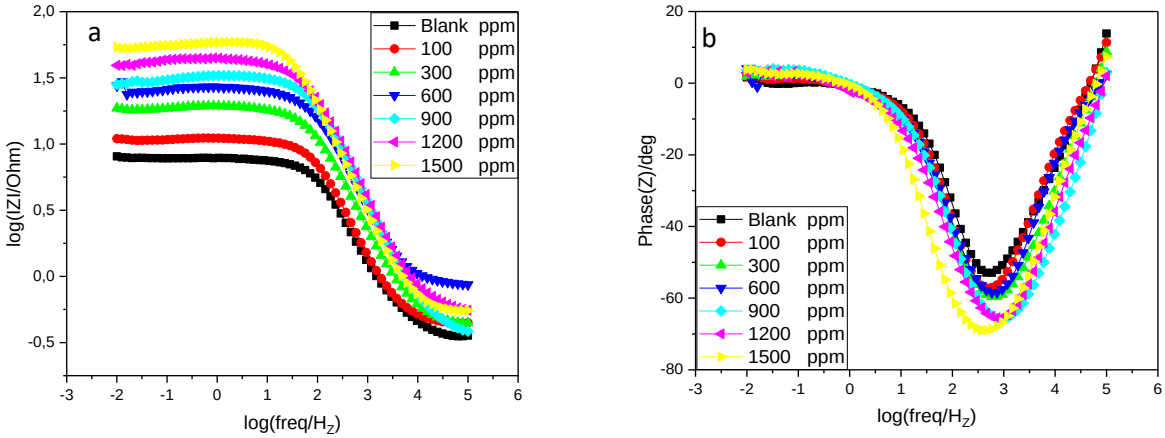


Figure 7. 15: Bode impedance magnitude plot (a) and Bode phase angle plot (b) of zinc metal in 1.0 M H_2SO_4 with and without various concentrations of *H. kraussii* inhibitor compound.

Table 7. 8: EIS parameters like the solution resistance (R_s), resistance of charge transfer (R_{ct}), constant phase element (CPE), constant phase element constant (n2), double layer capacitance (C_{dl}) and percentage inhibition efficiency ($\%IE_{EIS}$) using *H. kraussii* in 1.0 M H_2SO_4 in zinc metal.

Inhibitor	**Metal**	**Conc. (ppm)**	R_s **(Ωcm²)**	**CPE (F.S$^{(a-1)}$ x10^{-3}**	**n2**	R_{ct} **(Ωcm²)**	**C_{dl} (μF/cm^{-2})**	**τ (s)**	**$\%IE_{EIS}$**
H. kraussii extract	Zinc	00	0.3597	0.5629	0.8369	7.507	7020.9244	0.0527	
		100	0.448	0.3541	0.8796	10.46	3494.9680	0.0366	28.23
		300	0.4464	0.2717	0.8517	18.48	1173.2036	0.0217	59.38
		600	0.8712	0.1758	0.8636	25.3	643.7357	0.0163	70.33
		900	0.4008	0.1384	0.8701	30.97	402.2673	0.0125	75.76
		1200	0.5657	0.1410	0.8620	41.98	232.8906	0.0098	82.12
		1500	0.5542	0.1355	0.8975	56.48	110.9392	0.0063	86.71

The corrosion rate is directly related to the R_{ct} value, which is a measurement of electron transfer across the surface [390]. It is discovered that when the inhibitor's concentration rises, so do the R_{ct} values. This implies that the inhibitor was adsorbed into the metal surface, forming a protective film and reducing the corrosion rate [29]. The increase in the R_{ct} with the inhibitor concentration leads to an increase in the inhibition efficiency at the maximum concentration, and the %IE was found to be 86.71 %. The adsorption of the inhibitor molecules on the metal surface is considered proper if the R_{ct} values increase and the double layer capacitance (C_{dl})

© University of Venda

values decrease with increasing inhibitor concentration [227]. From the table, it can be noted that the values of C_{dl} decrease with the rise of extract inhibitor concentration. This decrease in C_{dl} is an indication of increased corrosion resistance of the zinc metal with increasing inhibitor concentration. The time constant values for zinc metal are observed to decrease as the inhibitor concentration increases. Based on this result, it can be inferred that the *H. kraussii* extract has a short adsorption time on aluminium metal, indicating a rapid adsorption process [282]. The constant phase element exponent (n) values describe the corrosion process on the metal surface. Its values range from -1 to 1, where -1 represents the inductance, 1 represents the capacitor [391], and zero represents the resistor. From the table, it can be observed that the values of n are approximately approaching 1, which suggests that the interface is of a capacitive nature [392]. The high value of n proves that the extract formed a film on the surface of zinc metal and improved its homogeneity. The CPE values do not form a proper trend, but generally, they were found to be in the opposite trend compared to the value of R_{ct}. Either a rise in the electrical double layer or a decrease in the local dielectric constant was the cause of the CPE decline. This behaviour shows that the extract inhibitor functions by the absorption process in which the inhibitor replaces water molecules on the surface of metal [390].

7.5.2.3. Potentiodynamic polarization (PDP)

Figure 7.16 shows the Tafel curves for zinc in 1.0 M H_2SO_4 solution in the non-existence and existence of *H. kraussii* extract. From the figure inspection, it can be observed that the introduction of the inhibitor extract in the aggressive electrolyte managed to reduce both the anodic and cathodic corrosion current densities [393, 394], indicating that the inhibitor was adsorbed onto the surface of the metal, forming a protective film. Electrochemical parameters like corrosion potential (E_{corr}), corrosion current density (i_{corr}), polarization resistance (R_P), anodic and cathodic Tafel slopes (β_a and β_c) and the calculated potentiodynamic polarization percentage inhibition efficiency (%IE_{PDP}), which are presented in Table 7.9 were obtained through the Tafel plot extrapolation. The polarization curves sometimes do not show the linear Tafel regions, making the extrapolation and the Tafel slope calculations somewhat inaccurate. This can be due to the slow diffusion process of the oxidizing species at the cathodic site or the deposition of the corrosion products at the anodic sites [395].

© University of Venda

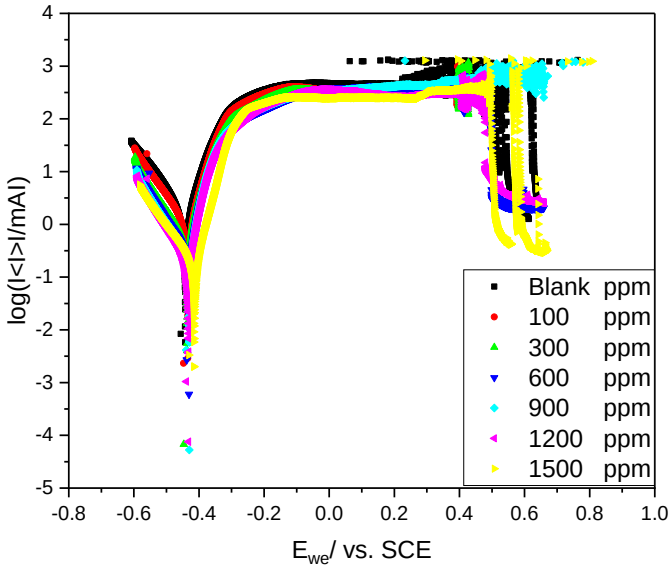


Figure 7. 16: Tafel plots for zinc in 1.0 M H_2SO_4 with and without various concentrations of *H. kraussii* extract inhibitor.

Table 7. 9: PDP parameters, including anodic and cathodic Tafel slopes (βa and β_c), polarization resistance (R_P), corrosion potential (E_{corr}), and corrosion current density (i_{corr}), measured in 1.0 M H_2SO_4 using different *H. kraussii* inhibitor concentrations.

Inhibitor	**Inhibitor Conc. (M)**	**-E_{corr} (mV) with Ag/AgCl**	**i_{corr} (mA.cm^{-2})**	**R_P (10^{-1}) (Ω)**	**βa (mV.dec^{-1})**	**β_c (mV.dec^{-1})**	**% IE$_{PDP}$**
Blank	0.00	-428.680	864.361	22.7	71.3	121.6	
H. kraussii extract	100	-434.387	1006.811	14.3	53.3	117.0	47.484
	300	-437.923	489.579	23.2	48.5	107.9	75.352
	600	-415.549	194.887	62.3	45.0	119.3	84.798
	900	-430.641	271.981	30.6	36.0	104.2	87.131
	1200	-429.998	247.847	33.3	34.5	110.3	88.719
	1500	-414.693	203.627	62.3	45.0	123.2	89.890

From the examination of Table 7.9, it can be observed that in most cases, the inhibitor's E_{corr} values are found to have shifted towards more positive values relative to that of the blank system. The shift in the E_{corr} values is not uniform, suggesting that the mechanism of inhibition is not by geometric blocking effects [395]. From the literature, the inhibitor can be categorised as anodic, cathodic or mixed inhibitor type based on the shifting of the E_{corr} values of the coated system with respect to the uncoated system. The E_{corr} value variation between the uncoated and

© University of Venda

coated system greater than -85 mV is indicative of the cathodic or anodic type of inhibitor. The E_{corr} values <-85 mV are associated with the mixed inhibitor type [395]. In the current study, the E_{corr} difference is less than -85 mV, suggesting that the inhibitor has a mixed type of inhibition action [396]. It can be said that the inhibitor inhibits both the cathodic and anodic reactions through the formation of a film on the metal surface, which results in the indirect blockage of the cathodic and anodic reaction sites [393]. The values of β_a and β_c show variation upon the inhibitor introduction in the corrosive electrolyte in relation to the blank system. The variation in β_a and β_c is due to several factors, such as the concentration of the electrolyte, the working electrode composition, the charge transfer coefficient, and the scan rate. The values of β_a and β_c can also be used to describe the magnitude of the variation of the E_{corr} values in categorising the inhibiting effects of the extract as anodic, cathodic or mixed type. From the table, it can be seen that the values of β_a and β_c do not follow a stable trend, which is an indication that the introduction of the extract inhibitor affects both the cathodic and anodic half-reactions and that the rate of the anodic and cathodic inhibition differs with inhibitor concentrations. Based on the difference significance between the β_a and β_c of the blank system and the inhibited system, it is observed that the inhibition effects of the extract are cathodic dominating. From the table, it can also be observed that the values of the corrosion current densities increase with an increase in the extract concentration, which leads to an increase in the %IE [302, 394].

7.6. Fourier Transform Infrared Spectroscopy (FTIR)

7.6.1. Mild steel

Figure 7.17 shows the variation in the absorption bands of different samples as outlined in the legend of the figure. It can be observed that the four spectra displayed are different from each other, especially when looking at the green spectrum and comparing it to the rest of the spectra. The variation in the spectra is an indication of the extract inhibitor adsorption on the mild steel metal surface. Table 7.10 shows the functional groups obtained from the four spectra displayed in Figure 7.17. The first and the last columns reveal the functional groups from the plant extract, which were retained after gravimetric analysis, which suggests that they are the ones that managed to absorb onto the metal surface, reducing the rate of corrosion of the mild steel metal. Such functional groups include O-H carboxylic acid, Sp^3 C-H (C-C-H), C=C alkene, C-N amine, Sp^3 C-O and C-H aromatic.

© University of Venda

University of Venda
Creating Future Leaders

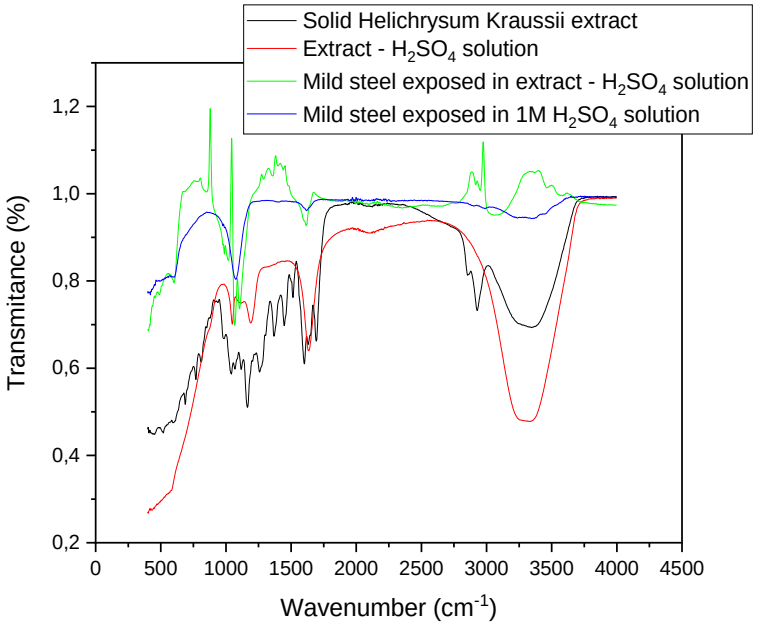


Figure 7. 17: FTIR spectra for solid *H. kraussii* plant extract (Black), 1500 ppm *H. kraussii* plant extract – 1.0 M H_2SO_4 solution (Red), the layer formed on mild steel metal exposed in 1500 ppm *H. kraussii* plant extract – 1.0 M H_2SO_4 solution (Green) and corrosion products formed on Mild steel metal exposed in 1.0 M H_2SO_4 solution (black).

Table 7. 10: Possible functional groups present in solid *H. kraussii* plant extract, corrosion products formed on mild steel metal exposed in 1.0 M H_2SO_4 solution, 1500 ppm *H. kraussii* plant extract – 1.0 M H_2SO_4 solution and layer formed on mild steel metal exposed in 1500 ppm *H. kraussii* plant extract – 1.0 M H_2SO_4 solution.

	Functional Groups			
Bands position (cm^{-1})	**Solid *H. kraussii***	**Mild steel metal exposed in H_2SO_4 blank solution**	***H. kraussii* - H_2SO_4 solution**	**Mild steel metal exposed in *H. kraussii* - H_2SO_4 solution**
2400 – 3600	O-H Carboxylic acid	O-H Carboxylic acid	O-H Carboxylic acid	O-H Carboxylic acid
3300 – 3500	O-H alcohol	O-H alcohol	O-H alcohol	
3200 – 3400	N-H amine N-H amide	N-H amine N-H amide	N-H amine N-H amide	
3260 – 3390				
3000 – 3100				Sp^2 (C=C-H)

© University of Venda

2850 – 2960	Sp^3 C-H (C-C-H)			Sp^3 C-H (C-C-H)
2700 – 2900				
2200 – 2270		nitrile C≡N		
2100 – 2250	C≡C alkyne	nitrile C≡N C≡C alkyne	C≡C alkyne	
1730 – 1750				
1680 – 1720	C=O ketone C=O aldehyde			
1600 – 1650	C=C alkene	C=C alkene	C=C alkene	C=C alkene
1500 – 1600				
1500 – 1570	NO_2 Nitro C=C aromatic		NO_2 Nitro C=C aromatic	
1450 – 1470				
1180 – 1360	amine C-N			amine C-N
1200 – 1250				
1000 – 1200	Sp^3 C-O	Sp^3 C-O	Sp^3 C-O	Sp^3 C-O
900 – 1000		C-H aromatic		C-H aromatic
600 – 900	C-Cl chloride C-C alkane C-H aromatic	C-H aromatic		C-H aromatic

7.6.2. Zinc metal

Figure 7.20 clearly shows the absorption regions of various peaks for *H. kraussii* peaked by the FTIR instrument. It can be observed that all the spectra portrayed differ from each other, which can be used as an indication of the adsorption of inhibitor on the zinc surface, especially comparing the spectrum of the plant extract (black) and zinc exposed in plant extract-H_2SO_4 solution spectrum (green). Table 7.11 compares all the functional groups peaked by the instrument to keep track of the functional groups from the plant extracts that were retained after the gravimetric analysis exposure. The functional groups obtained after gravimetric analysis on the zinc surface are the ones causing the inhibition efficiency. In this case, the first and last columns will be very helpful in keeping track of such functional groups. Looking at the table, it can be said that O-H carboxylic acid, O-H alcohol, N-H amine, N-H amide, Sp C-H (C≡C-H), nitrile C≡N, C≡C alkyne, NO2 Nitro, C=C aromatic, C=H alkene, C=H aldehyde, Sp^3 C-O, C-H alkane and C-H aromatic, are the functional groups retained after gravimetric analysis which can be said that they are the ones causing the corrosion inhibition on the zinc metal. However, a new functional group, nitrile C≡N, was formed during the corrosion process when

© University of Venda

the plant extracts, H_2SO_4, and zinc metal were reacting inside the beaker, contributing to the inhibition efficiency since it was found to be adsorbed on the metal surface.

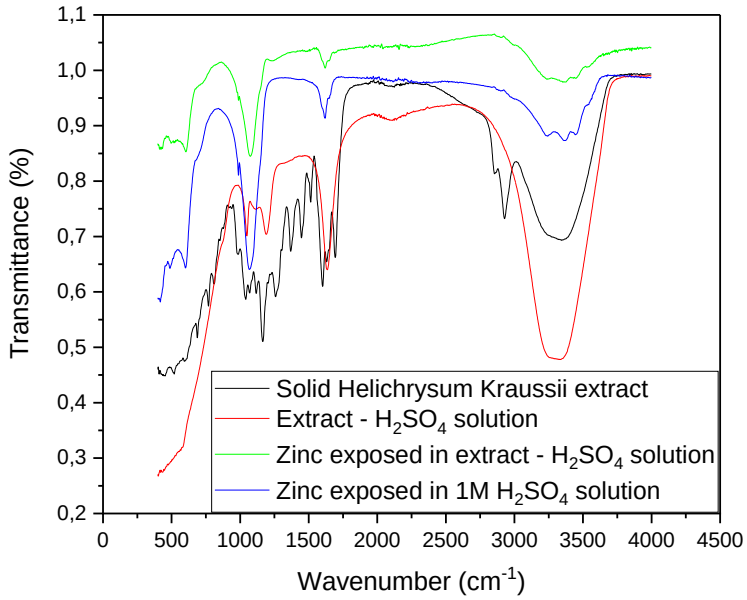


Figure 7. 18: FTIR spectra for solid *H. kraussii* plant extract (Black), 1500 ppm *H. kraussii* plant extract – 1.0 M H_2SO_4 solution (Red), the layer formed on zinc metal exposed in 1500 ppm *H. kraussii* plant extract – 1.0 M H_2SO_4 solution (Green) and corrosion products formed on zinc metal exposed in 1.0 M H_2SO_4 solution (black).

Table 7. 11: Possible functional groups present in solid *H. kraussii* plant extract, corrosion products formed on zinc metal exposed in 1.0 M H_2SO_4 solution, 1500 ppm *H. kraussii* plant extract – 1.0 M H_2SO_4 solution and layer formed on zinc metal exposed in 1500 ppm *H. kraussii* plant extract – 1.0 M H_2SO_4 solution.

	Functional Groups			
Bands position (cm^{-1})	**Solid *H. kraussii***	**Zinc metal exposed in H_2SO_4 blank solution**	***H. kraussii* - H_2SO_4 solution**	**Zinc metal exposed in *H. kraussii* - H_2SO_4 solution**
2400 – 3600	O-H Carboxylic acid	O-H Carboxylic acid	O-H Carboxylic acid	O-H Carboxylic acid
3300 – 3500	O-H alcohol	O-H alcohol	O-H alcohol	O-H alcohol
3200 – 3400	N-H amine N-H amide	N-H amine N-H amide	N-H amine N-H amide	N-H amine N-H amide
3260 – 3390		Sp C-H (C≡C-H)		Sp C-H (C≡C-H)

© University of Venda

2850 – 2960	Sp3 C-H (C-C-H)			
2700 – 2900				
2200 – 2270				nitrile C≡N
2100 – 2250	C≡C alkyne	C≡C alkyne	C≡C alkyne	C≡C alkyne
1730 – 1750				
1680 – 1720	C=O ketone C=O aldehyde			
1600 – 1650	C=C alkene	C=C alkene	C=C alkene	C=C alkene
1500 – 1600				
1500 – 1570	NO_2 Nitro C=C aromatic		NO_2 Nitro C=C aromatic	NO_2 Nitro C=C aromatic
1450 – 1470				
1180 – 1360	amine C-N			
1200 – 1250				
1000 – 1200	Sp^3 C-O	Sp^3 C-O	Sp^3 C-O	Sp^3 C-O
900 – 1000		C-H alkane		C-H alkane
600 – 900	C-Cl chloride C-C alkane C-H aromatic	C-H aromatic		C-H aromatic

© University of Venda

CHAPTER 8

UV-radiated *H. kraussii* in sulphuric acid

© University of Venda

8. Introduction

In this chapter, the results obtained for UV-radiated *H. kraussii* plant extract as corrosion inhibitor for mild steel and zinc metal in sulphuric acid using gravimetric analysis, adsorption isotherm, the effect of temperature, electrochemistry, and Fourier transform infrared spectroscopy are discussed.

8.1. Weight loss analysis

The weight loss method is utilized to monitor the corrosion of metal samples by keeping them in a specific environment for a given period, after which the metal sample is removed from that environment, and the change in mass before and after exposure is determined. It is also considered the most basic, precise, and accurate method for finding the corrosion rate of the metal [227]. The weight loss of mild steel and zinc metal for UV-radiated *H. kraussii* extract in 1.0 M H_2SO_4 solution at four different temperatures is listed in Table 8.1.

Table 8. 1: Gravimetric analysis in the presence of 1.0 M H_2SO_4 and UV-radiated *H. kraussii* extract for mild steel and zinc metals.

Inhibitor	**Metal**	**Concentration (ppm)**	**Weight loss (g)**			
			30° C	40° C	50° C	60° C
UV-radiated *H. kraussii* extract	Mild steel	0.00	0.4894	0.8193	1.3652	2.0949
		100	0.3445	0.6792	1.1482	1.7723
		300	0.2674	0.5724	0.9727	1.5661
		600	0.1882	0.4682	0.9136	1.4512
		900	0.1402	0.3747	0.8023	1.3422
		1200	0.0794	0.3111	0.6976	1.2198
		1500	0.0377	0.2655	0.5807	1.1066
	Zinc	0.00	0.5213	0.8274	1.3785	2.1379
		100	0.2679	0.5116	0.9493	1.6668
		300	0.2132	0.3975	0.6881	1.3639
		600	0.1516	0.3176	0.5936	1.1110
		900	0.1232	0.2415	0.5033	0.8479
		1200	0.1210	0.1627	0.3685	0.8298
		1500	0.1152	0.1287	0.3450	0.7215

© University of Venda

Table 8.1 shows the weight loss of mild steel and zinc metals in the presence of 1.0 M H_2SO_4. It can be noted that the weight loss of the two metals decreases with increasing extract inhibitor concentration [397]. However, as the temperature increased, the weight loss of the metals was found to be increasing. The 0.00 ppm concentration shows the weight loss of the metals in the absence of the inhibitors at the four different studied temperatures. The mild steel metal was the worst affected by H_2SO_4 since its weight loss is the highest at all temperatures and concentrations compared to those of zinc metal. The reduction in the weight loss of the two metals with an increase in the concentration of the inhibitor is solid evidence that the presence of the extract inhibitor in the aggressive acid solution managed to reduce the rate at which the metal corrodes. The increase in weight loss with an increase in the temperature shows that the inhibitor utilized is very effective at lower temperatures.

8.2. Corrosion rate and Percentage inhibition efficiency

The inhibitor's percentage inhibition efficiency and the metal's corrosion rate are used to determine the inhibitor's effectiveness. Table 8.2 shows the corrosion rate, surface coverage (θ), and percentage inhibition efficiency (%IE) of mild steel and zinc metals in 1.0 M H_2SO_4.

Table 8. 2: The corrosion parameters for mild steel, aluminium, and zinc in the aqueous solution of 1.0 M H_2SO_4 with and without various concentrations of UV-radiated *H. kraussii* extract from weight loss measurements at four various temperatures (30 – 60° C).

Inhibitor		**Temperature (° C)**	**Inhibitor Concentration (ppm)**	**Corrosion rate ($g.cm^{-2}.h^{-1}$)**	**Inhibition Efficiency (%)**	**Surface coverage (θ)**
		30	0.00	0.005094	-	-
			100	0.003585	29.623	0.29623
			300	0.002783	45.367	0.45367
			600	0.001959	61.543	0.61543
			900	0.001459	71.358	0.71358
			1200	0.000826	83.785	0.83785
			1500	0.000392	92.305	0.92305
		40	0.00	0.008527		
			100	0.007069	17.098	0.17098
			300	0.005957	30.140	0.30140
			600	0.004873	42.852	0.42852

© University of Venda

UV-radiated *H. Kraussii* extract	Mild steel		900	0.038997	54.266	0.54266
			1200	0.003238	62.027	0.62027
			1500	0.002763	67.597	0.67597
		50	0.00	0.014209		
			100	0.011950	15.898	0.15898
			300	0.010124	28.749	0.28749
			600	0.009508	33.085	0.33085
			900	0.008350	41.234	0.41234
			1200	0.007260	48.906	0.48906
			1500	0.006044	57.464	0.57464
		60	0.00	0.021803	-	-
			100	0.018445	15.402	0.15402
			300	0.016299	25.244	0.25244
			600	0.015104	30.725	0.30725
			900	0.013969	35.931	0.35931
			1200	0.012695	41.774	0.41774
			1500	0.011517	47.177	0.47177
	Zinc	30	0.00	0.005426		
			100	0.002788	48.618	0.48618
			300	0.002219	59.051	0.59051
			600	0.001578	70.918	0.70918
			900	0.001282	76.373	0.76373
			1200	0.001259	76.797	0.76797
			1500	0.001199	77.903	0.77903
		40	0.00	0.008611		-
			100	0.005325	38.160	0.36160
			300	0.004137	51.957	0.51957
			600	0.003305	61.619	0.61619
			900	0.002513	70.816	0.70816
			1200	0.001693	80.339	0.80339
			1500	0.001339	84.450	0.84450
		50	0.00	0.014347	-	-
			100	0.009880	31.135	0.31135
			300	0.007162	50.080	0.50080

© University of Venda

			600	0.006178	56.939	0.56393
			900	0.005238	63.491	0.63491
			1200	0.003835	73.270	0.73270
			1500	0.003591	76.646	0.76643
		60	0.00	0.022251	-	-
			100	0.017347	22.039	0.22039
			300	0.014195	36.205	0.36205
			600	0.011563	48.034	0.48034
			900	0.008825	60.339	0.60339
			1200	0.008636	61.188	0.61188
			1500	0.007509	66.253	0.66253

The percentage inhibition efficiency at all the studied temperatures and concentrations was found to increase with increasing inhibitor concentrations [397]. This increase in concentration is mainly due to the increase in the inhibitor molecules, meaning that more molecules are available for adsorption on the surface of the metal, thereby causing high corrosion inhibition. The formation of a protective layer as a result of the metal/solution interface transition from active dissolving to a passive state could potentially account for the improvement in inhibition efficiency [398]. The optimum %IE was found at a maximum concentration of 1500 ppm for all the temperatures studied. At 30℃ for 1500 ppm, the %IE was found to be 92.305 and 77.903 % for mild steel and zinc metals, respectively. This observation suggests that the UV-radiated extract functions optimally for mild steel in 1.0 M H_2SO_4 solution rather than in zinc metal. The surface coverage, which indicates how much of the metal surface was covered by the inhibitor molecules, was also calculated and was found to increase with rising extract inhibitor concentrations [399]. These values are also found to be very close to unity at the highest inhibitor concentration and lowest studied temperature of 30℃. This observation suggests that the inhibitor molecules managed to cover most of the metal's surface, thereby protecting the metal from corrosion. The rate of corrosion of mild steel and zinc metals was found to decrease with an increase in the extract inhibitor concentration and increase with an increase in temperature [400-402]. This means that the extract inhibitor works optimally at lower temperatures.

© University of Venda

Figures 8.1 and 8.2 show the variation in the %IE at four various temperatures and six different inhibitor concentrations in the presence of 1.0 M H_2SO_4. From the figures, it can be observed that the inhibition efficiency was found to increase with increasing inhibitor concentration.

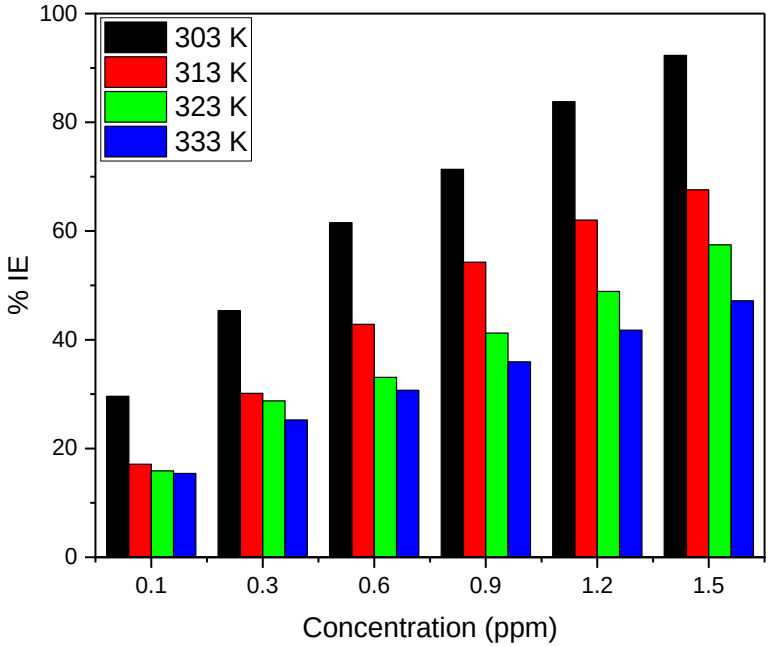
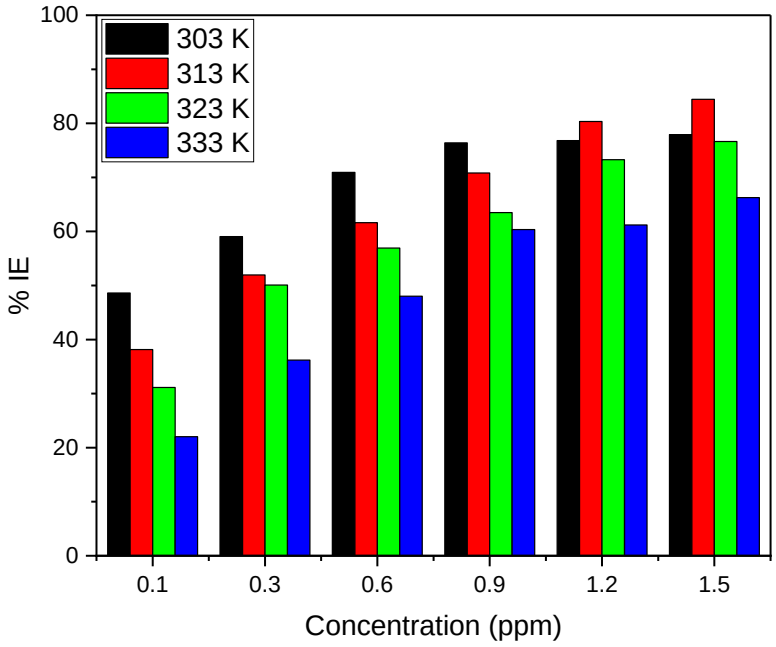


Figure 8. 1: The graph of inhibition efficiency using UV-radiated *H. kraussii* in 1.0 M H_2SO_4 for mild steel at various temperatures.



© University of Venda

Figure 8. 2: The graph of inhibition efficiency using UV-radiated *H. kraussii* in 1.0 M H_2SO_4 for zinc at various temperatures.

8.3. Langmuir adsorption isotherm

The adsorption of the inhibitor's molecules on the surface of the metal can result in a reaction at the surface of the metal. This reaction can produce secondary compounds for the formation of a protective layer. The isothermal models describe the adsorption of the inhibitor species on the surface of the metal [403]. Adsorption isotherms are used to obtain significant information on the interaction of the metal surface and the inhibitor compounds. In this work, adsorption isotherms were used to investigate the adsorption process of the UV-radiated *H. kraussii* on mild steel and zinc metals surface in 1.0 M H_2SO_4. The surface coverage values of the extract at different concentrations at 1.0 M H_2SO_4 were graphically fitted into different adsorption isotherms to find the suitable adsorption isotherm. In this study, the data from the gravimetric analysis was found to fit the Langmuir adsorption isotherm most perfectly compared to other isotherms [404]. This is evident by the values of the correlation coefficient, which are very close to unity, suggesting the close to perfect fit. From the Langmuir plot, the equilibrium constant (K_{ads}), the slope of the plots, and the change in Gibbs free energy (ΔG^o_{ads}) were determined and tabulated in Table 8.3.

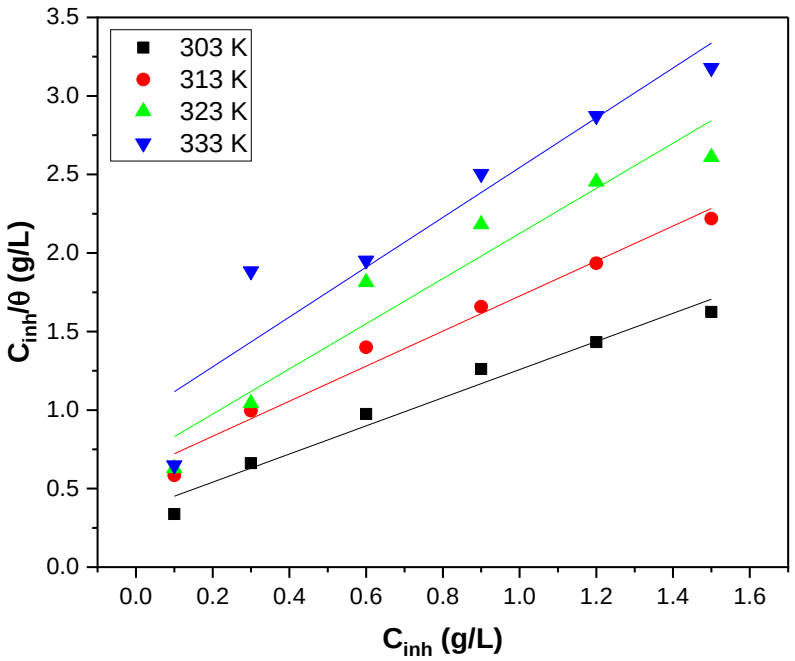


Figure 8. 3: Langmuir adsorption isotherm for UV-radiated *H. Kraussii* extract adsorption on mild steel metal in H_2SO_4 at 30, 40, 50 and 60°C.

© University of Venda

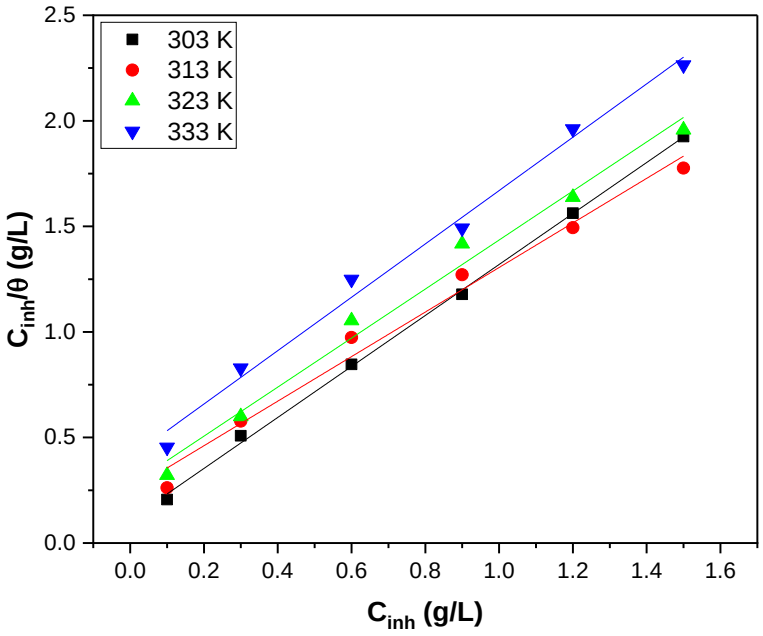


Figure 8. 4: Langmuir adsorption isotherm for UV-radiated *H. kraussii* extract adsorption on zinc metal in H_2SO_4 at 30, 40, 50 and 60°C.

Table 8. 3: Adsorption parameters from Langmuir Adsorption isotherm plots for UV-radiated *H. kraussii* extract in 1.0 M H_2SO_4.

Inhibitor	**Metals**	**Temperature (° C)**	**r^2**	**Slope**	**K_{ads} (L/g)**	**$-\Delta G^o_{ads}$ (kJ.mol^{-1})**
UV-radiated *H. Kraussii* extract	Mild steel	30	0.96331	0.89607	2764.49	38.600
		40	0.97113	1.11580	1638.94	37.240
		50	0.91620	1.43718	1455.71	38.111
		60	0.85779	1.43718	1043.73	38.370
	Zinc	30	0.99858	1.20770	8944.54	40.325
		40	0.98009	1.05545	4003.04	39.564
		50	0.98328	1.16137	3649.37	40.579
		60	0.98871	1.26398	2464.94	40.749

Adsorption is a process of separation that consists of two phases, which are accounted for by two primary forms of adsorption interaction: chemical and physical adsorption. [307]. It is known that the values of $\Delta G^o_{ads,}$ which are less than -20 kJ.mol^{-1}, indicate a physisorption kind of adsorption, and those more negative than -40 kJ.mol^{-1} indicate a chemisorption kind of

© University of Venda

adsorption [402, 405, 406]. The values of the ΔG^{o}_{ads} obtained for zinc range between -39.564 and -40.749 kJ.mol^{-1}, which means that both chemical and physical (comprehensive) adsorption took place, which is considered mixed adsorption [407]. However, for mild steel metal, the ΔG^{o}_{ads} values ranged between -37.240 and -38.600 kJ.mol^{-1}, which means that the adsorption of the extract on the metal was through physical adsorption. From Table 8.3 of the results, the values of the ΔG^{o}_{ads} did not follow any particular trend but, in most cases, were found to decrease (more negative) with an increase in temperature, which suggests an endothermic kind of adsorption [408]. The corrosion inhibitor inhibition efficiency depends on the inhibitor's K_{ads} (binding energy) values. The k_{ads} values provide the strength between the adsorbed species and the inhibitor surface; therefore, the higher the k_{ads} values, the stronger the interaction, as observed in Table 8.3, and the opposite is the case [403]. From the K_{ads} values obtained, it can be observed that the interaction of the UV-radiated *H. kraussii* extract with the surface of the metals decreases with temperature increase.

Although the r^2 values obtained in Table 8.3 suggest a good fit, the gradients obtained in the Langmuir plots are slightly above unity, which is inconsistent with the monolayer adsorption of inhibitor molecules on the metal surface assumption of the Langmuir adsorption isotherm. Due to this inconsistency, especially in a typical acid inhibition system like the one in this study, another adsorption parameter called dimensionless separation constant (K_L) is introduced to explain the inconsistency and to complement the r^2 values in terms of obeying the Langmuir adsorption isotherm. Table 8.4 shows K_L average values of mild steel and zinc metal in the presence of 1.0 M H_2SO_4 at different temperatures and concentrations of UV-radiated *H. kraussii* extract inhibitor. These values are calculated using Equation 91. From the table, the KL average values for mild steel and zinc metal are greater than unity, suggesting that the adsorption process is favourable and that the experimental data fit the Langmuir adsorption isotherm.

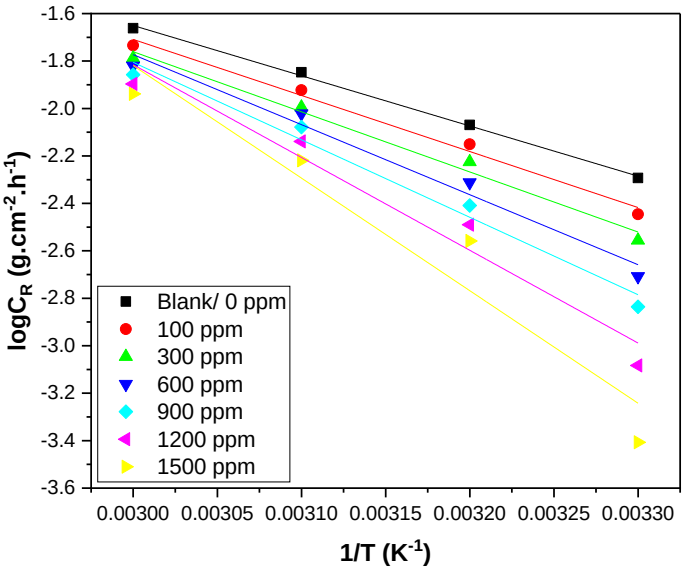
© University of Venda

Table 8. 4: Dimensionless separation factor (K_L) at various *H. kraussii* concentrations at four various temperatures for metals corrosion in 1.0 M H_2SO_4.

Metal	Concentration (ppm)	Temperature (℃)			
		30	40	50	60
Mild steel	100	0.003604266	0.006064502	0.006822632	0.009490097
	300	0.001204316	0.002029707	0.002284602	0.003183507
	600	0.000602521	0.001015884	0.001143607	0.001594291
	900	0.000401761	0.000677486	0.000762696	0.001063426
	1200	0.000301351	0.000508200	0.000572131	0.000797782
	1500	0.000241095	0.000406602	0.000457757	0.000638327
	Average	0.001059218	0.001783730	0.002007237	0.002794572
Zinc	100	0.001116752	0.002491876	0.002732711	0.004040502
	300	0.000372528	0.000832008	0.000912566	0.001350472
	600	0.000186299	0.000416177	0.000456491	0.000675692
	900	0.000124207	0.000277490	0.000304374	0.000450563
	1200	0.000093158	0.000208132	0.000228298	0.000337960
	1500	0.000074528	0.000166512	0.000182647	0.000270386
	Average	0.000327912	0.000732033	0.000802848	0.001187596

8.4. Thermodynamics and kinetic parameters

The Arrhenius and transition state plots can be used to obtain the kinetic and thermodynamic parameters like the activation energy (E_a), change in enthalpy (ΔH^*), and entropy (ΔS^*). These parameters are obtained from the transition state and Arrhenius plots presented in Figures 8.5-8.9. These parameters are presented in Table 8.5.



© University of Venda

Figure 8. 5: Arrhenius plots for mild steel metal corrosion in 1.0 M H_2SO_4 medium with and without various concentrations of UV-radiated *H. kraussii* as the inhibitor.

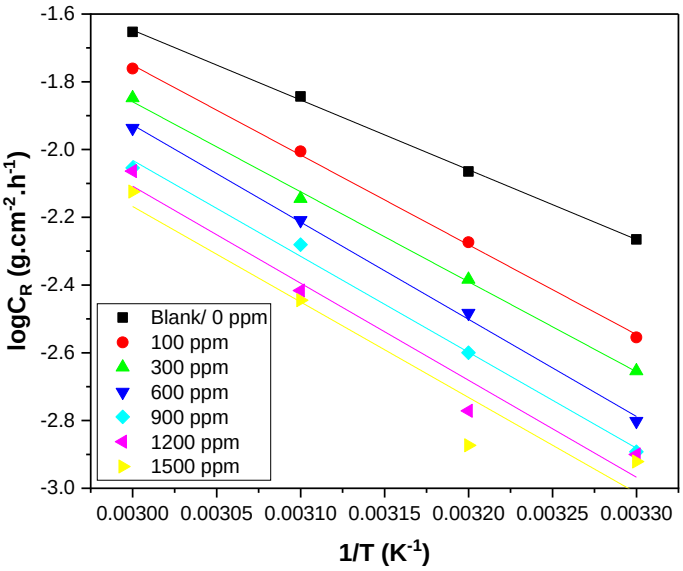


Figure 8. 6: Arrhenius plots for zinc metal corrosion in 1.0 M H_2SO_4 medium with and without various concentrations of UV-radiated *H. kraussii* as the extract inhibitor.

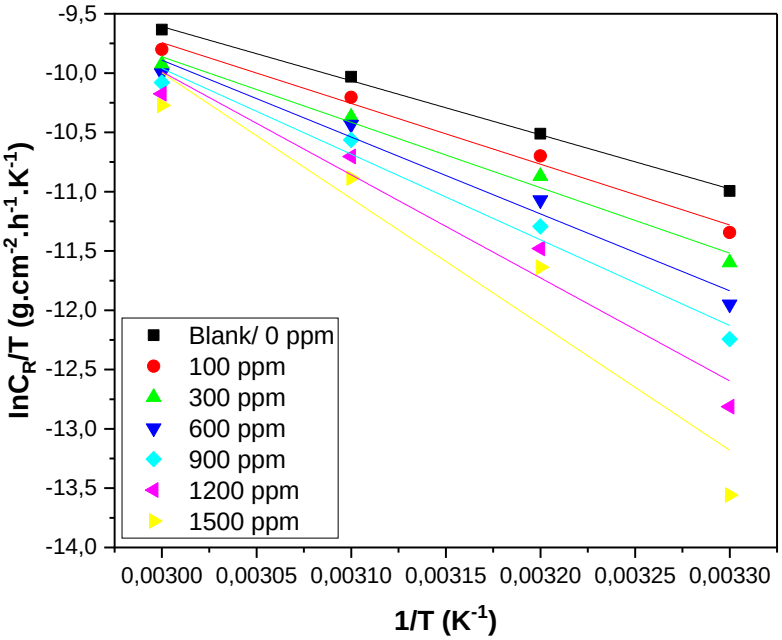


Figure 8. 7: Transition state plots for mild steel metal corrosion in 1.0 M H_2SO_4 medium with and without various concentrations of UV-radiated *H. kraussii* as the inhibitor.

© University of Venda

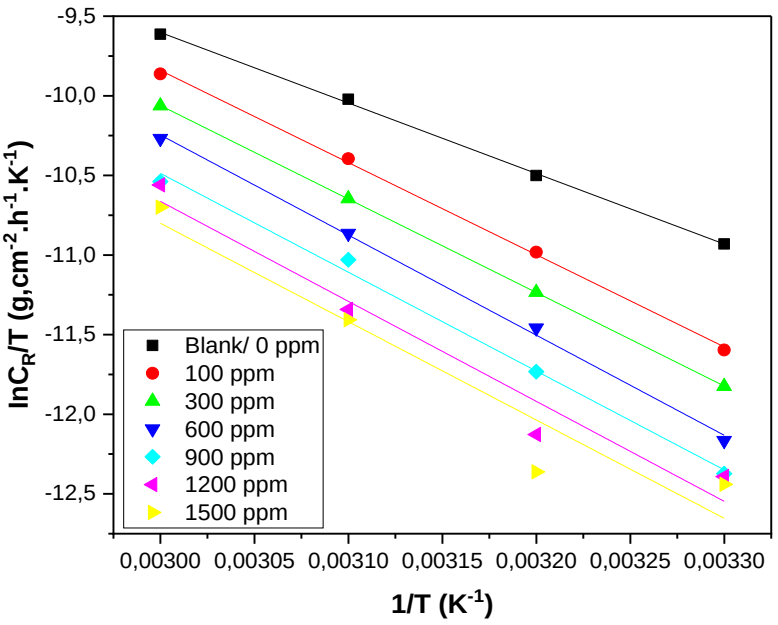


Figure 8. 8: Transition state plots for zinc metal corrosion in 1.0 M H_2SO_4 medium with and without various concentrations of UV-radiated *H. kraussii* as the extract inhibitor.

The E_a values were observed to be increasing with the rise in the inhibitor concentration, except for zinc metal, which showed some inconsistencies. This observation is an indication that the addition of inhibitors induced corrosion as the surface area was reduced because of the increase in the energy barrier. The formation of the film on the metal surface results in a lower corrosion rate because of the high activation energy [403]. The E_a values for the uninhibited system for mild steel and zinc metals (40.52047 and 39.45161 kJ.mol^{-1}) are lower than those of the inhibited system (45.23172-90.84123 kJ.mol^{-1}) for the two metals, respectively. This observation supports the formation of the absorptive layer. It is generally known that the values of E_a, which are less than 80 kJ.mol^{-1}, are indicative of physical adsorption; therefore, the mechanism of adsorption supported in this study is physical adsorption, except for the maximum temperature in mild steel.

© University of Venda

Table 8. 5: Transition state and Arrhenius parameters for the adsorption of various concentrations of UV-radiated *H. kraussii* in 1.0 M H_2SO_4 on mild steel and zinc metal.

Inhibitor	**Metals**	**Concentration of inhibitors (ppm)**	E_a **(kJ.mol^{-1})**	ΔH^* **(kJ.mol^{-1})**	ΔS^* **(J.mol^{-1}.k^{-1})**
UV-radiated *H. kraussii* extract	Mild steel	0.00	40.52047	37.89666	-163.75609
		100	45.23172	42.607323	-150.74507
		300	48.50780	45.88274	-141.91141
		600	56.51561	53.88885	-118.12820
		900	62.69151	60.04011	-100.26175
		1200	74.88151	72.25126	-63.85322
		1500	90.84123	88.20878	-16.04950
	Zinc	0.00	39.45161	36.82816	-166.90787
		100	50.74681	48.12175	-135.00913
		300	50.86323	48.79879	-134.82089
		600	54.88973	52.26358	-125.95605
		900	54.23639	51.61051	-129.91916
		1200	54.83976	52.21381	-29.57045
		1500	53.97368	51.34753	-133.3157

The transition state plot's slope, ΔH* /R, and intercept, In(CR/h+ΔS*/R), were used to compute the values of change in entropy (ΔS*) and enthalpy (ΔH*). It is possible to categorize the adsorption process between mild steel, zinc, and inhibitor molecules as either exothermic or endothermic. To elaborate, the exothermic process emits heat and can indicate physisorption or chemisorption, whereas the endothermic process absorbs heat and suggests chemisorption totally [169]. Physisorption is caused by charged metal and molecules interacting electrostatically. In contrast, chemisorption creates a coordinated bond by transferring or sharing charge from the inhibitor molecules to the metal surface. From Table 8.5, the values of ΔH^* are positive, which entails the fact that the dissolution process of mild steel and zinc in the presence of the inhibitor is endothermic, which entails a chemisorption kind of adsorption. Research indicates that the physisorption type of adsorption is linked with numerical values of ΔH* up to 41.86 kJ.mol^{-1}, while the chemisorption type of adsorption is associated with values around 100 kJ.mol^{-1} or higher [409]. From the table, it can be seen that the values of ΔH^* for

© University of Venda

mild steel and zinc are less than 100 $kJ.mol^{-1}$ and close to 41.86 $kJ.mol^{-1}$, which indicates chemisorption kind of adsorption.

For the mild steel and zinc metals, the values of ΔS^* are negative both in the presence and absence of inhibitor solutions. This suggests that rather than representing dissociation, the activated complex in the rate-determining step symbolizes association, indicating that there is a decrease in disordering as one proceeds from reactants to the activated complex.

[410]. The subsequent explanation can be applied to the negative values of ΔS^*: It's possible inhibitor molecules were freely circulating in the bulk solution before the inhibitors were adsorbed onto the zinc and mild steel surfaces. Put otherwise, there was a great deal of disorder among the inhibitor molecules. Entropy decreased as the inhibitor molecules were orderly adsorbed onto the mild steel and zinc surfaces due to the advancement in adsorption [411].

© University of Venda

8.5. UV-radiated H. *kraussii* extract in sulphuric acid

8.5.1. Mild steel

8.5.1.1. Open circuit voltage (OCV)

The OCV is essential in providing information about the thermodynamic stability of the sample surface in a given corrosive environment. OCV experiment was performed to study the effect of UV-radiated *H. kraussii* extract on the behaviour of mild steel metal in an H_2SO_4 solution. The OCV plot for mild steel electrodes in 98 % H_2SO_4 containing 100, 300, 600, 900, 1200, and 1500 ppm UV-radiated *H. kraussii* extract concentration is shown in Figure 8.9. The potential in the OCV varies with time because of the change in the oxidation tendency of the surface [412]. The OCV was performed for 3600 s in 1.0 M H_2SO_4 solution in the absence and presence of the extract inhibitor at 303 K. The OCV for the blank is found to have shifted towards more positive potential as compared to the OCV for the various concentrations of the inhibitor.

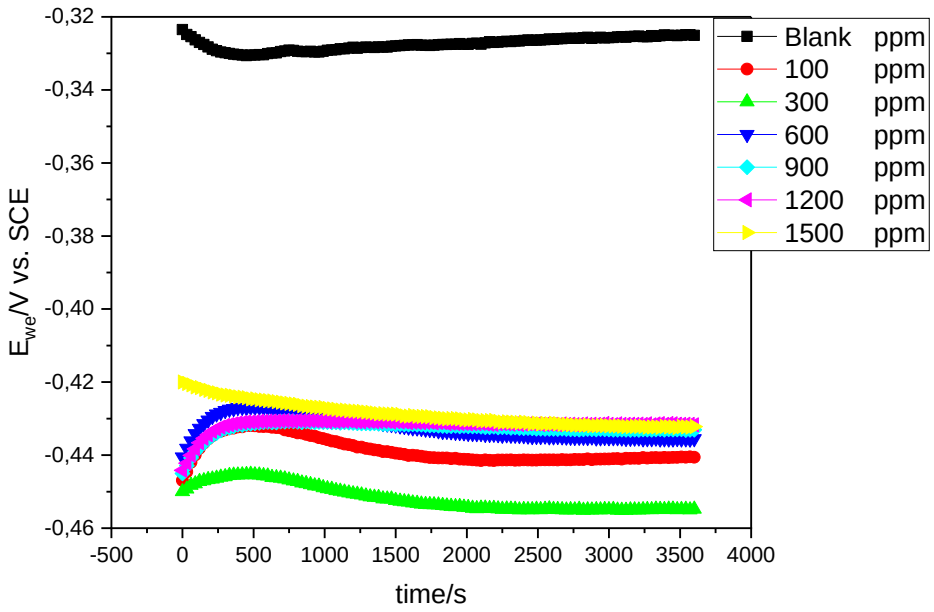


Figure 8. 9: Open circuit voltage for mild steel in 1.0 M H_2SO_4 medium and UV-radiated *H. kraussii* extract.

© University of Venda

8.5.1.2. Electrochemical impedance spectroscopy (EIS)

The electrochemical impedance spectroscopy technique is used to detect the changes in resistance on the substrate and how the charge carriers are rearranged at the electrolyte-metal interfacial capacitance [413]. Figure 8.10 represents the Nyquist plot for the blank and the inhibited system. The Nyquist plot for the blank and the inhibited system are of the same shape. This observation suggests that the corrosion mechanism was not altered upon the addition of the inhibitor. The Nyquist plot formed semi-circles that increased in diameter with increasing inhibitor concentration, which is an indication that the inhibitor was adsorbed onto the surface of the metal, protecting the metal from corrosion. In the event of dissolution, the presence of inhibitor molecules has no effect on the single charge transfer mechanism demonstrated by the existence of a single semi-circle [414].

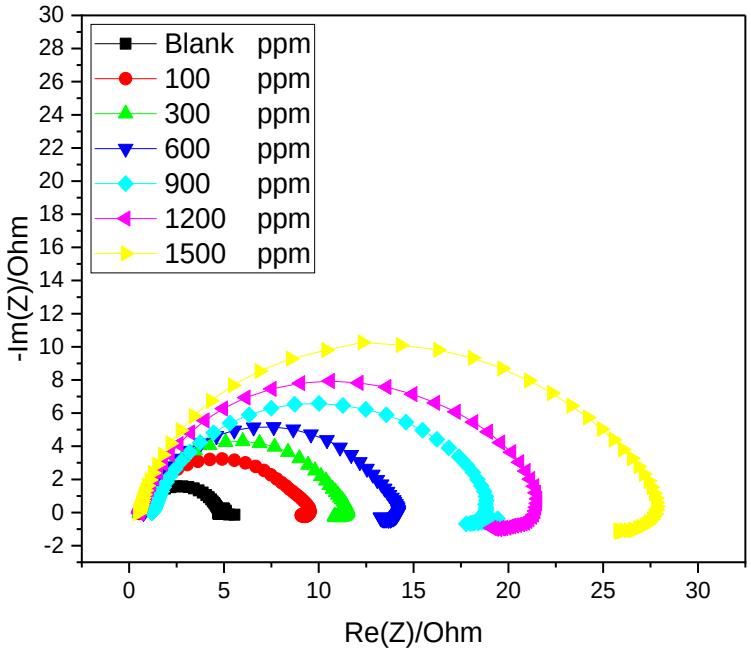


Figure 8. 10: Nyquist plot of m mild steel metal in 1.0 M H_2SO_4 with and without various concentrations of UV-radiated *H. kraussii* inhibitor compounds.

The magnitude of the Bode and the Bode phase angle plots are shown in Figure 8.11. The phase angles in the Bode plot are found to be increasing in the negative direction with a rise in the concentration of the extract inhibitor, which suggests the inhibitor adsorption onto the metal surface. The Bode phase angle shows one relaxation agreeing to a semi-circle in the Nyquist module. The maximum phase angle in the Bode plot is less than 90 ˚C. Such a tendency is due to the non-homogeneous character, unevenness in the surface, and variable dielectric constant [415]. The Bode modulus plot shows the single-phase downward curve in all the

© University of Venda

concentrations. The one phase correlates to the electric double layer of time constant, which is shown as the maximum value of log IZI at 1500 ppm. The lowest value of impedance modulus was found at 0 ppm solution and correlated to the lowest angle of the same solution in the Bode phase [416]. The phase angle values are approaching -90 ℃ at the intermediate frequencies. This phenomenon reveals the capacitative nature of the steel surface [417]. The increase in the log IZI values of the mild steel with rising inhibitor concentration indicates an improvement in the corrosion performance. This can be attributed to the formation of a protective layer on the metal surface due to the adhesion of the UV-radiated *H. kraussii* extract that redistricts the corrosion medium in the mild steel metal [417]. The extraction of the impedance parameters was performed by fitting the equivalent circuit represented in Figure 5.16 to the Nyquist plot, and the parameters obtained are tabulated in Table 8.6.

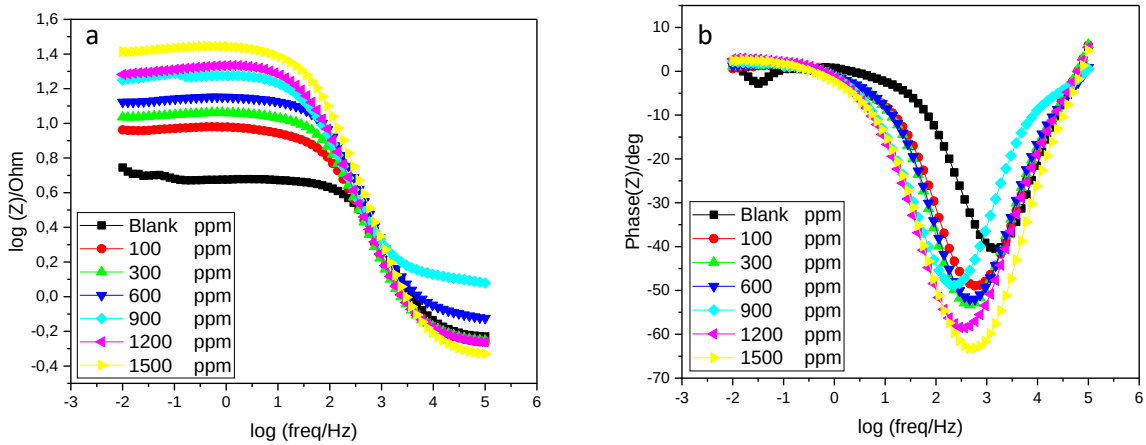


Figure 8. 11: Bode impedance magnitude plot (a) and Bode phase angle plot (b) of mild steel metal in 1.0 M H_2SO_4 solution in the absence and presence of various concentrations of UV-radiated *H. kraussii* inhibitor compound.

© University of Venda

Table 8. 6: EIS parameters like the solution resistance (R_s), resistance of charge transfer (R_{ct}), constant phase element (CPE), constant phase element constant (n2), double layer capacitance (C_{dl}) and percentage inhibition efficiency ($\%IE_{EIS}$), using UV-radiated *H. kraussii* in 1.0 M H_2SO_4 in mild steel metal.

Inhibitor	**Metal**	**Conc. (ppm)**	R_s **(Ωcm^2)**	**CPE (F.s$^{(a-1)}$) x10^{-3}**	**n2**	R_{ct} **(Ωcm^2)**	**C_{dl} (μF/cm^{-2})**	**τ (s)**	**$\%IE_{EIS}$**
UV-radiated *H. kraussii* extract	Mild steel	00	0.5866	0.3379	0.8377	4.221	23890.6700	0.1008	
		100	0.5517	0.5425	0.8177	8.751	5629.4522	0.0493	51.77
		300	0.5765	0.4274	0.8513	10.70	3459.6620	0.0370	60.55
		600	0.7731	0.3381	0.848	13.10	2355.0000	0.0309	67.78
		900	1.25	0.5375	0.8277	17.56	1377.2364	0.0242	75.96
		1200	05625	0.4309	0.8434	20.25	990.3615	0.0201	79.15
		1500	0.4746	0.2826	0.8565	26.52	585.1325	0.0155	84.08

From the inspection of Table 8.6, it is observed that the R_{ct} was found to increase with the rise in the inhibitor concentration. This increase led to a rise in the percentage inhibition efficiency, with the highest inhibition efficiency of 84.08% in the maximum concentration of 1500 ppm. It is evident in the table that increasing the UV-radiated *H. kraussii* extract concentration increases the R_{ct} values and decreases the double-layer capacitance (C_{dl}) values [418], leading to high %IE and increased n values. The time constant values for mild steel metal are observed to decrease as the concentration of the inhibitor increases. Based on this result, it can be inferred that the UV-radiated *H. kraussii* extract has a short adsorption time on mild steel metal, indicating a rapid adsorption process [282]. From the literature, it is stated that when the value of n is equal to -1, the CPE represents an inductor; when it is equal to 0, the CPE represent a pure resistor; and when it is equal to 1, the CPE represent a pure capacitor. We found the values of n to be in the range 0.8177 - 0.8565, which is very close to unity, suggesting that a pure capacitor is represented by CPE. The higher value of n in the inhibited solutions is an indication that the inhibitor extract forms an adsorptive layer on the metal surface and enhances their homogeneity [358].

© University of Venda

8.5.1.3. Potentiodynamic polarization (PDP)

Figure 8.12 shows the Tafel plot for mild steel in 1.0 M H_2SO_4 medium with and without various inhibitor concentrations. From the figure, it can be noted that anodic and cathodic branches are well represented. It can also be observed that the introduction of the inhibitor in the aggressive electrolyte managed to suppress both the anodic and cathodic current densities. This observation indicates that introducing the inhibitor in the corrosive solution reduced the corrosion rate of both the cathodic and anodic reactions. After extrapolating the Tafel plots linear parts to a junction with respect to the corrosion potential, valuable electrochemical parameters such as corrosion current density (i_{corr}), corrosion potential (E_{corr}), anodic Tafel slope (β_a), cathodic Tafel slope (β_c), and the calculated corrosion inhibition efficiency ($\%IE_{PDP}$) were obtained and are presented in Table 8.7 [293].

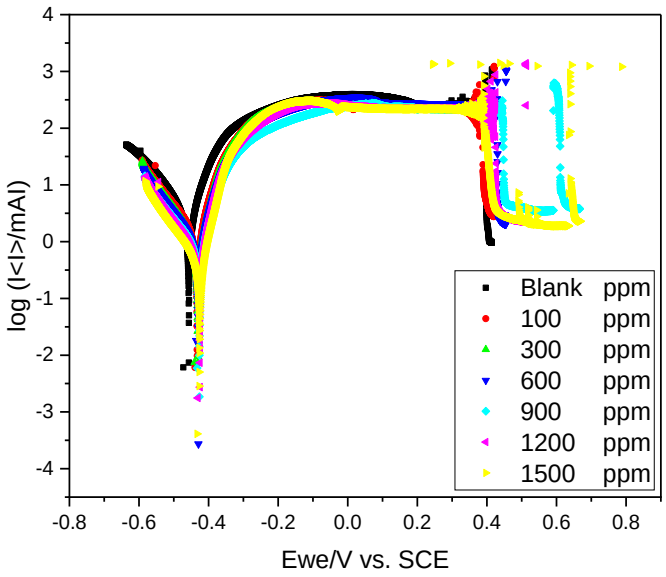


Figure 8. 12: Tafel plots for mild steel in 1.0 M H_2SO_4 solution with and without different UV-radiated *H. kraussii* extract inhibitor concentrations.

© University of Venda

Table 8. 7: PDP parameters, including anodic and cathodic Tafel slopes (βa and β_c), polarization resistance (R_P), corrosion potential (E_{corr}), and corrosion current density (i_{corr}), measured in 1.0 M H_2SO_4 using different UV-radiated *H. kraussii* inhibitor concentrations.

Inhibitor	**Inhibitor Conc. (ppm)**	**-E_{corr} (mV) with Ag/AgCl**	**i_{corr} (mA.cm^{-2})**	**R_P (Ω)**	**βa (mV.dec^{-1})**	**βc (mV.dec^{-1})**	**% IE$_{PDP}$**
Blank	0.00	-456.498	3556.426	5.64	74.5	143.0	
UV-radiated *H. kraussii* extract	100	-432.109	1395.884	10.2	55.8	130.0	60.75
	300	-430.585	1042.019	13.5	52.2	120.5	70.70
	600	-429.056	892.336	15.2	53.3	126.2	74.91
	900	-426.507	669.418	18.5	50.8	126.1	81.18
	1200	-424.099	513.944	20.2	41.1	118.3	85.55
	1500	-426.449	397.202	28.5	43.4	114.1	88.83

In the potentiodynamic polarization method, the polarization behaviour of a sample is investigated as a current response in the form of the function of the applied potential [419]. Table 8.7 shows that the values of the cathodic and anodic current densities obtained in the presence of the UV-radiated *H. kraussii* extract were smaller compared to those acquired in the absence of the extract. This makes the UV-radiated *H. kraussii* extract classified as a mixed corrosion inhibitor [276]. It can also be observed that the i_{corr} values were drastically reduced when the inhibitor was introduced to the corrosive electrolyte. For example, the i_{corr} value of the blank, which is 3556.426 mA.cm^{-2} was reduced to 397.202 mA.cm^{-2} upon the inhibitor presence, which yielded 88.83 % IE. This reduction is an indication of the drop in the deterioration rate of the mild steel metal, which suggests that the inhibitor molecules interacted with the metal surface, thereby shielding the metal active sites and preventing attacks from the corrosive electrolyte [293]. The %IE$_{PDP}$ was found to increase with the rise in the inhibitor's concentrations. The highest %IE$_{PDP}$ was found to be 88.83% for the highest concentration of the extract, which is 1500 ppm. It can be said that the inhibitive action of the UV-radiated *H. krausssii* extract could be due to the adsorption of its molecules on the surface of mild steel metal, making a mass and charge transfer barrier between the metal and the environment [420]. The E_{corr} values of the extract solution do not follow a definite pattern [419]. From the literature, the blank and the inhibitor E_{corr} values difference, which is greater than -85 mV, is indicative of either anodic or cathodic inhibitor [421], and the E_{corr} difference, which is less than or equal to -85 mV, is indicative of a mixed type inhibitor. From the results obtained, the

© University of Venda

E_{corr} difference is within -85 mV, which is an indication that the studied inhibitor is a mixed type [217]. This was also reported by Liao et al. (2023) [422]. The introduction of the extract in the aggressive solution led to the shifting of the E_{corr} values to more negative values compared to the blank sample. This is an indication of the cathodic inhibitory ability of extract in the corrosive solution. Since both the cathodic and anodic branches of the different concentrations of the extract are moved towards lower current densities than those of the blank, It can be concluded that the inhibition mechanism of the extract is of a mixed nature. The values of the cathodic and anodic Tafel slopes showed variation with respect to that of the blank upon introducing the extract, indicating that the extract managed to suppress both the cathodic and anodic reactions. With that said, the UV-radiated *H. kraussii* extract acts as a mixed inhibitor [356].

8.5.2. Zinc metal

8.5.2.1. Open circuit voltage (OCV)

The Open Circuit Voltage, also known as the corrosion potential (E_{corr}), allude to the working electrode's potential when no external current is applied to the system. It is widely known that the inhibited metal OCV values are more positive than those of the uninhibited metal. In the inhibitor free-solution, the OCV potential moved towards the negative potential direction, indicating the corrosion product's desorption on the metal surface [294]. When the inhibition coating on the metal fades away over time, the OCV values tend to become more negative until they equal the corrosion potential of the metal substrate. The OCV measurements can also give information about the disbandment of the coatings and the passive or active states of the metal substrate; for instance, a shift in the OCV towards more positive values when the inhibitors are present in the system is an indication of corrosion inhibition. The OCV-time profile for the zinc working electrode in the corrosive medium was monitored for 3600 s, which was found to be enough for the corrosion system to reach an equilibrium [292]. As can be observed from Figure 8.13, the time profile of the bare metal has a more negative potential than the inhibited metal profile, which shifted towards a less negative potential. This suggests that anodic protection could be the favoured process. No stable trend is observed in the OCV variation with time for the electrodes without or with varying concentrations of the inhibitor, indicating that the extract functions as a mixed type of inhibitor [293].

© University of Venda

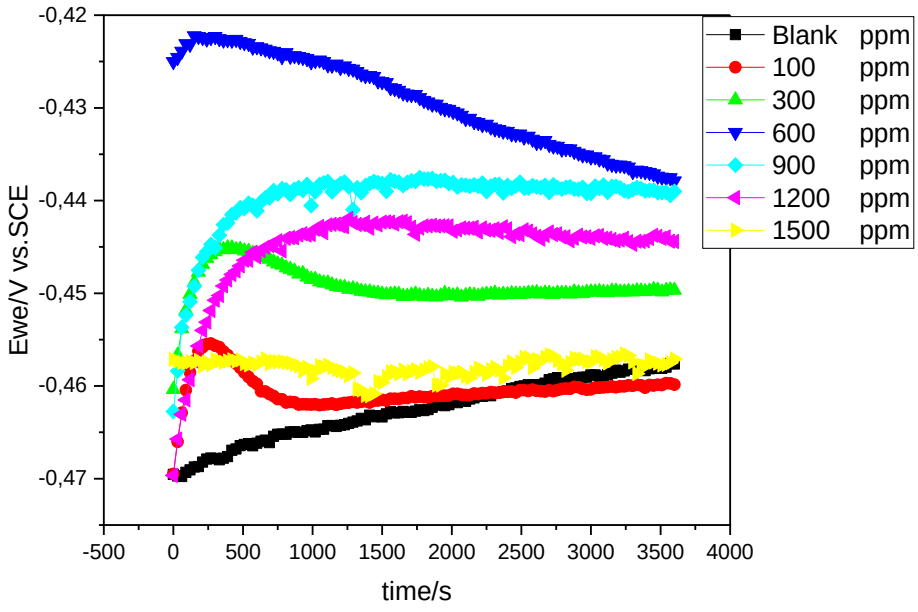


Figure 8. 13: Open circuit voltage for zinc in 1.0 M H_2SO_4 medium and UV-radiated *H. kraussii*.

8.5.2.2. Electrochemical impedance spectroscopy (EIS)

Electrochemical impedance spectroscopy is a very useful technique that is greatly utilised to evaluate a material's corrosion processes, coating and anti-corrosive performance. It is regarded as a destructive technique, which makes it suitable to be used to track the evaluation of a coated system subjected to an accelerated test and provide quantitative information about the corrosion kinetics and mechanisms [292]. The formation of the single Nyquist semi-circle in the absence and presence of the UV-radiated *H. kraussii* extract suggests that the working electrode's dissolution is a charge transfer process [297]. The Nyquist semi-circle of the blank and the inhibitor have similar shapes, which infer the same corrosion mechanism [423]. Furthermore, in the presence of the examined UV-radiated *H. kraussii* concentrations, the diameters of the Nyquist semi-circles are larger than those of the uninhibited (blank) and are increasing with an increase in the extract concentration [424, 425]. This indicates that the protective coating has been extremely well deposited on the metal surface and that the aggressive attack by Cl^- ions has been effectively prevented. The zinc metal in an aggressive solution demonstrates increased resistance in the presence of various UV-radiated *H. kraussii* concentrations, and the %IE increases as the UV-radiated *H. kraussii* extract concentration increases [417].

© University of Venda

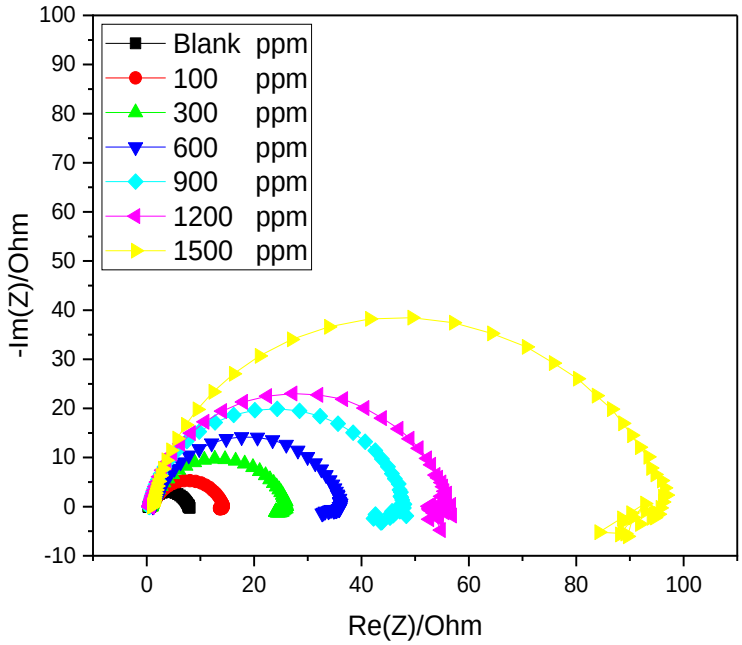


Figure 8. 14: Nyquist plot of zinc metal in 1.0 M H_2SO_4 solution with and without various concentrations of the UV-radiated *H. kraussii* extract inhibitor.

The Bode plots are represented in Figure 8.15. A single peak was observed in the phase angle both in the absence and presence of various concentrations of UV-radiated *H. kraussii* extract, confirming that a single time constant is present, just like in the Nyquist plot. The increase in the extract inhibitor concentration caused an increase in the impedance magnitude over the whole frequency range. This observation suggests the adsorption of the UV-radiated *H. kraussii* molecules on the surface of the metal [426]. The broadening nature of the Bode plots at higher concentrations indicated increased adsorption of the inhibitor extract molecules on the surface of the metal [427]. The high-frequency section of the Bode and phase angle plots explains the inhomogeneous surface layer behaviour, whilst the low-frequency region depicts the charge transfer reaction phenomenon [428]. In the phase angle and impedance plots, at 0 and 4 Hz, the values of the phase angle and log IZI are close to zero, which is an indication of the resistive behaviour of zinc metal and corresponds to the solution resistance confined between the reference and the zinc metal electrode [296]. The extraction of the impedance parameters was performed by fitting the equivalent circuit represented in Figure 5.16 to the Nyquist plot, and the parameters obtained are tabulated in Table 8.8.

© University of Venda

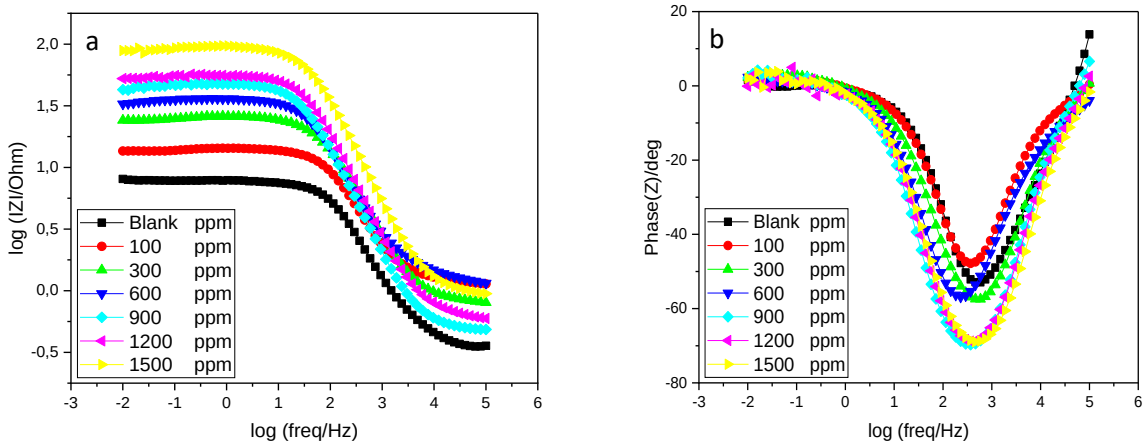


Figure 8. 15: Bode impedance magnitude plot (a) and Bode phase angle plot (b) of zinc metal in 1.0 M H_2SO_4 with and without various concentrations of UV-radiated *H. kraussii* extract inhibitor.

Table 8. 8: EIS parameters like the solution resistance (R_s), resistance of charge transfer (R_{ct}), constant phase element (CPE), constant phase element constant (n2), double layer capacitance (C_{dl}) and percentage inhibition efficiency ($\%IE_{EIS}$), using UV-radiated *H. kraussii* in 1.0 M H_2SO_4 in zinc metal.

Inhibitor	**Metal**	**Conc. (ppm)**	R_s **(Ωcm²)**	**CPE (F.S (a-1)**	**n2**	R_{ct} **(Ωcm²)**	C_{dl} **(μF/cm⁻²)**	**τ (s)**	**%IE$_{EIS}$**
UV-radiated *H. kraussii* extract	Zinc	00	0.3597	0.5629	0.8369	7.507	7020.9244	0.0527	
		100	1.1800	0.3143	0.8576	12.87	2337.3283	0.0301	41.53
		300	0.8163	0.2306	0.8527	24.5	673.8402	0.0165	69.36
		600	1.2530	0.2945	0.8309	34.59	326.1905	0.0113	78.30
		900	0.4963	0.1949	0.9025	46.06	173.5252	0.0080	83.70
		1200	0.6257	0.1543	0.8907	54.48	126.9367	0.0069	86.22
		1500	0.9681	84.563	0.8867	92.27	44.8293	0.0041	91.86

From Table 8.8 of the results inspection, the inhibition efficiency was found to increase with an increase in the concentration of the extract. The maximum percentage inhibition efficiency was found to be 91.86% for the maximum concentration of the extract, which is 1500 ppm. R_{ct} values of the extract were found to be higher than that of the blank, and they increased with an increase in the extract concentration [429]. The presence of the UV-radiated *H. kraussii* extracts enhanced the (R_{ct}) values, which also increased corrosion inhibition efficiency. The decrease in the CPE values upon the introduction of the extract in the corrosive electrolyte

© University of Venda

suggests that the surface smoothness is increasing because of the extract adsorption on the surface of the metal. This is further supported by the increase in the phase angles in the Bode plots [297]. The constant phase element exponent (n) values describe the corrosion process on the metal surface. Its values range from -1 to 1, in which the value of -1 represents the inductance, 1 represents the capacitor, and 0 represents the resistor. It is clear in the table that the n values are getting closer to 1, indicating that the interface may be capacitive. The high value of n indicates that the extract enhanced the homogeneity of the zinc metal surface by forming a coating on it. Although the CPE values do not properly trend, they typically decrease as the extract concentration rises. This shows that the extract is absorbed into the metal surface and prevents the development of corrosion and hostile cells. From the table, it is evident that the introduction of the extract inhibitor in the corrosive sulphuric solution resulted in a decrease in the double-layer capacitance (C_{dl}) [430], which is an indication of zinc metal increased corrosion resistance with increasing extract concentration. The C_{dl} decreased from 2337.3283 $\mu F/cm^{-2}$ to 44.8293 $\mu F/cm^{-2}$ with increasing extract inhibitor concentration. The time constant was observed to be decreasing with an increase in the extract inhibitor concentrations. For the blank, the time constant is found to be 0.0527 s, but at the highest concentration of 1500 ppm, it is found to be 0.0041 s, showing a sharp decline in the time constant. Based on this result, it can be inferred that the UV-radiated *H. kraussii* extract has a short adsorption time on zinc metal, indicating a rapid adsorption process [282]. The time constant has a direct proportional correlation with the double-layer capacitance.

8.5.2.3. Potentiodynamic polarization (PDP)

Figure 8.16 represents the Tafel plot for zinc in 1.0 M H_2SO_4 solution in the absence and presence of UV-radiated *H. kraussii* extract. From the figure, it can be observed that introducing the inhibitor in the corrosive electrolyte reduced both the cathodic and anodic branches of the Tafel plots compared to that of the blank system. Since both the cathodic and anodic branches of the different concentrations of the extract are shifted towards lower current densities than the blank. It can be concluded that the inhibition mechanism of the extract is of a mixed nature. This observation indicates that the inhibitor was adsorbed onto the surface of the metal, thereby forming a protective film. After extrapolating the linear parts of the Tafel plots to a junction with respect to the corrosion potential, valuable electrochemical parameters such as corrosion potential (E_{corr}), corrosion current density (i_{corr}), anodic Tafel slope (β_a),

© University of Venda

cathodic Tafel slope (β_c), and the calculated corrosion inhibition efficiencies (%IE_{PDP}) were obtained and presented in Table 8.9 [293].

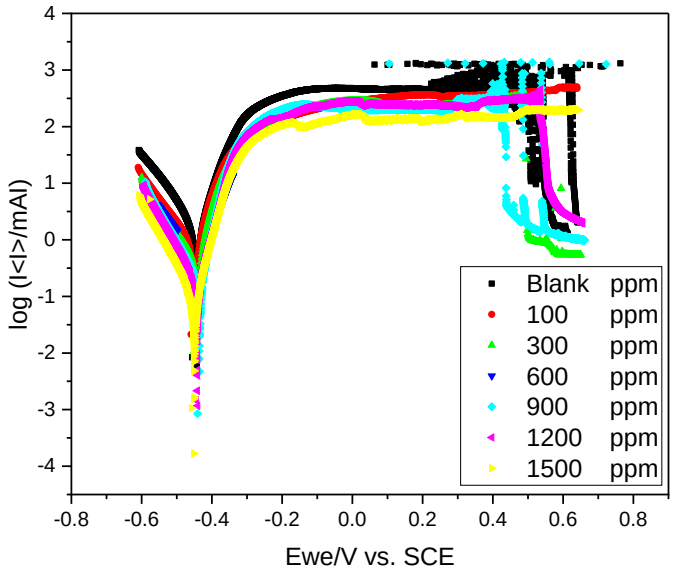


Figure 8. 16: Tafel plots for zinc in 1.0 M H_2SO_4 with and without different UV-radiated *H. kraussii* inhibitor extract concentrations.

Table 8. 9: PDP parameters, including anodic and cathodic Tafel slopes (βa and β_c), polarization resistance (R_P), corrosion potential (E_{corr}), and corrosion current density (i_{corr}), measured in 1.0 M H_2SO_4 using different UV-radiated *H. kraussii* inhibitor concentrations.

Inhibitor	**Inhibitor Conc. (ppm)**	**-E_{corr} (mV) With Ag/AgCl**	**i_{corr} (mA.cm^{-2})**	**R_P (10^{-1}) (Ω)**	**β_a (mV.dec^{-1})**	**β_c (mV.dec^{-1})**	**% IE_{PDP}**
Blank	0.00	-428.680	864.361	22.7	71.3	121.6	
UV-radiated *H. kraussiii*	100	-448.013	795.799	16.6	54.4	121.6	07.93
	300	-439.802	394.945	25.8	42.9	114.0	54.31
	600	-433.757	389.391	38.1	59.8	118.8	54.95
	900	-435.316	191.636	52.5	41.2	94.4	77.83
	1200	-440.171	177.495	67.5	56.4	93.7	79.47
	1500	-451.249	114.875	120	49.0	93.5	86.71

In the potentiodynamic polarization method, the polarization behaviour of a sample is investigated as a current response in the form of the function of the applied potential [419]. From the table, the values of the cathodic and anodic current densities obtained in the presence of the UV-radiated *H. kraussii* extract were smaller compared to those acquired in the absence

© University of Venda

of the extract. This makes the UV-radiated *H. kraussii* extract classified as a mixed corrosion inhibitor [276]. It can also be observed that the i_{corr} values were drastically reduced when the inhibitor was introduced to the corrosive electrolyte. For example, the i_{corr} value of the blank, which is 864.361 $mA.cm^{-2}$ was reduced to 114.875 $mA.cm^{-2}$ upon the inhibitor presence, which yielded a good corrosion inhibition efficiency. This decrease shows that the rate of zinc metal deterioration has decreased, indicating that the inhibitor molecules have interacted with the metal's surface to protect its active sites from the corrosive electrolyte [293]. The E_{corr} values of the extract solution do not follow a definite pattern [419]. From the results obtained, the E_{corr} difference between the blank and different concentrations of the inhibitor is within -85 mV, which is an indication that the inhibitor investigated is a mixed type [431]. The introduction of the extract in the corrosive solution led to the shifting of the E_{corr} values to more negative values compared to the blank sample. This is indicative of the cathodic inhibitory ability of extract in the corrosive solution. With increasing concentrations, a decrease in the current densities was observed with respect to the blank. This behaviour confirms the increase in the energy barrier of the zinc steel dissolution process and the rise in the relative ability of a material to resist corrosion [432]. Since both the anodic and cathodic branches of the different concentrations of the extract are shifted towards lower current densities than the blank. It can be concluded that the inhibition mechanism of the extract is of a mixed nature. The values of the cathodic and anodic Tafel slopes showed variation with respect to that of the blank upon the introduction of the extract, which indicates that the extract managed to suppress cathodic and anodic reactions. With that said, the UV-radiated *H. kraussii* extract acts as a mixed inhibitor [356]. The percentage inhibition efficiency was found to increase with the increase in the inhibitor concentrations. The highest inhibition efficiency was found to be 86.71% for the highest concentration of the extract, which is 1500 ppm. It can be said that the inhibitive action of the UV-radiated *H. kraussii* extract could be due to the adsorption of its molecules on the zinc surface, making a barrier for mass and charge transfer between the metal and the environment [420].

© University of Venda

8.6. Fourier Transform Infrared Spectroscopy (FTIR)

8.6.1. Mild steel

From Figure 8.17, it can be observed that the peaks display some variation in the adsorption peaks. The four spectra are used to find the functional groups present on them and then to compare and look for the functional groups present on the plant extract that were also found on the mild steel surface after gravimetric analysis. The functional groups that managed to survive the acid aggressiveness and adsorb on the surface of the metal are the ones that can be said to have caused the mild steel corrosion inhibition. Not only the remaining functional groups are responsible for the corrosion adsorption, but also the new functional groups which might form during the corrosion reaction process involving plant extract, H_2SO_4, water solution and mild steel metal can contribute to the corrosion inhibition efficiency if they are found adsorbed on the metal surface. Table 8.10 shows all the possible functional groups obtained from the four spectra. In determining which functional groups managed to course the corrosion inhibition, the first and the last columns were compared, and the functional groups present in the last column are responsible for hindering mild steel's corrosion process. These functional groups include O-H carboxylic acid, O-H alcohol, N-H amines, N-H amide, C≡C alkyne, C=C alkane, Sp^3 C-O and C-H aromatic.

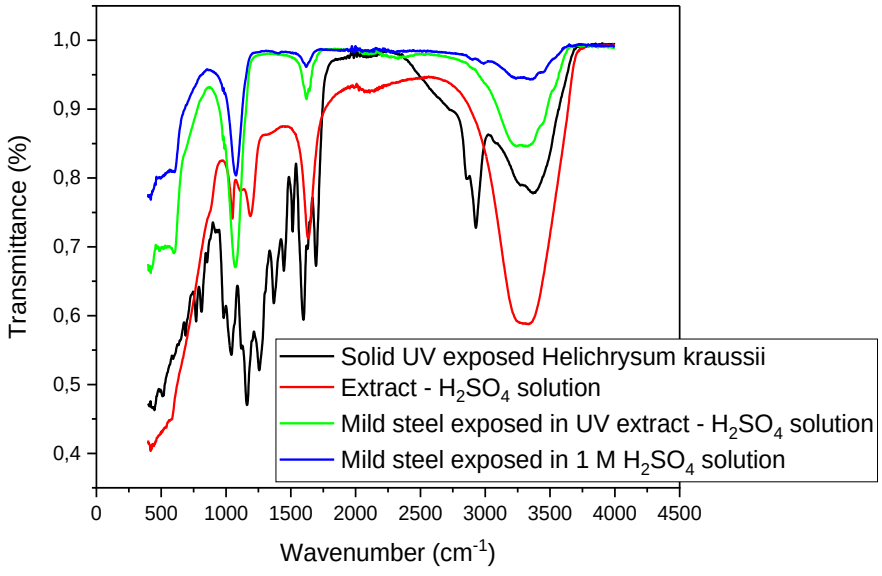


Figure 8. 17: FTIR spectra for solid UV-radiated *H. kraussii* plant extract (Black), 1500 ppm UV-radiated *H. kraussii* plant extract – 1.0 M H_2SO_4 solution (Red), the layer formed on mild steel metal exposed in 1500 ppm UV-radiated *H. kraussii* plant extract – 1.0 M H_2SO_4

© University of Venda

solution (Green) and corrosion products formed on Mild steel metal exposed in 1.0 M H_2SO_4 solution (black).

Table 8. 10: Possible functional groups present in solid UV-radiated *H. kraussii* plant extract, corrosion products formed on mild steel metal exposed in 1.0 M H_2SO_4 solution, 1500 ppm UV-radiated *H. kraussii* plant extract – 1.0 M H_2SO_4 solution and layer formed on mild steel metal exposed in 1500 ppm UV-radiated *H. kraussii* plant extract – 1.0 M H_2SO_4 solution.

	Functional Groups			
Bands position (cm^{-1})	**Solid UV-radiated *H. kraussii***	**Mild steel metal exposed in H_2SO_4 blank solution**	**UV-radiated *H. kraussii* - H_2SO_4 solution**	**Mild steel metal exposed in UV-radiated *H. kraussii* - H_2SO_4 solution**
2400 – 3600	O-H Carboxylic acid	O-H Carboxylic acid	O-H Carboxylic acid	O-H Carboxylic acid
3300 – 3500	O-H alcohol	O-H alcohol	O-H alcohol	O-H alcohol
3200 – 3400	N-H amine N-H amide	N-H amine N-H amide	N-H amine N-H amide	N-H amine N-H amide
3260 – 3390	Sp C-H (C≡C-H)			
2850 – 2960				
2700 – 2900				
2200 – 2270		nitrile C≡N		
2100 – 2250		nitrile C≡N C≡C alkyne	C≡C alkyne	C≡C alkyne
1680 – 1720	C=O ketone C=O aldehyde			
1600 – 1650		C=C alkene	C=C alkene	C=C alkene
1500 – 1600				
1500 – 1570	NO_2 Nitro C=C aromatic			
1450 – 1470				
1200 – 1250				
1000 – 1200	Sp^3 C-O	Sp^3 C-O	Sp^3 C-O	Sp^3 C-O
900 – 1000	C-H aromatic	C-H aromatic		C-H aromatic
600 – 900	C-Cl chloride C-C alkane C-H aromatic	C-H aromatic		

© University of Venda

8.6.2. Zinc metal

Figure 8.18 shows the four spectra of the four samples analysed using the FTIR instrument. The caption in the figure distinguishes the four spectra. From the figure observation, it can be seen that the four spectra show the vibration and shift in the adsorption peaks intensities and frequencies, which, from the literature, is associated with the metal surface and inhibitor interaction, which can also be associated with the inhibitor adsorption on the surface of the metal thereby causing corrosion inhibition [433, 434]. The table shows all the possible functional groups present on the four spectra analysed. The most important two spectra that can help in the determination of the functional groups that cause corrosion inhibition efficiency are the black and green spectra in Figure 8.18 and the first and last columns in Table 8.10. The black spectrum, which is represented by the first column in the table, is the plant extract used as a corrosion inhibitor, and the green spectrum, represented by the last column on the table, represents the corrosion products formed on the surface of zinc metal due to the adsorption of the UV-radiated *H. kraussii* plant extract. The functional groups that remained attached to the metal surface after gravimetric analysis are the ones that have been responsible for the formation of the film on the metal surface, thereby reducing the rate of corrosion of the zinc metal. Such functional groups can be found in the last column in comparison with the first column in Table 8.11, which are O-H carboxylic acid, O-H alcohol, N-H amine, N-H amide, Sp C-H (C≡C-H), C≡C alkyne, C=C alkene, Sp^3 C-O C-H alkane, C-H aromatic, with most of these found in 3260 – 3600 cm^{-1} adsorption band.

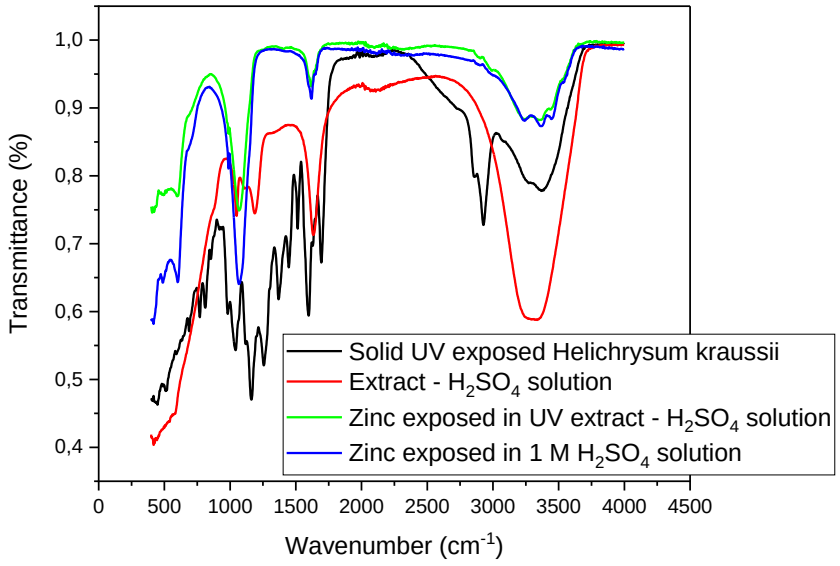


Figure 8. 18: FTIR spectra for solid UV-radiated *H. kraussii* plant extract (Black), 1500 ppm UV-radiated *H. kraussii* plant extract – 1.0 M H_2SO_4 solution (Red), the layer formed on zinc

© University of Venda

metal exposed in 1500 ppm UV-radiated *H. kraussii* plant extract – 1.0 M H_2SO_4 solution (Green) and corrosion products formed on zinc metal exposed in 1.0 M H_2SO_4 solution (black).

Table 8. 11: Possible functional groups present in solid UV-radiated *H. kraussii* plant extract, corrosion products formed on zinc metal exposed in 1.0 M H_2SO_4 solution, 1500 ppm UV-radiated *H. kraussii* plant extract – 1.0 M H_2SO_4 solution and layer formed on zinc metal exposed in 1500 ppm UV-radiated *H. kraussii* plant extract – 1.0 M H_2SO_4 solution.

	Functional Groups			
Bands position (cm^{-1})	**Solid UV-radiated *H. kraussii***	**Zinc metal exposed in H_2SO_4 blank solution**	**UV-radiated *H. kraussii* - H_2SO_4 solution**	**Zinc metal exposed in UV-radiated *H. kraussii* - H_2SO_4 solution**
2400 - 3600	O-H Carboxylic acid	O-H Carboxylic acid	O-H Carboxylic acid	O-H Carboxylic acid
3300 - 3500	O-H alcohol	O-H alcohol	O-H alcohol	O-H alcohol
3200 - 3400	N-H amine N-H amide	N-H amine N-H amide	N-H amine N-H amide	N-H amine N-H amide
3260 - 3390	Sp C-H (C≡C-H)	Sp C-H (C≡C-H)		Sp C-H (C≡C-H)
2850 - 2960				
2700 - 2900				
2200 - 2270				
2100 - 2250		C≡C alkyne	C≡C alkyne	C≡C alkyne
1680 - 1720	C=O ketone C=O aldehyde			
1600 - 1650		C=C alkene	C=C alkene	C=C alkene
1500 - 1600				
1500 - 1570	NO_2 Nitro C=C aromatic			
1450 - 1470				
1200 - 1250				
1000 - 1200	Sp^3 C-O	Sp^3 C-O	Sp^3 C-O	Sp^3 C-O
900 - 1000	C-H alkane	C-H alkane		C-H alkane
600 - 900	C-Cl chloride C-C alkane C-H aromatic	C-H aromatic		C-H aromatic

© University of Venda

CHAPTER 9

CONTACT ANGLES

© University of Venda

9. Introduction

This chapter discusses the surface morphology of mild steel, zinc and aluminium metal based on contact angle in hydrochloric and sulphuric acid in the absence and presence of non-radiated and UV-radiated *H. kraussii* extract.

9.1. Wettability study

The wettability of the surface of metals by water is an essential procedure for industries and chemical technologies, like in the corrosion processes of metals, for the contact of electrolyte-electrode in the electrochemical synthesis or the separation of the water-oil system in the oil industry and in many other applications such as corrosion behaviour or metallic nanoparticles preparation [435]. The effectiveness of the corrosion inhibitor in an acidic environment can also be determined from the water contact angle. The metal surface composition and wettability tend to change when the inhibitor molecules are adsorbed onto the metal surface [436]. The degree of wetness or wettability is the tendency of a liquid to maintain contact with the solid surface. Surface chemistry, free energy, surface shape, and liquid characteristics generally affect a surface's wettability. A liquid's wettability is typically described in terms of the liquid drop's contact angle. The contact angle is the angle formed between a tangent to the drop surface at the point of contact and a tangent to the supporting metal surface. The drop shape gives the adhesion and wettability between the metal surface and the liquid drop [437]. As a result, wettability decreases with increasing contact angle and vice versa. Hydrophilic surfaces have a contact angle of $< 90°$, whereas hydrophobic surfaces have a contact angle of $\geq 90°$ [438]. Hydrophilic surfaces have a high affinity for water, whereas hydrophobic surfaces have less attraction. It is obvious that a surface's hydrophobicity or hydrophilicity will impact how much corrosion occurs on the surface of steel when there is water present [439].

Inhibitors act as surfactants and adsorb to the internal metal surface, forming a hydrophobic layer that prevents water contact with the metal surface [437]. From the results obtained, it can be observed that the introduction of both non-radiated and UV-radiated *H. kraussii* extract resulted in an increase in the contact angle and in some cases, changed the metal surface to lipophilic layer, as the contact angles observed were higher than $\geq 90°$ [440]. Hydrophobic surfaces have been found to have better corrosion resistance [441]. Further discussion on the wettability of mild steel, zinc and aluminium metals in the presence of an aggressive solution is provided below.

© University of Venda

9.1.1. Mild steel metal in 1.0 M HCl for non and UV-radiated *H. kraussii* extract

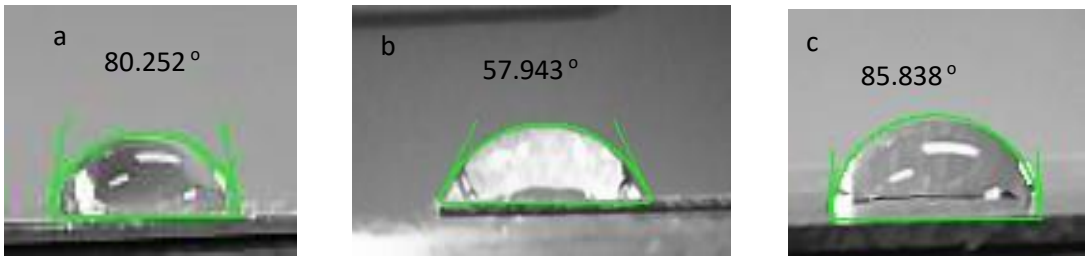


Figure 9. 1: Surface wettability behaviour of (a) polished untreated mild steel substrate, (b) mild steel substrate after 8 hours of immersion in 1.0 M HCl medium with no inhibitor, and (c) in the presence of 1500 ppm of Non-radiated *H. kraussii*.

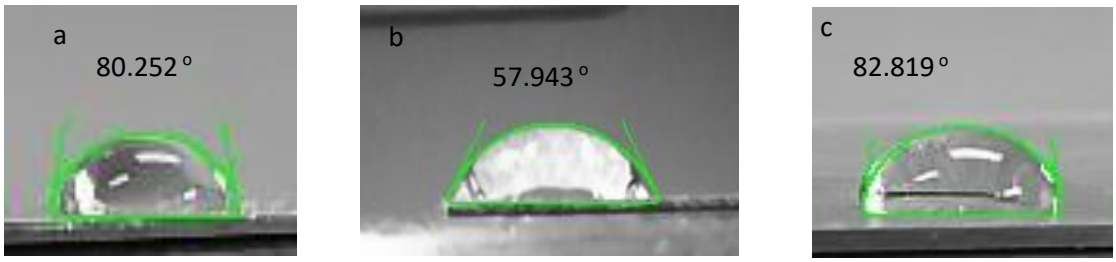


Figure 9. 2: Surface wettability behaviour of (a) polished untreated mild steel substrate, (b) mild steel substrate after 8 hours of immersion in 1.0 M HCl medium with no inhibitor, and (c) in the presence of 1500 ppm of UV-radiated *H. kraussii*.

For mild steel metal in Non-radiated and UV-radiated *H. kraussii* extract in hydrochloric acid, the contact angles observed for metal (c) in Figures 1 and 2, were < 90˚ which means that the introduction of the extract inhibitor did not change the metal surface. The angles observed for the extracted treated metals were 85.838 and 82.819° for non-radiated and UV-radiated extracts, higher than that of the untreated metal, 80.252° and the acid-treated metal, 57.94˚. The increase in the contact angle in the presence of the inhibitor is clear evidence that the extract inhibitors fortify the metal against the corrosion attack.

© University of Venda

9.1.2. Mild steel metal in 1.0 M H_2SO_4 for non and UV-radiated *H. kraussii* extract

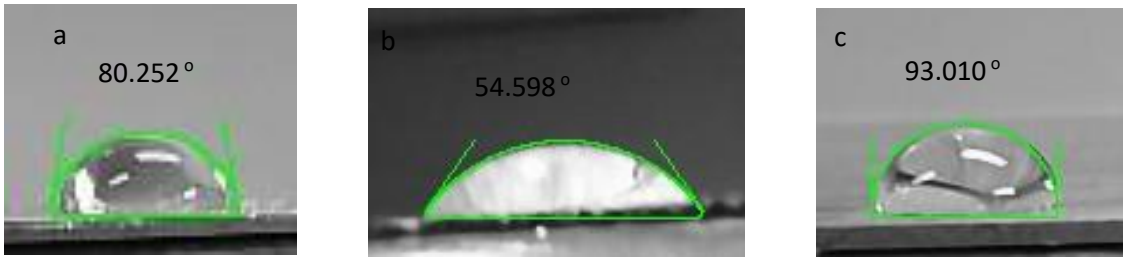


Figure 9. 3: Surface wettability behaviour of (a) polished untreated mild steel substrate, (b) mild steel substrate after 8 hours immersion time in 1.0 M H_2SO_4 medium without inhibitor, and (c) in the presence of 1500 ppm of Non-radiated *H. kraussii*.

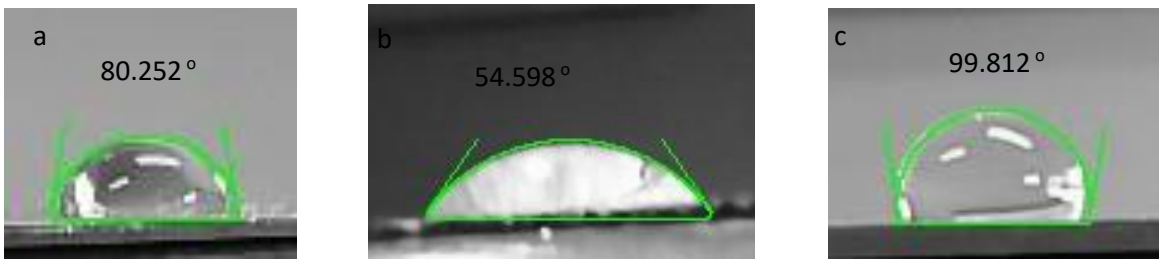


Figure 9. 4: Surface wettability behaviour of (a) polished untreated mild steel substrate, (b) mild steel substrate after 8 hours of immersion in 1.0 M H_2SO_4 medium with no inhibitor, and (c) in the presence of 1500 ppm of UV-radiated *H. kraussii*.

In sulphuric acid, the angle for the non-radiated and UV-radiated extract treated metals were found to be > 90° which means that the adsorption of the inhibitor onto the metal surface changed the metal surface from hydrophilic to hydrophobic [442, 443]. The angles obtained were 93.010˚ and 99.812° for non-radiated and UV-radiated extracts, respectively. The drop in the contact angle in the presence of HCl revealed a rise in the wettability of the metal surface due to corrosion attack [438].

© University of Venda

9.1.3. Zinc metal in 1.0 M HCl for non and UV-radiated *H. kraussii* extract

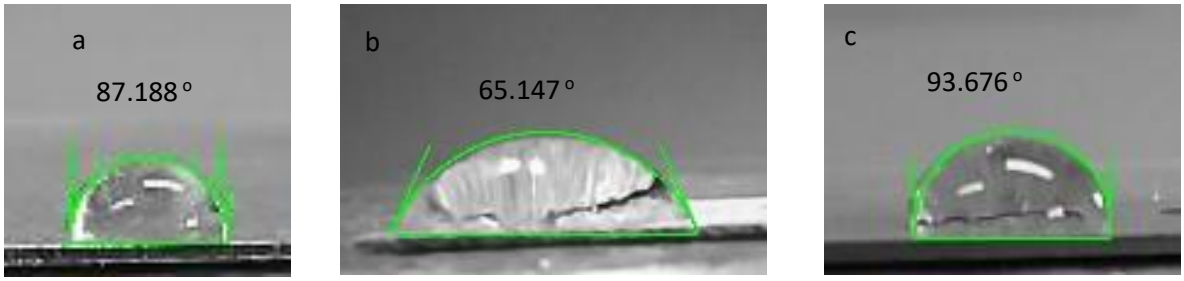


Figure 9. 5: Surface wettability behaviour of (a) polished untreated zinc metal substrate, (b) zinc metal substrate after 8 hours of immersion in 1.0 HCl medium with no inhibitor, and (c) in the presence of 1500 ppm of Non-radiated *H. kraussii*.

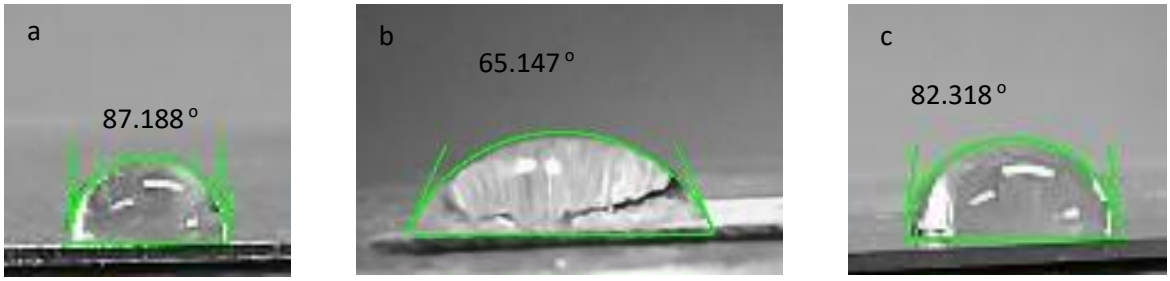


Figure 9. 6: Surface wettability behaviour of (a) polished untreated zinc metal substrate, (b) zinc metal substrate after 8 hours of immersion in 1.0 M HCl medium with no inhibitor, and (c) in the presence of 1500 ppm of UV-radiated *H. kraussii*.

The contact angle for the zinc metal treated with non-radiated extract was found to be > 90° (93.676°) as compared to the UV-radiated extract, which is < 90° (82.318°). This means that the non-radiated extract is a better inhibitor of zinc metal in HCl acid than the UV-radiated extract.

© University of Venda

9.1.4. Zinc metal in 1.0 M H_2SO_4 for non and UV-radiated *H. kraussii* extract

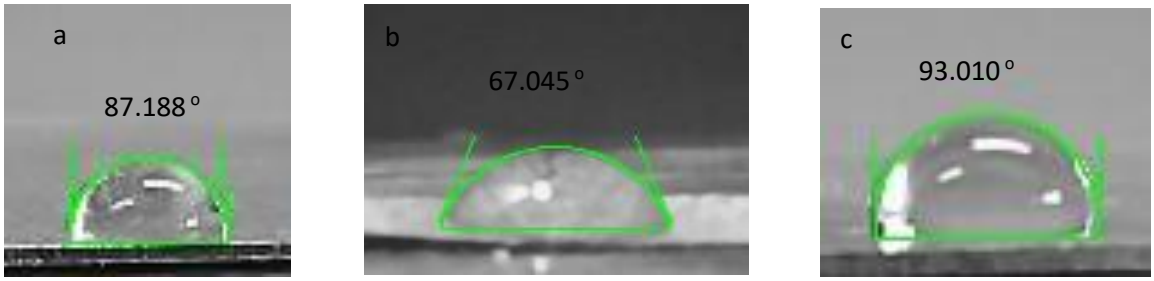


Figure 9. 7: Surface wettability behaviour of (a) polished untreated zinc metal substrate, (b) zinc metal substrate after 8 hours of immersion in 1.0 M H_2SO4 medium with no inhibitor, and (c) in the presence of 1500 ppm of Non-radiated *H. kraussii*.

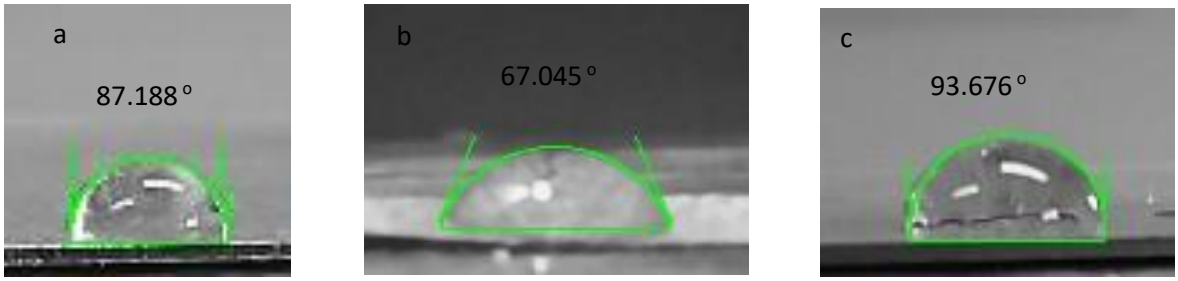


Figure 9. 8: Surface wettability behaviour of (a) polished untreated zinc metal substrate, (b) zinc metal substrate after 8 hours of immersion in 1.0 M H_2SO_4 medium with no inhibitor, and (c) in the presence of 1500 ppm of UV-radiated *H. kraussii*.

In the presence of sulphuric acid solution, the contact angle made on the zinc metal treated with the non-radiated and UV-radiated extracts were 93.010° and 93.676° respectively, which means that the two extracts managed to change the metal surface through adsorption from hydrophilic to hydrophobic [442, 443]. This shows that the two inhibitors are good corrosion inhibitors for zinc in a sulphuric acid medium. The decrease in the contact angle of zinc metal after exposure to sulphuric acid indicates an increase in the metal surface wettability [444].

© University of Venda

9.1.5. Aluminium metal in 1.0 M HCl for non and UV-radiated *H. kraussii* extract

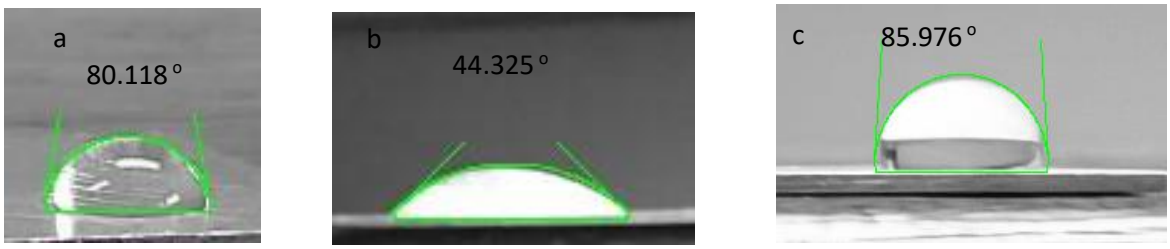


Figure 9. 9: Surface wettability behaviour of (a) polished untreated aluminium metal substrate, (b) aluminium metal substrate after 8 hours of immersion in 1.0 M HCl medium with no inhibitor, and (c) in the presence of 1500 ppm of Non-radiated *H. kraussii*.

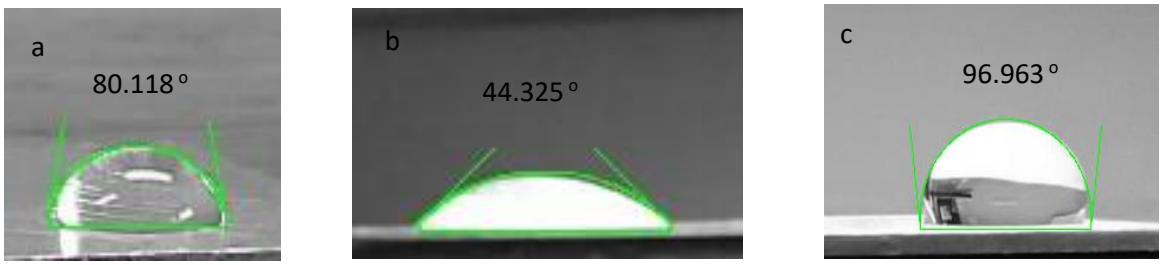


Figure 9. 10: Surface wettability behaviour of (a) polished untreated aluminium metal substrate, (b) aluminium metal substrate after 8 hours of immersion in 1.0 M HCl medium with no inhibitor, and (c) in the presence of 1500 ppm of UV-radiated *H. kraussii*.

For aluminium metal in hydrochloric acid in the presence of non-radiated and UV-radiated extracts, the contact angles made by the water drop on the aluminium surface were 85.976° and 96.963°, respectively. This behaviour shows that the adsorption of the UV-radiated extract inhibitor on the metal surface changed the metal surface from hydrophilic to hydrophobic, thereby reducing the wettability of the metal [442, 443]. This means that the UV-radiated extract performs better as a corrosion inhibitor for aluminium metal in hydrochloric acid than non-radiated extract.

© University of Venda

CHAPTER 10

Results and discussion on the computational studies on the interaction between selected inhibitors and metal surfaces

© University of Venda

10. Introduction

This chapter presents and analyses the results on the interaction between the surface of the metal and selected inhibitor molecules.

10.1. Computational studies on the interaction between selected inhibitors and metal surfaces.

This chapter presents and analyses the results on the interaction between the surface of the metal and selected inhibitor molecules. The relative energies of the inhibitors, the interaction energies, and bond distances are utilised to describe the preferred molecules arrangement on the surface as well as the preferred binding sites on the metal surfaces.

The binding energy (E_{ads}) is estimated following the equation given in Chapter 3. Adsorption energy values, which are large and negative, suggest a better inhibition performance [206]. The system or configuration with the strongest and most stable adsorption is the one with a large negative value [171, 445-447]. Adsorption energies greater than -100 kcal/mol signify chemical adsorption [448], and those lower than that are associated with physical adsorption [208, 449]. We compare herein among the different surfaces in order to determine the preferred metal surface on which the selected inhibitor molecules prefer to interact. We also compare for a given surface the preferred inhibitor to interact with the given surface.

The binding ability of the molecule is assessed not only in terms of energy but also in terms of bond distances at which the molecule atoms are from the surface of interest. The van der Waals interaction distances between the atoms of the metal surface and those of the inhibitor molecule would serve as a criterion to describe how good the interactions are between the molecules of interest and the metal surface.

The binding strength generally is discussed in terms of the orientation by which the inhibitor lies on the surface of the metal. Several possible arrangements can be considered, among which are parallel (flat) and perpendicular (vertical) arrangements, which are the most dominant. The parallel arrangement is known to maximise the surface coverage of the inhibitor on the metal surface, thereby efficiently protecting the metal from corrosion attack [450, 451]. The parallel arrangement also suggests that heteroatoms of extract inhibitor molecules might offer to the vacant d-orbital on the surface of the metal electron with ease to establish steady coordination

© University of Venda

bonds [206]. This makes parallel arrangement the most ideal arrangement of the compound used as a corrosion inhibitor.

Figure 10.1 shows the optimised structures of the six isolated inhibitor compounds and their energies. It is evident that the inhibitors have different electron donor centres, and because of that, their binding ability on the surfaces of the selected metals is likely to differ from each other.

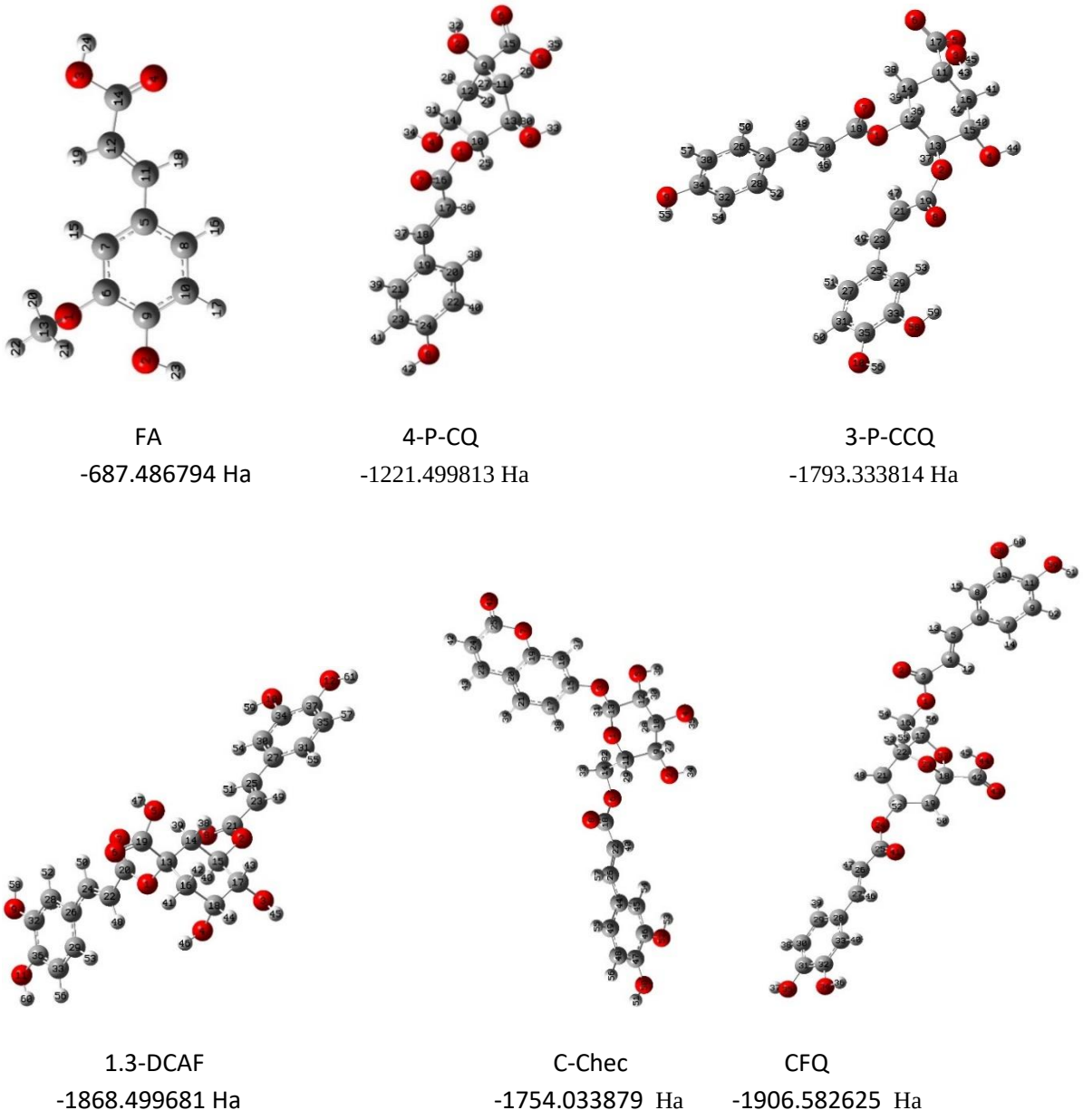


Figure 10. 1: Optimised structures for the isolated inhibitor compounds. The abbreviation FA denotes for ferulic acid, 4-P-CQ denotes for 4-P-Coumaroylquinic acid, 3-P-CCQ denotes 3-P-Coumaroyl-5-(E)-caffeic quinic acid, 1.3-DCAF denotes 1.3-Dicaffeoylquinic acid, C-Chec denotes Caffeoyl-checorin and CFQ denotes Caffeoyl-feruroyl-quinic acid.

© University of Venda

10.2. Interaction between aluminium metal surface and inhibitor molecules

The interactions involving the Ferulic acid (FA) inhibitor molecule, and the aluminium metal surface are shown in Figure 10.2, and the total energies, relative energies, interaction energies and bond distances are reported in Table 10.1. The different arrangements of the molecule on the metal surface are represented by alphabet letters *a*, *b*, *c*, d, *e, f* and *g.* It can be observed that in the configurations *a*, *b*, *c*, *d* and *f*, the inhibitor is oriented parallel to the aluminium surface. This kind of arrangement allows for better distribution of centres of electrophilic attack and nucleophilic attack by the entire inhibitor molecule [450]. Among these arrangements, the relative energy values suggest that only configuration *a* is the most preferred. In other words, the Al···FA interactions are better represented by the configuration *g*.

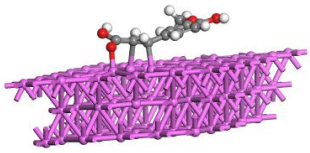
Configurations *a* and *e* show the bonds that form between the metal surface and the inhibitor molecule, which further confirm the adsorption of the inhibitor on the metal surface. The metal-inhibitor bonding distances in configurations *b, d, e, f* and *g* appear to suggest that the inhibitor molecule atoms are a distance from the aluminium surface, and the interactions can be said to be predominately governed by weak Van der Waals and electrostatic interactions. However, metal-inhibitor bonding distances shown in configurations *a* and *e* appear to suggest direct interactions between the metal surface and some atoms on the inhibitor molecule. For instance, the Al···O4 bond distance in configuration *e* has a value of 1.889 Å, and in configuration *a* has a value of 1.899 Å. These bond distances suggest that the interaction of the Al···O is through covalent bonding interaction. The covalent bonding interaction range is from 1.86 to 1.98 Å. Configuration *a* has a smaller bond distance than configuration *e,* meaning the Al···O4 interaction in configuration *a* is stronger and hence *a* is the preferred arrangement.

Even though configurations *a* and *e* show the bond interaction between the aluminium and inhibitor molecules, Configuration *a* can be regarded as the best arrangement and positioning that the FA inhibitor molecule prefers to align on the aluminium metal surface. This is due to the lower relative energies compared to the other configurations. The multiple bonds in configuration *a* are formed because the part of the molecule that contains sp^2 conjugated delocalised electrons is the one closest to the metal surface. Another reason could be that the part closest to the surface in configuration *a* contains three sp^2 centres (aromatic ring, C=O,

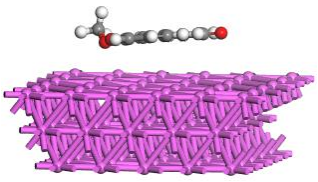
© University of Venda

and C=C), which are able to break from new bonds, as compared to one centre (C=O) in configuration *e*.

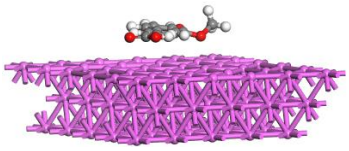
The highest interaction energy is found in arrangements *a* and *b*, which are parallel configurations. Based on this observation, it can be concluded that parallel configurations of the inhibitor geometries give high interaction energy and, therefore, offer stronger adsorption and good corrosion inhibition than the perpendicular configurations [278], Such as that shown in configuration *g*. This conclusion is also reported in the literature [306] and follows the suggested pattern reported herein. Configuration *a* is better than configuration *b* because of the shorter bond distances obtained and the low relative energy on *a*. The values of the adsorption energies obtained for aluminium metal for all the configurations are found to be less than -100 kcal/mol. Based on this information, it can be concluded that the interaction between the FA inhibitor and the aluminium metal surface takes place through physical adsorption. This observation is consistent with the conclusion drawn on the weight loss results presented in Chapter 5. This observation also suggests that the mechanism of the association of inhibitor molecules with the surface of the metal can be proposed to be predominantly through Van der Waals forces. From the literature, it has been reported that the higher the negative value of the system's total energy, the more efficiently the inhibitor will protect the metal surface from further corrosion [451]. In the table, configuration *e* gave the highest total energy of -18864,6572651 kcal/mol, which supports the suggestion that configuration *e* is the best arrangement of FA inhibitor on a zinc metal surface.



(AL···FA)-*a*

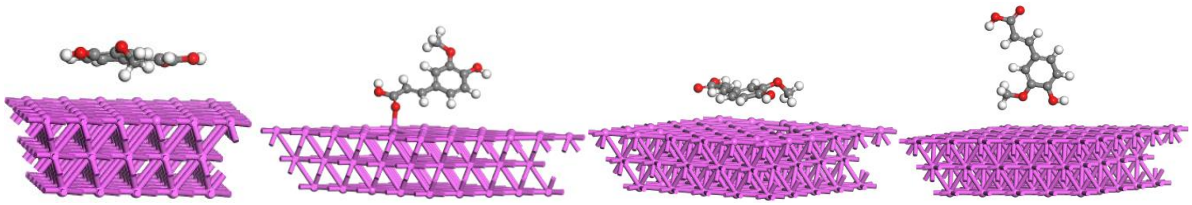


(AL···FA)-*b*



(AL···FA)-*c*

© University of Venda



(AL···FA)-*d* (AL···FA)-*e* (AL···FA)-*f* (AL···FA)-*g*

Figure 10. 2: Different adsorption geometries of ferulic acid (FA) molecules on the Al(111) surface in water solution.

Table 10. 1: Optimised energies for stable FA acid adsorption sites on Al(111) surface.

Configuration	**$E_{FA+metal}$ (Ha)**	**$\Delta E_{FA+metal}$ (kcal/mol)**	**ΔE_{inter} (kcal/mol)**	**Bond distance (Å)**
(Al···FA)-*a*	-18864,6572651	0.000	-51.5896	(Al···O4) 1.899 (Al···C12) 2.385 (Al···C11) 2.161
(Al···FA)-*b*	-18864,6382394	11.931	-39.6508	(Al···C11) 3.485
(Al···FA)-*c*	-18864,6305404	16.759	-34.8196	(Al···C11) 3.398 (Al···O1) 2.593
(Al···FA)-*d*	-18864,6288542	17.828	-33.761006	(Al···H22) 2.957 (Al···O4) 3.379
(Al···FA)-*e*	-18864,6265830	19.240	-32.3363	(Al···O4) 1.889
(Al···FA)-*f*	-18864,6252841	20.055	-31.5212	(Al···O4) 3.808 (Al···C11) 3.596 (Al···C8) 4.872
(Al···FA)-*g*	-18864,5935582	39.950	-11.6129	(Al···O1) 3.467 (Al···O2) 3.342

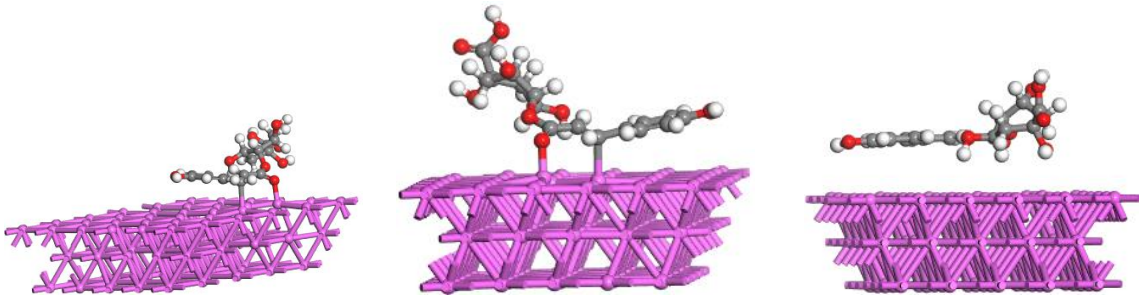
The interactions involving the 4-P-Coumaroylquinic acid (4-P CQ) inhibitor molecule and the aluminium surface are shown in Figure 10.3, and the total energies, relative energies, interaction energies and bond distances are reported in Table 10.2. The different arrangements of the molecule on the metal surface are represented by alphabet letters *a*, *b*, *c*, *d*, *e*, *f* and *g*. The results of the investigation suggest, in terms of relative energy, that configuration *a* is the most preferred, followed by *b* and *c*. This means that the inhibitor molecules prefer to arrange and position themselves according to configurations *a*, *b* and *c*, and these arrangements give the best interaction energies corresponding to high inhibition efficiencies.

Configurations *g*, *b*, *d* and *a* show short Al···4-P-CQ bond distances that would suggest strong interactions. The bond distance are (Al···O6 2.107 Å), (Al···O7 1.846 Å), (Al···O7 1.856 Å) and (Al···O 1.844 Å), respectively. Configurations *a* and *b* are almost similar, but what makes configuration *a to* have the best arrangement, and binding energy is due to the shorter Al···O7 bond formed, which has a bond distance of 1.844 Å compared to 1.846 Å of configuration *b*. Meanwhile, configurations *e*, *f* and *a* suggest minimal interactions between the metal and the

© University of Venda

surface because the bond distance in each case is greater than 2.2Å. Configurations *b*, *d* and *a* have bond distances that are within the covalent bond interaction, meaning that their Al···O interaction proceeds covalently.

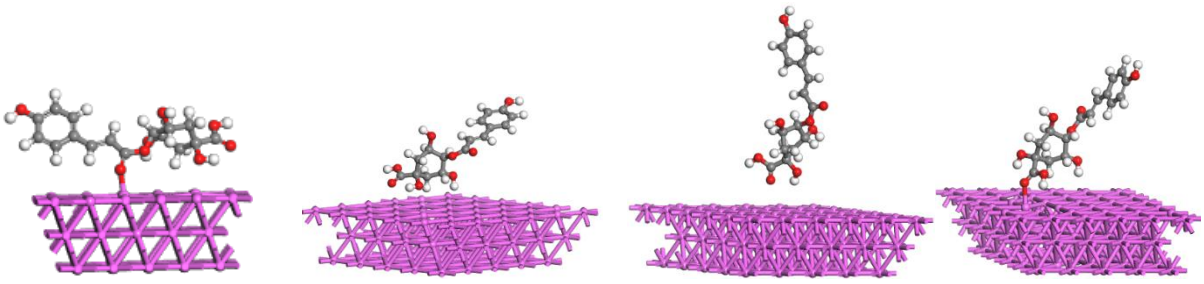
The binding energy values suggest that the parallel configurations, *a* and *b*, are the ones with the highest energies. The high interaction energy is due to the number of atoms interacting directly with the metal surface. The weakest interactions correspond to a perpendicular arrangement *c* for which there is minimal Al···4-P-CQ bond distances. In the 4-P-CQ inhibitor molecule, it is possible to conclude that the parallel configuration gives stronger interactions than the perpendicular arrangement, which suggests strong corrosion inhibition and large surface coverage for the parallel configuration [203]. The interaction energies obtained are all less than -100 kcal/mol, which is indicative of physical adsorption of extract inhibitor molecules on the aluminium metal surface. Configuration *a* is the best arrangement, also based on the atoms forming bonds with the aluminium surface. It can be noted that two conjugated sp^2 parts of the molecule, which are C=C and C=O, were responsible for adsorbing the aluminium metal surface, thereby forming the Al···C and Al···O bonds. Molecules in configurations *g* and *d* only contain one bond between the aluminium metal and the inhibitor C=O part of the molecule, explaining why their binding energy is less than that of configuration *a*. It can be concluded that the parallel arrangement gives high inhibition since molecules in configurations *g, e* and *f* gave the lower interaction energy, -20.7830, -24.1584 and -17.7128 kcal/mol compared to -60.7721, -48.8786, -63.1457, -53.6797 kcal/mol of configurations *b*, *d*, *a* and c respectively, which are parallel arrangements. Therefore, high interaction energy, which is equivalent to high binding energy, is indicative of high inhibition efficiency, as reported by Belghiti *et al.* (2018) [452].



AL···4-P-CQ)-*a* (AL···4-P-CQ)-*b* (AL···4-P-CQ)-*c*

© University of Venda

University of Venda
Creating Future Leaders



(AL···4-P-CQ)-*d* (AL···4-P-CQ)-*e* (AL···4-P-CQ)-*f* (AL···4-P-CQ)-*g*

Figure 10. 3: Different adsorption geometries of 4-P CQ acid molecule on the Al(111) surface in water solution.

Table 10. 2: Optimised energies for stable 4-P-CQ acid adsorption sites on Al(111) surface in solution.

Configuration	**$E_{4\text{-P CQ+metal}}$ (Ha)**	**$\Delta E_{4\text{-P CQ+metal}}$ (kcal/mol)**	**ΔE_{inter} (kcal/mol)**	**Bond distance (Å)**
(Al···4-P-CQ) -*a*	-19398.6887299	0.000	-63.1457	(Al···O7) 1.844 (Al···O18) 2.243
(Al···4-P-CQ) -*b*	-19398.6849473	2.3736	-60.7721	(Al···O7) 1.846 (Al···C18) 2.214
(Al···4-P-CQ) -*c*	-19398.6736449	9.466	-53.6797	(Al···O7) 3.513
(Al···4-P-CQ) -*d*	-19398.6659938	14.267	-48.8786	(Al···O7) 1.856
(Al···4-P-CQ) -e	-19398.6265997	38.987	-24.1584	(Al···O4) 2.820 (Al···H32) 2.891
(Al···4-P-CQ) -*f*	-19398.6163280	45.432	-17.7128	(Al···C12) 3.465
(Al···4-P-CQ) -*g*	-19398.6212207	42.362	-20.7830	(Al···O6) 2.107

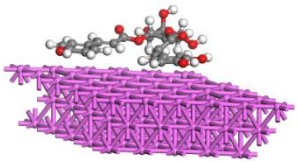
The interactions involving the 3-P-Coumaroyl-5-(E)-caffeic-quinic acid (3-P-CCQ) inhibitor molecule, and the aluminium metal surface are shown in Figure 10.4, and the total energies, relative energies, interaction energies and bond distances are reported in Table 10.3. The different arrangements of the molecules on the aluminium metal surface are represented by the alphabet letters *a*, *b*, *c*, *e,* and *d*. The interaction energies obtained in Table 10.3 are below -100 kcal/mol except for configuration *a*, which has -104.0355 kcal/mol energy. This means that interaction in configurations *b*, *c*, *d*, and *e* is through physisorption, and the interaction of configuration *a* is through chemisorption. Since the high interaction energy is equivalent to high inhibition efficiency, it can be said that configuration *a* is the best arrangement of the 3-P-CCQ on the aluminium metal surface. The molecules in configurations *a* and *b* are lying parallel to the aluminium metal surface and are found to have higher interaction energy than molecules in configurations *c*, *d* and *e,* which are more perpendicular to the aluminium metal surface. This observation supports the fact that the parallel arrangement of the molecules on

© University of Venda

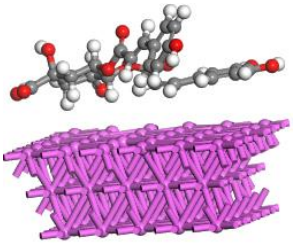
the metal surface maximises contact and surface coverage of the inhibitor molecule on the metal surface [203].

Configuration *a* and *b* are all lying parallel on the aluminium metal surface, but configuration *a* is the best arrangement based on the positioning of the sp^2 conjugated electron delocalised part of the inhibitor molecule. The conjugated part in configuration *a* is moving or pointing towards the aluminium metal surface, while in configuration *b*, it is moving away from the aluminium surface. Moving the conjugated electron delocalised region of the extract inhibitor molecule towards the aluminium metal surface gives high possibility of Al···3-P-CCQ bond formation.

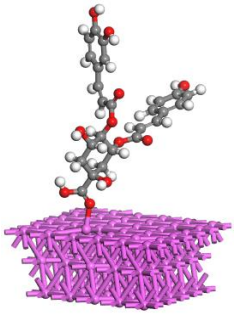
The relative energies can be used to determine the best arrangement of the inhibitor molecule on the metal surface. Configuration *a,* having the lowest relative energy, is the best possible arrangement that the 3-P-CCQ inhibitor prefers to position itself on the aluminium metal surface. The Al···C=O bond distance in configuration *c* is 4.015 Å, and in configuration *a,* it is 3.765 Å; this is the reason why configuration *a* has high interaction energy compared to configuration *c*. Values of interaction energies which are large and negative indicates a strong interaction between the surface of the metal and the extract inhibitor molecules as reported by Savaş et al. (2016) [453]. Therefore, configuration *a* give a stronger interaction of the 3-P-CCQ with the aluminium metal.



(AL···3-P-CCQ)-*a*

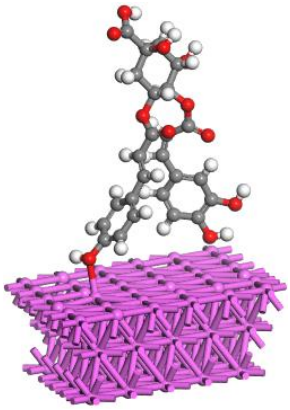


(AL···3-P-CCQ)-*b*

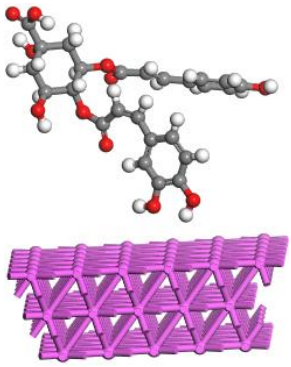


(AL···3-P-CCQ)-*c*

© University of Venda



(AL···3-P-CCQ)-*d*



(AL···3-P-CCQ)-*e*

Figure 10. 4: Different adsorption geometries of 3-P-CCQ acid molecule on the Al(111) surface in water solution.

Table 10. 3: Optimised energies for stable 3-P-CCQ acid adsorption sites on Al(111) surface.

Configuration	**$E_{3\text{-P-CCQ +metal}}$ (Ha)**	**$\Delta E_{3\text{-P-CCQ +metal}}$ (kcal/mol)**	**ΔE_{inter} (kcal/mol)**	**Bond distance (Å)**
(AL···3-P-CCQ)-*a*	- 19970.587893	0.000	-104.0355	(Al···O4) 3.675 (Al···H49) 3.335 (Al···C21) 3.738
(AL···3-P-CCQ)-*b*	-19970.554431	20.997	-83.0378	(Al···O8) 4.015 (Al···H41) 2.823 (Al···O4) 2.904
(AL···3-P-CCQ)-*c*	-19970.500877	54.603	-49.4322	(Al···O6) 1.963
(AL···3-P-CCQ)-*d*	-19970.499369	55.549	-48.4859	(Al···O9) 2.262
(AL···3-P-CCQ)-*e*	-19970.486609	63.556	-40.4788	(Al···O58) 3.072 (Al···H56) 3.046

The interactions involving the 1.3-Dicaffeoylquinic acid (1.3-DICAF) inhibitor molecule, and the aluminium metal surface are shown in Figure 10.5, and the total energies, relative energies, interaction energies and bond distances are reported in Table 10.4. The different arrangements of the molecule on the metal surface are represented by alphabet letters *a*, *b*, *c*, *d, e, f* and *g*. Based on the relative energy values, configuration *a* is the best arrangement. The lowest relative energy values give the best preferable arrangement of a molecule on the metal surface.

From Table 4 of the results, it can be observed that the interaction energy values are all greater than -100 kcal/mol, indicating that the adsorption of 1.3-DCAF on the metal surface is through chemisorption [448]. The highest energy was obtained by the parallel arrangement in configuration *a*, with -266.4994 kcal/mol energy. As expected, the lowest interaction energy is obtained for the perpendicular configuration with the energy of -231.1103 kcal/mol displayed

© University of Venda

by configuration *f*. This observation suggests that parallel arrangement is the best equilibrium arrangement [454] of the 1.3-DICAF inhibitor on the aluminium metal surface

Configurations *b*, *d* and *a* show the formation of Al···O bond but differ on the molecule's arrangement on the aluminium surface. The Al···O bond distance in configurations *b*, *d* and *a* are 2.023 Å, 1.870 Å and 2.112 Å. The bond distance of configuration *a,* which has the best arrangement, is longer than that in configurations *b* and *d*. The reason for configuration *a* to have high interaction energy, even though the Al···O bond distance formed is high, is because the inhibitor molecule in configuration *a* lie parallel to the aluminium surface with most of its atoms approaching the aluminium metal surface increasing the possibilities of adsorption, as compared to the arrangement in configuration *b* and *d*.

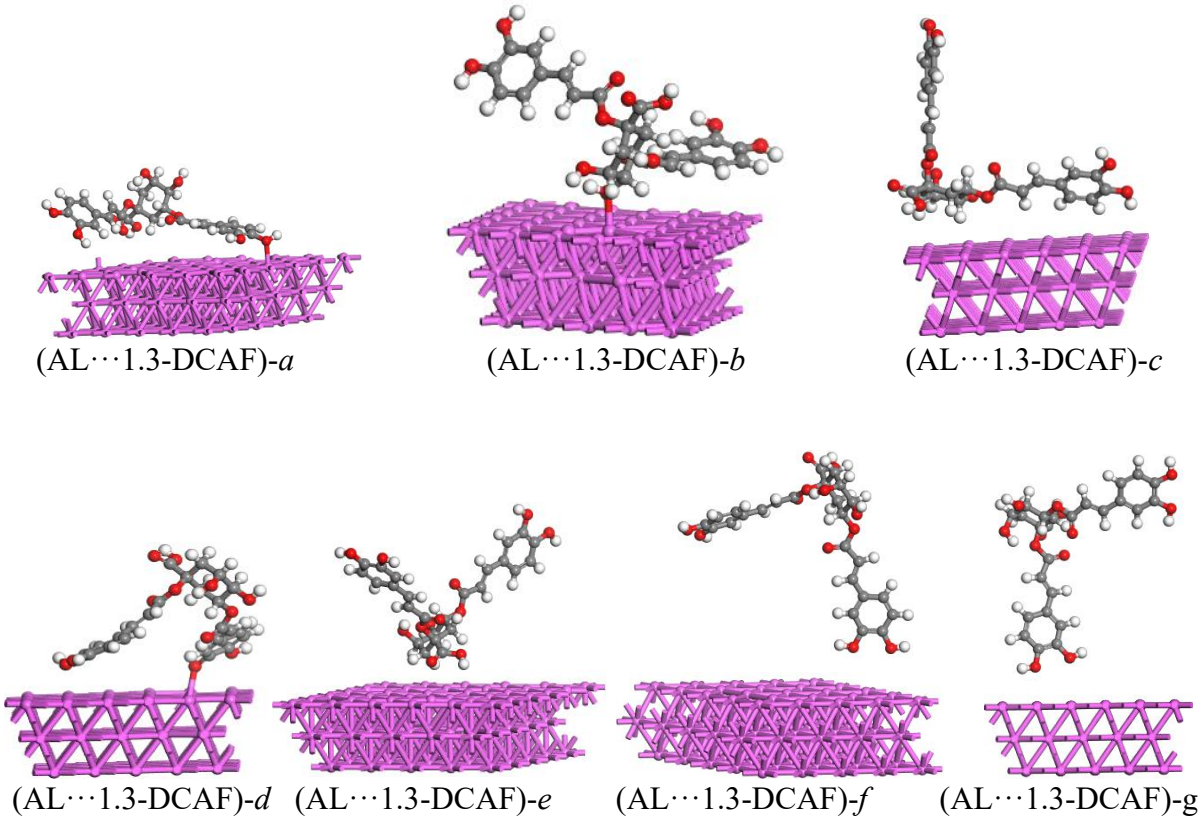


Figure 10. 5: Different adsorption geometries of 1.3-DCAF acid molecule on the Al(111) surface in water solution.

© University of Venda

Table 10. 4: Optimised energies for stable 1.3-DCAF acid adsorption sites on Al(111) surface.

Configuration	**$E_{1.3\text{-DCAF +metal}}$ (Ha)**	**$\Delta E_{1.3\text{-DCAF +metal}}$ (kcal/mol)**	**ΔE_{inter} (kcal/mol)**	**Bond distance (Å)**
(AL···1.3-DCAF)-*a*	-20046.012669	0.000	-266.4994	(Al···O8) 2.112
(AL···1.3-DCAF)-*b*	-20046.001316	7.124	-259.3754	(Al···O3) 2.023
(AL···1.3-DCAF)-*c*	-20045.989090	14.796	-251.7036	(Al···C35) 3.235 (Al···H40) 3.555
(AL···1.3-DCAF)-*d*	-20045.985841	16.834	-249.6648	(Al···O10) 1.870
(AL···1.3-DCAF)-*e*	-20045.957607	34.551	-231.9480	(Al···O8) 2.759
(AL···1.3-DCAF)-*f*	-20045.956756	35.085	-231.4140	(Al···H61) 3.704 (Al···O12) 3.484
(AL···1.3-DCAF)-*g*	-20045.956272	35.389	-231.1103	(Al···O12) 2.954

The interactions involving the Caffeoyl-checorin (C-Chec) inhibitor molecule and the aluminium metal surface are shown in Figure 10.6, and the total energies, relative energies, interaction energies and bond distances are reported in Table 10.5. The different arrangements of the molecules on the aluminium metal surface are represented by the alphabet letters *a*, *b*, *c*, *d, e,* and *f*. Based on the relative energy values, configuration *a* is by far the best arrangement of the C-Chec on the aluminium metal surface. This is because configuration *a* has 0.000 kcal/mol energy while other configurations have relative energy far greater than 4 kcal/ mol.

The interaction energies obtained are all above -100 kcal/mol, which is an indication that the C-Chec inhibitor adsorbs on the aluminium metal surface through chemical adsorption. Configuration *a,* which shows the parallel arrangement of C-Chec on the aluminium surface, has the highest interaction energy of -345.3153 kcal/mol, which suggests strong adsorption on the aluminium metal surface, thereby strong inhibition. The lowest energy was obtained for the perpendicular configuration (configuration *f*) with the interaction energy of -290.4285 kcal/mol. It can be concluded that the parallel configurations are the most preferred configuration for C-Chec as a corrosion inhibitor for aluminium metal surfaces.

Configuration *a* is the only arrangement that has formed a bond using its sp^2 conjugated C=O bond with the aluminium metal surface (Al···O5) with a bond distance of 2.152 Å. This bond distance is the lowest compared to the other Al···O bonds distances in the configurations *e*, *c*, *d*, *f* and *b,* having 3.036 Å, 3.165 Å, 3.604 Å, 2.647 Å and 3.812 Å. The shorter the bond distances between the inhibitor molecule and the metal surface, the stronger the adsorption. This means that configuration *e* offers strong adsorption, suggesting high corrosion inhibition. Configuration *d* and *b* have similar arrangements, but configuration *b* has higher interaction energy than Configuration *d*. The reason for this is that the Al···O2 bond distance of the sp^2 C=O in configuration *b* is shorter than that in configuration *d*. This is an indication that the

© University of Venda

inhibitor molecule in configuration *b* has slightly stronger adsorption on the metal surface than in configuration *d*.

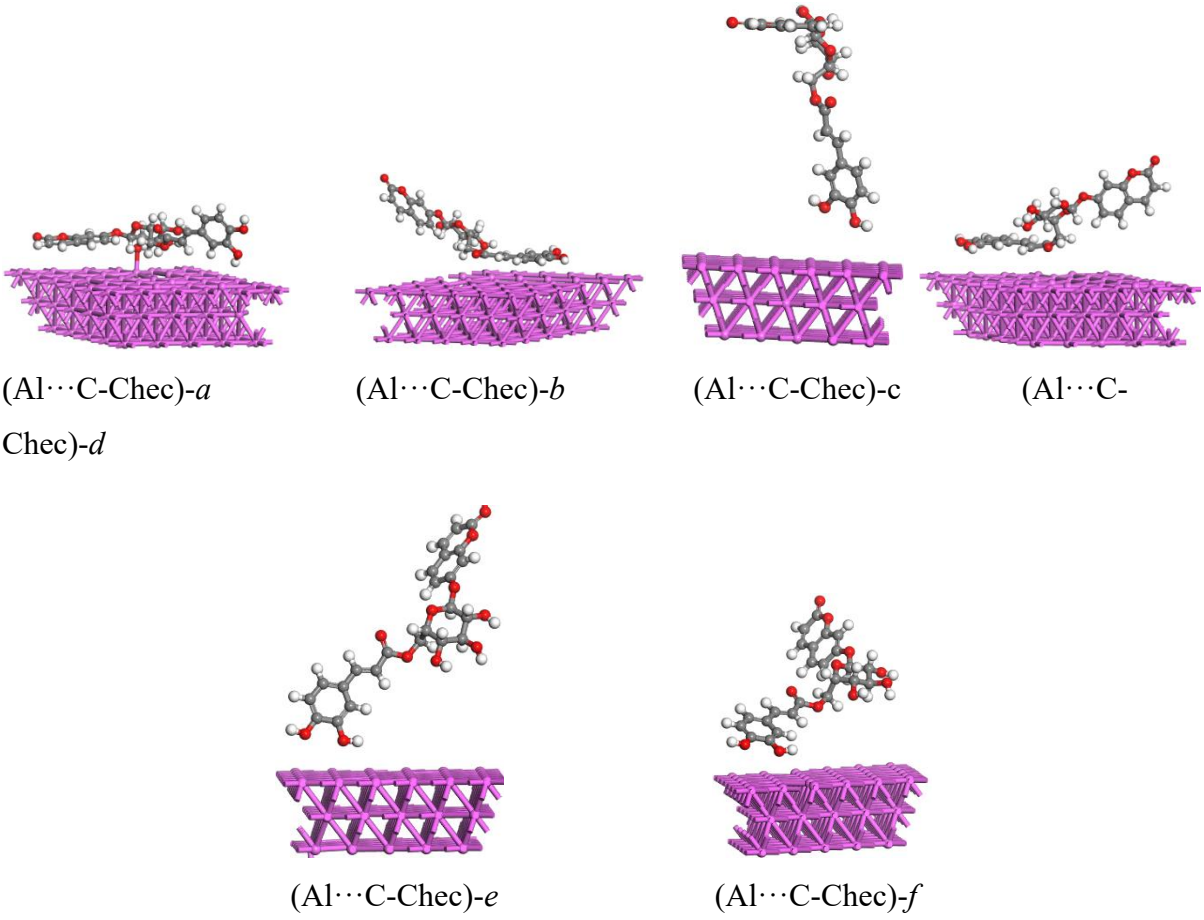


Figure 10. 6: Different adsorption geometries of C-Chec molecule on the Al(111) surface in water solution.

Table 10. 5: Optimised energies for stable C-Chec acid adsorption sites on Al(111) surface.

Configuration	**$E_{C\text{-}Chec+metal}$ (Ha)**	**$\Delta E_{C\text{-}Chec+metal}$ (kcal/mol)**	**ΔE_{inter} (kcal/mol)**	**Bond distance (Å)**
(Al···C-Chec)-*a*	-19931.672470	0.000	-345.3153	(Al···O5) 2.152
(Al···C-Chec)-*b*	-19931.628379	27.667	-317.6482	(Al···O2) 3.534 (Al···C22) 3.307
(Al···C-Chec)-*c*	-19931.624588	30.046	-315.2693	(Al···O50) 3.165 (Al···H51) 3.131
(Al···C-Chec)-*d*	-19931.614180	36.577	-308.7383	(Al···O8) 3.604
(Al···C-Chec)-*e*	-19931.593989	49.247	-296.0684	(Al···O52) 3.036 (Al···H53) 2.972
(Al···C-Chec)-*f*	-19931.585001	54.887	-290.4285	(Al···O52) 2.647

The interactions involving the Caffeoyl-feruroyl-quinic acid (CFQ) inhibitor molecule, and the aluminium metal surface are shown in Figure 10.7, and the total energies, relative energies,

© University of Venda

interaction energies and bond distances are reported in Table 10.6. The different configurations of the molecule on the aluminium metal surface are represented by alphabet letters *a* and *b*. It can be observed that the interaction energies obtained are less than -100 kcal/mol, which is an indication that the CFQ adsorbs on the aluminium metal through physisorption. The two configurations have similar arrangements but different positioning on the aluminium metal surface. Both have their conjugated electron delocalised part parallel to the surface of the aluminium metal. The only difference is that configuration *a* has three bonds formed from their conjugated electron delocalised part with the aluminium metal surface, while configuration *b* only formed one Al···O bond. It can be noted that the inhibitor molecules in the two configurations used their sp^2 conjugated regions C=C and C=O to form the bonds with the aluminium metal surface. The more the number of bonds formed with the aluminium metal surface, the better the adsorption of the inhibitor molecules on the metal surface thereby causing high inhibition. This can be supported by the higher adsorption energy obtained in configuration *a* compared to configuration *b*. This observation suggests that configuration *a* is the most preferred arrangement of the CFQ inhibitor on the metal surface.

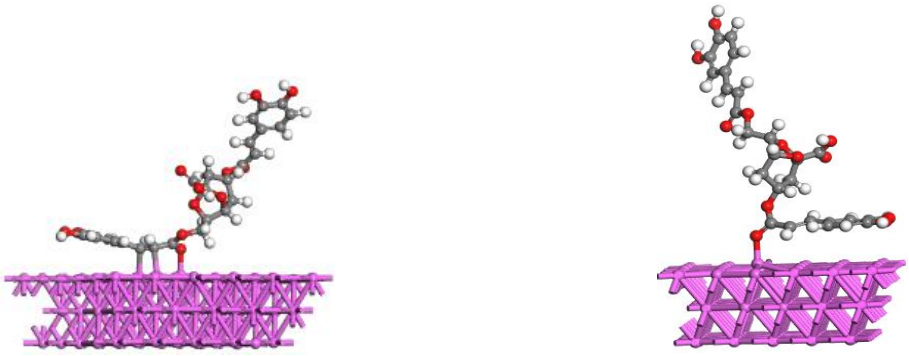
The relative energy can also be used to determine the most preferred inhibitor molecules arrangement on the surface of the metal. Configuration *a* has the lowest relative energy (0.000 kcal/mol) compared to configuration *b* (2.703 kcal/mol). This suggests that configuration *b* provides the best arrangement of CFQ on the aluminium surface. Relative energy values for the two configurations are less than 4 kcal/mol, which makes the two configurations a good representation of the arrangement of extract on aluminium surface, with configuration *a* being the most preferred.

The Al···CFQ bond distances formed in configuration *a* have bond distances (Al···O2 1.928 Å, Al···C4 2.239 Å and Al···C5 2.146 Å) while in configuration *b* the Al···O2 bond formed has a bond distance of 1.923 Å. The Al···O bond of configuration *b* is shorter than that in configuration *a*. The Al···O bond distances in the two configurations are within the range of Al and oxygen covalent bonding, which is 1.86-1.98 Å. Knowing that shorter bond distance corresponds to higher adsorption, the observation of configuration *b* having a shorter bond distance than configuration *a* does not change the fact that configuration *a* is the best arrangement because of the two Al···C bonds formed with the aluminium metal surface.

It can also be observed that the parallel configuration gave the highest interaction energy of -76.3473 kcal/mol, and the perpendicular arrangement gave a lower interaction energy of -

© University of Venda

70.0069 kcal/mol. Therefore, it can be concluded that the parallel arrangement offers stronger interaction than the perpendicular arrangement.



(Al···CFQ)-*a* (Al···CFQ)-*b*

Figure 10. 7: Different adsorption geometries of CFQ acid molecule on the Al(111) surface in water solution.

Table 10. 6: Optimised energies for stable CFQ acid adsorption sites on Al(111) surface.

Configuration	**$E_{CFQ+metal}$ (Ha)**	**$\Delta E_{CFQ+metal}$ (kcal/mol)**	**ΔE_{inter} (kcal/mol)**	**Bond distance (Å)**
(Al···CFQ)-*a*	-20083.792580	0.000	-76.3473	(Al···O2) 1.928 (Al···C4) 2.239 (Al···C5) 2.146
(Al···CFQ)-*b*	-20083.782476	2.703	-70.0069	(Al···O2) 1.923

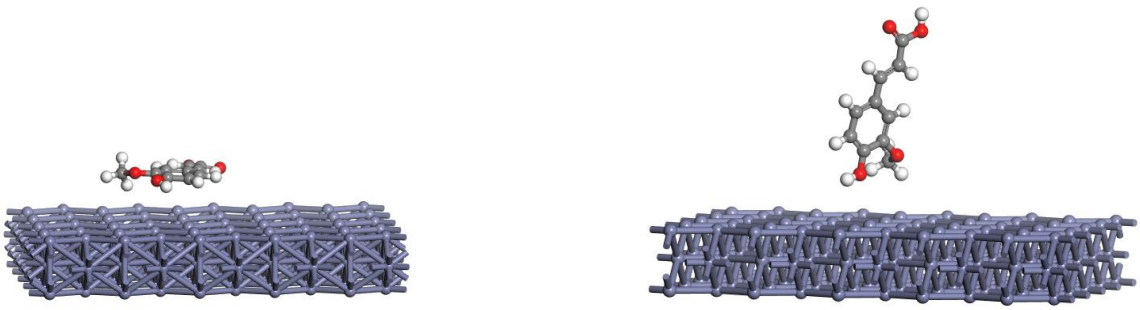
10.3. Interaction between zinc metal surface and inhibitor molecules

The interactions involving the Ferulic acid (FA) inhibitor molecule, and the zinc metal surface are shown in Figure 10.8, and the total energies, relative energies, interaction energies and bond distances are reported in Table 10.7. The different arrangements of the molecule on the metal surface are represented by alphabet letters *a* and *b*. Relative energy can be used to determine the most preferred arrangement of the inhibitor on the metal surface. Relative energies lower than 4 kcal/mol are regarded as the best arrangements. Configuration *a* has a lower relative energy of 0.000 kcal/mol compared to the 9.070 kcal/mol of configuration *b*. This observation suggests that configuration *a* is the most preferred arrangement of the FA molecules to align on the zinc surface.

© University of Venda

Configuration *a* has a parallel configuration with the metal surface, while configuration *b* has a perpendicular configuration with the metal surface. From the literature, it is known that parallel arrangement maximises the surface coverage of the inhibitor on the metal surface, thereby efficiently protecting the metal from corrosion attack better than the perpendicular arrangement [450]. The parallel arrangement (configuration *a*) has a higher interaction energy of -149.1532 kcal/mol compared to the perpendicular configuration (configuration b) with -140.0828 kcal/mol energy. Based on this observation, it can be concluded that the parallel configuration is the most preferred for corrosion inhibition, as stated in the literature. The energy values for the two configurations obtained are greater than -100 kcal/mol, which indicates a chemisorption behaviour.

The bond distances between the inhibitor molecules atoms and the zinc metal surface determine the strength of adsorption of the inhibitor molecules on the metal surface. The Zn···O bond distances for configurations *a* and *b* are 3.234 Å and 3.243 Å, respectively. These bond distances obtained are outside the Zn···O covalent interaction bond distance range, meaning that the interaction of Zn···FA does not take place through covalent bonding. The shorter the bond distance, the stronger the adsorption of the inhibitor molecules on the metal surface, thereby causing more corrosion inhibition. Configuration *a* can be said to have stronger adsorption than configuration *b*; hence, it is the most preferred arrangement of the FA on the zinc metal surface.



(Zn···FA)-*a* (Zn···FA)-*b*

Figure 10. 8: Different adsorption geometries of ferulic acid (FA) molecules on the Zn(110) surface in water solution.

© University of Venda

Table 10. 7: Optimised energies for stable FA acid adsorption sites on Zn(110) surface.

Configuration	$E_{FA+metal}$ (Ha)	$\Delta E_{FA+metal}$ (kcal/mol)	ΔE_{inter} (kcal/mol)	Bond distance (Å)
(Zn···FA)-*a*	-34776.0495410	0.000	-149.1532	(Zn···O3) 3.234 (Zn···C10) 3.214
(Zn···FA)-*b*	-34776.0350862	9.070	-140.0828	(Zn···O2) 3.243

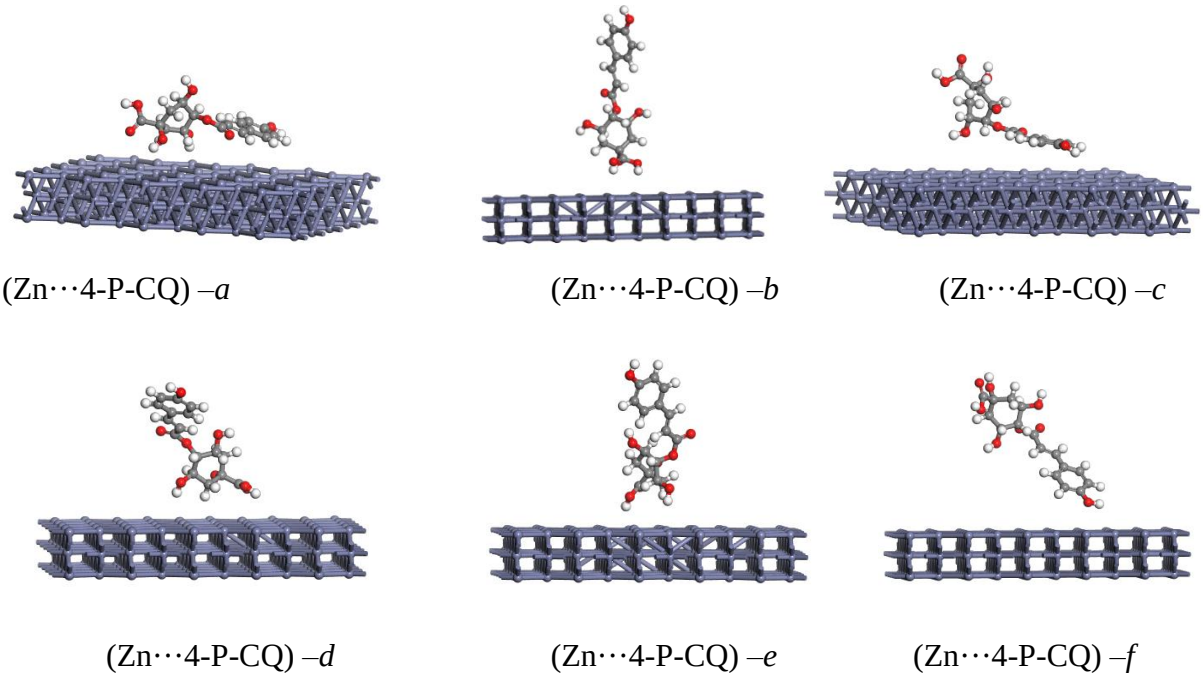
The interactions involving the 4-P-Coumaroylquinic acid Ferulic acid (4-P-CQ) inhibitor molecule and the zinc metal surface are shown in Figure 10.9, and the total energies, relative energies, interaction energies and bond distances are reported in Table 10.8. The different arrangements of the molecule on the metal surface are represented by alphabet letters *a*, *b*, *c*, *d*, *e* and *f*. The values of the interaction energies obtained for the six configurations are above -100 kcal/mol, which is an indication that the adsorption of the 4-P-CQ is through chemisorption. Comparing the energies of the six configurations, the lowest energy (-204.4095 kcal/mol) was obtained in configuration *f*, which is more of a perpendicular arrangement. The highest interaction energy (-218.1256 kcal/mol) was obtained in configuration *a*, which is a parallel arrangement of inhibitor on the surface of the metal. Since high energy is equivalent to high inhibition or adsorption on the surface of the metal, it can be concluded that the parallel arrangement of the 4-P-CQ (configuration *a*) is better for inhibiting the zinc corrosion than the perpendicular configurations since it maximises the contact of the inhibitor with the metal surface [455].

Configuration *a* is the most preferred arrangement of 4-P-CQ molecules on the zinc surface because it has a lower relative energy value compared to the other configurations. The reason configuration *a* has the lowest relative energy is because of its parallel arrangement on the zinc metal surface. Based on relative energy, the preference is in the following series: configuration *a* (0.00 kcal/mol) > configuration *b* (4.475 kcal/mol) > configuration *c* (6.390 kcal/mol) > configuration *d* (7.474 kcal/mol) > configuration *e* (7.997 kcal/mol) > configuration *f* (13.716 kcal/mol).

The bond distance between the metal surface and the inhibitor molecules can also be used to determine the best arrangement of extract molecules on the surface of the metal. The shorter the bond distance between the extract inhibitor molecule and the metal, the stronger the interaction between the metal and the inhibitor molecule. Configuration *a* has a Zn···O bond distance of 3.700 Å, which is shorter than the bond distances in configurations *e*, *c* and *b*. This observation explains why configuration *a* is the preferred arrangement. However, the bond distances in configurations *d* and *f* are shorter than those of configuration *a*. The reason

© University of Venda

configuration *a* has the high interaction energy and is the preferred arrangement even though it has longer bond distances than configurations *d* and *f* is because of the most parallel arrangements of the inhibitor molecules on the zinc metal surface than any other configuration in Table 10.8, exposing most of the inhibitor molecules atoms to be able to adsorb on the zinc metal surface, thereby causing corrosion inhibition.



(Zn···4-P-CQ) –*a* (Zn···4-P-CQ) –*b* (Zn···4-P-CQ) –*c*

(Zn···4-P-CQ) –*d* (Zn···4-P-CQ) –*e* (Zn···4-P-CQ) –*f*

Figure 10. 9: Different adsorption geometries of 4-P CQ acid molecule on the Zn(110) surface in water solution.

Table 10. 8: Optimised energies for stable 4-P-CQ acid adsorption sites on Zn(110) surface in solution.

Configuration	**$E_{4\text{-P CQ+metal}}$ (Ha)**	**$\Delta E_{4\text{-P CQ+metal}}$ (kcal/mol)**	**ΔE_{inter} (kcal/mol)**	**Bond length (Å)**
(Zn···4-P-CQ) –*a*	-35310.1724757	0.000	-218.1256	(Zn···O7) 3.700 (Zn···O6) 4.174
(Zn···4-P-CQ) –*b*	-35310.1653443	4.475	-213.6507	(Zn···O8) 3.277 (Zn···C22) 4.292
(Zn···4-P-CQ) –*c*	-35310.1622928	6.390	-211.7358	(Zn···C24) 3.784 (Zn···O7) 3.969
(Zn···4-P-CQ) –*d*	-35310.1605645	7.474	-210.6513	(Zn···O6) 2.861
(Zn···4-P-CQ) –*e*	-35310.1597288	7.997	-210.1269	(Zn···O5) 3.831
(Zn···4-P-CQ) –*f*	-35310.1506175	13.716 -204.4095		(Zn···O6) 3.277 Zn···C22) 4.292

The interactions involving the 3-P-Coumaroyl-5-(E)-caffeic-quinic acid (3-P-CCQ) inhibitor molecule and the zinc metal surface are shown in Figure 10.10, and the total energies, relative

© University of Venda

energies, interaction energies and bond distances are reported in Table 10.9. The different arrangements of the molecule on the zinc metal surface are represented by alphabet letters *a*, and *b*. The relative energy values suggest that configurations *a* and *b* are both the most favourable arrangements of the 3-P-CCQ inhibitor on the zinc metal surface since they have relative energies lower than 4 kcal/mol. However, configuration *a* is the most outstanding arrangement compared to configuration *b*.

Both configurations are parallel to the surface of the zinc metal. These arrangements yielded high interaction energy which is above -100 kcal/mol, which suggests that the arrangement of the 3-P-CCQ on the zinc metal surface is through chemical adsorption. High interaction energy suggests high inhibition. It is also known that the more negative the interaction between the metal surface and the inhibitor molecule is, the higher the binding energy, which leads to a stable metal-inhibitor interaction [455]. Configuration *a* has -341.4738 kcal/mol, and configuration *b* has -339.8869 kcal/mol interaction energy. Based on this observation, it can be concluded that the arrangement in configuration *a* offers better inhibition than configuration *b*.

Despite similar arrangement on the zinc metal surface, the preference of configuration *a* being the most preferred arrangement, can also be explained using the bond distance. Looking Zn···H at a bond distance to the zinc metal surface, configuration *a* has 2.747 Å and configuration *b* has 2.291 Å. The reason configuration b has shorter bond distances than configuration *a*, but configuration *a* is the preferred arrangement because of the inhibitor arrangement on the surface of the metal. It can be observed that the left part of the 3-PCCQ inhibitor appears to be moving up against the zinc metal surface, reducing the adsorption strength of the whole molecule. Meanwhile, the 3-P-CCQ in configuration *a* appears to be lying uniformly on the zinc metal surface, increasing the adsorption strength.



(Zn···3-P-CCQ)-*a* (Zn···3-P-CCQ)-*b*

Figure 10. 10: Different adsorption geometries of 3-P-CCQ acid molecule on the Zn(110) surface in water solution.

© University of Venda

Table 10. 9: Optimised energies for stable 3-P-CCQ acid adsorption sites on Zn(110) surface.

Configuration	$E_{3\text{-P-CCQ +metal}}$ (Ha)	$\Delta E_{3\text{-P-CCQ +metal}}$ (kcal/mol)	ΔE_{inter} (kcal/mol)	Bond distance (Å)
(Zn···3-P-CCQ)-*a*	-35882.2030466	0.000	-341.4738	(Zn···H41) 2.747
(Zn···3-P-CCQ)-*b*	-35882.2005176	1.586	-339.8869	(Zn···O3) 3.307 (Zn···H59) 2.291

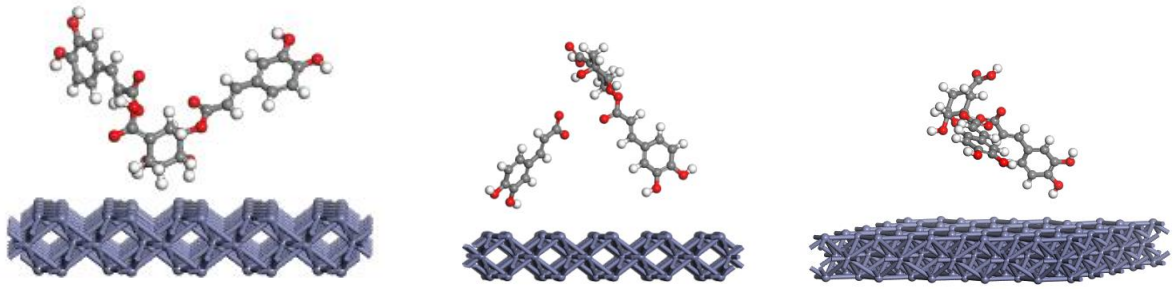
The interactions involving the 1.3-Dicaffeoylquinic acid (1.3-DICAF) inhibitor molecule and the zinc metal surface are shown in Figure 10.11, and the total energies, relative energies, interaction energies, and bond distances are reported in Table 10.10. The different arrangements of the molecule on the zinc metal surface are represented by alphabet letters *a*, *b,* and *c*. The relative energies of configurations *a*, *b,* and *c* are all less than 4 kcal/mol, which means that the three configurations represent the best arrangements of the 1.3-DICAF inhibitor molecules on the zinc metal surface. However, configuration *a* is the most preferred among the three since it has the lowest relative energy. The arrangement preference is in the following series: configuration *a* (0.000 kcal/mol) > configuration *b* (0.697 kcal/mol) > configuration *c* (3.442 kcal/mol).

Based on the interaction energy obtained after optimising the 1.3-Dicaffeoylquinic acid on the zinc metal surface, it can be observed that the values are greater than -100 kcal/mol, which suggests that the interaction of the studied 1.3-DICAF inhibitor on the zinc metal surface proceeds through chemisorption. Chemisorption is believed to offer more permanent adsorption than physisorption. This makes chemisorption to be an ideal kind of adsorption for a good corrosion inhibitor [447]. In configuration *b*, it can be observed that after optimisation, the compound was found to have broken into two parts, thereby spreading along the zinc metal surface to cover most of the surface, thereby exposing more molecules to be able to adsorb on the zinc metal surface. The interaction energy, which is equivalent to the strength of adsorption and inhibition, was through the following arrangement: configuration *a* (-391.8914 kcal/mol) > configuration *b* (-391.1945 kcal/mol)> configuration *c* (-388.4494 kcal/mol), therefore the higher the negative interaction energy values, the stable and stronger adsorption. Therefore configuration *a* is the most stable arrangement [171].

The bond distance between the inhibitor molecule and the zinc metal surface can be used to determine the adsorption strength of the inhibitor molecule on the zinc metal surface. A shorter bond distance means the extract inhibitor molecule is closest to the surface of the metal, making way for stronger adsorption on the metal surface. Configuration *a* has shorter bond distance Zn···H46 of 2.649 Å compared to the bond distances in configurations (Zn···H60) *c* (2.761 Å)

© University of Venda

and (Zn···H58) *b* (3.475 Å). This observation suggests that configuration *a* is the best arrangement of 1.3-DICAF on the zinc metal surface.



(Zn···1.3-DCAF)-a (Zn···1.3-DCAF)-b (Zn···1.3-DCAF)-c

Figure 10. 11: Different adsorption geometries of 1.3-DCAF acid molecule on the Zn(110) surface in water solution.

Table 10. 10: Optimised energies for stable 1.3-DCAF acid adsorption sites on Zn(110) surface.

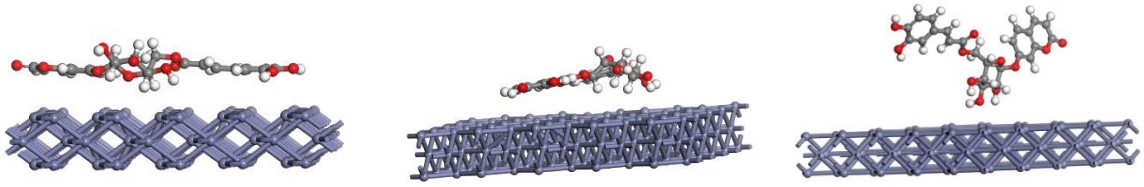
Configuration	**$E_{1.3\text{-DCAF +metal}}$ (Ha)**	**$\Delta E_{1.3\text{-DCAF +metal}}$ (kcal/mol)**	**ΔE_{inter} (kcal/mol)**	**Bond distances (Å)**
(Zn···1.3-DCAF)-*a*	-35957.4492600	0.000	-391.8914	(Zn···H46) 2.649 (Zn···H41) 3.250
(Zn···1.3-DCAF)-*b*	-35957.4481493	0.697	-391.1945	(Zn···O9) 3.553 (Zn···H58) 3.475
(Zn···1.3-DCAF)-*c*	-35957.4437747	3.442	-388.4494	(Zn···H60) 2.761

The interactions involving the Caffeoyl-checorin (C-Chec) inhibitor molecule and the zinc metal surface are shown in Figure 10.12, and the total energies, relative energies, interaction energies, and bond distances are reported in Table 10.11. The different arrangements of the molecule on the zinc metal surface are represented by alphabet letters *a*, *b,* and *c*. From the table, it can be observed that configuration *a* has the highest interaction energy, which is -324.6680 kcal/mol. This high energy is achieved through the parallel arrangement of C-Chec on the zinc surface. This interaction energy supports what has been reported in the literature, which is that the parallel arrangement of the compound along the metal surface provides better adsorption and surface coverage for molecules on the metal surface, thereby inhibiting corrosion [203]. The interaction energy values for the three configurations are greater than -100 kcal/mol, which suggests that the adsorption of C-Chec on the zinc metal surface takes place through chemical adsorption. The inhibitor molecules in configurations *a* and *b* are both positioned parallel to the surface of the zinc metal. The reason configuration *a* has higher interaction energy than configuration *b* is because the right part of the molecule in configuration *b* is shifting away from the metal surface, thereby reducing its adsorption strength, while the

© University of Venda

molecule in configuration c is spread out uniformly, increasing the adsorption strength because of the number of extract inhibitor molecule atoms close to zinc surface.

Relative energy and bond distance can also be used to determine the best-preferred arrangement of the inhibitor on the zinc metal surface. Configurations *a* and *b* have relative energies lower than 4 kcal/mol, which are 0.000 and 1.052 kcal/mol, respectively, making the two configurations the preferred arrangements. Configuration *a* can be said to be the first-choice preferred arrangement of C-Chec inhibitor molecule on the zinc metal surface than configuration *b* because of the lowest relative energy and highest interaction energy. The molecules in configuration *a* and *b* are all parallel to the surface of the metal, but the Zn···O bond distance in configuration *b* is 3.160 Å, which is shorter compared to that of configuration *a,* which is 3.501 Å. The reason for this is because part of the molecule in configuration *b* is moving towards the surface, with the other part moving away from the zinc metal surface. This shift towards the metal surface reduces the bond distance between Zn···C-Chec, hence lower bond distance in configuration *b*. This bond distance is outside the range of the covalent bonding interaction, meaning the Zn···C-Chec interactions do not proceed covalently.



(Zn···C-Chec)-a (Zn···C-Chec)-b (Zn···C-Chec)-c

Figure 10. 12: Different adsorption geometries of C-Chec molecule on the Zn(110) surface in water solution.

Table 10. 11: Optimised energies for stable C-Chec acid adsorption sites on Zn(110) surface.

Configuration	**$E_{C\text{-}Chec+metal}$ (Ha)**	**$\Delta E_{C\text{-}Chec+metal}$ (kcal/mol)**	**ΔE_{inter} (kcal/mol)**	**Bond distances (Å)**
(Zn···C-Chec)-*a*	-35842.8763287	0.000	-324.6680	(Zn···C26) 3.779 (Zn···O50) 3.501
(Zn···C-Chec)-*b*	-35842.8746519	1.052	-323.6156	(Zn···O5) 3.160 (Zn···H35) 2.738
(Zn···C-Chec)-*c*	-35842.8408379	22.270	-302.3974	(Zn···O4) 3.068

The interactions involving the Caffeoyl-feruroyl-quinic acid (CFQ) inhibitor molecule and the zinc metal surface are shown in Figure 10.13, and the total energies, relative energies, interaction energies and bond distances are reported in Table 10.12. The different arrangements of the molecule on the zinc metal surface are represented by alphabet letters *a*, *b*, *c*, *d* and *e*.

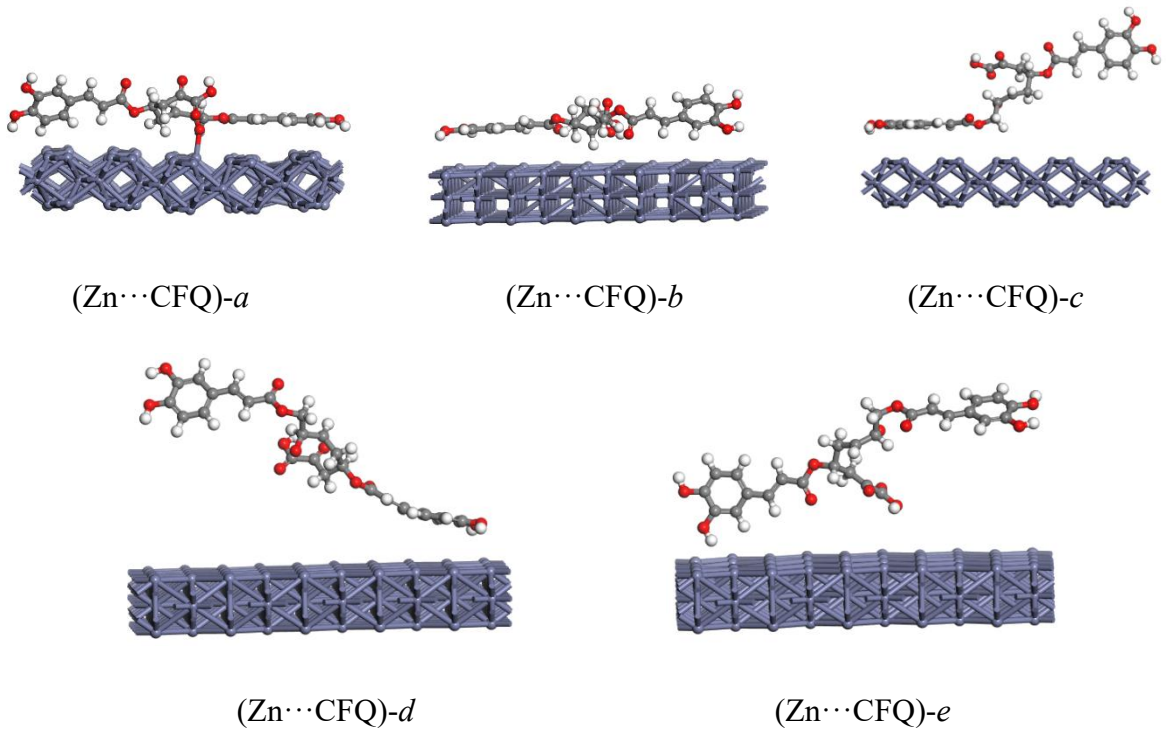
© University of Venda

All the configurations interaction energies obtained are found to be > -100 kcal/mol, suggesting that the CFQ compound's adsorption on the zinc metal surface proceeds through chemical adsorption. The arrangement of the molecules in the five configurations is parallel to the zinc metal surface. This means that most of the inhibitor's molecules are able to cover most of the zinc metal surface, thereby increasing the chances of adsorption on the zinc surface and hindering the metal corrosion process [203]. This claim is supported by the high interaction energies obtained in the table of results. The highest energy was obtained in configuration *a,* which is -415.9155 kcal/mol.

Though the inhibitor molecules in the five configurations appear to be parallel to the zinc metal surface, configuration *a*, is regarded as the best arrangement not only because of having the highest interaction energy. The formation of Zn···O43 bond with a bond distance of 2.160 Å, which is within the Zn and oxygen covalent bond range in configuration *a* is another reason why it is the best arrangement compared to other arrangements. The formation of the Zn···O bond is an indication that the inhibitor molecule in configuration *a* has a stronger adsorption ability to cause corrosion inhibition than the other configurations since the inhibitor molecules did not form a visible bond with the zinc metal surface.

The relative energy is also used to determine the best possible inhibitor molecules arrangement on the zinc surface. Smaller relative energy values suggest the best strong, favourable arrangement of inhibitor molecules on the surface of the metal. From the table configuration *a* is the best arrangement because of the lowest relative energy, which is 0.000 kcal/mol, compared to those of the other configurations, which is greater than 4 kcal/mol. Configuration *e* has the least interaction energy value of -383.6829 kcal/mol because the molecule is lying vertically along the zinc metal surface, meaning that fewer molecule atoms can interact with the zinc metal surface. Interaction energies, which are high and negative, suggest a more stabilised and stronger interaction between the inhibitor molecule and the metal surface. Configuration *a* having -415.9155144312 kcal/mol interaction energy is the most stable and, therefore, offers strong interaction of CFQ molecules on the zinc metal surface [456, 457].

© University of Venda



(Zn···CFQ)-*a* (Zn···CFQ)-*b* (Zn···CFQ)-*c*

(Zn···CFQ)-*d* (Zn···CFQ)-*e*

Figure 10. 13: Different adsorption geometries of CFQ acid molecule on the Zn(110) surface in water solution.

Table 10. 12: Optimised energies for stable CFQ acid adsorption sites on Zn(110) surface.

Configuration	**$E_{CFQ+metal}$ (Ha)**	**$\Delta E_{CFQ+metal}$ (kcal/mol)**	**ΔE_{inter} (kcal/mol)**	**Bond distance (Å)**
(Zn···CFQ)-*a*	-35995.5704892	0.000	-415.9155	(Zn···O43) 2.160
(Zn···CFQ)-*b*	-35995.5465542	15.019	-400.8962	(Zn···O41) 3.053 (Zn···O2) 3.580 (Zn···C3) 4.184
(Zn···CFQ)-*c*	-35995.5279963	26.664	-389.2511	(Zn···O50) 3.941 (Zn···C4) 4.500 (Zn···O2) 4.044
(Zn···CFQ)-*d*	-35995.5198392	31.783	-384.1325	(Zn···C5) 4.122 (Zn···C10) 3.399
(Zn···CFQ)-*e*	-35995.5191228	32.232	-383.6829	(Zn···O2) 4.152 (Zn···C5) 4.822 (Zn···C8) 3.891 (Zn···O58) 3.863

© University of Venda

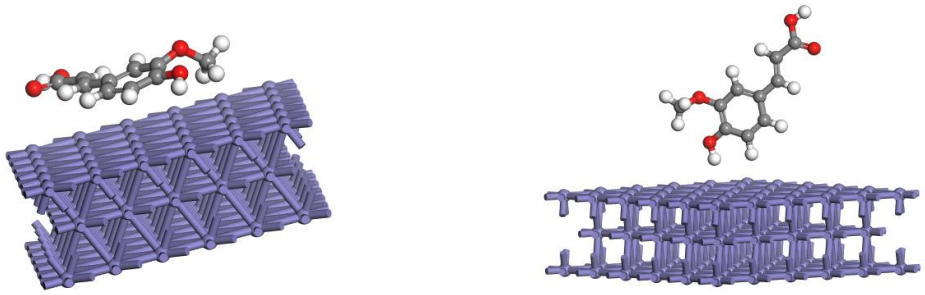
10.4. Interaction between iron metal surface and inhibitor molecules.

The interaction involving the ferulic acid (FA) inhibitor molecule, and the iron metal surface is shown in Figure 10.14, and the total energy, relative energy, interaction energy, and bond distances are reported in Table 10.13. The arrangement of the molecule on the metal surface is represented by alphabet letters *a* and *b*. The relative energy can be utilised to obtain the most stable and preferred arrangement of the inhibitor on the metal surface. Low relative energies are an indication of the stable preferred arrangement of the inhibitor. Configuration *a* gave lower relative energy than *b*. This result means that configuration *a* is the most stable configuration for the interactions between FA molecule and the Fe surface.

Configuration *a* has a parallel arrangement of FA molecule on the mild steel. The parallel arrangement maximise the surface coverage of the inhibitor molecule on the metal surface. This, in turn, results in high adsorption energy. Configuration *b* has a vertical arrangement of the FA molecule on the mild steel metal surface. This is the reason configuration *a* has a higher interaction energy (-207.0680975 kcal/mol) than configuration *b* (-176.6789000 kcal/mol). The high interaction energy also entails the inhibitor's most stable and preferred arrangement on the metal surface and, therefore, high inhibition [458]. The fact that the interaction energy was obtained as negative entails that the FA inhibitor was strongly adsorbed onto the mild steel surface [459]. The interaction energy of the two configurations arrangement is above -100 kcal/mol, indicating that the FA molecule's adsorption process on the mild steel metal proceeds through chemisorption. Chemisorption is known to be the preferred adsorption route for a powerful inhibitor since it entails permanent adsorption.

Short bond distances suggest the closeness of the inhibitor molecule atoms to the metal surface. The closer the inhibitor is to the metal surface, the stronger the interactions between the inhibitor and the metal surface. Configuration *a* has the shortest bond distance between the Fe atom on the Fe surface and C13 (Fe···C13 is 2.447). Configuration *a* is still the most preferred due to its parallel arrangement compared to configuration *b*.

© University of Venda



Fe···FA-*a* Fe···FA-*b*

Figure 10.14: Different adsorption geometries of FA acid molecule on the Fe(110) surface in water solution.

Table 10.13: Optimised energies for stable FA acid adsorption sites on Fe(110) surface in solution.

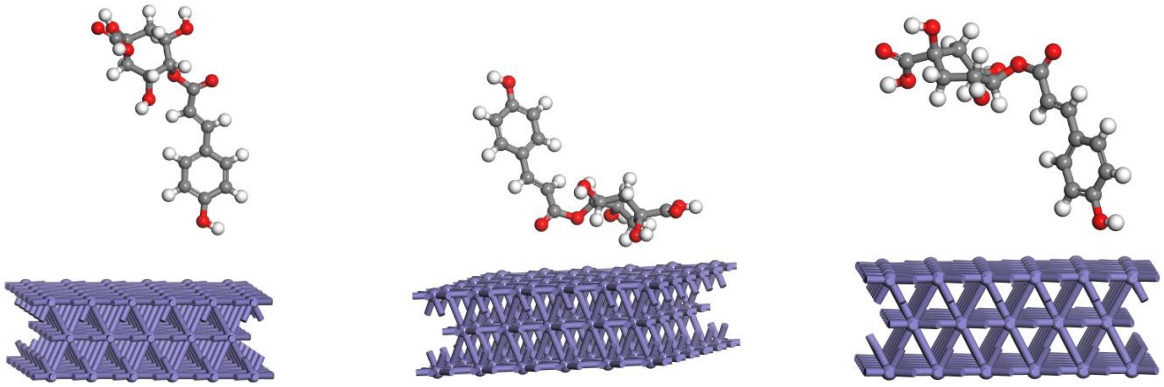
Configuration	**$E_{FA+metal}$ (Hartree)**	**$\Delta E_{FA+metal}$ (Kcal/mol)**	**ΔE_{inter} (Kcal/mol)**	**Bond distance (Å)**
(Fe···FA)-*b*	-11450.101696	0.000	-207.0680975	Fe···C13 2.447 Fe···O2 3.622
(Fe···FA)-*a*	-11450.053267	30.389	-176.6789000	Fe···H23 3.664

The interaction involving the 4-P-coumaryoul quinic acid (4-P-CQ) inhibitor molecule and the iron metal surface is shown in Figure 10.15, and the total energy, relative energy, interaction energy and bond distances are reported in Table 10.14. The arrangement of the molecule on the metal surface is represented by alphabet letters *a*, *b,* and *c.* based on the relative energy of the two configurations, it can be said that configuration *a* has the best arrangement of the 4-P-CQ molecule on the mild steel metal surface. This is because it has the lowest relative energy, which is less than 4 kcal/mol.

The arrangement of the inhibitor molecule onto the metal surface can be a deciding factor in the binding energy. Two dominating arrangements, parallel and vertical of the inhibitor molecule onto the metal surface, are mostly encountered. The parallel arrangement is known to give high binding energy because of the large number of the inhibitor molecules' atoms close to the surface of the metal, giving high chances for bond formation, thereby forming a protective layer. Configuration *a* has higher binding energy than configuration *b* even though it does not have the parallel arrangement of the 4-P-CQ inhibitor on the mild steel metal surface compared to the parallel arrangement in configuration *b*. The Fe···O bond distances for the three configurations are (Fe···O8) 4.212 Å for configuration *b*, (Fe···O2) 2.743 Å for

© University of Venda

configuration *c*, and (Fe···O8) 2.813 Å for configuration *c*. This observation suggests that the 4-P-CQ molecule in configuration *a* is closer to the surface than configuration *b*, indicating stronger interaction possibilities. This is also supported by higher interaction energy in configuration *a* than in configuration *b*.



(Fe···4-P-CQ)-*a* (Fe···4-P-CQ)-*b* (Fe···4-P-CQ)-*c*

Figure 10.15: Different adsorption geometries of 4-P CQ acid molecule on the Fe(110) surface in water solution.

Table 10.14: Optimised energies for stable 4-P-CQ acid adsorption sites on Fe(110) surface in solution.

Configurations	**$E_{4\text{-P-CQ +metal}}$ (Ha)**	**$\Delta E_{4\text{-P-CQ +metal}}$ (kcal/mol)**	**ΔE_{inter} (kcal/mol)**	**Bond distance (Å)**
(Fe···4-P-CQ)-*a*	-11984.253716	-0.000	-294.2912	(Fe···O8) 4.212
(Fe···4-P-CQ)-*b*	-11984.236284	-10.938	-283.3526	(Fe···O2) 2.743
(Fe···4-P-CQ)-*c*	-11984.210556	-27.082	-267.2083	(Fe···O8) 2.813

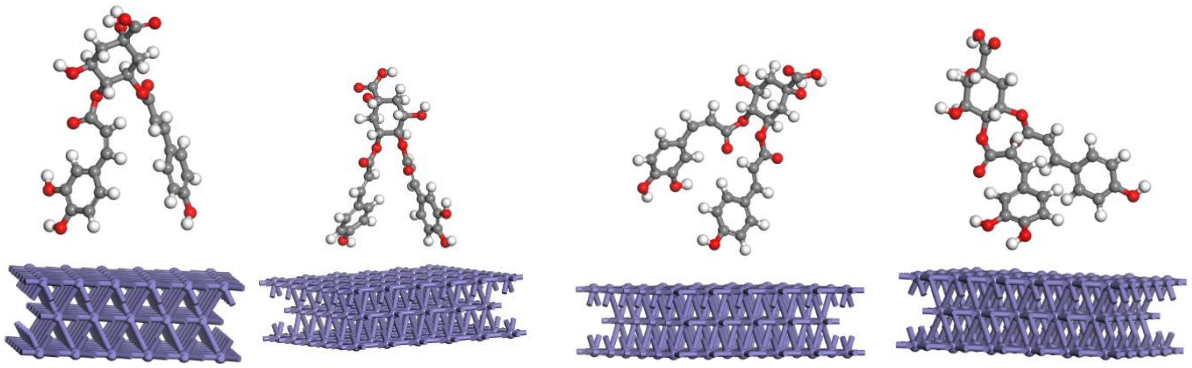
The interaction structures involving the 3-P-coumaroyl-5-(E)-caffeic-quinic acid (3-P-CCQ) inhibitor molecule, and the mild steel surface are shown in Figure 10.16, and the total energies, relative energies, interaction energies, and bond distances are reported in Table 10.15. The different arrangements of the molecule on the metal surface are represented by alphabet letters *a*, *b*, *c* and *d*. Based on relative energies, it can be observed that all four configurations have low relative energy values, which is an indication that they are all the most stable preferred arrangements of the 3-P-CCQ inhibitor onto the mild steel metal surface. The order of their

© University of Venda

preference is in the following range configuration *a* > configuration *b* > configuration *c* > configuration *d*, as outlined in Table 10.14.

Configuration *a* has the highest interaction energy of -429.4201 kcal/mol, meaning it is the most preferred among the four configurations. All the interaction energies are higher than -100 kcal/mol, meaning the adsorption of the 3-P-CCQ inhibitor on the mild steel metal is a chemisorption kind of adsorption.

Bond distances can be used to find the type of interaction and strength of the adsorption of the inhibitor onto the metal surface. Shorter bond distances of the inhibitor on the metal surface would suggest a high possibility of strong interaction of the inhibitor with the metal surface. Shorter bond distances were found in configuration *b*, having Fe···O bond distances of (Fe···O10) 2.841 Å and (Fe···O9) 2.921 Å. Configurations *a* and *b* have similar arrangements of the 3-P-CCQ inhibitor on the mild steel surface. The difference in the bond distances and interaction energies is due to the 3-P-CCQ orientation.



(Fe···3-P-CCQ)-*a* (Fe···3-P-CCQ)-*b* (Fe···3-P-CCQ)-*c* (Fe···3-P-CCQ)-*d*

Figure 10.16: Different adsorption geometries of the 3-P-CCQ acid molecule on the Fe(110) surface in water solution.

Table 10.15: Optimised energies for stable 3-P-CCQ acid adsorption sites on Fe(110) surface.

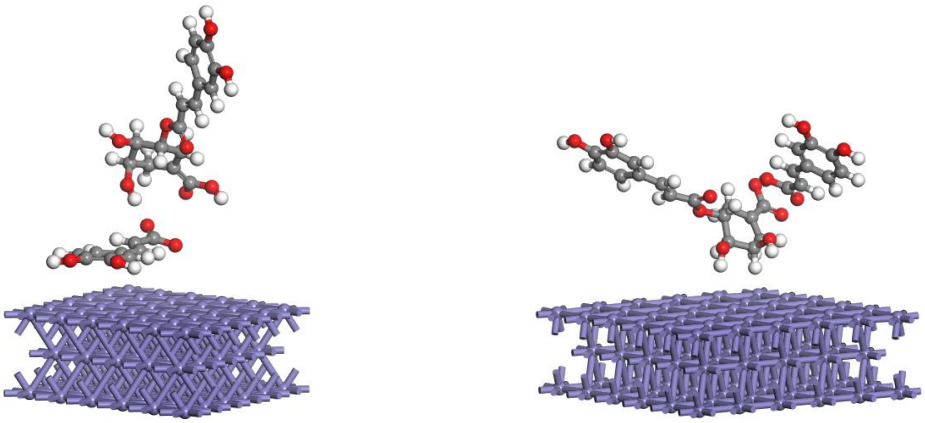
Configurations	**$E_{3\text{-P-CCQ}+metal}$ (Ha)**	**$\Delta E_{3\text{-P-CCQ}+metal}$ (kcal/mol)**	**ΔE_{inter} (kcal/mol)**	**Bond distance (Å)**
(Fe···3-P-CCQ)-*a*	-12556.3030619	0.000	-429.4201	(Fe···O10) 3.084
(Fe···3-P-CCQ)-*b*	-12556.3024857	0.362	-429.0586	(Fe···O10) 2.841 (Fe···O9) 2.921
(Fe···3-P-CCQ)-*c*	-12556.2969080	3.862	-425.5586	(Fe···O10) 3.101
(Fe···3-P-CCQ)-*d*	-12556.2962300	4.287	-425.1331	(Fe···O9) 3.437

© University of Venda

The interactions involving the 1.3-dicaffeoylquinic acid (1.3-DCAF) inhibitor molecule and the iron metal surface are shown in Figure 10.17, and the total energies, relative energies, interaction energies, and bond distances are reported in Table 10.16. The different arrangements of the molecule on the metal surface are represented by alphabet letters *a* and *b*. Configuration *a* and *b* have -0.000 and -19.904 kcal/mol relative energy values. Low relative energy values suggest the inhibitor's most stable and preferred arrangement on the metal surface. Based on that, configuration *a* can be said to be the most stable preferred arrangement of the inhibitor onto the mild steel metal surface.

Configuration *a* has the high interaction energy of -510.1060 kcal/mol compared to -490.2017 kcal/mol of configuration *b*. This means that configuration *a* is the most preferred arrangement of the 1.3-DCAF inhibitor on the mild steel metal surface. The interaction values obtained in configurations *a* and *b* are all greater than -100 kcal/mol, suggesting a chemisorption adsorption process of the 1.3-DCAF inhibitor molecule onto the mild steel metal surface. Configuration *a* has one part of the molecule parallel to the metal surface, and configuration *b* shows a vertical orientation. The parallel orientation in configuration *a* is the reason for the high interaction energy compared to configuration *b*.

Configuration *b* has the shortest bond distance through its hydrogen with the distance of Fe···H45 2.202 Å and Fe···H46 2.741 Å. However, the hydrogen cannot form bonds with the metal surface, which makes their distance not a true reflection of the closeness of the inhibitor molecule's atoms to the surface of the metal for possible bond formation.



(Fe···1.3-DCAF)-*a* (Fe···1.3-DCAF)-*b*

Figure 10.17: Different adsorption geometries of the 1.3-DCAF acid molecule on the Fe(110) surface in water solution.

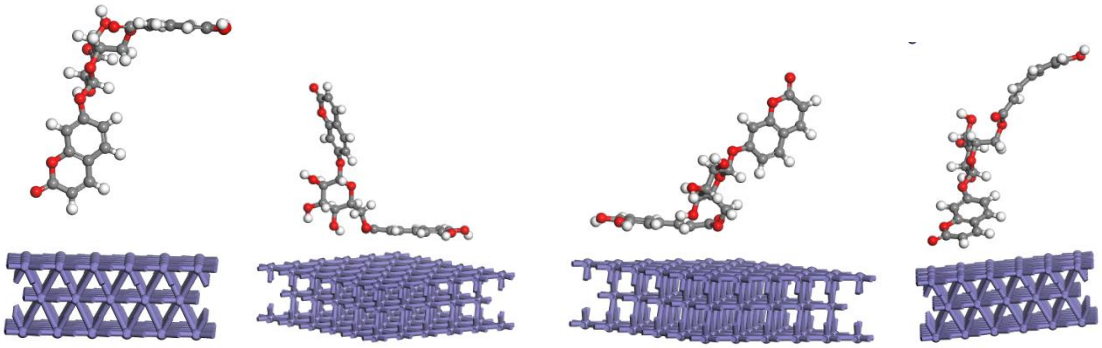
© University of Venda

Table 10.16: Optimised energies for stable 1.3-DCAF acid adsorption sites on Fe(110) surface.

Configurations	**$E_{1.3\text{-DCAF +metal}}$ (Ha)**	**$\Delta E_{1.3\text{-DCAF +metal}}$ (kcal/mol)**	**ΔE_{inter} (kcal/mol)**	**Bond distance (Å)**
(Fe···1.3-DCAF)-*a*	-12631.597512	0.000	-510.1060	(Fe···H45) 2.202 (Fe···H46) 2.741
(Fe···1.3-DCAF)-*b*	-12631.565792	19.904	-490.2017	(Fe···O11) 3.030 (Fe···C33) 2.996

The interactions involving the caffeoyl-checorin (C-Chec) inhibitor molecule and the iron metal surface are shown in Figure 10.18, and the total energies, relative energies, interaction energies, and bond distances are reported in Table 10.17. The four different arrangements of the molecule on the metal surface were obtained; they are noted with alphabet letters *a*, *b*, *c* and *d*. Configurations *a* and *b* are the most preferred arrangements of the C-Chec inhibitor onto the metal surface with 0.000 and 1.436 kcal/mol, respectively.

Configuration *a*, which has -426.1993 kcal/mol, is the most preferred arrangement. Configuration *d* was found to have the lowest interaction energy with -415.4063 kcal/mol, making it the least preferred arrangement of the C-Chec inhibitor onto the mild steel metal surface. All the interaction energies obtained in the table are above -100 kcal/mol, which is an indication that the interaction of the C-Chec with mild steel metal surface happens through chemisorption. The Fe···O bond distances have values of 5.292 Å for configuration *a*, 3.860 Å for configuration *b*, 3.768 Å for configuration *c* and 2.860 Å for configuration *d*.



(Fe···C-Chec)-*a* (Fe···C-Chec)-*b* (Fe···C-Chec)-*c* (Fe···C-Chec)-*d*

Figure 10.18: Different adsorption geometries of C-Chec molecule on the Fe(110) surface in water solution.

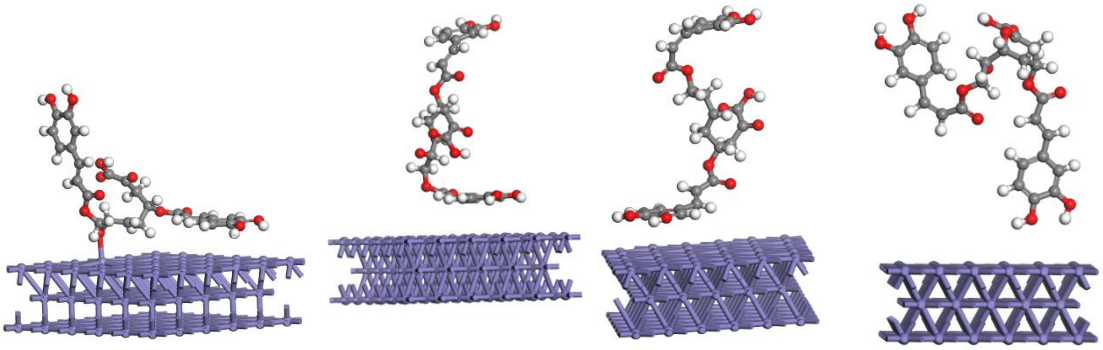
© University of Venda

Table 10.17: Optimised energies for stable C-Chec acid adsorption sites on Fe(110) surface.

Configurations	**$E_{C\text{-}Chec+metal}$ (Ha)**	**$\Delta E_{C\text{-}Chec+metal}$ (kcal/mol)**	**ΔE_{inter} (kcal/mol)**	**Bond distance (Å)**
(Fe···C-Chec)-*a*	-12516.997994	0.00	-426.1992	(Fe···O41) 5.292 (Fe···C24) 4.692
(Fe···C-Chec)-*b*	-12516.995705	1.436	-424.7629	(Fe···O52) 3.860 (Fe···C26) 3.517
(Fe···C-Chec)-*c*	-12516.986951	6.929	-419.2698	(Fe···O8) 3.768 (Fe···C18) 3.589 (Fe···C49) 3.206
(Fe···C-Chec)-*d*	-12516.980794	10.793	-415.4063	(Fe···O41) 2.860 (Fe···C24) 3.148

Structures representing interaction involving the caffeoyl-feruroyl-quinic acid (CFQ) inhibitor molecule and the mild steel metal surface are shown in Figure 10.19; the total energy, relative energy, interaction energy, and bond distances are reported in Table 10.18. The different arrangements of the inhibitor molecule on the metal surface are represented by alphabet letters *a*, *b*, *c*, and *d*. Configuration *a* is the only stable and preferred arrangement because all the other configurations have high energy with respect to it. The Fe···O bond in configuration in *a* has a distance of 2.237 Å, which is the shortest bond found amongst the four configurations. This observation further supports why configuration *a* is the most stable preferred arrangement of the CFQ on the mild steel metal surface compared to configurations *a*, *b*, and *c*.

The four configurations gave the interaction energies which are greater than -100 kcal/mol. Configuration *a* has high interaction energy of -521.4330 kcal/mol compared to -506.9296, -504.5596 and -467.1832 kcal mol for configurations *b*, *c*, and *d*. This observation makes configuration *a* the most preferred arrangement of CFQ onto the mild steel metal surface based on the energetic and bond distance parameter criteria.



(Fe···CFQ)-*a* (Fe···CFQ)-*b* (Fe···CFQ)-*c* (Fe···CFQ)-*d*

Figure 10.19: Different adsorption geometries of CFQ acid molecule on the Fe(110) surface in water solution.

© University of Venda

Table 10.18: Optimised energies for stable CFQ acid adsorption sites on Fe(110) surface.

Configurations	**$E_{CFQ+metal}$ (Ha)**	**$\Delta E_{CFQ+metal}$ (kcal/mol)**	**ΔE_{inter} (kcal/mol)**	**Bond distance (Å)**
(Fe···CFQ)-*a*	-12669.698509	0.000	-521.4330	(Fe···O43) 2.237
(Fe···CFQ)-*b*	-12669.675396	14.503	-506.9296	(Fe···O58) 3.272 (Fe···O59) 3.889
(Fe···CFQ)-*c*	-12669.671619	16.873	-504.5596	(Fe···O58) 3.720 (Fe···C11) 3.462
(Fe···CFQ)-*d*	-12669.612055	54.250	-467.1832	(Fe···O59) 3.537

The interaction of the ferulic acid compound in aluminium, zinc, and mild steel metal surfaces was found to have lower interaction energy values compared to other compounds. The reason for this finding is that chain length in the molecule plays an important role in the corrosion inhibition properties [453]. Therefore, comparing the chain length of ferulic acid to that of the other compounds, it can be observed that the ferulic acid chain is much smaller than the rest of the isolated compounds. From the thermodynamic point of view, the more stable system has the lowest energy state [460]. In this regard, it is expected that the system with more negative interaction energies is more stable. This view is in line with the results obtained. The interaction energies for all the configurations are negative, which suggests that the interaction energy between the inhibitor molecules and the metal surfaces is spontaneous, strong, and stable [461]. The highest interaction energy was obtained when the CFQ interacted with the iron metal having an interaction energy of -521.4330 kcal/mol. It has also been found that the parallel arrangement of the inhibitor on the metal surface gives the best interaction energy than the vertical arrangement. This is due to the fact the parallel arrangement gives more possibility for the inhibitor molecule atoms to form a bond with the metal surface, and that the inhibitor molecules cover a wide range of the surface area of the metal, thereby giving high inhibition efficiency. The bond distances can also be used to determine the type and strength of the bond that forms between the inhibitor molecule and the surface of the metal and the closeness of the inhibitor molecules to the metal surface. Most of the bond distances obtained were longer than 2.0, with only a few below that. FA and 4-P-CQ inhibitors for Al gave interaction energies lower than -100 kcal/mol, while all the other inhibitors in the three metals gave interaction energy higher than that, suggesting a chemisorption kind of adsorption.

© University of Venda

CHAPTER 11

Scanning electron microscopy, energy dispersive spectroscopy, and X-ray diffraction

© University of Venda

11. Introduction

This section investigates the surface morphology and the elemental composition of the metals before and after corrosion inhibition in the absence and presence of non-radiated and UV-radiated *H. kraussii* extract in 1.0 M HCl and H_2SO_4 solution.

11.1. Surface morphology and elemental composition

The surface morphology and elemental composition of mild steel, zinc, and aluminium metal immersed in 1.0 M HCl and H_2SO_4 corrosive solution before and after the introduction of the highest concentration of 1500 ppm of non-radiated and UV-radiated *H. kraussii* for 8 hours was carried out using SEM-coupled with EDS for elemental composition.

11.1.1. Aluminium metal

Figures 11.1 to 11.2 show the SEM images and EDS spectra for aluminium metals in 1.0 M HCl in the absence and presence of 1500 ppm concentration of non-radiated and UV-radiated *H. kraussii* plant extract. From the EDS spectra, aluminium was the dominant element observed in all the spectra. Calcium was one of the elements observed on the surface of aluminium metal in the presence of UV-radiated *H. kraussii* extract. This element can be said to be the difference maker in the smoothness of the inhibited aluminium surface compared to the acid-exposed aluminium metal. Comparing the aluminium metal exposed in the HCl solution to those exposed in the non-radiated and UV-radiated *H. kraussii* solution, it can be observed that the aluminium exposed in HCl was highly destroyed because of the free acid attack and showed high surface imperfection [297, 462], but when the aluminium was exposed in the presence of the inhibitor, the metal surface showed improved smoothness showing that the metal was protected to some extent from the acid.

Figures 11.3-11.6 show the SEM images mapping for different regions on the metal surface, while Table 11.1-11.3 shows the corresponding elements found in each selected region on the metal surface. It can be observed that the aluminium element was spotted in all the regions for all the metals. This observation is expected since we are dealing with aluminium metal. In the presence of UV-*radiated H. kraussii* extract, it can be observed that additional elements such as oxygen and calcium were present on the surface of the metal after being exposed to the HCl-inhibitor solution. These elements were present on the unexposed aluminium metal but were

© University of Venda

not present when the aluminium metal was exposed to the HCl solution. The compounds found in *H. kraussii plant* extract contain oxygen in their molecular structures. This suggests that the UV-radiated *H. kraussii* was adsorbed onto the aluminium surface, preserving the metal from the acid corrosion attack. The presence of oxygen could also indicate the formation of corrosion products in the form of aluminium oxide.

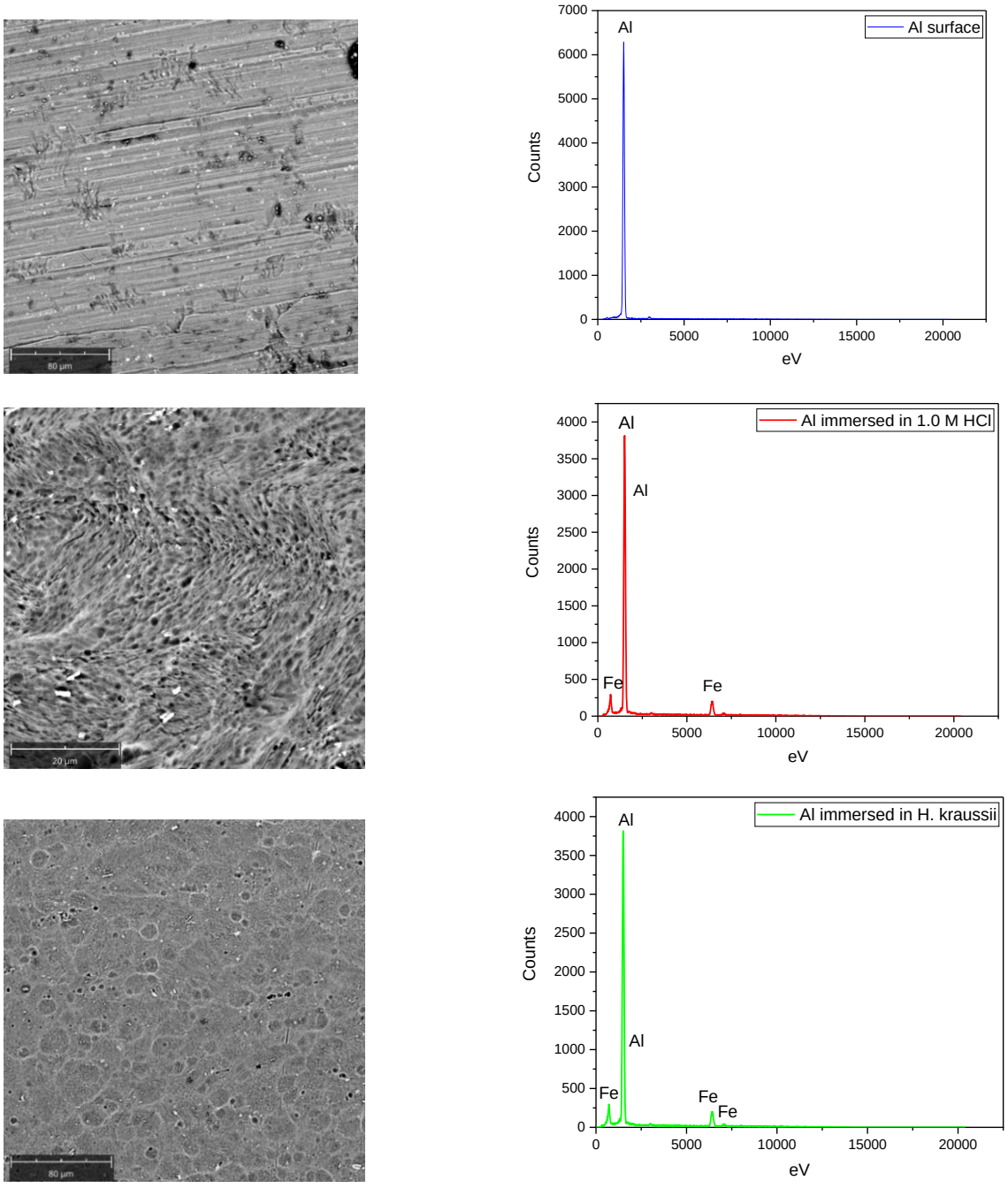


Figure 11. 1: SEM images and EDS spectra of unexposed aluminium surface, Aluminium immersed in uninhibited 1.0 M HCl, and Aluminium immersed in *H. kraussii*-inhibited 1.0 M HCl solution.

© University of Venda

University of Venda
Creating Future Leaders

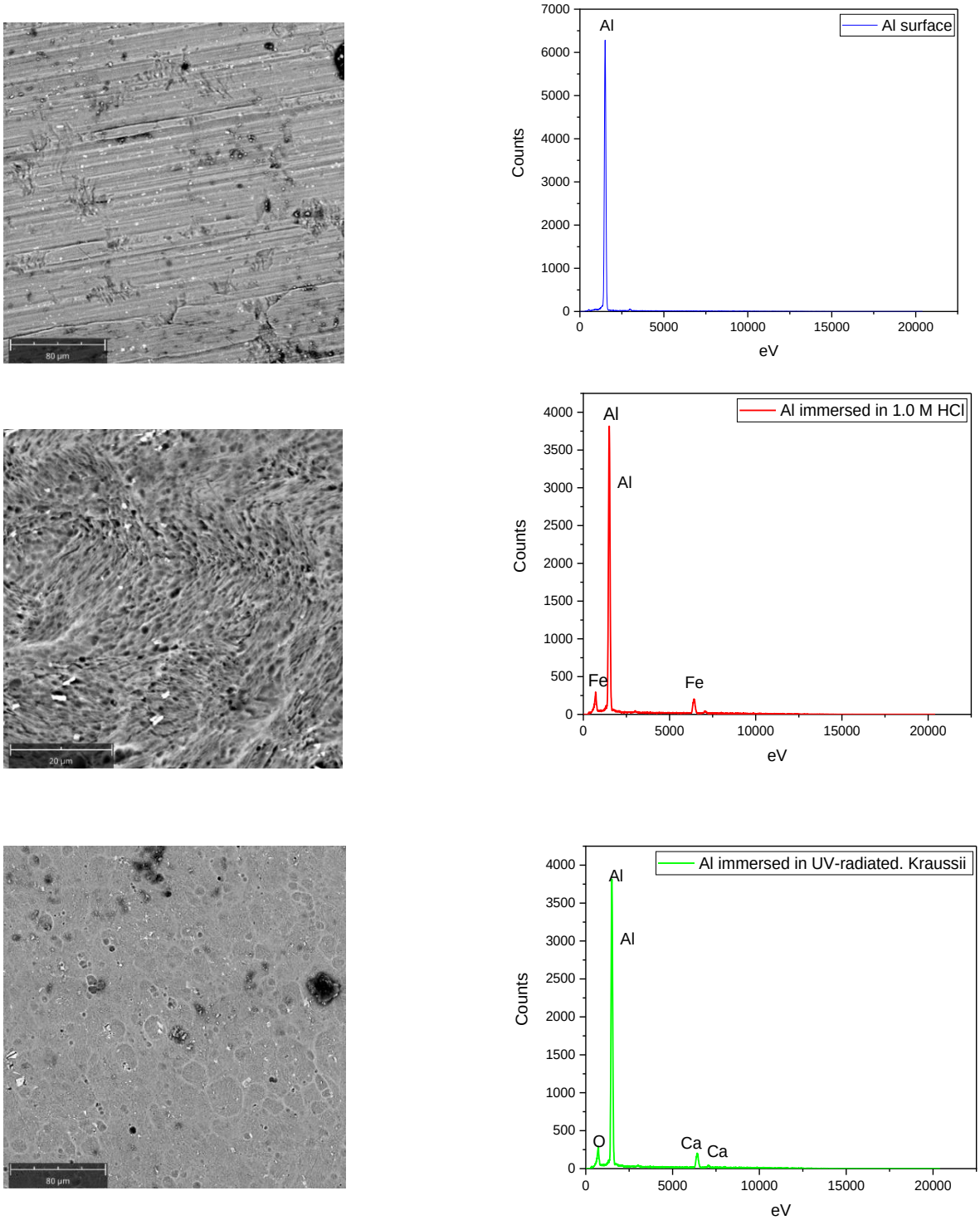


Figure 11. 2: SEM images and EDS spectra of unexposed aluminium surface, Aluminium immersed in uninhibited 1.0 M HCl, and Aluminium immersed in UV-radiated *H. kraussii*-inhibited 1.0 M HCl solution.

© University of Venda

11.1.1.1. Aluminium metal mapping

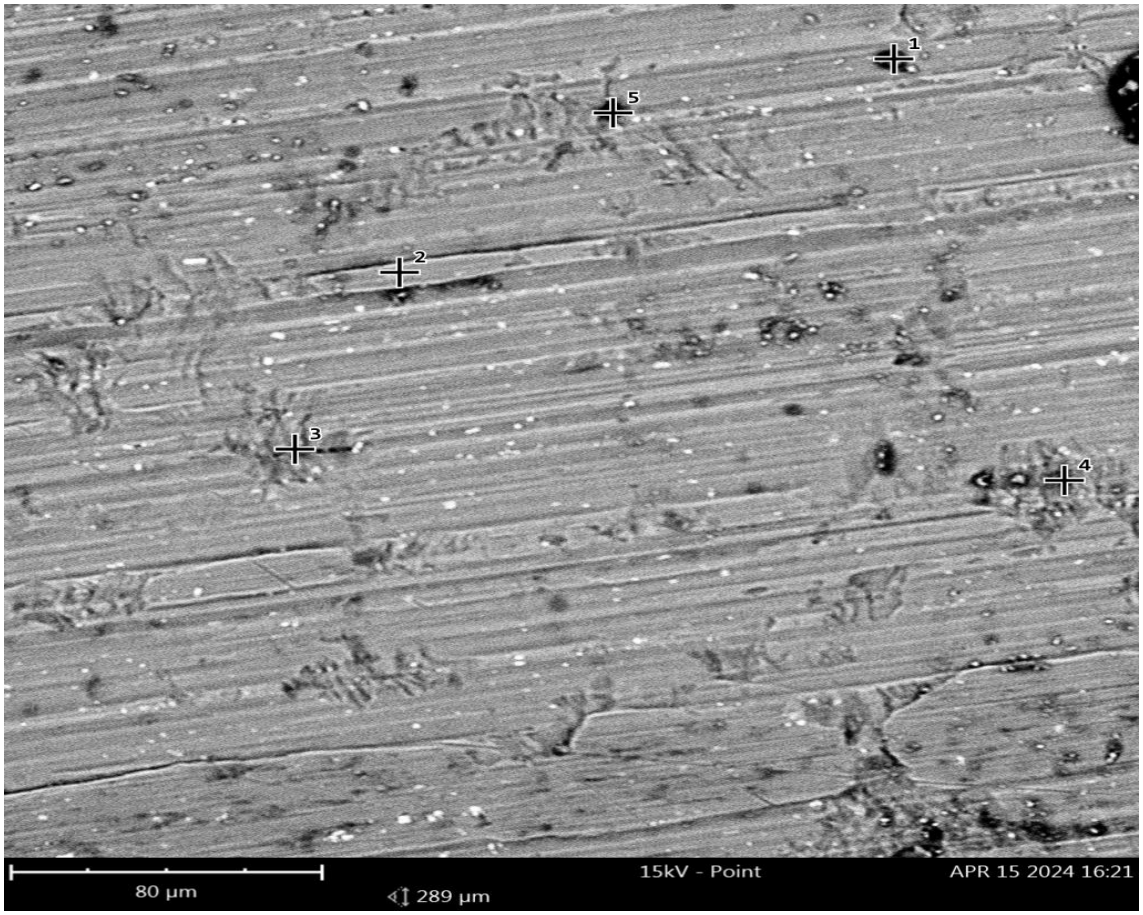


Figure 11. 3: SEM image of the unexposed aluminium metal surface.

Table 11. 1: Table showing the atomic number, element symbol, element name, concentration percentage and certainty of different regions on the aluminium metal surface.

Metal	Region	Atomic number	Element symbol	Element name	Concentration percentage (%)	Certainty
Aluminium metal	1	13	Al	Aluminium	59.9	1
		8	O	Oxygen	35.2	0.98
		20	Ca	Calcium	4.5	0.98
		70	Yb	Ytterbium	0.4	0.49
	2	13	Al	Aluminium	100	1
	3	13	Al	Aluminium	100	0.99
	4	13	Al	Aluminium	100	1
	5	13	Al	Aluminium	100	1

© University of Venda

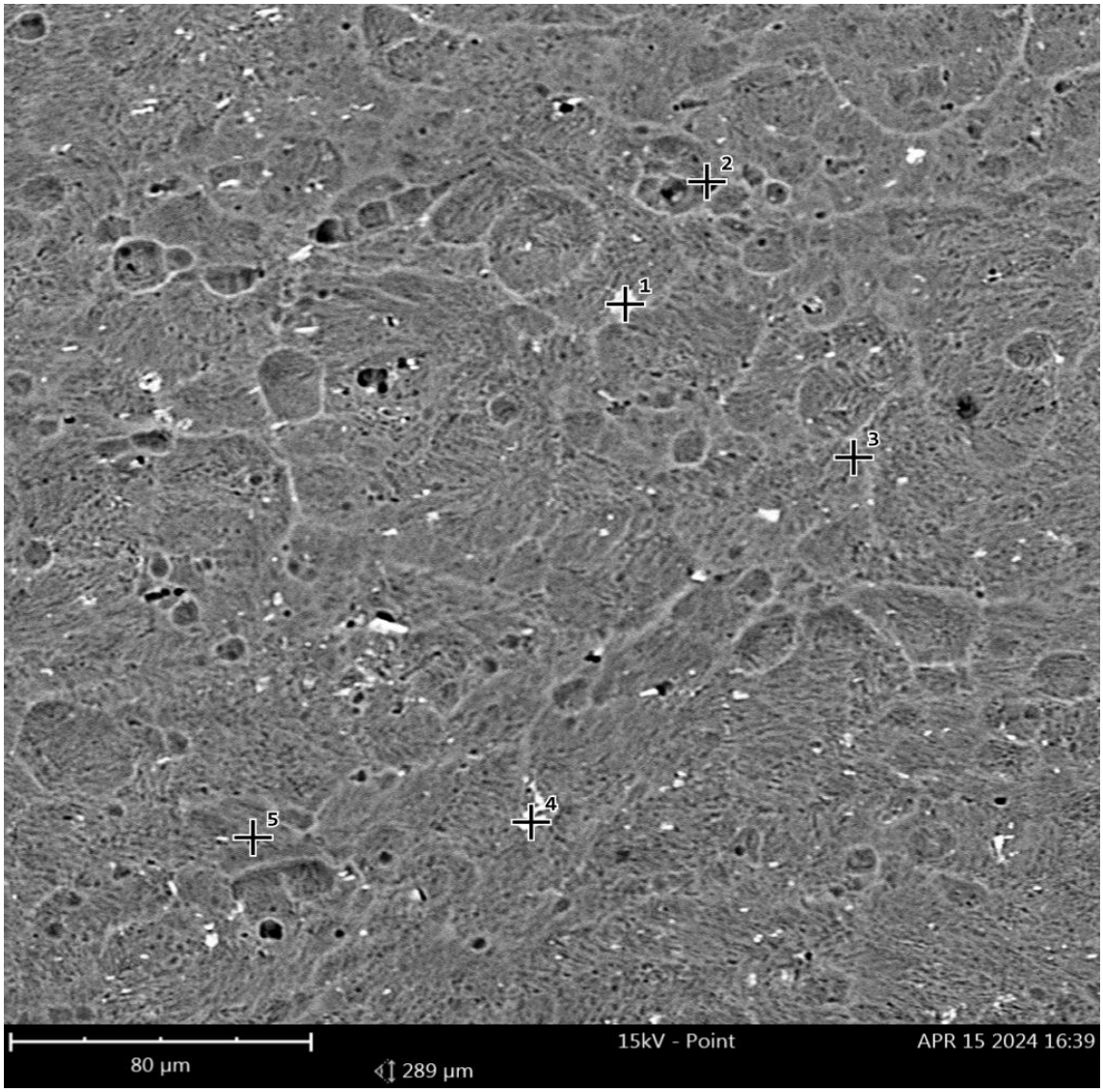


Figure 11. 4: SEM image of aluminium metal immersed in 1.0 M HCl solution.

Table 11. 2: Table showing the atomic number, element symbol, element name, concentration percentage and certainty of different regions on the aluminium metal surface.

Acid	Region	Atomic number	Element symbol	Element name	Concentration percentage (%)	Certainty
HCl	1	13	Al	Aluminium	86.1	1
		26	Fe	Iron	13.9	0.99
	2	13	Al	Aluminium	100	1
	3	13	Al	Aluminium	100	0.99
	4	13	Al	Aluminium	87	0.99
		26	Fe	Iron	13	0.98
	5	13	Al	Aluminium	100	1

© University of Venda

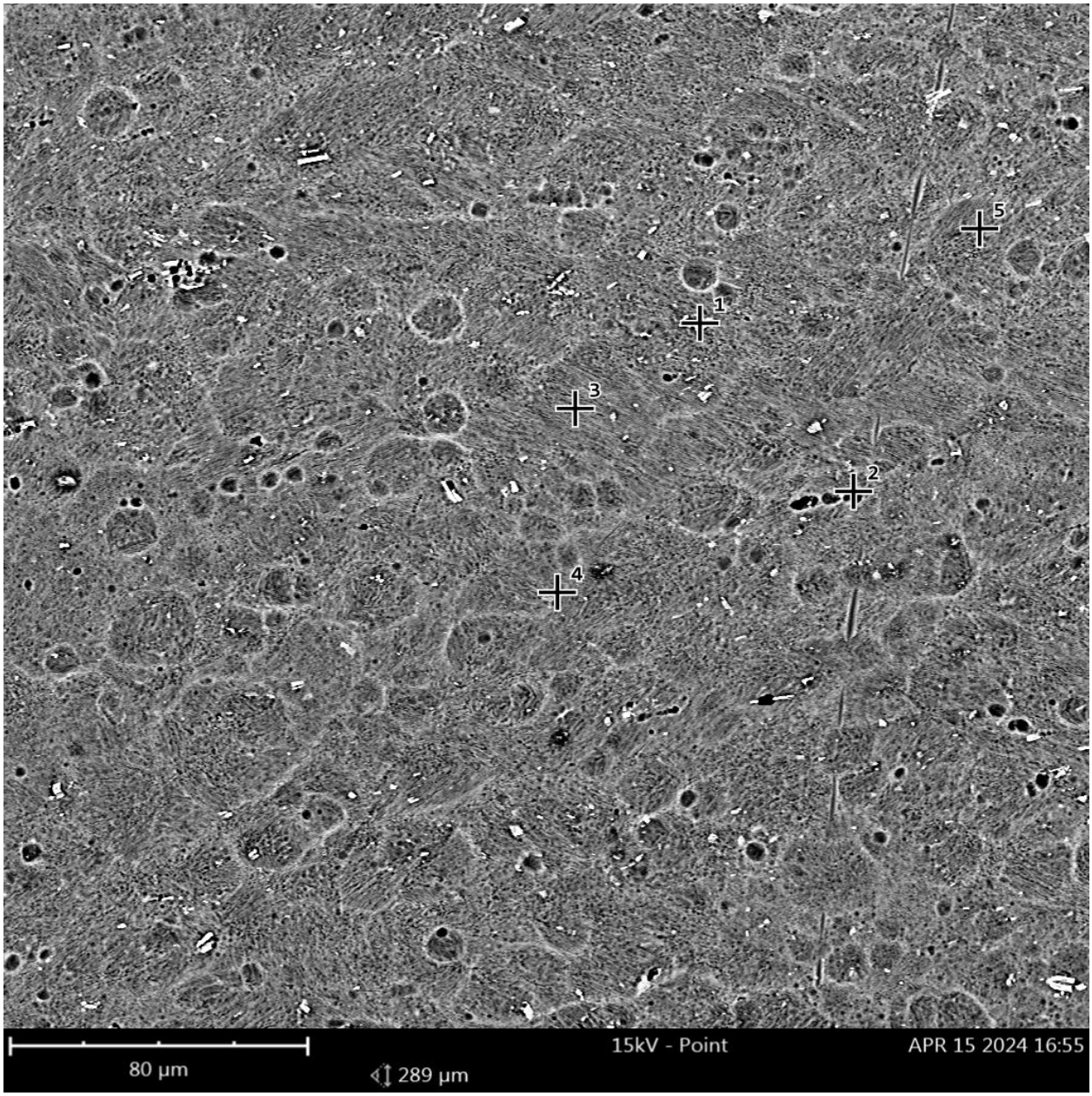


Figure 11. 5: SEM image of aluminium metal immersed in 1.0 M HCl and *H. kraussii* - inhibited solution.

Table 11. 3: Table showing the atomic number, element symbol, element name, concentration percentage and certainty of different regions on the metal surface.

Inhibitor	**Region**	**Atomic number**	**Element symbol**	**Element name**	**Concentration percentage (%)**	**Certainty**
H. kraussii extract	1	13	Al	Aluminium	86.1	1
		26	Fe	Iron	13.9	0.99
	2	13	Al	Aluminium	100	0.99
	3	13	Al	Aluminium	100	0.99
	4	13	Al	Aluminium	100	0.99
	5	13	Al	Aluminium	100	1

© University of Venda

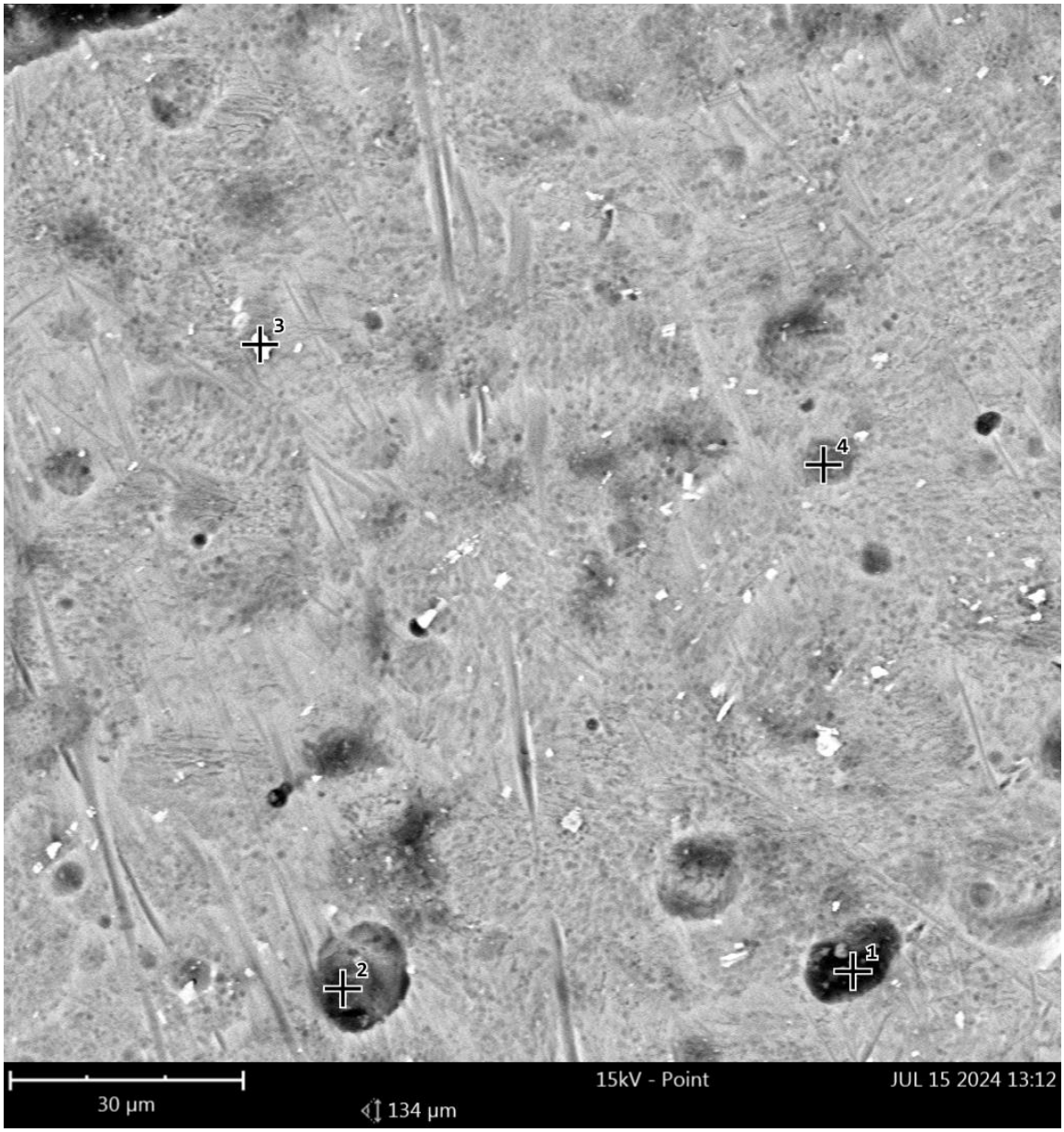


Figure 11. 6: SEM image of aluminium metal immersed in 1.0 M HCl and UV-radiated *H. kraussii* - inhibited solution.

Table 11. 4: Table showing the atomic number, element symbol, element name, concentration percentage and certainty of different regions on the aluminium metal surface.

Inhibitor	**Region**	**Atomic number**	**Element symbol**	**Element name**	**Concentration percentage (%)**	**Certainty**
UV-radiated *H. kraussii* extract	1	13	Al	Aluminium	50.6	0.99
		8	O	Oxygen	42.1	0.98
		20	Ca	Calcium	7.4	0.98
	2	13	Al	Aluminium	100	1
	3	13	Al	Aluminium	100	1
	4	13	Al	Aluminium	100	0.99

© University of Venda

11.1.2. Zinc metal

Figures 11.7 to 11.10 show the SEM images and EDS spectra for zinc metals in 1.0 M HCl and H_2SO_4 in the absence and presence of 1500 ppm of non-radiated and UV-radiated *H. kraussii* extract. It can be observed that in the presence of hydrochloric and sulphuric acid, the zinc metal was destroyed with many pits on the surface, as reported in the literature [463]. However, when the non-radiated and UV-radiated *H. kraussii* extracts were introduced into the acid solution, the metal was protected, and the surface of the metal resembled more of the unexposed metal surface. This is enough evidence to show the ability of the *H. kraussii* extract inhibitor to effectively hinder the corrosion progression on the metal surface. Comparing the inhibition in the presence of non-radiated and UV-radiated extract, the non-radiated extract was found to be an outstanding inhibitor looking at the smoothness of the surface of the metal.

It can also be observed that the zinc element was only observed in the EDS spectrum for unexposed zinc metal. This is because the zinc coupon used was iron metal galvanized by liquid zinc. When this galvanized metal was exposed to the acidic solutions, the zinc outer layer was destroyed by the presence of the acid. This is mostly observed in the mapping element table, with iron being the most dominant element. The surface mapping (Figures 11.11-11.17) shows different regions on the surface of the metal, and the elements found in each region are tabulated in Table 11.5-11.11. The mapping is very useful because the surface of the metal may be affected differently, which is evident from the elements observed in different regions. In the presence of both the corrosive solution and inhibitor concentrations, it can be observed in the EDS spectra that oxygen was one of the elements detected on the surface of the metal after gravimetric analysis. The presence of oxygen is an indication of the formation of corrosion products in the form of zinc oxide [462]. The formation of zinc oxide is the conformation that corrosion took place on the surface of the metal. The presence of elements such as cobalt, barium, carbon, and dysprosium in the presence of the two extracts that were not present in the unexposed metal is an indication that the inhibition and adsorption of the extract on the metal surface took place.

© University of Venda

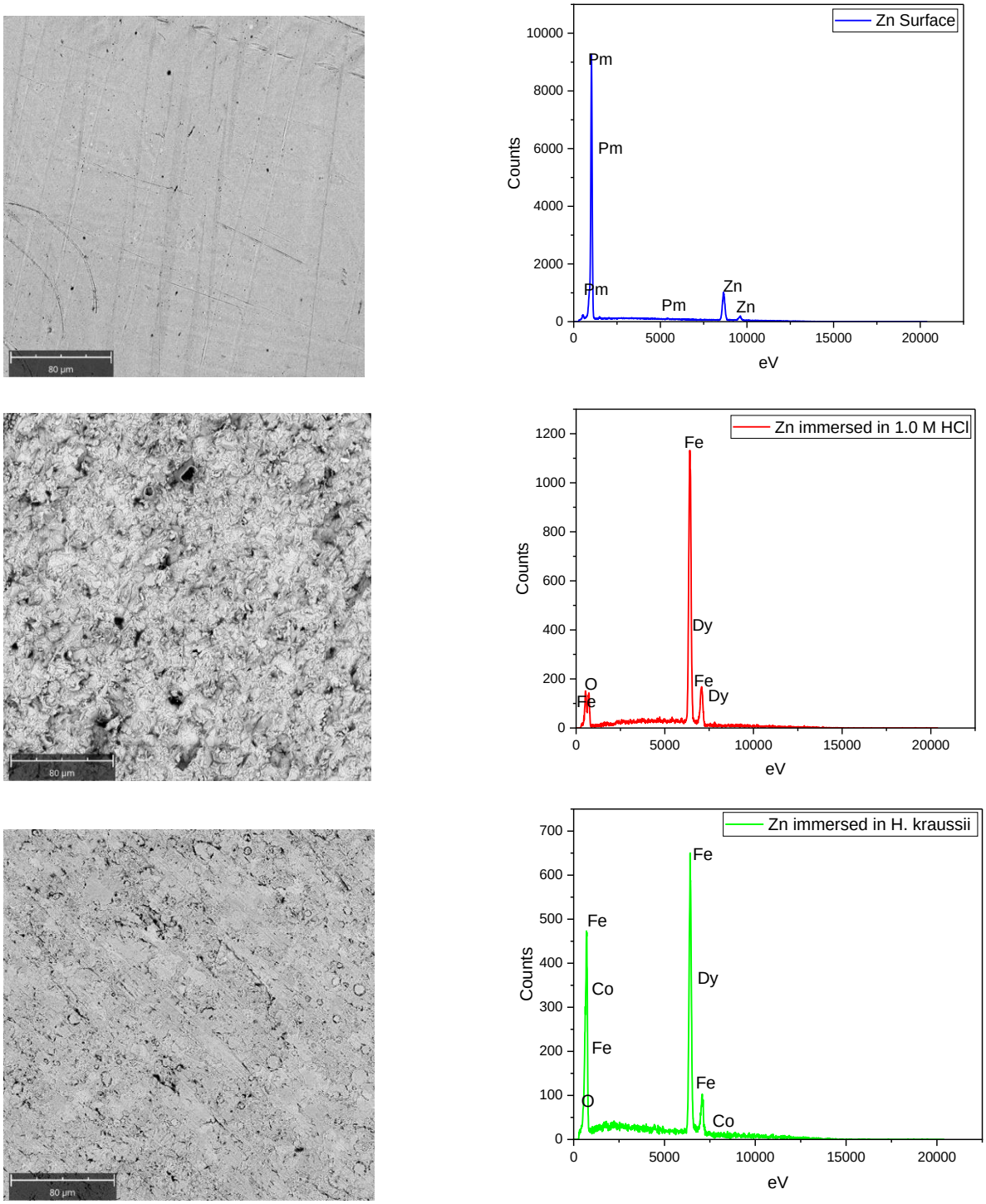


Figure 11. 7: SEM images and EDS spectra of unexposed zinc surface, zinc immersed in uninhibited 1.0 M HCl, and zinc immersed in UV-radiated *H. kraussii*-inhibited 1.0 M HCl solution.

© University of Venda

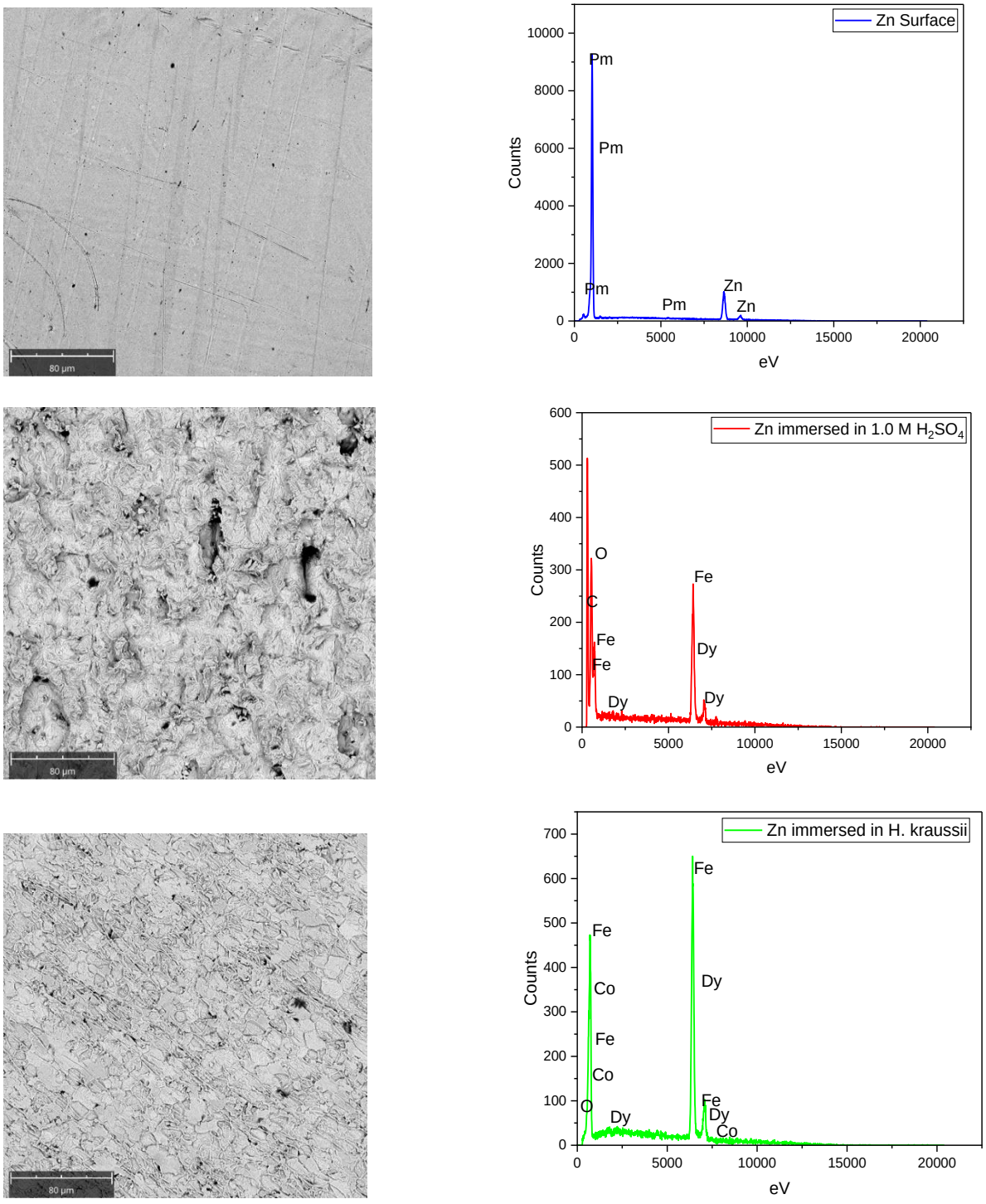


Figure 11. 8: SEM images and EDS spectra of unexposed zinc surface, zinc immersed in uninhibited 1.0 M H_2SO_4, and zinc immersed in *H. kraussii*-inhibited 1.0 M H_2SO_4 solution.

© University of Venda

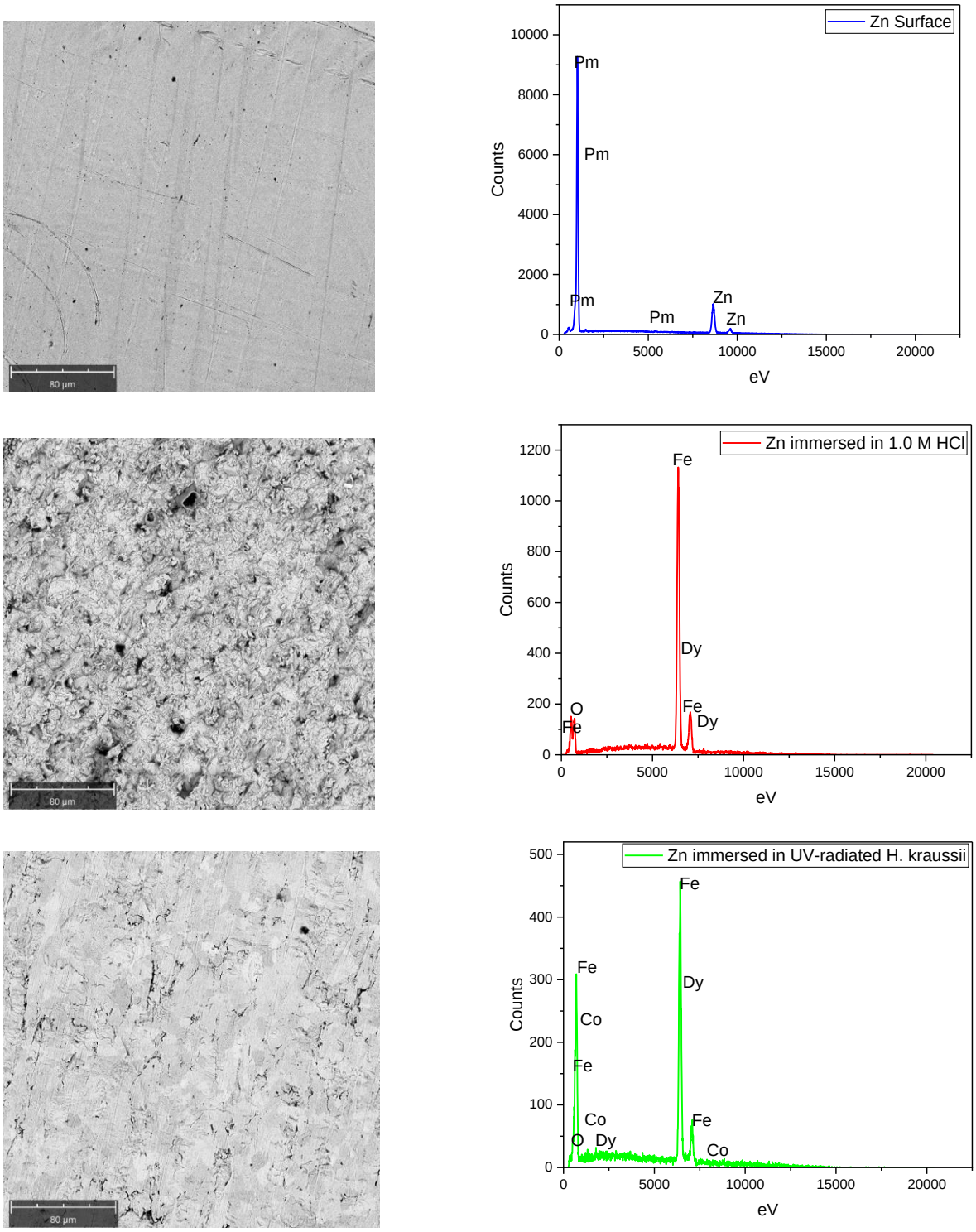


Figure 11. 9: SEM images and EDS spectra of unexposed zinc surface, zinc immersed in uninhibited 1.0 M HCl, and zinc immersed in UV-radiated *H. kraussii*-inhibited 1.0 M HCl solution.

© University of Venda

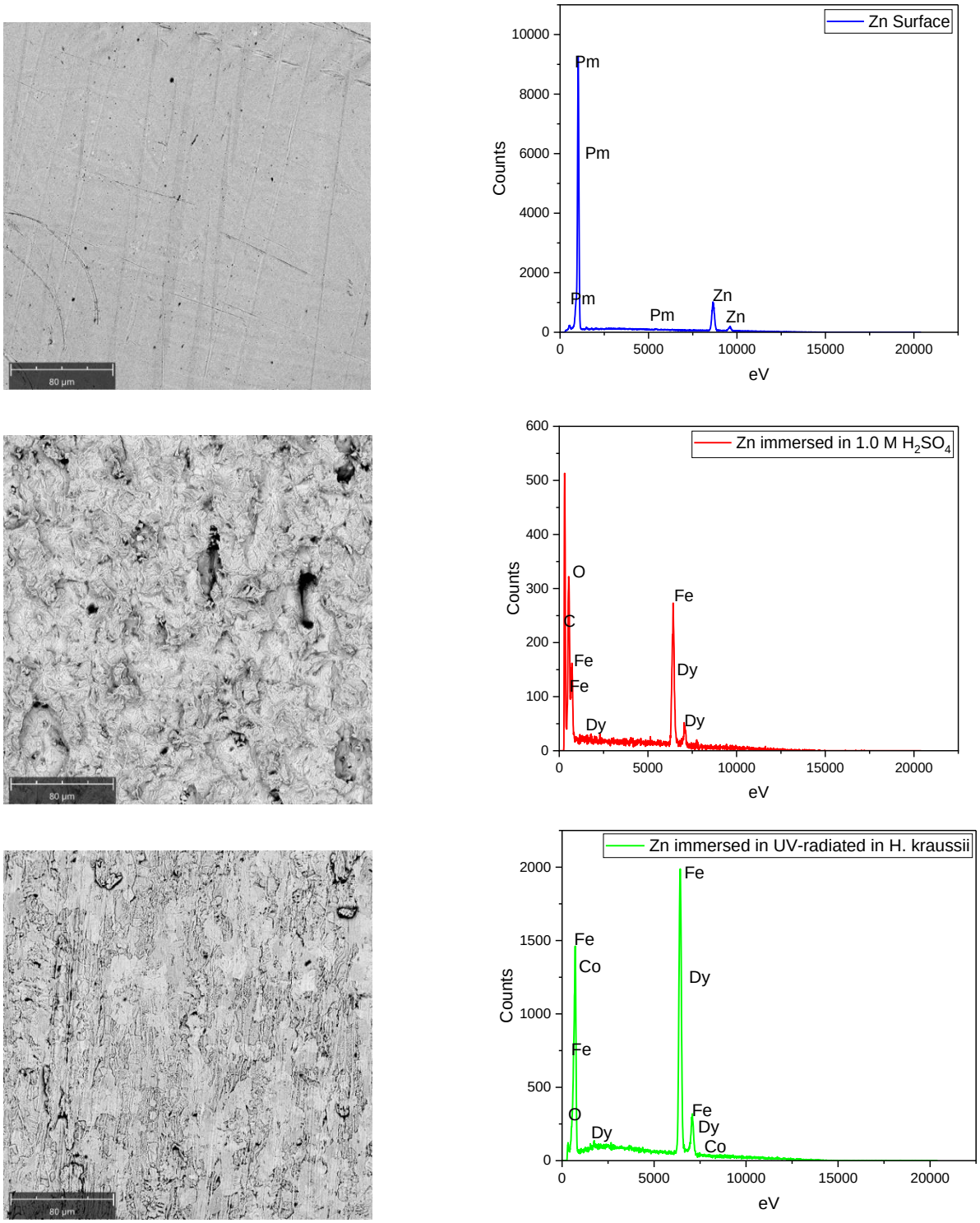


Figure 11. 10: SEM images and EDS spectra of unexposed zinc surface, zinc metal immersed in uninhibited 1.0 M H_2SO_4, and zinc immersed in UV-radited *H. kraussii*-inhibited 1.0 M H_2SO_4 solution.

© University of Venda

11.1.2.1. Zinc metal mapping

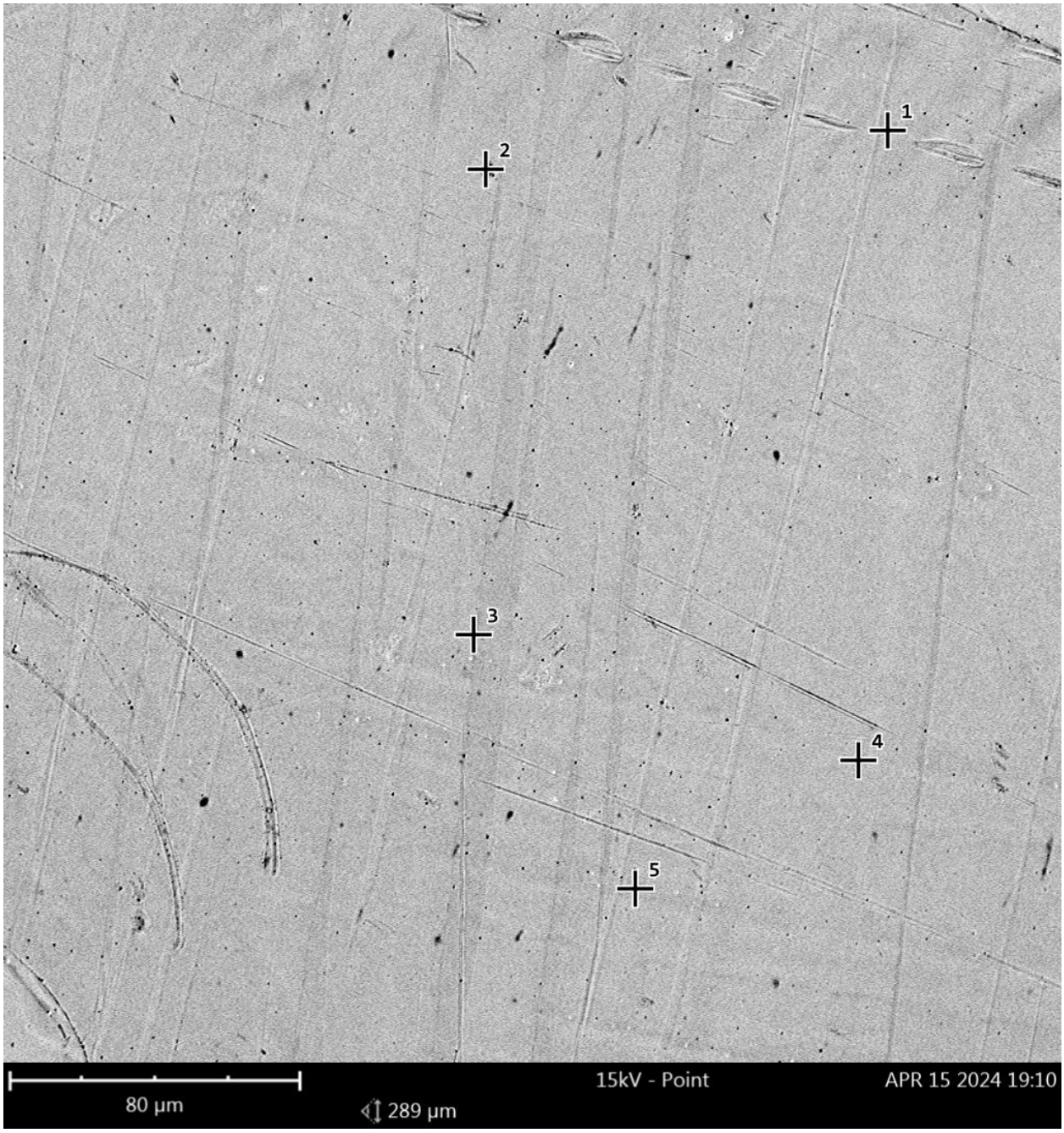


Figure 11. 11: SEM image of unexposed zinc metal surface.

© University of Venda

Table 11. 5: Table showing the atomic number, element symbol, element name, concentration percentage and certainty of different regions on the zinc metal surface.

Metal	Region	Atomic number	Element symbol	Element name	Concentration percentage (%)	Certainty
Zinc metal	1	30	Zn	Zinc	98.7	0.99
		61	Pm	Promethium	1.3	0.90
	2	8	O	Oxygen	47.9	0.97
		30	Zn	Zinc	40.4	0.97
		20	Ca	Calcium	10.7	0.97
		61	Pm	Promethium	0.9	0.72
	3	30	Zn	Zinc	100.0	0.98
	4	30	Zn	Zinc	100.0	0.99
	5	30	Zn	Zinc	93.3	0.99
		46	Pb	Palladium	5.4	0.96
		61	Pm	Promethium	1.4	0.86

© University of Venda

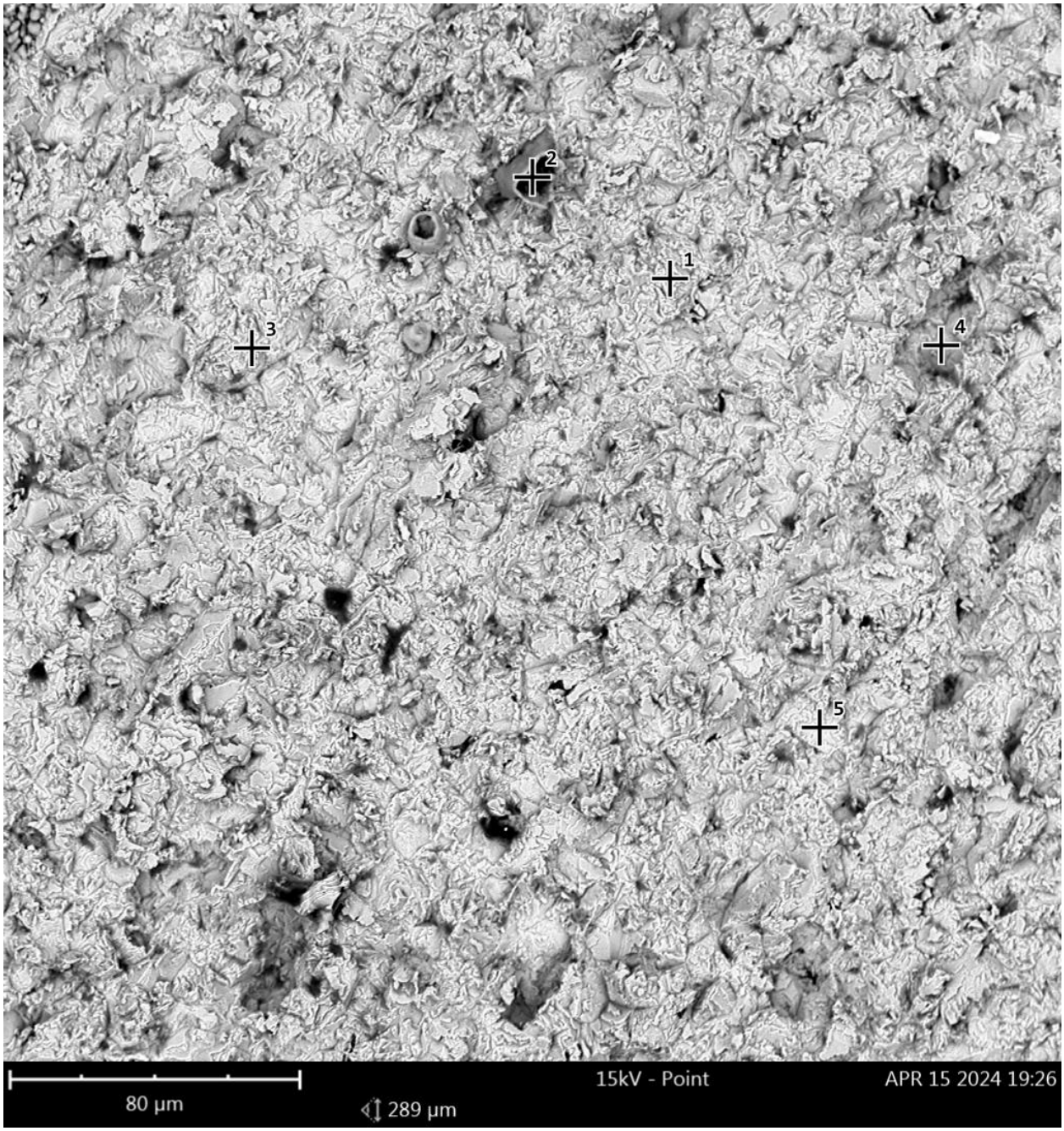


Figure 11. 12: SEM image of zinc metal immersed in 1.0 M HCl in solution.

© University of Venda

Table 11. 6: Table showing the atomic number, element symbol, element name, concentration percentage and certainty of different regions on the zinc metal surface.

Acid	Region	Atomic number	Element symbol	Element name	Concentration percentage (%)	Certainty
HCl	1	26	Fe	Iron	68.9	1.00
		66	Dy	Dysprosium	31.1	0.98
	2	26	Fe	Iron	60.2	0.99
		66	Dy	Dysprosium	26.6	0.97
		8	O	Oxygen	13.2	0.96
	3	26	Fe	Iron	60.3	0.99
		66	Dy	Dysprosium	26.6	0.98
		8	O	Oxygen	13.1	0.97
	4	26	Fe	Iron	67.2	0.99
		66	Dy	Dysprosium	32.8	0.96
	5	26	Fe	Iron	59.7	0.99
		66	Dy	Dysprosium	27.9	0.97
		8	O	Oxygen	12.4	0.96

© University of Venda

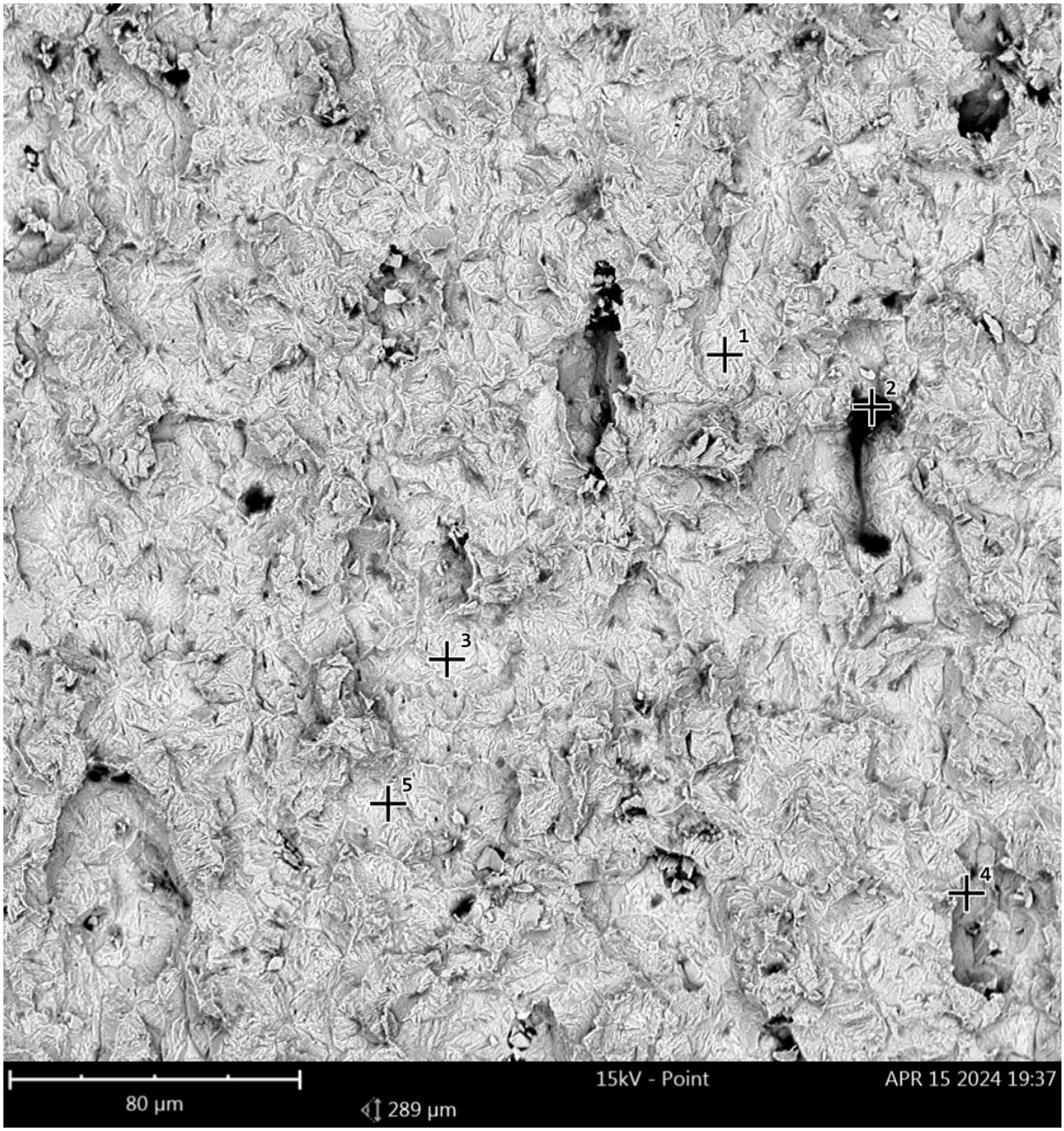


Figure 11. 13: SEM image of zinc metal immersed in 1.0 M H_2SO_4 solution.

© University of Venda

Table 11. 7: Table showing the atomic number, element symbol, element name, concentration percentage and certainty of different regions on the zinc metal surface.

Acid	Region	Atomic number	Element symbol	Element name	Concentration percentage (%)	Certainty
H_2SO_4	1	26	Fe	Iron	56.7	0.99
		66	Dy	Dysprosium	26.1	0.98
		8	O	Oxygen	17.2	0.98
	2	6	C	Carbon	56.7	0.98
		8	O	Oxygen	27.2	0.98
		26	Fe	Iron	11.4	0.98
		66	Dy	Dysprosium	4.7	0.95
	3	26	Fe	Iron	64.9	0.98
		66	Dy	Dysprosium	35.1	0.95
	4	26	Fe	Iron	63.0	0.98
		66	Dy	Dysprosium	26.4	0.92
		8	O	Oxygen	10.3	0.91
		56	Ba	Barium	0.2	0.21
	5	26	Fe	Iron	58.0	1.00
		66	Dy	Dysprosium	27.4	0.99
		8	O	Oxygen	14.6	0.98

© University of Venda

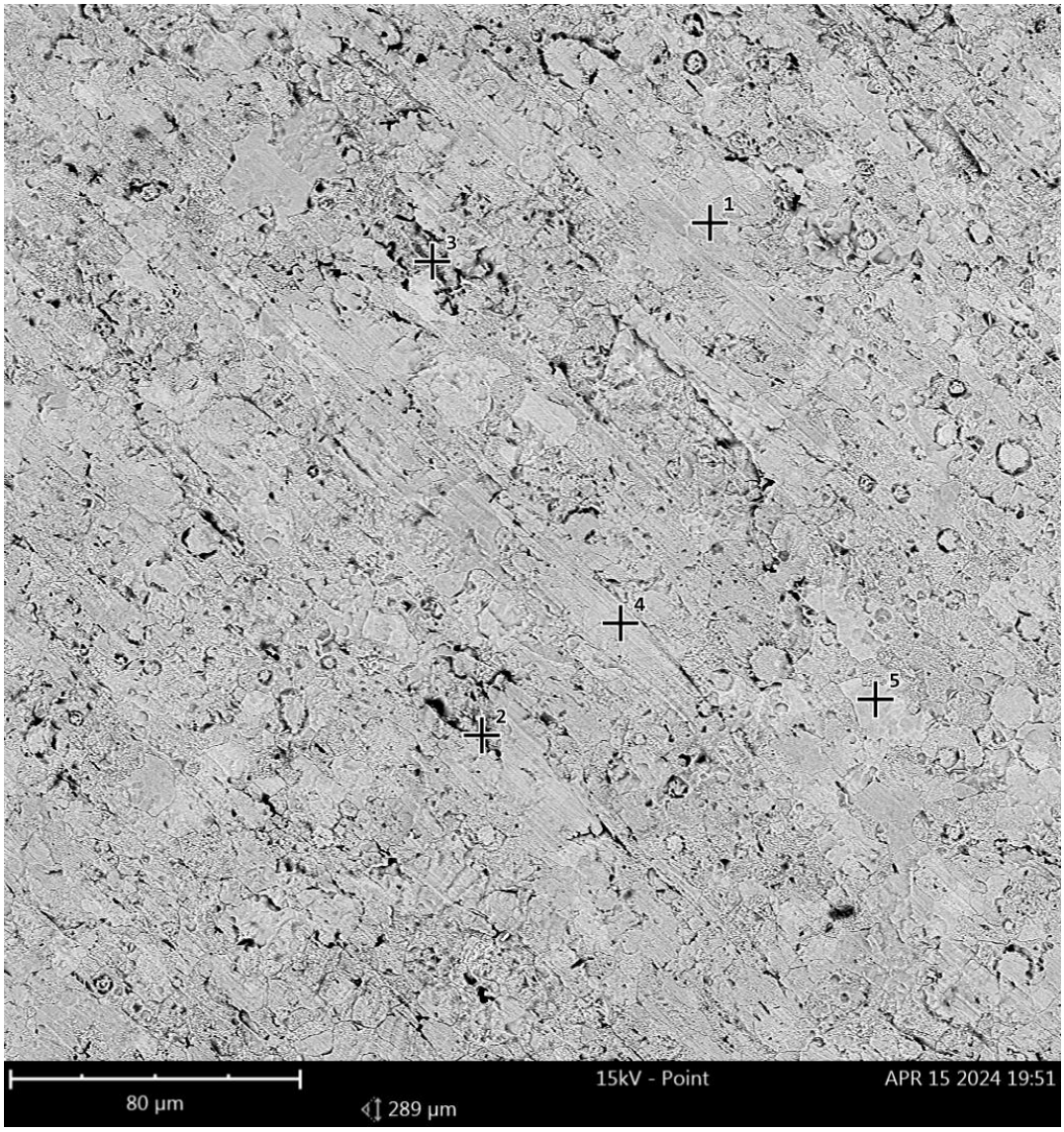


Figure 11. 14: SEM image of zinc metal immersed in 1.0 M HCl and *H. kraussii* - inhibited solution.

© University of Venda

Table 11. 8: Table showing the atomic number, element symbol, element name, concentration percentage and certainty of different regions on the zinc metal surface.

Inhibitor	Region	Atomic number	Element symbol	Element name	Concentration percentage (%)	Certainty
H. kraussii extract	1	26	Fe	Iron	60.8	0.99
		66	Dy	Dysprosium	29.1	0.98
		8	O	Oxygen	10.1	0.97
	2	26	Fe	Iron	61.0	0.99
		66	Dy	Dysprosium	30.1	0.96
		8	O	Oxygen	8.9	0.95
	3	26	Fe	Iron	50.1	0.99
		66	Dy	Dysprosium	26.8	0.98
		8	O	Oxygen	23.1	0.98
	4	26	Fe	Iron	59.0	0.99
		66	Dy	Dysprosium	30.0	0.98
		8	O	Oxygen	11.0	0.97
	5	26	Fe	Iron	61.1	1.00
		66	Dy	Dysprosium	28.5	0.99
		8	O	Oxygen	10.4	0.98

© University of Venda



Figure 11. 15: SEM image of zinc metal immersed in 1.0 M H_2SO_4 and *H. kraussii* - inhibited solution.

© University of Venda

Table 11. 9: Table showing the atomic number, element symbol, element name, concentration percentage and certainty of different regions on the zinc metal surface.

Inhibitor	**Region**	**Atomic number**	**Element symbol**	**Element name**	**Concentration percentage (%)**	**Certainty**
H. kraussii extract	1	26	Fe	Iron	60.6	0.99
		66	Dy	Dysprosium	29.1	0.98
		8	O	Oxygen	10.3	0.97
	2	26	Fe	Iron	77.1	0.99
		8	O	Oxygen	22.9	0.97
	3	26	Fe	Iron	61.4	0.99
		66	Dy	Dysprosium	27.5	0.95
		8	O	Oxygen	10.2	0.93
		27	Co	Cobalt	0.9	0.75
	4	26	Fe	Iron	59.0	0.99
		66	Dy	Dysprosium	27.5	0.95
		8	O	Oxygen	13.4	0.95
	5	26	Fe	Iron	61.6	0.99
		66	Dy	Dysprosium	28.0	0.98
		8	O	Oxygen	10.5	0.97

© University of Venda

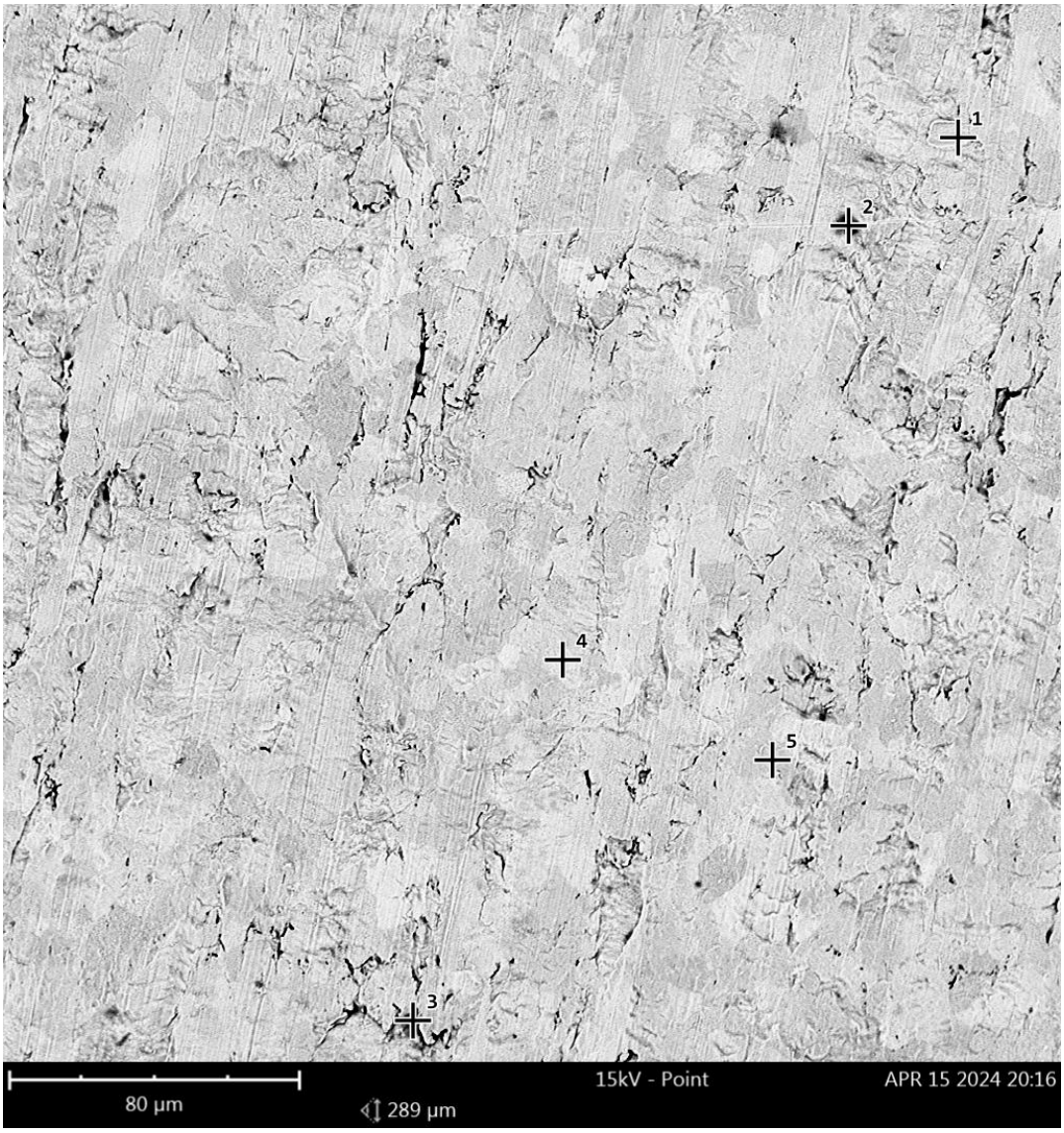


Figure 11. 16: SEM image of zinc metal immersed in 1.0 M HCl and UV-radiated *H. kraussii* - inhibited solution.

© University of Venda

Table 11. 10: Table showing the atomic number, element symbol, element name, concentration percentage and certainty of different regions on the zinc metal surface.

Inhibitor	Region	Atomic number	Element symbol	Element name	Concentration percentage (%)	Certainty
UV-radiated *H. kraussii* extract	1	26	Fe	Iron	61.8	0.99
		66	Dy	Dysprosium	28.5	0.98
		8	O	Oxygen	9.7	0.96
	2	26	Fe	Iron	26.5	0.98
		66	Dy	Dysprosium	15.0	0.95
		6	C	Carbon	58.5	0.97
	3	26	Fe	Iron	60.6	0.99
		66	Dy	Dysprosium	28.6	0.95
		14	Si	Silicon	2.9	0.93
		8	O	Oxygen	7.9	0.93
	4	26	Fe	Iron	61.8	0.98
		66	Dy	Dysprosium	26.9	0.94
		8	O	Oxygen	10.8	0.93
		27	Co	Cobalt	0.5	0.53
	5	26	Fe	Iron	60.7	0.99
		66	Dy	Dysprosium	29.5	0.97
		8	O	Oxygen	9.8	0.96

© University of Venda

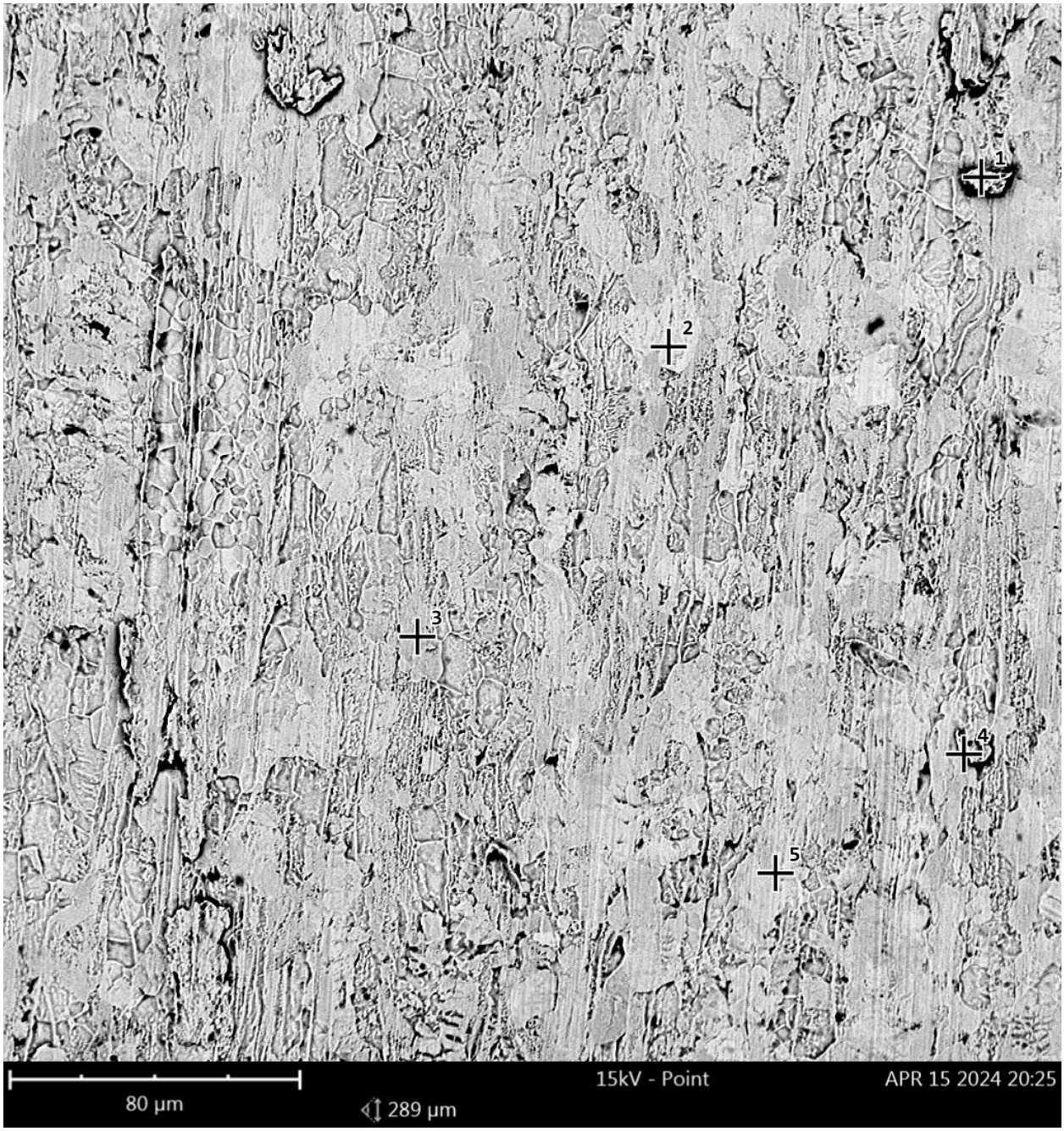


Figure 11. 17: SEM image of zinc metal immersed in 1.0 M H_2SO_4 and UV-radiated *H. kraussii* - inhibited solution.

© University of Venda

Table 11. 11: Table showing the atomic number, element symbol, element name, concentration percentage and certainty of different regions on the zinc metal surface.

Inhibitor	Region	Atomic number	Element symbol	Element name	Concentration percentage (%)	Certainty
UV-radiated *H. kraussii* extract	1	26	Fe	Iron	57.2	0.99
		66	Dy	Dysprosium	29.1	0.98
		8	O	Oxygen	14.1	0.97
		27	Co	Cobalt	0.6	0.94
	2	26	Fe	Iron	59.4	0.99
		66	Dy	Dysprosium	29.1	0.95
		8	O	Oxygen	11.5	0.93
	3	26	Fe	Iron	60.5	0.99
		66	Dy	Dysprosium	27.5	0.96
		8	O	Oxygen	10.6	0.93
		27	Co	Cobalt	1.4	0.85
	4	26	Fe	Iron	62.1	0.99
		66	Dy	Dysprosium	27.5	0.96
		8	O	Oxygen	10.4	0.94
	5	26	Fe	Iron	61.3	0.99
		66	Dy	Dysprosium	27.4	0.97
		8	O	Oxygen	11.3	0.96

© University of Venda

11.1.3. Mild steel metal

Figures 11.17-11.21 show the SEM images and corresponding EDS spectra of the unexposed mild steel surface, mild steel immersed in uninhibited 1.0 M HCl and H_2SO_4 solution, and mild steel immersed in non-radiated and UV-radiated *H. Kraussii* - inhibited 1.0 M HCl and H_2SO4 solution. The images were taken at different magnification ranges for the full view of the metal surface. It can be observed that the presence of the extract inhibitor in the corrosive HCl and H_2SO_4 solution managed to hinder the corrosion progression on the metal surface. This is observed by the improved smoothness of the metal surface after being exposed to the inhibited solution as compared to the uninhibited solution. In the presence of H_2SO_4, the metal exposed to non-radiated extract looked much more preserved than the one exposed to UV-radiated *H. kraussii* extract. However, in the presence of an HCl solution, the surface of the metal exposed to UV-radiated extract seems to be flatter than the one exposed to non-radiated extract. The mild steel metal both in the presence of HCl and H_2SO_4 shows uniform corrosion as reported in the literature [464].

Figures 11.22-11.28 show the SEM mapping images for different regions on the metal surface, and Table 1.12.-11.18 shows the corresponding elements found in each region, as the metal surface can be affected differently by corrosion. Looking at the blank images for HCl and H_2SO_4 solution, the elements obtained were the same as those found on the unexposed metal surface. In the presence of both the corrosive solution and inhibitors concentrations, it can be obsereved that in the EDS spectrum oxygen was one of the element detected on the surface of the metal after gravimetric analysis. The presence of oxygen is an indication of the formation of corrosion products in the form of iron oxide as reported by Ouakki et al. (2021) [462]. This observation is a clear indication that corrosion took place on the metal surface. In the presence of the non-radiated and UV-radiated *H. kraussii* extract, it can be observed that elements such as Nitrogen, Lanthanum, caesium, and cadmium were observed on the metal surface together with other elements observed in the unexposed and acid-exposed metals. This finding is solid evidence of the corrosion inhibition of the mild steel metal in the presence of the two extracts.

© University of Venda

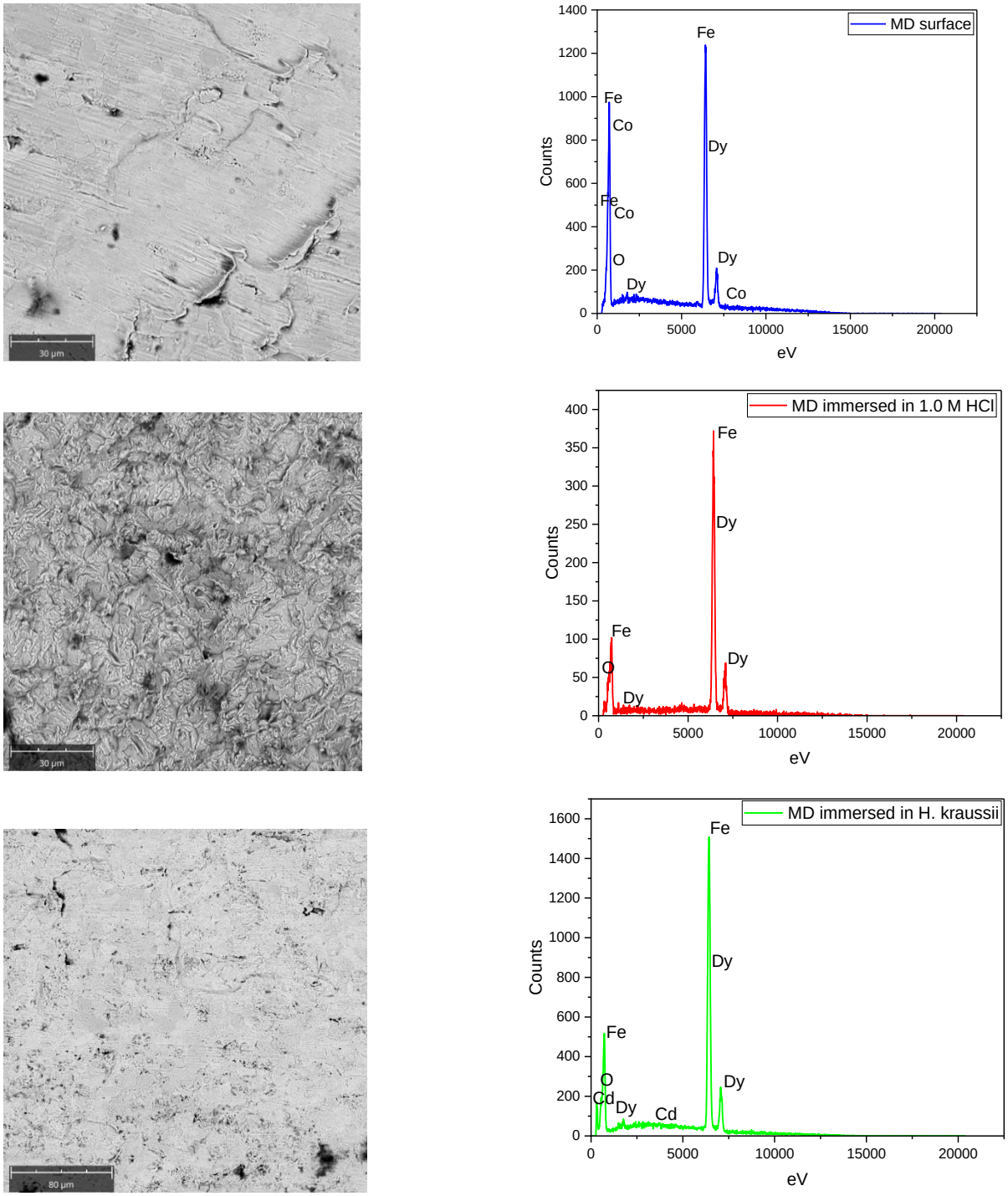


Figure 11. 18: SEM images and EDS spectra of unexposed mild steel surface, mild steel immersed in uninhibited 1.0 M HCl, and mild steel immersed in *H. kraussii*-inhibited 1.0 M HCl solution.

© University of Venda

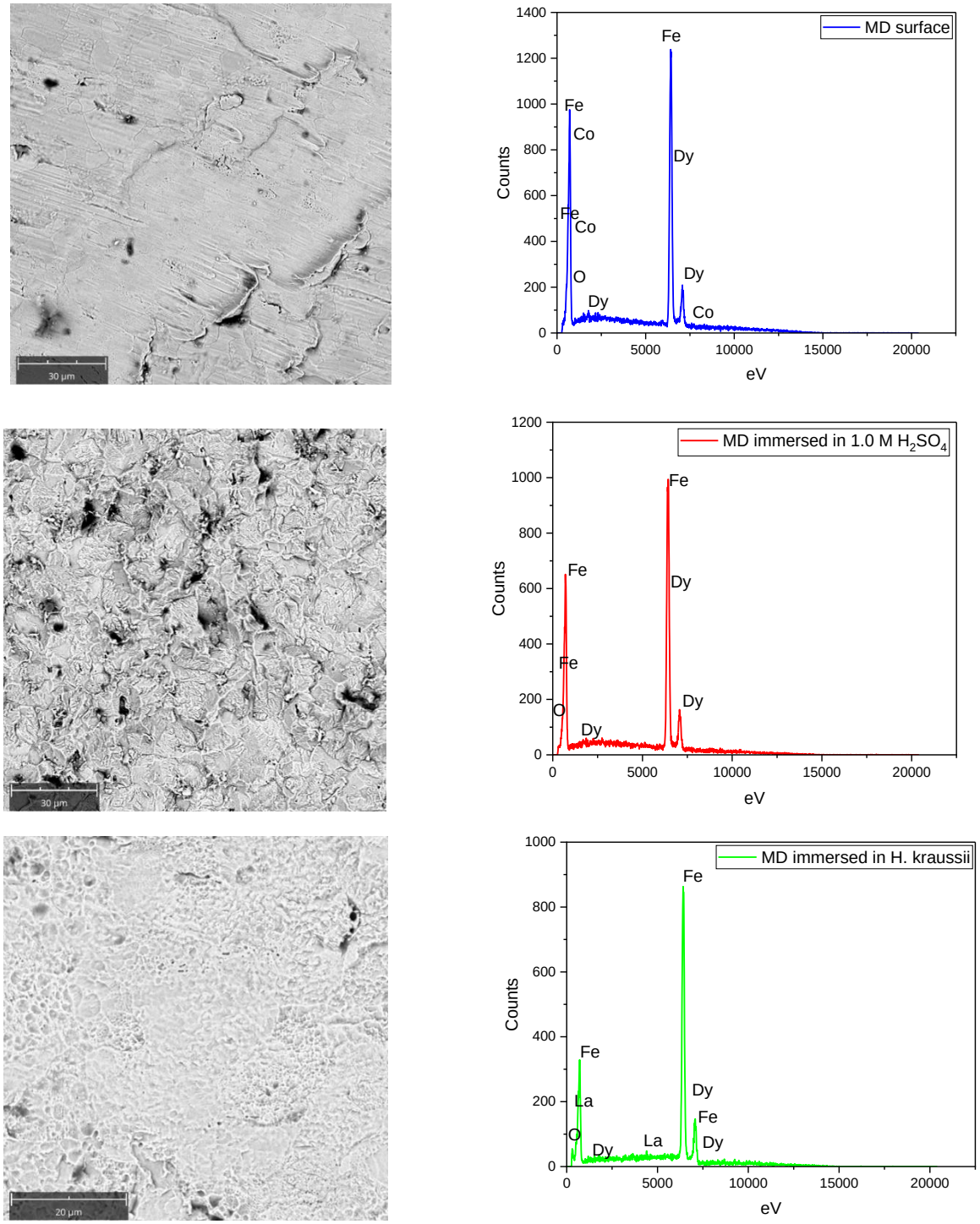


Figure 11. 19: SEM images and EDS spectra of unexposed mild steel surface, mild steel immersed in uninhibited 1.0 M H_2SO_4, and mild steel immersed in *H. kraussii*-inhibited 1.0 M H_2SO_4 solution.

© University of Venda

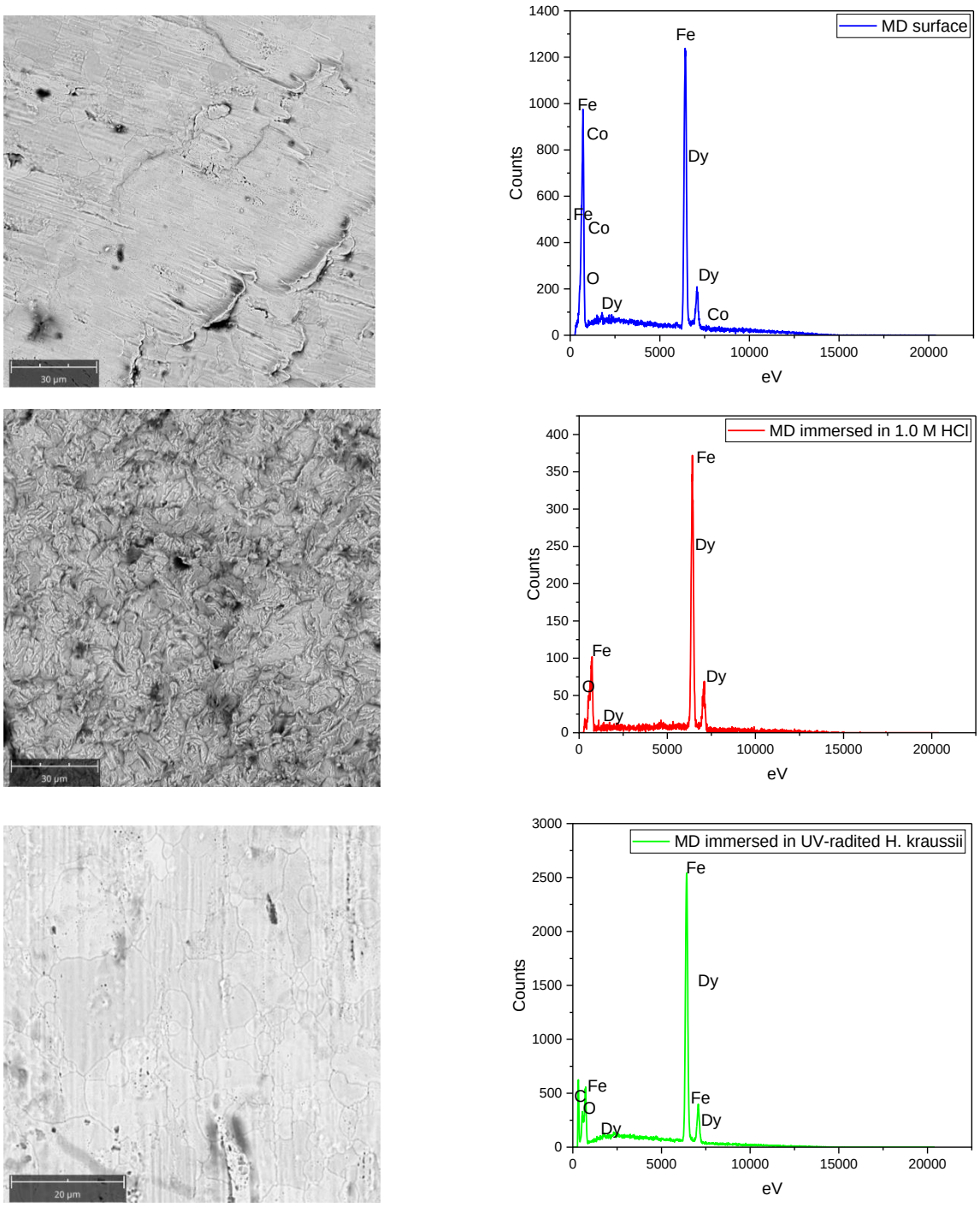


Figure 11. 20: SEM images and EDS spectra of unexposed mild steel surface, mild steel immersed in uninhibited 1.0 M HCl, and mild steel immersed in UV-radiated *H. kraussii*-inhibited 1.0 M HCl solution.

© University of Venda

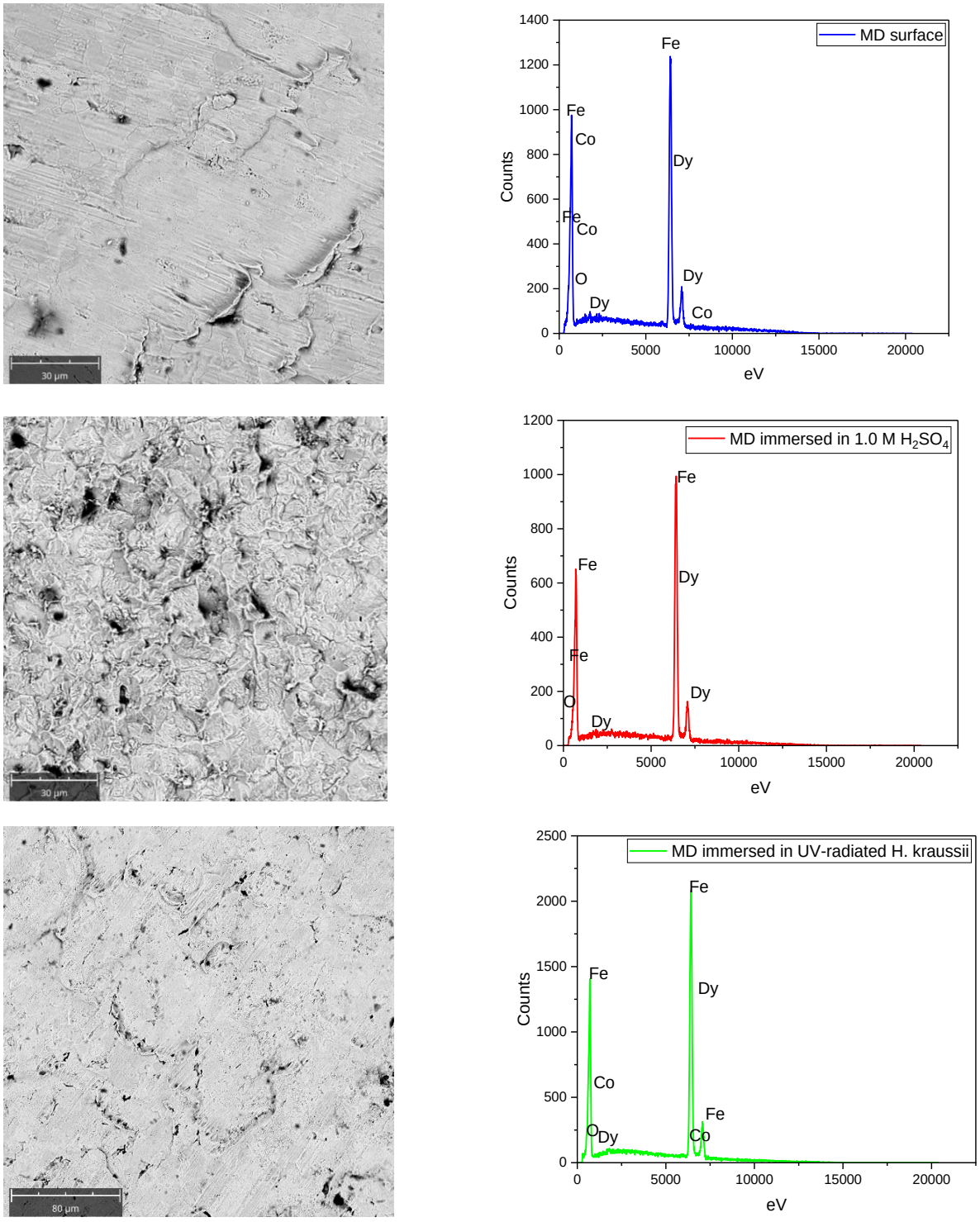


Figure 11. 21: SEM images and EDS spectra of unexposed mild steel surface, mild steel immersed in uninhibited 1.0 M H_2SO_4, and mild steel immersed in *H. kraussii*-inhibited 1.0 M H_2SO_4 solution.

© University of Venda

11.1.3.1. Mild steel metal mapping

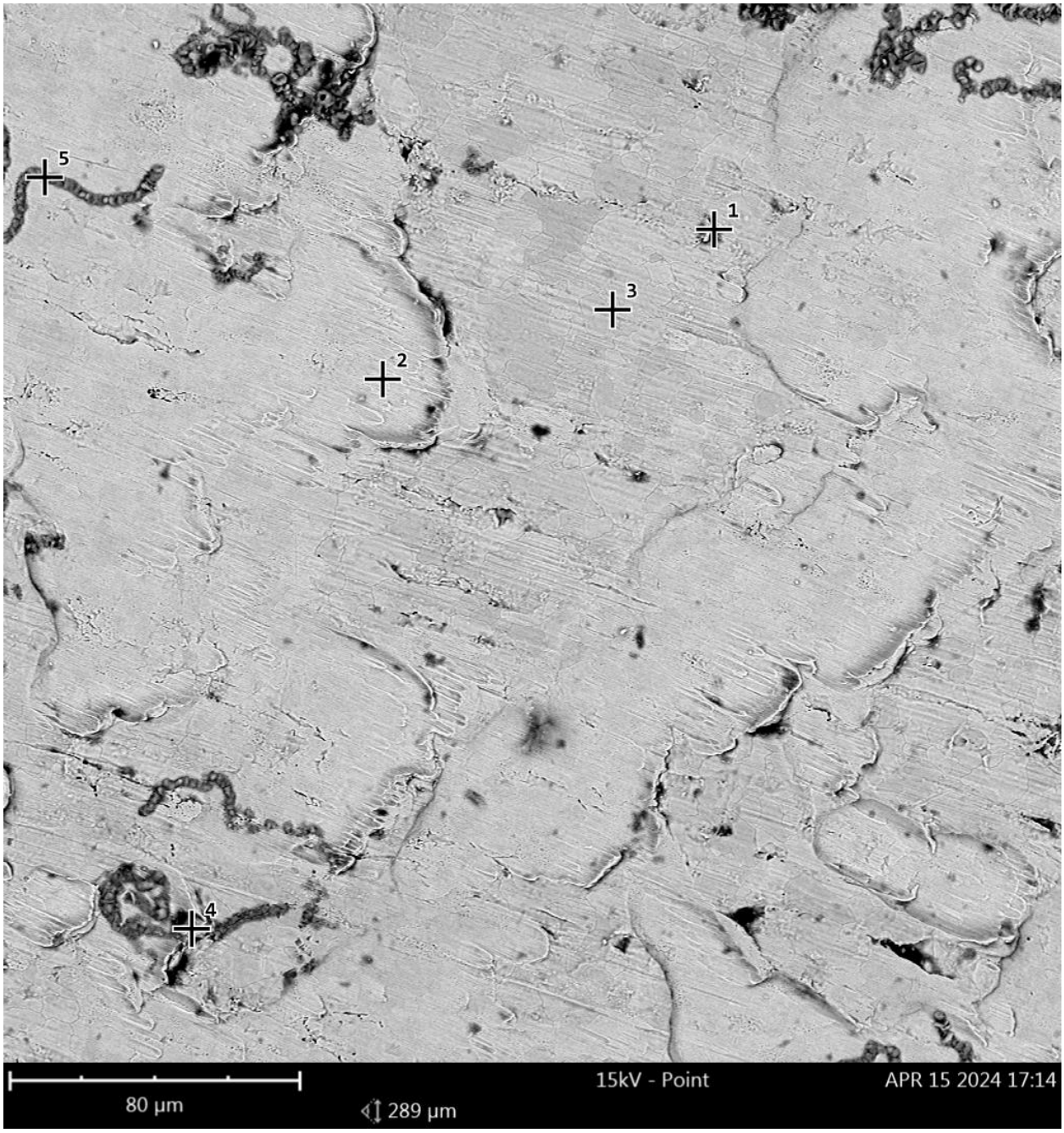


Figure 11. 22: SEM image of unexposed mild steel metal surface.

© University of Venda

Table 11. 12: Table showing the atomic number, element symbol, element name, concentration percentage and certainty of different regions on the mild steel metal surface.

Metal	Region	Atomic number	Element symbol	Element name	Concentration percentage (%)	Certainty
Mild steel metal	1	8	O	Oxygen	39.4	0.99
		26	Fe	Iron	30.9	1.00
		66	Dy	Dysprosium	18.2	0.99
		11	Na	Sodium	6.2	0.99
		20	Ca	Calcium	2.9	0.99
		14	Si	Silicon	1.3	0.97
		52	Te	Tellurium	0.7	0.96
		25	Mn	Manganese	0.4	0.92
	2	26	Fe	Iron	55.3	0.99
		66	Dy	Dysprosium	30.3	0.97
		8	O	Oxygen	13.4	0.96
		27	Co	Cobalt	0.9	0.86
	3	26	Fe	Iron	64.4	0.99
		66	Dy	Dysprosium	35.6	0.97
	4	26	Fe	Iron	53.5	0.99
		66	Dy	Dysprosium	29.0	0.96
		8	O	Oxygen	16.5	0.96
		27	Co	Cobalt	1.0	0.82
	5	8	O	Oxygen	48.1	0.99
		26	Fe	Iron	33.1	0.99
		66	Dy	Dysprosium	18.7	0.98

© University of Venda

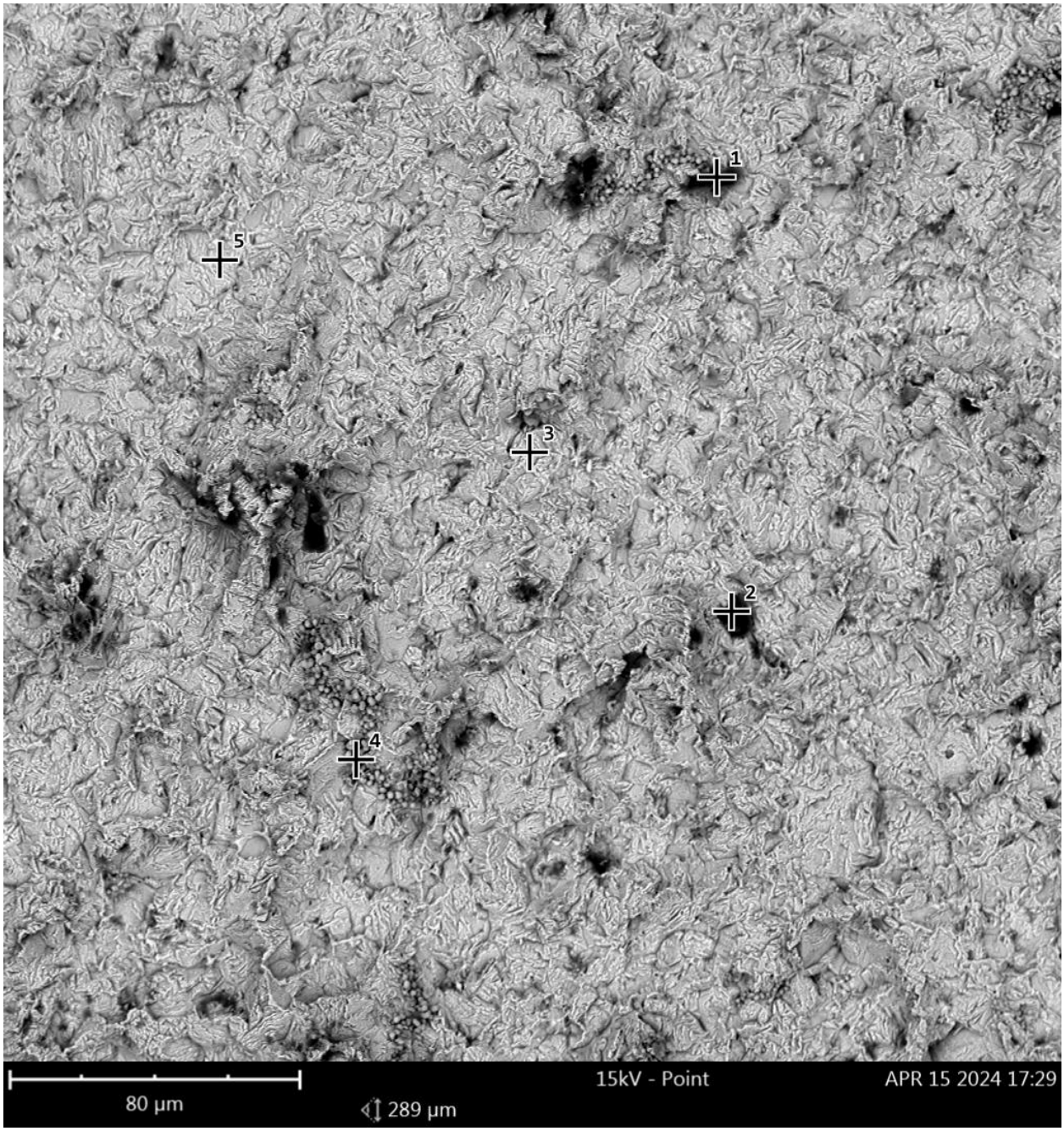


Figure 11. 23: SEM image of mild steel metal immersed in 1.0 M HCl solution.

© University of Venda

Table 11. 13: Table showing the atomic number, element symbol, element name, concentration percentage and certainty of different regions on the mild steel metal surface.

Acid	Region	Atomic number	Element symbol	Element name	Concentration percentage (%)	Certainty
HCl	1	6	C	Carbon	35.9	0.98
		26	Fe	Iron	21.5	0.99
		7	N	Nitrogen	14.5	0.97
		8	O	Oxygen	14.1	0.98
		66	Dy	Dysprosium	14	0.98
	2	6	C	Carbon	53	0.97
		8	O	Oxygen	28.1	0.97
		26	Fe	Iron	18.9	0.98
	3	26	Fe	Iron	62.5	0.99
		66	Dy	Dysprosium	37.5	0.96
	4	26	Fe	Iron	51.5	0.98
		66	Dy	Dysprosium	34.1	0.95
		8	O	Oxygen	14.4	0.94
	5	26	Fe	Iron	62	1
		66	Dy	Dysprosium	38	0.99

© University of Venda

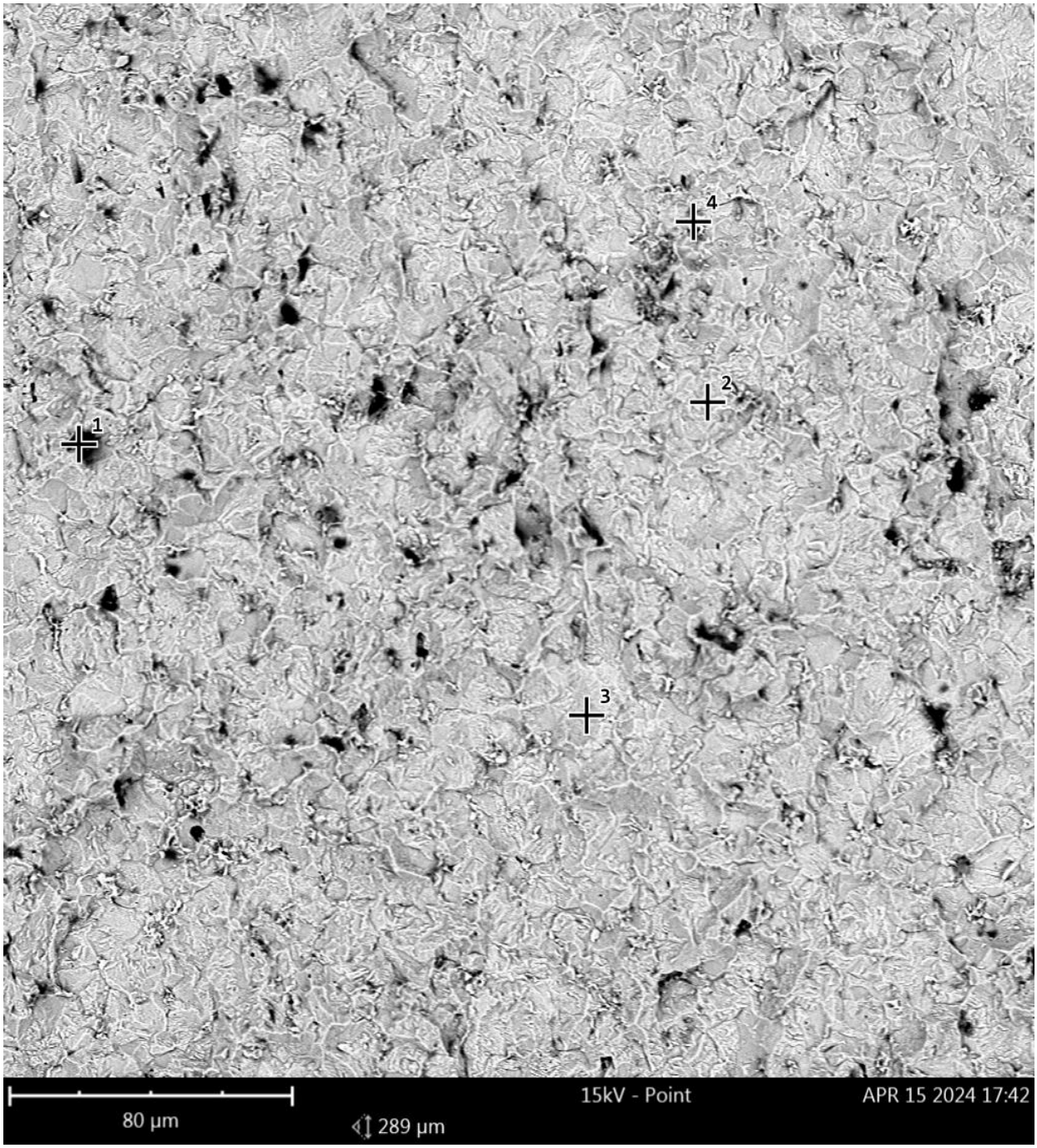


Figure 11. 24: SEM image of mild steel metal immersed in 1.0 M H_2SO_4 solution.

© University of Venda

Table 11. 14: Table showing the atomic number, element symbol, element name, concentration percentage and certainty of different regions on the mild steel metal surface.

Acid	Region	Atomic number	Element symbol	Element name	Concentration percentage (%)	Certainty
H_2SO_4	1	26	Fe	Iron	53.2	0.99
		66	Dy	Dysprosium	34	0.98
		8	O	Oxygen	12.8	0.97
	2	26	Fe	Iron	53.9	0.99
		66	Dy	Dysprosium	35	0.97
		8	O	Oxygen	11.2	0.95
	3	26	Fe	Iron	60.3	0.99
		66	Dy	Dysprosium	39.7	0.97
	4	26	Fe	Iron	48.8	1
		66	Dy	Dysprosium	30.7	0.99
		8	O	Oxygen	18.9	0.98
		27	Co	Cobalt	1.6	0.96

© University of Venda

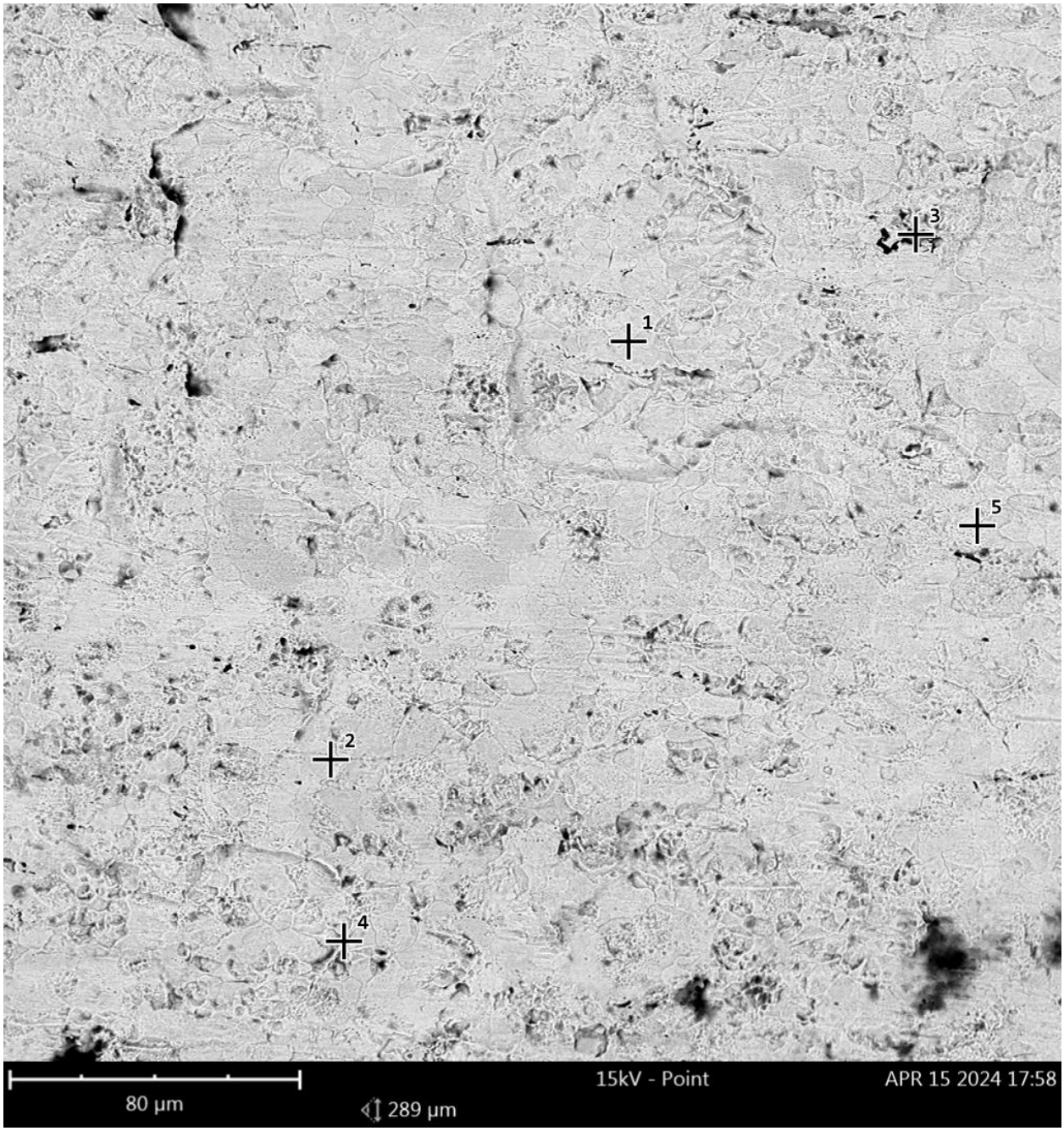


Figure 11. 25: SEM image of mild steel metal immersed in 1.0 M HCl and *H. kraussii* - inhibited solution.

© University of Venda

Table 11. 15: Table showing the atomic number, element symbol, element name, concentration percentage and certainty of different regions on the mild steel metal surface.

Inhibitor	Region	Atomic number	Element symbol	Element name	Concentration percentage (%)	Certainty
H. kraussii extract	1	26	Fe	Iron	61.6	0.99
		66	Dy	Dysprosium	38.4	0.99
	2	26	Fe	Iron	62.6	0.99
		66	Dy	Dysprosium	37.4	0.96
	3	26	Fe	Iron	62.1	0.99
		66	Dy	Dysprosium	37.9	0.96
	4	26	Fe	Iron	53	0.99
		66	Dy	Dysprosium	35.1	0.98
		8	O	Oxygen	11.8	0.97
		48	Cd	Cadmium	0.1	0.45
	5	26	Fe	Iron	55.4	0.99
		66	Dy	Dysprosium	33.5	0.98
		8	O	Oxygen	10.2	0.97
		27	Co	Cobalt	0.9	0.89

© University of Venda

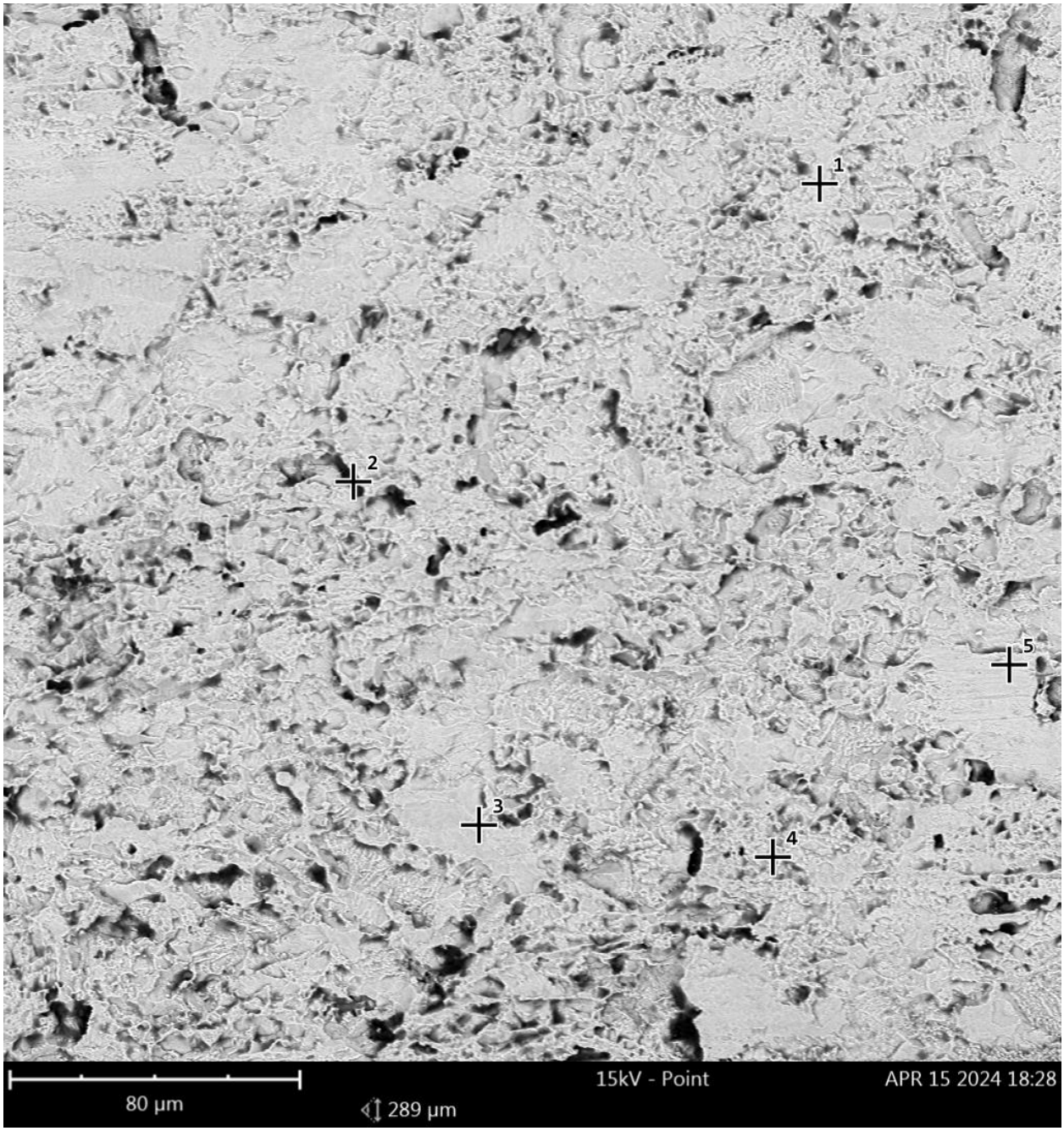


Figure 11. 26: SEM image of mild steel metal immersed in 1.0 M H_2SO_4 and *H. kraussii* inhibited solution.

© University of Venda

Table 11. 16: Table showing the atomic number, element symbol, element name, concentration percentage and certainty of different regions on the mild steel metal surface.

Inhibitor	Region	Atomic number	Element symbol	Element name	Concentration percentage	Certainty
H. kraussii extract	1	26	Fe	Iron	70.9	0.99
		66	Dy	Dysprosium	29.1	0.97
	2	26	Fe	Iron	62.3	0.99
		66	Dy	Dysprosium	27.1	0.96
		8	O	Oxygen	10.1	0.95
		57	La	Lanthanum	0.4	0.74
	3	26	Fe	Iron	100	0.98
	4	26	Fe	Iron	68.3	0.98
		66	Dy	Dysprosium	31.7	0.94
	5	26	Fe	Iron	61.8	0.99
		66	Dy	Dysprosium	29.3	0.98
		8	O	Oxygen	8.9	0.97

© University of Venda

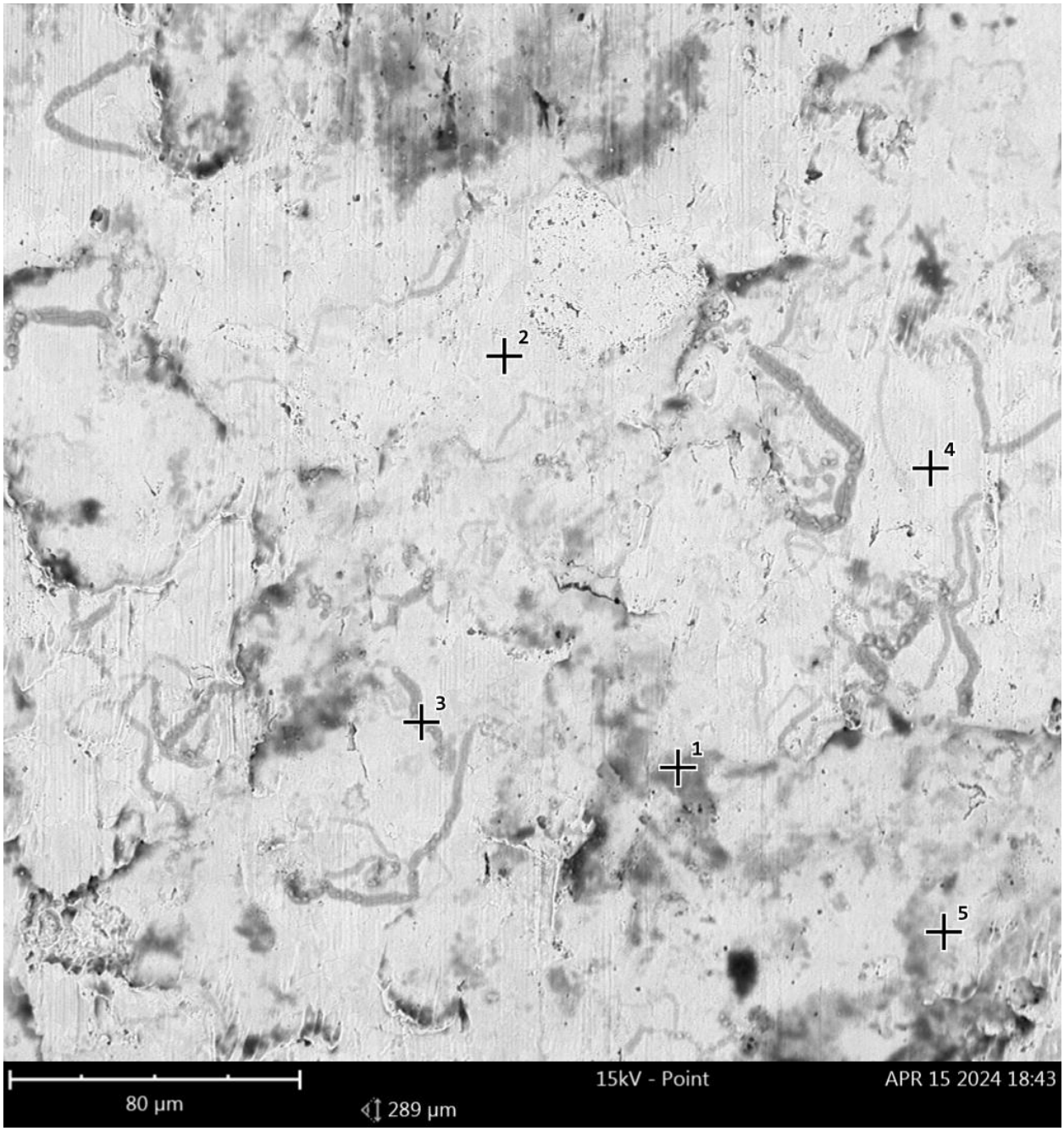


Figure 11. 27: SEM image of mild steel metal immersed in 1.0 M HCl and UV-radiated *H. kraussii* - inhibited solution.

© University of Venda

Table 11. 17: Table showing the atomic number, element symbol, element name, concentration percentage and certainty of different regions on the mild steel metal surface.

Inhibitor	Region	Atomic number	Element symbol	Element name	Concentration percentage (%)	Certainty
UV-radiated *H. kraussii* extract	1	26	Fe	Iron	39.2	0.99
		6	C	Carbon	34.1	0.99
		66	Dy	Dysprosium	17.8	0.98
		8	O	Oxygen	8.9	0.98
	2	26	Fe	Iron	57.9	0.97
		66	Dy	Dysprosium	30.4	0.90
		8	O	Oxygen	11.7	0.87
	3	26	Fe	Iron	74.3	0.97
		8	O	Oxygen	24.9	0.94
		55	Cs	Caesium	0.8	0.66
	4	26	Fe	Iron	87.1	0.97
		8	O	Oxygen	12.9	0.89
	5	26	Fe	Iron	60.8	0.99
		66	Dy	Dysprosium	27.2	0.98
		8	O	Oxygen	11.9	0.97

© University of Venda

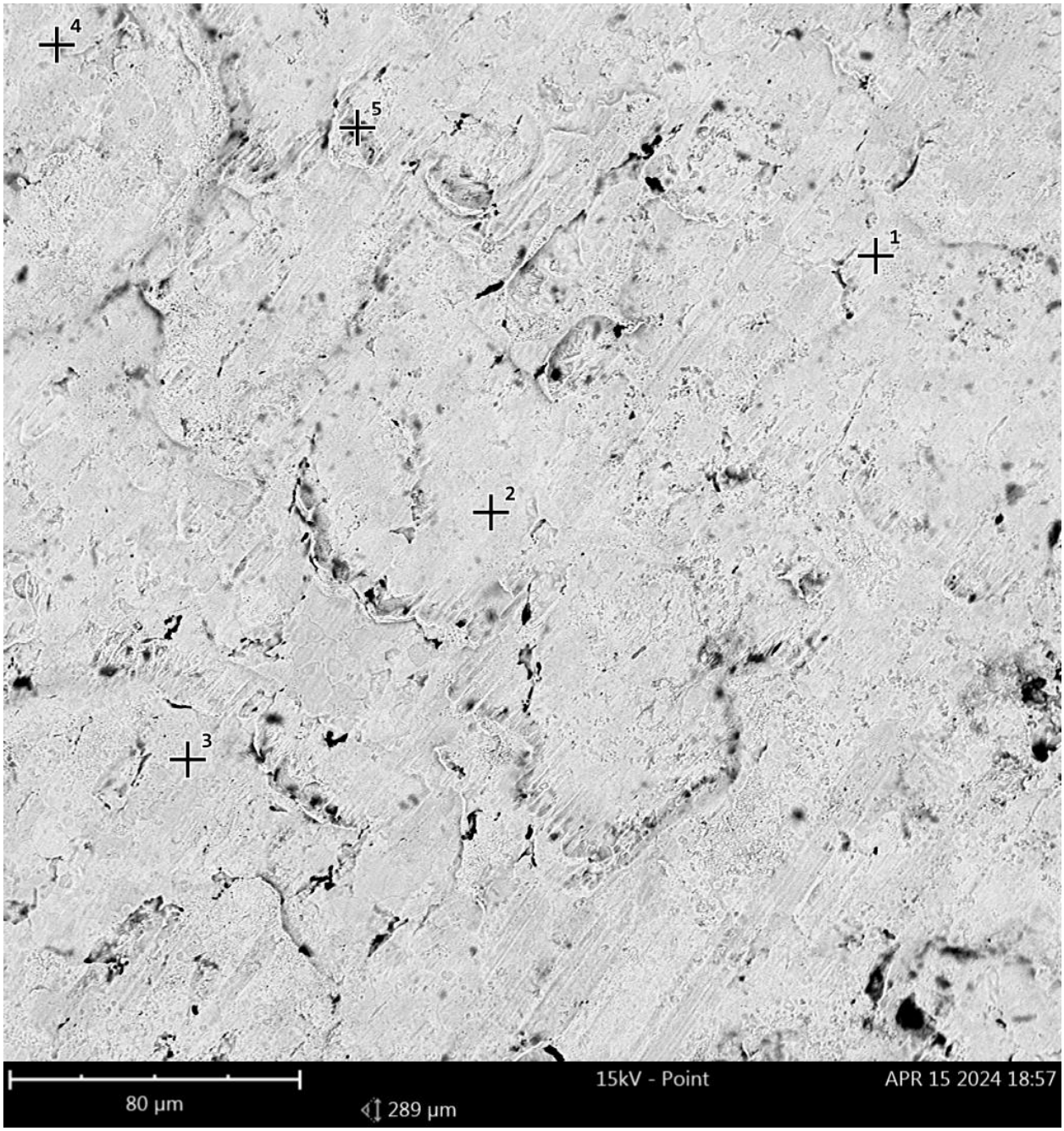


Figure 11. 28: SEM image of mild steel metal immersed in 1.0 M H_2SO_4 and UV-radiated *H. kraussii* - inhibited solution.

© University of Venda

Table 11. 18: Table showing the atomic number, element symbol, element name, concentration percentage and certainty of different regions on the mild steel metal surface.

Inhibitor	Region	Atomic number	Element symbol	Element name	Concentration percentage (%)	Certainty
UV-radiated *H. kraussii* extract	1	26	Fe	Iron	62.3	0.99
		66	Dy	Dysprosium	27.5	0.97
		8	O	Oxygen	9.1	0.96
		27	Co	Cobalt	1.2	0.91
	2	26	Fe	Iron	62.5	0.99
		66	Dy	Dysprosium	28.9	0.97
		8	O	Oxygen	8.6	0.95
	3	26	Fe	Iron	60.6	0.99
		66	Dy	Dysprosium	28.6	0.96
		8	O	Oxygen	10.7	0.95
	4	26	Fe	Iron	33.9	0.99
		8	O	Oxygen	27.4	0.97
		7	N	Nitrogen	21.0	0.94
		66	Dy	Dysprosium	17.1	0.96
	5	26	Fe	Iron	67.9	0.99
		66	Dy	Dysprosim	32.1	0.98

11.2. X-ray diffraction

Understanding corrosion processes requires identifying phase compositions rather than elemental compositions. Understanding the chemical stages can aid in explaining the corrosion process, identifying the corrosion source, and providing solutions [465]. X-ray diffraction (XRD) methods can be used for such purposes and to find microstructure information [466]. Recently, XRD has been one of the best tools for identifying the crystalline phase and identifying the nature of the protective layer formed on the metallic surface. Therefore, it can be utilized to study the constituent species of corrosion products resulting from the metal's interaction with the corrosive solution at different concentrations of the inhibitor [467]. This study uses XRD to investigate the oxide films [468] on mild steel, zinc and aluminium metal at 1500 ppm extracts inhibitor solution. Figures 11.29-11.38 represent the XRD patterns of the uninhibited and inhibited scratched samples of mild steel, zinc and aluminium metal in hydrochloric and sulphuric acid media.

The XRD for the scratched mild steel (Figures 11.29 and 11.30) and zinc (Figures 11.33 and 11.34) metal in the absence and the presence of non-radiated and UV-radiated *H. kraussii* extracts in 1.0 M HCl showed peaks of very little intensity. This observation is an indication of the non crystalline nature of the deposit protective oxide layers [469]. The diffraction pattern of Figures 11.29-11.30, and 11.33-11.34 in the absence and presence of the extracts inhibitor

© University of Venda

concentration is the same, which means that the extracts inhibitor are conceivably adsorbed on the metal surface through physisorption as opposed to shaping a defensive boundary type complex layer by chemisorptions [470]. In Figures 11.29 and 11.30 (for BM-HCl), a peak at around 2θ = 36° [467] was observed, indicating goethite FeOOH, which is common when working with carbon steel in chloride-containing environments. A peak at around 2θ = 28.5° [382] is related to the formation of the oxide film (mainly Fe2O3 and FeOOH) on the matal surface. The formed insoluble and persistent coating of FeOOH and Fe_2O_3 reduces ionic diffusion, improving the corrosion resistance in the steel surface in HCl media [382]. The presence of the *H. kraussii* extract effectively reduces the intensity of the iron peak at 2θ = 44.65° [467], indicating its ability to prevent metal dissolution.

In the presence of sulphuric acid, the two extracts can be observed to show some diffraction patterns. In Figures 11.31 and 11.32, the diffraction patterns in the absence and presence of the extract inhibitor look almost the same, with the variations only in the peak intensity. Similar observations have been observed in Figures 11.35 and 11.36 for the non-radiated and UV-radiated extracts. Thus, the introduction of the two extract inhibitors did not cause a severe change in the surface of the metals. The peaks in the observed diffraction patterns indicate that corrosion occurred on the metal surface.

For aluminium metal in 1.0 M HCl, both in the presence and absence of the non-radiated and UV-radiated *H. kraussii* extract, it can be observed that there are diffraction peaks observed. This observation confirms the formation of crystalline planes on the surface of the aluminium metal. A peak at 2θ = 38.5° was observed in both diffraction patterns in Figures 11.37 and 11.38, corresponding to the presence of aluminium. This peak corresponds to a (111) crystallographic plane, as observed by Ayieko et al. (2015) [471]. The reduction or disappearance of the peak intensity at 2θ = 29˚ in the presence of the two extracts (HKAL-HCl and VHKAL-HCl) as compared to the blank test (BAL-HCl) is indicative of the bonding between the metal surface and the molecules of the inhibitor contained in extract inhibitor, which might be due to metal complex formation as reported elsewhere [472].

© University of Venda

11.2.1. Mild steel metal

Mild steel metal exposed to *H. kraussii* – 1.0 M HCl solution.

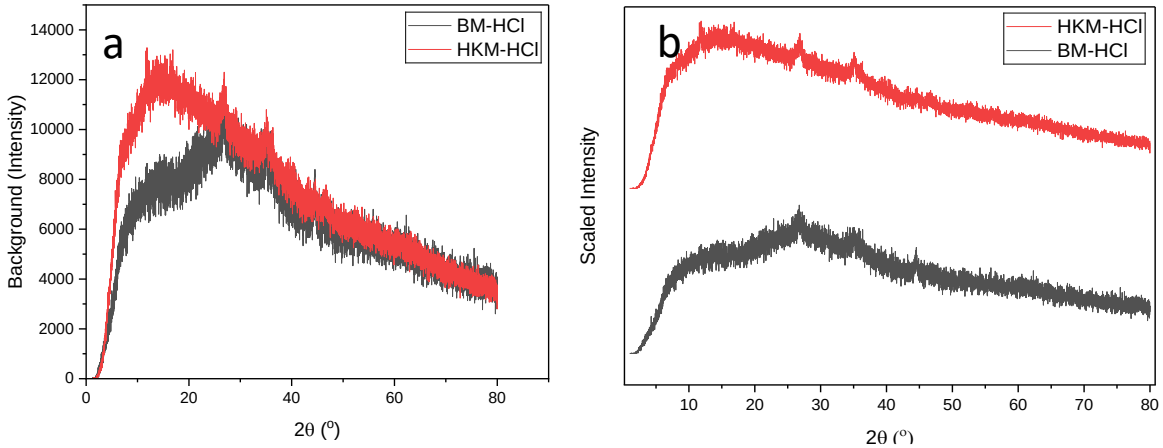


Figure 11. 29: XRD spectra for mild steel metal in the absence (BM-HCl) and presence (HKM-HCl) of *H. kraussii* extract in HCl (a) and their scale spectra (b).

Mild steel metal exposed to UV-radiated *H. kraussii* – 1.0 M HCl solution.

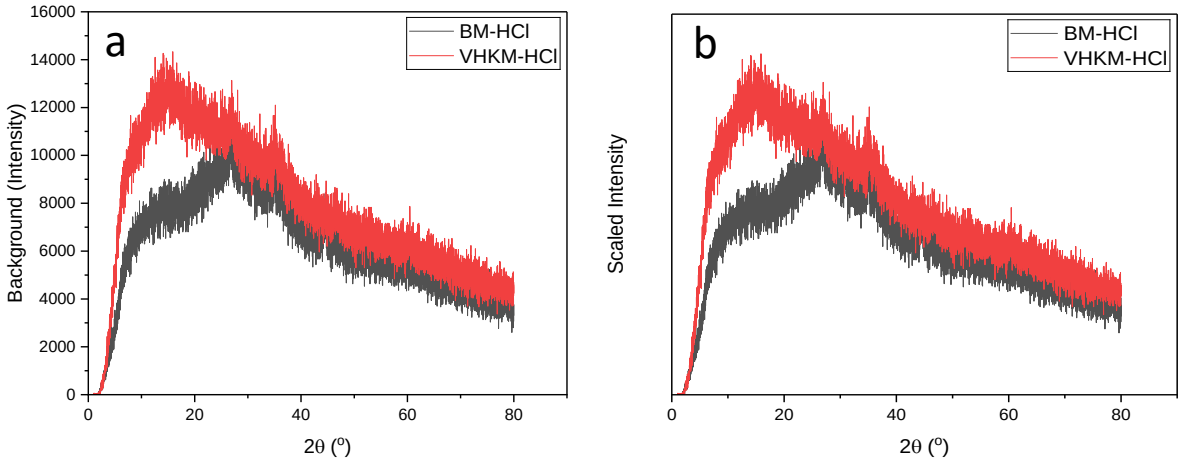


Figure 11. 30: XRD spectra for mild steel metal in the absence (BM-HCl) and presence (VHKM- HCl) of UV-radiated *H. kraussii* extract in HCl (a) and their scale spectra (b).

© University of Venda

Mild steel metal exposed to *H. kraussii* – 1.0 M H_2SO_4 solution.

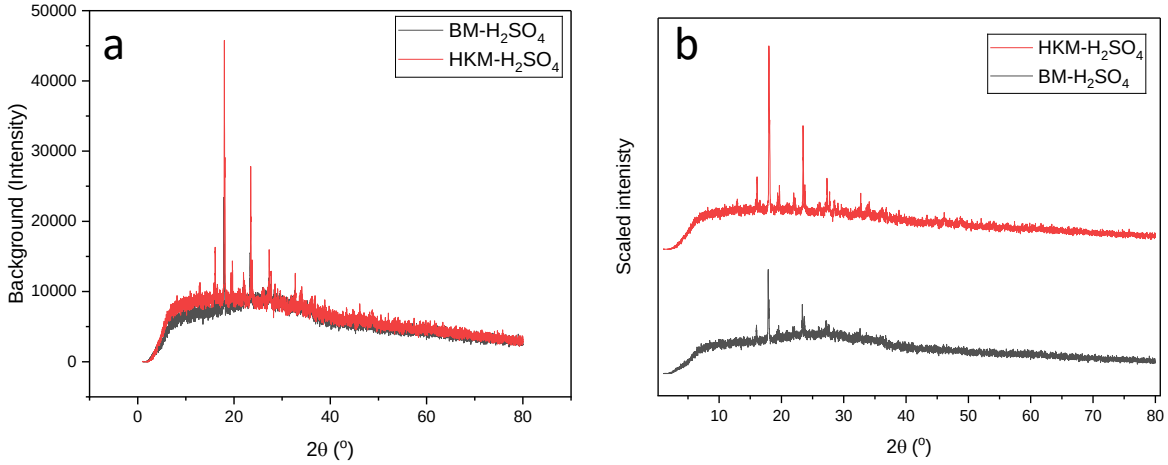


Figure 11. 31: XRD spectra for mild steel metal in the absence (BM-H_2SO_4) and presence (HKM- H_2SO_4) of *H. kraussii* extract in H_2SO_4 (a) and their scale spectra (b).

Mild steel metal exposed to UV-radiated *H. kraussii* – 1.0 M H_2SO_4 solution.

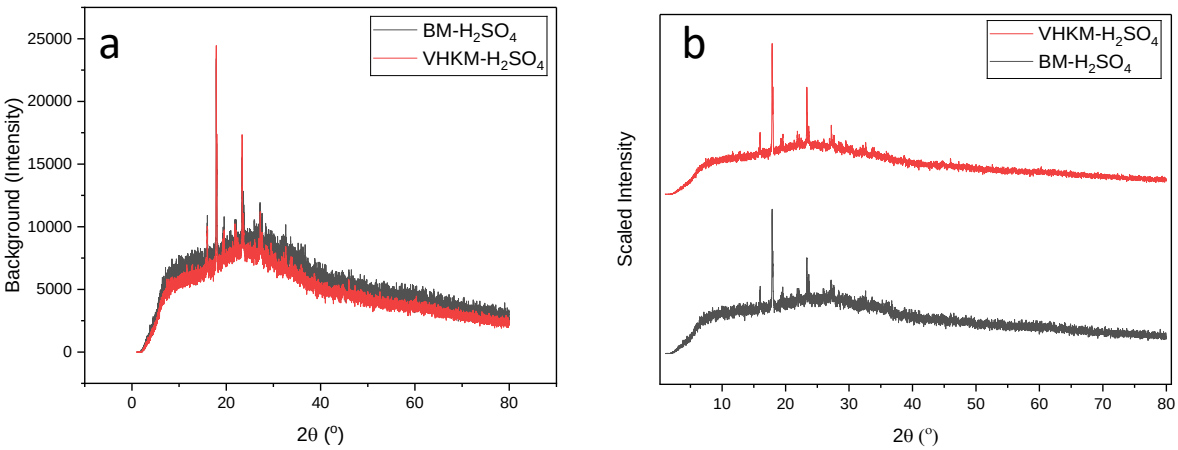


Figure 11. 32: XRD spectra for mild steel metal in the absence (BM- H_2SO_4) and presence (VHKM- H_2SO_4) of UV-radiated *H. kraussii* extract in H2SO4 (a) and their scale spectra (b).

© University of Venda

11.2.2. Zinc metal

Zinc metal exposed to *H. kraussii* – 1.0 M HCl solution.

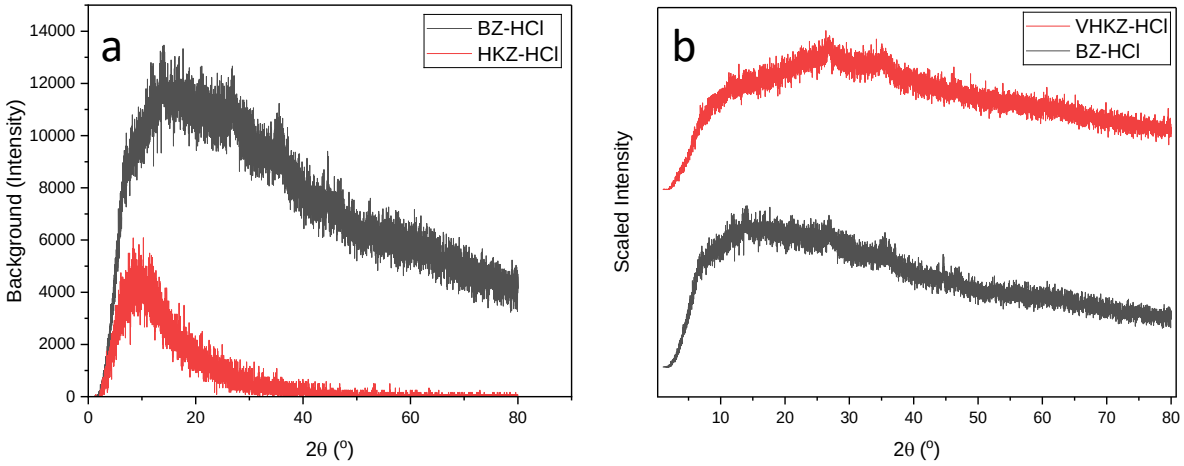


Figure 11. 33: XRD spectra for zinc metal in the absence (BZ-HCl) and presence (HKZ- HCl) of *H. kraussii* extract in HCl (a) and their scale spectra (b).

Zinc metal exposed to UV-radiated *H. kraussii* – 1.0 M HCl solution.

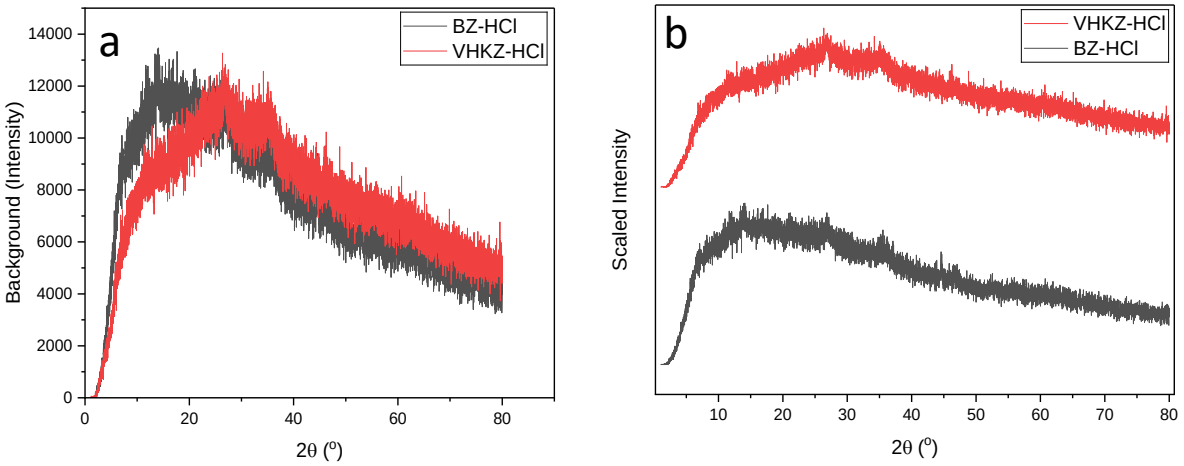


Figure 11. 34: XRD spectra for mild steel metal in the absence (BZ-HCl) and presence (VHKZ-HCl) of UV-radiated *H. kraussii* extract in HCl (a) and their scale spectra (b).

© University of Venda

Zinc metal exposed to *H. kraussii* – 1.0 M H_2SO_4 solution.

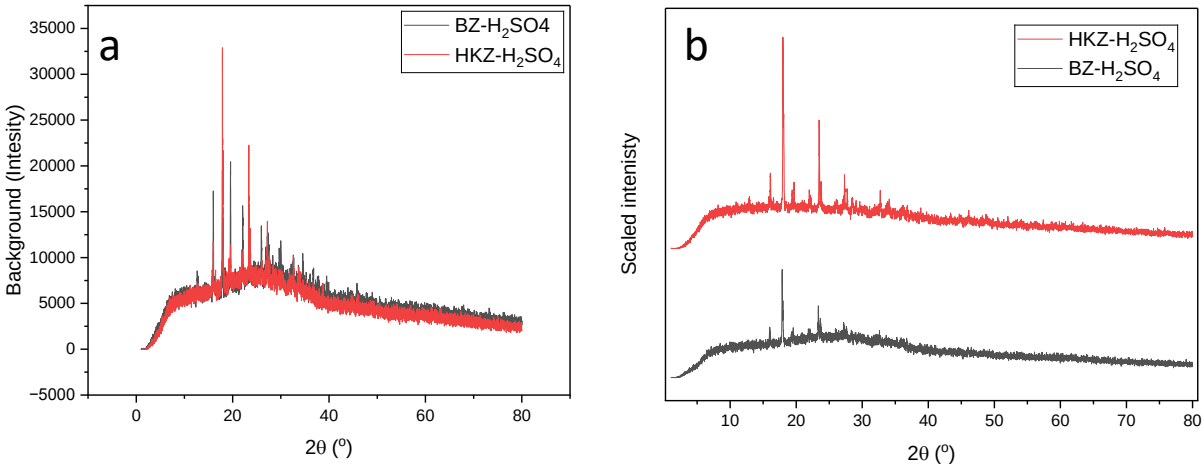


Figure 11. 35: XRD spectra for zinc metal in the absence (BZ- H_2SO_4) and presence (HKZ-H_2SO_4) of *H. kraussii* extract in H_2SO_4 (a) and their scale spectra (b).

Zinc metal exposed to UV-radiated *H. kraussii* – 1.0 M H_2SO_4 solution.

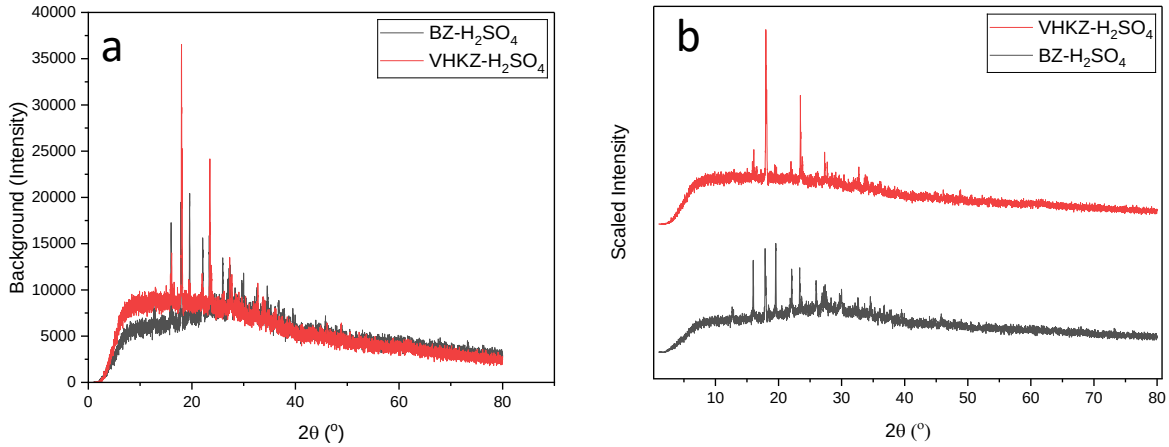


Figure 11. 36: XRD spectra for zinc metal in the absence (BM-H_2SO_4) and presence (VHKM-H_2SO_4) of UV-radiated *H. kraussii* extract in H_2SO_4 (a) and their scale spectra (b).

© University of Venda

11.2.3. Aluminium metal

Aluminium metal exposed to *H. kraussii* – 1.0 M HCl solution.

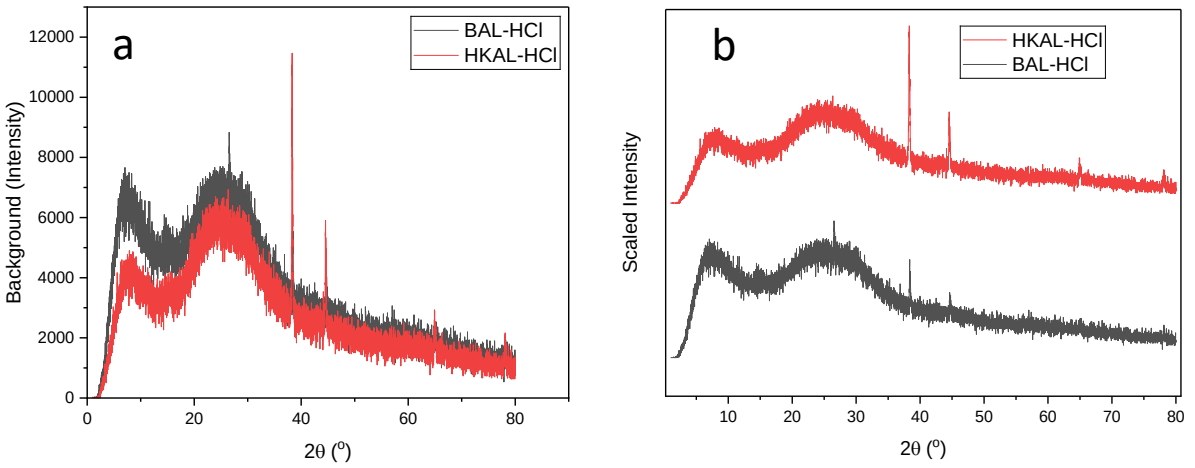


Figure 11. 37: XRD spectra for aluminium metal in the absence (BAL-HCl) and presence (VHKAL- HCl) of UV-radiated *H. kraussii* extract in HCl (a) and their scale spectra (b).

Aluminium metal exposed to UV-radiated *H. kraussii* – 1.0 M HCl solution.

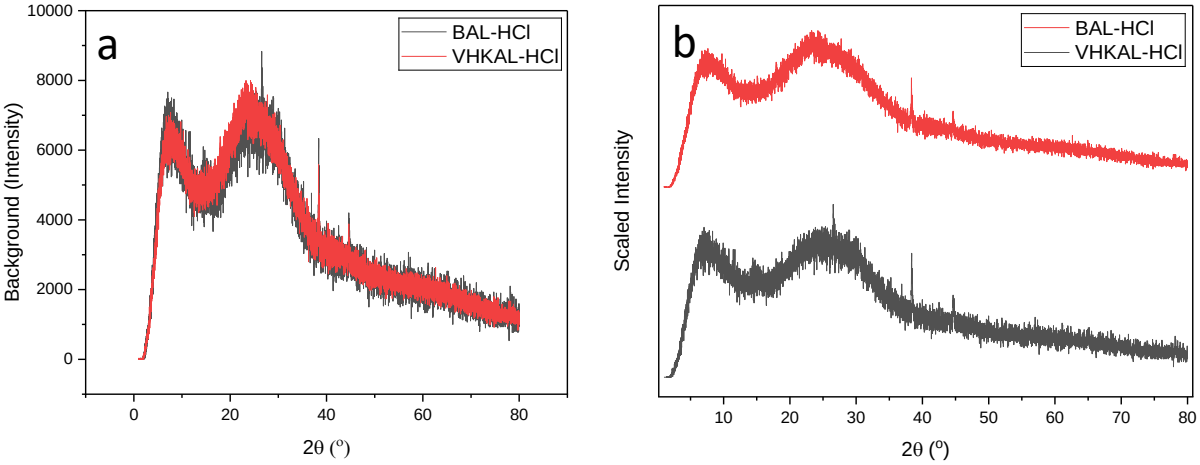


Figure 11. 38: XRD spectra for aluminium metal in the absence (BAL-HCl) and presence (VHKAL- HCl) of UV-radiated *H. kraussii* extract in HCl (a) and their scale spectra (b).

© University of Venda

CHAPTER 12

Summary, conclusions and recommendations

© University of Venda

12. Introduction

The findings reported in this study are summed up in Chapter 12, which also concludes the research work and offers recommendations and way forward.

12.1. Conclusion

After all the techniques have been conducted, in order to study the corrosion inhibition potential of non-radiated and UV-radiated *H. Kraussii* plant extract on mild steel, zinc, and aluminium metals in 1.0 M HCl and H_2SO_4 solution. The following conclusions based on the results obtained have been made.

- LCMS

LCMS chromatogram and FTIR spectrum revealed the difference between the non-radiated and UV-radiated extract, which is a confirmation of the formation of the geometrical isomers. It was also used to find the metabolites found in the *H. kraussii* extract.

- Gravimetric analysis

The gravimetric weight loss method used to get the weight loss of the mild steel, zinc, and aluminium metal in 1.0 M HCl and H_2SO_4 at different temperatures was used to calculate the corrosion rate and the percentage inhibition efficiency for the non-radiated and UV-radiated *H. kraussii* extract. The non-radiated extract was found to have a higher %IE than the UV-radiated extract.

- FTIR

The FTIR spectrum also showed that no new compounds with different functional groups were formed as there was only a shift in the adsorption peaks up and down with no new peaks formed. FTIR also confirmed the adsorption of the extract on the metal surface during the corrosion process, thereby protecting the metal from corrosion.

- PDP

The percentage inhibition efficiency obtained through PDP for non-radiated extract was higher than that of the UV-radiated extract, which confirms the effectiveness of the non-radiated extract as a corrosion inhibitor compared to the UV-radiated extract. The corrosion current density was also found to be decreasing with an increase in the inhibitor concentration.

© University of Venda

- EIS

The Nyquist plot semi-circle diameter for mild steel and zinc, and the circle diameter for aluminium metal for the two extracts was found to be increasing with an increase in the extracts concentration. This causes the increase in the corrosion inhibition efficiency. The non-radiated extract was found to have high percentage inhibition efficiency than the UV- radiated extract.

- Contact angle

The introduction of the two inhibitor extracts on the corrosive solution managed to reduce the wettability of the metal, thereby changing the metal surface from hydrophilic to hydrophobic.

- Computational study

The adsorption and interaction energy of the inhibitor molecules and the metal surface was studied and all the energies were obtained as negative suggesting a spontaneous interaction. All the energies obtained were above -100 kcal/mol except for ferulic acid in aluminium metal, meaning the compounds adsorbs through chemisorption in the metal surface. The energies obtained were also high suggesting high inhibition efficiency.

- SEM-EDS and XRD

SEM images showed that the introduction of the non-radiated and UV-radiated *H. kraussii* extract on the corrosive solution of 1.0 M HCl and H_2SO_4 managed to protect the metal surface and maintain the smoothness of the metal surface as that of the unexposed metal. The acid-exposed metals appeared to have many pits on the surface, which were not visible when the metals were now exposed to the extract inhibitor solution. EDS showed that elements such as Al, Fe, and Zn were the dominant elements found in aluminium, mild steel, and zinc metals, respectively. XRD for the non-radiated and UV-radiated extracts did not show much difference for all the metals. However, on most of the surface of the metals, the presence of metal oxide was observed, showing that corrosion took place.

© University of Venda

12.2. Contribution, recommendation and suggestions

This research has made some remarkable findings and contributions, including:

1. UV light radiation causes the formation of geometrical isomerization of the plant extract metabolites from trans to their cis isomerisation.
2. The exposure of *H. kraussii* plant extract to UV light radiation caused a minimal effect on the extract's inhibition efficiency, resulting in a minute decrease in the inhibition efficiency.
3. *H. kraussii* plant extract is an excellent corrosion inhibitor for mild steel, zinc, and aluminium metal in the sulphuric and hydrochloric acid medium at a lower temperature.
4. The *H. kraussii* extract is very effective at lower temperatures for mild steel and aluminium metal but works optimally at high temperatures for zinc metal in hydrochloric acid.
5. The two extracts work optimally in the presence of hydrochloric acid than sulphuric acid.
6. The best arrangement of the isolated inhibitor compounds on mild steel, zinc, and aluminium metal is found when they are lying parallel to the metals surface.
8. The *H. kraussii* extract must be used on materials that will be used in places with no UV radiation for its optimal effeceincy as corrosion inhibitor.
7. The geometrical optimization of the isolated compounds must be done at smaller smearing values corresponding to the experimental temperatures.

Based on the results obtained in this work, the researcher recommends the use of *H. kraussii* plant extract as excellent substitute for synthesized organic and inorganic corrosion inhibitors which are out of favour because of the environmental hazards. The researcher recommends further investigation into isolating the compounds responsible for corrosion inhibition from plant extracts, as well as exploring the use of different solvents for extraction and examining their inhibition potential.

© University of Venda

References

1. Obot, I., et al., *Corrosion inhibitors for acid cleaning of desalination heat exchangers: Progress, challenges and future perspectives.* Journal of Molecular Liquids, 2019. **296**: p. 111760.
2. Obot, I., et al., *Development of a green corrosion inhibitor for use in acid cleaning of MSF desalination plant.* Desalination, 2020. **495**: p. 114675.
3. Goyal, M., et al., *Organic corrosion inhibitors for industrial cleaning of ferrous and non-ferrous metals in acidic solutions: A review.* Journal of Molecular Liquids, 2018. **256**: p. 565-573.
4. Fouda, A., et al., *Corrosion inhibitors based on antibiotic derivatives for protection of carbon steel corrosion in hydrochloric acid solutions.* International Journal of Advanced Research, 2014. **2**(4): p. 788-807.
5. Wang, D.-Y., et al., *Investigation of efficient corrosion inhibitor during acid cleaning of reverse osmosis (RO) desalination plant.* Corrosion Science, 2022. **208**: p. 110609.
6. Caliskan, N. and E. Akbas, *Corrosion inhibition of austenitic stainless steel by some pyrimidine compounds in hydrochloric acid.* Materials and Corrosion, 2012. **63**(3): p. 231-237.
7. Raabe, D., *The materials science behind sustainable metals and alloys.* Chemical Reviews, 2023. **123**(5): p. 2436-2608.
8. Abbasov, V.M., et al., *Efficient complex surfactants from the type of fatty acids as corrosion inhibitors for mild steel C1018 in CO 2-environments.* Journal of the Korean Chemical Society, 2013. **57**(1): p. 25-34.
9. Popoola, L.T., *Progress on pharmaceutical drugs, plant extracts and ionic liquids as corrosion inhibitors.* Heliyon, 2019. **5**(2): p. e01143.
10. Koch, G., *Cost of corrosion.* Trends in oil and gas corrosion research and technologies, 2017: p. 3-30.
11. Mintek, *Corrosion costs SA R130bn: Mintek.* Brand South Africa, https://brandsouthafrica.com/105508/news-facts/26-may-11-1794/, 2011.
12. Ididama, R.O., V.I.E. Ajiwe, and C.N. Emeruwa, *Corrosion Inhibition of Mild Steel in Sulphuric Acid (H 2 SO 4) Medium of the Stem Extract of Tetrapleura Tetraptera.* American Journal of Applied Chemistry, 2019. **7**(3): p. 87-94.
13. Florio, J.J. and D.J. Miller, *Handbook of coating additives*. 2004: CRC Press.
14. Verma, C., E.E. Ebenso, and M. Quraishi, *Corrosion inhibitors for ferrous and non-ferrous metals and alloys in ionic sodium chloride solutions: A review.* Journal of Molecular Liquids, 2017. **248**: p. 927-942.
15. Abdel-Karim, A.M. and A.M. El-Shamy, *A review on green corrosion inhibitors for protection of archeological metal artifacts.* Journal of Bio-and Tribo-Corrosion, 2022. **8**(2): p. 1-21.
16. Guzen, K.P., et al., *Eco-friendly synthesis of imines by ultrasound irradiation.* Tetrahedron Letters, 2007. **48**(10): p. 1845-1848.
17. Namboodiri, V.V. and R.S. Varma, *Solvent-free sonochemical preparation of ionic liquids.* Organic letters, 2002. **4**(18): p. 3161-3163.
18. Singh, M.S. and S. Chowdhury, *Recent developments in solvent-free multicomponent reactions: a perfect synergy for eco-compatible organic synthesis.* Rsc Advances, 2012. **2**(11): p. 4547-4592.
19. Cioc, R.C., E. Ruijter, and R.V. Orru, *Multicomponent reactions: advanced tools for sustainable organic synthesis.* Green Chemistry, 2014. **16**(6): p. 2958-2975.
20. Aljuhani, A., et al., *Microwave-assisted synthesis of novel imidazolium, pyridinium and pyridazinium-based ionic liquids and/or salts and prediction of physico-chemical properties for their toxicity and antibacterial activity.* Journal of Molecular Liquids, 2018. **249**: p. 747-753.
21. Deng, Q., et al., *Novel triazolyl bis-amino acid derivatives readily synthesized via click chemistry as potential corrosion inhibitors for mild steel in HCl.* Corrosion science, 2012. **57**: p. 220-227.

© University of Venda

22. Ameta, G., et al., *Sonochemical synthesis and characterization of imidazolium based ionic liquids: A green pathway.* Journal of Molecular Liquids, 2015. **211**: p. 934-937.
23. Verma, C., et al., *An overview on plant extracts as environmental sustainable and green corrosion inhibitors for metals and alloys in aggressive corrosive media.* Journal of molecular liquids, 2018. **266**: p. 577-590.
24. Anastas, P. and N. Eghbali, *Green chemistry: principles and practice.* Chemical Society Reviews, 2010. **39**(1): p. 301-312.
25. Kidwai, M. and R. Mohan, *Green chemistry: an innovative technology.* Foundations of Chemistry, 2005. **7**(3): p. 269-287.
26. Northwood, D. and N. Faldu. *Corrosion: The Circular Materials Economy and Design for Sustainability*. in *Proceedings of the Australasian Corrosion Association's Annual Conference: Corrosion and Prevention, Melbourne, Australia*. 2019.
27. McCafferty, E., *Introduction to corrosion science*. 2010: Springer Science & Business Media.
28. Hays, G.F., *Now is the Time.* World Corrosion Organization, 2010.
29. Kumar, H., et al., *The inhibitive effect of cloxacillin on mild steel corrosion in 2 N sulphuric acid medium.* Materials Today: Proceedings, 2021. **36**: p. 898-902.
30. Zakeri, A., E. Bahmani, and A.S.R. Aghdam, *Plant extracts as sustainable and green corrosion inhibitors for protection of ferrous metals in corrosive media: A mini review.* Corrosion Communications, 2022.
31. Deepa, P. and R. Padmalatha, *Corrosion behaviour of 6063 aluminium alloy in acidic and in alkaline media.* Arabian Journal of chemistry, 2017. **10**: p. S2234-S2244.
32. Jane, M.N. and T.M. Nakara, *Determination of the Corrosion Inhibition Effect of Terminalia Ivorensis Leaves Extract on Galvanized and Mild Steel in Sulphuric Acid Media.* American Journal of Physical Chemistry, 2019. **8**(1): p. 11-16.
33. Ofuyekpone, O.D., et al., *Effect of inhibitor concentration on the potency of stylosanthes gracilis extract as corrosion inhibitor for AISI 304l in sulphuric acid solution.* Scientific African, 2021. **11**: p. e00714.
34. Loto, C.A. and M. Akinyele, *Effect of ginger, pomegranate and celery extracts on zinc electrodeposition, surface morphology and corrosion inhibition of mild steel.* Alexandria Engineering Journal, 2020. **59**(2): p. 933-941.
35. Vazirinasab, E., R. Jafari, and G. Momen, *Application of superhydrophobic coatings as a corrosion barrier: A review.* Surface and Coatings Technology, 2018. **341**: p. 40-56.
36. Palanisamy, G., *Corrosion inhibitors.* Corrosion inhibitors, 2019: p. 24.
37. Olasunkanmi, L.O., *Electrochemical, quantum chemical calculation and molecular dynamic simulation studies on some quinoxaline derivatives as corrosion inhibitors for mild steel in acidic medium*. 2015, North-West University (South Africa).
38. Davis, J., *The effects and economic impact of corrosion.* Corrosion: Understanding the Basics; ASM International: Almere, The Netherlands, 2000.
39. Onen, A.I., *Kinetic Studies of Selected Corrosion Inhibitors of Aluminium and Mild Steel in Acid Medium*. 2010.
40. Ismail, M.A., et al., *Novel cationic aryl bithiophene/terthiophene derivatives as corrosion inhibitors by chemical, electrochemical and surface investigations.* Scientific Reports, 2022. **12**(1): p. 1-16.
41. Brycki, B.E., et al., *Organic corrosion inhibitors.* Corrosion inhibitors, principles and recent applications, 2018. **3**: p. 33.
42. Ivonye, I.C., *Corrosion processes and mechanisms in the presence of MonoEthylene Glycol (MEG)*. 2014, University of Leeds.
43. Ukpai, J.I., *Erosion-corrosion characterisation for pipeline materials using combined acoustic emission and electrochemical monitoring*. 2014, University of Leeds.
44. Ghareba, S., *Inhibition of carbon steel corrosion by long alkyl-chain amino acid corrosion inhibitors.* 2011.

© University of Venda

45. Udabe Sánchez, E., *Innovative metal-free coumarate based ionic liquids and acrylic UV-coatings as corrosion inhibitors.* 2021.
46. Ebenso, E.E., *From Dust to Dust: The Chemistry Alternative.* 2011.
47. S Saji, V., *Contemporary developments in corrosion inhibitors-Review of patents.* Recent Patents on Corrosion Science, 2011. **1**(1): p. 63-71.
48. Quadri, T.W., et al., *Zinc oxide nanocomposites of selected polymers: synthesis, characterization, and corrosion inhibition studies on mild steel in HCl solution.* ACS omega, 2017. **2**(11): p. 8421-8437.
49. Syed, S., *Atmospheric corrosion of materials.* Emirates Journal for Engineering Research, 2006. **11**(1): p. 1-24.
50. Murulana, L.C., *Adsorption, thermodynamic and density functional theory investigation of some sulphonamides as corrosion inhibitors for some selected metals in acidic medium*. 2015, North-West University.
51. Kadhim, A., et al., *Corrosion inhibitors. A review.* International Journal of Corrosion and Scale Inhibition, 2021. **10**(1): p. 54-67.
52. Turkee, H.M., *Investigation of the Performance of Some Corrosion Inhibitors in Aerated Acid Solutions*. 2009, M. Sc. Thesis Dept. of Chem. Eng., University of AL-Nahrain, Baghdad.
53. Ts' oeunyane, G.M., *Corrosion Inhibition of Mild Steel in 1M HCL Using Synthesized Eco-friendly Polymer Composites*. 2017, University of Johannesburg.
54. Roberge, P.R., *Corrosion inspection and monitoring*. 2007: John Wiley & Sons.
55. Luu, T., *Corrosion, Corrosion Prevention & Solutions in System of Pipelines.* 2021.
56. Bardal, E. and J. Drugli, *Corrosion detection and diagnosis.* Materials science and engineering, 2004. **3**.
57. Anaee, R.A.M. and M.H. Abdulmajeed, *Tribocorrosion.* Advances in Tribology, 2016.
58. Singh, A.K., *Study on corrosion and inhibition behaviour of some aluminium alloys in hydrochloric acid contaminated by tungstate ions.*
59. SONI, A., *Studies of hydroxytriazenes as corrosion inhibitors for brass.* 2016.
60. Aslam, R., et al., *Corrosion inhibition of steel using different families of organic compounds: Past and present progress.* Journal of Molecular Liquids, 2022. **348**: p. 118373.
61. Nnaji, N.J., *Inhibition of aluminium corrosion using phthalocyanines–experimental and computational studies.* 2021.
62. Sastri, V.S., *Green corrosion inhibitors: theory and practice*. 2012: John Wiley & Sons.
63. Ramesh, M. and L. Rajeshkumar, *Case-studies on green corrosion inhibitors.* Sustainable Corrosion Inhibitors, 2021. **107**: p. 204-221.
64. Rashidi, N., S.R. Alavi-Soltani, and R. Asmatulu, *Crevice corrosion theory, mechanisms and prevention methods.* 2007.
65. Jiang, P., *Machine learning methods for corrosion and stress corrosion cracking risk analysis of engineered systems*. 2018, Doctoral dissertation). University of New South Wales.
66. Czaban, M., *Aircraft corrosion–review of corrosion processes and its effects in selected cases.* Fatigue of Aircraft Structures, 2018.
67. Loto, C., *Microbiological corrosion: mechanism, control and impact—a review.* The International Journal of Advanced Manufacturing Technology, 2017. **92**(9): p. 4241-4252.
68. Beech, I.B. and J. Sunner, *Biocorrosion: towards understanding interactions between biofilms and metals.* Current opinion in Biotechnology, 2004. **15**(3): p. 181-186.
69. Kvarekvål, J. and J. Moloney, *Sour corrosion.* Trends in Oil and Gas Corrosion Research and Technologies, 2017: p. 113-147.
70. Mohseni, E., et al., *A study on surface modification of Al7075-T6 alloy against fretting fatigue phenomenon.* Advances in Materials Science and Engineering, 2014. **2014**.
71. Gateman, S.M., *Investigating Corrosion of Simple and Complex Metallic Materials Using Macro and Micro Electrochemical Techniques*. 2020: McGill University (Canada).

© University of Venda

72. Ahuja, S.K., M.K. Shukla, and K.K. Ravulakollu, *Surface corrosion detection and classification for steel alloy using image processing and machine learning.* Helix, 2018. **8**(5): p. 3822-3827.
73. Nnoka, M., T.A. Jack, and J. Szpunar, *Effects of different microstructural parameters on the corrosion and cracking resistance of pipeline steels: A review.* Engineering Failure Analysis, 2024: p. 108065.
74. Chatterjee, U., S.K. Bose, and S.K. Roy, *Environmental degradation of metals: Corrosion technology series/14*. 2001: CRC Press.
75. McCafferty, E., *Kinetics of corrosion*, in *Introduction to Corrosion Science*. 2010, Springer. p. 119-175.
76. Mohd Isa, A.S.B., *Evaluation on Rust Stabilizer Paint for Maintenance Painting of Internal Pipeline.* 2009.
77. Nkhumeleni, M.R., *Application of modern analytical techniques for quantification of selected radioactive metals in environmental samples.* 2023.
78. Nwankwo, H.U., *Electrochemical, quantum chemical calculation, qsar and molecular dynamics simulation studies on some carbazole derivatives as corrosion and biocorrosion inhibitors for mild steel in acidic medium*. 2017, North-West University (South Africa).
79. Rahman, A., *Self-healable and conductive metal-nanocomposite double-network hydrogels with bioactive properties.* 2019.
80. Instruments, G., *Basics of electrochemical impedance spectroscopy.* G. Instruments, Complex impedance in Corrosion, 2007: p. 1-30.
81. Gil, P.M., *Exploring Corrosion Inhibition in Acidic and Oilfield Environments*. 2013: The University of Manchester (United Kingdom).
82. Shivakumar, S. and K. Mohana, *Corrosion behavior and adsorption thermodynamics of some Schiff bases on mild steel corrosion in industrial water medium.* International Journal of Corrosion, 2013. **2013**.
83. Saleh, B., et al., *Advanced corrosion protection through coatings and surface rebuilding*. 2023, MDPI. p. 180.
84. Perez, N., *Electrochemical corrosion*, in *Materials Science: Theory and Engineering*. 2024, Springer. p. 835-898.
85. Janiec-Anwar, J., *Galvanic Corrosion of Magnesium Alloys*. 2014: The University of Manchester (United Kingdom).
86. Thorn, T.D., et al., *Smart and repeatable easy-repairing and self-sensing composites with enhanced mechanical performance for extended components life.* Composites Part A: Applied Science and Manufacturing, 2023. **165**: p. 107337.
87. Liu, R., et al., *Influence of grain size and crystallographic orientation on microbially influenced corrosion of low-carbon steel in artificial seawater.* Materials & Design, 2023. **234**: p. 112353.
88. Gibon, E., et al., *The biological response to orthopaedic implants for joint replacement: Part I: Metals.* Journal of Biomedical Materials Research Part B: Applied Biomaterials, 2017. **105**(7): p. 2162-2173.
89. Islam, N., *Corrosion And Its Effect: A Critical Appraisal.* Journal of Survey in Fisheries Sciences, 2022: p. 396-408.
90. Popoola, A., O. Olorunniwo, and O. Ige, *Corrosion resistance through the application of anti-corrosion coatings.* Developments in corrosion protection, 2014. **13**(4): p. 241-270.
91. Khadom, A.A., A.N. Abd, and N.A. Ahmed, *Xanthium strumarium leaves extracts as a friendly corrosion inhibitor of low carbon steel in hydrochloric acid: kinetics and mathematical studies.* south african journal of chemical engineering, 2018. **25**: p. 13-21.
92. Sharma, N. and S. Joshi, *Experimental Study of Factors Affecting Corrosion in Gas Wells Using Potantio Acetate and Galvan Acetate Tests.* International Journal of Chemistry, 2013: p. 01.
93. Setoudeh, M., et al., *Experimental Study of Factors Affecting Corrosion in Gas Wells Using Potantio Acetate and Galvan Acetate Tests.* International Journal of science and investigations, 2012: p. 13-16.

© University of Venda

94. Sereda, P., *Weather factors affecting corrosion of metals*. 1974: ASTM International.
95. Craig, B.D., R.A. Lane, and D.H. Rose, *Corrosion prevention and control: A program management guide for selecting materials.* Advanced Materials, Manufacturing, and Testing Information Analysis Center (AMMTIAC), 2006.
96. Ismail, I.M., *Inhibition of pitting on carbon steel*. 2011, University of Leeds.
97. Harsimran, S., K. Santosh, and K. Rakesh, *Overview of corrosion and its control: A critical review.* Proc. Eng. Sci, 2021. **3**(1): p. 13-24.
98. Malik, A., et al., *The influence of pH and chloride concentration on the corrosion behaviour of AISI 316L steel in aqueous solutions.* Corrosion science, 1992. **33**(11): p. 1809-1827.
99. Kulshrestha, U., *Acid rain*. 2013: Taylor and Francis, Manila Typesetting Company, New York.
100. Cicek, V., *Corrosion engineering*. 2014: John Wiley & Sons.
101. Wang, J., et al., *Effects of oxygen concentration on the corrosion behavior of high entropy alloy AlCoCrFeNi in simulated deep sea.* Heliyon, 2024.
102. Madakson, P., et al., *Effect of anodization on the corrosion behavior of aluminium alloy in HCl acid and NaOH.* International Journal of Materials Engineering, 2012. **2**(4): p. 38-42.
103. Harb, M.B., et al., *Olive leaf extract as a green corrosion inhibitor of reinforced concrete contaminated with seawater.* Arabian Journal of Chemistry, 2020. **13**(3): p. 4846-4856.
104. GBERTYO, J.A., *EFFICACY OF ACIDIMETRY AS A CORROSION MONITORING TECHNIQUE IN DETERMINING THE KINETICS AND THERMODYNAMICS OF CORROSION INHIBITION BY L-LEUCINE, ASPARTIC ACID AND Sareocephalus Latifolius*. 2019.
105. Kruger, J. and M. Sc, *Electrochemistry of corrosion.* Electrochemistry Encyclopedia, 2001.
106. Martin, F.J., *Corrosion inhibitor mechanisms on reinforcing steel in Portland cement pastes*. 2001, Purdue University.
107. Yang, D., *Corrosion Inhibition Performance of Imidazolium Ionic Liquids and Their Influence On Surface Ferrous Carbonate Layer Formation*. 2016, University of Akron.
108. Arellanes-Lozada, P., et al., *The inhibition of aluminum corrosion in sulfuric acid by poly (1-vinyl-3-alkyl-imidazolium hexafluorophosphate).* Materials, 2014. **7**(8): p. 5711-5734.
109. Banerjee, S., et al., *Highly efficient polyurethane ionomer corrosion inhibitor: the effect of chain structure.* Rsc Advances, 2011. **1**(2): p. 199-210.
110. Guo, L., W. Dong, and S. Zhang, *Theoretical challenges in understanding the inhibition mechanism of copper corrosion in acid media in the presence of three triazole derivatives.* RSC advances, 2014. **4**(79): p. 41956-41967.
111. John, S. and A. Joseph, *Effective inhibition of mild steel corrosion in 1 M hydrochloric acid using substituted triazines: an experimental and theoretical study.* RSC advances, 2012. **2**(26): p. 9944-9951.
112. Mourya, P., S. Banerjee, and M. Singh, *Corrosion inhibition of mild steel in acidic solution by Tagetes erecta (Marigold flower) extract as a green inhibitor.* Corrosion Science, 2014. **85**: p. 352-363.
113. Rao, B.A., M.Y. Iqbal, and B. Sreedhar, *Electrochemical and surface analytical studies of the self-assembled monolayer of 5-methoxy-2-(octadecylthio) benzimidazole in corrosion protection of copper.* Electrochimica Acta, 2010. **55**(3): p. 620-631.
114. AL-KELABY, S.S.B., *INHIBITION OF GALVANIC CORROSION BY PHENYLTHIOUREA UNDER FLOWING CONDITIONS IN HYDROCHLORIC ACID SOLUTION.* 2007.
115. Fekry, A. and R.R. Mohamed, *Acetyl thiourea chitosan as an eco-friendly inhibitor for mild steel in sulphuric acid medium.* Electrochimica Acta, 2010. **55**(6): p. 1933-1939.
116. Tang, Y., et al., *Experimental and molecular dynamics studies on corrosion inhibition of mild steel by 2-amino-5-phenyl-1, 3, 4-thiadiazole.* Corrosion Science, 2010. **52**(1): p. 242-249.
117. Shanableh, A., *Studies on Natural Extracts as Inhibitors of Mild Steel Corrosion in 1M HC1 Solution*. 2011.
118. Davis, J.R., *Corrosion: Understanding the basics*. 2000: Asm International.

© University of Venda

119. Mercier, D. and M.-G. Barthés-Labrousse, *The role of chelating agents on the corrosion mechanisms of aluminium in alkaline aqueous solutions.* Corrosion Science, 2009. **51**(2): p. 339-348.
120. Winston, R., *Uhlig's corrosion handbook.* 2000.
121. Umoren, S. and M. Solomon, *Recent developments on the use of polymers as corrosion inhibitors-a review.* The Open Materials Science Journal, 2014. **8**(1).
122. Pehkonen, S.O. and S. Yuan, *Tailored thin coatings for corrosion inhibition using a molecular approach*. 2018: academic press.
123. Dariva, C.G. and A.F. Galio, *Corrosion inhibitors–principles, mechanisms and applications.* Developments in corrosion protection, 2014. **16**: p. 365-378.
124. Chiou, S.-Y., *A study of the effect of some inhibitors on the corrosion rates of austenitic stainless steels in sulfuric acid.* 1989.
125. Shang, Z. and J. Zhu, *Overview on plant extracts as green corrosion inhibitors in the oil and gas fields.* Journal of Materials Research and Technology, 2021. **15**: p. 5078-5094.
126. Zakeri, A., E. Bahmani, and A.S.R. Aghdam, *Plant extracts as sustainable and green corrosion inhibitors for protection of ferrous metals in corrosive media: A mini review.* Corrosion Communications, 2022. **5**: p. 25-38.
127. Al-Qasmi, M.N., *Natural products as corrosion inhibitors of some metals in aqueous media.* A Thesis, Umm Al-Qura University, Faculty of Applied Science for Girls, Chemistry Department, 2010.
128. Björlenstam, P., *Evaluation of corrosion in crevices in screw joints*. 2011.
129. Christian, V., *Corrosion of aluminium*. 2004, Elsevier Science.
130. Mahmood, N.J., *The effect of adding different percentages of Copper on corrosion of pure Aluminum.* Tikrit Journal of Pure Science, 2018. **23**(2): p. 123-128.
131. Fazal, B.R., et al., *A review of plant extracts as green corrosion inhibitors for CO2 corrosion of carbon steel.* npj Materials Degradation, 2022. **6**(1): p. 1-14.
132. Buchweishaija, J., *Plants as a source of green corrosion inhibitors: the case of gum exudates from Acacia species (A. drepanolobium and A. senegal).* Tanzania Journal of Science, 2009. **35**.
133. Miralrio, A. and A. Espinoza Vázquez, *Plant extracts as green corrosion inhibitors for different metal surfaces and corrosive media: a review.* Processes, 2020. **8**(8): p. 942.
134. Sedik, A., et al., *Dardagan Fruit extract as eco-friendly corrosion inhibitor for mild steel in 1 M HCl: Electrochemical and surface morphological studies.* Journal of the Taiwan Institute of Chemical Engineers, 2020. **107**: p. 189-200.
135. Dehghani, A., et al., *Potential of Borage flower aqueous extract as an environmentally sustainable corrosion inhibitor for acid corrosion of mild steel: electrochemical and theoretical studies.* Journal of Molecular Liquids, 2019. **277**: p. 895-911.
136. Chaubey, N., V.K. Singh, and M. Quraishi, *Papaya peel extract as potential corrosion inhibitor for Aluminium alloy in 1 M HCl: Electrochemical and quantum chemical study.* Ain Shams Engineering Journal, 2018. **9**(4): p. 1131-1140.
137. Jokar, M., T.S. Farahani, and B. Ramezanzadeh, *Electrochemical and surface characterizations of morus alba pendula leaves extract (MAPLE) as a green corrosion inhibitor for steel in 1 M HCl.* Journal of the Taiwan Institute of Chemical Engineers, 2016. **63**: p. 436-452.
138. Dehghani, A., et al., *Experimental complemented with microscopic (electronic/atomic)-level modeling explorations of Laurus nobilis extract as green inhibitor for carbon steel in acidic solution.* Journal of Industrial and Engineering Chemistry, 2020. **84**: p. 52-71.
139. Thakur, A. and A. Kumar, *Sustainable inhibitors for corrosion mitigation in aggressive corrosive media: a comprehensive study.* Journal of Bio-and Tribo-Corrosion, 2021. **7**: p. 1-48.
140. Lourens, A., A.M. Viljoen, and F. Van Heerden, *South African Helichrysum species: a review of the traditional uses, biological activity and phytochemistry.* Journal of Ethnopharmacology, 2008. **119**(3): p. 630-652.

© University of Venda

141. Yazdi, S.E., *Metabolomic analysis on anti-HIV activity of selected Helichrysum species*. 2019: University of Pretoria (South Africa).
142. Prinsloo, G. and J. Meyer, *In vitro production of phytoalexins by Helichrysum kraussii.* South African journal of botany, 2006. **72**(3): p. 482-483.
143. Dalton, B.P.A., *The coastal grasslands of Maputaland, South Africa: Effects of fire and grazing on vegetation structure, diversity, and composition*. 2007.
144. Hehre, W.J., *A guide to molecular mechanics and quantum chemical calculations*. Vol. 2. 2003: Wavefunction Irvine, CA.
145. Atkins, P., P.W. Atkins, and J. de Paula, *Atkins' physical chemistry*. 2014: Oxford university press.
146. Chen, B.W., L. Xu, and M. Mavrikakis, *Computational methods in heterogeneous catalysis.* Chemical Reviews, 2020. **121**(2): p. 1007-1048.
147. Sena, A.M.P., *Density functional theory studies of surface interactions and electron transfer in porphyrins and other molecules*. 2010, UCL (University College London).
148. Arora, P., *Development and application of QM/MM methods to study the solvation effects and surfaces.* 2010.
149. McKay, M., *Supramolecular resorcin [4] arene-capped porphyrins: ligands towards homogeneous catalysis*. 2008.
150. Van Mourik, T., M. Bühl, and M.-P. Gaigeot, *Density functional theory across chemistry, physics and biology*. 2014, The Royal Society Publishing. p. 20120488.
151. Engel, T., *Quantum chemistry and spectroscopy*. 2012: Pearson Higher Ed.
152. Ramachandran, K., D. Gopakumar, and K. Namboori, *Basis sets*. 2008: Springer.
153. López Álvarez, R.M., *Basis functions in computational chemisty: analysis of the second period diatomic hydrides.* 2021.
154. Reel, J., *A comparative review of computational methods as applied to gold (I) complexes and mechanisms*. 2016, Duke University.
155. Jensen, F., *Introduction to computational chemistry*. 2017: John wiley & sons.
156. Lynch, B.J., Y. Zhao, and D.G. Truhlar, *Effectiveness of diffuse basis functions for calculating relative energies by density functional theory.* The Journal of Physical Chemistry A, 2003. **107**(9): p. 1384-1388.
157. Mahamiya, V., P. Bhattacharyya, and A. Shukla, *Benchmarking Gaussian Basis Sets in Quantum-Chemical Calculations of Photoabsorption Spectra of Light Atomic Clusters.* ACS omega, 2022. **7**(51): p. 48261-48271.
158. Tanaka, T., *A theory of mean field approximation.* Advances in Neural Information Processing Systems, 1998. **11**.
159. Cremer, D., *Møller–Plesset perturbation theory: from small molecule methods to methods for thousands of atoms.* Wiley Interdisciplinary Reviews: Computational Molecular Science, 2011. **1**(4): p. 509-530.
160. Kordt, P., *Single-site Green function of the Dirac equation for full-potential electron scattering*. Vol. 34. 2012: Forschungszentrum Jülich.
161. Goerigk, L. and S. Grimme, *Double-hybrid density functionals.* Wiley Interdisciplinary Reviews: Computational Molecular Science, 2014. **4**(6): p. 576-600.
162. Perdew, J.P., K. Burke, and M. Ernzerhof, *Generalized gradient approximation made simple.* Physical review letters, 1996. **77**(18): p. 3865.
163. Li, M., et al., *Accurate prediction of the properties of materials using the CAM-B3LYP density functional.* Journal of Computational Chemistry, 2021. **42**(21): p. 1486-1497.
164. Cramer, C.J. and F. Bickelhaupt, *Essentials of computational chemistry.* ANGEWANDTE CHEMIE-INTERNATIONAL EDITION IN ENGLISH-, 2003. **42**(4): p. 381-381.
165. Verma, C., M. Quraishi, and K.Y. Rhee, *Electronic effect vs. Molecular size effect: Experimental and computational based designing of potential corrosion inhibitors.* Chemical Engineering Journal, 2022. **430**: p. 132645.

© University of Venda

166. Verma, C., et al., *Substituents effect on corrosion inhibition performance of organic compounds in aggressive ionic solutions: a review.* Journal of Molecular Liquids, 2018. **251**: p. 100-118.
167. Verma, C., E.E. Ebenso, and M. Quraishi, *Molecular structural aspects of organic corrosion inhibitors: Influence of–CN and–NO2 substituents on designing of potential corrosion inhibitors for aqueous media.* Journal of Molecular Liquids, 2020. **316**: p. 113874.
168. AKBAS, E., E. ERGAN, and H. DONMEZ, *Quantum Chemical Calculations for Corrosion Inhibition of Pyrimidine Derivatives.* The Eurasia Proceedings of Science Technology Engineering and Mathematics, 2019. **6**: p. 142-147.
169. MURULANA, L.C., *Adsorption, Thermodynamic and Density Functional Theory Investigation of Some Sulphonamides as Corrosion Inhibitors for Some Selected Metals in Acidic Medium.* North-West University (Mafikeng Campus), 2015.
170. Kabanda, M.M., et al., *Quantum chemical studies on the corrosion inhibition of mild steel by some triazoles and benzimidazole derivatives in acidic medium.* Int. J. Electrochem. Sci, 2012. **7**(5035): p. e5056.
171. Kaya, S., et al., *Determination of corrosion inhibition effects of amino acids: quantum chemical and molecular dynamic simulation study.* Journal of the Taiwan Institute of Chemical Engineers, 2016. **58**: p. 528-535.
172. Tüzün, B. and C. Kaya, *Investigation of DNA–RNA molecules for the efficiency and activity of corrosion inhibition by DFT and molecular docking.* Journal of Bio-and Tribo-Corrosion, 2018. **4**: p. 1-11.
173. Sánchez-Eleuterio, A., et al., *Experimental and Theoretical Studies on Acid Corrosion Inhibition of API 5L X70 Steel with Novel 1-N-α-d-Glucopyranosyl-1 H-1, 2, 3-Triazole Xanthines.* Molecules, 2023. **28**(1): p. 460.
174. Sands, D.E., *Introduction to crystallography*. 1993: Courier Corporation.
175. Callister, W.D. and D.G. Rethwisch, *Materials science and engineering: an introduction*. Vol. 7. 2007: John wiley & sons New York.
176. Sholl, D.S. and J.A. Steckel, *Density functional theory: a practical introduction*. 2022: John Wiley & Sons.
177. Elmagbari, F.M.A., *Synthesis and design of ligand copper complexes as anti-inflammatory drugs.* 2015.
178. Paul, A., et al., *UV irradiation of natural organic matter (NOM): impact on organic carbon and bacteria.* Aquatic sciences, 2012. **74**(3): p. 443-454.
179. Nikafshar, S., et al., *The effects of UV light on the chemical and mechanical properties of a transparent epoxy-diamine system in the presence of an organic UV absorber.* Materials, 2017. **10**(2): p. 180.
180. Muthukumarasamy, K., et al., *Adsorption and corrosion inhibition performance of Tunbergia fragrans extract on mild steel in acid medium.* Materials Today: Proceedings, 2020. **33**: p. 4054-4058.
181. Berrissoul, A., et al., *Evaluation of Lavandula mairei extract as green inhibitor for mild steel corrosion in 1 M HCl solution. Experimental and theoretical approach.* Journal of Molecular Liquids, 2020. **313**: p. 113493.
182. Ruvubu, S.B., *Corrosion Inhibiting Properties of Lignin and Sulfonated Lignin Derived from Selected Agro-waste Plant on Mild Steel in Acidic Condition.* American Journal of Physical Chemistry, 2021. **10**(2): p. 31-37.
183. Chigayo, K., et al., *Phytochemical and antioxidant properties of different solvent extracts of Kirkia wilmsii tubers.* Asian Pacific Journal of Tropical Biomedicine, 2016. **6**(12): p. 1037-1043.
184. Priya, B., *Studies on potential green corrosion inhibitors for mild steel in different media*. 2017, Ph. D. thesis. University of Kota.
185. Umoren, S.A., et al., *Date palm leaves extract as a green and sustainable corrosion inhibitor for low carbon steel in 15 wt.% HCl solution: The role of extraction solvent on inhibition effect.* Environmental Science and Pollution Research, 2021. **28**(30): p. 40879-40894.

© University of Venda

186. Mbedzi, D.T., et al., *Ultraviolet (UV) light-induced geometrical isomerization of cinnamic acid containing molecules: A plausible, non-enzymatic approach to modify metabolite composition of plant extracts.* South African Journal of Botany, 2022. **150**: p. 845-850.
187. Ramabulana, A.-T., et al., *Metabolomics and molecular networking to characterize the chemical space of four Momordica plant species.* Metabolites, 2021. **11**(11): p. 763.
188. Singh, M., S. Patra, and R.K. Singh, *Common techniques and methods for screening of natural products for developing of anticancer drugs*, in *Evolutionary diversity as a source for anticancer molecules*. 2021, Elsevier. p. 323-353.
189. Porot, L., et al., *Fourier-transform infrared analysis and interpretation for bituminous binders.* Road Materials and Pavement Design, 2022: p. 1-22.
190. Kamal, C. and M.G. Sethuraman, *Caulerpin • A bis-indole alkaloid as a green inhibitor for the corrosion of mild steel in 1 M HCl solution from the marine alga Caulerpa racemosa.* Industrial & Engineering Chemistry Research, 2012. **51**(31): p. 10399-10407.
191. Almzarzie, K., et al., *Electrochemical impedance spectroscopy (EIS) and study of iron corrosion inhibition by turmeric roots extract (TRE) in hydrochloric acid solution.* Egyptian Journal of Chemistry, 2019. **62**(3): p. 501-512.
192. Patel, A., et al., *Impedance spectroscopic study of corrosion inhibition of Al-Pure by organic Schiff base in hydrochloric acid.* Journal of Saudi Chemical Society, 2013. **17**(1): p. 53-59.
193. Hafez, B., et al., *Environmentally friendly inhibitor of the corrosion of mild steel: Commercial oil of Eucalyptus.* International Journal of Corrosion and Scale Inhibition, 2019. **8**(3): p. 573-585.
194. Zhu, J., et al., *Understanding the inhibition performance of novel dibenzimidazole derivatives on Fe (110) surface: DFT and MD simulation insights.* Journal of Materials Research and Technology, 2022. **17**: p. 211-222.
195. Kovačević, N. and A. Kokalj, *Chemistry of the interaction between azole type corrosion inhibitor molecules and metal surfaces.* Materials Chemistry and Physics, 2012. **137**(1): p. 331-339.
196. Vernack, E., et al., *DFT studies of 2-mercaptobenzothiazole and 2-mercaptobenzimidazole as corrosion inhibitors for copper.* Corrosion Science, 2020. **174**: p. 108840.
197. Basiuk, V.A., O.V. Prezhdo, and E.V. Basiuk, *Thermal smearing in DFT calculations: How small is really small? A case of La and Lu atoms adsorbed on graphene.* Materials Today Communications, 2020. **25**: p. 101595.
198. Li, J., et al., *Refinement of nanoporous copper by dealloying the Al–Cu alloy in NaOH solution containing sodium dodecyl sulfate.* Physical Chemistry Chemical Physics, 2023. **25**(29): p. 19492-19500.
199. Bedair, M., et al., *Benzidine-based Schiff base compounds for employing as corrosion inhibitors for carbon steel in 1.0 M HCl aqueous media by chemical, electrochemical and computational methods.* Journal of Molecular Liquids, 2020. **317**: p. 114015.
200. Nyangiwe, N.N. and C. Ouma, *Modelling the adsorption of natural organic matter on Ag (111) surface: Insights from dispersion corrected density functional theory calculations.* Journal of Molecular Graphics and Modelling, 2019. **92**: p. 313-319.
201. Xu, S., et al., *Experimental and theoretical studies on the corrosion inhibition of carbon steel by two indazole derivatives in HCl medium.* Materials, 2019. **12**(8): p. 1339.
202. Bourzi, H., et al., *Furfural analogs as sustainable corrosion inhibitors—predictive efficiency using DFT and Monte Carlo simulations on the Cu (111), Fe (110), Al (111) and Sn (111) surfaces in acid media.* Sustainability, 2020. **12**(8): p. 3304.
203. Oguzie, E.E., et al., *Understanding corrosion inhibition mechanisms—experimental and theoretical approach.* Rsc Advances, 2011. **1**(5): p. 866-873.
204. Haris, N.I.N., et al., *An overview of molecular dynamic simulation for corrosion inhibition of ferrous metals.* Metals, 2020. **11**(1): p. 46.
205. Obot, I., Z. Gasem, and S. Umoren, *Understanding the mechanism of 2-mercaptobenzimidazole adsorption on Fe (110), Cu (111) and Al (111) surfaces: DFT and*

© University of Venda

molecular dynamics simulations approaches. International Journal of Electrochemical Science, 2014. **9**(5): p. 2367-2378.

206. Bashir, S., et al., *Corrosion inhibition efficiency of bronopol on aluminium in 0.5 M HCl solution: Insights from experimental and quantum chemical studies.* Surfaces and Interfaces, 2020. **20**: p. 100542.
207. Iorhuna, F., S. Adulfatah, and A.M. Ayuba, *Quinazoline derivatives as corrosion inhibitors on aluminium metal surface: A theoretical study.* Advanced Journal of Chemistry-Section A, 2023. **6**(1): p. 71-84.
208. Ayuba, A.M. and U. Umar, *Modeling vitexin and isovitexin flavones as corrosion inhibitors for aluminium metal.* Karbala International Journal of Modern Science, 2021. **7**(3): p. 4.
209. Mansour, A.A., et al., *Interfacial phenomena and surface protection of N80-carbon steel in acidic environments using thiazolidinediones: An experimental and computational analysis.* Colloids and Surfaces A: Physicochemical and Engineering Aspects, 2023. **677**: p. 132415.
210. Ouakki, M., et al., *A detailed investigation on the corrosion inhibition effect of by newly synthesized pyran derivative on mild steel in 1.0 M HCl: Experimental, surface morphological (SEM-EDS, DRX& AFM) and computational analysis (DFT & MD simulation).* Journal of Molecular Liquids, 2021. **344**: p. 117777.
211. Fytianos, G., et al., *Corrosion Evaluation of MEA Solutions by SEM-EDS, ICP-MS and XRD.* Energy Procedia, 2016. **86**: p. 197-204.
212. Mukherjee, P., *LC–MS: A rapid technique for understanding the plant metabolite analysis.* Quality control and evaluation of herbal drugs, 2019: p. 459-479.
213. Hwang, J.T., et al., *Study of the UV light conversion of feruloyl amides from Portulaca oleracea and their inhibitory effect on IL-6-induced STAT3 activation.* Molecules, 2016. **21**(7): p. 865.
214. Masike, K., et al., *Revising reverse-phase chromatographic behavior for efficient differentiation of both positional and geometrical isomers of dicaffeoylquinic acids.* Journal of Analytical Methods in Chemistry, 2018. **2018**.
215. Srivastava, N., et al., *Advances in extraction technologies: Isolation and purification of bioactive compounds from biological materials*, in *Natural bioactive compounds*. 2021, Elsevier. p. 409-433.
216. Yang, H., et al., *Eupatorium adenophorum Spreng leaves extract/potassium iodide as a highly sustainable inhibitor for the corrosion protection of steel in citric acid solution.* Journal of Molecular Liquids, 2023. **387**: p. 122614.
217. Haldhar, R., et al., *Corrosion inhibition, surface adsorption and computational studies of Swertia chirata extract: A sustainable and green approach.* Materials Chemistry and Physics, 2021. **267**: p. 124613.
218. Leelavathi, S. and R. Rajalakshmi, *Dodonaea viscosa (L.) leaves extract as acid corrosion inhibitor for mild steel–a green approach.* J Mater Environ Sci, 2013. **4**(5): p. 625-638.
219. Zeng, J., et al., *The behavior of two indazole derivatives on the copper/sulfuric acid interface in terms of adsorption and corrosion inhibition.* Journal of the Taiwan Institute of Chemical Engineers, 2022. **140**: p. 104567.
220. Hsissou, R., et al., *Development and potential performance of prepolymer in corrosion inhibition for carbon steel in 1.0 M HCl: Outlooks from experimental and computational investigations.* Journal of colloid and interface science, 2020. **574**: p. 43-60.
221. Vijayalakshmi, P., R. Rajalakshmi, and S. Subhashini, *Corrosion inhibition of aqueous extract of Cocos nucifera-coconut palm-petiole extract from destructive distillation for the corrosion of mild steel in acidic medium.* Portugaliae Electrochimica Acta, 2011. **29**(1): p. 9-21.
222. Musa, H., et al., *Effect of Aniline as Corrosion inhibitor on the Corrosion of Aluminium in Hydrochloric acid solution.* Res. J. Chem. Environ, 2020. **24**(2).
223. Al-Amiery, A.A., W.N.R.W. Isahak, and W.K. Al-Azzawi, *Corrosion inhibitors: natural and synthetic organic inhibitors.* Lubricants, 2023. **11**(4): p. 174.

© University of Venda

224. Nasser, A.J.A. and M.A. Sathiq, *Comparative study of N-[(4-methoxyphenyl)(morpholin-4-yl) methyl] acetamide (MMPA) and N-[morpholin-4-yl (phenyl) methyl] acetamide (MPA) as corrosion inhibitors for mild steel in sulfuric acid solution.* Arabian Journal of Chemistry, 2017. **10**: p. S261-S273.
225. Gopiraman, M., et al., *Adsorption and corrosion inhibition behaviour of N-(phenylcarbamothioyl) benzamide on mild steel in acidic medium.* Progress in Organic Coatings, 2012. **73**(1): p. 104-111.
226. Ogunleye, O., et al., *Green corrosion inhibition and adsorption characteristics of Luffa cylindrica leaf extract on mild steel in hydrochloric acid environment.* Heliyon, 2020. **6**(1): p. e03205.
227. Sharma, S. and A. Kumar, *Recent advances in metallic corrosion inhibition: A review.* Journal of Molecular Liquids, 2021. **322**: p. 114862.
228. Bala, P., et al., *ADSORPTION AND ELECTROCHEMICAL BEHAVIOR OF CYPERUS ROTUNDUS ON OIL AND GAS PIPELINE STEEL IN 1.0 N HYDROCHLORIC ACID.*
229. Benali, O., et al., *Electrochemical, theoretical and XPS studies of 2-mercapto-1-methylimidazole adsorption on carbon steel in 1 M HClO4.* Applied surface science, 2007. **253**(14): p. 6130-6139.
230. Herrag, L., et al., *Adsorption properties and inhibition of mild steel corrosion in hydrochloric solution by some newly synthesized diamine derivatives: experimental and theoretical investigations.* Corrosion Science, 2010. **52**(9): p. 3042-3051.
231. Akinbulumo, O.A., O.J. Odejobi, and E.L. Odekanle, *Thermodynamics and adsorption study of the corrosion inhibition of mild steel by Euphorbia heterophylla L. extract in 1.5 M HCl.* Results in Materials, 2020. **5**: p. 100074.
232. Alinnor, I. and P. Ejikeme, *Corrosion inhibition of aluminium in acidic medium by different extracts of Ocimum Gratissimum.* Am. Chem. Sci. J, 2012. **2**(4): p. 122-135.
233. Dagdag, O., et al., *Epoxy pre-polymers as new and effective materials for corrosion inhibition of carbon steel in acidic medium: Computational and experimental studies.* Scientific reports, 2019. **9**(1): p. 11715.
234. Alaneme, K.K. and S.J. Olusegun, *Corrosion inhibition performance of lignin extract of sun flower (Tithonia diversifolia) on medium carbon low alloy steel immersed in H2SO4 solution.* Leonardo Journal of Sciences, 2012. **20**(11): p. 59-70.
235. Nwabanne, J.T. and V.N. Okafor, *Adsorption and thermodynamics study of the inhibition of corrosion of mild steel in H 2 SO 4 medium using Vernonia amygdalina.* Journal of Minerals and Materials Characterization and engineering, 2012. **11**(09): p. 885.
236. Dada, A., et al., *Langmuir, Freundlich, Temkin and Dubinin–Radushkevich isotherms studies of equilibrium sorption of Zn2+ unto phosphoric acid modified rice husk.* IOSR Journal of applied chemistry, 2012. **3**(1): p. 38-45.
237. Singh, A., et al., *Effect of electron donating functional groups on corrosion inhibition of mild steel in hydrochloric acid: Experimental and quantum chemical study.* Journal of the Taiwan Institute of Chemical Engineers, 2018. **82**: p. 233-251.
238. Liu, Z., et al., *Improved corrosion inhibition of calcium disodium EDTA for mild steel in chloride-contaminated concrete pore solution.* Cement and Concrete Composites, 2023. **140**: p. 105075.
239. Al Bahir, A., *Estimation of the performances of creatine and creatinine as eco-friendly corrosion inhibitors for copper in sodium hydroxide solution.* International Journal of Electrochemical Science, 2023. **18**(4): p. 100040.
240. Alamry, K.A., et al., *Corrosion inhibition of mild steel in hydrochloric acid solution by the expired Ampicillin drug.* Scientific Reports, 2023. **13**(1): p. 6724.
241. Betti, N., et al., *Corrosion inhibition properties of schiff base derivative against mild steel in HCl environment complemented with DFT investigations.* Scientific Reports, 2023. **13**(1): p. 8979.

© University of Venda

242. Ghazouani, T., et al., *Antioxidant activity and effect of quince pulp extract on the corrosion of C-steel in 1M HCl.* Research on Chemical Intermediates, 2015. **41**: p. 7463-7480.
243. Milonjić, S.K., *A consideration of the correct calculation of thermodynamic parameters of adsorption.* Journal of the Serbian chemical society, 2007. **72**(12): p. 1363-1367.
244. Jafari, H. and K. Akbarzade, *Effect of concentration and temperature on carbon steel corrosion inhibition.* Journal of Bio-and Tribo-Corrosion, 2017. **3**: p. 1-9.
245. Odewunmi, N.A., et al., *N1, N1, N12, N12-Tetramethyl-N1, N12-dioctyldodecane-1, 12-diaminium bromide: Its synthesis and application in inhibition of mild steel corrosion in 15% HCl.* Journal of Molecular Liquids, 2021. **338**: p. 116630.
246. Bouoidina, A., et al., *An effective and smart corrosion inhibitor in acidic environment: Experimental & theoretical studies.* Korean Journal of Chemical Engineering, 2023. **40**(1): p. 235-247.
247. Hmamou, D.B., et al., *Investigation of corrosion inhibition of carbon steel in 0.5 M H2SO4 by new bipyrazole derivative using experimental and theoretical approaches.* Journal of environmental chemical engineering, 2015. **3**(3): p. 2031-2041.
248. Eduok, U.M. and M. Khaled, *Corrosion inhibition for low-carbon steel in 1 MH 2 SO 4 solution by phenytoin: evaluation of the inhibition potency of another "anticorrosive drug".* Research on Chemical Intermediates, 2015. **41**: p. 6309-6324.
249. Ramesh Saliyan, V. and A.V. Adhikari, *Inhibition of corrosion of mild steel in acid media by N'-benzylidene-3-(quinolin-4-ylthio) propanohydrazide.* Bulletin of Materials Science, 2008. **31**(4): p. 699-711.
250. Kesari, P. and G. Udayabhanu, *Investigation of vitamin B12 as a corrosion inhibitor for mild steel in HCl solution through gravimetric and electrochemical studies.* Ain Shams Engineering Journal, 2023. **14**(4): p. 101920.
251. Iravani, D., et al., *The quaternary ammonium salts as corrosion inhibitors for X65 carbon steel under sour environment in NACE 1D182 solution: Experimental and computational studies.* Colloids and Surfaces A: Physicochemical and Engineering Aspects, 2023. **656**: p. 130544.
252. Radovici, O., *Proceedings of the Second European Symposium on Corrosion Inhibitors, Ferrara, Italy*. 1965, US Department of Energy Ferrara, Italy.
253. Laaroussi, H., et al., *Experimental and Theoretical Investigations of Argania spinosa's Extracts on the Antioxidant Activity and Mild Steel Corrosion's Inhibition in 1 M HCl.* Applied Sciences, 2022. **12**(24): p. 12641.
254. Kamal, A.-B., et al., *Corrosion inhibition behavior of the synthesized pyrazoline-sulfonamide hybrid of mild steel in aqueous solutions: experimental and quantum investigations.* Journal of Chemical Sciences, 2022. **134**(3): p. 90.
255. Yadav, D.K., B. Maiti, and M. Quraishi, *Electrochemical and quantum chemical studies of 3, 4-dihydropyrimidin-2 (1H)-ones as corrosion inhibitors for mild steel in hydrochloric acid solution.* Corrosion Science, 2010. **52**(11): p. 3586-3598.
256. Muthukrishnan, P., B. Jeyaprabha, and P. Prakash, *Corrosion inhibition and adsorption behavior of Setaria verticillata leaf extract in 1M sulphuric acid.* Journal of materials engineering and performance, 2013. **22**: p. 3792-3800.
257. Kumari, P.P., P. Shetty, and S.A. Rao, *Electrochemical measurements for the corrosion inhibition of mild steel in 1 M hydrochloric acid by using an aromatic hydrazide derivative.* Arabian Journal of Chemistry, 2017. **10**(5): p. 653-663.
258. Musa, A.Y., et al., *On the inhibition of mild steel corrosion by 4-amino-5-phenyl-4H-1, 2, 4-trizole-3-thiol.* Corrosion Science, 2010. **52**(2): p. 526-533.
259. Hong, X., et al., *New insights into the inhibition of hesperetin on polyphenol oxidase: inhibitory kinetics, binding characteristics, conformational change and computational simulation.* Foods, 2023. **12**(4): p. 905.

© University of Venda

260. Shukla, S.K. and E.E. Ebenso, *Corrosion inhibition, adsorption behavior and thermodynamic properties of streptomycin on mild steel in hydrochloric acid medium.* Int. J. Electrochem. Sci, 2011. **6**(8): p. 3277-3291.
261. Boudalia, M., et al., *Experimental and Theoretical Tests on the Corrosion Protection of Mild Steel in Hydrochloric Acid Environment by the Use of Pyrazole Derivative.* Materials, 2023. **16**(2): p. 678.
262. Chahul, H., G. Ndukwe, and S. Abawua, *Corrosion inhibition studies of mild steel with stem bark extract of Maranthes Polyandra (benth.) prance.* Journal of Chemical Society of Nigeria, 2017. **42**(1): p. 55-61.
263. Rahiman, A.F.S.A. and S. Sethumanickam, *Corrosion inhibition, adsorption and thermodynamic properties of poly (vinyl alcohol-cysteine) in molar HCl.* Arabian Journal of Chemistry, 2017. **10**: p. S3358-S3366.
264. Ferkous, H., et al., *Corrosion inhibition of mild steel by 2-(2-methoxybenzylidene) hydrazine-1-carbothioamide in hydrochloric acid solution: Experimental measurements and quantum chemical calculations.* Journal of Molecular Liquids, 2020. **307**: p. 112957.
265. Godlewska, E.M., et al., *Corrosion of Al (Co) CrFeNi high-entropy alloys.* Frontiers in Materials, 2020. **7**: p. 566336.
266. Kouhi, M., A. Mohebbi, and M. Mirzaei, *Evaluation of the corrosion inhibition effect of micro/nanocapsulated polymeric coatings: a comparative study by use of EIS and Tafel experiments and the area under the Bode plot.* Research on Chemical Intermediates, 2013. **39**: p. 2049-2062.
267. Stimpfling, T., et al., *Amino acid interleaved layered double hydroxides as promising hybrid materials for AA2024 corrosion inhibition.* European Journal of Inorganic Chemistry, 2016. **2016**(13-14): p. 2006-2016.
268. Verma, C., et al., *Pyrazole derivatives as environmental benign acid corrosion inhibitors for mild steel: Experimental and computational studies.* Journal of Molecular Liquids, 2020. **298**: p. 111943.
269. Khamaysa, O.M.A., et al., *Hydrazone-based green corrosion inhibitors for API grade carbon steel in HCl: Insights from electrochemical, XPS, and computational studies.* Colloids and Surfaces A: Physicochemical and Engineering Aspects, 2021. **626**: p. 127047.
270. Udabe, E., et al., *Design of polymeric corrosion inhibitors based on ionic coumarate groups.* ACS Applied Polymer Materials, 2021. **3**(4): p. 1739-1746.
271. Khattabi, M., et al., *Performance and computational studies of two soluble pyran derivatives as corrosion inhibitors for mild steel in HCl.* Journal of Molecular Structure, 2019. **1196**: p. 231-244.
272. Demir, K.Ç., *Corrosion behavior of electrodeposited WO3 thin films.* Ceramics International, 2020. **46**(4): p. 4358-4364.
273. Peng, Y., et al., *A study of rare-earth 3-(4-methylbenzoyl)-propanoate compounds as corrosion inhibitors for AS1020 mild steel in NaCl solutions.* Corrosion Science, 2018. **145**: p. 199-211.
274. Deyab, M., *Decyl glucoside as a corrosion inhibitor for magnesium–air battery.* Journal of Power Sources, 2016. **325**: p. 98-103.
275. El-Tabei, A., et al., *Novel macrocyclic cationic surfactants: Synthesis, experimental and theoretical studies of their corrosion inhibition activity for carbon steel and their antimicrobial activities.* Journal of Molecular Liquids, 2022. **345**: p. 116990.
276. Mendonça, G.L., et al., *Understanding the corrosion inhibition of carbon steel and copper in sulphuric acid medium by amino acids using electrochemical techniques allied to molecular modelling methods.* Corrosion Science, 2017. **115**: p. 41-55.
277. Moretti, G., F. Guidi, and G. Grion, *Tryptamine as a green iron corrosion inhibitor in 0.5 M deaerated sulphuric acid.* Corrosion science, 2004. **46**(2): p. 387-403.

© University of Venda

278. Kumar, H., et al., *Adsorption and inhibition mechanism of efficient and environment friendly corrosion inhibitor for mild steel: Experimental and theoretical study.* Journal of Molecular Liquids, 2021. **338**: p. 116634.
279. Farag, A.A., A.S. Ismail, and M. Migahed, *Inhibition of carbon steel corrosion in acidic solution using some newly polyester derivatives.* Journal of Molecular Liquids, 2015. **211**: p. 915-923.
280. Haldhar, R., et al., *Papaver somniferum as an efficient corrosion inhibitor for iron alloy in acidic condition: DFT, MC simulation, LCMS and electrochemical studies.* Journal of Molecular Structure, 2021. **1242**: p. 130822.
281. Turcio-Ortega, D., T. Pandiyan, and E.M. García-Ochoa, *Electrochemical impedance spectroscopy (EIS) study of the film formation of 2-imidazoline derivatives on carbon steel in acid solution.* Mater Sci, 2007. **13**(2): p. 163-166.
282. Fernine, Y., et al., *Anti-corrosion performance of Ocimum basilicum seed extract as environmental friendly inhibitors for mild steel in HCl solution: Evaluations of electrochemical, EDX, DFT and Monte Carlo.* Journal of Molecular Liquids, 2022. **355**: p. 118867.
283. Alias, M.N., *Some Applications of Electrochemical Impedance Spectroscopy.* 1992.
284. Gebril, M.A., et al., *Experimental and computational studies of the influence of non-ionic surfactants with coumarin moiety as corrosion inhibitors for carbon steel in 1.0 M HCl.* Journal of Molecular Liquids, 2022. **349**: p. 118445.
285. Abdulazeez, I., et al., *Mechanistic studies of the influence of halogen substituents on the corrosion inhibitive efficiency of selected imidazole molecules: A synergistic computational and experimental approach.* Applied Surface Science, 2019. **471**: p. 494-505.
286. Wang, Q., et al., *Application of biomass corrosion inhibitors in metal corrosion control: a review.* Molecules, 2023. **28**(6): p. 2832.
287. Somers, A.E., et al., *New, environmentally friendly, rare earth carboxylate corrosion inhibitors for mild steel.* Corrosion Science, 2018. **139**: p. 430-437.
288. Dahmani, K., et al., *Quantum chemical and molecular dynamic simulation studies for the identification of the extracted cinnamon essential oil constituent responsible for copper corrosion inhibition in acidified 3.0 áwt% NaCl medium.* Inorganic Chemistry Communications, 2021. **124**: p. 108409.
289. Madan, J., et al., *Serial analysis of the gut and respiratory microbiome in cystic fibrosis in infancy: interaction between intestinal and respiratory tracts and impact of nutritional exposures.* MBio, 2012. **3**(4): p. e00251-12.
290. Maginnis, M.S., et al., *Progressive multifocal leukoencephalopathy-associated mutations in the JC polyomavirus capsid disrupt lactoseries tetrasaccharide c binding.* MBio, 2013. **4**(3): p. 10.1128/mbio. 00247-13.
291. Zhu, Y., et al., *A review of surfactants as corrosion inhibitors and associated modeling.* Progress in Materials Science, 2017. **90**: p. 159-223.
292. Lamprakou, Z., *Novel Inhibitive Pigments for Corrosion Protection.* 2022.
293. Akpan, E.D., et al., *Formamidine-based thiuram disulfides as efficient inhibitors of acid corrosion of mild steel: electrochemical, surface, and density functional theory/monte carlo simulation studies.* ACS omega, 2022. **7**(30): p. 26076-26091.
294. Radovanović, M.B., et al., *Electrochemical and DFT studies of brass corrosion inhibition in 3% NaCl in the presence of environmentally friendly compounds.* Scientific Reports, 2019. **9**(1): p. 16081.
295. Bijapur, K., et al., *Recent trends and progress in corrosion inhibitors and electrochemical evaluation.* Applied Sciences, 2023. **13**(18): p. 10107.
296. Singh, A., et al., *Comprehensive investigation of steel corrosion inhibition at macro/micro level by ecofriendly green corrosion inhibitor in 15% HCl medium.* Journal of colloid and interface science, 2020. **560**: p. 225-236.

© University of Venda

297. Dagdag, O., et al., *Highly functionalized epoxy macromolecule as an anti-corrosive material for carbon steel: Computational (DFT, MDS), surface (SEM-EDS) and electrochemical (OCP, PDP, EIS) studies.* Journal of Molecular Liquids, 2020. **302**: p. 112535.
298. Fouda, A., et al., *Novel porphyrin derivatives as corrosion inhibitors for stainless steel 304 in acidic environment: synthesis, electrochemical and quantum calculation studies.* Scientific Reports, 2023. **13**(1): p. 17593.
299. Singh, A., S. Mohapatra, and B. Pani, *Corrosion inhibition effect of Aloe Vera gel: gravimetric and electrochemical study.* Journal of Industrial and Engineering Chemistry, 2016. **33**: p. 288-297.
300. Prajila, M., P.R. Ammal, and A. Joseph, *Comparative studies on the corrosion inhibition characteristics of three different triazine based Schiff's bases, HMMT, DHMMT and MHMMT, for mild steel exposed in sulfuric acid.* Egyptian journal of petroleum, 2018. **27**(4): p. 467-475.
301. Tribak, Z., et al., *Comparative studies on the corrosion inhibition of three different organic heterocyclic compounds as corrosion inhibitors for mild steel in hydrochloric acid.* Journal of the Mexican Chemical Society, 2020. **64**(4): p. 291-300.
302. Olasunkanmi, L.O., M.M. Kabanda, and E.E. Ebenso, *Quinoxaline derivatives as corrosion inhibitors for mild steel in hydrochloric acid medium: Electrochemical and quantum chemical studies.* Physica E: Low-dimensional Systems and Nanostructures, 2016. **76**: p. 109-126.
303. Guruprasad, A., et al., *Corrosion inhibition of zinc in 0.1 M hydrochloric acid medium with clotrimazole: experimental, theoretical and quantum studies.* Surfaces and Interfaces, 2020. **19**: p. 100478.
304. Mahdavian, M. and R. Naderi, *Corrosion inhibition of mild steel in sodium chloride solution by some zinc complexes.* Corrosion Science, 2011. **53**(4): p. 1194-1200.
305. Sithuba, T., et al., *Corrosion inhibitory potential of selected flavonoid derivatives: Electrochemical, molecular⋯ Zn surface interactions and quantum chemical approaches.* Results in Engineering, 2022. **16**: p. 100694.
306. Kumar, D., V. Jain, and B. Rai, *Imidazole derivatives as corrosion inhibitors for copper: A DFT and reactive force field study.* Corrosion Science, 2020. **171**: p. 108724.
307. Singh, A., et al., *Electrochemical and surface studies of some Porphines as corrosion inhibitor for J55 steel in sweet corrosion environment.* Applied Surface Science, 2015. **359**: p. 331-339.
308. Drewniak, Ł. and S. Kochowski, *The origin of constant phase element in equivalent circuit of MIS (n) GaAs structures.* Journal of Materials Science: Materials in Electronics, 2020. **31**: p. 19106-19118.
309. Chang, B.-Y., *The effective capacitance of a constant phase element with resistors in series.* Journal of Electrochemical Science and Technology, 2022. **13**(4): p. 479-485.
310. Shanthy, P., et al., *Corrosion inhibition by an aqueous extract of ervatamia divaricata.* International Journal of Corrosion and Scale Inhibition, 2021. **10**(1): p. 331-348.
311. Tan, J., et al., *Synergistic effect of potassium iodide and sodium dodecyl sulfonate on the corrosion inhibition of carbon steel in HCl medium: a combined experimental and theoretical investigation.* RSC advances, 2020. **10**(26): p. 15163-15170.
312. Ammal, P.R., M. Prajila, and A. Joseph, *Effect of substitution and temperature on the corrosion inhibition properties of benzimidazole bearing 1, 3, 4-oxadiazoles for mild steel in sulphuric acid: Physicochemical and theoretical studies.* Journal of environmental chemical engineering, 2018. **6**(1): p. 1072-1085.
313. Kozlica, D.K., A. Kokalj, and I. Milošev, *Synergistic effect of 2-mercaptobenzimidazole and octylphosphonic acid as corrosion inhibitors for copper and aluminium–An electrochemical, XPS, FTIR and DFT study.* Corrosion Science, 2021. **182**: p. 109082.
314. Ferkous, H., et al., *A comparative study of novel synthesized sulfamide compounds: Electrochemical, morphological, XPS, and theoretical investigations on copper corrosion inhibition in 1.0 M HCl.* Journal of Molecular Liquids, 2024. **394**: p. 123781.
315. Gándara, M.F., *Aluminium: the metal of choice.* Mater. Tehnol, 2013. **47**(3): p. 261-265.

© University of Venda

316. Zheng, H., et al., *Improved corrosion resistance of carbon steel in soft water with dendritic-polymer corrosion inhibitors.* Chemical Engineering Journal, 2023. **452**: p. 139043.
317. Eltmimi, A., et al., *Inhibitive effects of a novel efficient Schiff base on mild steel in hydrochloric acid environment.* International Journal of Corrosion and Scale Inhibition, 2021. **10**(2): p. 634-648.
318. Abdallah, M., et al., *Natural nutmeg oil as a green corrosion inhibitor for carbon steel in 1.0 M HCl solution: Chemical, electrochemical, and computational methods.* Journal of Molecular Liquids, 2021. **323**: p. 115036.
319. Gopiraman, M., et al., *An investigation of mild carbon steel corrosion inhibition in hydrochloric acid medium by environment friendly green inhibitors.* Journal of Coatings Technology and Research, 2012. **9**: p. 15-26.
320. Alkadir Aziz, I.A., et al., *Insights into corrosion inhibition behavior of a 5-mercapto-1, 2, 4-triazole derivative for mild steel in hydrochloric acid solution: experimental and DFT studies.* Lubricants, 2021. **9**(12): p. 122.
321. Farhadian, A., et al., *A theoretical and experimental study of castor oil-based inhibitor for corrosion inhibition of mild steel in acidic medium at elevated temperatures.* Corrosion Science, 2020. **175**: p. 108871.
322. Kang, Y., et al., *CO2-hierarchical activated carbon prepared from coal gasification residue: Adsorption equilibrium, isotherm, kinetic and thermodynamic studies for methylene blue removal.* Chinese Journal of Chemical Engineering, 2020. **28**(6): p. 1694-1700.
323. Suhasaria, A., et al., *Effect of the heterocyclic groups on the anti-corrosion performance of heterocyclic schiff bases of benzothiazole for mild steel in 1 M Aqueous HCl.* Journal of Bio-and Tribo-Corrosion, 2023. **9**(2): p. 26.
324. Gomes, E.E., *Green inhibition of mild steel corrosion in a CO2 saturated saline solution*. 2015.
325. Zarrouk, A., et al., *Temperature effect, activation energies and thermodynamic adsorption studies of L-cysteine methyl ester hydrochloride as copper corrosion inhibitor in nitric acid 2M.* Int. J. Electrochem. Sci, 2011. **6**(12): p. 6261-6274.
326. Saad, H., et al., *Azo-functionalized superparamagnetic Fe 3 O 4 nanoparticles: an efficient adsorbent for the removal of bromocresol green from contaminated water.* RSC advances, 2022. **12**(39): p. 25487-25499.
327. Cheng, S., et al., *Carboxymenthylchitosan as an ecofriendly inhibitor for mild steel in 1 M HCl.* Materials Letters, 2007. **61**(14-15): p. 3276-3280.
328. Méndez, C.M., et al., *Corrosion inhibition of aluminum in acidic solution by Ilex paraguariensis (Yerba Mate) extract as a green inhibitor.* Coatings, 2023. **13**(2): p. 434.
329. Yan, S., et al., *Oxidation Behavior and Corrosion Mechanism of Sic Ceramics at High Temperatures in Wet Air Environment.* Available at SSRN 4327695.
330. Lebrini, M., F. Robert, and C. Roos, *Adsorption properties and inhibition of C38 steel corrosion in hydrochloric solution by some indole derivates: temperature effect, activation energies, and thermodynamics of adsorption.* International Journal of corrosion, 2013. **2013**.
331. Berdimurodov, E., et al., *Thioglycoluril derivative as a new and effective corrosion inhibitor for low carbon steel in a 1 M HCl medium: Experimental and theoretical investigation.* Journal of Molecular Structure, 2021. **1234**: p. 130165.
332. Hjouji, K., et al., *Datura stramonium plant seed extracts as a new green corrosion inhibitor for mild steel in 1M HCl solution: Experimental and surface characterization studies.* Sustainable Chemistry and Pharmacy, 2023. **34**: p. 101170.
333. Umoren, S., I. Obot, and N. Obi-Egbedi, *Raphia hookeri gum as a potential eco-friendly inhibitor for mild steel in sulfuric acid.* Journal of materials science, 2009. **44**: p. 274-279.
334. Zinad, D., et al., *Adsorption, temperature and corrosion inhibition studies of a coumarin derivatives corrosion inhibitor for mild steel in acidic medium: gravimetric and theoretical investigations.* International Journal of Corrosion and Scale Inhibition, 2020. **9**(1): p. 134-151.

© University of Venda

335. Ouass, A., et al., *Poly (sodium acrylate) and Poly (acrylic acid sodium) as an eco-friendly corrosion inhibitor of mild steel in normal hydrochloric acid: Experimental, spectroscopic and theoretical approach.* Journal of Applied Electrochemistry, 2021. **51**: p. 1009-1032.
336. Saraswat, V. and M. Yadav, *Improved corrosion resistant performance of mild steel under acid environment by novel carbon dots as green corrosion inhibitor.* Colloids and Surfaces A: Physicochemical and Engineering Aspects, 2021. **627**: p. 127172.
337. Abd El-Lateef, H.M. and M.M. Khalaf, *Synergistic inhibition effect of novel counterion-coupled surfactant based on rice bran oil and halide ion on the C-steel corrosion in molar sulphuric acid: Experimental and computational approaches.* Journal of Molecular Liquids, 2021. **331**: p. 115797.
338. Palit, A. and S.O. Pehkonen, *Copper corrosion in distribution systems: evaluation of a homogeneous Cu2O film and a natural corrosion scale as corrosion inhibitors.* Corrosion Science, 2000. **42**(10): p. 1801-1822.
339. TK, B. and A. P, *Corrosion inhibition of mild steel in hydrochloric acid by leaves extract of Tephrosia purpurea.* Journal of Adhesion Science and Technology, 2020. **34**(22): p. 2424-2447.
340. Hamdy, A.S., et al., *Evaluation of corrosion and erosion–corrosion resistances of mild steel in sulfide-containing NaCl aerated solutions.* Electrochimica acta, 2007. **52**(24): p. 7068-7074.
341. Lopez, D., S.N. Simison, and S. De Sanchez, *Inhibitors performance in CO2 corrosion: EIS studies on the interaction between their molecular structure and steel microstructure.* Corrosion science, 2005. **47**(3): p. 735-755.
342. Burduhos-Nergis, D.-P., et al., *Evaluation of the corrosion resistance of phosphate coatings deposited on the surface of the carbon steel used for carabiners manufacturing.* Applied Sciences, 2020. **10**(8): p. 2753.
343. Al Otaibi, N. and H.H. Hammud, *Corrosion inhibition using harmal leaf extract as an eco-friendly corrosion inhibitor.* Molecules, 2021. **26**(22): p. 7024.
344. Ali, A. and Y.S. Mahrous, *Corrosion inhibition of C-steel in acidic media from fruiting bodies of Melia azedarach L extract and a synergistic Ni 2+ additive.* RSC advances, 2017. **7**(38): p. 23687-23698.
345. He, H., et al., *Exploiting machine learning for controlled synthesis of carbon dots-based corrosion inhibitors.* Journal of Cleaner Production, 2023. **419**: p. 138210.
346. Hashim, N.Z.N., et al., *XPS and DFT investigations of corrosion inhibition of substituted benzylidene Schiff bases on mild steel in hydrochloric acid.* Applied Surface Science, 2019. **476**: p. 861-877.
347. Khan, G., et al., *Electrochemical investigation on the corrosion inhibition of mild steel by Quinazoline Schiff base compounds in hydrochloric acid solution.* Journal of colloid and interface science, 2017. **502**: p. 134-145.
348. Sasikala, T., et al., *Synthesis and corrosion inhibition study of benzodiazepines on mild steel in sulphuric acid medium.* Measurement, 2017. **101**: p. 175-182.
349. Eldesoky, A. and S. Nozha, *The adsorption and corrosion inhibition of 8-hydroxy-7-quinolinecarboxaldehyde derivatives on C-steel surface in hydrochloric acid.* Chinese journal of chemical engineering, 2017. **25**(9): p. 1256-1265.
350. Bendaif, H., et al., *The study of the aqueous extract of leaves of Pancratium foetidum Pom as: characterization of polyphenols, flavonoids, antioxidant activities and ecofriendly corrosion inhibitor.* J Mater Environ Sci, 2017. **8**(12): p. 4475-86.
351. Fouda, A., O. Mohamed, and H. Elabbasy, *Ferula hermonis plant extract as safe corrosion inhibitor for zinc in hydrochloric acid solution.* Journal of Bio-and Tribo-Corrosion, 2021. **7**(4): p. 135.
352. Umoren, S.A., *Polypropylene glycol: A novel corrosion inhibitor for× 60 pipeline steel in 15% HCl solution.* Journal of Molecular Liquids, 2016. **219**: p. 946-958.

© University of Venda

353. Fouda, A.E.-A.S., et al., *Electrochemical and quantum chemical studies on the corrosion inhibition of 1037 carbon steel by different types of surfactants.* RSC advances, 2022. **12**(6): p. 3253-3273.
354. Kusumaningrum, I., et al., *Investigation of Artocarpus Heteropyllus peel extract as non-toxic corrosion inhibitor for pure copper protection in nitric acid.* Case Studies in Chemical and Environmental Engineering, 2022. **6**: p. 100223.
355. Shoair, A., et al., *Investigation on effects of avocado extract as eco-friendly inhibitor for 201 stainless steel corrosion in acidic environment.* International Journal of Electrochemical Science, 2022. **17**(6): p. 220642.
356. Benhiba, F., et al., *Corrosion inhibition performance of 4-(prop-2-ynyl)-[1, 4]-benzothiazin-3-one against mild steel in 1 M HCl solution: experimental and theoretical studies.* International Journal of Hydrogen Energy, 2021. **46**(51): p. 25800-25818.
357. Quraishi, M., et al., *Corrosion inhibition and adsorption studies of some barbiturates on mild steel/acid interface.* Int. J. Electrochem. Sci, 2012. **7**: p. 12301-12315.
358. Abd El-Lateef, H.M., Z.A. Abdallah, and M.S.M. Ahmed, *Solvent-free synthesis and corrosion inhibition performance of Ethyl 2-(1, 2, 3, 6-tetrahydro-6-oxo-2-thioxopyrimidin-4-yl) ethanoate on carbon steel in pickling acids: Experimental, quantum chemical and Monte Carlo simulation studies.* Journal of Molecular Liquids, 2019. **296**: p. 111800.
359. Guo, L., et al., *Multidimensional insights into the corrosion inhibition of 3, 3-dithiodipropionic acid on Q235 steel in H2SO4 medium: a combined experimental and in silico investigation.* Journal of colloid and interface science, 2020. **570**: p. 116-124.
360. Oguzie, E., Y. Li, and F. Wang, *Effect of surface nanocrystallization on corrosion and corrosion inhibition of low carbon steel: Synergistic effect of methionine and iodide ion.* Electrochimica Acta, 2007. **52**(24): p. 6988-6996.
361. Zhang, M., et al., *Akebia trifoliate koiaz peels extract as environmentally benign corrosion inhibitor for mild steel in HCl solutions: Integrated experimental and theoretical investigations.* Journal of Industrial and Engineering Chemistry, 2021. **101**: p. 227-236.
362. Rezaeivala, M., et al., *Experimental and theoretical investigation of corrosion inhibition effect of two piperazine-based ligands on carbon steel in acidic media.* Colloids and surfaces a: physicochemical and engineering aspects, 2022. **641**: p. 128538.
363. Pal, A. and C. Das, *A novel use of solid waste extract from tea factory as corrosion inhibitor in acidic media on boiler quality steel.* Industrial crops and products, 2020. **151**: p. 112468.
364. Bidi, M.A., M. Azadi, and M. Rassouli, *A new green inhibitor for lowering the corrosion rate of carbon steel in 1 M HCl solution: Hyalomma tick extract.* Materials today communications, 2020. **24**: p. 100996.
365. Ojha, L.K., B. Tüzün, and J. Bhawsar, *Experimental and theoretical study of effect of allium sativum extracts as corrosion inhibitor on mild steel in 1 M HCl medium.* Journal of bio-and tribo-corrosion, 2020. **6**: p. 1-10.
366. Salleh, S.Z., et al., *Plant extracts as green corrosion inhibitor for ferrous metal alloys: A review.* Journal of Cleaner Production, 2021. **304**: p. 127030.
367. Shyamvarnan, B., et al., *Corrosion inhibition effect of elettaria cardamomum extract on mild steel in 3.5% NaCl medium.* Materials Today: Proceedings, 2021. **40**: p. S192-S197.
368. Golchinvafa, A., et al., *The effect of natural inhibitor concentration of Fumaria officinalis and temperature on corrosion protection mechanism in API X80 pipeline steel in 1 M H2SO4 solution.* International Journal of Pressure Vessels and Piping, 2020. **188**: p. 104241.
369. Ogunleye, O., et al., *Green corrosion inhibition and adsorption characteristics of Luffa cylindrica leaf extract on mild steel in hydrochloric acid environment.* Heliyon, 2020. **6**(1).
370. Zakir Hossain, S., et al., *Effects of cinnamaldehyde as an eco-friendly corrosion inhibitor on mild steel in aerated NaCl solutions.* Arabian Journal for Science and Engineering, 2020. **45**: p. 229-239.

© University of Venda

371. Guo, L., et al., *Locust Bean Gum as a green and novel corrosion inhibitor for Q235 steel in 0.5 M H2SO4 medium.* Journal of Molecular Liquids, 2020. **310**: p. 113239.
372. Guruprasad, A. and H. Sachin, *Novel cost-effective aqueous Amorphophallus paeoniifolius leaves extract as a green corrosion inhibitor for mild steel corrosion in hydrochloric acid medium: A detailed experimental and surface characterization studies.* Chemical Data Collections, 2021. **34**: p. 100734.
373. Basik, M., M. Mobin, and M. Shoeb, *Cysteine-silver-gold Nanocomposite as potential stable green corrosion inhibitor for mild steel under acidic condition.* Scientific Reports, 2020. **10**(1): p. 279.
374. Noor, E.A., *Temperature effects on the corrosion inhibition of mild steel in acidic solutions by aqueous extract of fenugreek leaves.* International Journal of Electrochemical Science, 2007. **2**(12).
375. Ikpeseni, S., et al., *Thermodynamic parameters and adsorption mechanism of corrosion inhibition in mild steel using jatropha leaf extract in hydrochloric acid.* Arabian Journal for Science and Engineering, 2021. **46**: p. 7789-7799.
376. Ikeuba, A.I., et al., *Experimental and theoretical evaluation of aspirin as a green corrosion inhibitor for mild steel in acidic medium.* Results in Chemistry, 2022. **4**: p. 100543.
377. Padash, R., et al., *Corrosion control of aluminum in the solutions of NaCl, HCl and NaOH using 2, 6-dimethylpyridine inhibitor: Experimental and DFT insights.* Materials Chemistry and Physics, 2020. **244**: p. 122681.
378. Markhali, B., et al., *Electrochemical impedance spectroscopy and electrochemical noise measurements as tools to evaluate corrosion inhibition of azole compounds on stainless steel in acidic media.* Corrosion Science, 2013. **75**: p. 269-279.
379. Boudalia, M., et al., *Green approach to corrosion inhibition of stainless steel in phosphoric acid of Artemesia herba albamedium using plant extract.* Journal of Materials Research and Technology, 2019. **8**(6): p. 5763-5773.
380. Benzbiria, N., et al., *Novel synthetized benzodiazepine as efficient corrosion inhibitor for copper in 3.5% NaCl solution.* Materials Today: Proceedings, 2021. **37**: p. 3932-3939.
381. Salman, T.A., et al., *New environmental friendly corrosion inhibitor of mild steel in hydrochloric acid solution: Adsorption and thermal studies.* Cogent Engineering, 2020. **7**(1): p. 1826077.
382. Abd El-Lateef, H.M., *Corrosion inhibition characteristics of a novel salycilidene isatin hydrazine sodium sulfonate on carbon steel in HCl and a synergistic nickel ions additive: a combined experimental and theoretical perspective.* Applied Surface Science, 2020. **501**: p. 144237.
383. Liu, Z., et al., *Benzothiazole derivatives-based supramolecular assemblies as efficient corrosion inhibitors for copper in artificial seawater: Formation, interfacial release and protective mechanisms.* Corrosion Science, 2023. **212**: p. 110957.
384. Elgendy, A., et al., *Understanding the adsorption performance of two glycine derivatives as novel and environmentally safe anti-corrosion agents for copper in chloride solutions: Experimental, DFT, and MC studies.* RSC advances, 2019. **9**(72): p. 42120-42131.
385. Gouda, M., et al., *Synthesis and characterization of Zn–organic frameworks containing chitosan as a low-cost inhibitor for sulfuric-acid-induced steel corrosion: Practical and computational exploration.* Polymers, 2022. **14**(2): p. 228.
386. Naciri, M., et al., *Unveiling the Influence of Furan and Thiophene on the Corrosion Inhibition Capabilities of Novel Hydrazones Derivatives in Carbon steel/HCl interface: A Dual Experimental-Theoretical Study.* Colloids and Surfaces A: Physicochemical and Engineering Aspects, 2024: p. 133272.
387. Jmiai, A., et al., *Chitosan as an eco-friendly inhibitor for copper corrosion in acidic medium: protocol and characterization.* Cellulose, 2017. **24**: p. 3843-3867.
388. Madlangbayan, M.S., et al., *Corrosion inhibition of sodium silicate with nanosilica as coating in pre-corroded steel.* Civil Engineering Journal, 2021. **7**(11): p. 1806-1816.

© University of Venda

389. Yüce, A.O., *Corrosion inhibition behavior of Robinia pseudoacacia leaves extract as a eco-friendly inhibitor on mild steel in acidic media.* Metals and Materials International, 2020. **26**(4): p. 456-466.
390. Zulkifli, F., et al., *The effect of concentration of Lawsonia inermis as a corrosion inhibitor for aluminum alloy in seawater.* Advances in Physical Chemistry, 2017. **2017**.
391. Pi, J., et al., *Corrosion inhibition effect of 1-phenyl-5-mercaptotetrazole on nickel-aluminum bronze in seawater: A combined experimental and theoretical study.* Colloids and Surfaces A: Physicochemical and Engineering Aspects, 2023. **666**: p. 131354.
392. Kumar, R., et al., *Corrosion inhibition performance of chromone-3-acrylic acid derivatives for low alloy steel with theoretical modeling and experimental aspects.* Journal of Molecular Liquids, 2017. **243**: p. 439-450.
393. Meresht, E.S., T.S. Farahani, and J. Neshati, *2-Butyne-1, 4-diol as a novel corrosion inhibitor for API X65 steel pipeline in carbonate/bicarbonate solution.* Corrosion Science, 2012. **54**: p. 36-44.
394. Yadav, M., U. Sharma, and P. Yadav, *Isatin compounds as corrosion inhibitors for N80 steel in 15% HCl.* Egyptian Journal of Petroleum, 2013. **22**(3): p. 335-344.
395. Rani, A.J., T. Sreelakshmi, and A. Joseph, *Effect of the addition of potassium iodide and thiourea on the corrosion inhibition effect of aqueous extract of Ayapana triplinervis towards mild steel in HCl at elevated temperatures-theoretical, electrochemical and surface studies.* Journal of Molecular Liquids, 2022. **366**: p. 120211.
396. Yadav, M., et al., *Substituted amines as corrosion inhibitors for N80 steel in 15% HCl.* Journal of Material and Environmental Science, 2013. **4**(5): p. 691-700.
397. Amin, M.A., *Weight loss, polarization, electrochemical impedance spectroscopy, SEM and EDX studies of the corrosion inhibition of copper in aerated NaCl solutions.* Journal of applied electrochemistry, 2006. **36**: p. 215-226.
398. Odusote, J., et al., *Inhibition efficiency of gold nanoparticles on corrosion of mild steel, stainless steel and aluminium in 1M HCl solution.* Materials Today: Proceedings, 2021. **38**: p. 578-583.
399. Ashassi-Sorkhabi, H., M. Majidi, and K. Seyyedi, *Investigation of inhibition effect of some amino acids against steel corrosion in HCl solution.* Applied surface science, 2004. **225**(1-4): p. 176-185.
400. Desimone, M., G. Gordillo, and S.N. Simison, *The effect of temperature and concentration on the corrosion inhibition mechanism of an amphiphilic amido-amine in CO2 saturated solution.* Corrosion Science, 2011. **53**(12): p. 4033-4043.
401. Jiang, X., Y. Zheng, and W. Ke, *Effect of flow velocity and entrained sand on inhibition performances of two inhibitors for CO2 corrosion of N80 steel in 3% NaCl solution.* Corrosion science, 2005. **47**(11): p. 2636-2658.
402. Al-Amiery, A.A., W.K. Al-Azzawi, and W.N.R.W. Isahak, *Isatin Schiff base is an effective corrosion inhibitor for mild steel in hydrochloric acid solution: Gravimetrical, electrochemical, and computational investigation.* Scientific Reports, 2022. **12**(1): p. 17773.
403. Adebayo, M.A., et al., *Equilibrium and thermodynamic characteristics of the corrosion inhibition of mild steel using sweet prayer leaf extract in alkaline medium.* Prog. Chem. Biochem. Res, 2021. **4**(1): p. 80-91.
404. Chauhan, L. and G. Gunasekaran, *Corrosion inhibition of mild steel by plant extract in dilute HCl medium.* Corrosion science, 2007. **49**(3): p. 1143-1161.
405. Abdel-Gaber, A., H. Rahal, and F. Beqai, *Eucalyptus leaf extract as a eco-friendly corrosion inhibitor for mild steel in sulfuric and phosphoric acid solutions.* International Journal of Industrial Chemistry, 2020. **11**: p. 123-132.
406. Dehghani, A., et al., *Potential role of a novel green eco-friendly inhibitor in corrosion inhibition of mild steel in HCl solution: Detailed macro/micro-scale experimental and computational explorations.* Construction and Building Materials, 2020. **245**: p. 118464.

© University of Venda

407. Ogundipe, K.D. and A. Babarinde, *Comparative study on batch equilibrium biosorption of Cd (II), Pb (II) and Zn (II) using plantain (Musa paradisiaca) flower: kinetics, isotherm, and thermodynamics.* Chem. Int, 2017. **3**(2): p. 135-149.
408. Raji, F. and M. Pakizeh, *Kinetic and thermodynamic studies of Hg (II) adsorption onto MCM-41 modified by ZnCl2.* Applied Surface Science, 2014. **301**: p. 568-575.
409. Zarrouk, A., et al., *New 1H-pyrrole-2, 5-dione derivatives as efficient organic inhibitors of carbon steel corrosion in hydrochloric acid medium: electrochemical, XPS and DFT studies.* Corrosion Science, 2015. **90**: p. 572-584.
410. Bouklah, M., et al., *Thermodynamic properties of 2, 5-bis (4-methoxyphenyl)-1, 3, 4-oxadiazole as a corrosion inhibitor for mild steel in normal sulfuric acid medium.* Corrosion science, 2006. **48**(9): p. 2831-2842.
411. Li, X., et al., *Synergistic inhibition between o-phenanthroline and chloride ion for steel corrosion in sulphuric acid.* Corrosion science, 2006. **48**(2): p. 308-321.
412. Choudhary, S., A. Garg, and K. Mondal, *Relation between open circuit potential and polarization resistance with rust and corrosion monitoring of mild steel.* Journal of Materials Engineering and Performance, 2016. **25**: p. 2969-2976.
413. Abdel-Karim, A.M. and A.M. El-Shamy, *A review on green corrosion inhibitors for protection of archeological metal artifacts.* Journal of Bio-and Tribo-Corrosion, 2022. **8**(2): p. 35.
414. Elmsellem, H., et al., *Adsorption properties and inhibition of mild steel corrosion in 1 M HCl solution by some bipyrazolic derivatives: experimental and theoretical investigations.* Protection of Metals and Physical Chemistry of Surfaces, 2015. **51**: p. 873-884.
415. Kumar, H. and V. Yadav, *Highly efficient and eco-friendly corrosion inhibitor for mild steel in 5 M HCl: An anti-pitting and anti-cracking agent.* Chemical Data Collections, 2020. **30**: p. 100552.
416. Kaban, A.P.S., et al., *Experimental and modelling waste rice husk ash as a novel green corrosion inhibitor under acidic environment.* Materials Today: Proceedings, 2022. **62**: p. 4225-4234.
417. Hsissou, R., et al., *Evaluation of corrosion inhibition performance of phosphorus polymer for carbon steel in [1 M] HCl: Computational studies (DFT, MC and MD simulations).* Journal of Materials Research and Technology, 2020. **9**(3): p. 2691-2703.
418. Abdel-Gaber, A.M., H.T. Rahal, and M.S. El-Rifai, *Green approach towards corrosion inhibition in hydrochloric acid solutions.* Biointerface Res Appl Chem, 2021. **11**(6): p. 14185-14195.
419. Thomas, A., et al., *A green approach to corrosion inhibition of mild steel in hydrochloric acid using fruit rind extract of Garcinia indica (Binda).* Journal of Molecular Liquids, 2020. **312**: p. 113369.
420. El-Etre, A., M. Abdallah, and Z. El-Tantawy, *Corrosion inhibition of some metals using lawsonia extract.* Corrosion science, 2005. **47**(2): p. 385-395.
421. Ibrahim, T.H., Y. Chehade, and M. Abou Zour, *Corrosion inhibition of mild steel using potato peel extract in 2M HCL solution.* International Journal of Electrochemical Science, 2011. **6**(12): p. 6542-6556.
422. Liao, B., et al., *Insight into the anti-corrosion performance of Acanthopanax senticosus leaf extract as eco-friendly corrosion inhibitor for carbon steel in acidic medium.* Journal of Industrial and Engineering Chemistry, 2023. **117**: p. 238-246.
423. Odewunmi, N.A., et al., *Comparative studies of the corrosion inhibition efficacy of a dicationic monomer and its polymer against API X60 steel corrosion in simulated acidizing fluid under static and hydrodynamic conditions.* ACS omega, 2020. **5**(42): p. 27057-27071.
424. Ghaderi, M., et al., *Corrosion inhibition of a novel antihistamine-based compound for mild steel in hydrochloric acid solution: Experimental and computational studies.* Scientific Reports, 2022. **12**(1): p. 13450.
425. Ibrahim, T. and M. Habbab, *Corrosion inhibition of mild steel in 2M HCl using aqueous extract of eggplant peel.* International Journal of Electrochemical Science, 2011. **6**(11): p. 5357-5371.

© University of Venda

426. Saraswat, V., R. Kumari, and M. Yadav, *Novel carbon dots as efficient green corrosion inhibitor for mild steel in HCl solution: Electrochemical, gravimetric and XPS studies.* Journal of Physics and Chemistry of Solids, 2022. **160**: p. 110341.
427. Saraswat, V. and M. Yadav, *Computational and electrochemical analysis on quinoxalines as corrosion inhibitors for mild steel in acidic medium.* Journal of Molecular Liquids, 2020. **297**: p. 111883.
428. Yeganeh, M., et al., *Corrosion inhibition of L-methionine amino acid as a Green corrosion inhibitor for stainless steel in the H 2 SO 4 solution.* Journal of Materials Engineering and Performance, 2020. **29**: p. 3983-3994.
429. Chauhan, D.S., et al., *Chitosan-cinnamaldehyde Schiff base: A bioinspired macromolecule as corrosion inhibitor for oil and gas industry.* International Journal of Biological Macromolecules, 2020. **158**: p. 127-138.
430. Negi, R., et al., *Double-layer protection of stainless steel by using triethylammonium-3-silatranylpropyldithiocarbamate as a corrosion inhibitor: Experimental and computational studies.* Journal of Molecular Structure, 2024: p. 138166.
431. Haldhar, R., et al., *Corrosion inhibition, surface adsorption and computational studies of Momordica charantia extract: a sustainable and green approach.* SN Applied Sciences, 2021. **3**: p. 1-13.
432. Alsabagh, A.M., et al., *Corrosion inhibition efficiency of some hydrophobically modified chitosan surfactants in relation to their surface active properties.* Egyptian Journal of Petroleum, 2014. **23**(4): p. 349-359.
433. Nazir, U., et al., *Experimental and theoretical insights into the corrosion inhibition activity of novel Schiff bases for aluminum alloy in acidic medium.* RSC advances, 2019. **9**(62): p. 36455-36470.
434. Nnaji, N., et al., *Corrosion resistance of aluminum against acid activation: Impact of benzothiazole-substituted gallium phthalocyanine.* Molecules, 2019. **24**(1): p. 207.
435. Somlyai-Sipos, L. and P. Baumli, *Wettability of metals by water.* Metals, 2022. **12**(8): p. 1274.
436. Saha, S.K. and P. Banerjee, *Introduction of newly synthesized Schiff base molecules as efficient corrosion inhibitors for mild steel in 1 M HCl medium: an experimental, density functional theory and molecular dynamics simulation study.* Materials Chemistry Frontiers, 2018. **2**(9): p. 1674-1691.
437. Hirano, S., et al. *Characterization of Corrosion Inhibitor with Contact Angle Measurement*. in *NACE CORROSION*. 2021. NACE.
438. Elsharif, A.M., et al., *Synthesis, characterization and corrosion inhibition studies of polyunsaturated fatty acid derivatives on the acidic corrosion of mild steel: Experimental and computational studies.* Journal of Molecular Liquids, 2020. **319**: p. 114162.
439. Sajid, H.U. and R. Kiran, *Influence of corrosion and surface roughness on wettability of ASTM A36 steels.* Journal of Constructional Steel Research, 2018. **144**: p. 310-326.
440. Li, Y., D. Wang, and L. Zhang, *Experimental and theoretical research on a new corrosion inhibitor for effective oil and gas acidification.* RSC advances, 2019. **9**(45): p. 26464-26475.
441. Deepika, A.U., et al. *Wetting and corrosion studies on SS304 material surfaces*. in *AIP Conference Proceedings*. 2021. AIP Publishing.
442. Mathew, Z.P., et al., *Corrosion inhibition of mild steel using poly (2-ethyl-2-oxazoline) in 0.1 M HCl solution.* Heliyon, 2020. **6**(11).
443. Kerstner, E.K., et al., *Anticorrosive performance of commercial nanoceramic coatings on AISI 1010 steel.* Materials Research, 2014. **17**: p. 1497-1506.
444. Souza, F.S.d., R.S. Gonçalves, and A. Spinelli, *Assessment of caffeine adsorption onto mild steel surface as an eco-friendly corrosion inhibitor.* Journal of the Brazilian Chemical Society, 2014. **25**: p. 81-90.
445. Awe, F., et al., *Theoretical and experimental inhibitive properties of mild steel in HCl by ethanolic extract of Boscia senegalensis.* Cogent Chemistry, 2015. **1**(1): p. 1112676.

© University of Venda

446. Ayuba, A., et al., *Theoretical study of aspartic and glutamic acids as corrosion inhibitors on aluminium metal surface.* Moroccan journal of chemistry, 2018. **6**(1): p. 6-1 (2018) 160-172.
447. Akalezi, C.O., et al., *Corrosion inhibition of aluminium pigments in aqueous alkaline medium using plant extracts.* Environment and Pollution, 2012. **1**(2): p. 45.
448. Umar, U.U.U., *Computational study of anticorrosive effects of some thiazole derivatives against the corrosion of aluminium.* RHAZES: Green and Applied Chemistry, 2020. **10**: p. 113-128.
449. Ayuba, A., et al., *Hydroxycarboxylic acids as corrosion inhibitors on aluminium metal: a computational study.* Journal of materials and environmental sciences, 2018. **9**(11): p. 3026-3034.
450. Kasprzhitskii, A. and G. Lazorenko, *Corrosion inhibition properties of small peptides: DFT and Monte Carlo simulation studies.* Journal of Molecular Liquids, 2021. **331**: p. 115782.
451. Verma, D.K., et al., *Computational modeling: theoretical predictive tools for designing of potential organic corrosion inhibitors.* Journal of Molecular Structure, 2021. **1236**: p. 130294.
452. Belghiti, M., et al., *Piperine derivatives as green corrosion inhibitors on iron surface; DFT, Monte Carlo dynamics study and complexation modes.* Journal of Molecular Liquids, 2018. **261**: p. 62-75.
453. Kaya, S., et al., *Quantum chemical and molecular dynamics simulation studies on inhibition performances of some thiazole and thiadiazole derivatives against corrosion of iron.* Journal of Molecular Liquids, 2016. **219**: p. 497-504.
454. Mi, H., G. Xiao, and X. Chen, *Theoretical evaluation of corrosion inhibition performance of three antipyrine compounds.* Computational and Theoretical Chemistry, 2015. **1072**: p. 7-14.
455. Obot, I. and Z. Gasem, *Theoretical evaluation of corrosion inhibition performance of some pyrazine derivatives.* Corrosion Science, 2014. **83**: p. 359-366.
456. Erdoğan, Ş., et al., *A computational study on corrosion inhibition performances of novel quinoline derivatives against the corrosion of iron.* Journal of Molecular Structure, 2017. **1134**: p. 751-761.
457. Singh, A., et al., *Effect of electron donating functional groups on corrosion inhibition of J55 steel in a sweet corrosive environment: experimental, density functional theory, and molecular dynamic simulation.* Materials, 2018. **12**(1): p. 17.
458. Amin, M.A., et al., *A study of the inhibition of iron corrosion in HCl solutions by some amino acids.* Corrosion science, 2010. **52**(5): p. 1684-1695.
459. Dohare, P., M. Quraishi, and I. Obot, *A combined electrochemical and theoretical study of pyridine-based Schiff bases as novel corrosion inhibitors for mild steel in hydrochloric acid medium.* Journal of Chemical Sciences, 2018. **130**: p. 1-19.
460. Dehdab, M., M. Shahraki, and S.M. Habibi-Khorassani, *Theoretical study of inhibition efficiencies of some amino acids on corrosion of carbon steel in acidic media: green corrosion inhibitors.* Amino acids, 2016. **48**(1): p. 291-306.
461. Hossam, K., et al., *Understanding corrosion inhibition of C38 steel in HCl media by omeprazole: insights for experimental and computational studies.* Journal of Failure Analysis and Prevention, 2021. **21**: p. 213-227.
462. Ouakki, M., et al., *Insights into corrosion inhibition mechanism of mild steel in 1 M HCl solution by quinoxaline derivatives: electrochemical, SEM/EDAX, UV-visible, FT-IR and theoretical approaches.* Colloids and Surfaces A: Physicochemical and Engineering Aspects, 2021. **611**: p. 125810.
463. Fakhry, H., et al., *A newly synthesized quinoline derivative as corrosion inhibitor for mild steel in molar acid medium: Characterization (SEM/EDS), experimental and theoretical approach.* Colloids and Surfaces A: Physicochemical and Engineering Aspects, 2021. **610**: p. 125746.
464. Zhao, P., Q. Liang, and Y. Li, *Electrochemical, SEM/EDS and quantum chemical study of phthalocyanines as corrosion inhibitors for mild steel in 1 mol/l HCl.* Applied Surface Science, 2005. **252**(5): p. 1596-1607.

© University of Venda

465. Hamdy, A. and N.S. El-Gendy, *Thermodynamic, adsorption and electrochemical studies for corrosion inhibition of carbon steel by henna extract in acid medium.* Egyptian Journal of Petroleum, 2013. **22**(1): p. 17-25.
466. Malinovschi, V., et al., *Study of carbon steel corrosion layer by X-ray diffraction and absorption methods.* Journal of nuclear materials, 2006. **352**(1-3): p. 107-115.
467. Naciri, M., et al., *Exploring the potential of a new 1, 2, 4-triazole derivative for corrosion protection of carbon steel in HCl: A computational and experimental evaluation.* Colloids and Surfaces A: Physicochemical and Engineering Aspects, 2020. **597**: p. 124604.
468. Karthik, R., et al., *Anti-corrosion inhibition of mild steel in 1M hydrochloric acid solution by using Tiliacora accuminata leaves extract.* International Journal of Electrochemical Science, 2015. **10**(5): p. 3707-3725.
469. Verma, D.K., et al., *Experimental and computational studies on hydroxamic acids as environmental friendly chelating corrosion inhibitors for mild steel in aqueous acidic medium.* Journal of Molecular Liquids, 2020. **314**: p. 113651.
470. Prasad, D., et al., *Natural corrosion inhibitor of renewable eco-waste for SS-410 in sulfuric acid medium: Adsorption, electrochemical, and computational studies.* Journal of Molecular Liquids, 2022. **351**: p. 118671.
471. Ayieko, C.O., et al., *Controlled texturing of aluminum sheet for solar energy applications.* Advances in Materials Physics and Chemistry, 2015. **5**(11): p. 458-466.
472. Şahin, E.A., et al., *Adsorption ability, stability and corrosion inhibition mechanism of phoenix dactylifera extrat on mild steel.* Materials Research Express, 2020. **7**(1): p. 016585.

© University of Venda